Deep Underground Neutrino Experiment (DUNE)

Near Detector
Preliminary Design Report

Volume III – SAND

April 15, 2026

The DUNE Collaboration

DRAFT

DEEP UNDERGROUND NEUTRINO EXPERIMENT

DRAFT

Contents

Contents i

List of Figures vii

List of Tables xiv

1 Overview 2
- 1.1 Requirements and SAND Role . . . 3
- 1.2 The Overall Design of SAND . . . 5
- 1.3 Derived SAND Capabilities . . . 6
- 1.4 Opportunities for SAND . . . 6
- 1.5 Simulation framework . . . 8
- 1.6 SAND Physics Reach . . . 12

2 Organization & Management 20
- 2.1 Consortium Organization . . . 20
- 2.2 Institutional Framework . . . 21
  - 2.2.1 Contribution by Istituto Nazionale di Fisica Nucleare . . . 21
  - 2.2.2 Contribution by Fermi National Accelerator Laboratory . . . 22
- 2.3 Risk Management . . . 22
- 2.4 Schedule . . . 24
  - 2.4.1 High Level Schedule . . . 25
  - 2.4.2 Major Milestones . . . 25

3 The Superconducting Magnet 28
- 3.1 Magnet Specifications . . . 28
  - 3.1.1 Coil Shell and Conductor . . . 30
  - 3.1.2 Radiation Screen . . . 31
  - 3.1.3 Service Turret . . . 31
  - 3.1.4 Power Supply and Control Instrumentation . . . 32
- 3.2 Magnet Maintenance and Revamping Options . . . 32
  - 3.2.1 Magnet Power Supply Overview . . . 33
  - 3.2.2 Uninterruptible Power Supply . . . 33
  - 3.2.3 Control System Interfaces . . . 34
  - 3.2.4 Busbars . . . 35
  - 3.2.5 Quench Detection . . . 35

DRAFT

3.2.6 Warm-up Power Supply . . . 36
3.2.7 Power Supply Revamped and Salvaged Parts . . . 36
3.3 Activities at LNF . . . 40
3.3.1 Magnet Cool-Down . . . 40
3.3.2 Coil Cryostat Extraction . . . 43
3.3.3 Dismounting of the Iron Yoke . . . 45
3.3.4 Tools, Packaging, and Shipping to FNAL . . . 45
3.4 Installation and Integration at FNAL . . . 45
3.4.1 Storage at FNAL . . . 47
3.4.2 Tools and Mounting Procedure . . . 47
3.4.3 Cryogenic Refrigeration Plant for Continuous Operation . . . 48
3.5 Risk Management . . . 48
3.5.1 Detailed Risk Analysis . . . 48
3.6 Schedule and Milestones . . . 50

4 Lead/Scintillating-Fiber Calorimeter (ECAL) 51
4.1 Design and Structure . . . 51
4.1.1 Scintillating Fibers . . . 53
4.1.2 Photomultiplier Tubes . . . 53
4.1.3 SiPMs as Possible Spares for PMT . . . 54
4.2 Performance in the KLOE Experiment . . . 55
4.3 Requirements for ECAL . . . 61
4.4 Calibration and Monitor System . . . 61
4.5 Electronics . . . 65
4.5.1 Studies for the Optimization of the PMT Working Point . . . 65
4.5.2 FEE and DAQ . . . 77
4.5.3 High-Voltage . . . 91
4.5.4 Low-Voltage . . . 92
4.6 Dismounting Procedures . . . 92
4.6.1 Barrel Modules . . . 94
4.6.2 Endcap Modules . . . 98
4.7 Refurbishment and Test before SAND Installation . . . 102
4.7.1 Light Tightness and Tests with Cosmic Rays . . . 105
4.8 Installation & Integration . . . 105
4.8.1 Packaging and Shipping . . . 105
4.8.2 Activities at FNAL . . . 106
4.9 Risk Management . . . 106
4.9.1 Detailed Risk Analysis . . . 107
4.10 Schedule and Milestones . . . 109

5 GRanular Argon for Interactions of Neutrinos (GRAIN) 110
5.1 Introduction and Physics Requirements . . . 110
5.2 Mechanical Design . . . 111
5.3 Cryogenic System . . . 113
5.4 Optical Detector . . . 116
5.4.1 Lens-based Optical Detector . . . 117
5.4.2 Coded Mask Detector . . . 121

DRAFT

5.4.3 Detector Layout in GRAIN . . . 122
5.4.4 Camera Prototypes . . . 124
5.5 Readout System . . . 128
5.5.1 GRAIN Camera Board . . . 129
5.5.2 ASIC Design . . . 129
5.5.3 Cryo-Vacuum Flanges and Cold Interface Board . . . 136
5.6 Data Acquisition and Slow Control System . . . 137
5.7 GRAIN Assembly and Comissioning . . . 137
5.8 Detector Performance . . . 138
5.8.1 Reconstruction performance with lens-based detector . . . 138
5.8.2 Reconstruction performance with Coded Mask detector . . . 143
5.8.3 Acceptance enhancement with GRAIN . . . 145
5.8.4 Neutrino energy reconstruction . . . 147
5.9 Calibration System . . . 154

6 Straw Tube Tracker 165
6.1 A Compact Modular Design . . . 165
6.2 Nuclear and "Solid" Hydrogen Targets . . . 166
6.3 Detector Requirements . . . 167
6.4 Initial STT Configuration and Upgrades . . . 172
6.5 Engineering Model . . . 175
6.5.1 Design of STT Modules . . . 175
6.5.2 Assembly Procedure . . . 180
6.5.3 Super-module Assembly . . . 188
6.5.4 Mechanical Analysis . . . 189
6.6 Detector Technology . . . 195
6.7 Electronic Readout . . . 200
6.7.1 Integrated Readout Boards . . . 200
6.7.2 VMM3a Readout . . . 205
6.7.3 Custom ASIC Upgrade . . . 208
6.8 Cooling System . . . 212
6.8.1 Self-Cooling Design . . . 212
6.8.2 Thermal Analysis . . . 213
6.9 System Integration . . . 219
6.9.1 Gas Connections . . . 220
6.9.2 Electrical Connections . . . 221
6.9.3 Grounding . . . 223
6.9.4 HV and LV Components . . . 225
6.9.5 Cabling . . . 226
6.9.6 Metrology Fixtures . . . 227
6.10 Data Acquisition and Slow Control System . . . 228
6.11 Gas System . . . 229
6.12 Prototyping and Tests . . . 237
6.12.1 Measurements of Straw Properties . . . 237
6.12.2 Mockup Prototypes . . . 240
6.12.3 Wiring Tests . . . 241
6.12.4 Prototypes of a 1.2 m STT Module . . . 243

DRAFT

6.12.5 Prototypes of Readout Boards . . . 245
6.12.6 Mockup Cooling Prototype . . . 249
6.12.7 Target and Radiator Prototypes . . . 250
6.12.8 Test Beam Measurements . . . 252
6.12.9 Full-Scale 3.9 m Prototype of a STT Module . . . 254
6.13 Quality Controls for Mass Production . . . 256
6.13.1 Industrial Supply Chain . . . 256
6.13.2 Tests of Straw Welding . . . 257
6.13.3 Tests of End-plugs . . . 260
6.13.4 Tests of Wire Spacers . . . 261
6.13.5 Tests of Crimping Pins . . . 262
6.13.6 Tests of Anode Wires . . . 263
6.13.7 Tests of C-fiber Frames . . . 264
6.13.8 Tests of VMM3a Chips . . . 265
6.13.9 Quality Controls for Straw Production . . . 266
6.13.10 Quality Controls for Module Assembly . . . 269
6.14 Detector Construction . . . 272
6.14.1 Straw Production unit . . . 272
6.14.2 Module Assembly Unit . . . 275
6.14.3 Production Sites . . . 280
6.14.4 Transportation to Fermilab . . . 282
6.14.5 Installation and Integration at Fermilab . . . 283
6.14.6 Organization and Schedule . . . 284
6.15 Operating Conditions . . . 287
6.15.1 Operational Modularity . . . 287
6.15.2 Straw Creep Rate . . . 288
6.15.3 Relative humidity . . . 290
6.15.4 Ambient temperature . . . 290
6.15.5 Detector aging . . . 291
6.16 Risk Register and Contingencies . . . 293
6.17 Alignment, Monitoring, and Calibration . . . 293
6.17.1 Alignment and Monitoring with Rock Muons . . . 293
6.17.2 Calibration with V^0 Decays . . . 295
6.18 Detector Performance . . . 297
6.18.1 Particle acceptance . . . 298
6.18.2 Track Reconstruction . . . 300
6.18.3 Vertex Reconstruction . . . 306
6.18.4 Particle Identification . . . 307
6.18.5 Application to $\bar{\nu}_\mu \mathrm{H} \to \mu^+ n$ with Initial STT . . . 312

7 Drift Chamber **317**

8 DAQ Architecture **318**
8.1 Description of the SAND subsystems and their interfaces . . . 318
8.1.1 GRAIN . . . 318
8.1.2 Tracker . . . 319
8.1.3 ECAL . . . 319

DRAFT

8.2 DUNE-DAQ and DTS Systems . . . 319
8.3 Physical Interfaces . . . 321
8.3.1 Timing . . . 321
8.3.2 Data . . . 322
8.4 Data formats and protocols . . . 322
8.4.1 Timing . . . 322
8.4.2 Data . . . 323
8.5 Data synchronization . . . 323
8.6 Synchronous Interfaces . . . 323
8.6.1 Performance requirements for synchronization . . . 323
8.6.2 Trigger and Calibration . . . 324

9 Detector Control and Safety systems (DCS-DSS) 326
9.1 DCS Devices . . . 326
9.2 Unifying Standards . . . 327
9.3 Detector Operation . . . 327
9.4 Basic and Advanced Operations . . . 327
9.5 Detector Safety Systems (DSS) . . . 328
9.5.1 DSS Devices . . . 328
9.5.2 DSS Control Hardware . . . 329

10 Installation & Integration 332
10.1 Work Organization and Sharing of Responsibilities . . . 332
10.2 Fermilab Requirements for Equipment Approval . . . 334
10.2.1 Cryogenics and Pressure Engineering Requirements . . . 334
10.2.2 Mechanical Engineering Requirements . . . 336
10.2.3 Electrical Engineering Requirements . . . 336
10.3 Transport and Handling . . . 338
10.4 Experimental Hall and Facilities . . . 339
10.4.1 Detector Access and Transport Infrastructure . . . 339
10.4.2 Space Allocation and Infrastructure Interfaces . . . 339
10.4.3 Facility Services and Utilities . . . 343
10.4.4 Environmental and Safety Considerations . . . 343
10.5 Helium Cryogenics and Distribution . . . 344
10.5.1 Cooling Requirements . . . 344
10.5.2 Design Scheme . . . 346
10.5.3 Operation Modes . . . 347
10.5.4 Cryogenic Facilities . . . 348
10.5.5 Layout Plan . . . 349
10.5.6 Estimated Heat Loads . . . 350
10.5.7 Final Remarks about Cryogenic Helium System . . . 350
10.6 Installation Sequence . . . 351
10.7 Critical and Engineered Lifts . . . 353
10.8 Risks . . . 354
10.9 Safety . . . 355

A Engineering Codes and Standards 357

DRAFT

Glossary **361**

References **370**

DRAFT

List of Figures

1.1 SAND sketch . . . 3
1.2 SAND exploded-view . . . 3

2.1 SAND High-Level Schedule . . . 26

3.1 KLOE solenoid . . . 29
3.2 KLOE magnetic field . . . 30
3.3 Schematic of the new power supply . . . 34
3.4 Diagnostic Rack . . . 36
3.5 KLOE Magnet Power Supply Cabinet . . . 38
3.6 KLOE coil lead clamps . . . 41
3.7 KLOE pipe cuts . . . 41
3.8 KLOE cooling with existing refrigerator . . . 42
3.9 KLOE cooling with cryo liquid . . . 43
3.10 Coil extraction and transport . . . 44

4.1 KLOE ECAL schematic view . . . 52
4.2 Light guides . . . 53
4.3 KLOE PMT-base . . . 54
4.4 SiPM test . . . 55
4.5 ECAL photon efficiency vs energy . . . 57
4.6 KLOE ECAL photon time resolution . . . 58
4.7 KLOE ECAL photon energy linearity and resolution . . . 59
4.8 KLOE ECAL Efficiency to neutrons . . . 60
4.9 Vertex coordinates . . . 62
4.10 MIP peaks . . . 62
4.11 fit peaks . . . 63
4.12 MIP occupancy . . . 63
4.13 Δt_0 example . . . 64
4.14 T0 determination . . . 65
4.15 Simulation - Neutrino energy spectrum for all events . . . 66
4.16 Simulation - Neutrino energy spectrum in the FV . . . 66
4.17 PE distributions . . . 67
4.18 PE for different neutrino energy ranges - 1 . . . 67
4.19 PE for different neutrino energy ranges - 2 . . . 68
4.20 Number of hits for each cell . . . 69

DRAFT

4.21 Hit cell probability . . . 70
4.22 Schematic of the HV divider . . . 72
4.23 Schematic of the preamplifier . . . 72
4.24 Typical signal from the PMT-base . . . 72
4.25 Preamplifier linearity test . . . 74
4.26 Preamplifier charge linearity test . . . 75
4.27 Preamplifier linearity test . . . 75
4.28 Linearity test - Experimental setup . . . 77
4.29 PMT linearity test - 1 . . . 78
4.30 PMT linearity test - 2 . . . 79
4.31 PMT signal vs attenuation scale factor . . . 80
4.32 PicoTDC test - set-up . . . 81
4.33 Walk-ToT picoTDC calibration curves . . . 82
4.34 ΔT before and after walk correction - low threshold . . . 83
4.35 ΔT before and after walk correction - high threshold . . . 84
4.36 ToT-Amplitude picoTDC calibration curves . . . 85
4.37 ToT before and after amplitude correction - low threshold . . . 86
4.38 ToT before and after amplitude correction - high threshold . . . 87
4.39 Amplitude distribution from ToT and from digitizer . . . 88
4.40 Correlation between amplitude from ToT and from digitizer . . . 88
4.41 ToT resolution vs. ECAL resolution . . . 90
4.42 ECAL HV system . . . 91
4.43 Cable removal . . . 92
4.44 Chamber extraction . . . 93
4.45 Barrel module design . . . 94
4.46 Barrel layout . . . 94
4.47 Barrel extraction tool . . . 95
4.48 Platform . . . 95
4.49 Barrel guides . . . 96
4.50 Barrel modules . . . 96
4.51 Pillar . . . 97
4.52 Extraction scheme . . . 98
4.53 First Module . . . 99
4.54 Test area . . . 99
4.55 Tools for endcap disassembling . . . 100
4.56 Delaminated module . . . 102
4.57 Light-guides . . . 103
4.58 PMT-grid . . . 103
4.59 Tape-wrapping . . . 104

5.1 3D GRAIN sketch . . . 112
5.2 GRAIN Inner Vessel . . . 112
5.3 GRAIN Inner Vessel . . . 113
5.4 GRAIN Inner Vessel . . . 114
5.5 GRAIN Inner Vessel . . . 114
5.6 cryogenics P&ID for GRAIN. . . . 115
5.7 Lens-based camera . . . 118

DRAFT

5.8 Lens design . . . 119
5.9 Spot vs. a . . . 120
5.10 Typical image for lens based detector . . . 120
5.11 Coded aperture concept . . . 121
5.12 Coded-mask-based camera . . . 122
5.13 Coded aperture images . . . 123
5.14 Lens layout in GRAIN . . . 123
5.15 Coded-mask detector layout in GRAIN . . . 124
5.16 First lens prototype . . . 125
5.17 First mask prototype . . . 125
5.18 Cold demo hardware . . . 126
5.19 ARTIC facility . . . 127
5.20 Cosmic ray tagger for ARTIC . . . 128
5.21 Block diagram of the GRAIN electronic system. . . . 129
5.22 Events detected in GRAIN within a spill . . . 130
5.23 DENEB channel's block scheme . . . 131
5.24 Behavioral simulation output . . . 134
5.25 Simulations for validating the ASIC design . . . 135
5.26 Distribution of ΔT for pure Argon. . . . 136
5.27 Images from neutrino interactions in GRAIN . . . 139
5.28 True tracks vs. visible tracks . . . 140
5.29 Vertex reconstruction with lens-based cameras . . . 140
5.30 Vertex reconstruction in GRAIN . . . 141
5.31 Angle residual for track direction reconstruction . . . 142
5.32 Mask-based reconstruction and track clusterization . . . 144
5.33 Single track reconstruction performance with coded mask detector . . . 145
5.34 Vertex reconstruction performance with coded mask detector . . . 146
5.35 Detection efficiency in STT and GRAIN . . . 148
5.36 Neutrino energy for ν_μ 0πNp0n events in GRAIN . . . 150
5.37 Relative ν energy for ν_μ interactions with and without pions in GRAIN . . . 151
5.38 Multiplicity of tracks entering STT from GRAIN . . . 152
5.39 Specific energy loss of charged particles in GRAIN . . . 153
5.40 Energy loss vs. path-length in GRAIN . . . 153
5.41 Momentum error for particles from GRAIN entering the tracker . . . 154
5.42 Error on neutrino energy in GRAIN . . . 155
5.43 Reconstructed photon number as a function of deposited energy . . . 156
5.44 Energy loss of muons crossing GRAIN . . . 157
5.45 Simulated muon beam crossing GRAIN . . . 158
5.46 Calibration curve from a muon beam . . . 159
5.47 Simulated muon beam crossing GRAIN at Y = 300 mm . . . 160
5.48 Calibration curve from a decentralized muon beam . . . 160
5.49 Simulated muon beams crossing GRAIN . . . 161
5.50 Simulated muon beams crossing GRAIN . . . 162
5.51 Interaction vertices in yoke and ECAL with a muon . . . 163
5.52 Calibration function from yoke muons . . . 163
5.53 Reconstructed energy for ECAL muons from calibration function . . . 164

DRAFT

6.1 Drawing of the CH_2 and C STT modules . . . 166
6.2 Threshold for protons on H in STT . . . 168
6.3 Electron identification in STT . . . 170
6.4 Initial STT configuration . . . 172
6.5 Initial STT configuration 3D . . . 173
6.6 Maximal STT configuration . . . 174
6.7 Details of the straw assembly . . . 176
6.8 Temporary bars holding the end-plugs during wiring . . . 176
6.9 Details of the C-fiber STT frame . . . 178
6.10 Removable lid and sealing of the STT frame . . . 179
6.11 Assembly of a STT module with C-fiber frame . . . 181
6.12 STT targets . . . 182
6.13 Details of the graphite target and polypropylene radiator . . . 183
6.14 Gluing of the 1.2 m STT prototype . . . 184
6.15 Completion of the 1.2 m STT prototype . . . 185
6.16 STT super-module . . . 188
6.17 STT super-module assembly . . . 189
6.18 STT super-module vertical assembly . . . 190
6.19 STT super-module assembly structure . . . 191
6.20 STT super-module external support . . . 192
6.21 Deformations of a 4 m straw with fixed ends . . . 192
6.22 Deformations of full-scale STT frame during assembly . . . 193
6.23 Relative displacement of straws during assembly . . . 194
6.24 Straw variations from creep rate over time . . . 194
6.25 Ultrasonic welding technology . . . 196
6.26 Fraunhofer metallized film . . . 196
6.27 Integration of the UV laser into the straw production line . . . 197
6.28 Removal of the Al metallization in the welding area of the straw film . . . 198
6.29 Straw production line . . . 199
6.30 Straw production components . . . 199
6.31 Integrated readout boards for STT . . . 200
6.32 Front-end readout and flexible kapton PCBs for STT . . . 200
6.33 BUS connections of FEBs for STT . . . 202
6.34 Flipped readout and ghost tracks . . . 202
6.35 VMM3a and NRL architectures . . . 204
6.36 VMM3a noise and timing resolution . . . 204
6.37 Differential driver for VMM3a output to ADC . . . 205
6.38 VMM3a readout for STT . . . 206
6.39 Straw occupancy in STT . . . 208
6.40 Timing resolution of the straws . . . 209
6.41 Expected charge deposition in the straws . . . 209
6.42 Custom ASIC architecture . . . 211
6.43 Custom ASIC floor-plan and packaging . . . 211
6.44 Thermal analysis of STT module . . . 214
6.45 Gas flow in STT module . . . 214
6.46 Thermal analysis of super-module . . . 215
6.47 Temperature map of super-module . . . 216

DRAFT

6.48 Thermal analysis of super-module: ambient temperature . . . 216
6.49 Thermal analysis of super-module: air heat transfer coefficient . . . 217
6.50 Temperature uniformity along straws . . . 218
6.51 Temperature uniformity along straws . . . 218
6.52 Maximal temperature vs. active time window . . . 219
6.53 STT Al CornerBlocks . . . 220
6.54 Terminations for the gas connections . . . 221
6.55 STT DAQ+LV-connections . . . 222
6.56 Ribbon and FPC cables for FEBs . . . 223
6.57 STT ground plane . . . 223
6.58 STT DAQ+LV-connections . . . 224
6.59 STT services through magnet end-caps . . . 226
6.60 STT Metrology fixtures . . . 228
6.61 DAQ/DTS prototype board . . . 228
6.62 STT Initial gas system layout . . . 231
6.63 STT Maximal gas system layout . . . 232
6.64 STT Gas Xe Mixer . . . 233
6.65 STT Gas Pump . . . 233
6.66 STT Gas distribution circuit . . . 234
6.67 STT Gas Distribution . . . 234
6.68 STT Gas Xe Recuperation . . . 235
6.69 Pressure tests of straws . . . 237
6.70 Pressure tests of straws . . . 238
6.71 Gas tightness tests of straws . . . 239
6.72 Measurement of the gas leak rate . . . 239
6.73 Gas gain as a function of HV . . . 240
6.74 Mockup STT prototype . . . 241
6.75 Crimping tests for STT . . . 242
6.76 Wiring 4 m straws with spacers . . . 242
6.77 Wiring tests with production spacers . . . 244
6.78 Prototype of 1.2 m STT module at CERN . . . 244
6.79 Test of 1.2 m STT prototype . . . 245
6.80 Prototype of 1.2 m STT module in Pisa . . . 246
6.81 Prototype of 1.2 m STT module in Pisa . . . 247
6.82 Tests of prototype readout board . . . 248
6.83 Tests of the solid state relay . . . 248
6.84 Mockup cooling prototype . . . 249
6.85 Graphite tiles for STT . . . 250
6.86 Prototype of STT radiator . . . 251
6.87 STT test beam setup 2022-2024 . . . 252
6.88 STT test beam setup 2024 . . . 252
6.89 Straw timing resolution from H4 test beam . . . 253
6.90 Straw dE/dx from H4 test beam . . . 254
6.91 Prototype of 3.9 m STT module . . . 255
6.92 Assembly table for 3.9 m STT prototype . . . 255
6.93 Mould for STT wire spacers . . . 256
6.94 Mould for frames of STT modules . . . 257

DRAFT

6.95 Straw welding inspection . . . 258
6.96 Straw welding tests . . . 259
6.97 Longitudinal tests of straw welding . . . 259
6.98 Summary of weld tests . . . 259
6.99 Test of end-plugs . . . 260
6.100 Test of final wire spacers . . . 261
6.101 Test of final crimping pins . . . 262
6.102 Wire measurements with SEM . . . 263
6.103 Wire measurements with SEM . . . 264
6.104 Tests of carbon fiber frames . . . 265
6.105 Tests of VMM3a chips for STT . . . 266
6.106 Quality controls for straws . . . 267
6.107 QC for straws: outer diameter . . . 267
6.108 QC for straws: pressure tests . . . 268
6.109 QC for assembly: ground connections . . . 269
6.110 QC for assembly: HV . . . 270
6.111 QC for assembly: wire tension . . . 270
6.112 Straw production line JINR . . . 272
6.113 Straw production line GTU . . . 273
6.114 Straw production line INP . . . 273
6.115 Straw production unit 12 m long . . . 274
6.116 Module assembly tooling . . . 276
6.117 Module assembly tooling for wiring . . . 277
6.118 Module assembly tooling for frame support . . . 278
6.119 STT contributions . . . 280
6.120 STT Transportation . . . 282
6.121 STT shipping 20ft HC . . . 283
6.122 Preliminary organizational chart for the construction of STT. . . . 285
6.123 Preliminary schedule for the construction of the initial STT including contingency. . . . 286
6.124 Measurement of the straw creep rate . . . 288
6.125 Results for the straw creep rate . . . 289
6.126 Humidity dependence of straws . . . 290
6.127 STT risk register . . . 292
6.128 Core costs for the initial STT . . . 294
6.129 Interaction vertex for rock muons crossing STT . . . 294
6.130 Rock muons crossing STT straws . . . 294
6.131 V^0 decays in STT volume . . . 296
6.132 Muon acceptance in STT . . . 298
6.133 Acceptance difference between targets . . . 299
6.134 Momentum resolution vs. momentum in STT . . . 301
6.135 Momentum resolution vs. track length in STT . . . 301
6.136 Angular resolution vs. momentum in STT . . . 301
6.137 Radial dependence of single hit resolution . . . 302
6.138 Non-Gaussian hit resolution . . . 303
6.139 Particle resolutions vs. momentum . . . 304
6.140 Particle resolution vs. track length . . . 304
6.141 Vertex reconstruction with initial STT . . . 305

DRAFT

6.142 Vertex resolution with initial STT . . . 305
6.143 Vertex resolution for QE with initial STT . . . 306
6.144 STT and NOMAD Transition Radiation (TR) detection planes . . . 308
6.145 Performance of the TR electron identification in NOMAD . . . 308
6.146 STT and NOMAD TR detection planes . . . 309
6.147 STT and NOMAD TR detection planes . . . 310
6.148 Vertex distribution of tracks with limited pion rejection . . . 311
6.149 Resolution of dE/dx in inclusive ν_μ CC interactions . . . 311
6.150 Simulation of a neutrino spill for QE on H . . . 312
6.151 Momentum and angular resolutions for muons in QE on H . . . 312
6.152 Momentum and angular resolutions for neutrons in QE on H . . . 313
6.153 Neutron line-of-flight in QE on H . . . 314
6.154 Neutron candidates in QE on H . . . 315
6.155 Selection of $\bar{\nu}_\mu H \to \mu^+ n$ in the initial STT . . . 315
6.156 Reconstructed Q^2 distribution in selected $\bar{\nu}_\mu H \to \mu^+ n$ . . . 316

8.1 TDAQ basic layout . . . 320

9.1 DSS basic layout . . . 330

10.1 I&I organization . . . 333
10.2 ECAL disassembly and assembly . . . 337
10.3 ND facility - 1 . . . 340
10.4 ND facility - 2 . . . 341
10.5 ND facility - 3 . . . 341
10.6 ND facility - 4 . . . 342
10.7 ND facility - 5 . . . 344
10.8 ND facility - 6 . . . 345
10.9 Scheme of DUNE NS helium cryo system . . . 348
10.10 Preliminary PFD of DUNE NS SAND helium cryo system . . . 349
10.11 Layout of the NS Cryo LHe cryo system . . . 350
10.12 Assembly sequence for SAND . . . 352

DRAFT

List of Tables

1.1 SAND capability requirements for Neutrino-based Beam Monitoring System (NuMS). . . 7
1.2 Capability requirements and opportunities for the inner tracker of SAND. 7
1.3 Sensitivity to beam variations 13
1.4 Events on H 14

2.1 SAND high-level milestones 27

3.1 Magnet specifications 29
3.2 Coil parameters 29
3.3 Heat Loads 31
3.4 Power Supply and Control Instrumentation 32
3.5 Power Supply Requirements 39
3.6 Tools for handling the Coil Cryostat. 46

4.1 SiPM vs PMT 55
4.2 Fraction of events with at least one cell above PE threshold 68
4.3 Fraction of hit cells above PE threshold 68
4.4 Average probabilities that a cell is hit in a neutrino interaction 70
4.5 Pile-up of PMT signals (w/o time smearing) 71
4.6 Pile-up of PMT signals (w/ time smearing) 71
4.7 Maximum and minimum number of PEs 73
4.8 Maximum and minimum number of PEs given by a cell 76
4.9 HV values in linear and saturation regimes of the preamplifier 76
4.10 Amplitude resolution from ToT. 79
4.11 Time resolutions on reconstructed ΔT peaks 82
4.12 Resolutions on reconstructed amplitude peaks from ToT for low and high thresholds. . . 82
4.13 Resolutions on reconstructed amplitude peaks from ToT, digitizer, and their difference. . 85

5.1 SiPM features 117
5.2 ASIC specifications 133
5.3 Tracks classified as fully contained in GRAIN 142
5.4 Fraction of primary particles in STT, GRAIN and ECAL 146

6.1 Main requirements for the design of the STT 169
6.2 Key numbers for STT 174
6.3 Types of glue for the assembling of STT 188
6.4 Ghost track rejection in STT 203

DRAFT

6.5 Timing resolution of VMM3a readout boards . . . 206
6.6 Timing resolution of VMM3a readout boards . . . 208
6.7 Custom ASIC requirements for STT . . . 210
6.8 Selection of the neutron candidate in $\bar{\nu}_\mu H \to \mu^+ n$ events . . . 217
6.9 Gas tubing for STT . . . 221
6.10 HV and LV components for STT . . . 226
6.11 Cabling for STT . . . 227
6.12 List of refurbished components from ATLAS TRT . . . 237
6.13 Measurement of straw tensions for STT . . . 238
6.14 Measurement of the straw leak rate for different gas types . . . 240
6.15 Industrial tooling for STT . . . 256
6.16 Tolerances for the C-fiber frames of the STT modules . . . 264
6.17 Existing SP units for STT . . . 275
6.18 Person-power requirements for STT . . . 281
6.19 Operational modularity of STT . . . 287
6.20 Straw creep rate with different films . . . 289
6.21 Rock muons for STT . . . 293
6.22 V0 decays for STT . . . 296
6.23 Particle acceptance for STT . . . 298
6.24 Effect of energy threshold on particle acceptance . . . 300
6.25 Effect of energy threshold on particle acceptance . . . 300
6.26 Reconstruction efficiency for STT . . . 300
6.27 Vertex resolution for initial STT . . . 307
6.28 Electron identification with Transition Radiation (TR) in the initial STT . . . 310
6.29 Neutron candidates in $\bar{\nu}_\mu H \to \mu^+ n$ events . . . 314
6.30 Expected $\bar{\nu}_\mu H \to \mu^+ n$ events in the initial STT . . . 316

8.1 Expected data rates from single subdetector . . . 321
8.2 Timing requirements for the SAND subdetectors . . . 324

10.1 Main parameters of SAND magnet and its cryostat with service turret. . . . 345
10.2 Cooling requirements of SAND magnet. . . . 346
10.3 Heat loads at 4 K . . . 350
10.4 Heat loads at 70 K . . . 351

A.1 A.1 - First part - Engineering codes and standards used in the beamline design. . . . 358
A.2 A.1 - Second part - Engineering codes and standards used in the beamline design. . . . 359
A.3 A.1 - Third part - Engineering codes and standards used in the beamline design. $\star$ = latest addition appproved by Electrical AHJ. . . . 360
A.4 A.2 - Engineering codes and standards used in the beamline installation and construction. 360

DRAFT

Todo list

Why don't we show the preliminary plot here? 15
Fix missing section references based on new organization. 110
Fix missing section references based on new organization. 122
ref al primo capitolo 142
ref al primo capitolo 152
Fix missing section references based on new organization. 157
probabilmente manca una parte conclusiva..ma verrà scritta dopo la revisione se richiesta LDN . . 164

DRAFT

Chapter 1

Overview

All Deep Underground Neutrino Experiment (DUNE) accelerator-based physics studies take into account flux uncertainties, assuming that parameters such as horn positions and currents are known within certain tolerances. Beamline instrumentation is being developed to monitor these parameters; however, many potential deviations from the expected tolerances are more effectively identified by observing distortions in the neutrino energy spectra measured in near detector (ND). Typical sources of beamline distortion are most easily detected and diagnosed in neutrino energy spectra measured on the beam axis, while such effects are diluted in off-axis measurements. However, the DUNE Precision Reaction-Independent Spectrum Measurement (DUNE-PRISM) measurement program requires the Near Detector Liquid Argon system (ND-LAr) and the Temporary Muon Spectrometer (TMS) to spend approximately 50% of the time collecting data at off-axis positions. DUNE-PRISM relies on the well-understood relationship between the off-axis angle and the neutrino energy spectrum. For DUNE-PRISM to be effective, it is essential that the beam remains stable during data collection at various positions—or, if not, that any beam distortions can be promptly identified and accurately modeled. As a result, DUNE requires a component of the ND complex [2] to remain on-axis, where beam monitoring is most sensitive and a sufficient number of ν_μ (or $\bar{\nu}_\mu$) charged current (CC) interactions can be collected. This continuous monitoring role is primarily fulfilled by the System for on-Axis Neutrino Detection (SAND), as illustrated in Figure 1.1.

SAND is not designed to match the latter minimal-requirements specification, as it is based on a largely in-kind reuse of the electromagnetic calorimeter (ECAL, Section 4) and the superconducting magnet (Section 3) from the K-LOng Experiment (KLOE). All the more so, it will be capable of fulfilling the monitoring role, as demonstrated in the following. The well-known performance of the KLOE components [3] is further enhanced by the addition of a LAr active target (GRAIN, Section 5) and a low density tracking system (Section 6 and Section 7). An exploded view drawing is shown in Figure 1.2.

The design of SAND is also driven by physics opportunities and the necessity to operate in a high-rate environment and measure external backgrounds, including cosmic rays and beam-induced activity. As a result, SAND goes beyond the basic requirement of monitoring the ν beam stability, further motivated by leveraging the KLOE detector not only to enhance the overall DUNE scientific

DRAFT

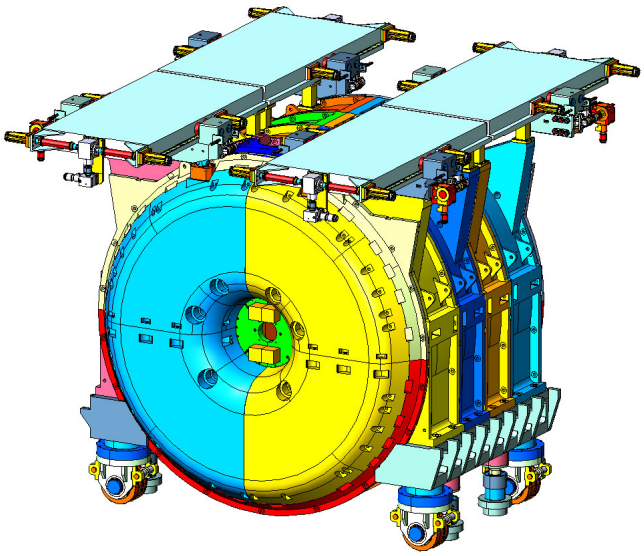


Figure 1.1: SAND sketch.

program. The SAND configuration yields a multipurpose detector capable of providing unique measurements to constrain systematic uncertainties relevant for the long-baseline analysis, as well as supporting a broad physics program of precision measurements and searches for new physics. The overall performance of SAND will be extensively detailed throughout this technical report.

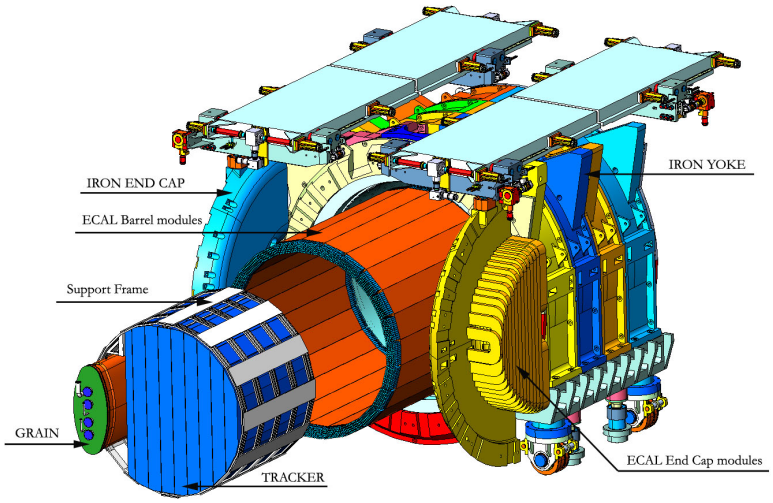


Figure 1.2: Exploded view drawing of SAND. Starting from the left, one can see GRAIN, the tracker, the calorimeter (barrel and endcap) and the magnet system.

1.1 Requirements and SAND Role

SAND contributes to the primary neutrino oscillation physics program in two distinct ways. First, as a permanent and magnetized on-axis detector, it fulfills the requirement for monitoring the neutrino beam spectrum, so the movable ND-LAr+TMS system does not need to make regular

on-axis stops for this purpose. Second, it enables measurements of neutrino interactions that complement those of the ND-LAr+TMS program. SAND can measure neutrino interactions on both argon and 'solid hydrogen' targets, using a fundamentally different detection technique from that of ND-LAr, thus providing complementary information. In this way, SAND improves the long-baseline physics reach and broadens the overall DUNE physics program with additional Beyond the Standard Model (BSM) sensitivity.

The overarching requirements for SAND are to monitor the on-axis spectrum and position information to detect typical variations in the neutrino beam, and to operate effectively in a high-rate environment. Beam monitoring involves two main tasks:

(a) Detecting a 1% change in the muon rate in near-real time.

(b) Monitoring the neutrino interaction rate on the axis with a sensitivity better than 1% over the course of a week.

SAND also enhances the robustness of the neutrino oscillation program by measuring the muon and neutrino energy and vertex distributions. To meet the second overarching requirement, SAND must be able to separate cosmic rays, rock muons, and other beam-induced activity from neutrino interactions occurring in the fiducial volume (FV), and must be able to identify neutrino interactions even in the presence of event pile-up.

To provide statistically significant feedback on beam variations over short time periods (one week), SAND must monitor the on-axis beam using a target mass large enough to ensure a high rate of neutrino interactions. For the collection and identification of ν_μ charged current (CC) events, the required mass is estimated to exceed 20 t for reliable reconstruction of p_μ, and more than 5 t for reconstruction of E_ν.

SAND must measure the muon and neutrino energy and vertex distributions to detect changes in the beamline. To capture spectral variations, the muon energy resolution must be $\sigma_{E_\mu}/E_\mu < 10\%$ at 5 GeV/c, improving to 5% at 1 GeV/c, or alternatively, the neutrino energy resolution must be $\sigma_{E_\nu}/E_\nu < 15\%$. Furthermore, the interaction vertices in ν_μ CC events must be reconstructed with sufficient precision to locate the events relative to the beam center. A vertex resolution better than 5 cm is sufficient to distinguish interactions occurring at positions where the neutrino spectrum may vary.

Due to the shallow site and the intensity of the neutrino beam, the ND operates in a high-rate environment characterized by cosmic rays, beam-induced background activity, and neutrino interaction pileup. To ensure that these backgrounds are properly accounted for and modeled — and to distinguish neutrino interactions occurring within the same time window — the SAND timing system must be capable of identifying and selecting activity within the neutrino beam spill. This requires a time resolution of $\sigma_t < 10$ ns on the tracker and $\sigma_t < 400$ ps on ECAL hits.

An improved resolution of 1 ns on the tracker would further enhance directional reconstruction capabilities. These timing requirements also support the vertex resolution goals mentioned earlier.

All requirements for SAND to function as a ν beam monitoring system are summarized in Table 1.1.

1.2 The Overall Design of SAND

SAND must reconstruct the vertices of ν_μ CC interactions, and the outgoing muons must be reconstructed with good momentum resolution over a broad momentum range (approximately $0.5 \lesssim p_\mu \lesssim 10\,\mathrm{GeV}/c$). This requires a tracking detector operating within a magnetic field.

SAND is largely based on the reuse of the electromagnetic calorimeter (ECAL) and the solenoidal superconducting magnet from KLOE [3]. The KLOE detector was originally designed for the study of the violation of charge parity (CP) in neutral-kaon decays in the DAΦ NE ϕ factory. KLOE collected data from April 1999 to March 2018, during which the detector performance remained stable. In the KLOE experiment, the inner volume enclosed by the magnet and the ECAL was occupied by a large drift chamber.

In DUNE ND, the detector will be installed so that the neutrino beam enters through the side of the barrel, perpendicular to the magnetic field. The drift chamber KLOE has been removed (Section 4.6), and the now vacant volume will be instrumented for neutrino studies according to DUNE requirements. The 4π ECAL (Section4) serves not only as a target mass for beam monitoring but also offers additional capabilities discussed in the following sections. The solenoid (Section 3) provides a 0.6 T magnetic field over a large volume (approximately $43\,\mathrm{m}^3$), which is partially instrumented with a tracking system combined with hydrocarbon target masses ("target/tracker"). The remaining magnetized volume will be occupied by a thin liquid argon (LAr) target with a mass of approximately 1 t.

The tracking system (Section 6) occupies most of the magnetic volume, with Straw Tube Tracker (STT) planes arranged orthogonally to the beam, interleaved with thin carbon and hydrocarbon layers that serve as targets for neutrino interactions. A backup option under study is a drift chamber (Section 7) with a reduced number of channels. All capability requirements and opportunities for the inner tracker are summarized in Table 1.2. This inner tracker design represents the optimal approach (Section 6.18) to fully exploit the existing magnet and calorimeter, considering the intensity of the beam.

Since argon is the target material in DUNE FD, the inclusion of GRanular Argon for Interactions of Neutrinos (GRAIN) is particularly appropriate. This LAr component is not only a target but also functions as an imaging detector (Section 5), located within the magnetic volume between the tracking region and the upstream inner edge of the ECAL. It consists of a cryostat shaped like an elliptical tube, instrumented with innovative devices for photon detection in the vacuum ultraviolet range. Two different technologies are being tested: lenses and coded masks, both coupled to arrays of silicon photomultipliers (SiPMs) for photon readout. The tracker enables precise momentum reconstruction of particles exiting GRAIN.

The performance studies demonstrating how SAND meets the beam monitoring requirements are presented in [4]. Meeting these requirements also implies a set of derived detector capabilities, as described below.

DRAFT

1.3 Derived SAND Capabilities

Since SAND is required to measure the charge and momentum of muons, it is also capable of performing similar measurements for charged hadrons. The target/tracking systems provide particle identification through dE/dx, while ECAL can measure the energy of photons and electrons via calorimetry, further enhancing particle identification. These capabilities originate from the beam monitoring requirements but also enable SAND to carry out a neutrino interaction measurement program that complements DUNE's oscillation physics goals. In particular, SAND provides the following additional capabilities:

- SAND is capable of providing an independent measurement of the interaction rates and energy spectra of the ν_μ, $\bar{\nu}_\mu$, ν_e, and $\bar{\nu}_e$ beam components. Its ability to identify and reconstruct various types of interactions enables complementary measurements of both the flux normalization and its energy dependence. This redundancy enhances the reliability of the extrapolation of neutrino and antineutrino fluxes to the far detector.
- Nuclear effects represent a major source of uncertainty for DUNE. Significant uncertainties exist in the modeling of (anti)neutrino–nucleus cross sections, particularly in the treatment of final state interactions, which affect the final state hadron composition and energies. Using argon as the primary target in the ND helps mitigate these uncertainties in the near-to-far comparison. However, such uncertainties cannot be completely canceled, even with the implementation of DUNE-PRISM. SAND supports a program of measurements on additional targets (carbon, hydrocarbons, and others beyond lead and argon) to help constrain systematic uncertainties associated with nuclear effects.
- The hydrocarbon used in the target/tracker provides a large sample of interactions on carbon and a smaller yet statistically significant sample on hydrogen. In certain interaction channels, hydrogen-enriched samples can be selected using Transverse Kinematic Imbalance (TKI) techniques [5–18]. Isolating neutrino–hydrogen interaction samples is extremely valuable, as nuclear uncertainties are confined to the background and can potentially be mitigated using kinematic sidebands or by matching carbon targets with identical acceptance. This allows for model-independent background subtraction.
- SAND can combine information from the ECAL and the target/tracker to tag neutrons and measure their energies. Incorporating this information improves the neutrino energy resolution and reduces biases in energy reconstruction, leading to decreased systematic uncertainties. Neutron measurements also enhance the reconstruction of event kinematics.

In summary, the contribution of SAND to the DUNE scientific program is not limited to monitoring variations in the neutrino beam. SAND is capable of measuring different neutrino spectra and reducing systematic uncertainties in the extrapolation of the beam to the FD. Furthermore, it can provide significant constraints on cross-section models and nuclear effects.

1.4 Opportunities for SAND

The use of polyethylene $(C_2H_4)_n$ as a target, combined with a thin passive pure carbon (graphite) target, it enables a unique 'solid hydrogen' measurement. Neutrino-nucleus interaction models — including those employed in the DUNE oscillation analysis — typically factorize the scattering on

Table 1.1: SAND capability requirements for Neutrino-based Beam Monitoring System (NuMS).

Name	Requirement	Rationale
Continuous on-axis monitor	SAND shall continuously stay on-axis to monitor the ν-beam	The other ND detectors are not required to stay periodically on-axis to monitor the ν-beam
NuMS statistics	SAND inner tracker shall have a fiducial mass higher than 5 t	This mass is large enough to provide a precise measure of ν_μ CC energy spectrum in one week
μ momentum resolution	SAND inner tracker shall reconstruct muon momentum with a resolution better than 5% at 1 GeV/c and better than 10% at 5 GeV/c	The muon momentum resolution shall be sufficient for a precise measurement of its spectrum
Vertex position	The position of ν-interaction vertex shall be measured to < 5 cm	The localization of the ν interaction is required in order to measure the beam spectrum as a function of the position, which elucidates beamline variations
Timing resolution	The inner tracker shall have a timing resolution < 10 ns	The timing resolution shall be sufficient to resolve activity from different beam buckets (18.83 ns)

Table 1.2: Capability requirements and opportunities for the inner tracker of SAND.

Name	Requirement	Rationale
Density	The inner tracker shall have average density $\rho < 0.22\,\mathrm{g/cm^3}$	Low density is essential to minimize multiple scattering and to allow precise magnetic spectrometry
Momentum resolution	The inner tracker shall have charged particle momentum resolution $< 5\%$ up to $p \sim 5$ GeV/c	Precise momentum measurements via curvature are needed to perform kinematic reconstruction
Radiation length	The inner tracker shall have less than 1 radiation length from its center to ECAL	Minimize radiation lengths allow precise curvature measurement, particularly for $e^{\pm}$
Interaction length	The inner tracker shall have less than 1 interaction length from its center to ECAL	Minimize interaction lengths minimizes secondary hadronic interactions
Carbon & Hydrocarbon targets	The inner tracker shall have both hydrogen-rich and pure carbon targets	A mixture of pure carbon and hydrocarbon target allows to isolate interactions on free protons via subtraction
Nuclear target	The inner tracker shall be configurable with other nuclear targets	Deploying other nuclear targets allows to investigate A-dependence of cross section
Argon target (GRAIN)	The inner SAND volume shall have an argon target	Argon target allows a direct comparison of ν-Ar interactions with ν-H ones

DRAFT

free nucleons with the effects of the nuclear medium. These models are inherently biased due to the predominance of neutrino-nucleus data over neutrino-nucleon data, most of which originates from outdated bubble chamber experiments. The solid hydrogen subtraction technique offers a way to perform high-statistics measurements of neutrino-proton scattering using a modern, well-characterized neutrino beam.

The ability to measure interactions on different nuclei enables comparisons of neutrino cross sections across various nuclear targets, especially argon. A program studying the 'A-dependence' of neutrino cross sections was previously conducted by MINERvA. With significantly improved vertex resolution and a low-density tracker, SAND could substantially enhance these measurements, including the use of additional nuclear targets. Moreover, SAND has the potential to perform ratio measurements where the denominator consists of free protons and to carry out complementary measurements by exploiting its magnetic field.

The high intensity of the LBNF beam, combined with the KLOE solenoid and high-performance calorimeter, enables the use of a low-density target in a neutrino beam. This approach adopts a detection strategy commonly employed in collider experiments: precise particle tracking in a low-density material within a magnetic field, surrounded by calorimeters. Such a strategy was previously unfeasible at neutrino facilities, as the low density would have required an extremely large volume to achieve a sufficient event rate. However, at LBNF with a beam power of 1.2 MW, a 5 t tracker is expected to observe more than 5×10^6 ν_μ CC events per year.

A search for Heavy Neutral Leptons (HNL) becomes very promising because the signal — i.e., a neutral particle decaying within the detector volume — scales with the volume, while the background from standard neutrino interactions scales with the detector mass. Additionally, the ability to reject events involving nuclear breakup on the carbon target is excellent, making searches for processes that do not break the nucleus (such as HNL, trident production, $\nu + e$ scattering, and similar channels) particularly clean and pure.

1.5 Simulation framework

The SAND consortium has established the Physics and Software WG to evaluate the detector's physics performance and capabilities. One of the main activities of the WG is the development of a complete simulation and event-reconstruction chain. It takes as input the energy spectrum of the incident neutrino flux, together with the detailed geometry of the detector (and its subdetectors: ECAL, GRAIN, and the Tracker) in which the interactions occur. Neutrino interactions are generated using the GENIE software framework [19]. The transport of the resulting final-state particles and their interactions with the detector materials are subsequently simulated with GEANT4 [20]. The detector response to the deposited energy is modeled using several dedicated software tools, each tailored to a specific sub-detector. These consist of a suite of C++ and Python applications that simulate the different stages of the signal-formation process, offering multiple levels of detail and accuracy depending on the needs of the study. The event reconstruction identifies neutrino interactions occurring within the detector's inner volume and infers the properties of both the neutrino and the interaction from the reconstructed final-state particles, using information provided by all three sub-detectors. The reconstruction workflow consists of several steps, including neutrino-interaction identification, pattern recognition, physics-object reconstruction,

DRAFT

and the integration of information from the different sub-detectors. Each of these steps has been studied independently to evaluate their performance and to enable their implementation within a fast-event-reconstruction framework designed to produce high-level physics results. All software components are developed, maintained, and continuously updated by the working group.

Neutrino Fluxes Neutrino fluxes were generated using a Geant4-based simulation of the Long-Baseline Neutrino Facility (LBNF) neutrino beam. The simulation was configured to use a detailed description of the LBNF optimized beam design. That design starts with a 1.2 MW, 120 GeV primary proton beam that impinges on a cylindrical graphite target. Hadrons produced in the target are focused by three magnetic horns operated with 300 kA currents. The target is followed by a 194 m helium-filled decay pipe and a hadron absorber. The focusing horns can be operated in forward or reverse current configurations, creating neutrino- or antineutrino-enriched beams, respectively. Following guidance from the beam group, a predefined selection of LBNF beam simulation files (in dk2nu format), available in `https://glaucus.crc.nd.edu/DUNEFluxes`, was used. These records contain information about the decay of hadrons and muons that give rise to neutrinos in the beam system and integrate into GENIE to then calculate the neutrino 4-momentum and weight at the detector location.

Detector Geometries Several components of the detector required design optimization; consequently, a fast tool for producing alternative geometry configurations is essential. For this purpose, the General Geometry Description (GGD) software was adopted, as it enables the rapid generation of configurable geometries. The geometry is described using the GDML format, which integrates with GENIE, Geant4, and ROOT.
The SAND detector is composed of a superconducting solenoidal magnet and three subdetectors. The magnet consists of a superconducting coil housed in a cryostat and surrounded by an iron yoke. It provides a 0.7 T magnetic field in its inner volume, where three sub-detectors are installed. The ECAL subdetector is composed of a barrel and two endcaps. The barrel consists of 24 trapezoidal cross-sections, 4.3 m-long modules, while each endcap is composed of 32 C-shaped modules, both with a thickness of 23 cm. Each module is a spaghetti electro-magnetic calorimeter composed of scintillating fibers in lead-grooved foils. In the geometry description, the complex internal structure of the modules is approximated by alternating scintillator and lead layers with a thickness of 700 µm and 400 µm. The total thickness matches the actual detector's radiation length. The photon-collection system, consisting of an array of PMTs coupled to the module through Winston cones, is not included in the geometry description; however, it is fully simulated in the subsequent detector-response stage.
The GRAIN subdetector consists of an outer carbon-fiber vessel and an inner steel vessel. The latter houses a liquid-argon volume, which is instrumented with optical systems coupled to SiPM matrices. Two optical-system configurations are implemented: coded-mask cameras, in which the sensor is enclosed within an opaque housing, and lens-based cameras employing a gas-filled optical assembly. The number, placement, orientation, and type of optical systems are configurable.
The tracker sub-detector is composed of vertical planar tracking stations interleaved with layers of target material. Two alternative technologies have been implemented in the geometry descriptions for the tracking planes:

- the STT, whose basic module includes a solid plastic CH_2 (C) target slab with scalable thick-

ness, a polypropylene radiator alternating with air gaps, and four layers of straws arranged in an XXYY pattern;
- the Drift Chamber, arranged in a structure of super-modules, consists of one module with carbon as a target, followed by nine where it is replaced by C_3H_6; the base module consists of a position-dependent height (3 to 4 m) solid polypropylene (carbon) 5 mm-thick (4 mm-thick) target and three wire-plane layers interspaced with Mylar foils, filled with Ar/CO_2 gas (85/15%) with alternating field wires and sensing wires oriented XXY.

The number of modules, their dimensions, and the distribution of the target material along the tracker volume have not yet been finalized.

Neutrino event generation The GENIE code is a neutrino event generator for the experimental neutrino physics community. It has a focus on low energies (≤ 1 TeV) and is currently used by a large number of experiments working in the neutrino oscillation field. A GENIE-based application to generate neutrino-induced events in the ND has been developed. It uses an input detector geometry and the dk2nu flux files to simulate neutrino interactions in the entire geometry or in part of it. Depending on the input flux files, it can simulate single or multi-flavor neutrino beams crossing the detector, with the neutrino energy and type randomly generated according to the input file.

Event overlays The neutrino interactions can be overlaid by grouping those associated with the same spill. The purpose of this step is to distribute events realistically in time, reproducing the LBNF beam spill structure. The neutrino interaction time is modified by accounting for all contributions from proton production up to the neutrino interaction. In this step, the neutrino interaction time is estimated in a way that is as close to reality as possible.

Particle propagation The primary particles produced by the neutrino interaction are propagated in the detector geometry to simulate energy deposition and geometric effects. This step is performed with the Energy Deposition Simulation (EDEP-SIM) software, a wrapper around the Geant4 simulation tool. In most cases, it exploits the QGSP_BERT physics list to simulate the possible processes that could occur during particle propagation. This includes elastic, inelastic, and capture processes for the purely hadronic part, while the electromagnetic processes include Multiple Coulomb Scattering (MCS), Bremsstrahlung, and ionization for electrons, muons, pions, kaons, and (anti)protons. For the photons, e^-/e^+ pair production, Compton and Rayleigh scatterings, and the photoelectric effect are included. The simulation implements a detailed energy deposition model, the NEST (Noble Element Simulation Technique) model, for both ionizing and non-ionizing (scintillation) energy losses in liquid argon, taking into account the energy and field dependence, as well as the intrinsic fluctuations and recombination physics, deposits, and full Monte Carlo truth.

ECAL Simulation and Reconstruction As a first step, the energy deposits in the scintillator layers of the ECAL modules are converted into an expected number of photoelectrons, accounting for several aspects such as scintillation, light propagation and collection, and the photomultiplier tube (PMT) response. The scintillation in the fibers includes a calibrated light-yield factor, the Poissonian nature of the photon-production process, and the characteristic photon-emission time profile. Light propagation along the fiber is simulated by incorporating both the effective speed of

light in the medium and the attenuation length. The photons are then grouped according to the corresponding PMT, thereby simulating the segmentation of the photon-detection system. The portion of the module volume between two PMTs facing each other is hereafter referred to as a cell. The PMT signal simulation consists of a simplified model of the PMT response and the trigger logic implemented in the front-end electronics. The digitized signal is built from the PEs in an integration time of 30 ns window, exceeding a 2.5 PEs threshold. In all the fired PMT, the corresponding digitized photo-signals are stored with their ADC and TDC values. The position, time, and deposited energy of a particle crossing a cell are estimated from the signals recorded by the two PMTs. These energy deposits are then grouped into reconstructed objects using a clustering algorithm.

Starting from a seed cell, spatial neighboring cells are first added to the pre-cluster. This process iterates, continuing to add complete cells until no further neighbors remain. Once a pre-cluster is formed, a new seed cell is selected from those not yet assigned to any pre-cluster, and the process repeats until all complete cells have been processed. For each pre-cluster, the reconstructed energy, position, and time are calculated, taking into account the cell quantities. To eliminate potential overlapping clusters grouped during the pre-clustering step, a splitting procedure is applied to each pre-cluster, evaluating the spread in time of the grouped cells through the calculation of the energy-weighted cluster time. If the pre-cluster satisfies the threshold condition, it is split into four quadrants, which are populated with the cells according to the single-cell signal times. After splitting, the cluster variables are recalculated, and the process repeats until no pre-clusters meet the splitting criteria. To combine pre-clusters that were incorrectly split or contain cells that are not spatially adjacent, a merging procedure is implemented. This routine compares pairs of pre-clusters, and if the spatial distance between their centroids is less than 40 cm and their time difference is less than 2.5 ns, the two clusters are merged. The parameters for the resulting merged cluster are then recalculated. The newly formed clusters are analyzed to determine their direction and apex origin. For each module layer where the cluster spreads, the weighted average cluster position is calculated. The cluster's direction vector and apex coordinates are obtained by performing a linear regression on these layer-wise positions.

Tracker Simulation and Reconstruction The signal readout is simulated by assigning each true particle ionization segment in the gas a TDC time for the nearest wire. This time is given by the sum of the ionization time, the free electron drift time, and the signal propagation time along the wire to the electronics. In the case of multiple ionization segments for a given wire, the earliest signal is stored as the ADC and TDC values of the corresponding wire channel. The reconstruction of the event in the tracker starts with an initial vertex position estimation based on the longitudinal spread of tracker digits. This vertex serves as input to a global track-finding method based on coordinate transformations, which turns curved tracks into straight lines in the transformed space. Peaks in the ϕ distribution identify the tracks, whose associated hits are then passed to the fitting stage. A charged particle in the SAND tracker follows an approximately helical trajectory in the 0.6 T magnetic field, and its track is reconstructed by fitting a helical model to the drift radii inferred from TDC times. The method uses likelihood minimization and is validated on simulated muon tracks from charged-current neutrino interactions. A Kalman-filter–based algorithm for track reconstruction has been developed and tested on simulated single-track samples of muons and protons. For targeted high-level physics analyses, these reconstruction steps are emulated by applying a smearing to the true particle momentum based on the expected momentum resolution given by the Gluckstern formula.

DRAFT

GRAIN Simulation and Reconstruction A dedicated Geant4 simulation is used to model the emission and propagation of liquid-argon scintillation light in GRAIN. Starting from the deposited energies, scintillation photons are generated following the liquid-argon emission spectrum, singlet-to-triplet ratio, and decay time constants. Emitted photons are then propagated through the argon volume, accounting for effects that alter their transport, principally absorption by impurities and Rayleigh scattering, each implemented with a constant characteristic length. The sensor-matrix and readout-electronics response are simulated with dedicated software that operates independently of the optical simulation's geometry output, enabling evaluation of different sensor configurations from the same dataset. Two modes are provided: a "fast" mode that approximates the SiPM response by counting photons incident on each detector, applying geometric effects and photon-detection efficiency to estimate detected counts; and a "full" mode that models the complete SiPM and readout-ASIC behavior and produces data formatted like the DAQ output.
Track reconstruction using the lens-based design for GRAIN has the set of two-dimensional images from all the cameras as a starting point. Combining two views is enough to identify the source's true position in space. However, extracting reliable information on ν interactions from images requires a custom reconstruction infrastructure that coherently integrates data from all views. The reconstruction workflow in its present implementation assumes no pile-up, i.e., a single interaction per event, and entails two key steps: a two-dimensional phase, where a combination of algorithms is employed for clustering, track fitting, and, if $N > 1$ lines are identified, candidate vertex projection identification; and a three-dimensional stage to identify a 3D volume that consistently matches the 2D outputs. While the 2D step is unique and uses the Hough transform method, two methods for back-projection in 3D exist: the former is a simple and coarse approach based on the voxelization of the volume, while the latter leverages Multiple-View Geometry.
The reconstruction of the Coded Aperture cameras' signals is based on an iterative Maximum Likelihood Expectation-Maximization (MLEM) algorithm. The algorithm computes the probability that a given initial distribution of the photon source within the detector could have produced the observed images, according to a mathematical model of the detection process. Among all possible source distributions, the one with the highest probability is identified as the *Maximum Likelihood Estimate* of the original photon source distribution. In practice, starting from an initial three-dimensional, non-negative distribution—assumed uniform in the absence of other information—the algorithm iteratively updates the estimate of the photon source distribution until the required accuracy for numerical convergence is achieved.

1.6 SAND Physics Reach

The SAND detector's performance on the LBNF neutrino beam has been evaluated through detailed simulations, dedicated tests of prototypes, and by utilizing the operational experience and physics outcomes of the KLOE experiments at Laboratori Nazionali di Frascati (LNF). In the following, the results achieved so far in terms of reconstruction capabilities in response to the primary requirements by SAND, as part of the near detector complex, are outlined, together with the opportunities offered to enhance the DUNE physics program. These include both complementing the neutrino interaction phase space explored by other ND detectors and opening the possibility of expanding the neutrino cross-section measurement program and BSM physics searches.

DRAFT

Beam monitor Being the only component of the ND complex to be permanently located on-axis, the SAND detector's main target is to monitor the rate, spectrum, and profile of the neutrino beam by measuring the momentum and energy of the particles produced in neutrino interactions. The key features for this aim are: available target mass, resolution on the reconstructed neutrino energy, and transverse size with respect to the beam axis; a large target mass is crucial for reducing the minimum data taking period needed to detect potential variations in the beam (~ 1 week time scale); an accurate reconstruction of the neutrino energy is also required to minimize the effect of the reconstruction smearing in monitoring the beam spectrum; finally, the capability to measure the beam profile over a wide cross-sectional area provides additional sensitivity, as the kinematics of the parent meson decays implies spectral variations with the distance from the beam axis. The SAND detector meets the three requirements described above.

Most of the sensitivity for beam monitoring is provided by neutrino interactions in the upstream barrel ECAL (fiducial mass 22.8 t), with the momentum of the charged tracks exiting from ECAL being reconstructed in the tracker (the STT, for example). Interactions occurring in the STT volume and in GRAIN (fiducial mass 7.7 t) further enhance the overall beam monitoring capability of the detector. As shown in Table 1.3, comparing the reconstructed energy spectra of ν_μ CC events in the upstream barrel ECAL and in the STT + GRAIN SAND is able to identify with a $\gtrsim 3\sigma$ significance the following 8 variations of the beam parameters: (a) horn current; (b) water layer thickness in the horns; (c) decay pipe radius; (d) proton target density; (e) proton beam radius; (f) proton beam offset (X or Y); (g) horn 1 X shift; (h) horn 1 Y shift in one week of data taking. Another important task for beam monitoring is to detect potential changes in the beam direction in real time. Comparing the reconstructed neutrino energy spectra of the events located at larger and smaller X values with respect to the SAND center, SAND will identify a shift of the beam center along the X direction down to 8.4 cm with a $\gtrsim 3\sigma$ significance in a week of data-taking.

Table 1.3: Sensitivity to variations of the main beam parameters with respect to the nominal FHC beam settings. The values of $\Delta\chi^2$ are calculated for both the neutrino (E_ν) and muon (E_μ) energy distributions in the front ECAL and STT with inclusive ν_μ CC samples equivalent to one week of data taking (7 days, 3.78×10^{19} POT). The values obtained using both the true and the reconstructed variables with 80 bins are reported for comparison.

		ECAL				STT			
Beam parameter	Variation	$\Delta\chi^2(E_\nu)$		$\Delta\chi^2(E_\mu)$		$\Delta\chi^2(E_\nu)$		$\Delta\chi^2(E_\mu)$	
		true	rec	true	rec	true	rec	true	rec
Horn current	+3 kA	107.6	76.1	26.0	25.4	50.6	29.5	11.4	10.4
Water layer thickness	+0.5 mm	21.2	16.2	8.7	8.5	9.1	6.0	3.4	3.0
Decay pipe radius	+0.1 m	42.0	34.3	12.0	11.9	19.9	13.7	5.1	4.8
Proton target density	+2%	18.0	14.3	8.9	8.7	7.6	5.3	3.3	3.1
Proton beam radius	+0.1 mm	34.9	27.6	18.2	17.8	13.5	9.8	6.6	6.1
Proton beam offset X	+0.45 mm	24.6	16.9	9.0	8.7	9.5	5.3	3.0	2.7
Proton beam θ, ϕ	0.07 mrad, 1.57 rad	0.5	0.1	0.1	0.1	0.3	0.1	0.0	0.0
Proton beam θ, ϕ	0.07 mrad, 0.0 rad	0.7	0.2	0.1	0.1	0.4	0.1	0.0	0.0
Horn 1 X shift	+0.5 mm	16.2	10.7	4.3	4.1	7.2	3.9	1.7	1.6
Horn 1 Y shift	+0.5 mm	20.6	13.6	5.7	5.5	7.3	4.1	1.8	1.7
Horn 2 X shift	+0.5 mm	0.4	0.2	0.1	0.1	0.2	0.1	0.0	0.0
Horn 2 Y shift	+0.5 mm	0.4	0.1	0.0	0.0	0.2	0.1	0.0	0.0

DRAFT

***Solid Hydrogen* sample** Approximately 97% of the total tracker mass is contained in the diffuse target, which consists of thin foils of polyethylene (C_3H_6) and graphite (C) interleaved with tracking planes. This configuration allows interactions to be associated with the correct target material with very high purity, enabling the extraction of hydrogen interactions through "statistical subtraction". The study of (anti)neutrino scattering on hydrogen (i.e., on free protons) is crucial for the DUNE near detector physics program, as it represents the only interaction process, together with ν-e elastic scattering, entirely free from nuclear effects. In particular, it allows to directly constrain nuclear effects from a comparison with corresponding measurements on heavy materials within the same detector, and a precise determination of neutrino and antineutrino fluxes as well.

The hydrogen content by weight in the tracker targets is 14.4%, a very high percentage achievable with standard plastic materials; yet, most interactions still originate from carbon nuclei. To enhance the signal-to-background ratio in the selection of hydrogen interactions, the complete event kinematics can be exploited. For a hydrogen target at rest, CC events are expected to be transversely balanced with respect to the beam axis. In contrast, interactions on nuclear targets are affected by Fermi motion, nuclear binding, and final-state interactions, resulting in significant missing transverse momentum. This kinematic handle provides strong rejection of the carbon background.

The most readily accessible exclusive topology is $\nu_\mu(\bar{\nu}_\mu)\, p \rightarrow \mu^{\mp} p\, \pi^{\pm}$, dominated by resonance production, in which all final-state particles are reconstructed in the tracker. The quasi-elastic process $\bar{\nu}_\mu\, p \rightarrow \mu^+\, n$ on hydrogen is also of particular importance. In this case, the neutron direction is inferred from the reconstructed primary vertex and the neutron interaction point within the detector. Assuming the target proton is at rest, the neutron energy E_n is obtained from energy-momentum conservation, allowing full kinematic reconstruction and the application of the transverse-balance selection. This approach generalizes to all exclusive channels, as well as to the inclusive ν_μ and $\bar{\nu}_\mu$ CC interactions on hydrogen. The corresponding selected events are listed in Table 1.4 for all the available channels.

Table 1.4: Number of events expected in the selection of all the various processes on H, assuming 5+5 years of data taking with the default FHC and RHC beams. The first two columns (CH_2 and H targets) refer to the initial statistics, while the last three include all selection cuts based on kinematics criteria. For the CH_2 and C targets the numbers refer to the given final state topologies originated from either p or n interactions. The fourth column shows the total residual C background to be subtracted from the corresponding CH_2 selected samples.

CC process	CH_2 target	H target	CH_2 selected	C bkgnd	H selected
$\nu_\mu p \rightarrow \mu^- p \pi^+$	5.233×10^3	2.286×10^3	2.148×10^3	107×10^3	2.041×10^3
$\nu_\mu p \rightarrow \mu^- p \pi^+ X$	10.665×10^3	890×10^3	817×10^3	57×10^3	760×10^3
$\nu_\mu p \rightarrow \mu^- n \pi^+ \pi^+ X$	3.293×10^3	171×10^3	134×10^3	41×10^3	93×10^3
ν_μ CC inclusive	32.526×10^3	3.347×10^3	3.099×10^3	205×10^3	2.894×10^3
$\bar{\nu}_\mu p \rightarrow \mu^+ n$	4.168×10^3	1.581×10^3	1.078×10^3	216×10^3	862×10^3
$\bar{\nu}_\mu p \rightarrow \mu^+ p \pi^-$	775×10^3	348×10^3	320×10^3	16×10^3	304×10^3
$\bar{\nu}_\mu p \rightarrow \mu^+ n \pi^0$	741×10^3	343×10^3	250×10^3	41×10^3	209×10^3
$\bar{\nu}_\mu p \rightarrow \mu^+ p \pi^- X$	2.126×10^3	165×10^3	143×10^3	8×10^3	135×10^3
$\bar{\nu}_\mu p \rightarrow \mu^+ n \pi \pi X$	2.177×10^3	262×10^3	186×10^3	30×10^3	156×10^3
$\bar{\nu}_\mu$ CC inclusive	12.176×10^3	2.699×10^3	1.977×10^3	311×10^3	1.666×10^3

Beyond cross-section measurements, interactions on free protons provide a nuclear-smearing-free

tool for the determination of the relative ν_μ flux as a function of neutrino energy. The process $\nu_\mu p \rightarrow \mu^- p \pi^+$ is particularly well suited for this purpose: the momentum resolution of the tracker ($\delta p/p \sim 3\%$) enables precise unfolding of the detector response, and the energy dependence of the resonant cross-section on hydrogen is controlled by well-known proton form factors, with uncertainties substantially smaller than those in any nuclear target. Restricting the analysis to events with low hadronic energy can further reduce the uncertainty on the energy dependence of the cross-section to the sub-percent level. The absolute flux normalization is provided independently by ν-e elastic scattering. Additionally, the possibility of using multiple nuclear targets, including argon from the GRAIN active target, allows for measurements of the A-dependence of neutrino cross sections, complementing and extending prior work by MINERvA with improved vertex resolution and the unique capability to form ratios with respect to a free-proton reference.

Search for Dark Neutrinos Being exposed to the world's most powerful neutrino beam at that time (i.e., the LBNF beam), the ND complex in general, and the SAND detector in particular, will experience an intense neutrino flux and thus provide an excellent environment to search for rare BSM physics, especially Heavy Neutral Leptons (HNL). A class of HNL models that has recently gained attention within the accelerator-neutrino community is that of Dark Neutrinos, which postulate a minimal $U(1)'$ gauge group and one or more HNLs, whose associated flavor states, the *dark neutrinos*, carry the new gauge charge. In such a scenario, HNLs are produced in the scattering of an active flavor state on a nuclear target and can decay to e^+e^- pairs. Either prompt (proper lifetime $c\tau \ll 10\,\text{cm}$) or displaced decays ($c\tau \gg 10\,\text{cm}$) are possible, depending on the model parameters. The SAND detector is well suited for searches for BSM physics, owing to its high neutrino flux and the use of a complementary suite of subsystems. The low-density STT ($\rho \sim 0.18\,\text{g/cm}^3$) allows for a precise measurement of vertex activity and the detection of electromagnetic BSM signatures that are difficult to observe in liquid argon. The low tracker density additionally provides an optimal signal-to-background ratio for displaced decays. The ECAL can be leveraged to reduce the main background from $\pi^0 \rightarrow \gamma\gamma$ decays. The use of a magnetic field for the detector will further enable charge identification.
A preliminary simulation and analysis pipeline for the search for dark neutrinos decaying in the inner volume has been developed, allowing for the estimation of the discovery potential for a range of models with dark photon masses $M_{Z'} = 30\,\text{MeV}$ and dark neutrino masses $35\,\text{MeV} \leq M_N \leq 1\,\text{GeV}$. The SAND detector can test unexplored areas of the dark neutrino coupling parameter space down to $|U_{\mu 4}|^2 \simeq 10^{-11}$ at $M_N \simeq 100\,\text{MeV}$ at 95% C.L.

Why don't we show the preliminary plot here?

Complementary ν-Ar interaction measurements with GRAIN Samples of inclusive and exclusive ν-Ar interactions in GRAIN play an important complementary role in achieving the SAND physics goals within the ND complex. While ND-LAr, which shares the same target nucleus as the FD, is essential for reducing systematic uncertainties, particularly those related to FSI models, its measurements are limited since it is not magnetized. As a result, the momentum and charge of the outgoing muon, and consequently the nature of the incoming neutrino, cannot be determined. In addition, neutron detection is extremely challenging, and its inefficiency can degrade the reconstructed neutrino energy resolution.
Despite its smaller mass (1 t compared to 67 t) and different detection technology, GRAIN offers

key complementary capabilities for oscillation analysis. Located inside SAND, it benefits from the magnetic field and the combined performance of the tracker and the ECAL to precisely measure the momentum and sign of muons, even at large angles, reaching an overall $\sim 80\%$ neutron detection efficiency. Thus, exploiting GRAIN, the SAND detector can perform cross-calibrations with ND-LAr and constrain the neutrino interaction models by utilizing its multi-target configuration to study argon-specific nuclear effects across different interaction channels. To this end, maximizing acceptance for neutrino interactions with primary vertices inside GRAIN is crucial. Studies using MC simulated samples of ν_μ-CC events show that optical reconstruction enlarges the accessible phase space of muons and charged pions compared to tracker-only reconstruction, especially at large angles relative to the beam. It also improves the detection efficiency of short proton tracks (from $\sim 13\%$ to $\sim 23\%$), especially for ν_μ CCQE-like events.

Physics Facility for Precision Measurements and Searches The possibility of collecting a large statistic of neutrino interactions and determining the neutrino and antineutrino fluxes with unprecedented precision using $\nu(\bar{\nu})$-H interactions can be exploited to perform studies of fundamental interactions with a broad program of precision measurements and searches.

SAND can determine $\sin^2\theta_W$ from the ratio of NC and CC DIS interactions induced by neutrinos $R_\nu \equiv \sigma^\nu_{NC}/\sigma^\nu_{CC}$. The use of the high-resolution tracker significantly reduces experimental systematic uncertainties and enables efficient identification of ν_e CC interactions and event-by-event kinematic analysis that separates NC and CC interactions. By doing so, it seems feasible to achieve a total relative uncertainty on the value of $\sin^2\theta_W$ extracted from νN DIS of 0.35%. A second independent measurement of $\sin^2\theta_W$ can be obtained from NC $\nu_\mu e$ elastic scattering. This channel is free from hadronic uncertainties, but it is limited by the statistics due to its tiny cross-section. The value of $\sin^2\theta_W$ can be extracted from the ratio $R_{\nu e}(Q^2) \equiv \sigma(\bar{\nu}_\mu e \to \bar{\nu}_\mu e)/\sigma(\nu_\mu e \to \nu_\mu e)$, in which systematic uncertainties related to the selection and the electron identification cancel out. A high-purity $\nu_\mu e$ elastic scattering event sample, which can be calibrated in-situ with data, can be obtained. An overall relative precision of $\sin^2\theta_W$ from $\nu - e$ of 1% or better seems feasible. The DIS and $\nu - e$ elastic channels are characterized by substantially different scales of momentum transfer, providing a tool to test the running of $\sin^2\theta_W$ in a single experiment.

SAND can investigate isospin physics using both neutrino and antineutrino interactions. The availability of large samples of $\nu(\bar{\nu})$-H interactions allows a precision test of the Adler sum rule (in the quark-parton model, the difference between the number of valence u and d quarks of the target), $S_A = 0.5\int_0^1 dx/x(F_2^{\bar{\nu}p} - F_2^{\nu p}) = I_p$, which gives the isospin of the target and was tested only by the BEBC experiment with a few thousand events. The Adler sum rule survives the strong-interaction effects because of the conserved vector current (CVC) and provides an exact relation to test the local current commutator algebra of the weak hadronic current. The value of S_A can be measured as a function of the momentum transfer Q^2 from the structure functions $F_2^{\bar{\nu}p}$ and $F_2^{\nu p}$ determined from the corresponding differential cross-sections on hydrogen. This measurement is sensitive to possible violations of isospin (charge) symmetry, heavy quark (charm) production, and strange sea asymmetries $s - \bar{s}$. Furthermore, the measurement from H can be compared with the values of S_A obtained from the C target ($S_A = 0$). The Gross-Llewellyn-Smith (GLS) sum rule $S_{GLS} = 0.5\int_0^1 dx/x(xF_3^{\bar{\nu}p} - xF_3^{\nu p})$ can also be measured precisely as a function of Q^2 using $\nu(\bar{\nu})$-H interactions. The value of S_{GLS} in the quark-parton model gives the number of valence quarks in the nucleon. This sum rule receives both perturbative and non-perturbative QCD corrections,

and its Q^2 dependence can be used to extract the strong coupling constant $\alpha_s(Q^2)$. The presence of both H and various nuclear targets in STT would allow an investigation of the isovector and nuclear corrections, adding a tool to test isospin (charge) symmetry.

SAND can accurately determine the strange axial-vector form factors from a measurement of the NC elastic scattering off protons $\nu_\mu(\bar{\nu}_\mu)p \to \nu_\mu(\bar{\nu}_\mu)p$. In the limit $Q^2 \to 0$, the NC differential cross-section is proportional to the axial-vector form factor $d\sigma/dQ^2 \propto G_1^2 = (-G_A/2 + G_A^s/2)^2$, where G_A is the known axial form factor and G_A^s is the strange form factor. This process provides the most direct measurement of Δs by extrapolating the NC differential cross-section to $Q^2 = 0$, since in this limit $G_A^s \to \Delta s$. The ratios of NC elastic scattering to the corresponding QE processes $R_{\nu p}(Q^2) \equiv \sigma(\nu_\mu p \to \nu_\mu p)/\sigma(\nu_\mu n \to \mu^- p)$ and $R_{\bar{\nu}p}(Q^2) \equiv \sigma(\bar{\nu}_\mu p \to \bar{\nu}_\mu p)/\sigma(\bar{\nu}_\mu n \to \mu^+ n)$ can be measured over an extended Q^2 range, using the CCQE process to determine GA. This latter can also be used to extract the axial current charge radius, which can be compared to the results from muon capture in hydrogen to investigate existing discrepancies regarding this quantity. The SAND resolution will enable precision measurements of exclusive decay modes of charmed hadrons (e.g., D^{*+}, D_s, Λ_c) and measurements of charm fragmentation and production parameters. In addition, the low density of the tracker will provide access to both the $\mu\mu$ and μe inclusive semi-leptonic charm decay channels, with statistics more than one order of magnitude higher than the largest sample of charm dimuon events available from other experiments.

The precise calibration of the energy scale uncertainties in SAND and the unprecedented precision in the determination of the (anti)neutrino fluxes allow measurements of structure functions and cross-sections with accuracies comparable to electron scattering experiments. Using both neutrino and antineutrino DIS, the different structure functions F_2, xF_3, F_L, and F_T can be determined, elucidating the flavor structure of the nucleon. It is possible to perform global QCD analyses of (anti)neutrino data from the proposed detector to study parton distribution functions (PDFs) as well as perturbative and non-perturbative corrections in a broad range of Q^2 and Bjorken x, given the statistics and energies available in DUNE. Data from both H and the various nuclear targets can be used to separate valence and sea quark distributions, d and u quark distributions, and the strange quark s and $\bar{s}$ distributions. A study of F_L will not only provide information on the gluon distribution but also a determination of $R = F_L/F_T$, which is expected to have a different behavior at small Q^2 with respect to electromagnetic interactions. All of these studies of nucleon structure in the proposed detector can provide unique information complementary to the ongoing programs at colliders and fixed-target electron DIS experiments.

The possibility of integrating various thin nuclear targets within the tracker allows for detailed studies of nuclear structure and the related nuclear effects on structure functions, form factors, and cross-sections. An important issue is how the structure of a nucleon is modified when said nucleon is inside the medium of a heavy nucleus, including the determination of nuclear PDFs as well as non-perturbative effects. The study of final state interactions (FSI) is also relevant, as FSI can introduce substantial smearing of the kinematic variables reconstructed from the observed final state particles. The flavor separation provided by the weak current and the availability of nuclear targets with the same atomic weight, like Ar and Ca, would clarify the flavor dependence of nuclear effects. A comparison between interactions on H and on the various nuclear targets available in the tracker can provide a direct model-independent measurement of nuclear effects. In particular, the isospin symmetry provides a determination of the free neutron structure function and hence that of the average isoscalar nucleon $F_{2,3}^{\nu N} \equiv (F_{2,3}^{\nu p} + F_{2,3}^{\bar{\nu} p})/2$. Then, the first direct measurement of

the nuclear ratios $R_A \equiv F_{2,3}^{\nu A}/F_{2,3}^{\nu N}$ can be obtained.

External background evaluation The DUNE ND complex will operate in shallow depth in an intense LBNF neutrino beam environment, where activity not originating from neutrino interactions within the detector fiducial volumes can overlap with or mimic the signals used for beam monitoring and physics measurements. This high-rate environment leads to the requirement to separate cosmic rays, rock muons, and other beam-induced activity from genuine neutrino interactions, and to measure and validate the level and modeling of these backgrounds so that their residual contribution after selections can be quantified and included in the systematic uncertainty budget.

Achieving this with the SAND detector relies on the ability to collect large on-axis samples of neutrino interactions for continuous monitoring, as well as robust reconstruction performance. The high resolution on muon momentum and neutrino energy, vertex reconstruction, and especially precise timing in the tracker and ECAL allow for the localization of activity in space and time, defining background-enriched control samples and determining background rejection and residual contamination.

The relevant backgrounds for neutrino-beam events can be grouped into three main classes: cosmic rays, natural radioactivity from the surrounding rock and detector materials, and beam-induced neutrino interactions in the material surrounding the detector fiducial volume. The first two sources are strongly suppressed by requiring time coincidence with the beam spill and are therefore expected to be negligible for the analyses considered here. The most critical contribution is due to beam-related external activity, both because of the high interaction rate in the material surrounding the fiducial volume and because the detector fiducial mass is small compared to the mass of the surrounding mechanical structure. In the following, some preliminary studies are summarized, considering both backgrounds overlapping during the spill, due to random particles from other beam-induced interactions within the same spill, and external neutrino interactions misidentified as occurring in the fiducial volume. All of the studies summarized below are based on Monte Carlo simulations including the spill time structure and event overlay with a geometry that makes use of the STT configuration for the tracker.

Neutron Background One of the most critical beam-related backgrounds for the $\nu(\bar{\nu})$-H program comes from random neutron candidates produced by other beam-induced interactions outside the fiducial volume but occurring in the same spill. This is studied using the benchmark channel $\bar{\nu}_\mu p \to \mu^+ n$ (QE) on H in the tracker targets, where only one muon track is present and the neutron constitutes the full hadronic system. Neutron candidates are defined as isolated neutral activity above threshold in the STT or ECAL channels, with no associated charged track. Before timing preselection, the spill overlay yields, on average, 8.15 external neutron candidates per spill, reduced to 0.047 by requiring the measured neutron time of flight relative to the interaction vertex to satisfy $-4 < \Delta t < 300$ ns. The background candidates are not related to the signal vertex, but they constitute the pool of external neutrons that can be wrongly associated with it. A multivariate ranking based on timing and topology then selects one candidate per event and identifies the true primary neutron in 85.4% of $\bar{\nu}_\mu p \to \mu^+ n$ signal events, suppressing neutron contamination in the spill before the final kinematic selection.

In general, for inclusive $\nu(\bar{\nu})$ CC interactions in the STT fiducial volume, random neutrons mainly introduce an additional smearing of the reconstructed neutrino energy. A timing combined with an ANN selection retains 85.6% of the signal neutron candidates while reducing the external-neutron

background to $\mathcal{O}(10^{-2})$ candidates per spill.

Rock Muon Background A complementary study addresses the rejection of rock muons and neutrino interactions in the magnet for event selections in the upstream barrel ECAL, relevant in particular for beam monitoring. A preselection requiring a reconstructed STT track and energy in the ECAL fiducial volume retains 72.9% of genuine ECAL events while reducing the rock-muon background to 0.42%. A further layer-dependent ANN, based on ECAL timing and topological observables, leads to a combined background rejection factor of about 7×10^{-5} while retaining an overall signal efficiency of about 70% in the upstream ECAL fiducial volume.

Beam Neutrino Related External Background The rejection of neutrino interactions originating outside the STT fiducial volume, mainly in the surrounding magnet and ECAL, which can be reconstructed as genuine interactions inside the STT fiducial volume, has also been studied. Since the surrounding magnet and ECAL mass is much larger than the STT fiducial mass, rejection factors above 10^4 are required. The rejection that has been studied relies mainly on low-level timing and topological information from STT and ECAL, combined in an ANN. The resulting selection reaches an external-background efficiency of about 3×10^{-5}, while retaining 92.7% signal efficiency and achieving 99.65% purity.

Pile-up in ECAL Finally, the effect of pile-up activity in the upstream barrel ECAL modules was studied. Even though about 19% of genuine charged-current neutrino interactions in the upstream barrel ECAL fiducial volume have some ECAL activity contaminated by at least one hit contribution above the threshold from particles produced in other interactions within the same spill, the average impact on the event reconstruction remains small: for a 30 ns integration window, only about 0.1% of ECAL cells and only 0.04% of the total reconstructed ECAL energy is contributed by pile-up activity hits. These results indicate that pile-up has a negligible impact on event samples selected in the upstream barrel ECAL fiducial volume, and that residual out-of-time activity can be further identified using the timing mismatch between STT tracks matched with ECAL clusters.

Summary. The combined performance of the STT, ECAL, and GRAIN magnetic spectrometer, along with embedded nuclear targets, provides SAND with a uniquely broad and precise physics reach. From sub-percent flux measurements and high-fidelity CC reconstruction to real-time beam diagnostics and stringent nuclear-effect constraints, SAND plays an essential role in controlling the systematic uncertainties required for the DUNE long-baseline oscillation program.

DRAFT

Chapter 2

Organization & Management

Effective coordination among the institutions participating in the design, construction, installation, and operation of System for on-Axis Neutrino Detection (SAND) is essential to achieving the scientific objectives of the program. For this purpose, the SAND Consortium was established in 2020 within the DUNE organizational framework.

2.1 Consortium Organization

The Consortium is structured around a leadership model consisting of a Consortium Leader and a Technical Leader, appointed within the DUNE governance structure. The Technical Leader is responsible for technical coordination across all subsystems, while the Consortium Leader oversees institutional coordination and strategic alignment.

The governance structure includes advisory and steering bodies that provide strategic guidance and oversight. The Consortium Board consists of representatives from participating institutions and serves as the primary forum for discussion of major technical and strategic matters. Technical decisions impacting multiple subsystems are reviewed within this framework and, when appropriate, escalated to higher-level bodies in accordance with the DUNE governance process.

The Consortium is organized into dedicated working groups (WGs), each responsible for a specific subsystem or functional area. These include:

- Magnet and Yoke;
- electromagnetic calorimeter (ECAL);
- GRanular Argon for Interactions of Neutrinos (GRAIN);
- Inner Tracker;
- Data acquisition, trigger, timing, and slow control;
- Physics and software;
- Calibrations;

DRAFT

- Installation and Integration (I&I).

Each WG is responsible for subsystem-level technical development, documentation, scheduling, and resource planning, operating under the coordination of the Technical Leader and within the overall Consortium structure.

The adequacy of the required resources has been evaluated through:

- A detailed financial planning exercise;
- A detailed human resources plan.

Resource commitments are tracked and reviewed periodically to ensure alignment with the project schedule and technical milestones.

2.2 Institutional Framework

A significant component of the SAND program involves the refurbishment, transportation, and reuse of the K-LOng Experiment (KLOE) detector elements. These activities are governed by a memorandum of understanding (MoU) between DOE and Istituto Nazionale di Fisica Nucleare (INFN), signed in April 2024, which defines the scope of INFN's contributions to DUNE, including SAND.

The MoU establishes that SAND is an integral component of the international DUNE program, while operating outside the scope of the current U.S. Long-Baseline Neutrino Facility (LBNF)/DUNE capital project. The installation schedule and operational coordination are therefore carried out in close collaboration between Fermilab, INFN, and the broader DUNE management structure.

Within this framework, Fermilab provides site coordination, infrastructure support, and safety oversight for installation and operation activities, while the Consortium institutions retain responsibility for subsystem construction and in-kind contributions.

2.2.1 Contribution by Istituto Nazionale di Fisica Nucleare

Still from the above MoU, and specifically related to the SAND contribution, "INFN shall contribute resources in the form of hardware and scientific, engineering, and technical personnel as follows.

For the DUNE ND, in-kind contributions for the following items:

1. The magnet and calorimeter system that was deployed in the KLOE experiment's detector at the DAΦNE collider at INFN's Laboratori Nazionali di Frascati (LNF) (hereinafter "KLOE Components") being understood to imply that INFN's activities for the KLOE Components shall include their necessary refurbishment, maintenance, and subsequent delivery to Fermi National Accelerator Laboratory in accordance with the schedule and acceptance criteria to be developed by the DUNE Collaboration in consultation with the Participants. Once

delivered, the refurbished KLOE Components shall form detector subsystems of the SAND detector;

2. Cryogenic components for the magnet and for the liquid argon (LAr) target are to be built, installed, and operated in collaboration with Fermilab;

3. Electronics, power supplies, and trigger systems for the SAND calorimeter and magnet; and

4. Contribution to the development of the inner tracking system of SAND and an active compact LAr target to be installed within the volume of the refurbished KLOE Components."

2.2.2 Contribution by Fermi National Accelerator Laboratory

The excerpt from the above MoU indicates that "Fermilab shall contribute resources as follows:

1. Provide facilities for the execution of the DUNE Program, including: Accelerators and the associated neutrino beamline for DUNE; Experimental halls including infrastructure such as AC power distribution, computer and data networking, and building cranes; Safe working environments to conduct activities; and Engineering support for external cryogenic systems, cryogenic system integration, and process control systems to be built, installed by INFN, and operated in collaboration with INFN.

2. Support for the installation of the DUNE ND and FD in their respective experimental halls. This support includes: Providing technical coordination for each detector and associated subsystems; and Providing certain specialized technical services such as crane operation and welding services.

3. Along with the DUNE Collaboration, support for the commissioning, experimental, and physics operation of DUNE that shall include: Technical staff to operate the cryogenic systems; and Physics control room facilities located near the DUNE ND and FD experimental halls.

4. Provide oversight of activities regarding environmental and safety standards; provide support for carrying out safety reviews and obtaining necessary operational readiness clearances; and provide the necessary training for users to carry out the functions of installation, maintenance, and operation of the detectors."

2.3 Risk Management

The methodology adopted for identifying, evaluating, monitoring, and mitigating risks associated with SAND follows standard project management practices and is intended to ensure transparency, traceability, and timely corrective action.

Risks are identified through:

- Technical reviews and design assessments;

DRAFT

- Interface definition meetings;
- Installation planning exercises;
- Safety and compliance evaluations;
- Lessons learned from comparable detector projects.

Risks are categorized into the following classes:

1. **Technical Risks:** mechanical integration, alignment tolerances, cryogenic performance, services routing, and compatibility of electronics and infrastructure.

2. **Schedule Risks:** delays in subsystem delivery, transportation constraints, sequencing conflicts, and long-lead procurements.

3. **Resource Risks:** manpower availability, engineering support, and facility access windows.

4. **Interface Risks:** inconsistencies between subsystem specifications and host-laboratory infrastructure.

5. **Safety and Compliance Risks:** installation hazards, lifting operations, cryogenic safety, electrical certification, and regulatory approvals.

6. **Configuration Risks:** late design changes impacting installation procedures.

All identified risks are recorded in a Risk Register.

Each risk is evaluated using a qualitative likelihood–impact matrix.

- **Likelihood** is ranked as Low, Medium, or High.
- **Impact** is evaluated independently for:
  - Technical performance,
  - Schedule,
  - Cost,
  - Safety.

The overall risk level is determined from the combined likelihood and impact ranking according to a predefined matrix. Risks classified as Medium or High require a mitigation plan and regular monitoring.

Mitigation strategies may include:

- Early prototyping and validation tests;
- Formal interface control documentation;
- Redundant technical solutions where appropriate;
- Schedule contingency buffers;

DRAFT

- Advance logistics planning;
- Parallel development of fallback options.

The Risk Register is reviewed at regular intervals and at each major project milestone. Updates include:

- Status of mitigation actions;
- Changes in likelihood or impact assessment;
- Closure of resolved risks;
- Identification of new risks.

High-level summaries are presented to the SAND management and, when appropriate, to the DUNE coordination bodies.

Because installation and integration occur at Fermilab while subsystem construction is distributed internationally, particular attention is given to:

- Validation of mechanical and service interfaces prior to shipment;
- Verification of transportation tolerances and environmental constraints;
- Early definition of installation tooling and access requirements;
- Coordination between subsystem readiness and site availability;
- Alignment between subsystem documentation and installation procedures.

Formal interface documents and readiness reviews are used to reduce integration risk prior to component delivery to the installation site.

Where feasible, contingency measures are identified in advance for risks that could significantly impact the installation sequence or detector readiness. These may include alternative sequencing strategies, temporary bypass solutions, or staged integration approaches.

This risk management framework provides a structured and transparent approach to identifying and mitigating risks during installation and integration. Its systematic application is intended to preserve technical robustness, schedule integrity, and operational safety throughout the SAND deployment phase.

2.4 Schedule

SAND is progressing through the final phases of detector dismounting in Frascati (Italy) and the associated refurbishment activities. In parallel, preparations for shipment to Fermilab are ongoing, including logistics planning, identification of temporary storage locations at Fermilab, and the definition of post-delivery quality assurance (QA)/quality control (QC) procedures for major subsystems such as the magnet and the ECAL modules.

DRAFT

The primary objective of the SAND schedule is to ensure readiness for data taking at the time of the first beam delivery. Achieving this objective requires that SAND be prepared to begin assembly immediately upon the beneficial occupancy of the near detector (ND) hall, as described in Section 10. The schedule, therefore, integrates subsystem refurbishment, transportation, installation planning, and commissioning activities within a coordinated timeline.

The development of the schedule is driven by the following principles:

- alignment with the overall DUNE ND program timeline;
- early identification of long-lead activities and critical path elements;
- incorporation of appropriate float and contingency;
- coordination between international construction activities and on-site installation readiness.

The following sections present a high-level schedule and a summary of major milestones that define the path toward detector assembly, integration, and commissioning.

2.4.1 High Level Schedule

Figure 2.1 presents the high-level schedule for SAND, derived from the detailed subsystem schedules described in the corresponding chapters and from the installation sequence outlined in the Integration & Installation chapter (Section 10.6).

Schedule float is incorporated within the timeline and is, therefore, not explicitly displayed. For example, transportation of detector components from Europe to Fermilab is allocated approximately three months, whereas the typical shipment time is on the order of six weeks or less. Post-delivery QA/QC activities are scheduled with sufficient margin to accommodate potential minor repairs or adjustments identified upon arrival.

Throughout this document, the availability of the ND building for installation is assumed at the end of the third quarter of 2029. Beam checkout is assumed at the end of 2031. It is further assumed that SAND installation will commence immediately upon the availability of the ND Hall and will proceed without interference from the installation activities of the other Near Detectors (Near Detector Liquid Argon system (ND-LAr), Temporary Muon Spectrometer (TMS), Precision Reaction-Independent Spectrum Measurement (PRISM)).

The detailed final installation schedule will be developed in coordination with the schedules of the other Near Detector systems and will be presented in a separate document.

2.4.2 Major Milestones

SAND's major milestones at the present stage of the project are summarized in Table 2.1, organized by subsystem or activity. The milestones listed correspond to the completion of the activities required to bring each subsystem to the point of delivery to Fermi National Accelerator Laboratory (Fermilab).

For Installation and Integration (I&I), the relevant milestones concern: (i) completion of the

DRAFT

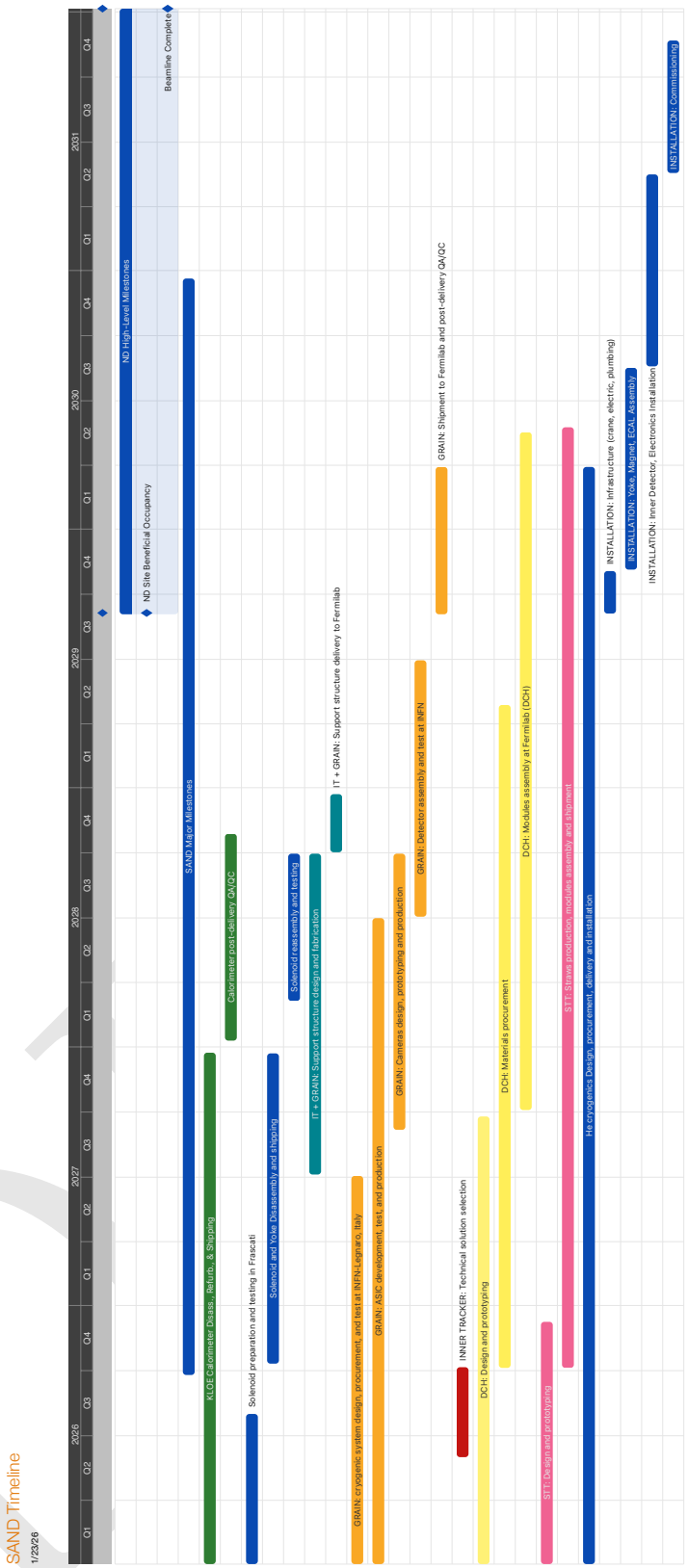


Figure 2.1: SAND high-level schedule

final design of the helium system for the magnet, (ii) definition of the QA/QC protocols required for subsystem acceptance, and (iii) qualification of the magnet for operation. The latter two are directly linked to readiness for operational acceptance of the subsystems. Completion of the helium system design is a prerequisite for initiating procurement, which is subject to both extended administrative procedures (including bidding) and long production lead times.

Table 2.1: High-level milestones for SAND subsystems and integration activities.

System	Milestone	Date
External	ND Site Beneficial Occupancy	Sep 3, 2029
	Beamline Complete	Jan 5, 2032
KLOE to SAND	New ECAL readout electronics selection	Oct 2, 2026
	ECAL modules revamping complete	Jul 30, 2027
	Solenoid Cold Test and Fitness for Service qualification	Sep 25, 2026
Inner Tracker	Module 0 construction and test complete	May 28, 2027
	Final design complete	Sep 24, 2027
	Modules production and test complete	Dec 20, 2030
GRAIN	Masks and lenses proof of principle	Dec 18, 2026
	Final detector design	Dec 20, 2027
	ASIC delivery complete	Apr 28, 2028
	Detector tested at the assembly site	Jul 27, 2029
Integration and Installation	He system and transfer lines design complete	May 28, 2027
	Complete definition of QA/QC protocols for acceptance	Jul 30, 2027
	Solenoid Fitness for Service qualification (Fermilab)	Dec 22, 2028

DRAFT

Chapter 3

The Superconducting Magnet

3.1 Magnet Specifications

The K-LOng Experiment (KLOE) Magnet is an iron-shielded superconducting solenoid that utilizes a thermo-siphoning cooling method, manufactured by Oxford Instruments A.T.G. (England). A schematic of the design is shown in Figure 3.1.

The cryostat is equipped with its own valve box, a Joule-Thomson (JT) valve, and a liquid helium (LHe) reservoir of approximately 150 liter. The total liquid volume in the system is approximately 200 liter. All controls for magnet operation (including cool-down and warm-up) are an integral part of the system. The main features of the cryogenic configuration are listed below:

1. **Coil Cooling:** A thermo-siphoning cycle cools the coil. Gaseous helium (GHe) at 5.2 K and 3 bar is supplied from the cryogenic plant and is liquefied through the JT valve into the LHe reservoir.

2. **Radiation Shield:** Cooled with 70 K GHe from the cryogenic plant.

3. **Current Leads:** Cooled with LHe from the reservoir; the returning 300 K GHe is sent back to the cryogenic plant.

4. The magnet operates under continuous cooling.

The superconducting magnet and its iron yoke were jointly designed to produce a 0.6 T magnetic field over a volume 4.3 m long and 4.8 m in diameter. The magnet specifications and major coil parameters are listed in Tables 3.1 and 3.2, respectively.

The KLOE magnetic field was mapped in 1997 using a Hall probe integrated into a dedicated positioning device called MagAx. The main body of the MagAx was a precisely machined beam, approximately 7 m long, made of a special aluminum alloy. The 5 mm $\times$ 14 mm flat encasing of the Hall probe was positioned precisely normal to the longitudinal axis on the front face of a

DRAFT

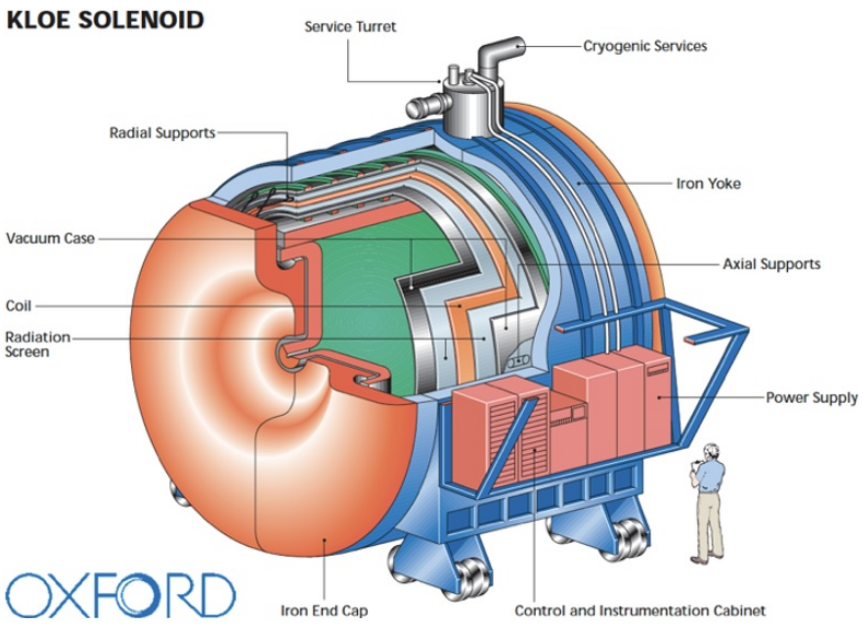


Figure 3.1: Schematic of the KLOE solenoid.

Table 3.1: Magnet specifications.

Central magnetic field	0.6 T
Vacuum case length	4.4 m
Vacuum case inner diameter	4.86 m
Vacuum case outer diameter	5.76 m
Coil shell inner diameter	5.19 m
Cold mass	10 t
Vacuum case mass	26 t
Iron return yoke mass	475 t

Table 3.2: Coil parameters.

Layers	2
Turns/layer	368
Ampere-turns	2.14 MA-T
Operating current	2902 A
Stored energy	14.3 MJ
Inductance at full field	3.4 H
Discharge voltage	250 V
Peak quench temperature	80 K

DRAFT

$1\,\text{cm} \times 1\,\text{cm} \times 170\,\text{mm}$ support finger. Further details of the device can be found in [21]. Figure 3.2 shows the longitudinal component of the solenoid's magnetic field along its axis.

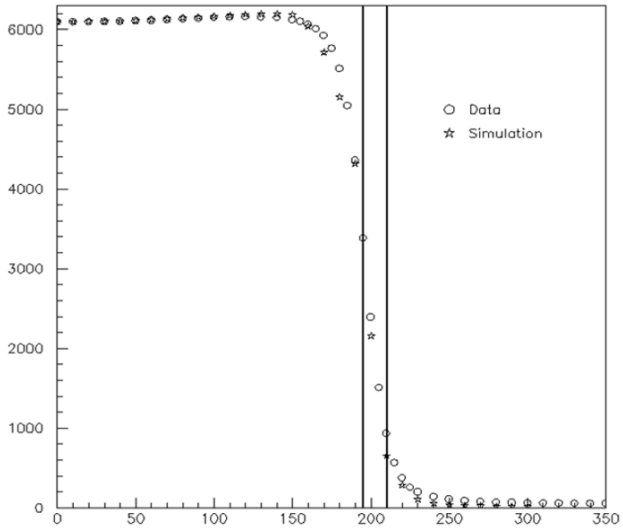


Figure 3.2: The longitudinal field component (Gauss) of the KLOE solenoid along its magnetic axis (cm), where 0 is the center of the barrel. The MagAx measurements are compared with a Monte Carlo simulation.

3.1.1 Coil Shell and Conductor

Oxford Instruments designed the coil shell to be fabricated from a number of 12 mm thick aluminum sheets and cooling channels. This design relied on achieving the diametrical tolerances (specified by INFN as $\pm 8\,\text{mm}$) by fabricating the shell on an adjustable spider, which allowed the ribs to be moved until the tolerances were met. The inner skin was fully welded to the ribs, while the outer skin was partially welded. No machining was performed on the shell; however, the inner welds were all dressed by hand. This manufacturing approach was successfully executed by Vosper Thorneycroft (Southampton, UK). The new coil shell was designed, manufactured, and delivered in six months, minimizing the delay to the system manufacturing schedule that resulted from a contractor substitution initiated by Istituto Nazionale di Fisica Nucleare (INFN).

The conductor is a 10 mm by 5 mm composite consisting of a Rutherford cable co-extruded with high-purity aluminum. The conductor, supplied by LMI (`https://lmi-srl.it/`), was cleaned and wrapped with two half-lapped layers of 0.125 mm glass tape. The two-layer coil was wound inside the coil shell by rotating the shell on motorized rollers in a controlled manner while the conductor was fed from a spool onto the shell face.

The conductor was wound flat, and 1 mm thick, high-purity aluminum sheets were placed between the two layers to improve quench propagation velocities and reduce peak quench temperatures. After winding, the coil was lined with aluminum to serve as an impregnation vessel before being oriented with its axis vertical and placed inside a 7 m cubic impregnation oven. The aluminum liner was supported against collapse by a fabricated structure before the coil space was evacuated, filled with epoxy resin, and cured at 100°C for 48 hours.

3.1.2 Radiation Screen

The radiation screen is cooled by helium gas from the dedicated refrigerator. The inner and outer radiation screen cylinders are end-cooled screens, each constructed from eight prefabricated panels. Each panel has a sandwich construction, consisting of two 1 mm thick flat aluminum sheets bonded and riveted to a central 1 mm corrugated aluminum sheet. The cooling pipe is welded to the panels over a length equivalent to 30% of their circumferential extent. This minimal approach to cooling the radiation screens is possible due to the extremely low radiant and conducted heat loads. The guaranteed heat loads are given in Table 3.3. The screen is supported from the vacuum case by stainless steel cables.

Table 3.3: Guaranteed Heat Loads.

Source	Heat Load
Current Leads	0.6 g/s
4 K Radiation and Conduction	55 W
77 K Radiation and Conduction	530 W

3.1.3 Service Turret

The space available for the service turret was highly restricted by the need to minimize the cutout in the iron yoke and by severe height limitations. The service turret provides the following functions:

- Supply and control of LHe
- A 150 liter helium storage volume
- Supply and control of 70 K helium gas for cooling the radiation screens
- 3 kA current leads from 300 K
- Instrumentation connections to the coil and radiation screens

Design delays meant that connections to the refrigerator were finalized after the service turret was already in manufacturing. This, combined with the lack of space, necessitated the addition of a separate valve box. This box was designed to be mounted on top of the iron yoke and contains several valves to facilitate a safe and easy connection to the refrigerator.

3.1.4 Power Supply and Control Instrumentation

Initially, a thyristor-controlled switch-mode power supply was planned. However, due to concerns about electromagnetic interference (EMI) with the experimental detectors, a series-regulated supply designed for low EMI was provided instead. The control and instrumentation system is subdivided as shown in Table 3.4. The system features distributed control with centralized monitoring via LabVIEW.

Table 3.4: Power Supply and Control Instrumentation.

Overall control + monitoring	LabVIEW running on a Pentium PC
Temperature measurement	Oxford Instruments ITC-600
Helium valve control	Weka valve controlled by LabVIEW driver
Current leads control	Northvale Korting Bossmatic valve controlled by a separate P&ID controller

3.2 Magnet Maintenance and Revamping Options

The KLOE magnet was operational at LNF until December 2018. From a fluidics perspective, the system generally operated smoothly, with only one major unscheduled shutdown. This two-month shutdown in the summer of 2010 was caused by a helium leak from the 4.4 K line into the insulating vacuum, originating from a faulty VCR gasket that was undetectable by vacuum gauges.

From a P&ID (Piping and Instrumentation Diagram) perspective, the magnet has only three actively controlled devices:

- The Joule-Thomson valve, which maintains the LHe level in the magnet turret at its set point.
- The valve controlling the He flow through the Current Leads.
- The heaters that prevent frosting on the warm side of the Current Leads.

The replacement of all these subsystems, along with all Teflon gaskets in the cryogenic valves, is foreseen.

In recent years of operation, the power supply (PS) has shown signs of aging in some components. The cooling pipes for the transistor bank and the freewheeling diodes have developed several water leaks, and the PS control system, based on an old version of LabVIEW (3.0), requires revamping. Nevertheless, several passive components (e.g., inductors, dump resistors), high-current contactors, and the busbars—which were tailored to the overall dimensional constraints—can be reused after proper functionality tests. This option will allow for significant cost savings while guaranteeing perfect compatibility with the magnet apparatus, as the busbars connected to the PS output terminal and the overall PS dimensions and location can remain the same.

Therefore, INFN is finalizing a market survey of companies with expertise in power converters that have previously supplied power supplies with satisfactory performance to INFN. The required PS

performance specifications are the same as those of the old power converter and are summarized in Table 3.5. The new PS must accommodate several configurations to handle all potential fault scenarios, which are presented later.

3.2.1 Magnet Power Supply Overview

After discussions with several companies, a basic PS scheme has been defined, as shown in Figure 3.3. This design features three one-quadrant power converter modules (1000 A, 10 V) connected in parallel to reach a maximum current setpoint of 3000 A. The modules will operate in a master-slave configuration (one master, two slaves) and will communicate via optical fibers. This solution ensures redundancy and higher reliability in the event of a fault. Each module is connected in series with a diode to protect it from unbalanced output voltages, thereby preventing reverse energy flow between modules. During normal magnet operation, contactors T1 and T3 are closed, while T4 and T2 are open.

In the event that the magnet loses its superconducting state (a quench), the stored energy (approximately 14 MJ) must be dissipated as rapidly as possible. A loss of the superconducting state is detected by the quench detector, which triggers an energy dump circuit (OCB rundown). The energy is then dumped into a permanently connected 85 mΩ resistor (the "Dump Load"). At the nominal power supply terminal voltage, this resistor dissipates very little energy. However, when the quench signal is sent, contactor T3 opens, disconnecting the power supply from the magnet. The magnet current is now forced through the resistor, causing the voltage across the busbars to rise to about 250 V, and the current decays with a time constant of 50 s. Diode D4 ensures that no current flows through the dump resistor when the magnet is in its superconducting state.

Other, less severe failures are also managed by the power supply design. For instance, in the event of a main power failure or an internal PS failure, contactor T1 opens, and also T4 and T2 remain open. The current then flows through a stack of freewheeling diodes (D5 to D12), maintaining the magnet current path and causing the magnet to ramp down gently (FWD rundown) over approximately 20 minutes.

During a nominal ramp-up, the three modules provide a 0.6 A/s current ramp. For the ramp-down, since the PS modules are 1-quadrant, contactor T4 is closed and T1 is opened, creating a bypass around the freewheeling diodes D5 to D10. In this configuration, the current flows only through diodes D11 and D12, providing a negative voltage of −2 V and allowing a −0.6 A/s current ramp-down.

Since all freewheeling diodes are water-cooled, they are protected against overheating from a failure in the cooling water flow by contactor T2. In this scenario, T2 closes and T1 opens, de-energizing and 'crowbarring' the power supply output (CBD rundown). The magnet current then decays over a period of 2.5 hours, with the only power dissipation being due to the resistance of the magnet busbars.

3.2.2 Uninterruptible Power Supply

All relays that drive the contactors, along with the power supply control circuits, are powered by an uninterruptible power supply (UPS) built into the magnet power supply cabinet. The UPS will

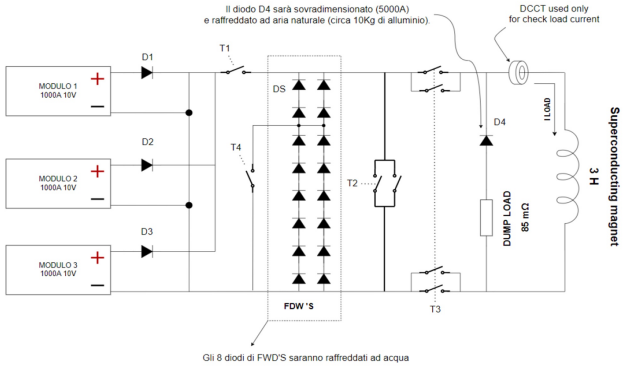


Figure 3.3: Schematic of the new power supply.

maintain power to all control circuits, including the quench detector unit mounted externally in the control rack. The UPS can power these critical circuits for more than 30 minutes, allowing a freewheel diode rundown to be completed.

In the event that the UPS fails, the quench breaker contactor T3 will open, and any residual stored energy in the magnet will be dissipated in the discharge resistor.

If a mains input power failure occurs in conjunction with a cooling water flow failure, there will still be appreciable stored energy when the UPS eventually runs out of power. This energy will then be dissipated in the discharge resistor when T3 opens upon UPS failure.

3.2.3 Control System Interfaces

The PS control system interface architecture will follow that of the old KLOE solenoid PS. The power supply receives interlocks from several external locations in addition to its internal protection interlocks. These interlocks are functionally divided into three classes:

- **Fast Energy Dump (OCB):** Forces the magnet current through the discharge resistor.
- **Freewheel Diode Rundown (FWD):** Causes the PSU to turn off and forces the current to decay through the diodes.
- **Crowbar Rundown (CBD):** Causes the magnet to run down very slowly through the busbar resistance.

All interlocks are implemented via an external contact closure, which is sensed by the magnet power supply's built-in 24 V supply, itself fed from the built-in UPS. All contacts will be connected to a board that will be rebuilt during the revamping phase. A new PLC will also be introduced and configured to manage all interlocks and perform internal PS control. Remote computer control is implemented via an Ethernet link to the main control PC; however, a local control panel and a local alarm panel are provided for front-panel operation. The UPS power is fed to the control rack, where it powers the quench detector. The quench detector sends signals back to trigger a fast energy dump if a quench is detected and to trigger a freewheeling diode rundown if the current lead voltage drop is excessive.

DRAFT

The control rack also triggers a freewheel diode rundown for several other conditions detected by the control software. The system monitors the temperature of the magnet current leads, which will initially trigger a freewheel diode rundown. If the temperature continues to rise, it will trigger a rapid energy dump. The front-panel power-off and magnet fast-energy-dump buttons can also be duplicated by two series-connected emergency buttons wired around the experimental area. The helium refrigerator can be configured to provide an interlock to trigger a freewheel diode rundown, and the power supply provides a contact closure that opens to signal that a fast energy dump is in progress, coordinating the actions of the rest of the INFN installation.

3.2.4 Busbars

The main busbars from the power supply unit to the coil terminals are items being salvaged from the old KLOE magnet. They are made of aluminum and are internally water-cooled. The ends of each busbar section are copper-plated to ensure good long-term electrical contacts, and all bolts have disk springs to maintain the clamping force. The busbars are Kapton-insulated and covered with heat-shrink sleeving for mechanical protection. The joint areas and water pipe connections are covered with an elastomer, as it is not possible to apply sleeving in these areas. Voltage taps on the busbars allow for the identification of higher-resistance sections of the busbar circuit. The expected busbar voltage drop is about 300 mV at 2963 A. At each end of the busbar run, there are flexible copper braids to ease assembly and avoid undue forces on the PSU or current lead terminals.

All connections to the PSU and to each end of the busbars are made with insulated water hoses. The nominal water flow rate is 33 liter/min, and the resistive loss in the busbars is 2.6 kW, which results in a temperature rise of 1°C in this part of the circuit. The loss of water flow is sensed by an indicator within the PSU, and appropriate action is taken to reduce the current.

3.2.5 Quench Detection

The quench detector unit monitors the voltage taps of the magnet and the associated current leads. It detects a quench by looking for small differential voltages against the background of a large common-mode voltage. All boards, wires, and quench signals will be thoroughly tested during the revamping phase, and all aged parts will be replaced. The working principle will remain the same as in the old system, where several potential taps are used for both the inner and outer coil layers. Specifically, there are two redundant potential taps at each monitored point, connected to two completely separate detector cards in the quench detector unit.

The outer layer of the coil has potential taps at the start and end of the layer. The inner layer has a potential tap at its end, as well as one part-way along the winding. Thus, four potential taps are present, defining three magnet sections of dissimilar inductances. The quench detector has a precisely adjusted resistor chain with resistance ratios identical to the inductance ratios of the magnet sections. The voltages across each section of this chain are compared to the voltages across the corresponding sections of the magnet. During ramping, the back-EMF across the coil will be proportional to the inductance; when at a steady field, all voltages will be zero. If a quench occurs, the resistive voltage of the normal zone will appear in one or two of these sections, upsetting the balance of the detector and triggering a 'magnet has quenched' signal.

DRAFT

The detector is housed in a 19-inch, 3U-high unit (Figure 3.4) and has up to eight channels (including current leads) that can withstand voltages of up to 5 kV on the magnet taps and up to 500 V across the magnet terminals during a fast discharge. It is powered by the UPS located in the power supply cabinet. Internal test voltages can be used during setup.



Figure 3.4: KLOE Magnet Diagnostic Rack. The Quench Detector (QD) is marked in red.

3.2.6 Warm-up Power Supply

The warm-up power supply can be used to drive 25 A at up to 230 V into the magnet terminals to bring it to room temperature once it is no longer superconducting. This is a small, current-controlled unit that must be wired into the circuit, and the main magnet busbar must be removed before it can be used. The warm-up power supply must always be switched off during normal operation. It is only powered up after the main magnet circuit is disconnected, which would otherwise short-circuit the warm-up power supply output through the discharge resistor.

3.2.7 Power Supply Revamped and Salvaged Parts

The power supply revamping will primarily involve the power unit, which will be completely replaced with three parallel AC/DC power modules, including their DCCTs and control units. Communication between modules will be based on the Modbus TCP/IP Ethernet interface. The input power will comply with the USA standard (208 V 3-phase at 60 Hz), while a dedicated front end will be used for tests at LNF. The new power units will replace the old transistor banks, which

have operated for a long time and are no longer serviceable due to water leakages in the cooling circuit.

Another significant intervention will be the installation of two new contactors (T1 and T4 in Figure 3.3) for disconnecting the power units from the load and for bypassing several diodes to adjust the current ramp-down during an FWD rundown or a normal 0.6 A/s ramp-down. All diodes shown in Figure 3.3 will be new and indirectly water-cooled by new aluminum plates and pipes. The warm-up and UPS power supplies will be replaced, and a new interlock board will be designed according to the old scheme to collect all signals from the diagnostic rack. A new PLC for signal management and internal control will also be installed.

The new control system will be based on LabVIEW and will have the same main functions as the previous one, which was built on LabVIEW 3.0. This task will be handled by a company with long-standing, positive experience with INFN in the field of automation. Regarding the salvaged parts, contactors T3 and T2 (Figure 3.3) will be reused after functional tests are performed by the power converter supplier. The dump resistor and all passive devices that still meet their nominal parameters will also be salvaged after testing. The original DCCT head and its electronics will be surveyed; if they are still functional, they will be used for diagnostic monitoring of the load current. If a mismatch is detected between the sum of the currents from the three power unit DCCTs and the current measured by the upstream DCCT, the control system will issue a warning.

The old busbars connected to the magnet will be salvaged, preserving the original voltage drop and avoiding changes to the PS cabinet's position and configuration. All new and revamped parts will be hosted in a cabinet with the same dimensions as the previous one. Figure 3.5 shows the current PS cabinet with its overall dimensions.

DRAFT

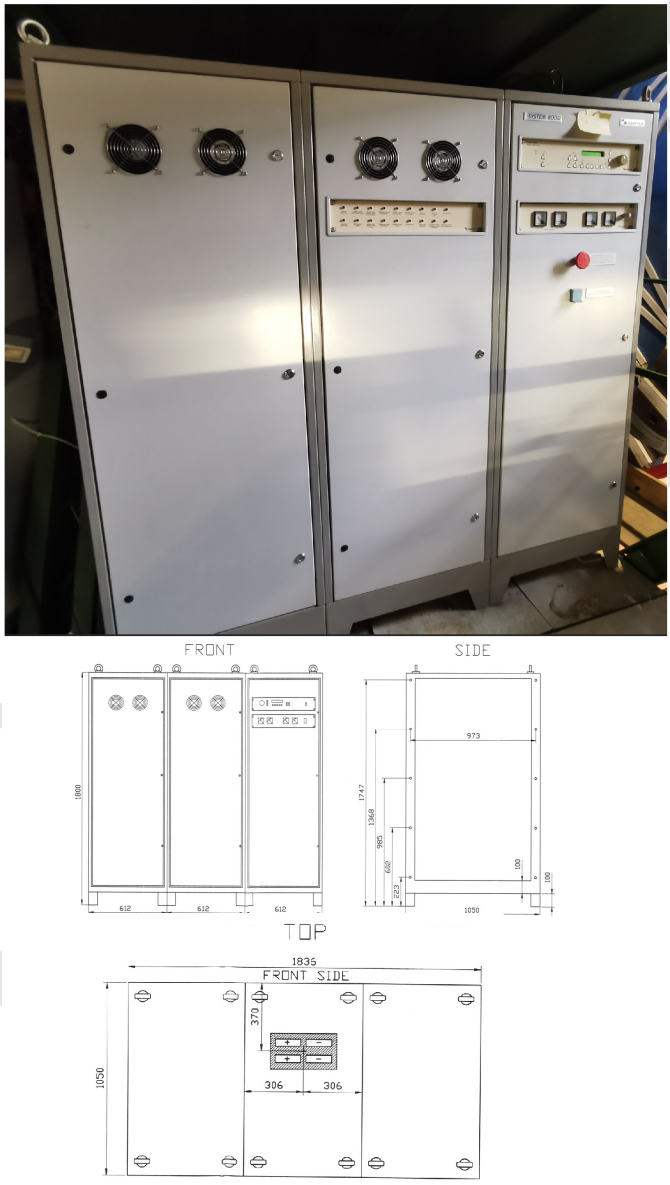


Figure 3.5: The KLOE Magnet Power Supply Cabinet (top) with its overall dimensions (bottom).

Table 3.5: Power Supply Requirements.

DC OUTPUT RATINGS	
Power Range	30 kW
Current range	3000 A
Maximum output Voltage	10 V
Nominal Ramp Rate	0.6 A/s
Output Polarity	Unipolar
STABILITY $\star$	
Short term (30 min)	$\pm$ 10 ppm
Long term (8 hours)	$\pm$ 10 ppm
WATER COOLING	
Flow Rate	18–25 l/min
Inlet Water Temperature	$25 - 32^{\circ}$C
Current setting resolution	18 Bit
Current readback resolution	16 Bit (16 ppm)
AC SUPPLY POWER	
Mains voltage	3×208 VAC $\pm 10\%$ @ 60 Hz (with 400 VAC connection for LNF Tests)

$\star$ These are nominal PS parameters; they will be improved with the 3H magnet load.

DRAFT

3.3 Activities at LNF

Before shipment, an operational test will be performed to confirm the integrity of the magnet. The activities are listed below:

1. **Warm Test:** System vacuum check, pressure test of the safety valve, leak test of pipe connections and the LHe tank, hydraulic and actuator tests for valves, and insulation tests of pressure, temperature, and LHe level sensors.

2. **Cold Test:** Cooling of the magnet from 300 K down to 4.2 K, functional testing of sensors at LHe temperature, coil insulation check, protection system check, and thermal loss measurement.

3. **Commissioning:** Commissioning of the new Power Supply and Control system.

4. **Coil Energizing:** Sensor checks, heat loss measurement at steady state, coil de-energizing, and warm-up.

5. **Final Check:** Final functionality check upon return to 300 K.

At the end of the tests, the service turret must be removed before shipment to Fermilab due to interference with the hall door. This process can be summarized as follows:

1. Disconnect the signal sensor cables (airside).

2. Remove the cylindrical shell of the vacuum case.

3. Remove the Multi-Layer Insulation (MLI).

4. Disconnect the signal sensor cables (vacuum side).

5. Disconnect the coil terminals (see Figure 3.6).

6. Cut the four cryogenic lines (see Figure 3.7).

The turret will be reconnected at Fermilab. The re-assembly procedure (to be used in reverse for removal) is described in Oxford Instrument drawing AJL0550, "Service Turret Assy KLOE," sheets 1 to 5. Due to the critical nature of this operation, INFN will award a contract to ASG Superconductors to perform the entire process of removal at LNF and reconnection at Fermilab.

These tests will be performed again at Fermilab before re-installation in the iron yoke to exclude any damage incurred during transportation.

3.3.1 Magnet Cool-Down

Two options for cooling the magnet have been investigated: reconnecting it to the Linde TCF 50 refrigerator or cooling it by direct filling with cryogenic liquids. The evaluation for each option is

DRAFT

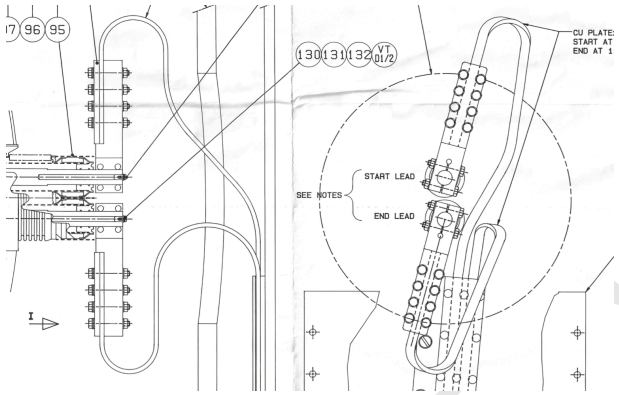


Figure 3.6: Detail of the KLOE coil lead clamps.

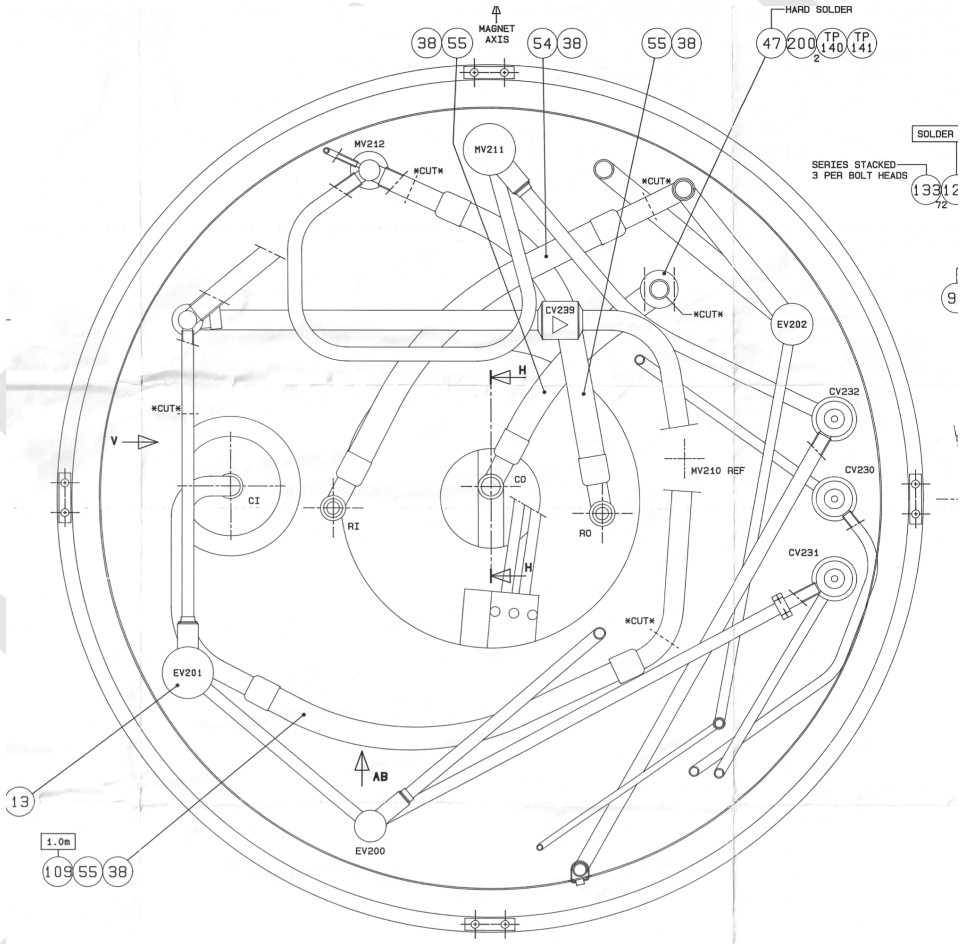


Figure 3.7: Location of pipe cuts for service turret removal.

reported below.

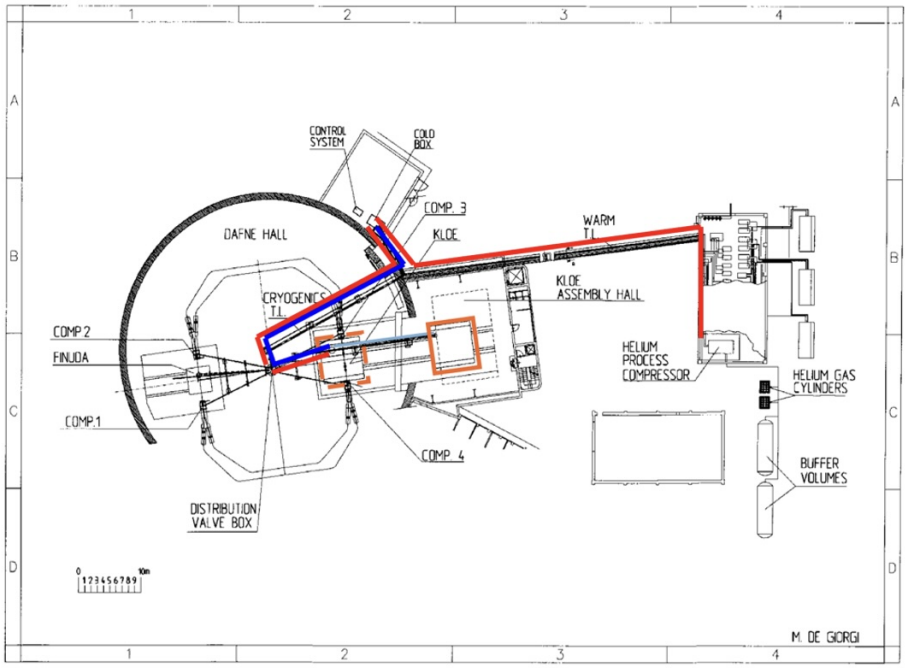


Figure 3.8: Plant layout for cooling the KLOE magnet with the existing refrigerator.

Magnet Cooling with the Existing Refrigerator The KLOE magnet was first cooled down outside the beamline in 1997. Over the years, the transfer line (TL) extension and its support bridge have been decommissioned and will need to be procured again.

- **Pros:**
  1. A very well-known process was performed several times by Laboratori Nazionali di Frascati (LNF) personnel from 1998 to 2018.
- **Cons:**
  1. Requires non-trivial re-manufacturing and re-installation of the KLOE TL extension and bridge.
  2. Requires a full re-installation of the fluidic subsystems.
  3. Requires the cryo plant to be put back in service after 5 years for only a few weeks of operation.
  4. Most of the required hardware and services would not be useful for repeating the test in the US.

Magnet Cooling with Cryogenic Liquids The KLOE magnet was cooled down at Oxford Instruments in 1996 before shipment to Italy. The process is briefly described in [22].

- **Pros:**
  1. Requires very limited re-installation of the original fluidic subsystems; LN2 flexible TLs are already in place (with a 3000 liter LN2 tank for preliminary tests).

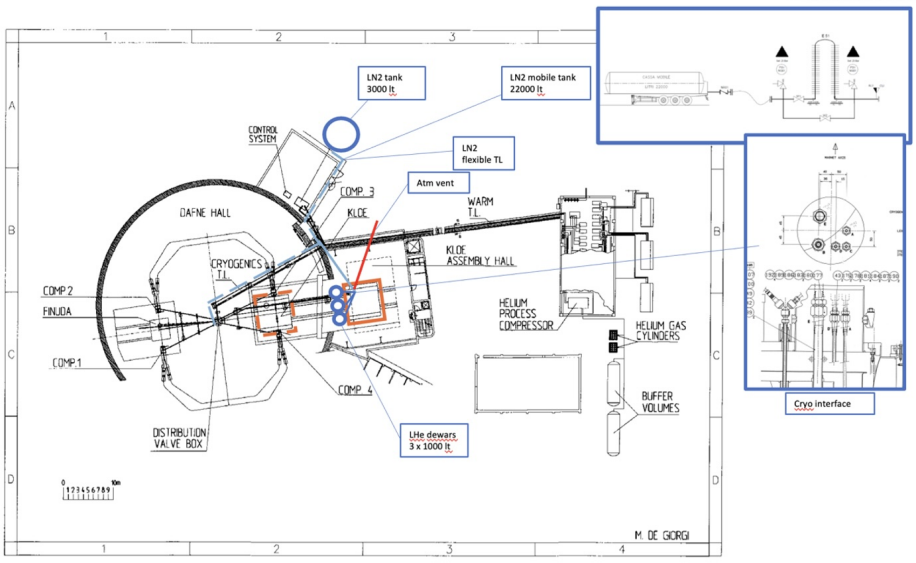


Figure 3.9: Plant layout for cooling the KLOE magnet with cryogenic liquids.

2. LHe dewars (3000 liter total) are available in-house.
3. Requires the manufacture of only non-complex cryogenic interfaces.
4. The hardware is self-contained, allowing the test to be repeated "turnkey" before magnet re-integration into the yoke at Fermilab.

- **Cons:**
  1. The process was performed only once at Oxford Instruments before 1996.
  2. Extending or repeating the test could consistently increase costs.

After careful consideration, the option of cooling the magnet with cryogenic liquids has been selected. Some services and goods have been procured, and the administrative process for other orders has been concluded.

INFN is negotiating with ASG Superconductors for support during the test activities, which is mandatory given the re-procurement of the power supply, quench detector, and control system. Support for the magnet turret removal is another critical activity that INFN has requested from ASG Superconductors.

3.3.2 Coil Cryostat Extraction

The extraction and handling of the Coil Cryostat will take place inside the KLOE experimental hall at LNF, while preparations for transport will be carried out in the yard in front of the building. The Coil Cryostat is a cylindrical structure with a 5.8 m diameter, a 4.4 m length, and a weight of approximately 40 t. It is installed inside the support structure (hereafter referred to as the "Yoke") of the KLOE apparatus. Removing it for transport to Fermilab requires a series of equipment to allow the cryostat to slide out of the Yoke, be lifted, and be positioned onto a loading platform for its exit from the assembly hall. The main equipment includes:

- The Insertion/Extraction Rails (Figure 3.10, left).
- The Handling Cradle (Figure 3.10, center).
- The Transport Cradle (Figure 3.10, right).

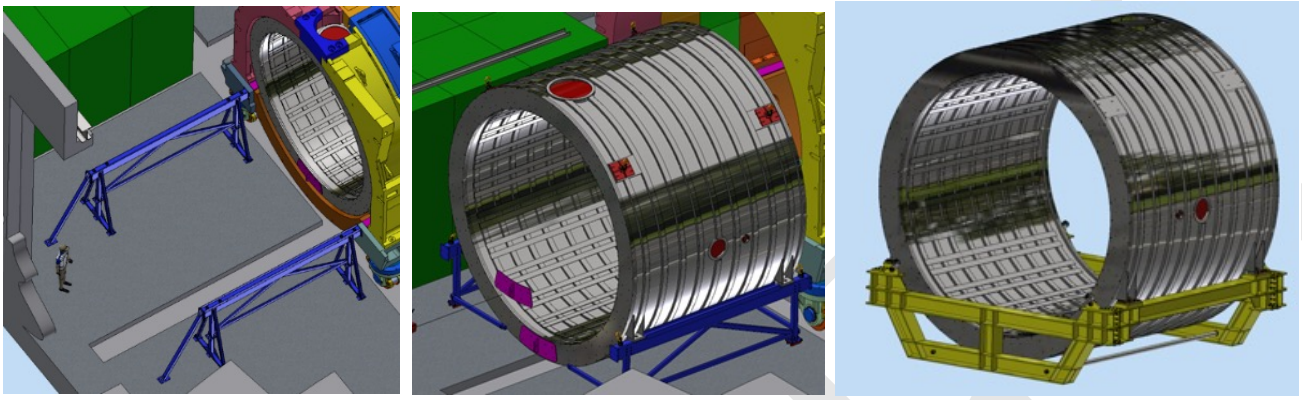


Figure 3.10: Tools for the extraction, transport, and insertion of the coil. Left: insertion/extraction rails. Center: handling cradle. Right: transport cradle.

The procedure for removing the Coil Cryostat from the KLOE apparatus can be summarized in the following steps:

1. Prepare the work area.
2. Assemble the extraction/insertion rails.
3. Assemble the pulling system (Tirfor© System).
4. Extract the Coil Cryostat from the Yoke.
5. Lift and move the Coil Cryostat to a temporary parking area.
6. Assemble the loading platform and rails.
7. Lift and move the Coil Cryostat onto the loading platform.
8. Move the Coil Cryostat outside the KLOE hall.
9. Transfer the Coil Cryostat into the Transport Cradle.
10. Load the Coil Cryostat onto the truck.

To extract the Coil Cryostat from the Yoke, two rails must be installed on which the cryostat can slide while being pulled by a mechanical system. For safety, to prevent uncontrolled sliding, it will be restrained on the opposite side by a similar mechanical system. As soon as the cryostat is completely extracted, four lifting points will be installed. The cryostat will be connected to the overhead crane, lifted to allow the removal of the roller skids, placed back on the rails, and secured to them. The cryostat and rails will then be lifted to remove the leg extensions that support the

DRAFT

rails. Bracing bars will be installed, and the cryostat with the Handling Cradle will be repositioned on the floor.

Since the space between the overhead crane hook and the lifting points is insufficient to lift the cryostat directly onto the loading platform, the crane slings will be attached to the Handling Cradle. The assembly will be moved inside the hall to facilitate the installation of the loading platform, which was previously removed. Once the platform is ready, the cryostat will be moved onto it and taken out of the hall by sliding it on special rails. Outside, the cryostat will be placed into the Transport Cradle using two mobile cranes and loaded onto the truck.

3.3.3 Dismounting of the Iron Yoke

The iron yoke of the KLOE magnet has a total weight of 600 t. It is composed of 32 pieces, the heaviest of which weighs 20 t.

A specialized company in large mechanical assemblies, which originally mounted the yoke for the KLOE experiment in 1997, will be contracted to dismount it at LNF. This work, coordinated by INFN personnel, includes the ancillary operations needed for the extraction of the coil cryostat. The same company will re-mount the yoke and coil at Fermilab once it is ready to be installed in the ND Hall, according to the project schedule.

3.3.4 Tools, Packaging, and Shipping to FNAL

The main tools necessary to complete the extraction, handling, and transportation of the Coil Cryostat are listed in Table 3.6.

The Coil Cryostat, protected by a waterproof cover, will be transported by land to a suitable port near LNF and then loaded onto a specially equipped ship. Unloading the cryostat from the truck and loading it onto the ship will be performed using a mobile crane. The insertion/extraction system and lifting points will be shipped to Fermilab along with the Coil Cryostat and the Transport Cradle. Refer to Section 4.8.1 for details regarding the shipping of all KLOE elements.

3.4 Installation and Integration at FNAL

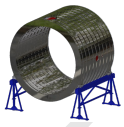
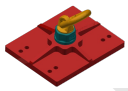
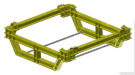
The KLOE magnet is provided with a 180 liter LHe reservoir intended to limit its temperature below 20 K in the event of a quench; therefore, it must comply with Fermilab internal regulations. Cryogenic tanks at Fermilab must be designed, fabricated, tested, and operated according to the Fermilab internal standard 'FESHM 5031: PRESSURE VESSELS'.

Since the magnet was built almost 30 years ago—posing issues regarding different design and manufacturing standards and a lack of records such as material certificates and test reports—point 4 of the procedure, "Exceptional Vessels / Director's Exception," shall be applied. The exceptional vessels process requires the approval of the Laboratory Director or their designee. An Extended Engineering Note shall be prepared, including the following information:

a. **Reason for Exception:** The Division/Section/Project Head or designee shall provide justifi-

DRAFT

Table 3.6: Tools for handling the Coil Cryostat.

Tool	Description	Purpose
	Elevating platform (H = 10 m)	Assembly of lifting lugs and slings
	Overhead crane and related accessories (ropes, eyebolts, etc.)	Handling of coil cryostat and heavy materials
	Various tools	Assembly
	Tirfor©	Extraction/insertion of coil cryostat
	Forklift	Extraction/insertion of coil cryostat
	Extraction/insertion tools	Extraction/insertion of coil cryostat
	Lugs	Handling of coil cryostat
	Trolley	Handling of coil cryostat
	Cradle	Transport of coil cryostat
	Mobile crane	Handling of coil cryostat
	Pallet jack	Handling of components

DRAFT

cation.

b. **Analysis/Burst Test:** For exceptions based on stresses above code-allowable limits, the system designer shall provide a stress analysis of all exceptional parts of the vessel, including data, formulas, or test results that demonstrate the anticipated safety factor. Alternatively, burst test data from samples demonstrating the safety factor may be provided. If the relief system does not conform to the ASME BPVC, calculations or test results must demonstrate that the venting system capacity exceeds the maximum required flow rate.

c. **Fabrication:** The system designer shall provide a fabrication procedure, a list of planned and completed inspections, and any other quality control procedures, including weld or braze procedure specifications and qualification records.

d. **Hazard Analysis:** The system designer shall provide a description of personnel hazards associated with vessel operation and the methods used for protection. This analysis shall address the vessel's application, operating limits, controls, possible effects in the event of failure, and inherent safeguards.

e. **Pressure Test:** A pressure test shall be performed in accordance with Chapter 5034 of the Fermilab ES&H Manual.

f. The division/section/project head or designee shall provide a written record of the decisions, judgments, tests, administrative controls, and hazard analyzes necessary to approve this type of vessel.

3.4.1 Storage at FNAL

The Coil Cryostat must be stored inside a building, while the tools can be stored outdoors if they are adequately protected from environmental degradation.

The magnet (cryostat with the superconducting coil inside) will be stored in a suitably sized building that can provide the necessary environmental conditions. The detector components located inside the magnetic volume will be installed in the same storage site. The resulting assembly will then be moved to the DUNE-ND experimental hall for final installation.

3.4.2 Tools and Mounting Procedure

The Coil Cryostat will be installed at Fermilab in the SAND experimental apparatus. The same equipment used for extraction at LNF will be employed. The installation procedure will follow the reverse of the extraction process:

1. Prepare the work area.

2. Assemble the insertion rails.

3. Assemble the pulling system (Tirfor© System).

4. Move the Coil Cryostat into the SAND assembly hall.

5. Transfer the Coil Cryostat from the Transport Cradle to the insertion rails.

6. Insert the Coil Cryostat into the Yoke.

7. Remove the insertion rails.

3.4.3 Cryogenic Refrigeration Plant for Continuous Operation

The procurement of a new refrigeration plant to be installed at Fermilab is under investigation. The most natural course of action is to consult Linde, the provider of the TCF 50 refrigerator that has reliably supplied the KLOE magnet for almost 20 years.

The company has been contacted and has stated that the TCF 50 is no longer in their catalog. They have provided a preliminary offer for a plant with reduced cryogenic power, as the cryogenic load in DUNE will be lower than that required by DAΦNE [23, 24], and the compensator magnets will not be present.

3.5 Risk Management

The topics covered in Section 4.9 regarding the risks of dismantling, shipping, and reassembling the KLOE detector are not repeated here. However, it is necessary to stress that the risk analyzes primarily focus on the possible damage occurring during transport from LNF to Fermilab. Furthermore, it should be noted that the magnet was transported from Great Britain, where it was built, to LNF by truck and ship (via the Atlantic Ocean and the Mediterranean Sea) without suffering any damage.

3.5.1 Detailed Risk Analysis

1. **Event: Leak (fissure) in the magnet cryostat**

   - **Possible Causes:** Shock, impact, or vibrations occurring during transport.
   - **Possible Consequences:** Inoperability of the magnet. Locating and repairing the leak requires access to the cryostat surface. If detected during commissioning, this would require partial disassembly of the yoke and potentially the extraction of the magnet, as well as the removal of internal detector components. These operations cannot take place in the alcove. The estimated time ranges from 6 months (un-cabling, moving to the cavern, partial yoke disassembly, leak localization and repair, re-assembly, re-cabling) to 12 months (including magnet removal, detector component extraction, and re-insertion). This would occupy the main cavern space for 3 to 9 months, interfering with other ND activities.
   - **Estimated Probability:** Moderate, 2% to 5% (based on long-distance transport statistics).
   - **Detection:** Visual inspection and review of accelerometer recordings upon delivery to Fermilab. Vacuum pumping of the cryostat and helium leak checking.

DRAFT

- **Intervention:** Seal the leak(s) by welding and re-test the vacuum tightness.
- **Mitigation:** Detailed transport engineering with shock and vibration analysis, definition of maximum accelerations and road speeds, and specification of supports and shock absorbers. Transport with online shock logging and periodic checkpoints. Use of a carrier with the highest reliability for special transports. Early detection via inspection and vacuum tightness tests upon arrival at Fermilab and before the installation of internal detector components.

2. **Event: Leak in the internal cooling circuit**

- **Possible Causes:** A loose connection on an internal interface inside the turret. Shock, impact, or vibrations during transport can cause cracks in the piping.
- **Possible Consequences:** Loss of the cryostat's insulating vacuum and inoperability of the magnet. Locating the leak requires access to the turret, which necessitates partial disassembly of the yoke. If the leak is on an internal interface, repair may only require turret access. If it is regarding the heat exchangers inside the cryostat, repair would require opening the cryostat and extracting the internal coil and radiation shields. This is a major undertaking that would likely require transferring the magnet to an external company. The estimated time ranges from 6 months to 24 months (including transfer to an external company). The occupation of the main cavern would be 3 to 9 months.
- **Estimated Probability:** Moderate for leaks at internal interfaces ($\sim 5\%$). Very low for leaks in the radiation shields.
- **Detection:** Visual inspection and review of accelerometer recordings upon delivery. Monitor the cryostat vacuum level while injecting helium into the cooling circuit.
- **Intervention:** Seal the leak by tightening or replacing the connections inside the turret. If the leak is elsewhere, it should be repaired by an external company. Re-test the tightness at room temperature before re-installation.
- **Mitigation:** Detailed transport engineering, as described above. Early detection is achieved by flowing nitrogen and then helium into the circuit and cooling to LN2 or LHe temperatures after delivery to Fermilab and before installing the internal detector components.

3. **Event: Break or short in the superconducting coil**

- **Possible Causes:** A loose connection on an internal interface inside the turret. Shock, impact, or vibrations during transport can cause the deformation or breakage of the coil.
- **Possible Consequences:** Inoperability of the magnet. If the break/short is on the coil itself, repair would require opening the cryostat and would likely need to be performed by an external company. This is a major event. The estimated time for operations ranges from 6 months to 30 months (including repair or substitution by an external company). The occupation of the main cavern would last 3 to 9 months.
- **Estimated Probability:** Moderate for a loose connection at internal interfaces ($\sim 2\%$). Very low for a coil break/short.

- **Detection:** Visual inspection and review of accelerometer recordings upon delivery. Monitor the current flow in the coil.
- **Intervention:** Check and adjust the connections inside the turret. If the break is in the coil, it should be repaired or replaced by an external company. Re-test the coil before delivery and again at Fermilab prior to installing the internal detector components.
- **Mitigation:** Detailed transport engineering, as described above. Early detection can be achieved by operating the magnet in superconducting mode at low current after delivery to Fermilab and before installing the internal detector components.

4. **Event: Malfunction or break of the main power supply (new equipment)**

- **Possible Causes:** Infancy defect, transport damage, or over-voltages from the power grid.
- **Possible Consequences:** Inoperability of the magnet. A stop in commissioning for repair/substitution. As the power supply is a custom product, replacement could take 8 to 12 months.
- **Estimated Probability:** Moderate ($\sim 2\%$).
- **Detection:** Operate the unit and monitor the output current, paying close attention to the current setpoint, stability, and ramp. Test all PS fault scenarios (quench, power grid failure, etc.).
- **Intervention:** Remove the unit, assess the problem in the lab, and define the required repair or substitution.
- **Mitigation:** Early detection by stress-testing the power supply in the lab before installation and during Factory Acceptance Tests (FAT) at the supplier's premises.

5. **Event: Issue with service cryogenic equipment (cryo box, valve box, interfaces, cryo controls)**

- **Possible Causes:** Infancy defects or transport damage.
- **Possible Consequences:** Inoperability of the magnet. A stop in commissioning for the time required for repairs, substitutions, or modifications could take several months if component rebuilding is required.
- **Estimated Probability:** Moderate (2% to 5%).
- **Detection:** Operate the unit and monitor its behavior through the control system.
- **Intervention:** Assess the problem in the lab and define the required repair, substitution, or modification.
- **Mitigation:** Early detection through the pre-commissioning of the plant.

3.6 Schedule and Milestones

The schedule for the magnet dismounting and shipping is summarized in Figure **??**.

DRAFT

Chapter 4

Lead/Scintillating-Fiber Calorimeter (ECAL)

The design and performance of the electromagnetic calorimeter K-LOng Experiment (KLOE) (electromagnetic calorimeter (ECAL)) are presented in this section, together with all studies and tests carried out to operate it within SAND. The ECAL is a lead–scintillating fiber sampling calorimeter. Scintillating fibers provide high light transmission over several meters and subnanosecond timing resolution. The geometry of ECAL also ensures very good hermeticity.

4.1 Design and Structure

The KLOE ECAL [3] is a fine sampling lead-scintillating calorimeter with photomultiplier tube (PMT) readout. The central part (barrel) approximating a cylindrical shell of 4 m inner diameter, 4.3 m active length and 23 cm thickness ($\sim 15\ X_0$), consists of 24 modules with trapezoidal cross section and fibers running parallel to the cylinder axis. Two endcaps hermetically close the barrel. Each of them consists of 32 "C" shaped modules arranged vertically along the chords of the circle inscribed in the barrel (see Figure 4.1). In the endcap modules, fibers run perpendicular to the cylinder axis, therefore, for the entire ECAL, the fibers are mostly transverse to the particle trajectories.

The modules are read on both sides through optically coupled Plexiglas light guides to a fine mesh PMTs. The readout granularity is $\sim 4.4 \times 4.4\,\mathrm{cm}^2$, corresponding to the dimensions of the basic elements of each module, called cells, arranged in five layers. Each barrel module has 60 channels per side, while endcap modules have 10, 15, or 30 channels per side, depending on their width. The total number of readout channels is 4880, corresponding to a total of 2440 cells which are read out at both ends. Both in the barrel and in the endcaps, PMT axes are almost parallel to the magnetic field to decrease the field effects on PMT response and to increase hermeticity (see Figure 4.1).

The basic calorimeter structure consists of an alternating stack of 1 mm scintillating fiber layers glued between thin, grooved lead foils, obtained by passing 0.5 mm thick lead foils through rollers of the appropriate shape. The grooves on the two sides of each foil are displaced half a pitch, so that fibers are located at the corners of adjacent, quasi-equilateral triangles, resulting in an optimal

DRAFT

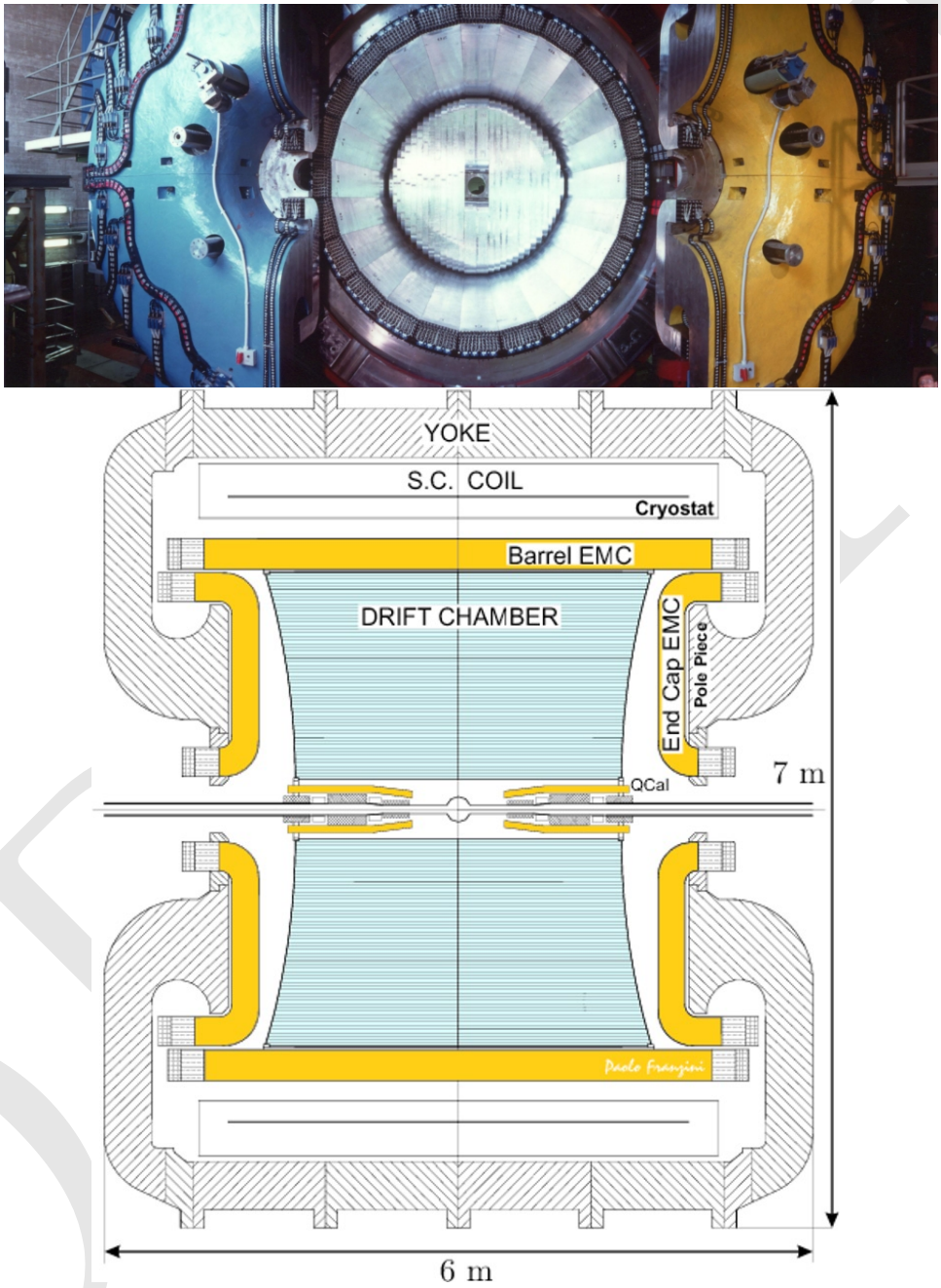


Figure 4.1: Picture of the KLOE ECAL and magnet (top) and KLOE detector cross section (bottom).

and uniform arrangement of fibers in the stack. The final composite has a fiber : lead : glue volume ratio of approximately 48 : 42 : 10, a density of $\sim 5\,\mathrm{g/cm^3}$, and a radiation length X_0 of $\sim 1.6\,\mathrm{cm}$. Furthermore, it is self-supporting and can be easily machined. The efficiency for low-energy photons is high because of the very small lead foil thickness ($< 0.1\ X_0$).

4.1.1 Scintillating Fibers

Two types of fibers (Kuraray SCSF-813 and Pol.Hi.Tech. 0046) with a total length of 15,000 km have been used to assemble the ECAL. The former has higher light output and a longer attenuation length; the latter is less expensive. The performance differences are not significant, and the Kuraray fibers are used in the inner half of the calorimeter. All fibers have an attenuation length between 3 and 5 m and produce ~ 1 PE for 1 mm of crossed fiber at a distance of 2 m from a PMT. The emitted light is in the blue-green region ($\lambda_{peak} \sim 460\,\mathrm{nm}$).

4.1.2 Photomultiplier Tubes

The light guides matching the module end faces to the photo-tube windows begin with a mixing section and terminate with a Winston cone [25], passing from an approximately square to a circular area with a concentration factor of ~ 4 (see Figure 4.2).

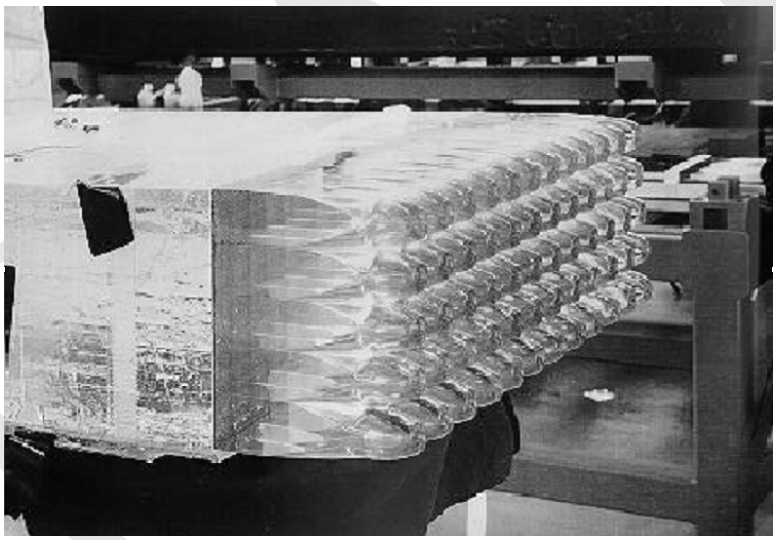


Figure 4.2: Light guides at one end of a KLOE ECAL barrel module before PMT installation.

The PMTs must operate in a magnetic field with suitable efficiency, linearity, timing resolution, and dynamic range. The Hamamatsu R5946/01 1.5" tubes [26] have been chosen because the electron multiplication occurs between dynodes made of fine mesh, very close to each other. Then, the effect of the magnetic field on the electron path is very small. The field intensity at the PMT location is less than 0.2 T, and the PMT alignment is such that the component transverse to the tube axis is less than 0.07 T. Measurements show that the PMT gain decreases by 10% when the field is on, but linearity and resolution are not affected.

The PMTs are operated with grounded cathodes in order to eliminate leakage, a possible origin of noise and field distortions. A thin aluminum cylinder holds each PMT mechanically in place,

and a spring pushes it gently against the light guide. Bicron optical gel BC-630 forms the optical contact between the PMT and the light guide.

Each PMT is connected to a base that hosts the high-voltage divider and a preamplifier (see Figure 4.3). The PMT-base has low noise, high bandwidth, and a high output dynamic range in order to avoid distortion of the fast pulses from the PMT. The cables carrying high and low voltage, a test pulse, and the output signal are connected to the PMT-base through its rear connector.

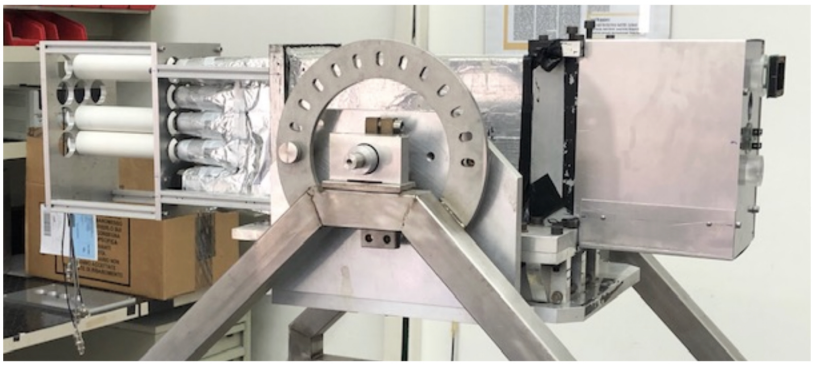


Figure 4.3: KLOE PMT-base.

4.1.3 SiPMs as Possible Spares for PMT

The silicon photomultipliers (SiPMs) work efficiently in a range compatible with the typical wavelength-shifted light of the scintillating fibers and are insensitive to magnetic fields, unlike PMTs. In addition, since SiPMs operate at low voltage, the high voltage power supply would no longer be required, providing convenience in compactness and cost. Therefore, the substitution of SiPMs for PMTs in the SAND ECAL, with a possible improvement in efficiency and timing resolution, has been investigated [27]. The SiPMs used in this test are the 4×4 arrays of the Hamamatsu S13361-3050 series. Anyway, it is excluded to substitute the single PMT channel with 16 readout channels. Thus, in the measurements, the SiPM array is considered a unique element. The MPPC series has been chosen since it achieves the maximum Photo-Detection Efficiency (PDE_{MAX}) close to the peak wavelength of the scintillating fibers (typically $\mathrm{PDE}_{MAX} = 40\%$ at $\lambda = 450\,\mathrm{nm}$), while the quantum efficiency of the Hamamatsu R5946 1.5-inch mesh photomultiplier is 23% at $\lambda = 390\,\mathrm{nm}$. A block ($24.5 \times 13.5 \times 40\,\mathrm{cm}^3$) of the lead-scintillating fiber calorimeter has been equipped (Figure 4.4, left) with light guides like those in KLOE. These light guides are shaped to cover the PMT surface and are not optimal for the smaller SiPM surface. Excluding the option to remove the present light guides and the mounting of new ones in the calorimeter have been performed by gluing a small adapter onto the light guide to optimize the coupling with the SiPM (Figure 4.4, right).

Signals induced by cosmic-ray muons have been collected on one side by SiPMs and on the opposite side by standard KLOE PMTs. This setup allowed for a direct comparison of the different performances. The measurements were performed for two SiPMs and two PMTs. The average



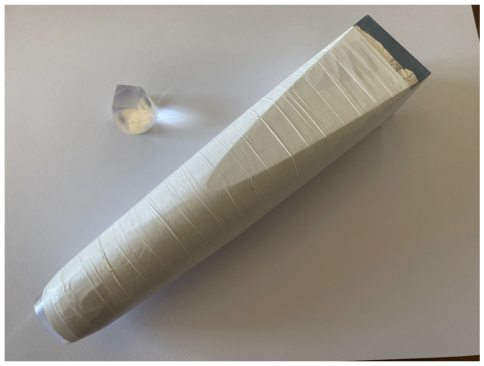


Figure 4.4: Left: experimental setup to compare PMT and SiPM. The SiPMs are on the right, the calorimeter block is at the center, the PMTs are on the left. Right: light guide and adapter for SiPM.

results for efficiency and timing resolution in these conditions are reported in Table 4.1. Even if the differences are small, PMTs performs better in the present setup. The difficulties in coupling SiPMs with the light guides without deep mechanical changes, the lack of improvement, the cost, and the necessary commissioning time advise against the substitution of 4880 available and tested PMTs with new SiPMs. Nevertheless, the results from this study do not exclude the use of SiPMs as replacements for failed PMTs. A mechanical setup is under study.

Table 4.1: Comparison of SiPM performance with PMT ones.

	Efficiency (%)	Time Resolution (ps)
PMT	91.6 ± 0.2	197 ± 4
SiPM	90.8 ± 0.3	240 ± 3

4.2 Performance in the KLOE Experiment

In KLOE the signal from the PMT is split three ways. One split signal is used for analog sums for triggering purposes. Two split signals are sent to analog-to-digital converter (ADC) and Time-to-Digital Converter (TDC) boards after discrimination [3]. The TDC signal is delayed by a monostable, while a continuous sampling technique is used for the ADC. The ADC is coupled to an analog integrator, and the signal from the integrator is sampled every 450 ns by two sample and hold circuits. After the trigger, a third sampling of the integrator is performed, and the value of the buffered signal is subtracted to compute the signal charge. A calibration and equalization of the response of the calorimeter have been performed with cosmic rays by selecting minimum ionizing particles (MIPs) and measuring the peak of the energy released at the center of the calorimeter for each calorimeter channel. The accuracy of MIPs determination is typically 1%. By adjusting the PMT high voltages, the entire calorimeter is equalized to a 5% level. In KLOE, run-by-run PMT relative gain variations (a typical run lasted about one hour) are corrected by recalibrating each cell response using Bhabha scattering events ($e^+e^- \to e^+e^-$), copiously produced at the DAΦNE collider [28]. The absolute energy scale is set run by run using $e^+e^- \to \gamma\gamma$ events with photons of energy 510 MeV. The mean time of each cell is obtained from the measured times t^A, t^B at both

ends as

$$t = \frac{t^A - t_0^A}{2} + \frac{t^B - t_0^B}{2} - \frac{L}{2v} - t_0^G \tag{4.1}$$

where t_0^A, t_0^B are the time offsets for each channel, v is the light velocity in the fiber, L is the calorimeter cell length, and t_0^G is an overall time offset related to the trigger start time. Using cosmic ray events, the $t^A - t^B$ difference distribution is measured. The mean value of this distribution is used to set the difference $t_0^A - t_0^B$, while the width is used to determine v.

The position of the impinging particle along the fibers (conventionally the z-coordinate in the KLOE reference system) is determined using the relation:

$$z = \left(\frac{t^A - t_0^A}{2} - \frac{t^B - t_0^B}{2} \right) v \tag{4.2}$$

The previous determination of $t_0^A - t_0^B$ allows for the reconstruction of the longitudinal position z. This information is used in cosmic ray analysis to associate the energy deposit in the fibers with a cosmic ray track in the KLOE drift chamber. The cosmic rays selected in this way are used to inter-calibrate t_0^A and t_0^B among the cells, imposing that the difference in time between two cells is the expected propagation time of the cosmic ray. Finer calibrations were performed run by run using $e^+e^- \to \gamma\gamma$ events. With this sample, the time offset t_0^A, t_0^B of the hit cells is calibrated by imposing $t - r/c = 0$, where r is the photon path length and t is its reconstructed time.

The trigger formation time has a spread of a few tens of nanoseconds. In order to avoid a worsening of the time resolution, the trigger signal is phase locked with the RF signal. The event time is therefore discretized according to the bunch crossings. The delay due to the cable length shifts the time of flight (ToF) by a constant quantity. This shift is determined from the position of the largest peak of the $t - r/c$ distribution for $e^+e^- \to \gamma\gamma$ events. The association of an event to the correct bunch crossing is performed off-line and depends on the event topology, where the bunch crossing time spacing is 2.7 ns. For example, in events with prompt photons, the correct bunch is easily determined by imposing the $t - r/c = 0$ constraint. On the other hand, for $K_S \to \pi^+\pi^-$ events, the bunch crossing is determined by requiring $t - l/v_\pi = 0$, where l is the pion track length and v_π is the pion velocity determined by the measurement of its momentum in the KLOE Drift Chamber. Cells close in space and time are grouped into energy clusters. The cluster energy E is the sum of the cell energies; the cluster time and position are energy-weighted averages.

The efficiency has been evaluated with different data samples (see Figure 4.5): $e^+e^- \to e^+e^-\gamma$, $\phi \to \pi^+\pi^-\pi^0$, and $K_L \to \pi^+\pi^-\pi^0$. In the first case, selected events require two tracks and zero missing mass; in the other cases, two tracks and one neutral cluster (i.e., a cluster not connected to a track) are required. The position of the second cluster is evaluated by missing momentum from the photon direction and pion momenta. For energies larger than 100 MeV, a constant value of more than 98% is observed. The loss in efficiency below 100 MeV is mainly due to ADC and TDC thresholds and the clustering algorithm.

The time resolution has been evaluated using $\phi \to \eta\gamma$, $\phi \to \pi^0\gamma$, $e^+e^- \to e^+e^-\gamma$ events (see Figure 4.6). The resolution is evaluated from the standard deviation of the $t - r/c$ distribution, yielding:

$$\sigma_t = \frac{54\,\text{ps}}{\sqrt{E(GeV)}} \oplus 140\,\text{ps} \tag{4.3}$$

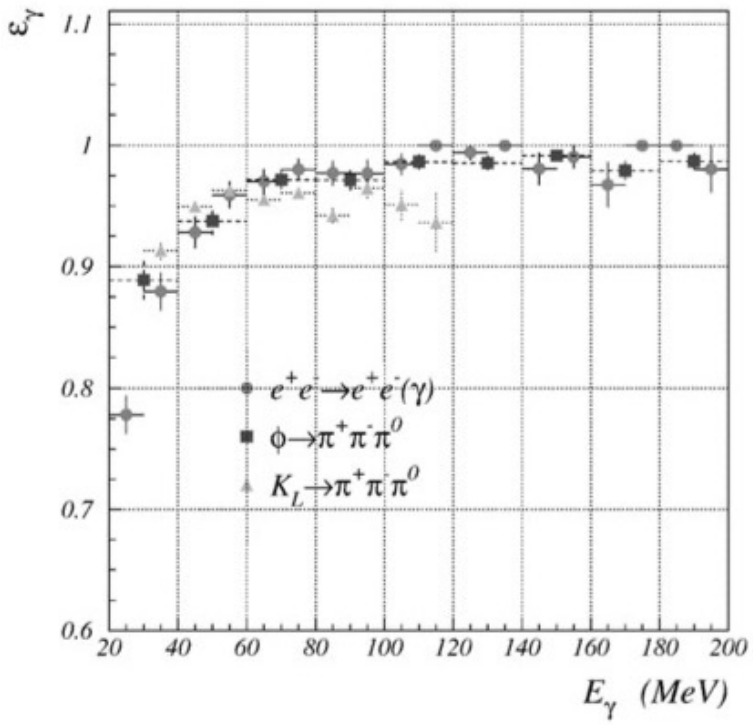


Figure 4.5: KLOE ECAL photon efficiency vs energy.

The constant term of 140 ps is due to residual detector miscalibration of $\mathcal{O}(100\,\text{ps})$, the time jitter of the RF coincidence, and the uncertainty on the interaction point position due to the finite length of the bunches.

Cluster positions are measured with a resolution of 1.3 cm in the coordinate transverse to the fibers and with a resolution of $1.2\,\text{cm}/\sqrt{E(GeV)}$ in the longitudinal coordinate, using time differences (Eq. 4.2).

The energy response and resolution are studied using $e^+e^- \to e^+e^-\gamma$ events. The photon energies are evaluated with high precision by the e^+e^- momenta and then compared with the reconstructed cluster energies (see Figure 4.7). The ECAL response is linear within 2% for $E_\gamma > 75\,\text{MeV}$, while a 5% deviation is observed at lower energy. The energy resolution is:

$$\frac{\sigma(E)}{E} = \frac{5.7\%}{\sqrt{E(GeV)}} \tag{4.4}$$

with a negligible contribution from the constant term in the explored range of energies relevant for KLOE.

At energies higher than $\sim 1\,\text{GeV}$, a constant term of $\sim 2\%$ added in quadrature to the stochastic term should be considered due to the longitudinal electromagnetic shower leakage, as evaluated from Refs. [29, 30] for a 15 X_0 thick calorimeter.

The time and energy resolution performance (4.3) and (4.4) of the KLOE ECAL did not show signs of worsening during the first KLOE data-taking campaign (years 2001-2006) and the second

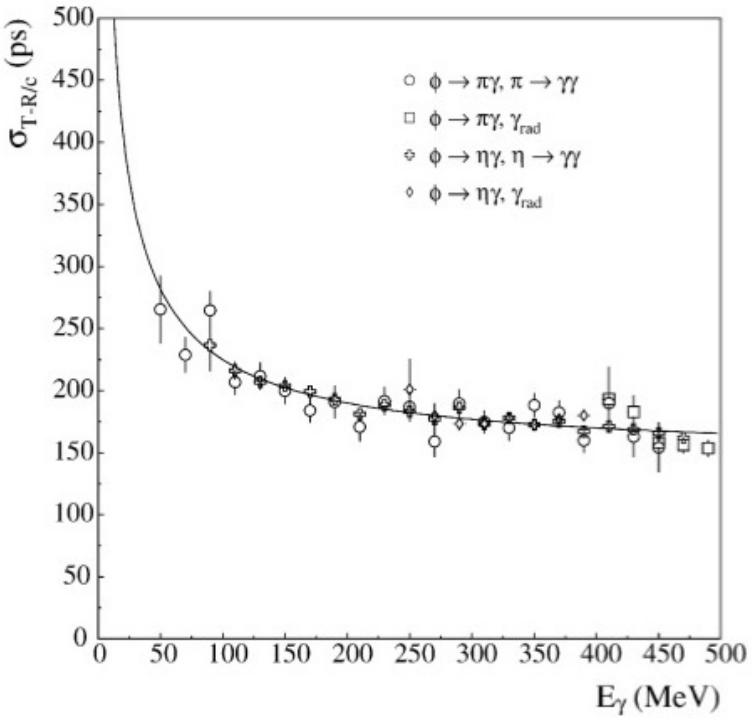


Figure 4.6: KLOE ECAL photon time resolution vs energy. The fit result $\sigma_t = 54\,\text{ps}/\sqrt{E(GeV)}$ is superimposed.

campaign for the KLOE-2 experiment (years 2014-2018). Resolutions were measured again during KLOE-2, confirming the previous results:

$$\begin{aligned} \sigma_t &= \frac{58\,\text{ps}}{\sqrt{E(GeV)}} \oplus 135\,\text{ps}, \\ \frac{\sigma(E)}{E} &= \frac{5.6\%}{\sqrt{E(GeV)}}. \end{aligned} \tag{4.5}$$

The overall detection efficiency of neutrons for a small prototype of KLOE ECAL has been measured at the neutron beam facility of the Svedberg Laboratory (TSL), Uppsala, in the kinetic energy range from 5 to 175 MeV [31].

The measurement of the neutron detection efficiency of a NE110 scintillator provided a reference calibration. At the lowest trigger threshold, the overall ECAL prototype efficiency ϵ_{calo} ranges from 40% to 50%. This value largely exceeds the estimated $8-16\,\%$ expected if the response were proportional only to the scintillator equivalent thickness (see Figure 4.8).

A detailed simulation of the calorimeter and the TSL beamline has been performed, showing an overall neutron efficiency of about 50%, when no trigger threshold is applied. The efficiency enhancement, in comparison with typical scintillator-based neutron counters, is explained by the existence of a contribution from the passive material to neutron detection efficiency in a high-sampling calorimeter configuration, as in KLOE ECAL.

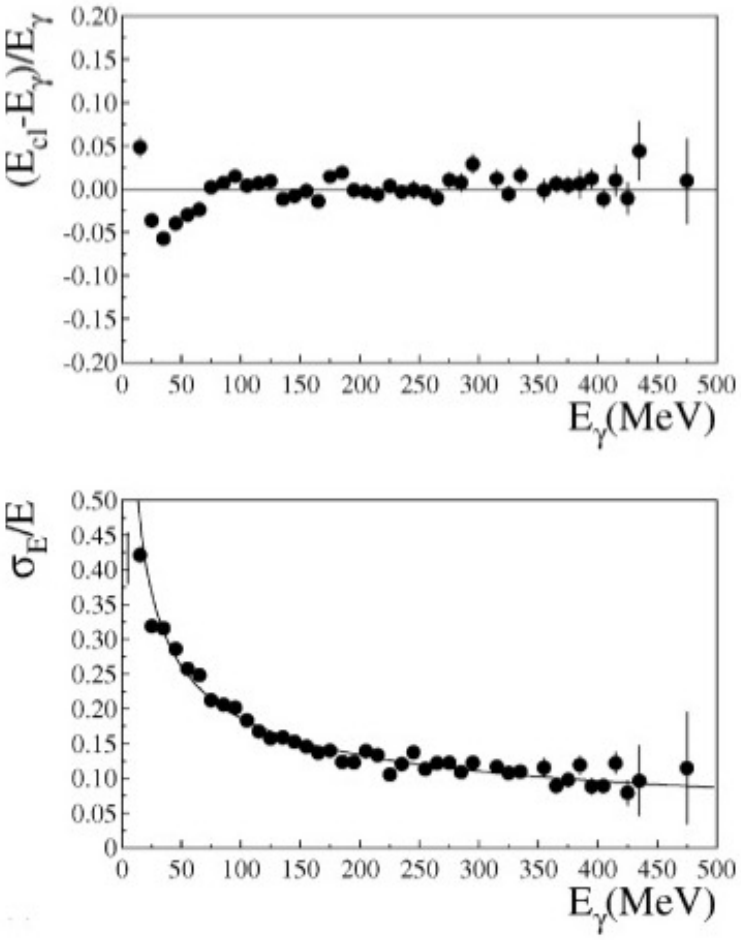


Figure 4.7: KLOE ECAL energy linearity (top) and resolution (bottom) vs energy. The fit result $\sigma(E)/E = 5.7\%/\sqrt{E(GeV)}$ is superimposed.

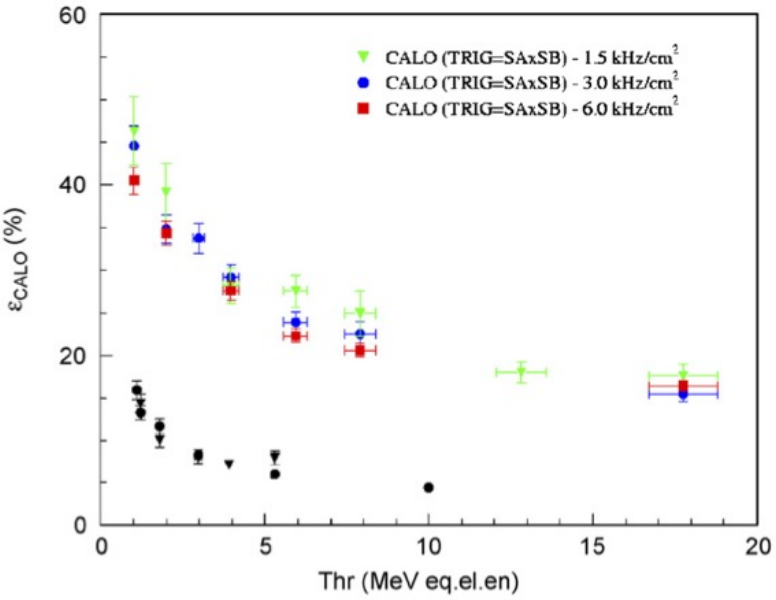


Figure 4.8: Dependence of the neutron efficiency ϵ_{calo} of the KLOE ECAL prototype on the trigger threshold. The horizontal scale is in MeV set for electron response. The scintillator efficiency measurements are reported (black points), scaled by the ratio between the two scintillator thicknesses.

4.3 Requirements for ECAL

The expected physics performance of SAND exposed to the DUNE neutrino beam has been extensively studied with a complete Monte Carlo (MC) simulation of the proposed detector [32]. For the calorimeter, the mentioned KLOE ECAL performance in terms of photon efficiency, time and energy resolutions (Eq.s 4.3 and 4.4), and efficiency to neutrons has been assumed in the simulation, and proven to be more than adequate to satisfy the requirements mentioned in Section 1.1.

The ECAL impact on the SAND event reconstruction and background rejection capabilities is important, especially for time resolution, as it affects the particle identification capabilities with the ToF technique and the detection efficiency of low-energy photons and neutrons. The energy resolution appears to be a less critical parameter, being at the level of some percent for the highest photon and electron energies of a few GeVs (with longitudinal leakage that starts becoming important for a 15 X_0 thick calorimeter, corresponding to a constant term of $\sim 2\%$ – see Section 4.2), and dominated for hadrons by large fluctuations due to the limited shower containment[1]. These fluctuations can be reduced by adding information on the event from the tracker system and by imposing kinematic constraints when possible.

In order to maintain the ECAL performance at the same level as in KLOE, special attention should be devoted to the ECAL dismounting and refurbishment operations and in re-designing the front-end electronics, as described in the following.

4.4 Calibration and Monitor System

The plan to calibrate the SAND ECAL follows the experience of many years of operation of the ECAL in the KLOE experiment, described in Section 4.2. A several-step process is envisioned:

1. Cell-by-cell response equalization and time-offset alignment with MIPs;

2. Setting the absolute energy scale at the cluster level with photons from π^0 decays and electrons from beam events;

3. Timing alignment with the rest of the SAND detector by using muons, pions, and electrons from events with reconstructed vertices in the inner tracker.

For the first step, cosmic-ray muons selected with a dedicated trigger during the period of no beam can be used as MIPs. A simulation has been performed to estimate the fraction of cosmic muons reaching the SAND hall under about 60 m of soil and rock. The rate of cosmic muons turns out to be reduced by a factor of about 100 compared to the surface. Due to this reduced rate and to the fact that the best orientation for calibration tracks is perpendicular to the ECAL module surface, a sample of almost horizontal MIPs would be very useful. Muons produced in neutrino interactions in the rocks of the ND hall and in the material in front of the ECAL, including the iron yoke of the magnet, can be exploited. A sample of 1×10^6 ν_μ events from MC, originating in the rock surrounding the ND hall, as well as in the iron yoke and in the ECAL volume itself, has

[1] The ECAL thickness corresponds to about one interaction length.

been generated. By requiring at least one muon detected in the ECAL, about 1×10^5 events are selected (see Figure 4.9).

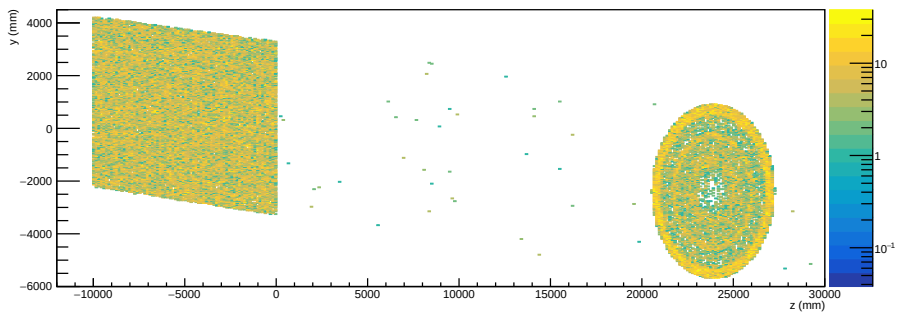


Figure 4.9: Production vertex position of the generated ν_μ events.

The distribution of the energy deposited in the ECAL cells is shown in Figure 4.10 for three different possible selections: *(i)* no selection, *(ii)* at least three hits in the same column of cells, and *(iii)* the muons cross an entire column of five aligned cells ("golden MIP" selection). The left tail of Figures 4.10 left and center is due to the muons not crossing a whole cell.

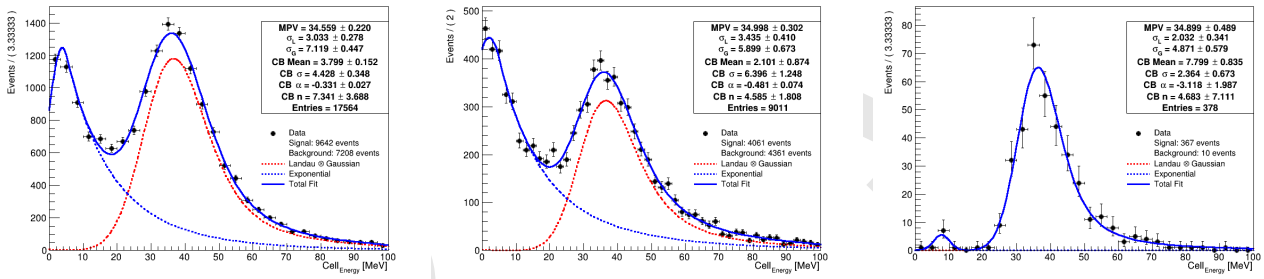


Figure 4.10: Distribution of the deposited energy in the ECAL cells for the different selections applied to a sample of MC simulated muons: no selection (left), three cells in a column (center), and "golden MIPs" *i.e.* five cells in a column (right). The fit is performed with the convolution of a Landau curve with a Gaussian and an exponential for the left tail.

The peaks of distributions such as these will provide the calibration constants for the equalization of the response of the ECAL cells. In the example of the peaks obtained for one of the most populated modules shown in Figure 4.11 is clearly visible that the energy deposited in the last layer of the ECAL is higher than in the other layers due to the different thickness.

The sample of 1×10^6 ν_μ events used for this study has been generated under the hypothesis of a 1.2 MW beam with 7.5×10^{13} POTs per spill and corresponds to about 4×10^3 spills, equivalent to about 1.3 hours data-taking; this implies that one can expect about 25 such muons per beam spill.
In Figure 4.12, the occupancy per barrel cells is shown; if no selection is applied to the muons, the barrel is almost uniformly illuminated. However, when applying the criteria *(ii)* or *(iii)*, the modules closer to the beam line are more populated. Last plot is complementary with what expected from cosmic muons.

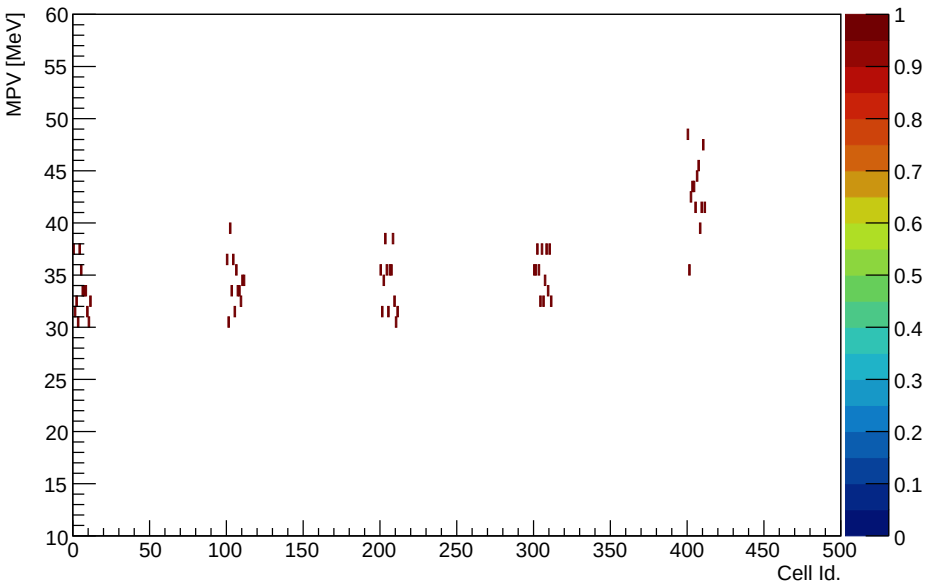


Figure 4.11: Example of MIP peaks for a barrel module close to the median horizontal plane (MC simulation).

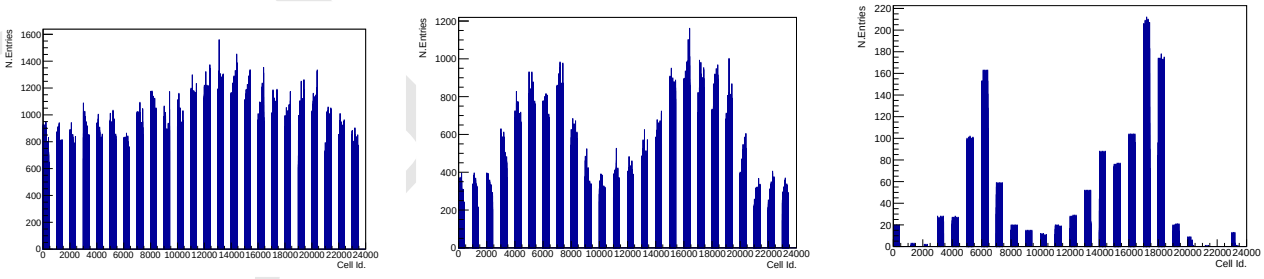


Figure 4.12: Barrel cell ccupancy for the different selections applied to simulated muons: no selection (left), three cells in a column (center), and "golden MIPs" (right). The first two digits of the Cell ID refers to the module number, ranging from zero to 23.

A large number of π^0' are produced in the neutrino interactions in the internal volume of ECAL. By exploiting the information from the vertex reconstructed with the inner tracker, the invariant mass of the two photon decay of π^0's can be used to set the absolute energy scale. Moreover, the probability for a photon to convert into an e^+e^- pair in the tracker is on the order of 30% [32]; then about 50% of the π^0's will have at least one $\gamma \to e^+e^-$. With the information on the momentum of the electrons, the energy of the photons can be reconstructed and compared to the measured one in the ECAL. The electrons themselves can be used for energy scale calibration.
There are also many electrons coming from interactions of electron neutrinos in the tracker, useful for setting the scale in a different energy range with respect to the photons from π^0's.

The time offset alignment among the ECAL cells involves determining, for each cell, the two constants $t_0^{A,B}$ of Eq. 4.1 and 4.2, or equivalently, their combinations:

$$t_0 = \frac{1}{2}\left(t_0^A + t_0^B\right) \qquad \Delta t_0 = \frac{1}{2}\left(t_0^A - t_0^B\right) \tag{4.6}$$

By exploiting the almost uniform illumination of the ECAL cells with MIPs, the $t^A - t^B$ distributions can be constructed. From a fit to a double Fermi-Dirac-like function (see Figure 4.13), the Δt_0 can be determined as the center of the distribution, while from the width, the effective velocity of light in the scintillating fibers, v, can be obtained, with the cell length L fixed.

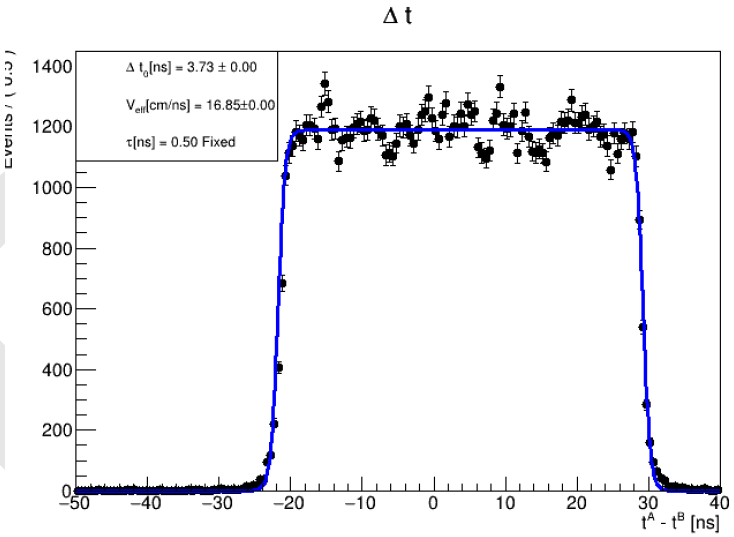


Figure 4.13: MC simulation: example of Δt_0 determination from the $t^A - t^B$ distribution.

The other set of offsets, t_0's, can be determined by selecting events with almost straight tracks (muons with high momentum) that cross the ECAL in two different regions and connect as many parts of the ECAL as possible. Both muons from cosmic rays and beam events should be used to achieve as many different track orientations as possible. A linear fit of time versus the y- or z-coordinate, at least five plus five points per each track, is performed for all the selected tracks (see Figure 4.14), and the fit residuals are used to fill the corresponding cell histograms. The centers of the residual distributions are the corrections to the t_0's. Then the calorimeter cells and clusters are reconstructed again using the new t_0's, and the whole procedure is repeated until the averages of the residuals are compatible with zero.

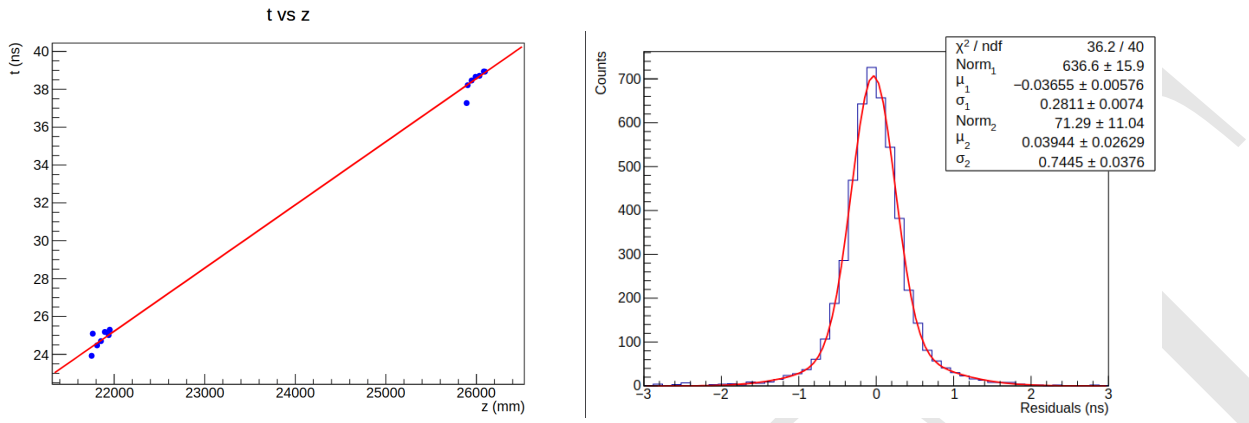


Figure 4.14: MC simulation: example of the linear fit of cell time vs.the z-coordinate (left); example of the residual distribution expected on one cell (right).

4.5 Electronics

The neutrino interactions inside the System for on-Axis Neutrino Detection (SAND) detector must be identified by reconstructing the particles in the final state of the various processes. In particular, when these particles reach the ECAL modules, the PMT signals from both sides of the hit cells are read out and converted by the ECAL electronics into digital counts for time and amplitude. From this information, the energy released into the hit cells, and their times and positions are derived [3].

As the existing ECAL electronics were optimized to work under the conditions of the KLOE experiment, which are different from those in SAND, a comparative study of the physical requirements in SAND and the characteristics of the existing front-end electronics (FEE) is therefore important for the final choice of the SAND readout electronics.

4.5.1 Studies for the Optimization of the PMT Working Point

The neutrino interaction processes inside the detector are simulated with the neutrino event generator GENIE. The response of the detector, reconstructed with *gegede* and *dunendggd* algorithms and framework described in [32], is performed with Energy Deposition Simulation (EDEP-SIM) and digitized with SAND Detector Simulation and Event Reconstruction Tool (sandreco) [32]. In particular, the tracks are used for vertex reconstruction, whose position is useful for event classification. A fiducial volume (FV) for the interesting neutrino events is defined as the volume delimited by the surface at 20 cm distance from the inner ECAL surface.

The Monte Carlo (MC) sample used for the analysis presented in the following contains 118,592 events of neutrino interactions with the SAND detector (the same sample has been used in other studies presented in [32]) and the beam in the forward horn current (ν_μ mode) (FHC) polarization mode, corresponding to a total of 1.011×10^{17} protons on target (POT). At 1.2 MW beam power and an expected rate of 7.5×10^{13} POTs/spill, these events correspond to $\sim$ 27 minutes of data taking, or equivalently $\sim$ 15 minutes at 2.1 MW beam power.

The associated neutrino energy spectrum is shown in Figure 4.15 for all events and in Figure 4.16,

only for events with the primary vertex in the FV. It is worth noting that the spectra of the different neutrino components in the beam have a tail extending up to $\mathcal{O}(100\,\mathrm{GeV})$.

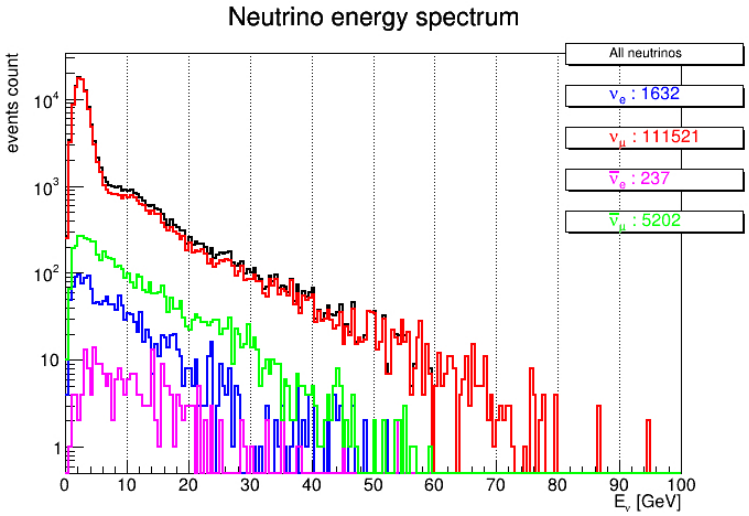


Figure 4.15: Neutrino energy spectrum for all events in the MC simulation.

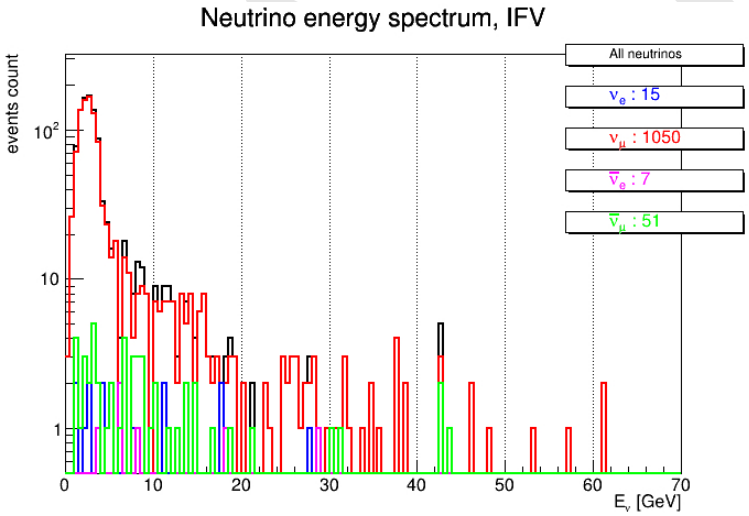


Figure 4.16: Neutrino energy spectrum for simulated events with the primary neutrino interaction vertex contained in the FV.

The response of ECAL is digitized similarly to that in the official KLOE MC simulation. The deposited energy in the cells is propagated to PMT with a double exponential attenuation curve, according to the attenuation length of light in the fibers, and is converted into photoelectron (PE). The light yield is $\sim$ 1 PE/MeV of the total energy of the particle at the center of the cell of a barrel module. The discriminator threshold is set to 2.5 PE, and a constant fraction discriminator at 15% of the signal is simulated, as well as a multihit TDC (30 ns integration time + 50 ns dead time).

For each of the 118,592 events of neutrino interaction, and for each cell of all the ECAL modules, barrel and endcaps, the number of PEs is recorded. Furthermore, the same analysis can be performed by selecting only the primary vertex of the neutrino interaction in the FV. The distribution

of the number of PEs of all the cells involved for each event was produced. These distributions are shown in Figure 4.17. It can be noticed that the number of PEs can reach the value of about 25,000 for a single cell.

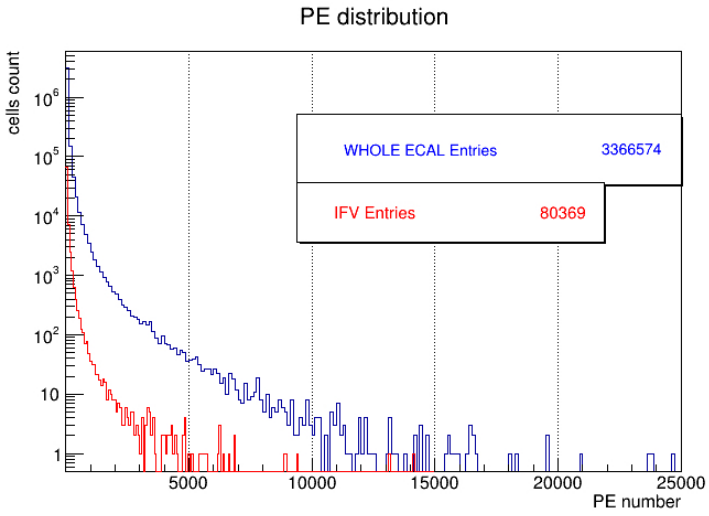


Figure 4.17: Distribution of the number of PEs released per cell and per event, for all simulated events (blue) and for events in the FV (red).

The next step is to relate the PE distribution to the neutrino energies. The neutrino energy range 0 - 100 GeV is considered, with a particular focus on the energy range below 10 GeV, relevant for the neutrino oscillation analyzes in DUNE. Figures 4.18 and 4.19 show the distributions of the number of PEs corresponding to different slices of the neutrino energy spectrum. It can be observed that there is a correlation between the number of PEs and the neutrino energy.

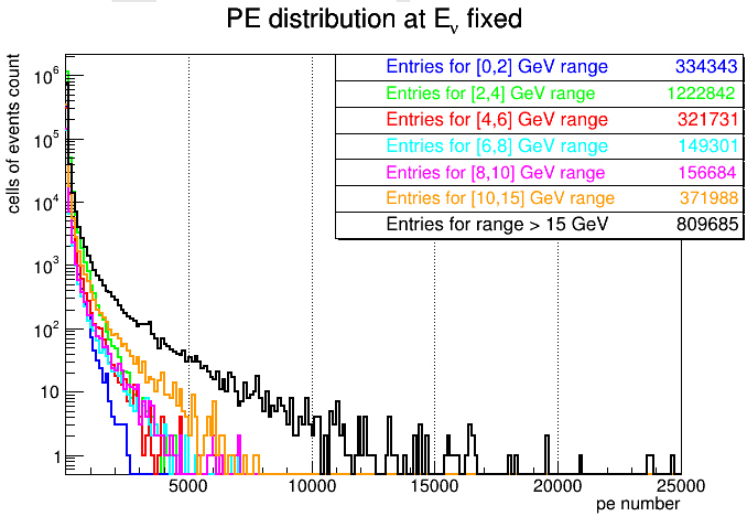


Figure 4.18: Distribution of the number of PEs released per cell and per event, for all simulated events and for different neutrino energy ranges.

Then, the same distributions are evaluated, considering only those cells with a number of PEs greater than a chosen threshold.

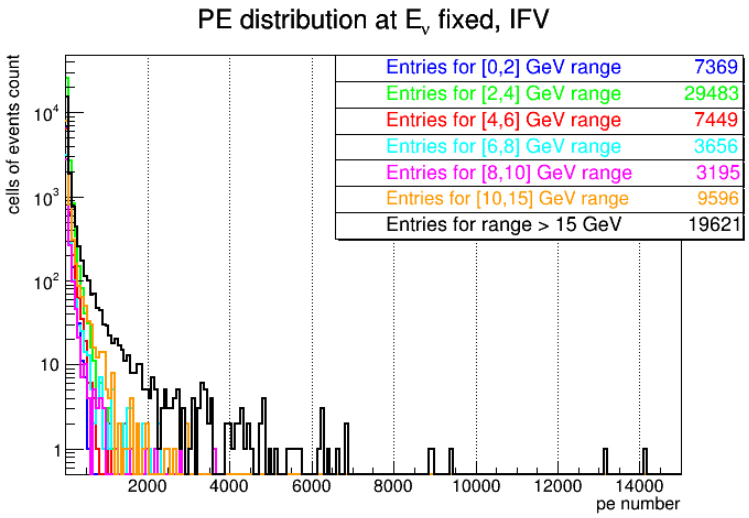


Figure 4.19: Distribution of the number of PEs released per cell and per event, for simulated events in the FV and for different neutrino energy ranges.

Counting the number of events for the slices of energy below 10 GeV, the conclusion that only a fraction of 2.58% or 0.49% of the events has at least one cell above the thresholds of 1000 or 2000 PE, respectively, is reached. The values for these thresholds and for the other ones are shown in Table 4.2, while Table 4.3 reports also the fraction of cells hit above the mentioned thresholds for all events.

Table 4.2: Fraction of events with at least one cell above PE threshold in the neutrino energy range 0-10 GeV.

PE threshold	Fraction of events (%)
1000	2.58
2000	0.49
3000	0.13
4000	3.64×10^{-2}

Table 4.3: Fraction of hit cells above PE threshold in the neutrino energy range 0-110 GeV.

PE threshold	Fraction of hit cells (%)
1000	0.19
2000	3.0×10^{-2}
3000	7.2×10^{-3}
4000	2.1×10^{-3}

The number of PEs ranges from 1 to 2.5×10^3; however, this upper limit corresponds to events with an energy range beyond the scope of interest for DUNE oscillation analysis. The minimum number of PEs considered in the simulation is chosen to be 3 to avoid background noise, while the maximum number that could be considered of interest is 1000 or 2000 PEs, as discussed in the following. These numbers set the dynamic range for the PMT signals, which must match the

readout electronics. In particular, a linearity of the electronics for signals up to 2000 PEs would guarantee a linear response for more than 99.5% of the events, as can be inferred from Table 4.2.

The next step corresponds to evaluating the probability that a single cell is hit in a neutrino interaction event. To extract this information from the MC sample, the cell occupancy plots are evaluated for the modules of the two endcaps and the 24 modules of the barrel, using the ID cell code for the barrel $\mathrm{ID}_{barrel} = 1000\ mod + 100\ plane + column$, where *mod* is the module index (from 0 to 23), *plane* is the plane index (from 0 to 4), and *column* is the column index (from 0 to 11). For the two endcaps, the module numbers are 30 for endcap A and 40 for endcap B, while the columns are grouped by the plane to which they belong. Figure 4.20 shows the occupancy plots of a module of the barrel and the two endcaps.

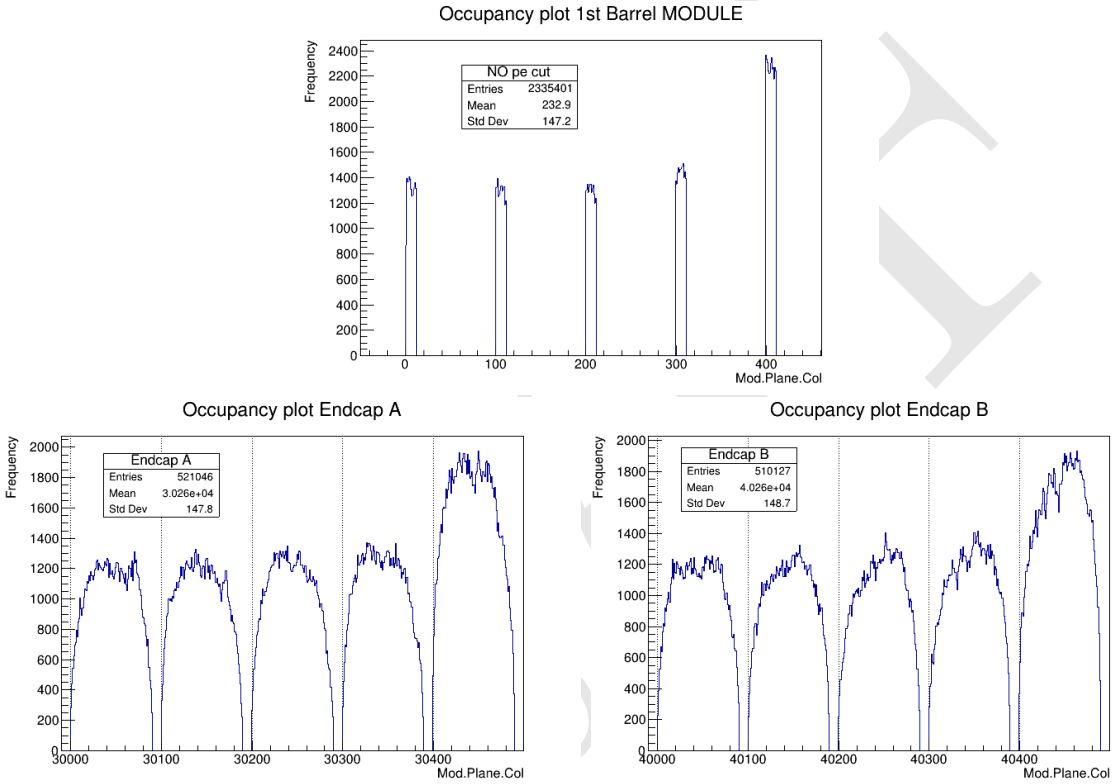


Figure 4.20: (Top) Number of hits for each cell (occupancy plot) of one ECAL barrel module as an example (# 1). (Bottom) Number of hits for each cell (occupancy plot) of ECAL endcap A modules (left), and endcap B modules (right). Each bin in the histograms represents a cell. Cells in the fifth plane have, on average, more hits than in other planes.

It is noteworthy that the cells belonging to the fifth plane make the largest contribution to the occupancy plot. This is in part due to the fact that planes do not have equal thickness; in fact, plane 5 is thicker than the others, namely 5.2 cm against 4.4 cm. Partly, it is due to the more probable neutrino interaction in the iron yoke than in the FV, with more secondary particles entering ECAL from the fifth planes.
From the occupancy plot, it is possible to estimate the probability that a cell is hit in a neutrino interaction event. Figure 4.21 shows the probabilities for all 24 modules of the barrel separately for planes 1-5, and averaged for the cells of each plane.

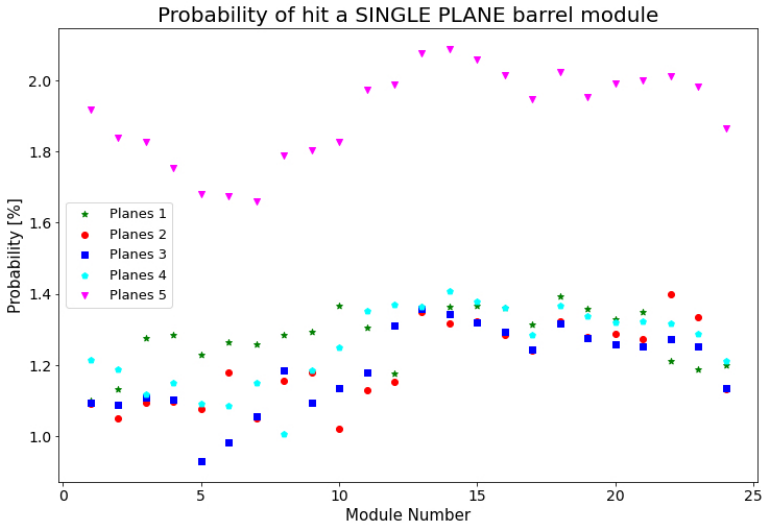


Figure 4.21: Probability of hitting a cell in a barrel module, separately for the 24 modules and the 5 planes.

The average probabilities for the first 4 planes and for plane 5 for all 24 barrel modules are easily evaluated. The same analysis is performed for the endcaps A and B. The results are summarized in Table 4.4:

Table 4.4: Average probabilities that a cell is hit in a neutrino interaction event.

ECAL	planes 1-4	plane 5	planes 1-5
Barrel	1.23%	1.91%	1.37%
Endcap A	0.80%	1.21%	0.88%
Endcap B	0.79%	1.15%	0.86%

A global weighted average is calculated using the weights of the number of cells in the barrel (1440), the endcap A (500), and the endcap B (500):

$$P_{cell} = \frac{1440\ P_{\text{barrel}} + 500\ (P_{\text{endcapA}} + P_{\text{endcapB}})}{2440} = 1.16\% \tag{4.7}$$

This single value for the probability that a cell is hit in a neutrino interaction event will be considered in the next section for the evaluation of the pile-up, therefore assuming that all cells have the same probability.

The beam time structure is reconstructed to simulate the time of the neutrino interaction event and calculate the pile-up probability that, given a PMT signal, a second signal arrives within a fixed time window after the first signal. The times of N interactions per spill (on average, N=84 with 1.2 MW beam) are extracted uniformly between 0 and 9.6 μs. All time differences between two consecutive interactions in a spill are calculated (the distribution follows – as expected – an exponential distribution with $\tau_{\text{spill}} = 114$ ns). From this, the distribution of time differences for a single cell with a probability of being hit of $P_{cell} = 1.16\%$ is evaluated, and then the pile-up probabilities for different time windows (50, 100, 150, 200 ns) are also evaluated, as shown in Table 4.5, where the cases of higher $P_{cell} = 1.5\%, 2.0\%$ are also considered. The effect of the time

spread of the cell hits within a single neutrino interaction event is negligible on the time scale of the spill, as shown in Table 4.6.

Table 4.5: Pile-up probability of PMT signals (without neutrino event time smearing).

Time window [ns]	$P_{cell} = 1.16\%$	$P_{cell} = 1.5\%$	$P_{cell} = 2.0\%$
50	0.67%	0.90%	1.28%
100	1.33%	1.81%	2.52%
150	1.95%	2.71%	3.72%
200	2.59%	3.58%	4.87%

Table 4.6: Pile-up probability of PMT signals (with neutrino event time smearing).

Time window [ns]	$P_{cell} = 1.16\%$	$P_{cell} = 1.5\%$	$P_{cell} = 2.0\%$
50	0.64%	0.86%	1.36%
100	1.32%	1.71%	2.56%
150	1.91%	2.60%	3.78%
200	2.52%	3.48%	4.93%

Since the KLOE detector had high demands on time and energy resolutions, a high-performance front-end electronics (FEE) was required. This task is accomplished by the base of the PMTs. This consists of a high voltage (HV) divider and a preamplifier that must have low noise, high bandwidth, and high output dynamic range in order to avoid distortion of the fast pulses from the photomultiplier.

The HV divider has a cathode that is grounded, and a positive voltage is applied to the anode; this reduces the noise associated with the charging surfaces in contact with the PMT envelopes. The voltage of the first stage is 300 V and is independent of the high voltage supplied, while the remaining HV is divided among the other 15 stages (see Figure 4.22). For example, a typical divider current for a high voltage of 2000 V is 150 μA. To increase the linearity of the HV divider, the last five resistors are used in conjunction with capacitors to reduce the voltage fluctuations due to current spikes.

The preamplifier is necessary for the base because it provides optimal coupling to the PMT and drives the cable that carries the signal to the next stage. It is a three-transistor transimpedance device AC coupled to the PMT, with a conversion gain $G_C = 247$ V/A (see Figure 4.23). A high gain-bandwidth product and a high dynamic range are required both to avoid distortion of the signal edges and to keep the non-linearity below 0.2% over the whole range of interest for KLOE. The first stage is a common base with low input impedance. The second stage (common emitter) is necessary to increase the open loop gain; the third stage is an emitter follower that drives a 50 Ω coaxial cable. A typical PMT signal produced by the PMT-base is shown in Figure 4.24.

This signal can be approximated as a triangular pulse with a base $\Delta t \sim 14$ ns and a height $V^{\text{out}}_{\text{peak}}$. Until the preamplifier works within its linearity range, the output voltage signal has the same shape as the input current signal, and its amplitude is given by $V^{\text{out}}_{\text{peak}} = I^{\text{in}}_{\text{peak}}\, G_C$.

The dynamic range in terms of N_{PE} and the PMT gain G_{PMT} can be evaluated in KLOE using the following constraints:

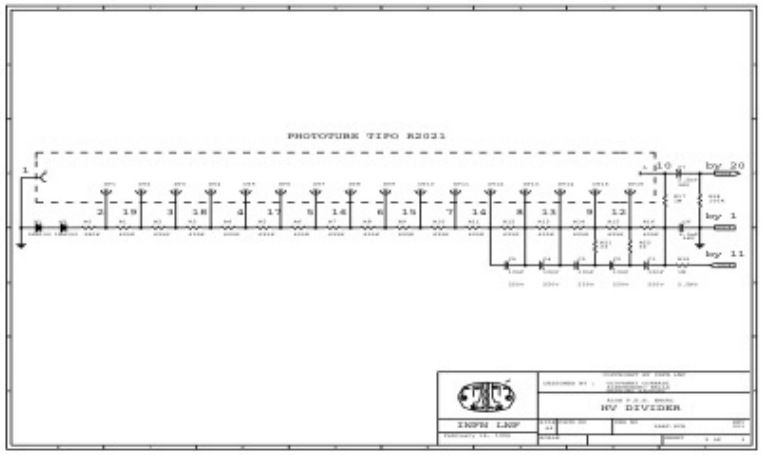


Figure 4.22: Electrical schematic of the HV divider in the PMT-base.

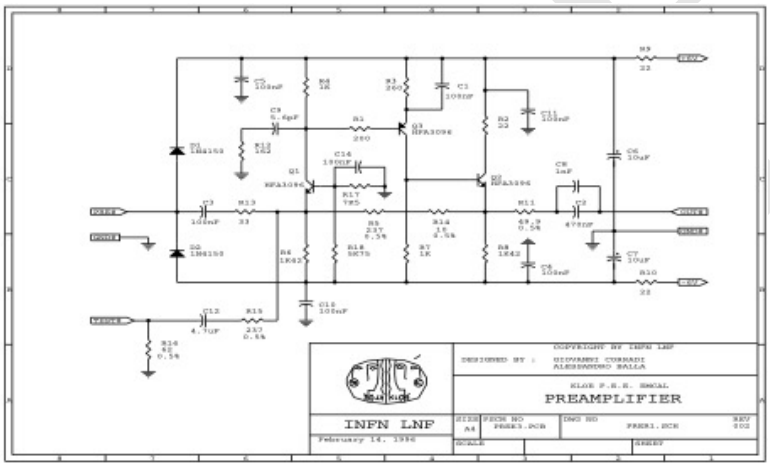


Figure 4.23: Electrical schematic of the preamplifier in the PMT-base.

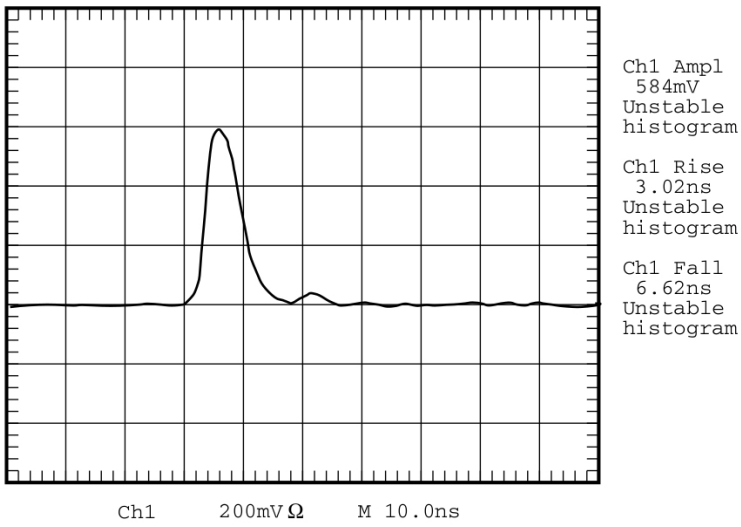


Figure 4.24: Typical signal from the PMT-base.

1. Minimum discriminator threshold $V_{TH} = 5\,\mathrm{mV}$;
2. Preamplifier linearity (within 0.2%) range = [0, 4.7] V; $V_{preamp}(max) = 4.7\,\mathrm{V}$;
3. preamp transimpedance gain $G = 250\ V/A$; $I_{peak}(max) = V_{preamp}(max)/G = 19\,\mathrm{mA}$;
4. max signal charge $Q(max) = 133\,\mathrm{pC}$ (triangle approx.);
   from $Q = e\ N_{pe}\ G_{PMT}$ follows $(N_{PE}\ G_{PMT})(max) = 83 \times 10^7$;
5. light yield of 1 PE/MeV at cell center; ~ 1.8 PE at the cell end (close to the PMT);
6. max energy release in one cell: 410 MeV, implying $N_{PE}(max)$ of $\mathcal{O}(1000)$;
7. $G_{TOT} = G_{PMT}\ G_{\mathrm{preamp}}$, with $G_{\mathrm{preamp}} = 2.5$;
8. 12 m long cable attenuation: $C_{ATT} = 0.74$;
9. maximum HV for divider is 2300 V; typical HV 1700-1800 V corresponding to $G \sim 1-3\times10^6$;
10. the maximum single pulse amplitude at the discriminator/digitizer input is:
    $V_{dis}(max) = V_{preamp}(max)\ 0.5\ C_{ATT} = 1.74\,\mathrm{V}$;
11. signal amplitude:
    (signal ampl) $= V_{dis}(max)/N_{PE}(max)$
    $N_{PE}(min) = V_{TH}/$(signal ampl)
    $N_{PE}(max)/N_{PE}(min) = V_{dis}(max)/V_{TH}$.

From these constraints, possible choices of $N_{PE}(max)$ and G_{PMT} follow, as reported in Table 4.7. In KLOE the effective choice provided $N_{PE}(max) \sim 1000$ and $G_{PMT} \sim 2 \times 10^6$.

Table 4.7: Maximum and minimum number of PEs given by a calorimeter readout cell as a function of the gain $G_{tot} = G_{PMT} \times G_{preamp}$.

G_{PMT} ($\times10^5$)	G_{TOT} ($\times10^6$)	$N_{PE}(max)$	signal amplitude (mV/PE)	$N_{PE}(min)$ $V_{TH} = 5\,\mathrm{mV}$	MeV at module center
4.2	1.04	~ 2000	0.87	~ 6	6.0
5.5	1.38	~ 1500	1.16	~ 4	4.0
8.3	2.1	~ 1000	1.74	~ 3	3.0
10	2.5	~ 800	2.18	~ 2	2.0

As mentioned above, the preamplifier in the PMT-base provides an optimal coupling to the PMT and drives the cable carrying the signal to the next stage. A high gain bandwidth and a high dynamic range are required both to avoid distortions of the signal rise edges and to maintain the non-linearity below 0.2% across the entire range of interest. As $V_{dis}(max)$ depends directly on $V_{preamp}(max)$, the linearity of the preamplifier has been tested with the specific goal of investigating the possibility of slightly extending the dynamic range of signals by increasing $V_{preamp}(max)$, while keeping linearity at an acceptable level, e.g., 1%. The test has been performed on a preamplifier

using the test input specifically modified to get unity voltage gain and a total input resistance of $50\,\Omega$.

The preamplifier response has been characterized in two different ways. First, a square pulse at 1 MHz was generated using the Tektronix AFG 3252 signal generator, with an amplitude of -5 V and a width of 30 ns. Subsequently, the signal was passed through two calibrated attenuators in series in order to modulate the input voltage to the preamplifier. Then, the input voltage, the output voltage, and the integral of the output voltage (which represents the charge) were measured with a LeCroy HDO6104 oscilloscope. The results are shown in Figures 4.25. The output saturation is clearly visible at an output value of ~ 3.4 V. A linear fit to the integrated charge of the output signal Q_{int} vs input voltage V_{in} is performed and shown in Figure 4.26.

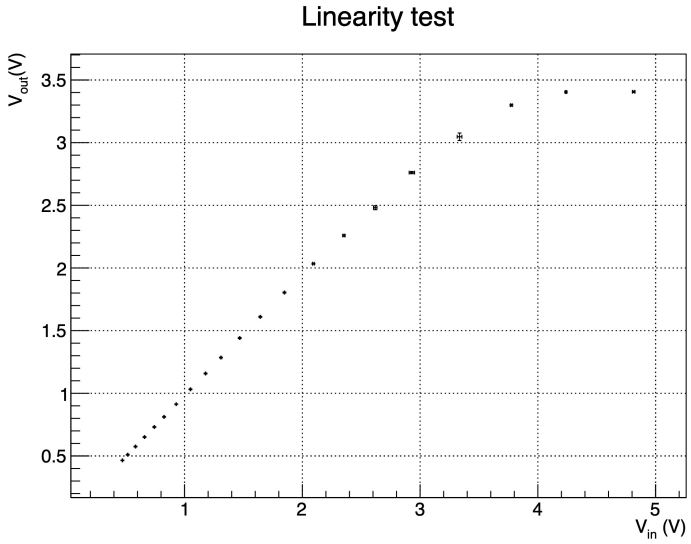


Figure 4.25: Preamplifier linearity test, showing output voltage V_{out} vs input voltage V_{in}.

To better understand the linearity of the amplifier, the linearity of the experimental setup chain was studied by bypassing the amplifier and inputting the same signal into the oscilloscope. The residuals of the data without the preamplifier were then subtracted from the residuals of the data with the preamplifier included in the chain. The residuals after this operation are shown in Figure 4.27.

From the results of this test, it can be concluded that by accepting the linearity of the preamplifier at 1% level, $V_{preamp}(max)$ can be extended by $\sim 15\%$, from 4.7 V to 5.4 V, corresponding to

$$V_{dis}(max) = V_{preamp}(max)\ 0.5\ C_{ATT} = 2.0\,\text{V}. \tag{4.8}$$

Assuming a very low noise environment, as in KLOE, and lowering the minimum discriminator threshold to $V_{TH} = 2.5$ mV, suitable choices for the dynamic range of signals in SAND are obtained, as shown in Table 4.8. Different dynamic ranges can be implemented by changing G_{PMT}: the final choice should be a compromise between an affordable level of events with energy saturated cells, depending on $N_{PE}(max)$, and an acceptable neutron detection efficiency, depending on $N_{PE}(min)$.

It is worth noting that the use of a preamplifier lowers the effective PMT gain and HV values, with a beneficial effect on PMT lifetime.

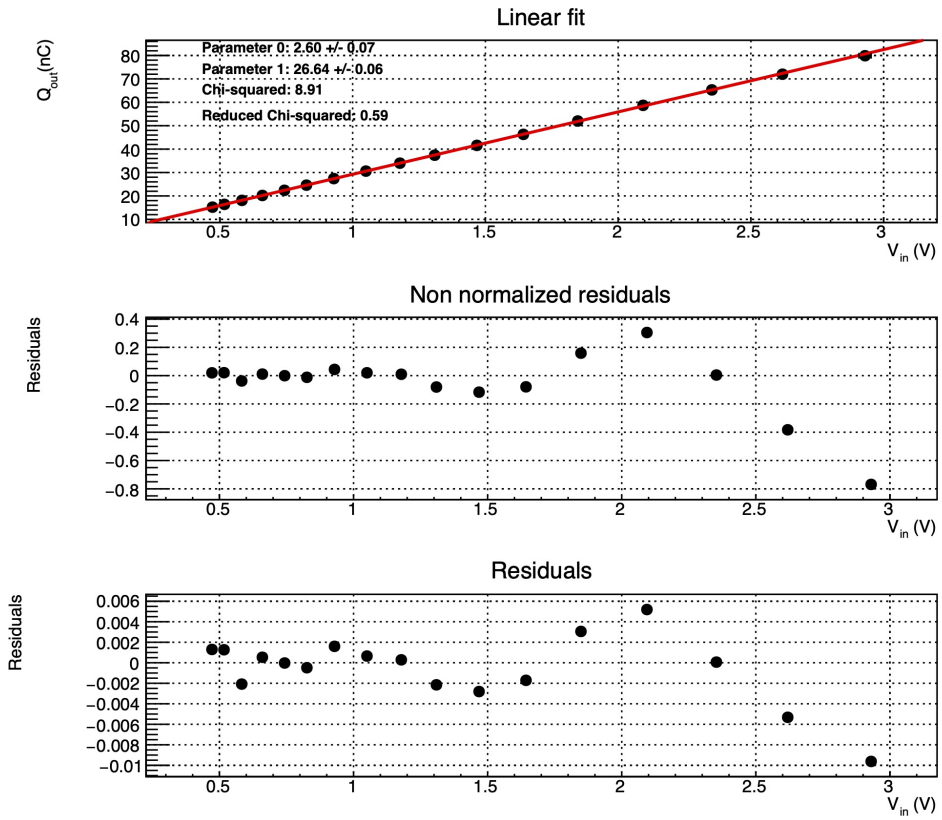


Figure 4.26: Preamplifier integrated charge linearity test, showing integrated charge of the output signal Q_{int} vs input voltage V_{in} (top). The absolute (center) and fractional (bottom) fit residuals are also shown vs input voltage V_{in}.

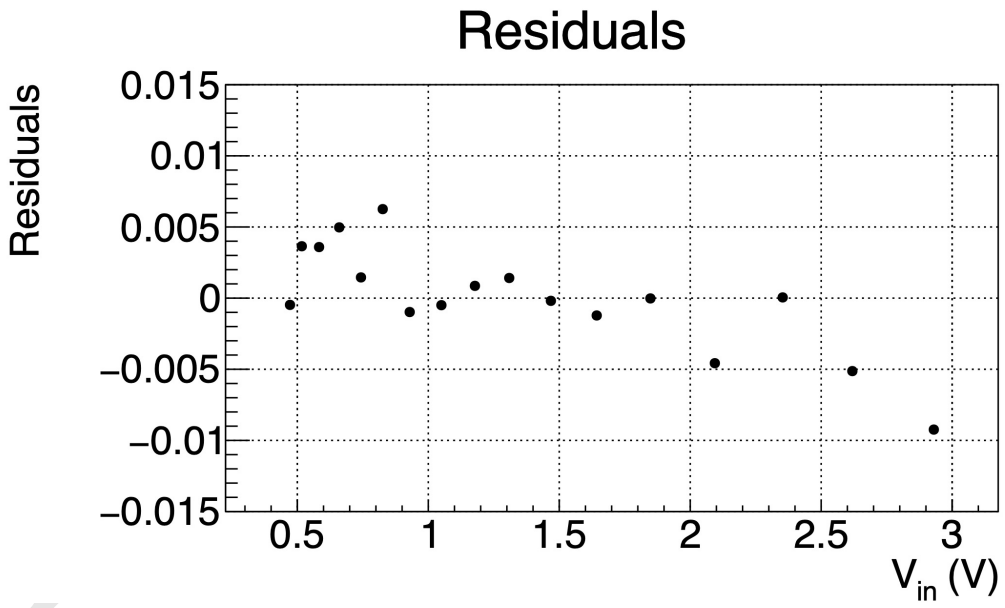


Figure 4.27: Normalized fit residuals to the setup linearity.

Table 4.8: Maximum and minimum number of PEs given by a calorimeter readout cell as a function of the gain $G_{tot} = G_{PMT} \times G_{preamp}$.

G_{PMT} ($\times 10^5$)	G_{TOT} ($\times 10^6$)	$N_{PE}(max)$	signal amplitude (mV/PE)	N_{PE}(min) $V_{TH} = 2.5$ mV	MeV at module center
4.8	1.2	$\sim$ 2000	1.0	$\sim$ 3	3.0
6.4	1.6	$\sim$ 1500	1.3	$\sim$ 2	2.0
9.5	2.4	$\sim$ 1000	2.0	$\sim$ 1	1.0

The preamplifier linearity, with a special focus on the saturation regime, has also been studied directly with PMT signals. Two PMTs were connected to a CAEN SP5601 LED driver using scintillating fibers (see Figure 4.28). For each position of the light attenuator of the Led Driver, measurements were taken at two different high voltages for the two PMTs. Using a lower voltage ensured operation and the study of the system in the linear response region of the preamplifier. Subsequently, a higher voltage was used to study the system in the saturation regime of the preamplifier. The HV values used to characterize the response in the two regions for the two PMTs are reported in Table 4.9.

Table 4.9: HV values for the study of the PMT signals in the linear and saturation regimes of the preamplifier.

	PMT1 (V)	PMT2 (V)
Linearity regime	1700	1650
Saturation regime	2100	1900

The scan with the Led Driver light attenuator spans the two regimes, and the attenuation scales have been inter-calibrated and coherently combined in order to have a unique attenuation scale factor, with unity corresponding to the maximum intensity. The result is shown in Figure 4.29 for the output voltage and in Figure 4.30 for the integrated charge vs. the attenuation scale factor.

Since it was observed that the integrated charge exceeds the expected linear behavior when the attenuation scale factor approaches unity, instead of saturating, the trend of the full-width at half-maximum of the signals as a function of the attenuation was studied. The measurements are presented in Figure 4.31. They are compared with the expected behavior for the PMT signal in a triangular model approximation with saturation implemented for the amplitude, but without a corresponding increase in the signal width, as observed in the data. This phenomenon is fully clarified by directly looking at the PMT signals on the oscilloscope. The time baseline is distorted during saturation. The recovery time from saturation to the linear regime depends on the input signal amplitude. In conclusion, the input information is not fully lost during the saturation regime. The "over-linearity" of the integrated charge, or the signal width increase versus the input signal amplitude, could be exploited to characterize signals beyond the preamplifier saturation regime and measure their amplitude also in this region. This feature is going to be implemented in the MC simulation, and its impact on ECAL performance will be evaluated.

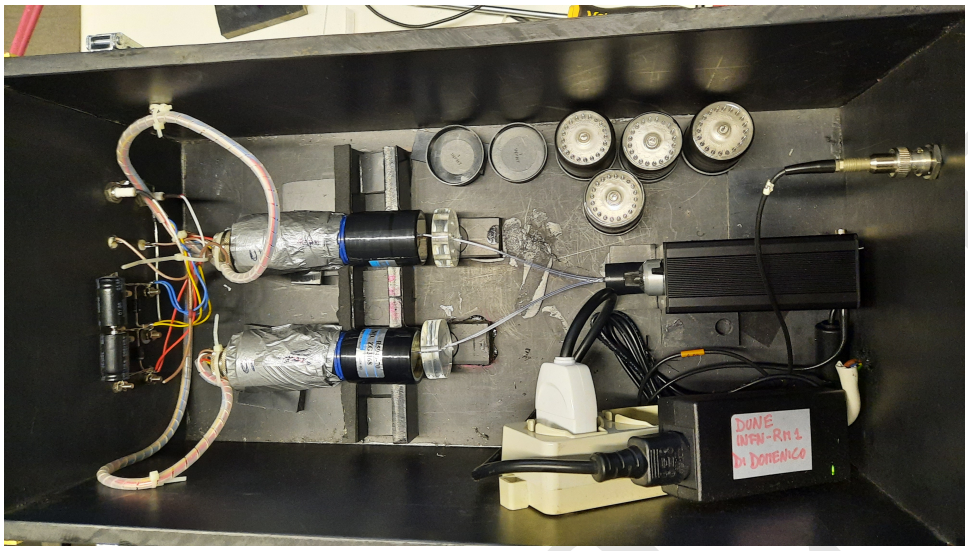


Figure 4.28: Experimental setup for the linearity test with PMTs.

4.5.2 FEE and DAQ

Three possible schemes can be envisaged for the ECAL front-end electronics (FEE):

1. A digitizer with a sampling rate of $\sim 1\ GS/s$; this option is rather expensive, so a compromise with a slower digitizer, having a sampling rate of $\sim 128\ MS/s$, complemented by a signal slow shaper;

2. a picoTDC based on the application-specific integrated circuit (ASIC) developed at European Organization for Nuclear Research (CERN) coupled with a double threshold discriminator to reconstruct the amplitude of the signal with the Time over Threshold (ToT) technique;

3. a more conventional solution involves splitting the signal into two paths: a fast one to a TDC (or picoTDC) for the time measurement and a slower one to a QDC for the integrated charge measurement.

Possible solutions for the FEE that should constitute a good compromise between cost and performance are being investigated in collaboration with CAEN S.p.A. In particular, several tests have been performed on the picoTDC option using the commercial CAEN board DT5203 with a double threshold discriminator A5256.

A preliminary test was conducted by CAEN using a signal function generator, AFG3252. The output from the signal generator was sent to the picoTDC installed on a FERS (DT5203+A5256) through a calibrated attenuator in order to vary the amplitude of the signals in a precise and controlled way. At 0 dB of attenuation, the amplitude was set to 3.85 V with a rise time of 2.5 ns. The low threshold was set to 5 mV and the high threshold to 300 mV.

First, calibration data for the ToT and ΔT (Walk) at different amplitudes (from 0 to 52 dB, in 3 dB steps) were acquired. Then, pulses were acquired at 6 different amplitudes spanning a 50 dB dynamic range in separate runs and independently of the calibration data. The walk effect caused

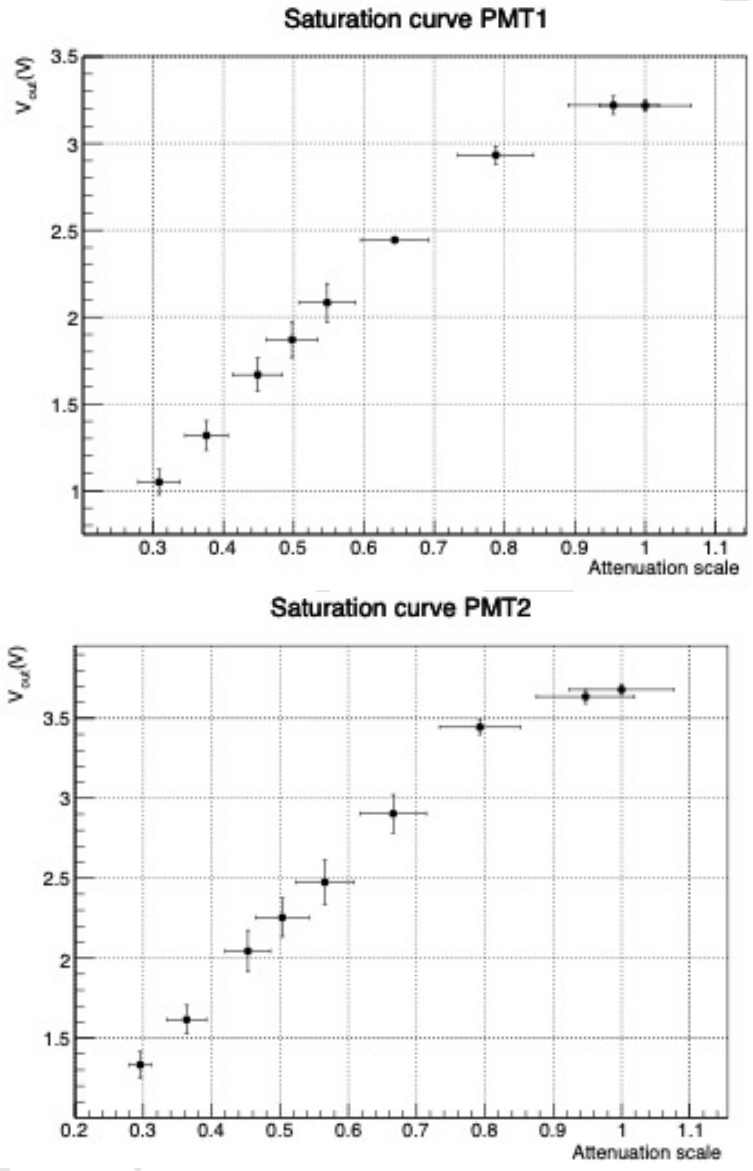


Figure 4.29: Preamplifier linearity test with PMT signals, PMT1 (Top) and PMT2 (Bottom) showing output voltage V_{out} vs attenuation scale factor.

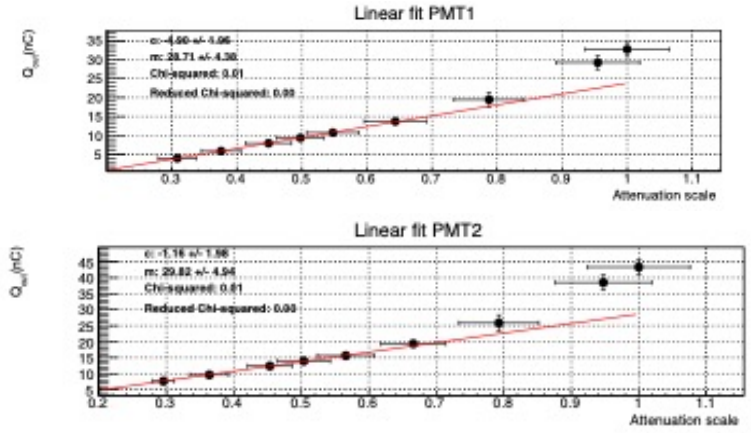


Figure 4.30: Preamplifier linearity test with PMT signals, PMT1 (Top) and PMT2 (Bottom) showing integrated charge Q_{int} vs attenuation scale factor.

approximately a 2 ns spread in ΔT, resulting in 6 separate peaks. ΔT was corrected using ToT data with a 5^{th} order polynomial fit of the ToT-ΔT points collected at a lower threshold (5 mV). The corrected ΔT distribution shows a single peak. Using this correction, a time resolution $\sigma_{\Delta T} \sim 18$ ps over the full 50 dB dynamic range was achieved.

Finally, using the calibration curve ToT-A, the amplitude A was reconstructed. The achieved resolution σ_A on the different reconstructed amplitude peaks, ranging from 12 mV to 3850 mV, is reported in Table 4.10.

Table 4.10: Resolution on reconstructed amplitudes from ToT.

A (mV)	σ_A (%)
12.2	1.1
38.0	3.1
121.8	3.3
385.9	0.1
1217.5	0.6
3850.0	0.8

A second test of the picoTDC has been conducted with PMT signals using the same set-up used to study the linearity of the preamplifier in the PMT-base, with two PMTs connected to a Led driver through scintillating fibers. In this case, the output signal from the calibrated attenuator is split into two branches: one branch is sent to the picoTDC chain, while the other is sent as input to a CAEN 730S 14-bit Digitizer module, serving as a reference measurement for the amplitude (see Figure 4.32).

After performing a calibration similar to the previous case, data were acquired from 0 to 40 dB attenuation in 5 dB steps, with thresholds of 10 mV and 100 mV for the picoTDC, while no threshold was applied on the digitizer (synchronized with an external trigger).

As in the previous case, a fit of the Walk-ToT correlation plot was performed to correct the time

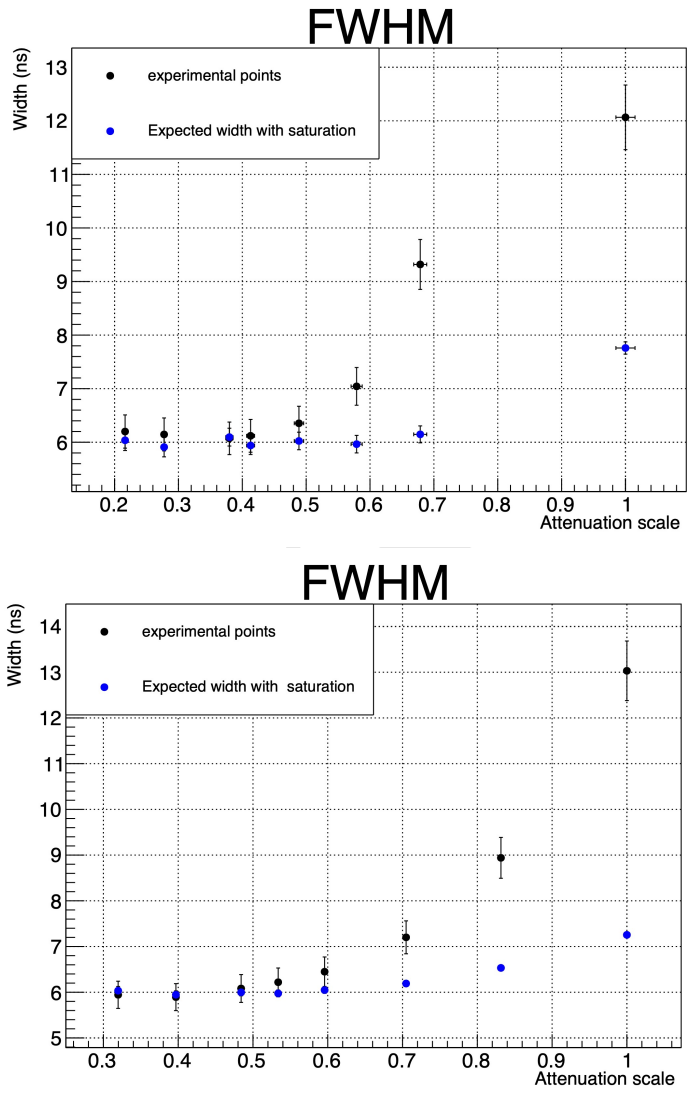


Figure 4.31: Behavior of the FWHM of the PMT1 signal (Top) and PMT2 (Bottom) vs attenuation scale factor. The expected behavior for the PMT signal in a triangular model approximation is also shown (blue points) with saturation implemented for the amplitude but without a corresponding increase in the signal width.

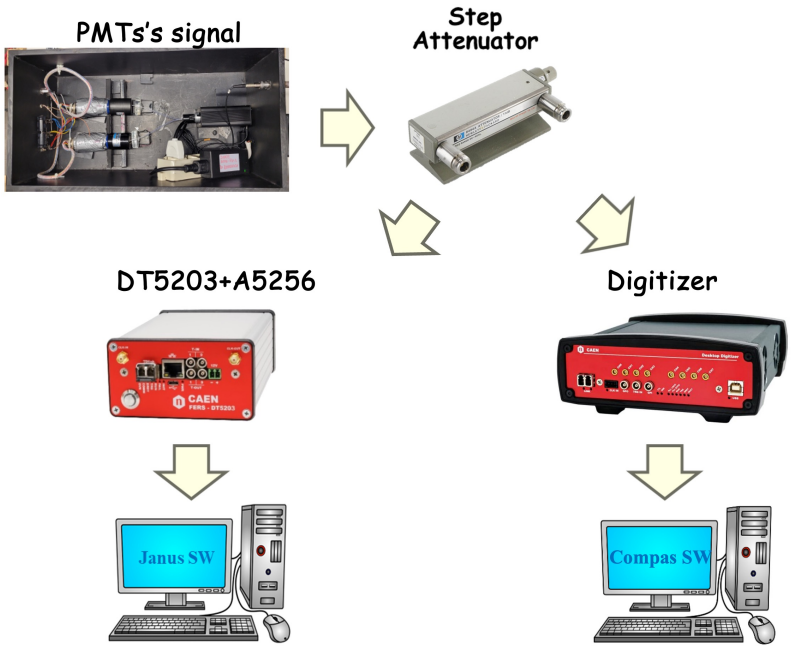


Figure 4.32: Set-up of the picoTDC test with PMT signals.

resolution for both high and low thresholds, as shown in Figure 4.33. The ΔT distributions before and after walk correction are shown in Figures 4.34 and 4.35 for the two thresholds. After the correction, a fit to the ΔT peaks yields a global time resolution of ~ 70 ps for the low threshold and ~ 60 ps for the high threshold.

The peak centered at 119.1 ns on the lower edge of the low threshold scan had an issue due to a secondary peak sometimes detected by the ToT measurement (see the bottom plot of Figure 4.34), it is not considered in the analysis. The time resolution results are summarized in Table 4.11. All values improve after the walk correction. Even though the obtained resolutions are affected by the non-negligible light intensity fluctuations of the Led Driver (at the level of a few percent of the PMT signal amplitudes), it does not come as a surprise that they are worse than the value (~ 18 ps) obtained using the pulse generator test; nonetheless, they are already better than the intrinsic ECAL time resolution when considering its constant term.

The ToT distributions were studied by applying the calibration curves shown in Figure 4.36. In this way, from the ToT histograms, the corresponding amplitude histograms were derived for the two thresholds, as shown in Figures 4.37 and 4.38.

The obtained reconstructed amplitude resolutions are presented in Table 4.12.

From these results, it is evident that the best resolution for a given threshold is achieved for the closest amplitude to the threshold value, as expected, even in a simple triangular PMT signal model, with a progressive worsening of resolution for increasing amplitudes.

The best resolution results from the two threshold scans were merged into a single histogram. This merged amplitude distribution from ToT and the amplitude distribution measured with the

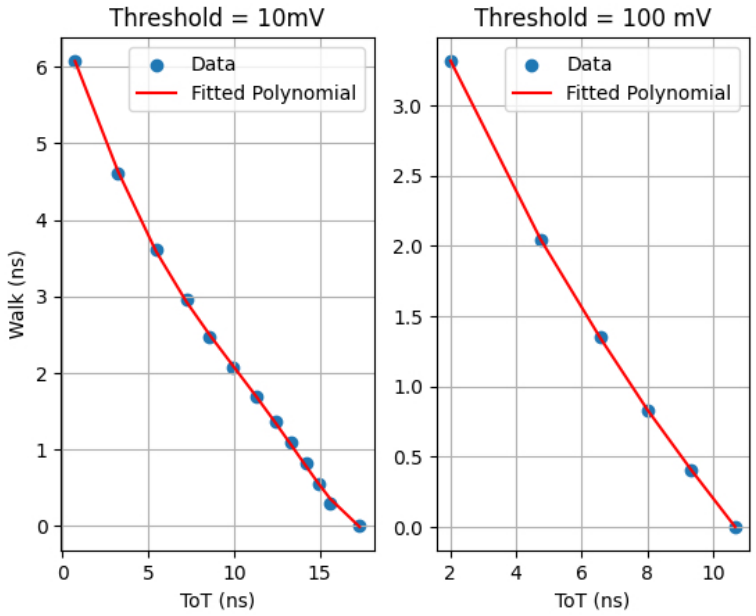


Figure 4.33: ToT-Walk picoTDC calibration curves; fit to calibration data points for low (left) and high (right) thresholds.

Table 4.11: Time resolution on reconstructed ΔT before and after walk correction for low and high thresholds.

Threshold	mean ΔT (ns)	$\sigma_{\Delta T}$ (ps) before corr.	$\sigma_{\Delta T}$ (ps) after corr.
Low	119.1	-	-
Low	119.6	89	72
Low	120.0	81	71
Low	120.5	75	70
Low	121.1	74	65
Low	121.8	77	63
Low	122.8	100	71
High	120.8	74	69
High	121.4	72	61
High	122.3	82	62

Table 4.12: Resolutions on reconstructed amplitude from ToT for low and high thresholds.

mean A (mV)	σ_A (%) (low thr.)	σ_A (%) (high thr.)
722.0	-	4.2
406.0	8.0	3.8
228.3	5.9	3.2
128.4	5.4	-
72.2	4.0	-
40.6	4.0	-
22.8	3.2	-

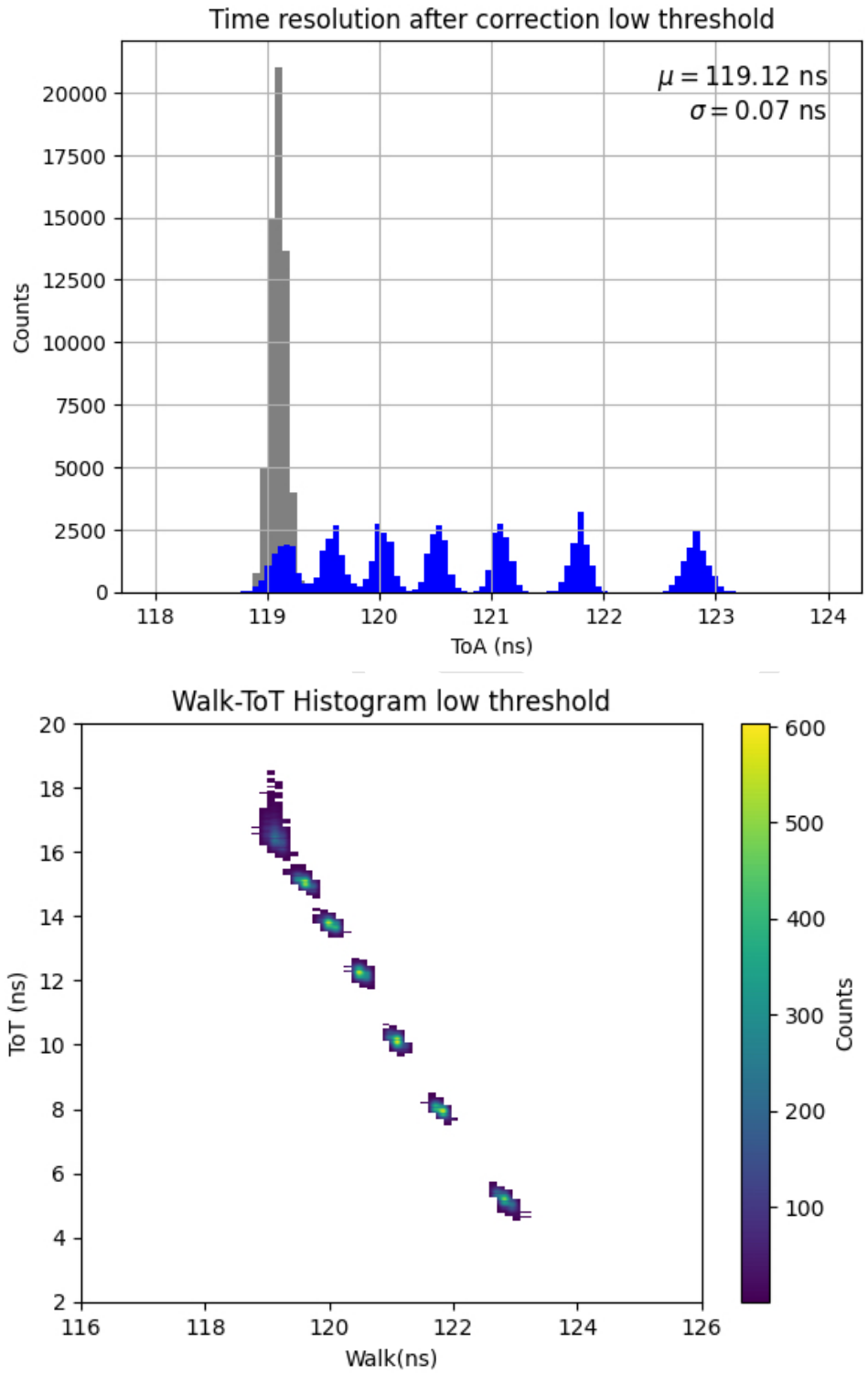


Figure 4.34: (Top) ΔT distributions before (blue peaks) and after (grey peak) walk correction for the low threshold. μ and σ values in the top-right corner of the plot refer to a Gaussian fit to the grey distribution. (Bottom) ToT vs. ΔT correlation histogram before walk correction for the low threshold.

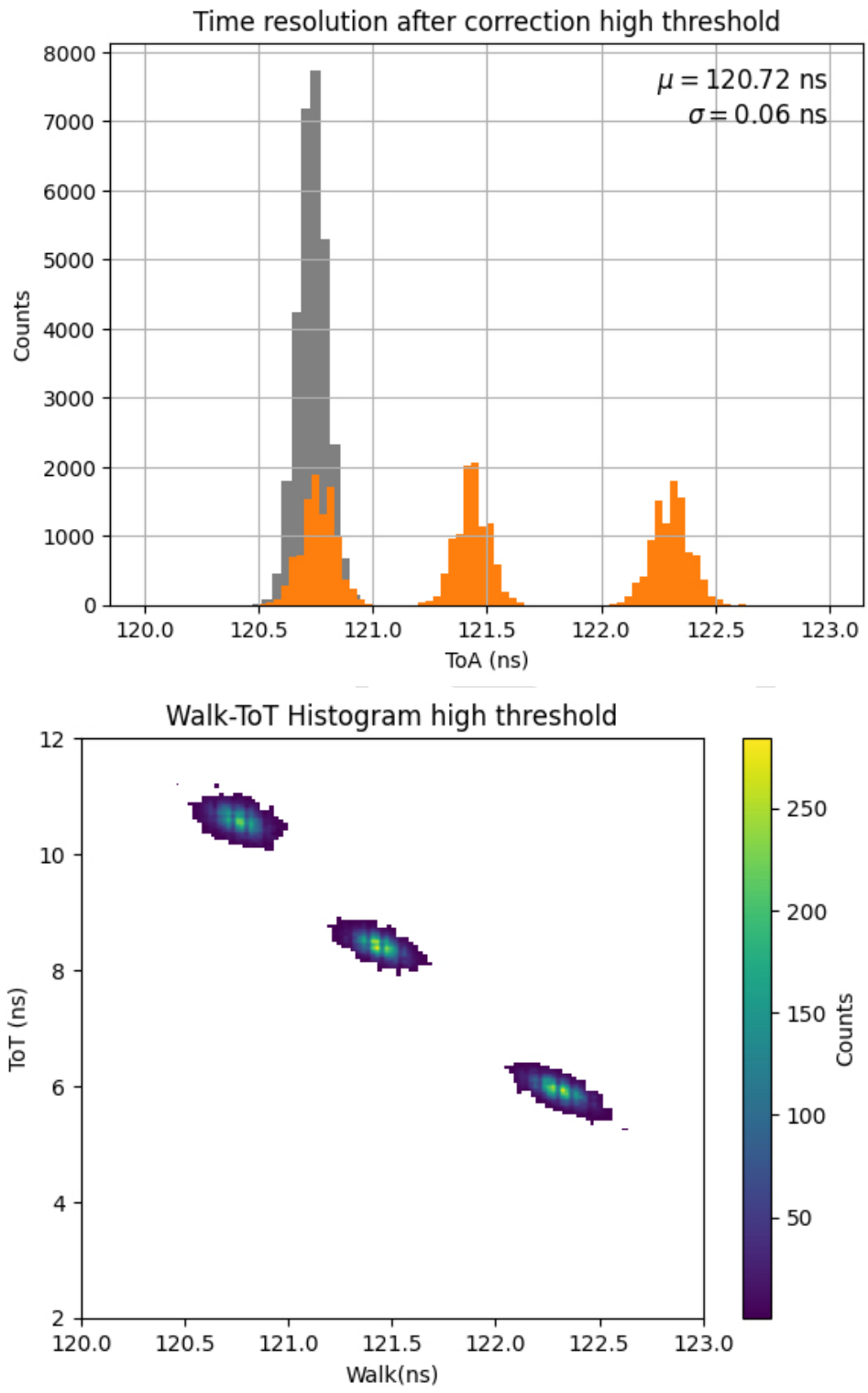


Figure 4.35: (Top) ΔT distributions before (ochre peaks) and after (grey peak) walk correction for the low threshold. μ and σ values in the top-right corner of the plot refer to a Gaussian fit to the grey distribution. (Bottom) ToT vs. ΔT correlation histogram before walk correction for the low threshold.

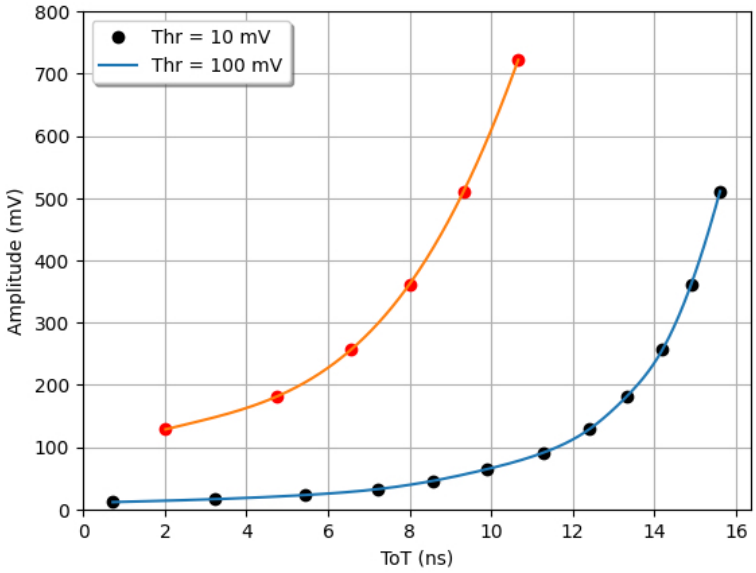


Figure 4.36: ToT-Amplitude picoTDC calibration curves; fit to calibration data points for low (blue) and high (ochre) thresholds.

digitizer were then compared (see Figure 4.39), and their correlation was probed with a linear fit, as shown in Figure 4.40. The fit indicates good linearity, with a slope coefficient $c = 0.987 \pm 0.05$ compatible with unity within the uncertainty, and the intercept at zero $m = -1.78 \pm 0.65$ mV, still compatible with zero and indicating that an offset – if present – should be very small.

The amplitude resolution was then calculated for each peak by considering the difference between the amplitudes from the digitizer and from the ToT in order to subtract possible common sources of signal fluctuations, such as the fluctuations of the LED Driver light pulse. The results for the amplitude resolutions are summarized in Table 4.13.

Table 4.13: Resolutions on reconstructed amplitude peaks from ToT, digitizer, and their difference.

mean A (mV)	σ_A from ToT (%)	σ_A digitizer (%)	difference (%)	best from ToT (%)
722.0	3.2	4.2	3.3	3.3
406.0	3.2	3.8	2.4	2.4
228.3	3.3	3.2	1.5	1.5
128.4	3.6	5.4	4.7	4.7
72.2	4.2	4.0	4.3	4.0
40.6	5.3	4.0	5.2	4.0
22.8	10.8	3.2	10.6	3.2

It is worth noting that the digitizer experiences a worsening of resolution at low amplitudes due to the presence of residual noise; therefore, it cannot be considered a reference to be subtracted for the lowest values of amplitude. The best resolutions achieved regarding the amplitude resolution from ToT, considering this limitation, are reported in the last column of Table 4.13.

Finally, assuming the PMT gain and the dynamic range of N_{PE} according to the first row of

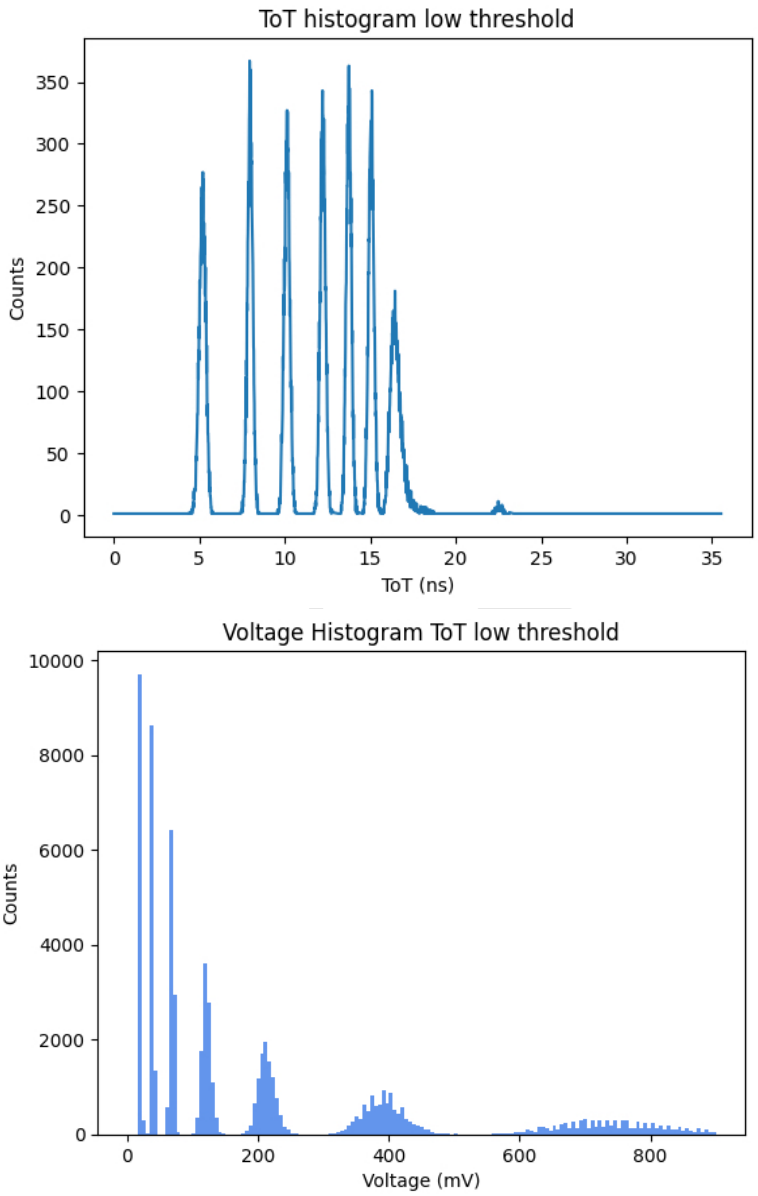


Figure 4.37: ToT distributions (Top) and amplitude from ToT after calibration correction (Bottom) for the low threshold.

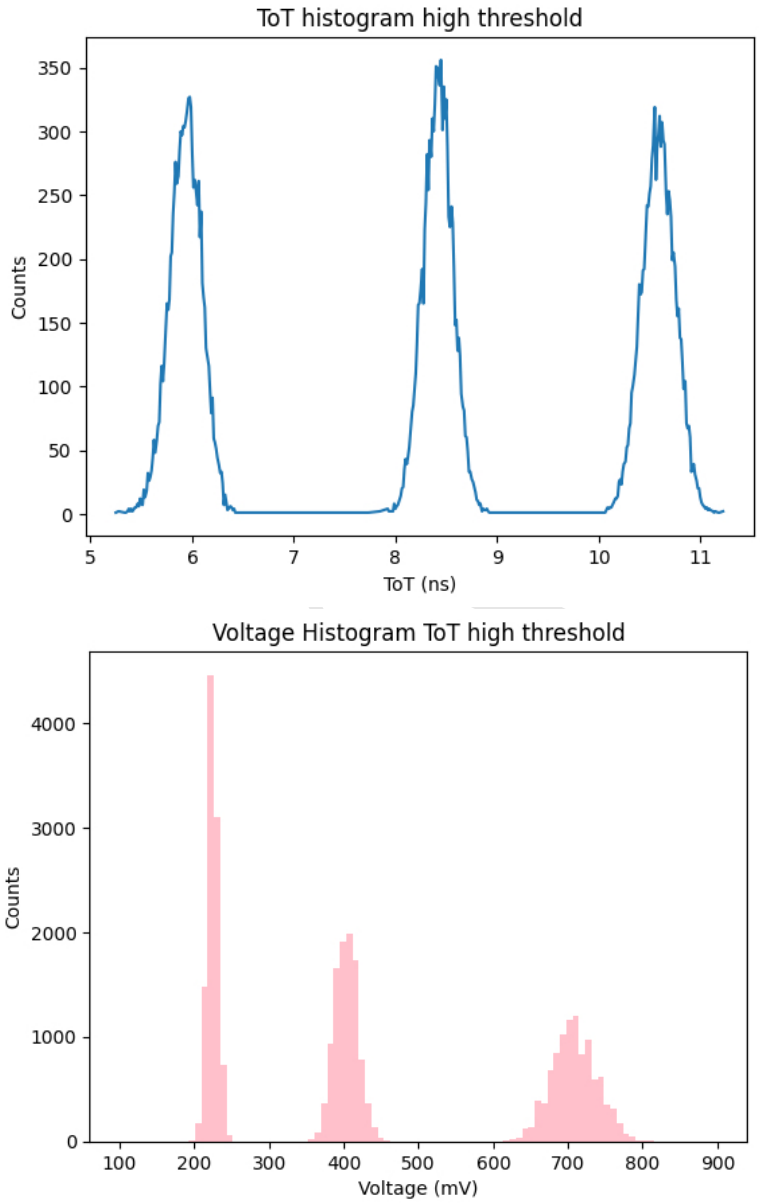


Figure 4.38: ToT distributions (Top) and amplitude from ToT after calibration correction (Bottom) for the high threshold.

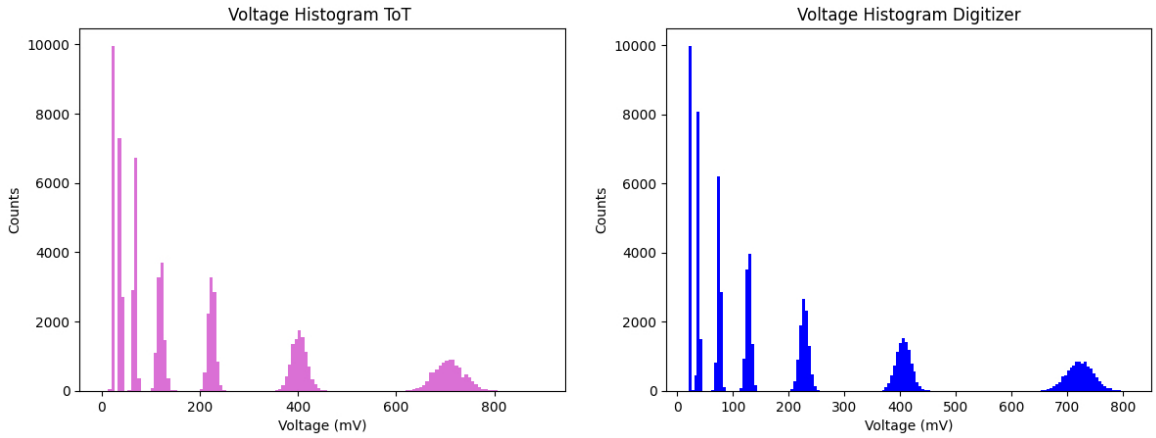


Figure 4.39: (Left) Amplitude distribution from ToT (low and high thresholds merged) and (Right) from digitizer.

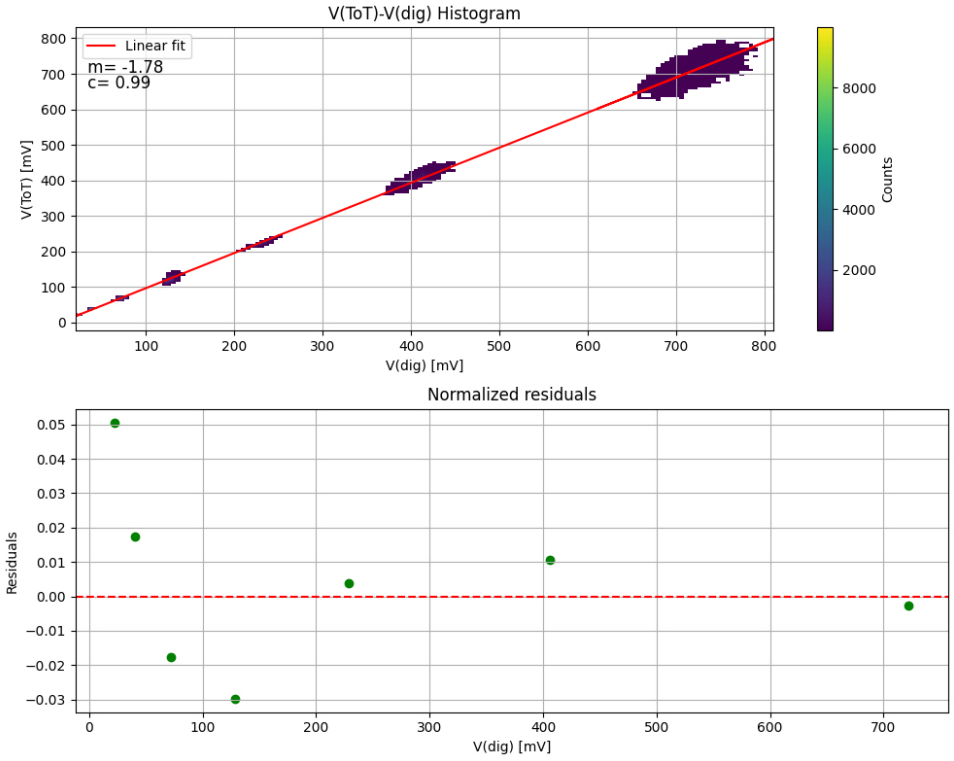


Figure 4.40: Correlation between amplitude from ToT (low and high thresholds merged) and from digitizer.

Table 4.8, by setting the ECAL energy scale 1 MeV = 1 PE = 1 mV, the amplitude resolution from ToT can be compared to the intrinsic energy resolution of ECAL, Eq. 4.4, as shown in Figure 4.41.

It is worth noting that the resolutions achieved with the picoTDC using the PMT are lower than the intrinsic ECAL resolution throughout the entire explored range (20-700 mV). In the whole range shown in the bottom plot of Figure 4.41, the following considerations are in order:

1. The two threshold values (10 mV and 100 mV) were not optimized, and there are margins for improvement that remain to be investigated. In particular, the high threshold can be set at higher values than 100 mV to cope with the need to keep the amplitude resolution below the intrinsic ECAL resolution in the higher end of the energy scale.

2. At an amplitude of 2000 mV, corresponding to 2000 MeV, the limit to keep the preamplifier response linear within the 1 % level is reached.

3. At an amplitude of 2500 mV, corresponding to 2500 MeV, the saturation level of the preamplifier is reached.

4. The shower leakage effects for ECAL ($\sim 15\ X_0$ thick) are limiting its intrinsic resolution at a scale beyond 1000 MeV, as discussed in Section 4.2.

The foreseen next steps are:

1. Optimization of the thresholds for the best performance in the entire expected dynamic range (2.5 - 2000 mV) and in the preamp saturation regime.

2. Improve the simulation of the PMT signal and FEE in the official SAND MC simulation; implementation of Walk-ToT correction, ToT amplitude reconstruction, preamp saturation, etc.

3. Test of PicoTDC and ToT with KLOE ECAL modules at the test stand at LNF.

4. Other solutions based on PicoTDC are being investigated in collaboration with CAEN and appear very promising. In particular, a solution implementing both a TDC and a QDC (QTDC) on a single board has been developed. In this architecture, the input signal is split into two branches: one branch is sent to a PicoTDC equipped with a single-threshold discriminator, providing excellent time resolution and amplitude reconstruction through the ToT technique; the other branch is sent to a specially designed charge preamplifier followed by a digital pulse-height analyzer, achieving excellent amplitude resolution.

In general, once the most suitable solution for ECAL FEE is chosen, it must be integrated into the SAND data acquisition (DAQ) scheme, with possible synergies with other SAND subdetector electronics (see Section 8).

DRAFT

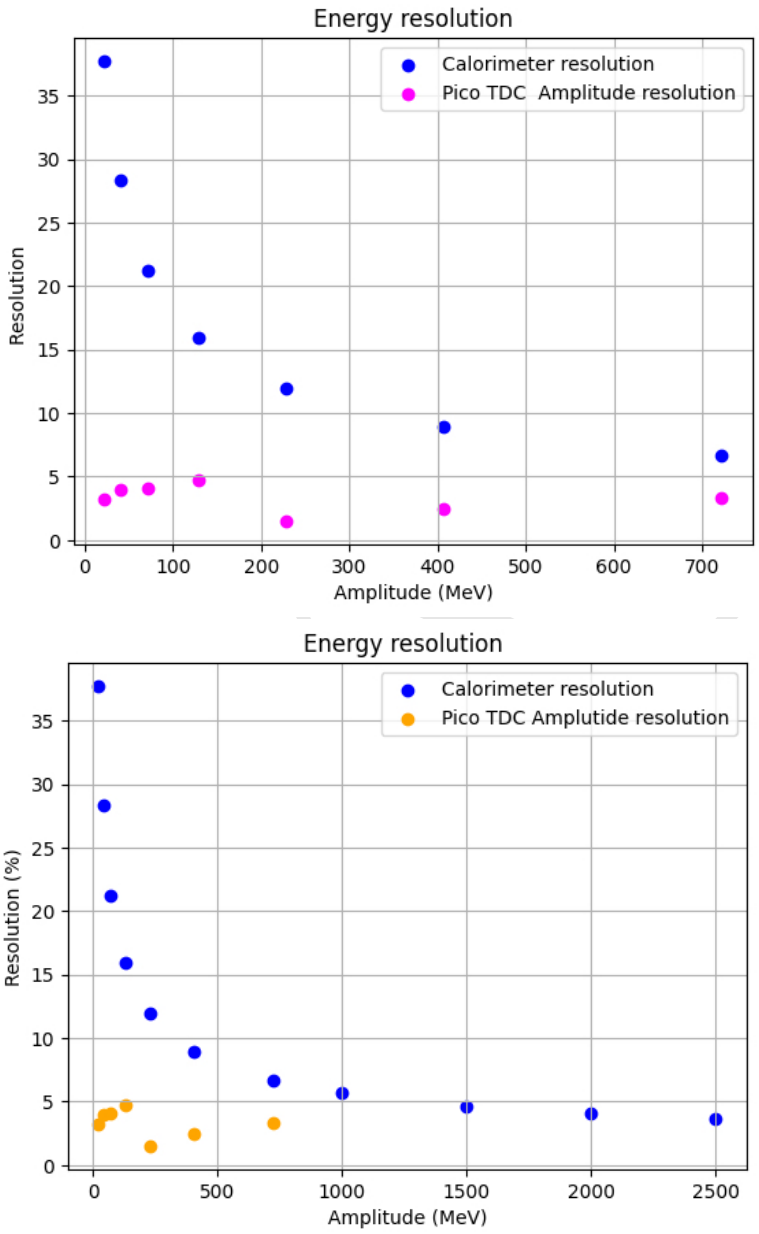


Figure 4.41: Comparison between the intrinsic ECAL energy resolution and the amplitude resolution from ToT vs. energy in the explored range (20-700 mV) (Top) and in the whole energy range expected for signals (Bottom).

4.5.3 High-Voltage

The Hamamatsu R5946/01 PMTs requires a maximum high voltage of 2.3 kV, absorbing an average anode current of 0.015 mA. The CAEN SY4527 mainframe is capable of hosting up to 16 HV A7030P modules suitable for powering the ECAL PMTs. The CAEN A7030P is a module able to independently control up to 48 channels, with an output range of 3 kV/1 mA (1.5 W) at a low ripple ($< 20\,\mathrm{mV}_{pp-max}$ in the range $10 \div 1000$ Hz and $< 10\,\mathrm{mV}_{pp-max}$ over 1000 Hz). The A7030P module is supplied with a high density multipin Radiall 691803004 connector. The described system includes a complete set of software tools for remote control (*via* Gigabit Ethernet) of both the mainframe and the high voltage boards, from low-level libraries to graphical application software. Furthermore, proprietary software introduces easy logging capability to the system. Through this tool, it is possible to record every command sent to the system and every warning/alarm detected by the system. In this way, it is possible to automatically monitor the behavior of every single parameter during operations. The system will be integrated into the slow control.



Figure 4.42: HV system to power 768 ECAL PMTs. In order to power all the PMTs, 8 of these systems are required.

Powering 4880 PMTs requires 100 CAEN A7030P HV modules that will be hosted in 8 CAEN SY4527 mainframes. In addition, 100 CAEN R648 Radiall to SHV connector adapters will be used to transfer HV power from HV module to PMTs. The unused mainframe slots can be used to save HV spare modules (Figure 4.42).

4.5.4 Low-Voltage

Each preamplifier on a PMT base is supplied with $\pm$ 6 V and has a power consumption of 60 mW. Few CAEN A2551 boards, each with 8 full floating channels 8 V/12 A, are sufficient to power all 4880 PMT bases. The output voltage range is $0 \div 8$ V, with 0.2 mV monitor resolution (connector and sense voltages). The maximum output current is 12 A with 500 µA monitor resolution. The maximum channel power is 60 W. These boards can be hosted in the same CAEN SY4527 mainframes used for HV.

4.6 Dismounting Procedures

The first step for dismounting the KLOE detector was the removal of cables, racks hosting the electronics, and other items in the experimental hall. A huge quantity of cables was unplugged from the calorimeter and the ancillary devices. Only the signal and HV cables were stored to be reused at Fermi National Accelerator Laboratory (Fermilab). Twelve boxes were filled with 4880 signal cables and 4880 HV ones (Figure 4.43). Both types of cables are 15 m long. From the six platforms aside KLOE, 32 FEE+HV racks, 150 crates, and 3000 boards were removed.



Figure 4.43: Left: cables (red) connected to the endcap PMTs. Right: removed cables assembled for shipping.

The second step was the extraction of the Drift Chamber (DC) from the calorimeter. Although the DC will not be reused at Fermilab, the extraction required special care for two main reasons. First, it was essential to avoid damaging the adjacent ECAL barrel modules. Second, the DC itself is planned for display at the Laboratori Nazionali di Frascati (LNF) visitor center as a historical artifact of the KLOE experiment. The delicate nature of the DC's construction necessitated this careful approach. The structure is built from carbon fibers, with spherical endplates held apart by 12 rods. An external ring is coupled to each endplate with 48 screws to counteract deforma-

tion caused by the tension from approximately 60.000 wires stretched between the plates. Each wire is crimped onto a copper feed-through, and the chamber's gas seal is provided by an inner cylinder and 12 panels. Consequently, the extraction procedure was designed with three primary objectives: to preserve the DC's integrity, to prevent wire breakage, and to ensure personnel safety.

The extraction of the DC was based on the insertion of a beam (Figure 4.44, right) on the axis of the cylindrical chamber, its clamping on the endplates, and the extraction of the beam and chamber as a unique piece. More in detail, the procedure started with the beam (HEA200, 6 and 5 m long) placed on 3 reinforced concrete pillars. Then the 6 m beam was inserted inside the DC. The beam and the DC were lifted a few millimeters by means of the crane. This was enough to unload the DC weight from the static supports inside the calorimeter. A system with trolleys, suitably positioned on the end plates, allowed the DC to slide along the beam. Once the chamber was extracted from the calorimeter (Figure 4.44, left), it was lifted with a suitable sling bar and placed on a handling trolley located at the entrance of the experimental hall. Then it was ready to be taken away.

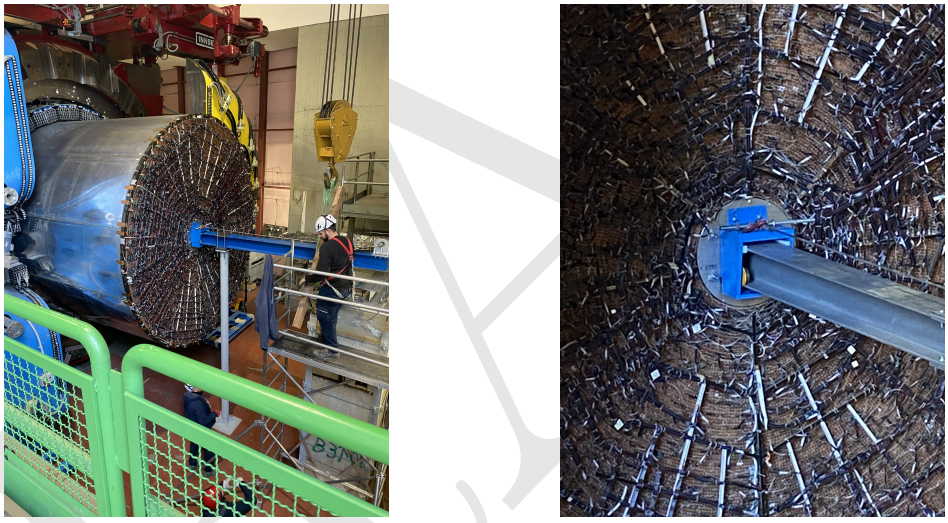


Figure 4.44: Left: extraction of the drift chamber from the KLOE calorimeter at LNF. Right: zoom on the HEA200 beam and the trolley (detail in the text).

DRAFT

4.6.1 Barrel Modules

The dismantling operation on the calorimeter cylindrical part consists of the extraction of 24 modules located inside the KLOE apparatus. The module dimensions and mass are reported in Figure 4.45. Each module has a mass of 3500 kg and is made of several layers of lead and scintillating fibers glued together. The layout of the calorimeter is shown in Figure 4.46 together with the numbering scheme used.

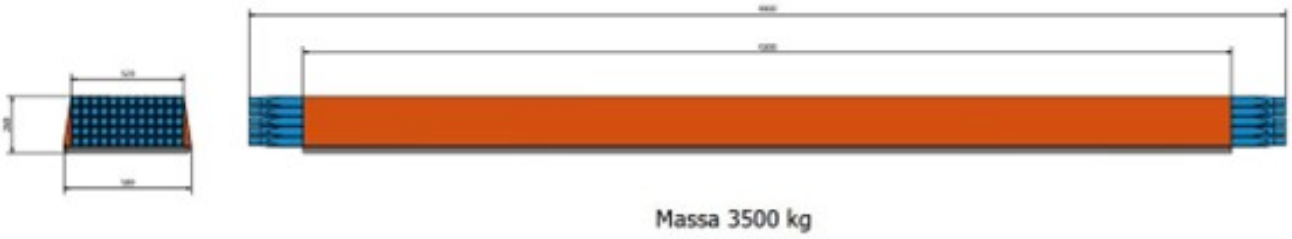


Figure 4.45: Scheme of a module of the barrel.

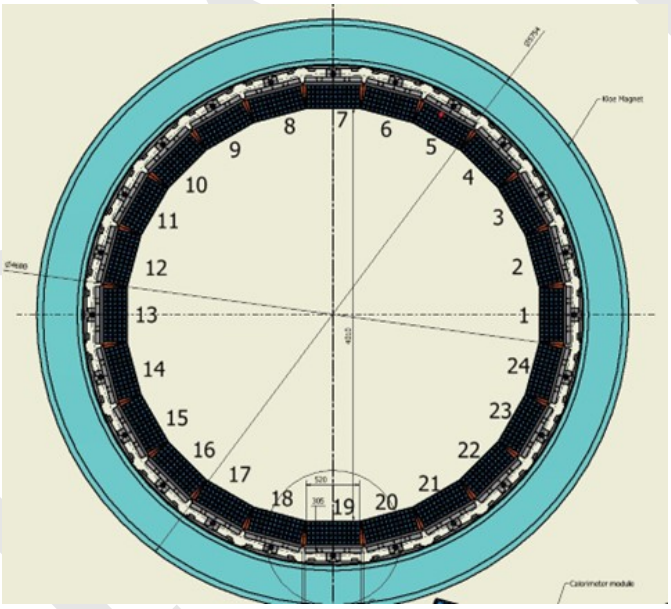


Figure 4.46: Scheme of the 24 modules of the calorimeter barrel.

For this operation, the old insertion tool has been thoroughly refurbished and used as an extraction tool (see Figure 4.47). It required an external platform to be placed at the proper height, which has also been designed and customarily realized by an external company under ECAL group supervision (see Figure 4.48). Both are suitable for the insertion of the modules and comply with US safety regulations. The 24 modules can slide through bearings on the bars fixed to the internal wall of the magnet cryostat vessel (see Figure 4.49). The extraction tool has a steel shaft (Figure 4.50 left) that, once engaged with the support bar, allows for the extraction of the module. The shaft is fixed to the upper frame of the extraction tool, which can be moved longitudinally and rotated in all three spatial axes independently from the base, with precise fine-tuning screws in order to perfectly align the two shafts without moving the heavy base part.

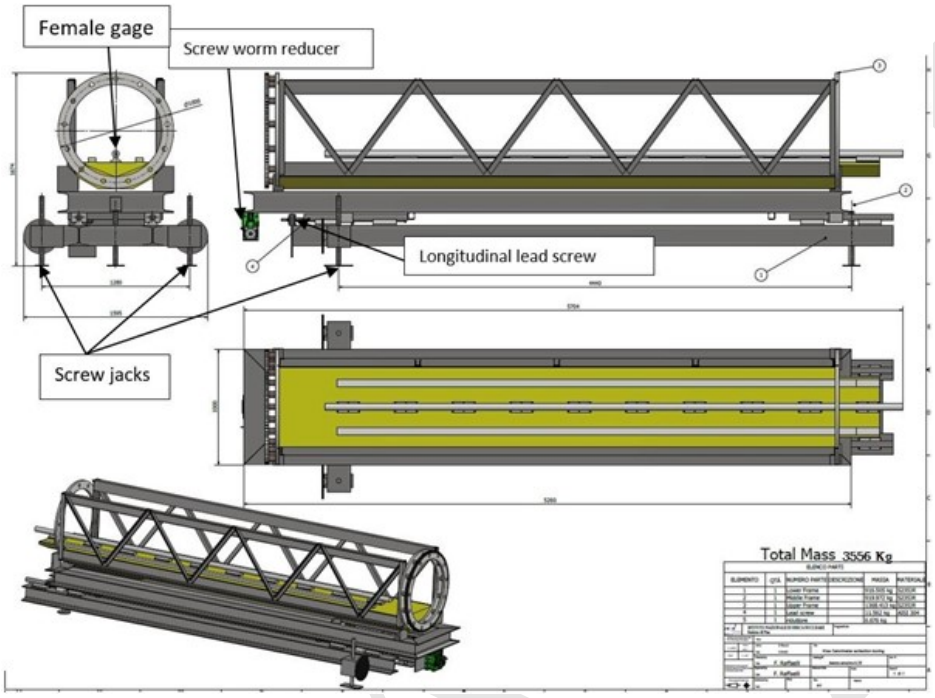


Figure 4.47: Drawing of the tool for the barrel modules extraction.

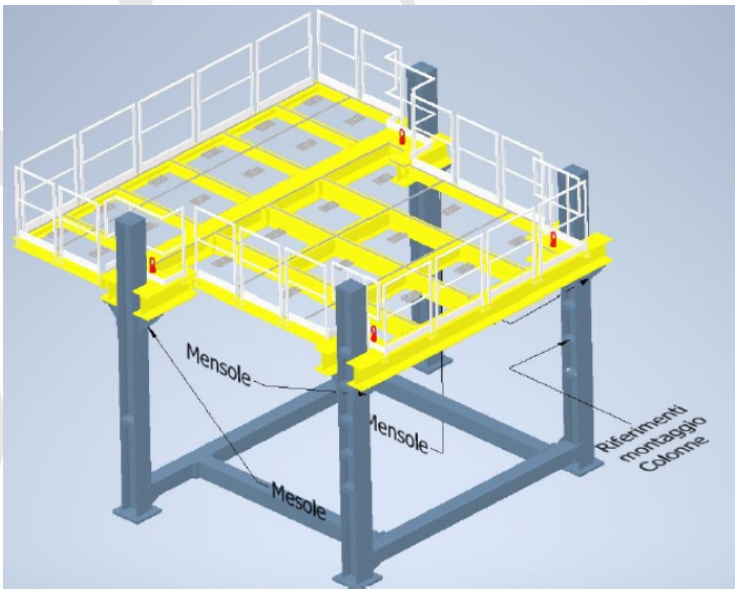


Figure 4.48: Drawing of platform used to position the extraction tool in front of the calorimeter.

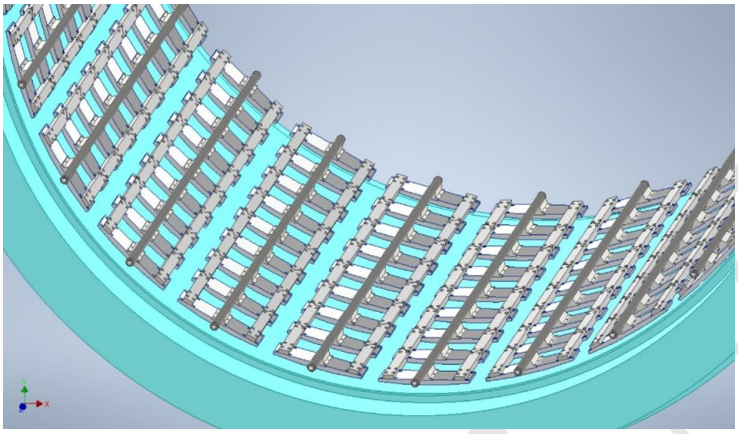


Figure 4.49: Detail of the supporting bars inside the cryostat.



Figure 4.50: Extraction tool (left) for the calorimeter modules and its operating position on the movable platform (right).

DRAFT

The complete list of steps for barrel dismantling is as follows:

1. Insertion of internal support pillars. Nine pillars have been used to hold up the 7 upper modules: 3 on the moving module with rolling elements and 3 fixed on each of the neighboring modules (see Figure 4.51).

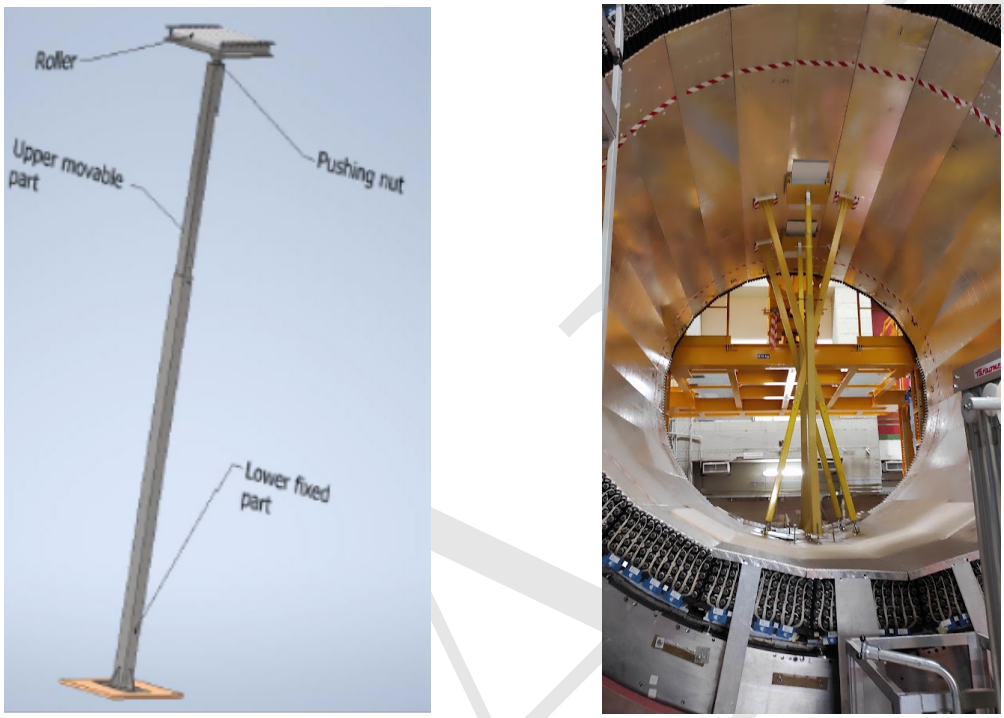


Figure 4.51: Drawing of the safety support pillar (left) and the pillars mounted inside the calorimeter (right).

2. Setup of the external platform at the appropriate height. For each pair of modules at the same height, the platform is moved correctly on its legs. The same position is used for the group of the 3 uppermost modules, thanks to a limited vertical adjustment of the extraction machine.

3. Setup of the extraction tool on the platform with the crane. Once positioned, the extraction tool is aligned to the module by adjusting the upper frame, which has independent movement controls in all 3 spatial planes. When the extraction shaft and the module shaft are aligned, the upper frame is rotated to the right angle corresponding to the module (see Figure 4.51). Finally, the frame is longitudinally moved towards the module until the two shafts are engaged through their conical coupling ends.

4. Pull out of the module. A belt is fixed to the module and to a chain hoist used to manually extract the module. Four screws inserted in the bottom plates of the modules, at their ends, act as guides, scraping their heads on rails mounted on the extraction machine. Adjusting the screws allows one to slightly rotate the module around its supporting shaft to gain a few tenths of a millimeter of clearance between the adjacent modules. The friction of the screws on the rails creates the most force needed to move the module, measured by a dynamo-meter in several thousand newtons.

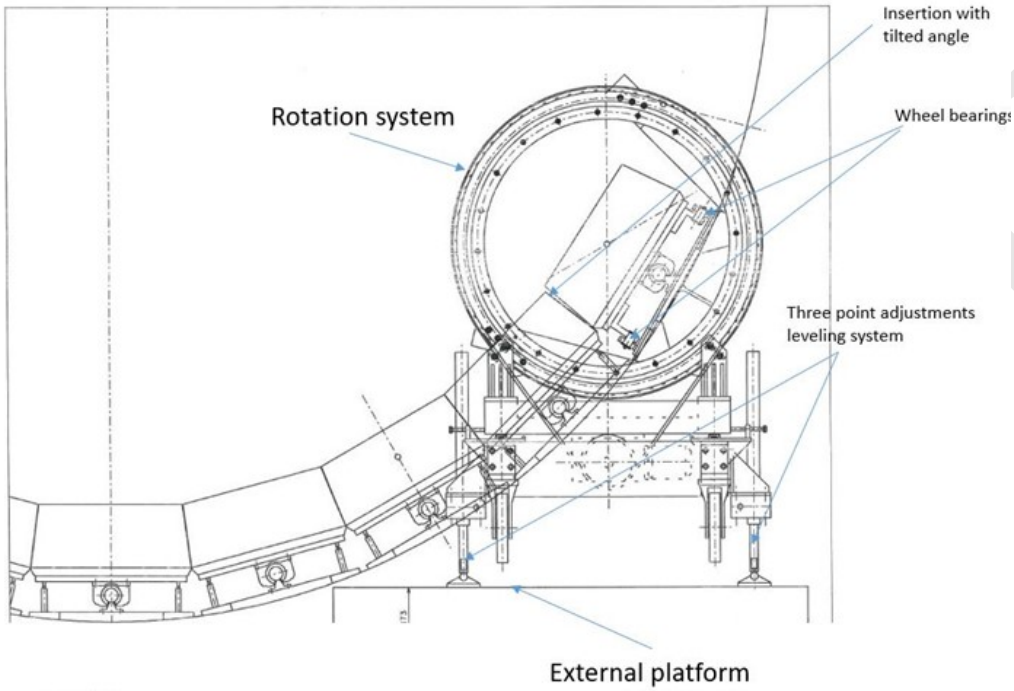


Figure 4.52: Scheme of the extraction of a barrel module.

5. Secure the module with confining straps. While the module is extracted from the magnet vessel, straps are placed every meter to wrap the lead layers and avoid possible delamination.

6. Positioning of the extracted module. When the module has completely shifted from the support shaft to the extraction tool shaft, the upper frame is first retracted to the rear stop position and then rotated until the module is placed horizontally with the support plates at the bottom.

7. Lift the module and move it to the storage area. The module is disconnected by the support plates and the bearings, lifted with the crane from the extraction tool, and moved to the test area (see Figures 4.53, 4.54).

4.6.2 Endcap Modules

Here, the operation list is presented for the endcap dismantling.

At the very beginning, the disassembly tool is positioned in front of the KLOE apparatus. Once the overhead crane has also been positioned, the first module is extracted after having previously disconnected it from the plate (see Figure 4.55). Then the module Cradle is assembled; it will also be used to transport and place the module on the transport support.

The disassembly procedure involves the use of the upper holes with a diameter of 21 mm present on the tool to insert a pin with a nut, which is then screwed into the two M12 threaded holes of the revolving eyebolts with a joint. This operation allows the straps to be hooked to the overhead crane, which enables the module to start rotating and be brought to an almost vertical position.

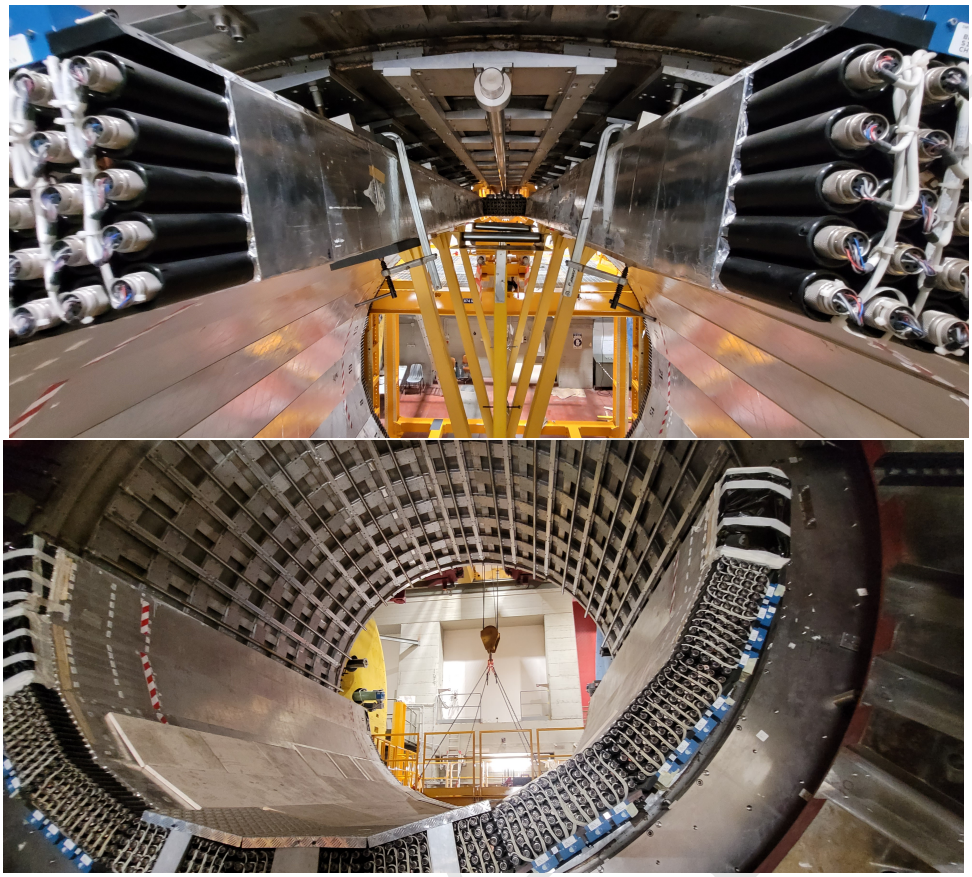


Figure 4.53: Extraction of the first barrel module (top) and progress in the extraction operation (bottom) from magnet cryostat.



Figure 4.54: Test area for ECAL modules at LNF.

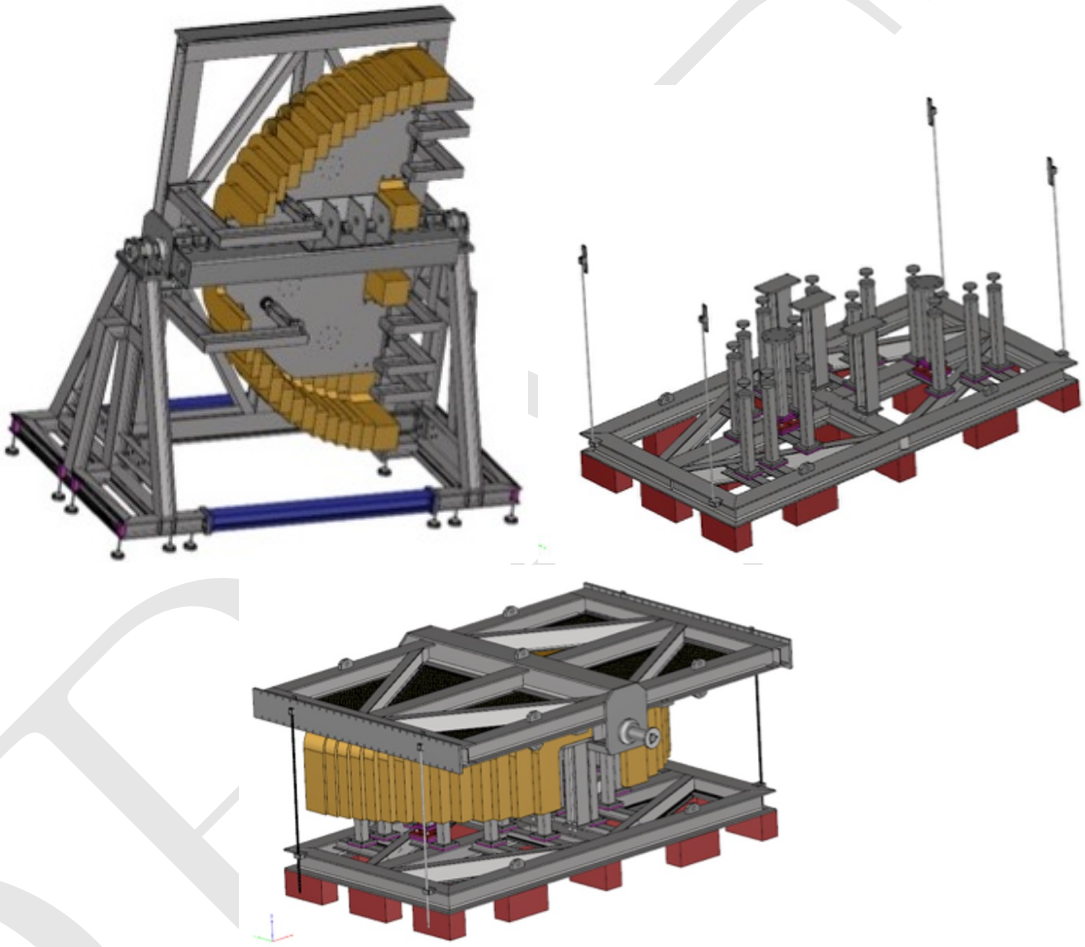


Figure 4.55: Disassembling, rotation, and handling mechanical tools for endcaps.

DRAFT

By positioning a rotating eyebolt with a joint, the unhooking of the structure commences. In this phase, the pushers present in the calorimeter plate are activated, and a gap is created between the iron part and the bearing plate of the calorimeter. This operation allows for the insertion of the aluminum shelves, on which a sliding beam will be moved, aligned with the M24 threaded holes on the half-plate and subsequently blocked with screws.

The tool with the rotating table (tipper), using the holes present on both ends, blocks the barycentric subsystem, which will allow the rotation of the rotating table dragged by the overhead crane. The rotating plane/center of gravity system is transported to the half-plate via the overhead crane. Through the centering of the eight M36 holes present on the blue beam, the entire system becomes integral.

The next phase consists of assembling the 2 "C" supports on one side and the other 6 small ones on the other side; this operation serves to minimize the possible deformations that the calorimeter plate could undergo.

The movement of the rotating table/calorimeter system begins at the support, which allows for the rotation of the table from vertical to horizontal. Additionally, the first pair of the braking system is introduced, which secures the table in a vertical position. Subsequently, it is blocked with the second braking couple and the rotation maneuver can proceed. It consists of using the coupled support to ensure that the system stops in an almost horizontal position, dismantles the barycentric system, and assembles the system to center the calorimeter with the support on the rotating table used for shipping.

The next phase is to prepare the shipping tool and proceed with the assembly of the 14 supports, adjusting them to a height of 955 mm. The centering system is positioned through perforated plates, blocked on the frame for shipping, and utilizes a clamp system.

Afterwards, it is possible to transfer the calorimeter using the overhead crane to the shipping support and to place the calorimeter on the shipping frame on the 14 mentioned supports. The calorimeter half-plate can be secured using the M16 holes, which are used to connect the pushers, along with the 2 supports and the centering system made up of several slotted plates connected integrally to the shipping frame, compensating for any difference in height with threaded bars.

Using the holes present on the sliding beam, it is necessary to insert eyebolts in order to hook the straps, which, when attached to the overhead crane, will allow for the dismantling of the screws connecting the sliding beam to the half-plate. The half-plate will be placed on translating tables to facilitate its extraction from under the calorimeter.

As a final phase, everything is transported to the storage position using the revolving table.

DRAFT

4.7 Refurbishment and Test before SAND Installation

The 24 modules composing the barrel of ECAL will be thoroughly revamped after their dismantling. The list of operations needed in order to have all the elements ready to be mounted again is:

- gluing of delaminated lead foils;
- gluing of the unstuck light-guides;
- repair of aluminum grids holding PMTs;
- repair or replacement of the aluminum protection of PMTs;
- wrapping of modules with aluminum tape reinforced with glass-fiber.

Delamination of lead foils from the support plate notoriously occurs in the three top-most modules just after the calorimeter assembly. During the years of KLOE operation, the position of the internal face of these modules has been monitored with gages, but no evidence of further detachment has been registered. A laser-tracker 3D mapping of the calorimeter has been performed before the dismantling, which confirmed the delamination of the three top-most modules resulting in an increase in the overall thickness of about 20 mm. Minor increases of the order of 1 mm have been measured for other modules mounted on the top part of the cryostat. All these modules have been supported by pushing rods during their extraction to avoid any additional damage and for safety reasons. The revamping procedure involves injecting an epoxy adhesive into the delaminated layers and pressing the module, possibly with a vacuum-bag. The Loctite EA-9483 is quite suitable, thanks to its very low viscosity and high optical transparency. This gluing process is needed for about six modules (see Figure 4.56).



Figure 4.56: Delaminated ECAL modules.

In only one case during the extraction, the light-guides suffered a disconnection from the lead. Neither of the parts has been damaged, so it was possible to proceed to the polishing of the surfaces and a new gluing (see Figure 4.57).

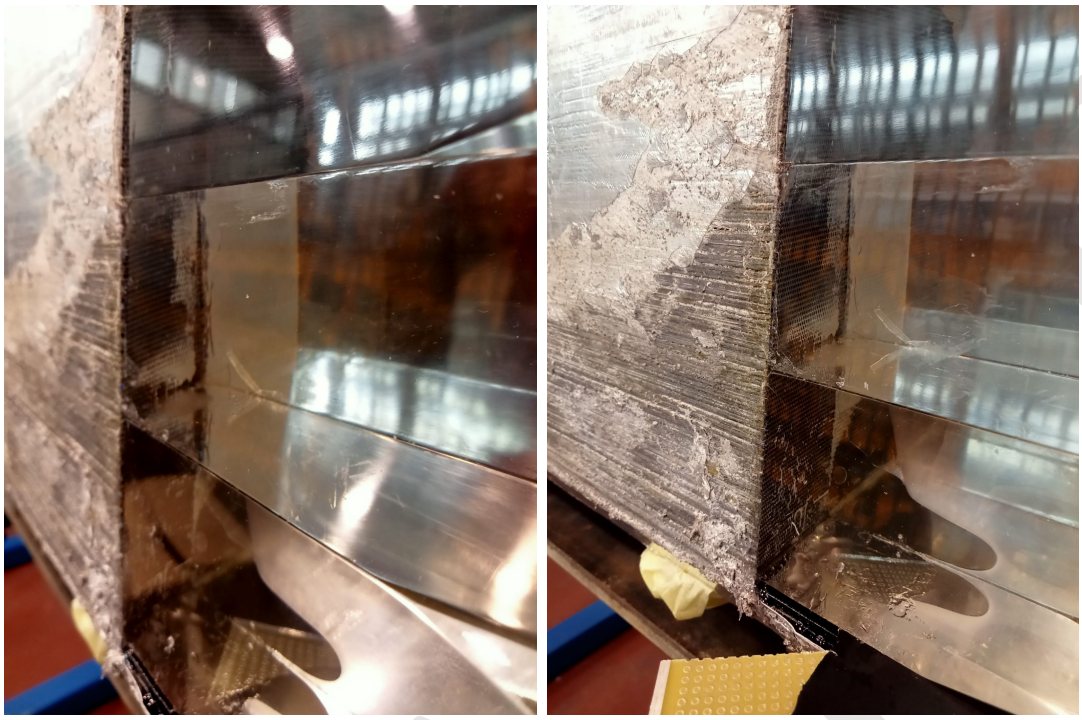


Figure 4.57: Light-guides before and after gluing.

In the same module, the grid in front of the PMTs has been bent during the extraction. A new one is going to be machined (see Figure 4.58).



Figure 4.58: The aluminum grid supporting PMTs going to be replaced.

On their side-ends, the light-guides have additional protective foils made of aluminum 0.25 mm thick. In a few cases, these have been damaged and will be installed as new.

Finally, the most time-consuming revamping activity is the new wrapping of the modules. The 3M-363 tape has been identified as the most suitable wrapping tape among those available. It is made of aluminum and fiberglass, 450 mm wide and 0.19 mm thick. The old tape will be removed and replaced on all parts where it is deteriorated, while on the parts that are perfectly intact, the new tape will be placed above (see Figure 4.59).



Figure 4.59: A barrel module during the tape wrapping.

DRAFT

Although not damaged, the support plates of the modules will be partially revamped. Each module hosts three (or five, depending on the position of the module) aluminum plates 30 mm thick, fixed with screws to the long bottom plate, which acts as a base for the lead and scintillating fiber layers. These plates hold the cylindrical cushions that bind the modules to the support bars fixed in the inner wall of the magnet cryostat. All the screws will be replaced with new ones, and the possibility of machining the plates is studied, thinning them by a few millimeters. In this way, the modules will be closer to the magnet and clearance would increase between the side faces of modules by hundreds of microns, allowing for smoother and easier assembly.

4.7.1 Light Tightness and Tests with Cosmic Rays

The tape wrapped around the modules has not only a mechanical role but is also mandatory for light tightness. After the complete re-wrapping, a test of the light tightness of the modules is necessary. Most of PMTs have already been dismounted for safety reasons during the extraction operation of the modules from the magnet. All PMTs will be dismounted, and after a proper cleaning of the light guides and the PMT photocathode window from the old optical grease, they will be reinstalled in the ECAL modules, applying a new optical gel for optimal optical contact.

Afterwards, the single PMTs and the entire module will be tested. The PMT check consists of the readout of the output signal from each tube. A test stand will be equipped with the KLOE readout electronics (constant fraction discriminators, ADCs, and TDCs) to check the operation of two complete barrel modules (240 PMTs) by collecting signals induced by cosmic rays. The module performance in terms of light yield, energy and time resolution, and coordinate reconstruction along the fibers will be measured according to the procedures already developed during the commissioning in KLOE at a similar cosmic ray test stand [33]. The consistency of the results with the expected ECAL performance will be checked.

Comparative tests of the prototypes of the new FEE chosen for ECAL will be performed, with respect to KLOE FEE, the latter guaranteeing the ECAL performance cited in Section 4.2. After the test, the option of dismounting all PMTs again from the ECAL modules and shipping them to Fermilab separately from the modules will be evaluated based on the experience during the test at LNF (e.g., failure rate in dismounting/re-mounting PMTs, connector or pin problems, etc.) and a proper risk analysis.

4.8 Installation & Integration

The main operations related to the packaging and sea shipment of the ECAL are briefly described, along with the requirements and support needed at the Fermilab for temporary storage and transport to the experimental hall. More details about I&I procedures are in Section 10.

4.8.1 Packaging and Shipping

The calorimeter can be shipped from LNF to Fermilab either by ship or by plane. At the present time, both options are being considered.

The 24 modules of the barrel will be fixed to their own steel supports, and each one will be closed in

a box. The complete list of sensors to be inserted in the box is still under definition; most likely, an accelerometer, a thermometer, and a hygrometer are mandatory. For each sensor, a minimum and maximum value of the measured quantity will be agreed upon with the transportation company for the dual purpose of recording the environmental conditions during the travel and defining the insurance policy. All the boxes will be equipped with a GPS tracking device. The 4 endcap modules will have dedicated supports and boxes.

A preliminary study of the viability and possible routing of the shipping has been commissioned to a specialized company. Being a dedicated boat for the ocean crossing out of budget, scheduled routes are considered. Possible starting harbors not too far from LNF could be Naples, Civitavecchia, or Livorno, while the arriving harbor in the US is still to be defined. It will be chosen considering the proximity to Fermilab, but also the connection with suitable roads. In fact, if the transportation of the calorimeter modules does not require overload or special shipping, it must be planned together with the magnet transportation, which, on the other hand, does require oversize shipping. For instance, the 5.80 m height of the coil is more than the usual clearance of highway bridges, ranging from 4.50 to 4.90 m. For this reason, the possibility of reaching Fermilab via internal waterways and loading the magnet onto canal boats is analyzed.

The iron yoke will be dismounted into 32 pieces, each fitting in a standard 20' container and with a maximum weight of 20 t. The use of boxes for this is not foreseen; rather, it is intended to protect the parts prone to oxidation with grease and to wrap them with a vinyl film.

4.8.2 Activities at FNAL

Upon arrival at Fermilab, ECAL modules will be stored in a proper area equipped with a crane of 5 t maximum load for handling barrel modules, and 15-20 t for handling endcap modules. A controlled temperature environment is required in the storage and test area of ECAL modules, avoiding thermal stresses and keeping temperature changes within about $\pm 10^{\circ}$ C throughout the entire period.

The location of these areas is being identified, and their availability for the required period (see the detailed time-schedule in Sect. 4.10) will be agreed upon with Fermilab, according to Fermilab and DOE regulatory requirements.

The quality assurance (QA) and quality control (QC) operations will be performed, repeating the tests on each module done at LNF, as described above. In particular, the ECAL module performance will be checked again at a cosmic ray test stand with the same equipment used at LNF before installation in the SAND detector.

4.9 Risk Management

The existing components, repurposed from the KLOE detector, have operated for several years at the INFN Laboratori Nazionali di Frascati. Their functionality is amply demonstrated, and their performance is well known and documented [34]. As part of the preparatory work to be performed before the delivery of the components to Fermilab, all subcomponents, after minor repairs and eventual upgrades, will be extensively tested at LNF. These tests, in addition to confirming the

functionality of the subcomponents before travel, will also establish the protocols to be used for QA and QC upon arrival at Fermilab. Development of appropriate documentation for the approval of operation at Fermilab is being conducted in close cooperation with a dedicated Fermilab engineering team, which is also involved in the definition of the necessary QA/QC protocols. Finally, the same teams and companies involved in the disassembly and testing of the repurposed subcomponents will conduct the tests and the re-assembly at Fermilab. The strategy described above covers most of the risks associated with the installation and utilization of the existing subcomponents of the KLOE detector at Fermilab. The risk analyzes in this Section and in Section 4.9 mostly focus on possible damages occurring during the transport from LNF to Fermilab. Catastrophic events, such as the destruction or loss of significant portions of the ECAL, are not considered, as they would imply a significant re-definition of the experimental program. It has to be noted that the ECAL modules have been transported by truck from their production sites to LNF (about 100 km), without any issues. Other events considered in the risk analysis are related to reassembly operations and the non-functionality of newly constructed components.

4.9.1 Detailed Risk Analysis

1. Event: External damage with inelastic deformation of the lead or the aluminum cover in the hit point, or partial detachment of light guides

   - Possible causes - Shock, bump or vibrations occurred during the transport.
   - Possible consequences - Impossibility of installation of the damaged module due to the deformed geometry, inoperability of the ECAL cells corresponding to the damaged portion of the module. Localization and repair of the damage, by partial disassembly of protective tape and aluminum covers if needed, machining and milling the surface on the hit point, or by re-gluing possible delaminated lead foils, re-gluing or substituting the damaged light guides during the QA/QC phase at Fermilab. These operations cannot take place in the alcove. The estimated time for the operations ranges from few days to four weeks depending on the severity of the damage and the number of interested modules.
   - Estimated Probability - Moderate, 2% to 5% (from long distance transport statistics).
   - Detection - Visual inspection after delivery to Fermilab, check the recording of the accelerometers. Test of module before insertion in the detector.
   - Intervention- Repair the module and re-test its functionality and performance with cosmic rays.
   - Mitigation - Detailed engineering of the transport with shock and vibration analysis and thermal shock analysis; definition of maximum accelerations, of maximum speeds of road transport, definition of supports and shock absorbers, definition of maximum thermal variation and of controlled temperature container or environment during transport. Transport with online shock logs and periodic check-points. Choice of carrier with highest reliability for special transports. Early detection by inspection and test upon arrival at Fermilab and before installation of detector components in the magnetized volume.

2. Event: thermal stress with possible partial detachment of light guides or partial damage of

scintillating fibers

- Possible causes - Large temperature variations during the transport or temporary storage.
- Possible consequences - reduced light collection efficiency and Physical performance of the modules. Localization and repair of the damage, by partial disassembly of protective tape and aluminum covers if needed, re-gluing light guides during the QA/QC phase at Fermilab. These operations cannot take place in the alcove. The estimated time for the operations ranges from few days to four weeks depending on the severity of the damage and the number of interested modules.
- Estimated Probability - Moderate, 2% to 5% (from long distance transport statistics).
- Detection - Visual inspection after delivery to Fermilab, check the recording of the thermometers. Test of module before insertion in the detector.
- Intervention- Repair the module and re-test its functionality and performance with cosmic rays.
- Mitigation - Detailed engineering of the transport with thermal shock analysis; definition of maximum thermal variation and of controlled temperature container or environment during transport. Transport with online temperature logs and periodic check-points. Choice of carrier with highest reliability for special transports. Early detection by inspection and test upon arrival at Fermilab and before installation of detector components in the magnetized volume.

3. Event: thermal or mechanical stress of PMTs with possible vacuum leak

- Possible causes - Shock, bump or vibrations occurred during the transport, or thermal shock during the transport or temporary storage.
- Possible consequences - Inoperability of PMTs. Broken units need to be replaced before installation in ECAL modules during the QA/QC phase at Fermilab. These operations cannot take place in the alcove.
- Estimated Probability - Moderate, 2% to 5% (from long distance transport statistics).
- Detection - Visual inspection after delivery to Fermilab, check the recording of the thermometers. Test of module before insertion in the detector.
- Intervention - Repair the module and re-test its functionality and performance with cosmic rays.
- Mitigation - Detailed engineering of the transport with shock and vibration analysis and thermal shock analysis; definition of maximum accelerations, of maximum speeds of road transport, definition of supports and shock absorbers, definition of maximum thermal variation and of controlled temperature container or environment during transport. Transport with online shock and temperature logs and periodic check-points. Choice of carrier with highest reliability for special transports. Early detection by inspection and test upon arrival at Fermilab and before installation in ECAL modules.

  Depending on the experience acquired during the ECAL module test at LNF, the option of dismounting all PMTs from the ECAL modules and shipping them separately in smaller and easier to handle boxes (as delivered by Hamamatsu from Japan to Italy)

might be considered.

4. Event: Malfunctioning or break of ECAL electronics - High Voltage and Low Voltage power supply and FEE (new equipment).

   - Possible causes - Infancy defect. Damage due to transport.
   - Possible consequences - Inoperability of corresponding ECAL modules. If detected during the commissioning it would result in a stop of the commissioning for the time required for repair/substitution. Spare units are available for a prompt substitution if needed.
   - Estimated Probability - Moderate $\sim 2\%$.
   - Detection - Operate the unit and monitor its functionality and corresponding ECAL module performance.
   - Intervention - Remove the unit. Assess the problem in the lab and define the required repair or substitution.
   - Mitigation - Early detection by testing electronics in the lab or during QA/QC phase before installation.

4.10 Schedule and Milestones

A detailed time-schedule of the ECAL dismounting and shipping is summarized in Figure **??**.

DRAFT

Chapter 5

GRanular Argon for Interactions of Neutrinos (GRAIN)

Fix missing section references based on new organization.

An active LAr target (GRanular Argon for Interactions of Neutrinos (GRAIN)) has been designed to be installed inside ECAL, upstream of the tracking system, with the goal of complementing measurements of the neutrino flux and the ν-Ar cross-section. In contrast to time projection chambers (TPCs), event detection does not rely on drift electrons but rather on scintillation photons.

5.1 Introduction and Physics Requirements

GRAIN is a 1 t LAr target that will be placed upstream inside the magnetized volume of SAND. It will provide measurements of both inclusive and exclusive Ar interactions for nuclear-effect studies, as well as a complementary Ar target for cross-calibration with the other DUNE ND components, which will be off-axis for 50% of the total run time.
In the near detector (ND) complex, the primary LAr target will be ND-LAr, which employs a detector technology similar to that used in the far detector (FD). However, ND-LAr cannot guarantee full containment of neutrino interaction events. Consequently, the momentum and charge of muons must be measured by another detector placed upstream.

Since the neutrino interactions in GRAIN are not affected by the same systematics, SAND can provide an additional sample which acts as important complement to ND-LAr in the context of oscillation analyses.
The strength of GRAIN is primarily determined by its location inside SAND, as the full potential of the tracker and the ECAL can be exploited to analyze ν–Ar interactions. In particular, the neutron-detection efficiency of the tracker and the electromagnetic calorimeter allows for their inclusion in the reconstruction process, preventing degradation of the energy resolution. Moreover, thanks to the magnetic field, the momentum and charge of muons can be measured directly with a larger

acceptance than the forward-going fraction of ND-LAr, since the internal GRAIN reconstruction and the calorimeter also ensure coverage for muons at large angles. This synergy between the independent measurements from the large mass of ND-LAr (67 t), which uses a technology closer to that of the FD, and the smaller mass of GRAIN (1 t), located in a magnetic field and subject to different systematic effects, will strengthen the overall robustness of the ND detector complex. The contribution of GRAIN samples to the long-baseline oscillation analysis is twofold:

- GRAIN can provide data samples from the different flavor components of the beam for neutrino flux evaluation, as well as constrain background processes in the analysis, such as wrong-sign contamination, neutral current interactions, π^0 and γ production, meson decays, and others;
- GRAIN can constrain systematic uncertainties in ν–Ar cross-section measurements at DUNE energies. In addition, the neutrino interaction model can be tuned using data acquired from different nuclear targets, all collected within the same detector infrastructure (SAND).

A high-precision reconstruction of neutrino interactions in GRAIN is therefore crucial for the DUNE physics program. In particular, since low-energy particles are absorbed in the liquid argon (LAr) volume or in the GRAIN cryostat, and particles emitted at large angles relative to the beam direction fall outside the tracker acceptance, biases in topological reconstruction and energy estimation may occur. These limitations can only be mitigated by instrumenting the LAr volume. In the current design, to collect scintillation light for reconstructing charged particle tracks produced in neutrino interactions, GRAIN will be instrumented with innovative detectors based on silicon photomultiplier (SiPM) matrices coupled to dedicated optical systems. On the one hand, the light readout in GRAIN will provide event timing and calorimetric measurements of the total energy deposited in the LAr volume. On the other hand, if the optical system operates at full efficiency, the acquired images could deliver additional information for event topology reconstruction, such as the number of primary and secondary tracks, the position of the neutrino interaction vertex, and particle identification. This would enable neutrino interactions in GRAIN to be reconstructed with very high accuracy.

5.2 Mechanical Design

As depicted in Figure 5.1, the GRAIN cryostat consists of an Internal Vessel housed within a Vacuum Vessel, both with an elliptical transverse shape. The Internal Vessel, made of Stainless Steel (AISI 316L), has an elliptical transverse base with axes measuring 49 cm and 148 cm and a longitudinal length of 150 cm. It is designed to store 1 t of LAr and withstand an internal pressure of 1.5 bar.

The Internal Vessel includes the main body within a 6 mm thick shell, reinforced by two H-shaped ribs, each 6 mm thick, to ensure structural rigidity while minimizing the material budget transverse to the beam axis. The two open bases are closed by two endcaps 30 mm thick, each equipped with instrumentation flanges: 4 CF-DN160, 2 CF-DN63, and 2 CF-DN40, fitted with feedthroughs for signals and detector power, as shown in Figure 5.3. The thickness of the endcap was chosen to ensure sufficient rigidity to avoid deformations that would compromise the sealing of the "Helicoflex" seal. A detailed finite element analysis (FEA) was commissioned to an external

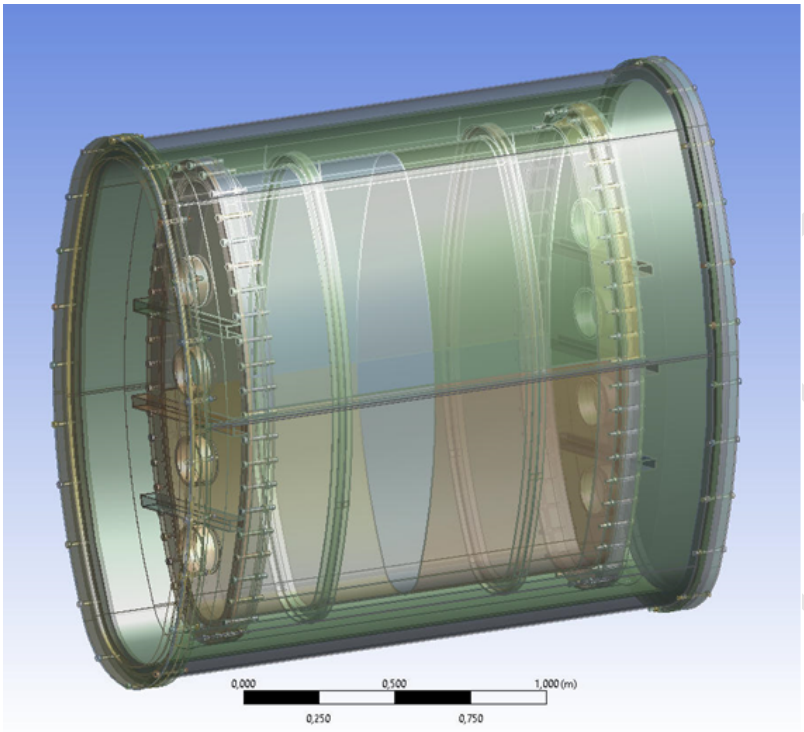


Figure 5.1: GRAIN cryostat.

Engineering Studio to verify that the deformations and the strengths were within the acceptable tolerances. In particular, this study was fundamental in choosing the correct Helicoflex sealing.

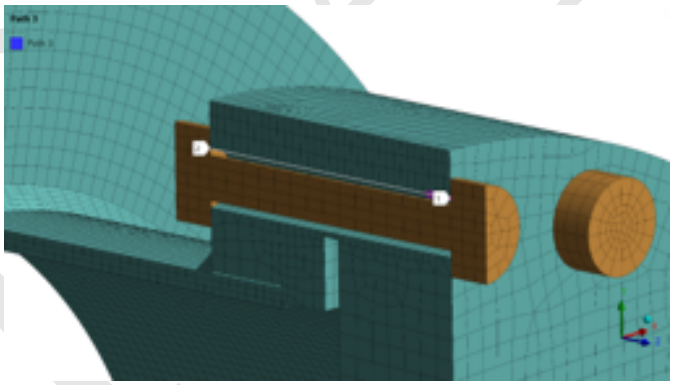


Figure 5.2: GRAIN - Details of FEA.

The imaging detectors will be mounted on frames attached to the end caps.
In the current design, there are two pipes welded to the top of the Internal Vessel: one for the input of LAr coming from the recondenser and one for the boil off of GAr. The thermal insulation of the Internal Vessel relies on the vacuum, which is maintained at about 1×10^{-5} mbar inside the Vacuum Vessel, ensured by a dedicated pumping system. Additional insulation is provided by minimized thermal conduction through the suspension and multi-layer insulation loosely wrapped around the internal vessel.

The Vacuum Vessel originally was foreseen to be made of a composite structure based on a sandwich made of a 40 mm overexpanded Nomex core and two 6 mm CFRP (Carbon Fiber Reinforced

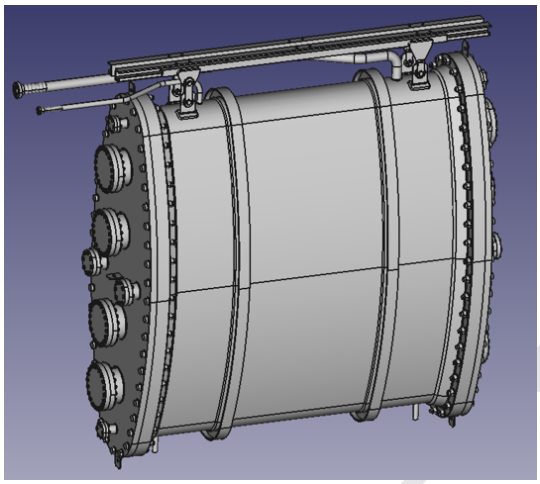


Figure 5.3: GRAIN Internal Vessel.

Plastics) skins. Technical challenges and cost considerations suggested to abandon this solution in favor of a more traditional and safe approach. Presently a new design in under way based on an Aluminum vessel with a body of elliptical shape and two endcaps featuring the same number of flanges as the Internal Vessel, thereby enabling signal transmission and power distribution to the detector. The tests of the Inner Vessel, while waiting for the GRAIN Outer Vessel, will be done inside a cylindrical Vacuum Tank made of stainless Steal.

To facilitate maintenance operations and detector upgrades, the Internal Vessel will be inserted and extracted using a sliding system (see Figure 5.4). This system consists of two Teflon bars, one fixed and one sliding on the other, ensuring minimal friction and eliminating the need for extreme planar tolerance due to the Teflon-on-Teflon contact. The Teflon is glass-reinforced to prevent long-term deformation that could result in the Internal Vessel becoming stuck inside the Vacuum Vessel. To mitigate damage risks caused by the different thermal contraction rates of Teflon and stainless steel, the Teflon bars are composed of separate segments placed side by side. The fixed Teflon bar is riveted to a C-shaped stainless steel bar mounted on the vacuum vessel, while the sliding Teflon bar is riveted to a carriage attached to the internal vessel. To minimize thermal conductivity through the suspension system, G10 bushings serve as thermal breaks between the internal vessel and the support rods. On one side, each rod is hinged to accommodate the longitudinal thermal contraction of the Internal Vessel, while the other side remains rigidly fixed.

5.3 Cryogenic System

A schematic view of the cryogenic system is depicted in Figure 5.5. Instead of having a forced circulation of liquid argon by means of a pump and filters, as was foreseen in the initial design, a quasi-passive recirculation will be implemented. The static heat load, along with the heat dissipated by the detectors, vaporizes part of the LAr contained in the cryostat. The produced gaseous argon (GAr) is liquefied in the re-condenser and then sent back to the cryostat by gravity. If the boiloff, caused mainly by the electronics of the detectors, is not sufficient to sustain the circulation, a heating element will be inserted into the circuit, along with a pump and a filter operating on gas. The purification achieved with this scheme is not at the level of that obtainable with forced circulation in liquid, but it should be sufficient to guarantee the purity for optical

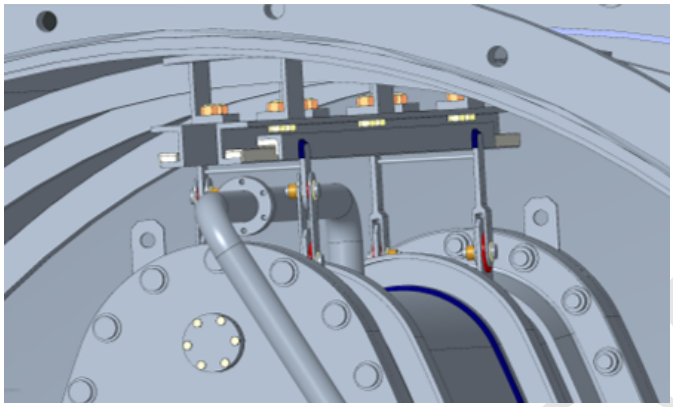


Figure 5.4: GRAIN Internal Vessel sliding system.

transparency, namely $O_2 \leq 0.1\,\text{ppm}$, $N_2 \leq 1\,\text{ppm}$.

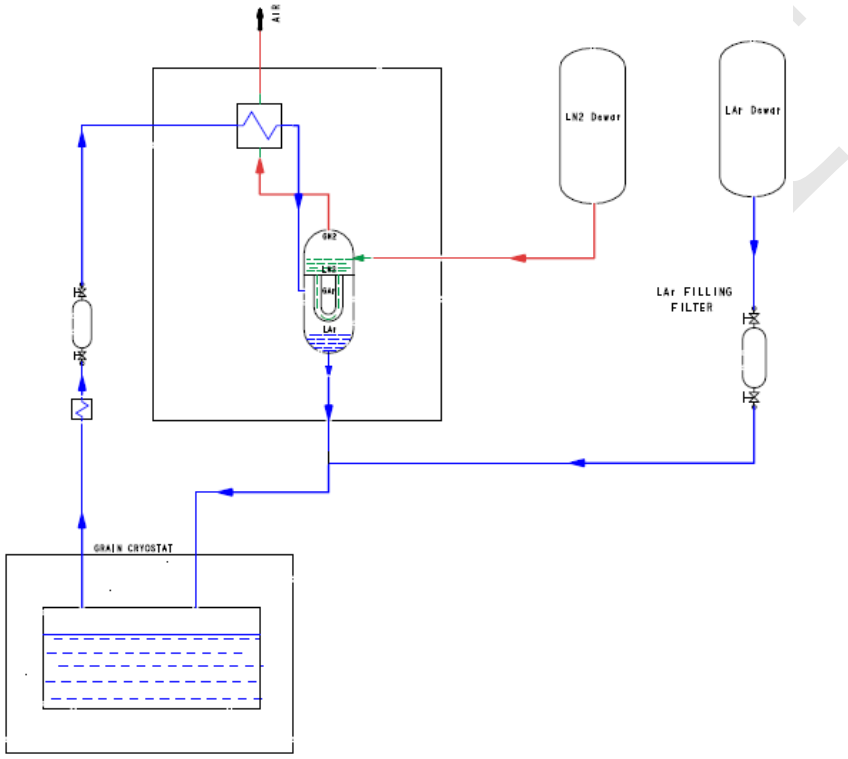


Figure 5.5: Scheme of GRAIN cryogenic system.

Since a large number of active electrical components will be immersed in LAr, resulting in a significant amount of heat being injected, particular care should be taken to avoid bubble formation that could deteriorate optical transparency, generate microphonic noise, and create large thermal gradients. Particular care will be taken to reduce the power density through the dissipator on the application-specific integrated circuit (ASIC) surface and the extended metal layers in the front-end (FE) printed circuit board.

The cryostat will be filled starting with high purity commercial Argon gas (Argon 6.0). Filling the cryostat with gas instead of liquid will reduce the mechanical stress on the inner vessel. During

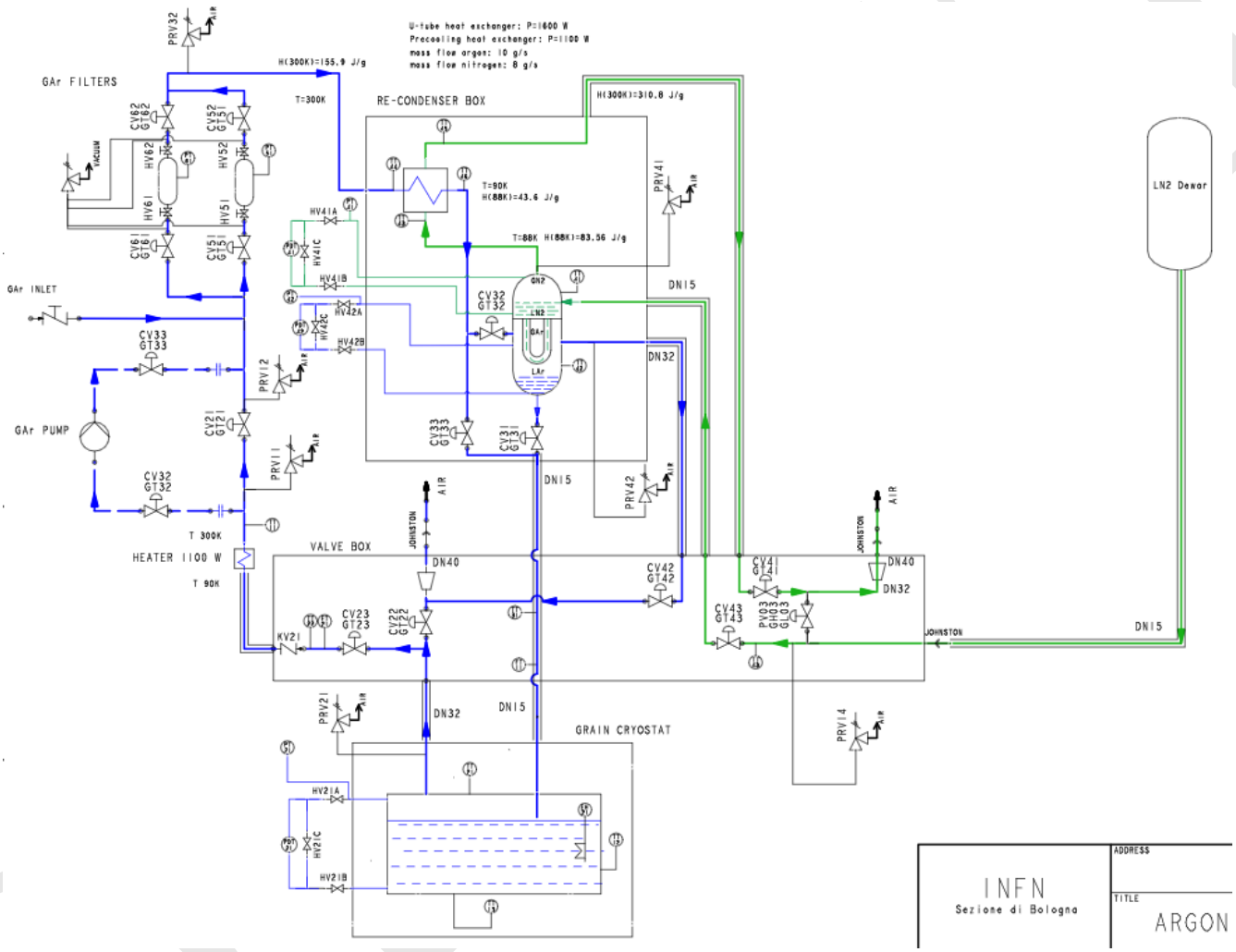


Figure 5.6: cryogenics P&ID for GRAIN.

normal operation mode, the level of purity will be guaranteed by means of a filter and a pump that will ensure proper circulation of the Argon necessary to maintain the desired purity in case the passive circulation is not sufficient.

The total heat load, i.e., the static heat load of the cryostat plus the heat load from the detector, must be limited to 1500 W, resulting in a boil-off mass flow of approximately 9 g/s within the cryostat that needs to be re-condensed. The generated GAr is delivered to the re-condenser, where liquid nitrogen, maintained at a suitable pressure to avoid Ar solidification, is used to provide cooling power in a U-tube configuration heat exchanger. Nitrogen is operated in a loss configuration: after being used to recondense LAr, it is not recovered, while the LAr feeds the cryostat by gravity. In Figure 5.6, a detailed diagram of the components of the cryogenic system is shown, including all temperature and pressure sensors, flow meters, and valves required to control and monitor the system. A facility test in INFN Laboratori Nazionali di Legnaro (INFN-LNL) is scheduled to verify the functionality of all proximity cryogenics prior to shipment to Fermilab.

5.4 Optical Detector

Optical systems are necessary for collecting and possibly focusing photons from argon scintillation in order to image tracks and vertices from neutrino interactions. Currently, two technologies for optical detectors are under evaluation for their use in GRAIN, based either on UV lenses or on coded apertures.

- **UV Lenses:** lenses are traditional imaging systems, but their use for LAr scintillation light (vacuum ultra-violet (VUV)) poses some challenges regarding material properties (transmittance, index of refraction) and the choice of the main optical parameters. Currently, different materials are under test; some of these have high transmittance only at wavelengths higher than 180 nm. In this case, the use of xenon doping to shift the 128 nm wavelength of argon scintillation light is thus necessary.
- **Coded Apertures:** this technique is the direct evolution of the pinhole camera, the simplest imaging device. A perforated mask is placed in front of the photo-detector. This optical system will form an image on the sensor plane, from which a 3D reconstruction can be extracted through iterative numerical algorithms. This is independent of the light wavelength, but it requires a large amount of collected light for good reconstruction.

In both technologies, the impinging photons are acquired by matrices of 32 by 32 SiPMs. GRAIN will use SiPM matrices with pixel sizes ranging from 1×1 to $4 \times 4\,\mathrm{mm}^2$, with a cell size ranging from 30 to 50 μm. The baseline option for lens-based cameras will be a 32×32 matrix, with SiPM dimensions of $2 \times 2\,\mathrm{mm}^2$. Currently, the Hamamatsu S13361-2050 8×8 matrix is commercially available, which has a fill factor of 75%, a cell pitch of 50 μm, and photon detection efficiency (PDE) of 40% at 450 nm [35]. In this case, 16 matrices can be employed to achieve the 32×32 channels configuration. For the lens-based system, an alternative solution that might improve the final resolution in the spatial reconstruction is to use a matrix of 64×64 channels of $1 \times 1\,\mathrm{mm}^2$ each. In this case, the 16×16 Hamamatsu S13615-1050N-16 matrix can be considered, which has a fill factor of 74%, a cell pitch of 50 μm, and PDE of 50% at 450 nm [36]. Again, 16 matrices can be employed to achieve the 64×64 configuration, but now the number of channels will increase

by a factor of 4 with respect to the 2 mm configuration.
For the coded aperture-based detector, the baseline option is a 32×32 matrix with SiPM dimensions of $3 \times 3\,\mathrm{mm}^2$ provided by, e.g., 16 matrices Hamamatsu S14161-3050HS-08 (fill factor of 74%, cell pitch of 50 μm and PDE of 50%). However, currently, the option to use matrices with $4 \times 4\,\mathrm{mm}^2$ is also under evaluation and must be considered for the ASIC design of the FE electronics. Properties of representative SiPMs from Hamamatsu are listed in Table 5.1, where the terminal capacitance assumes lower values for smaller SiPM dimensions.

Table 5.1: Properties of representative SiPMs from Hamamatsu.

Parameter	Minimum	Maximum
Terminal Capacitance	40 pF	900 pF
Gain	1×10^6	7×10^6
Bias	35 V	60 V
Warm Dark Current	-	3.3 μA

Finally, the Single Photon Timing Resolution (SPTR), which represents the timing jitter measured when a single photo-electron is detected by the photodetector, will be responsible for the final time accuracy. If the cell dimension is in the $30 - 50\,\mu$m range, as in the current baseline design, the SPTR is expected to be less than 100 ps.

5.4.1 Lens-based Optical Detector

Lenses have traditionally been used as imaging systems in countless camera applications. However, their use in a cryogenic liquid, such as argon, would be innovative, as the material choice must satisfy several requirements. In particular, the material must be compatible with the cryogenic environment, have a proper refractive index with respect to the LAr index, and exhibit a high transmittance at the relevant light wavelength.

Considering the 127 nm LAr scintillation wavelength, the only two materials commercially employed for the production of UV lenses are magnesium fluoride (MgF_2) and calcium fluoride (CaF_2), whose transmittance at 128 nm is on the order of 60%. However, their use in a cryogenic environment has not been documented yet, posing questions about the mechanical and thermal stability of large lenses (up to 6 cm in diameter) made from these materials. In order to include other materials, a possible solution is to work at a higher light wavelength by doping LAr with a small amount (a few tens of ppm) of xenon (Xe). It has been demonstrated that dissolving xenon in LAr can efficiently convert the VUV light from 127 nm to 174 nm, also slightly enhancing the light yield [37]. The energy transfer between the argon excimers and xenon is quick (~ 1 ns) [38], so no degradation of spatial resolution is expected to occur. An efficient imaging system based on lenses would, therefore, be possible with Xe-doping: the PDE is 10% higher at 174 nm, and also more common materials, such as fused silica, become suitable. The only downside of adding Xe is the change in the time distribution of the shifted emission: the fast component (6 ns) is not affected and remains at 127 nm, possibly also suppressed, while the slow component is shortened by up to a few hundred ns (160 ns at 25 ppm) [39].

In order to design a lens-based optical system, the refractive indices of the different materials have to be considered. For what concerns LAr refractive index, the uncertainty in the UV range is

quite high. The refractive index at 127 nm can be calculated using the Sellmeier equation, with coefficients extracted from fits to historical datasets in the visible range. These calculations predict a value between 1.35 and 1.45 [40]. More recently, from a measurement of the group velocity at 127 nm, the refractive index is reported as $n = 1.358 \pm 0.003$ [41], while the extrapolated value at 174 nm is around 1.26. Since typical VUV transparent materials or silica glass have a refractive index around 1.3-1.4, which is very similar to the LAr value, a normal bi-convex lens with spherical surfaces might not be usable for achieving the desired focal length. In fact, since the difference between the refractive indices of the media is reduced, stronger curvatures are needed to achieve the same focusing effect. However, reducing the radii while keeping the same diameter makes the lens very thick. Thus, the lens design is based on a gas volume enclosed between two surfaces of materials, with a refractive index similar to that of argon. In this way, the surface does not influence the optical system behavior, which is dominated by the LAr-gas refractive index difference. The design of the lens-based optical setup is shown in Figure 5.7. It consists of four elements: the optical lens system, the light shield that supports the lens system, and the SiPM matrix mounted on a front-end board.

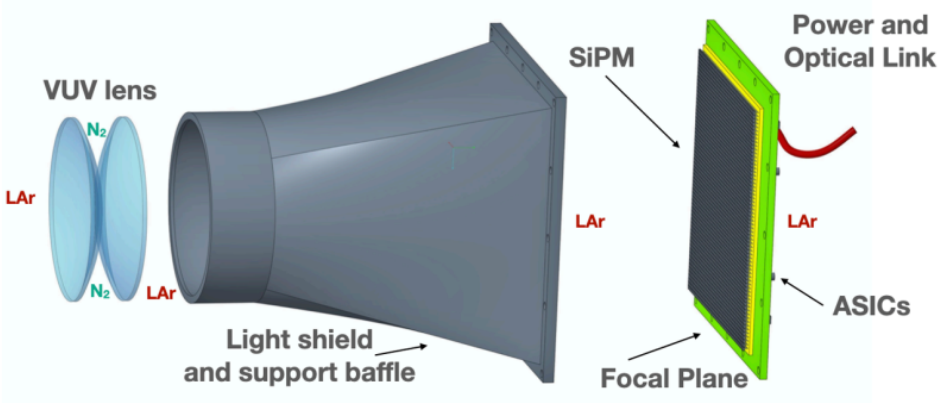


Figure 5.7: Exploded view of the lens-based camera components: the lenses, the light shield, SiPM matrix on a supporting PCB.

The design of the VUV lens focusing system was developed by considering dedicated ray-tracing simulations, guided by the following requirements:

- the track thickness on the detector image must be smaller than 5-6 mm (equivalent to 2-3 SiPMs), since all the tracks in the image must be clearly distinguished, even for neutrino interactions at high energy, where more than 3 tracks can be produced;
- a large field of view is desirable to cover a larger fiducial volume; in this volume, the detected tracks must satisfy the previous condition;
- the lens dimensions must be suitable to ensure a large number of photons are detected for each track in the field of view;
- the distance between the lens and the SiPM surface must be smaller than 10 cm.

The final configuration for the lens system is shown in Figure 5.8, where two plane-convex lenses with an effective diameter of 60 mm and a curvature radius of 79 mm are placed at a minimum distance of 2 mm. Preliminary simulations showed that the diameter is adequate for collecting

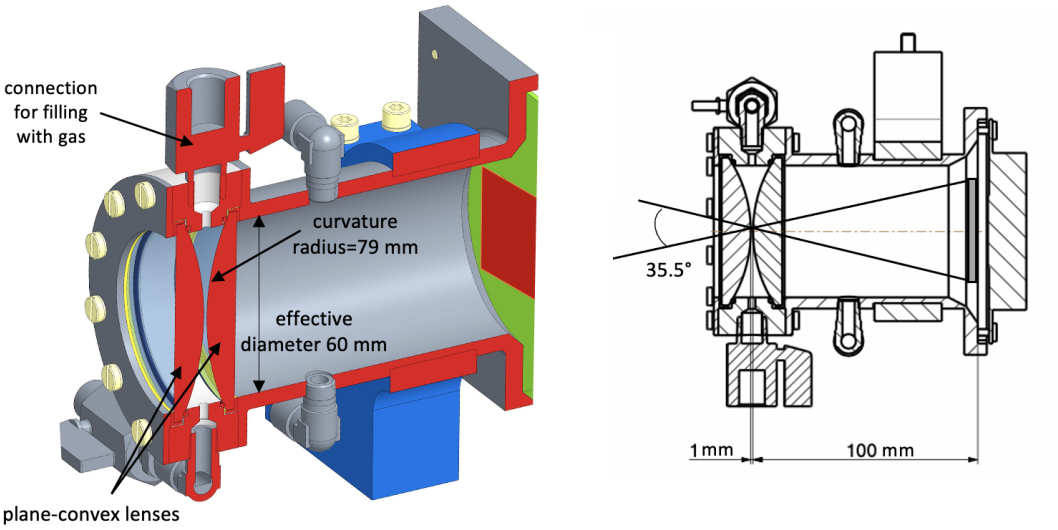


Figure 5.8: Design of the optical system based on two plano-convex lenses.

enough light from tracks crossing the LAr volume at a maximum distance of 130 cm from the lens surface. The selected material is Corning HPFS 8655, a UV-grade fused silica that provides a $> 99.6\%$ transmittance in the relevant part of the spectrum (i.e., for $\lambda > 170$ nm) and features a refractive index of ~ 1.6. The focal length of this system is 88.8 mm if the LAr refractive index is 1.26 for the wavelength of 178 nm.
Due to the fixed distance between the lens and the sensor, any object located outside the focal plane will appear out of focus on the sensor plane. This means that a point-like source will be imaged as a small point if it lies in the focal plane, while it will appear as a circle with increasing dimensions the farther the source is from the optical plane. In order to characterize the focusing effect and to estimate the effective field of view of the camera, many point light sources emitting a number of photons corresponding to 100 MeV of deposited energy were simulated at different distances a from the lens surface. The plot of the spot radius detected on the sensor plane as a function of a is shown in Figure 5.9.

As shown in the plot, the spot diameter remains smaller than 7 mm for sources placed at a distance greater than 400 mm. This value determines the effective field of view of each lens, which is formed by a cone, or more precisely, a frustum of a square pyramid, originating at 400 mm from the lens and increasing with the distance from the camera. This behavior results from the chosen focal length of 88.8 mm in combination with the distance b between the lens and SiPM plane, which is set to 100 mm. Finally, the angular opening of the field of view of cameras, which is the angle of the square pyramid, is fixed by half of the sensor dimension ($L/2 = 32$ mm) and b, and it results in $\alpha = 2\ \arctan(L/(2b)) = 35.5°$.

A typical image of tracks crossing the LAr volume inside a lens field of view and thus well focused on the sensor plane is shown in Figure 5.10.

For tracks crossing the LAr volume and falling outside the field of view, the reconstructed image can be completely empty or almost full, depending on whether the track is outside the ”cone” or inside the cone region but at a distance from the lens surface smaller than 40 cm, respectively.

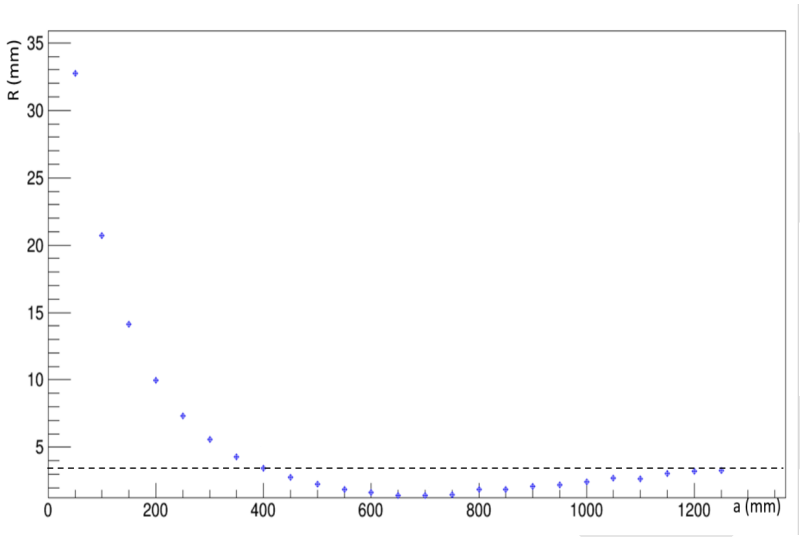


Figure 5.9: Spot radius as a function of a, the distance from the point light source and the lens surface. Note that for $a > 400$ mm the spot radius is smaller than 3.5 mm as highlighted by the dashed horizontal line.

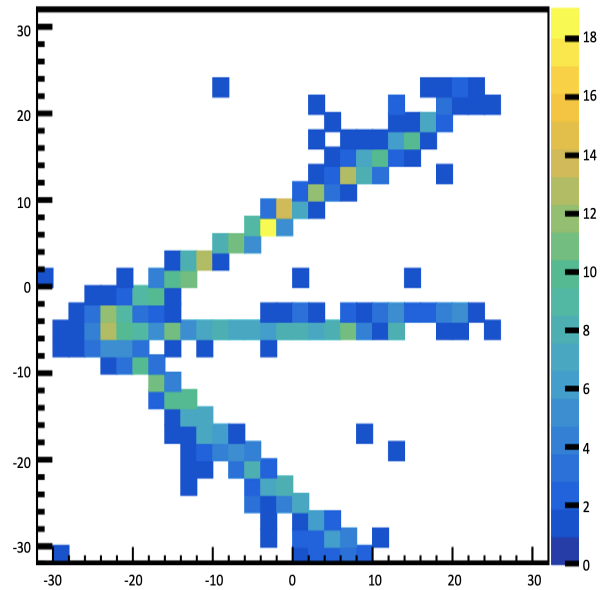


Figure 5.10: Typical image for well-focused tracks with lens-based optical detectors. In this example, three tracks originate from a neutrino interaction vertex placed within the field of view of the considered camera. The geometrical coordinates (in mm) of the fired pixels are reported on the X and Y axes, while the color palette highlights the number of collected photons.

5.4.2 Coded Mask Detector

Coded-aperture imaging can be a viable alternative when the wavelength—such as the scintillation light from liquid argon—poses challenge to design a traditional optical system. The technique was originally developed for X-ray astronomy an is as an extension of the pinhole camera concept. Although the pinhole camera is capable of excellent angular resolution, it is inherently inefficient in light collection. Coded aperture imaging was introduced as a means of preserving angular resolution while improving efficiency. Figure 5.11 shows a schematic comparison of a pinhole camera and a coded-aperture camera. Instead of a single aperture in an attenuating plane, a mask formed from an array of opaque elements and holes is placed between the incoming light flux and the sensor array. [42]. The elements of this so-called *coded aperture mask* are all of equal size and are arranged in a predetermined pattern on a regular grid.

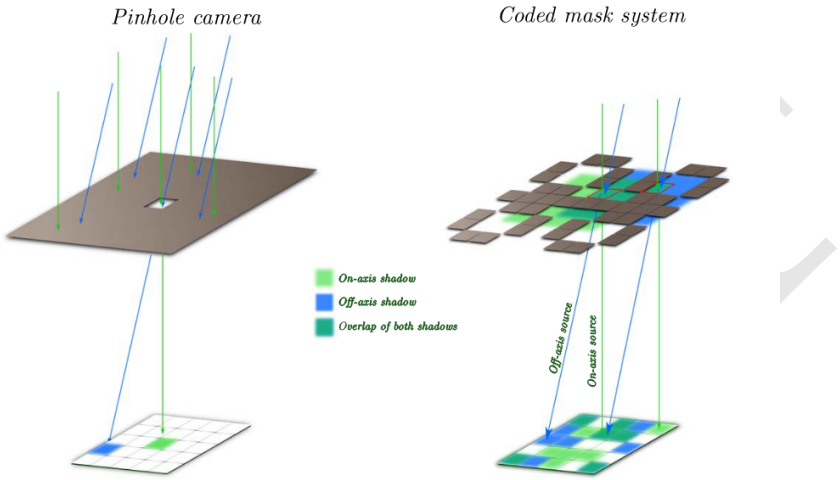


Figure 5.11: Left: a pinhole camera. The detector plane registers an image of the source field with relatively low significance peaks, since the detecting area corresponds to only one mask element. Right: a coded aperture mask camera. The detector plane registers an overlapping set of multiple images, each set associated with one point source.

Each light source within the camera field of view projects a shadow of the aperture onto the detection plane. For an isolated point source, the detected two-dimensional distribution replicates the mask pattern, or a portion of it, but shifted from the central position by by an amount that is uniquely related to the source position. For extended sources or multiple point sources, the recorded data is the linear superposition of the individual shifted mask patterns produced by each source element. To reconstruct the original source position several algorithm exists, such as deconvolution, [42], where the decoding matrix is retrieved by the mask pattern itself, or iterative methods based on maximum likelihood estimation [43], as summarized in Section 5.8.2.

This imaging technique offers several practical advantages: the hardware is simple, passive, and lightweight —just a thin patterned mask positioned in front of the detector. That simplicity makes systems compact and robust, since there are no delicate lenses or moving parts. Redundant coding distributes the light source information so that partial mask or detector damage degrades performance gracefully. The approach enables wide field of view and thin, compact camera designs because focusing optics are unnecessary, and the focal length can be tuned through the size of the mask holes. It also works across a broad range of wavelengths because imaging relies on geometric

coding rather than wavelength-dependent refraction or reflection, enabling versatile, lightweight solutions where conventional optics are impractical.

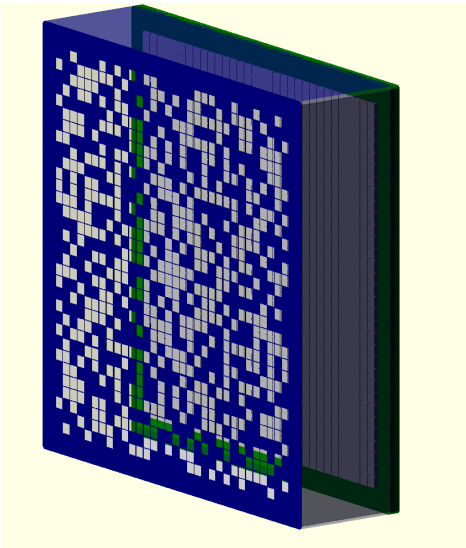


Figure 5.12: Coded-mask-based camera.

The coded-mask camera design for GRAIN is shown in Figure 5.12. The mask is fabricated from a 0.1 mm laser-cut aluminum sheet and is mounted 30 mm from the sensor plane; it is supported by a rigid frame that provides structural integrity and also shields the sensor from stray light entering from the sides. To reduce internal reflections that could degrade image quality, both the mask and the frame surfaces will be anodized. The mask pattern is identical across all cameras: each mask cell is assigned randomly to be either an open hole or a solid element, with half of the mask area occupied by solid material. Liquid argon flows through the mask openings and fills the optical detector volume, so there is continuous optical coupling between the camera interior and the surrounding medium and no refractive-index discontinuity at the mask plane. Figure 5.13 shows examples of typical images detected in GRAIN with this camera design.

5.4.3 Detector Layout in GRAIN

Fix missing section references based on new organization.

The detector layout in GRAIN is not yet finalized. Currently, two configurations are under study: one optimized with a lens-based detector and one optimized with coded aperture masks. Once the full characterization of the two technologies is performed (see Section 5.4.4), the reconstruction performance achieved with the two different layouts will be evaluated. Thus, a final optimized layout of the detectors inside GRAIN will be developed at this stage and might exploit both technologies.

The detector layout of lens-based optical detectors in GRAIN is shown in Figure 5.14, where the placement of 53 cameras inside the vessel is depicted. Given the inner vessel geometry, as described in Section 5.2, the lens based detector placement is optimized in order to enlarge the fiducial volume (FV).

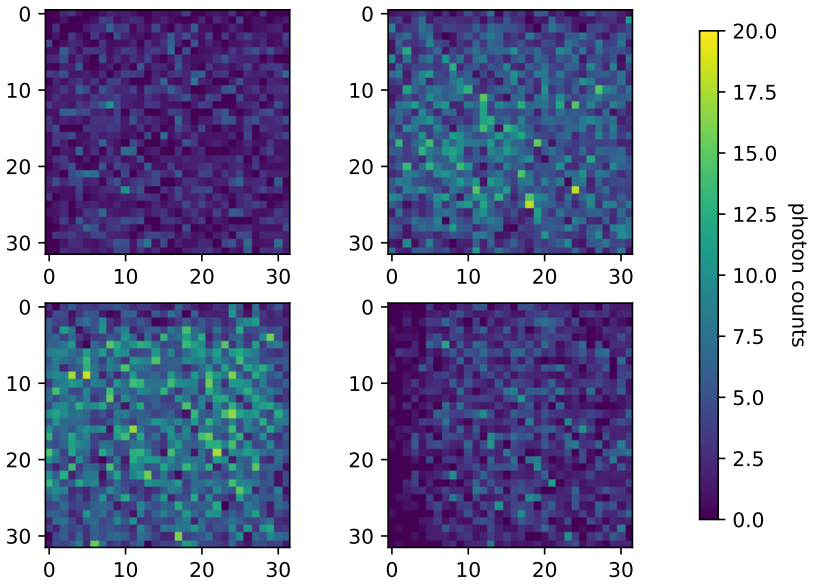


Figure 5.13: Typical images detected with coded aperture cameras in GRAIN. The pixel indices are reported on the axes.

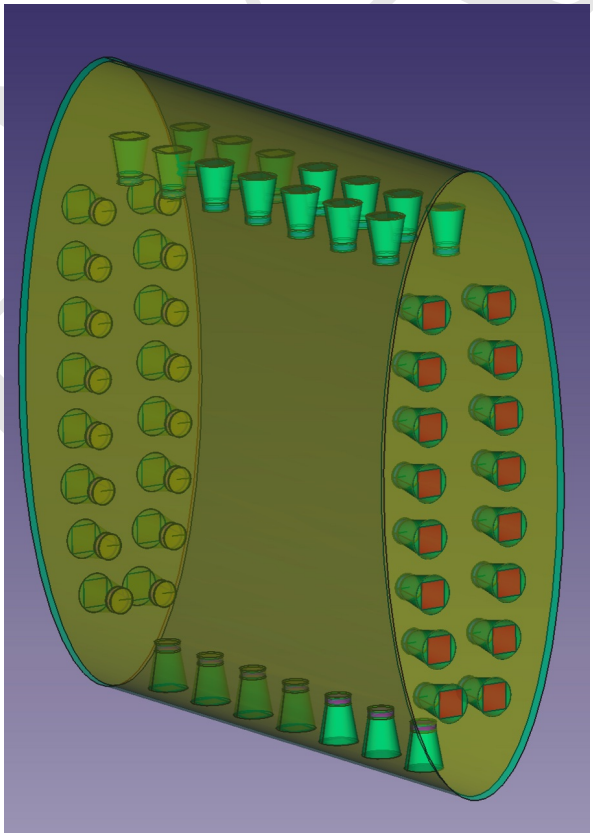


Figure 5.14: Lens-based detector layout in GRAIN (53 cameras).

DRAFT

The design of the cameras is the one described in Section 5.4.1, using 60 mm diameter lenses with a focal length of about 9 cm and a lens-sensor distance of 10 cm, which makes them perfectly suitable for covering the 1.5 m longitudinal dimension of the inner vessel. In this design, 16 pairs of cameras are positioned in two columns on the elliptical sides of the inner vessel, and 21 additional cameras are also placed on the top and bottom of GRAIN to provide orthogonal views of the interactions. A single row of 7 cameras is placed as close as possible to the bottom of GRAIN, while a double row of 7 detectors is placed at about 10 cm from the top of the cryostat. This distance guaranties that a sufficient fraction of space is left free for the evaporation of LAr. The second column on the vertical walls and on the top of GRAIN is very important to expand the transverse coverage of the system. Since each camera has a field of view with an angular opening of 35.5° and is positioned at a distance of about 40 cm from the lens surface, the relative positions of the cameras were chosen in a way that ensures that combining their fields of view would leave no blind space at $a = 40$ cm. In other words, the overlap of the fields of view of the various cameras at the middle plane of the vessel fills the elliptical section with minimal gaps.

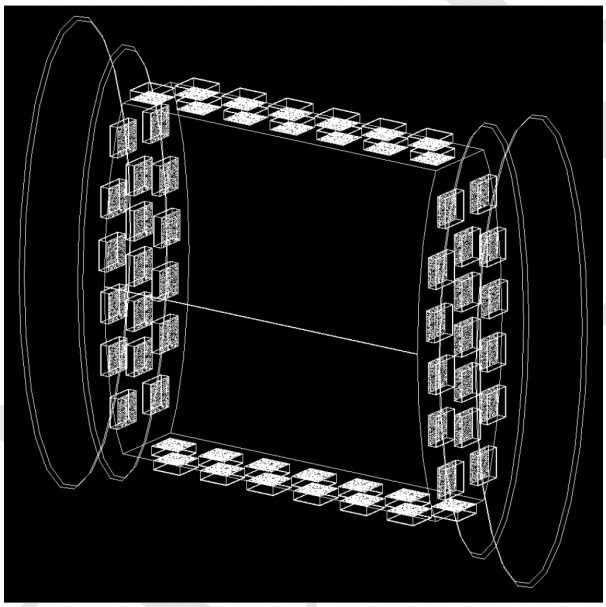


Figure 5.15: Coded mask-based cameras located inside GRAIN geometry.

In the coded aperture based system, 60 imaging devices are positioned within the GRAIN detector in accordance with the layout depicted in Figure 5.15. Along the elliptical sides, 17 cameras are distributed across three staggered columns to ensure uniform coverage. A clearance of approximately 5 cm is maintained between the rear of each camera and the vessel wall. This gap accommodates the necessary components, including the camera readout electronics, the cabling, and the supporting structure. On the top and bottom sections of the vessel, 13 cameras are positioned in two staggered rows. The upper rows are positioned at a height 12 cm from the topmost point, leaving sufficient space to accommodate a layer of GAr. Similarly, the bottom rows are symmetrically aligned with respect to the upper configuration.

5.4.4 Camera Prototypes

In order to validate the simulations and the design of the optical detector, dedicated tests are currently performed with prototypes.

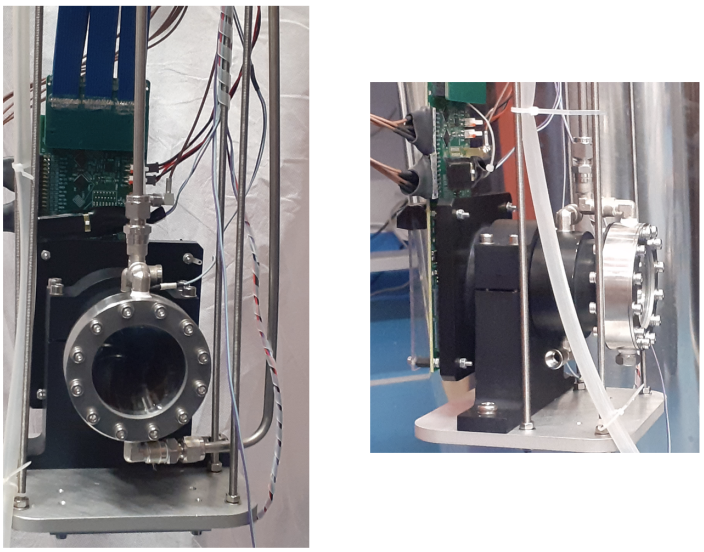


Figure 5.16: First prototype of the lens-based detector.

A first prototype of the lens-based detector, which is currently under test, is shown in Figure 5.16. The lens curvature and diameter are those considered in the simulations, as well as the distance between the lens and the SiPM plane. The lens prototypes were produced by GestioneSILO, an external company specialized in the construction of precision optics. Other types of lenses are already built with different curvature radii and made from different materials (MgF_2), but with similar focal lengths.

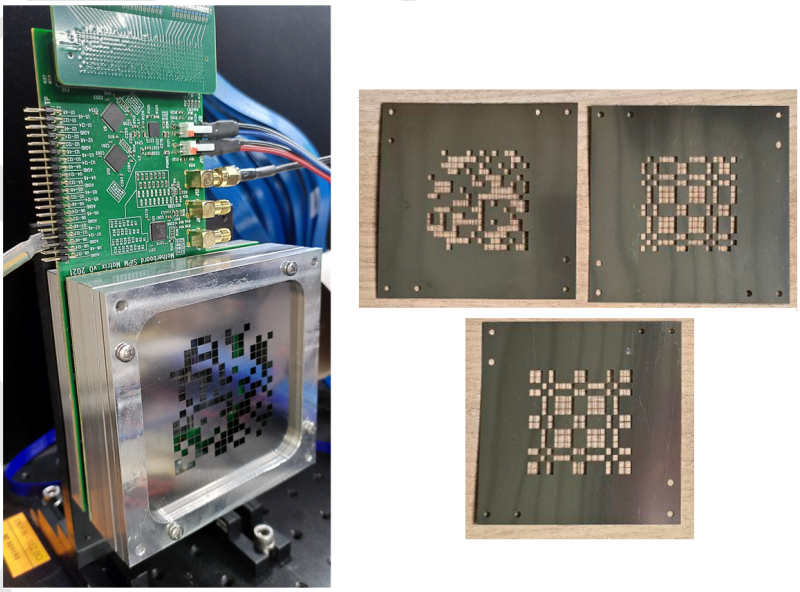


Figure 5.17: Left: First prototype of the mask-based detector. Right: mask patterns.

Figure 5.17 shows the prototype coded mask-based detector. The mask is fabricated from a 0.1 mm laser-cut steel sheet and mounted on a steel frame that is attached to the SiPM matrix board. The frame consists of several 5 mm-thick plates aligned with dowel pins, allowing the mask to be

positioned at multiple distances from the sensor, from 0.5 to 4 cm. For testing and validation of simulations, masks with different patterns, optimized for either track reconstruction or point-source reconstruction, were produced.

While the construction of a full scale prototype of a camera with 1024 channels will require a dedicated ASIC, a readout system for testing prototypes with matrices of 16×16 (256 channels) was built. The readout chain consists of a SiPM matrix (16×16), connected to a custom PCB hosting eight ALCORs (A Low-power Circuit for Optical sensor Readout), i.e., 32-channel integrated circuits suitable for a cryogenic environment developed by INFN Sez. Torino [44]. This board is connected via an FMC extension cable to a Virtex-7 VC707 FPGA with custom firmware based on the IPbus protocol. The readout system chain for the demonstrator is shown in Figure 5.18. This readout system was designed to accommodate SiPM matrices with different pitches. A matrix of 1 mm SiPMs is directly available in a monolithic 16×16 array by Hamamatsu (S13615-1050N-16), while for the configuration with 2 mm and 3 mm SiPM size, four 8×8 arrays (S13361-2050NE-08 and S14161-3050HS-08, respectively) have been mounted on the same board as close as possible to form a 16×16 matrix. Either the lens or the coded mask prototype can be coupled interchangeably to the SiPM matrix boards. One of these boards is shown in Figure 5.18. The gap between the four arrays in the present configuration is only slightly larger than the dead space between the remaining SiPMs. All the SiPMs are designed to be fully operational in the visible range and will therefore require TPB deposition to be sensitive to UV wavelengths.

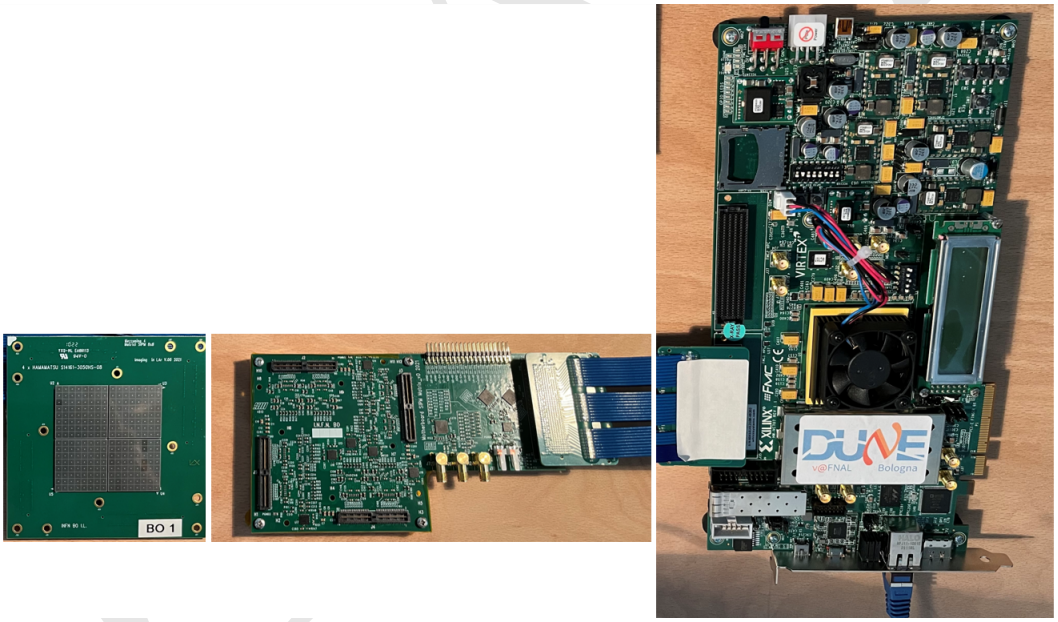


Figure 5.18: Readout system chain composed of a SiPM matrix (here the 3 mm one is shown), a PCB hosting the ALCOR ASIC and an FPGA, which communicates with a computer through Ethernet.

For each channel, together with the timing information of the first detected photon, which is measured with a global time resolution of 50 ps, the time-over-threshold is acquired in order to estimate the number of detected photons in each acquisition window.

ARgon Test InfrastruCture (ARTIC) The full characterization and validation of the lens-based cameras will be performed inside the cryogenic facility called ARgon Test InfrastruCture (ARTIC), located in the DIFILab at the Department of Physics of the University of Genoa (Italy).

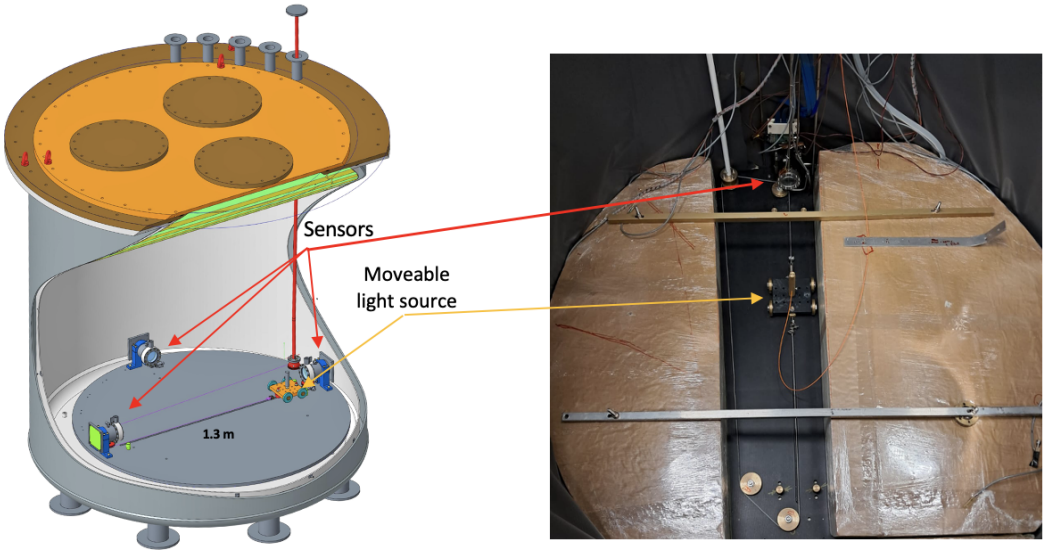


Figure 5.19: The ARTIC facility at the DIFILab of the University of Genova and the setup for testing prototypes with an artificial light source.

ARTIC is a cylindrical, vacuum-insulated cryostat with a 1.5 m diameter and a capacity of about 150 liter (maximum height of liquid 50 cm). This dimension matches the characteristic longitudinal length of GRAIN, allowing for the testing of the cameras under similar working conditions. ARTIC will be supplied by an ancillary plant for the recirculation and purification of LAr in order to guarantee an adequate light yield for the measurement of LAr scintillation light. If necessary, an ancillary doping system is available for the doping of liquid argon with xenon at the ppm level. A drawing of the facility and a possible configuration of the setup to test optical detector prototypes is shown in Figure 5.19.

A campaign of tests with a lens-based detector prototype is in progress. As shown in Figure 5.19, different cameras can be mounted on a perforated plate and placed close to the bottom of ARTIC, thereby allowing for the filling of ARTIC with the minimum amount of LAr necessary ($\sim$ 150 liter). In the first phase, the prototypes will be tested using a point-like UV light source placed at different desired positions inside the LAr volume. The UV artificial light source consists of an external xenon lamp, coupled with a monochromator and matched with an optical fiber, that will be located in the LAr volume and anchored onto a movable support. The first prototypes will be tested at different distances and orientations relative to the light source to precisely estimate the field of view and point spread function, enabling a complete characterization of the UV focusing system.
In the second phase, the detectors will be fully validated by using scintillation light emitted by radioactive sources or cosmic rays. In this case, a few prototypes will be installed in the same mechanical setup in order to provide three stereoscopic images of the same event. A dedicated cosmic ray tagger was built to trigger cosmic rays and double-check the track reconstruction capability.

Cosmic Ray Tagger (CRT) In order to evaluate the performance of the optical detector prototypes, an external trigger system has been installed in the ARTIC facility (Figure 5.20). Two scintillator planes are positioned on the top of the ARTIC Dewar; two additional planes are located below the bottom of the Dewar. These planes are composed of bars whose signals are read on one

side by SiPMs. Each top plane is made of 8 bars with 2 cm width and 8 bars with 4 cm width, for a total area of $50 \times 50\,\mathrm{cm}^2$. Each bottom plane is made of 8 bars with 2 cm width and 4 bars with 4 cm width, for a total area of $34 \times 34\,\mathrm{cm}^2$.
When a cosmic muon activates all four planes, a trigger signal is generated. The path of the muon is easily reconstructed because the bars of the coupled planes are perpendicular to each other. Then, two hits are available in the XZ view and two others in the YZ view, making it possible to compare the signal collected in the ARTIC Dewar with the muon track. A similar trigger device is foreseen for the commissioning and first calibration of GRAIN, described in Section 5.7.



Figure 5.20: Cosmic Ray Tagger for ARTIC. Two scintillator planes are placed on the top and two others on the bottom of the cryostat. The fourfold coincidence activates the trigger. Left: rendering of the setup. Right: actual CRT device.

5.5 Readout System

The conceptual scheme of the GRAIN readout system is shown in Figure 5.21. Listed from the outer to the inner volume, the main components are:

- the GRAIN Warm Interface Board (GWIB) that interfaces the GRAIN detector with the DAQ, timing and Slow Control system; there will be 8 GWIBs, each one directly mounted on the outer flange of the Vacuum Vessel;
- the GRAIN Cold Interface Board (GCIB), which routes the signals, communications, and power from GWIBs to the GRAIN Camera Boards (GCBs); there will be 8 GCIB, each one directly mounted on the inner flange of the Inner Vessel;
- the GCBs, which hosts the SiPM matrices and their front-end mixed-signal ASIC; there will be 1 GCB for each camera.

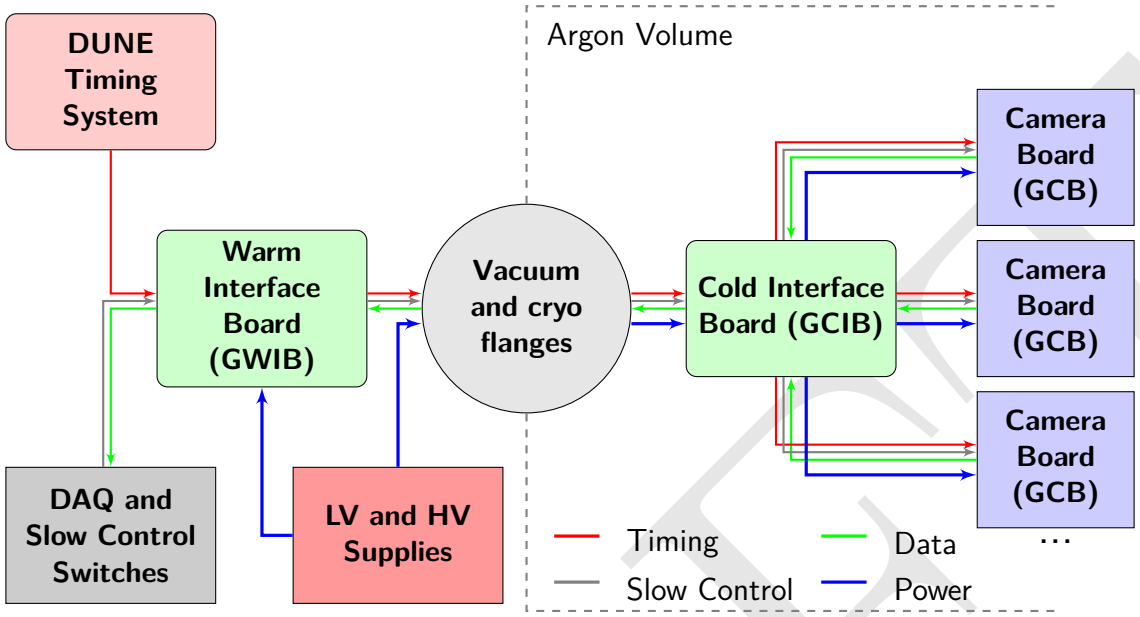


Figure 5.21: Block diagram of the GRAIN electronic system.

5.5.1 GRAIN Camera Board

Each GRAIN camera, regardless of the optical system, will be equipped with a square matrix of 32 by 32 SiPMs, independently read out for a total of 1024 channels. Different optical systems may use a different number of cameras, as well as SiPMs of different sizes, requiring a differently sized PCB. However, the channel count per camera will remain the same.

The size, power, and wiring constraints of the system necessitate the use of ASIC front-end with a large channel count, mounted on the camera itself. Alternative readout schemes using warm electronics (with or without cold amplifiers) would require an enormous number of feed-throughs and likely suffer from signal integrity issues.

The design of the GCB foresees a single PCB per camera, hosting the required SiPM matrix on the front side and a mixed signal ASIC on the back side (with both analog and digital components). The only additional active components of this board would be the power conditioning circuits for the ASIC itself.

The only mixed-signal ASIC in production that is capable of reading out SiPMs in cryogenic conditions is ALCOR [44]. While ALCOR has been used in the construction of prototype cameras, it is not well suited for large scale use in GRAIN, due to its relatively high power consumption and a relatively low channel count of only 32. For this reason, a new ASIC is being designed specifically for GRAIN by the same group that developed ALCOR.

5.5.2 ASIC Design

Due to the high channel density (32×32 channels per SiPM matrix), a dedicated readout ASIC is required for each camera. Consequently, the Dune Integrated Electronics for NEutrino Beams (DENEB) ASIC is currently under development. The main design requirements are guided by the detector layout and by the needs for the physics reach of SAND.

DRAFT

ASIC Requirements A 1024-channel ASIC is optimal for a sensor with a 32×32 SiPM matrix or, alternatively, for a 64×64 SiPM configuration. Due to the large number of channels and the need to minimize noise, each ASIC must be placed inside the LAr tank, close to the SiPM matrix, and must be capable of operating at the LAr temperature in the GRAIN cryostat (87 K). The ASIC will be characterized at room temperature (300 K) and in liquid nitrogen (77 K); therefore, its design must ensure compatibility with both operating conditions.

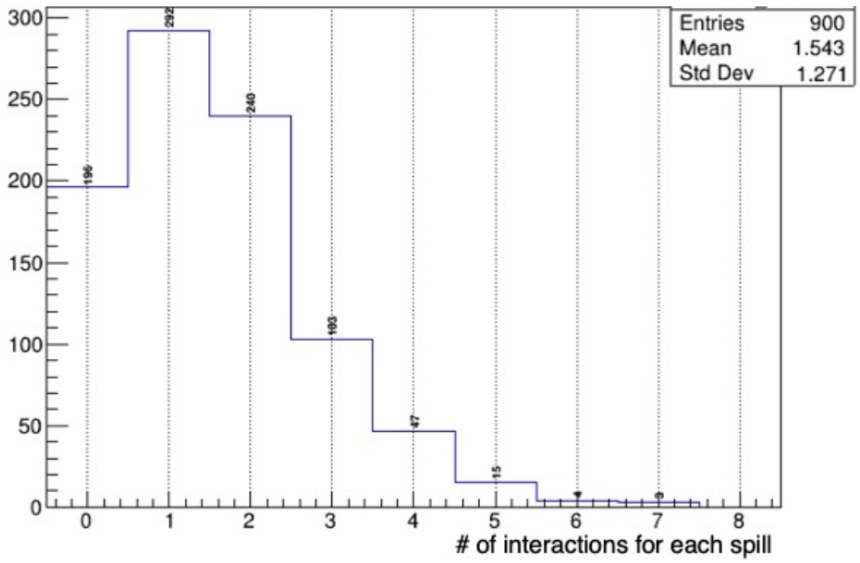


Figure 5.22: Number of neutrino interactions detectable in GRAIN within a spill. An interaction is considered detectable if at least one track deposits more than 6 MeV in the LAr volume.

As shown in Figure 5.22, in each spill, tracks from different neutrino interactions cross the GRAIN volume and can be detected by the cameras. Considering a beam intensity of $7.5 \cdot 10^{13}$ POT per spill, on average, about 2 events are expected within 10 μs of spill duration, and for a small number of spills, up to 6-7 events can occur. For GRAIN's physics goals, precise track reconstruction is required. The ASIC must process the current generated in each SiPM pixel by impinging photons during the spill, providing single-photon sensitivity, the capability to count photons, and the time structure of the detection windows.

In order to satisfy the original goal of distinguishing overlapping neutrino events, the ASIC must be capable of separating pulses whose photons are more than $\mathcal{O}(100\,\text{ns})$ apart. In this condition, offline data analysis will be able to distinguish a distribution of events with a single signal from one containing overlapping signals likely induced by multiple neutrino interactions in SAND within the same spill. In addition, to fully exploit GRAIN's capability as a fast detector and accurately reconstruct the neutrino interaction time, the time tagging for each channel must achieve a resolution better than 200 ps root mean square (RMS).

Moreover, the ASIC should be able to provide precise information on the number of photons detected from each interaction. In particular, for an efficient reconstruction of tracks with coded aperture masks, the number of photons in each channel must be known precisely in the range of 0 to 20 photons, while for the calorimetric reconstruction, a dynamic range of about 80 to 100 photons is necessary.

While the capability to collect off-beam data for cosmic ray events, useful for calibration and

background studies, is desirable, a duty cycle working limitation is acceptable if necessary to meet constraints on power consumption and data throughput. Thus, the ASIC can leverage the spill structure by embedding power gating in the analog components and logic circuits with higher power consumption.
The target average power consumption for the ASIC is set at 5 W per camera, corresponding to an average of 5 mW per channel for a 1024-channel ASIC.

ASIC Architecture Overview The ASIC is being developed using a 110 nm CMOS process, leveraging the expertise gained from previous designs and tests of readout ASICs, which were fabricated using the same technology and tested in liquid nitrogen. The DENEB ASIC features a pixelated structure, consisting of a 32×32 matrix of pixel channels. Using some silicon-proven blocks to reduce the development timeline and meet the GRAIN detector delivery deadline, the design team opted for a channel readout architecture based on two branches for time and charge measurements.

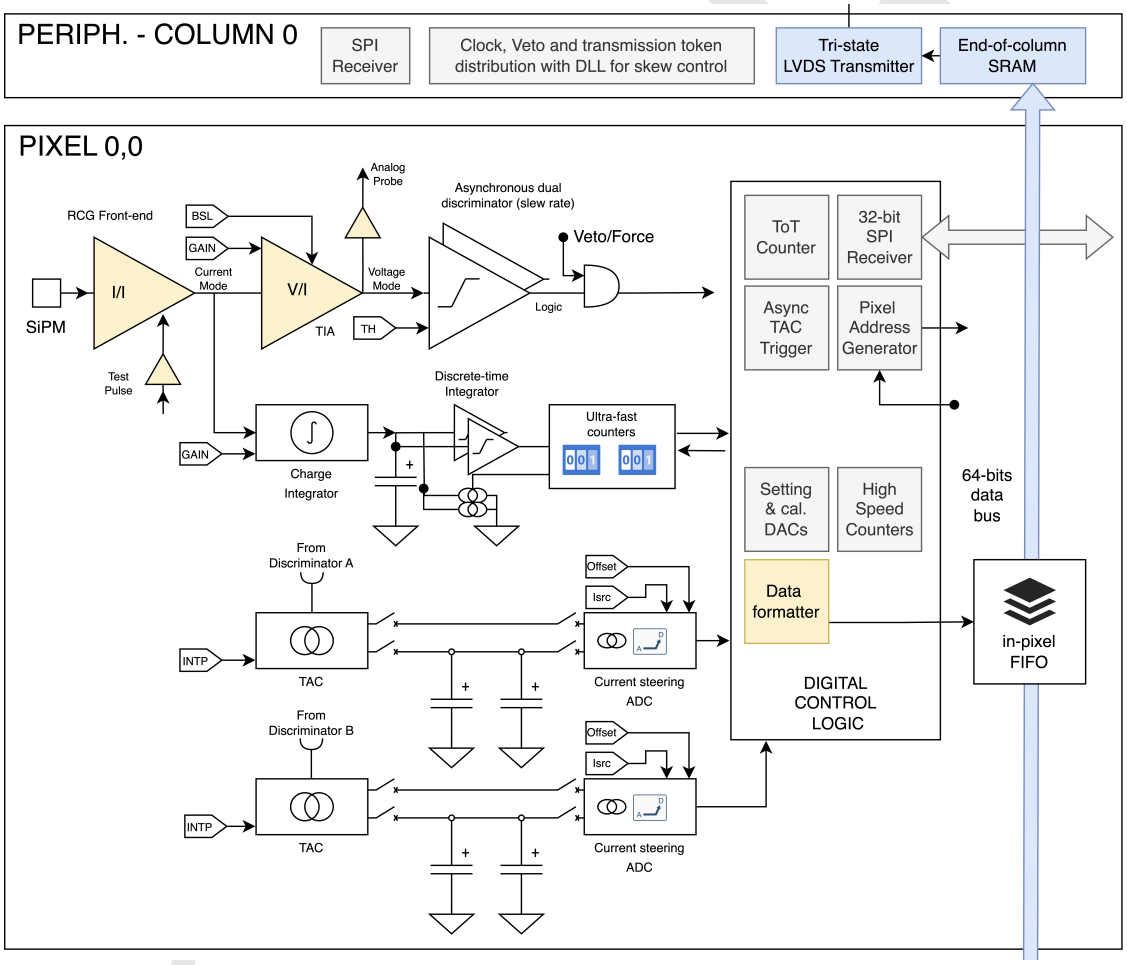


Figure 5.23: DENEB channel's block scheme.

The present pixel architecture scheme is illustrated in Figure 5.23. The sensing node is DC-coupled to a current amplification stage based on a regulated common-gate topology (RCG). The signal is mirrored to a transimpedance amplifier (TIA) and a dual-threshold timing discriminator for time-of-arrival and slew-rate measurements, enabling time-walk correction. In the second branch,

the RCG signal is integrated using a current-to-frequency converter, which provides sub-single-photon resolution and an input dynamic range exceeding 200 photons. Both signal polarities are supported in the front end. The chip works at a supply voltage of 1.2 V.

Fine time measurements are performed with four on-pixel TDCs by interpolating a 1.5 clock period (1.5×3.2 ns). The Time-to-Digital Converters (TDCs) are based on a Time to Analog Converter (TAC) and an 8-bit SAR ADC, integrated at the channel level, with time binning down to 17 ps. However, 4 bits are sufficient to provide ~ 291 ps time binning, i.e., 85 ps RMS, which is compatible with a 200 ps time resolution. The ADC can also work in Wilkinson mode, with a slower conversion time but high linearity. The four on-pixel converters enable a fourfold derandomization scheme to mitigate pile-up from consecutive events in the same spill window. When operating in slew-rate mode, the derandomization factor is halved to provide the time-of-arrival measurements on the same leading edge at two different threshold crossing times. Alternatively, the second discriminator can be configured as a falling edge sensitive comparator, enabling ToT measurements by using a coarse counter that measures how long the signal remains above the threshold. It also controls the integration windows. A programmable hold-on time, on the order of tens of nanoseconds following the ToT, allows for grouping consecutive events. If a new event crosses the discriminator's threshold during this hold-on period, it is merged with the previous one.

Each pixel word is propagated through its column to the end-of-column periphery, where it is stored in dedicated memory. Each column periodically sends a packet containing the event words to the output transceiver, and the packet has a header and footer indicating the column ID. Each column has an SLVS data transceiver operating at a base clock frequency of 312.5 Mbps (equal to the clock frequency) and an extended mode at 1.28 Gbps. Due to constraints on the number of differential lines that can be used per board in GRAIN, the data bandwidth will be limited to one or two lines.

Time-division multiplexing provides flexibility in output bandwidth, supporting configurations with 1 to 32 parallel transceivers, enabling a maximum bandwidth of 32×625 Mbps (in DDR). The dynamic random access memory (DRAM) size is chosen to store at least 2000 events per column, which exceeds the expected data throughput per column during a spill. The slow control interface is implemented via an SPI protocol.

Table 5.2 presents the ASIC design specifications.

The DENEB pixel channel has a size of $500 \times 500\,\mu\text{m}^2$. Considering the 32×32 channel matrix, along with the EoC SRAM, logic, and data transceiver, the ASIC occupies $2 \times 2\,\text{cm}^2$. An engineering run is required, as the ASIC covers most of the reticle area, which is approximately $2 \times 3\,\text{cm}^2$. The padframe consists of a 40×40 pad grid with a $500\,\mu$m pitch, supporting three distinct power domains. It includes 1024 on-pixel input pads for interconnection with the SiPM, analog probe pads, 64 pads for Tx differential signals, 1 pad for analog test pulse injection (for data converter calibration), and additional pads for clock, low-power mode, power gating, analog and digital calibration, and reset differential signals.

Given the high input/output pad density ($> 40 \times 40$), Flip-Chip Ball Grid Array (BGA) packaging is required. In this configuration, the ASIC is bump-bonded to an interposer, which is connected to the board via package balls. The board also integrates the SiPM matrix, ensuring efficient signal transmission and mechanical stability.

Special consideration must be given to the selection of the interposer material and soldering balls, as mechanical stress on the interconnection caused by differences in the coefficient of thermal expansion (CTE) must be minimized. At present, a ceramic interposer is under consideration since it offers a suitable CTE match.

DRAFT

Table 5.2: DENEB ASIC design specifications.

Features	DENEB×1024
Channel Modularity	1024
Input Signal Polarity	Positive and Negative
Measurements	ToA, Time over Threshold (ToT), Charge Integral
Single Photon Time of Arrival Resolution	150 ps
Time over Threshold Resolution	1 ns
Charge Integral Resolution	3 codes/photoelectron (PE)
Charge Dynamic Range	$1 \div 200$ PE
AVG Power Density	5 mW/channel
Silicon Die Size	$18 \times 22\,\text{mm}^2$
Operating Temperature	77 K ÷ 300 K
Number of SLVS Transceiver	32 columns
SLVS Transceiver Speed	312.5 Mbps - 625 Mbps
Clock Frequency	312.5 MHz
Power Gating Feature	DUNE Compatible (triggered)

To meet the required operating temperature range of the detector and characterization procedures, the ASIC is partially designed using silicon-proven blocks whose performance has been previously tested under cryogenic conditions (liquid nitrogen, 77 K). However, a set of features dictated by the specific application necessitates modifications and the development of new IP blocks. To ensure optimal performance across different thermal conditions, simulations are conducted at 77 K, 87 K, and 300 K. Additionally, key parameters are being designed with built-in flexibility to compensate for temperature-dependent effects. Whenever possible, design rules established in previous works [45, 46] are applied to mitigate aging and performance variations induced by cryogenic conditions.

ASIC development timeline A first engineering run is scheduled for early 2026 to ensure the availability of the DENEB chip for testing in the course of 2026. The reticle will include the first full-scale DENEB demonstrator, integrating 1024 channels.
The package design is currently under discussion. A cryogenic-compatible package will be sent for production once the pad frame design is finalized. In 2026, initial chip testing will begin using a probe card to verify functionality at room temperature. Once the cryogenic package is received, the ASIC characterization will proceed at room temperature and in liquid nitrogen, including optical tests with the SiPM matrix and electrical and functional characterization without it.
A second run will follow in 2027, providing the final version of the ASIC. A second possible package production with modifications is considered to meet variations in the final version of the ASIC submitted to the foundry in 2027.

ASIC design validation The first validation of the channel architecture was performed using reconstruction simulations based on a behavioral software model of the channel, incorporating key variables to study critical architectural parameters.

From the analysis of spill simulations, the design concept was validated by considering both the

coded mask layout and the lens layout in pure LAr as well as in xenon-doped argon.

This validation yielded a range of values for critical parameters, such as the data converter's conversion time and the charge dynamic range.

By means of a behavioral simulation, the electronic response to spill events for each channel was simulated as shown in Figure 5.24. In the simulation, the waveform signal is generated together with the final information delivered by the electronics, including the time of the opening windows (orange edges), the time of the closing window (green edges), and the number of integrated photons for each window (not shown in the figure).

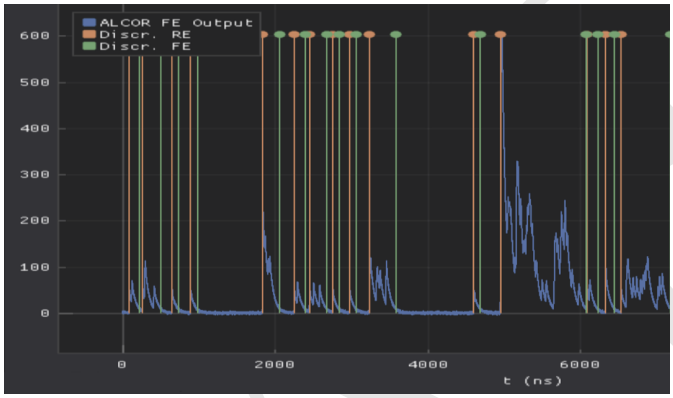


Figure 5.24: Output of the simulated electronics response for a single channel for a simulated spill event. The signal waveform from the behavioral simulation is shown in blue, the rising edge (in orange) and the falling edge (in green) of each integration window are reported in the same plot.

From the analysis of the spill simulations, the preliminary design was validated by considering both the coded mask layout and the lens layout in pure LAr or in xenon-doped argon.

As shown in Figure 5.25, the results indicate that the design satisfies the main requirements: the fraction of photons lost for each channel can be reduced to less than a few percent if the ADC conversion is fast enough (top plot), and the dynamic range is guaranteed to be above 200 photons (bottom right plot). As shown in the bottom left plot, the signal generated by some photons can be lost if their arrival time separation is larger than 200 ns and more than one integration window is necessary to fully contain each spill. This loss is, however, kept to a minimum if the ADC conversion time is fast enough to allow ADC to be free in a shorter time.

Finally, it was demonstrated that the electronic response does not preclude the possibility of reconstructing the neutrino interaction time within the beam spill. A dedicated study was performed to evaluate how often the integration window for the current event is opened by a photon coming from the previously detected interaction, which would prevent measuring the correct interaction time.

To evaluate this, for each channel detecting at least 10 photons for each interaction, the time of the first photon T_{first} was saved, and the time interval ΔT between T_{first} and the previously detected photon was saved. As shown in Figure 5.26, for pure LAr with the lens-based optical detector, ΔT is below 500 ns in less than 1% of the cases, implying that in over 99% of cases, the time distance

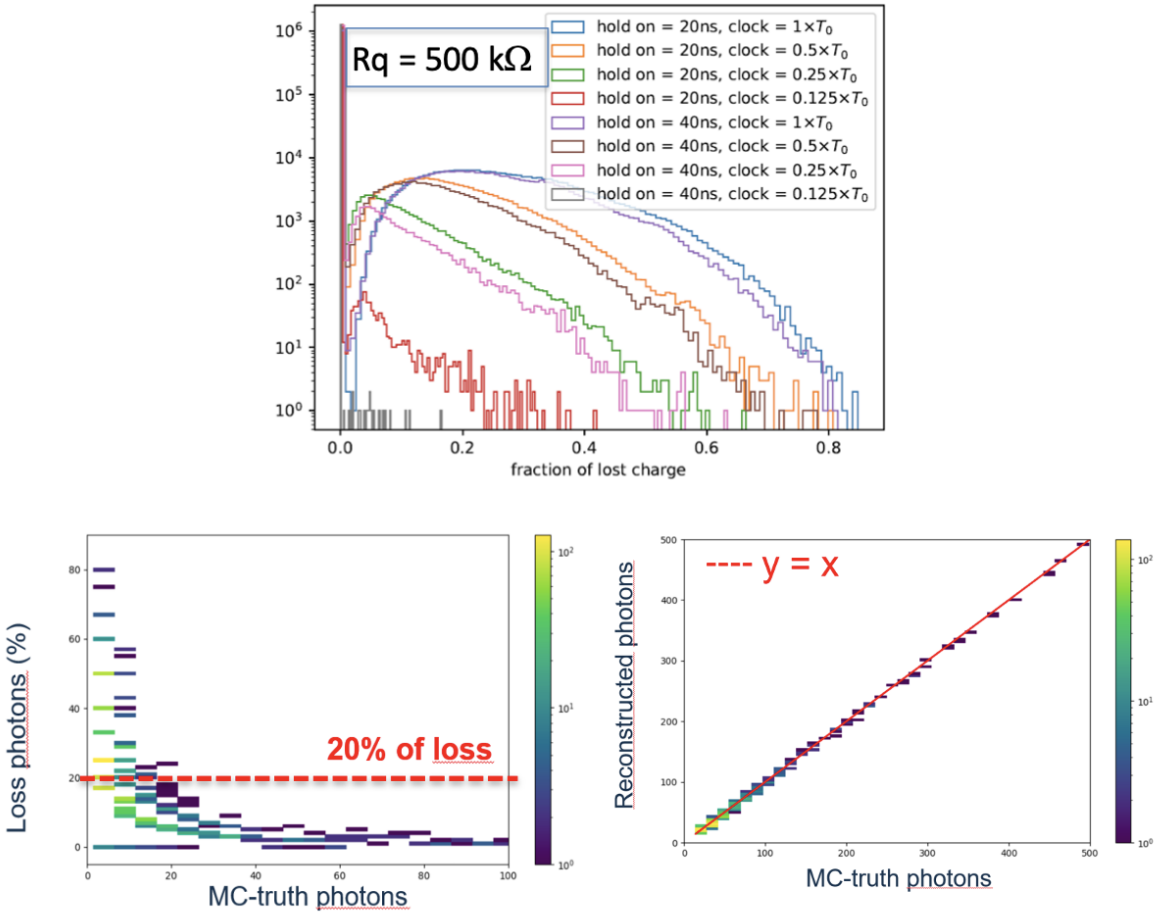


Figure 5.25: Results from simulations for the validation of the ASIC design. Top: Fraction of lost charge for different values of ADC velocity and hold-on duration. In this plot, 250 beam spills were simulated with the coded mask layout. Bottom left: Percentage of lost photons as a function of the number of true photons per spill. In this plot, the lens layout and the channels with typical values of 1-7 integration windows are considered. Bottom right: Number of reconstructed photons as a function of the number of detectable (true) photons. In this plot, the lens layout was considered and the channels with a large number of photons for each integration window are displayed.

between the first photon of the current interaction and the last photon of the previous one exceeds 500 ns. The interaction time can, therefore, be reliably reconstructed from GRAIN.

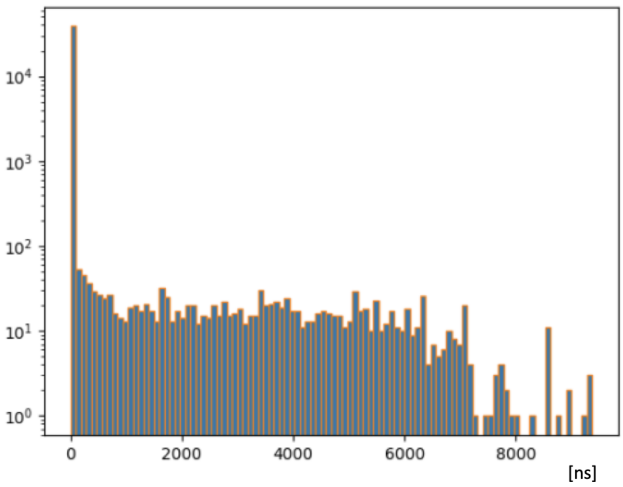


Figure 5.26: Distribution of ΔT for pure Argon (see text).

5.5.3 Cryo-Vacuum Flanges and Cold Interface Board

Electrical connections between the internal GCB and the external GWIB are routed through the GRAIN Cold Interface Board (GCIB) and a pair of DN160CF flanges. These flanges provide the physical interface from air to vacuum and from vacuum to LAr. Each endcap of the GRAIN Inner and Vacuum Vessel contains four pairs of flanges, with each pair servicing up to eight cameras. This configuration supports a maximum of 64 cameras, accommodating layouts with only lens-based detectors, only coded-mask systems, or a combination of both.

Identical custom-manufactured D-SUB connectors, incorporating regular pins, high-current pins, and coaxial pins, are planned for both sides of each flange. The final connector layout is yet to be defined, pending tests to evaluate the noise immunity and signal integrity of digital LVDS lines and bias voltage lines. The primary options are:

- Regular Pins: This option offers higher density, allowing each GCB to have independent power and data lines routed through a completely passive GCIB. It is the preferred solution from a reliability and cost perspective, though it may compromise signal quality.
- Coaxial Pins: This option provides superior signal quality but at a lower density, which prevents fully independent connections for each GCB. This would require the GCIB to become an active board, splitting power lines and/or buffering digital signals. While feasible, this approach reduces system robustness, as a single point of failure on the GCIB could disable multiple cameras.

Mechanically, the GCIBs boards will be located in the flange neck on the endcap to preserve internal space, plugging directly into the inner connector of the flange. Separate cables will then run from each GCIB to the GCBs. The GCIBs may also host additional environmental sensors and power filters if required in that location.

5.6 Data Acquisition and Slow Control System

The GWIB functions are the data acquisition (DAQ), timing, and slow control endpoints for GRAIN. Each of the 8 GWIBs is attached to the corresponding flange through short cables and is housed in a dedicated air-cooled enclosure. The GWIB is built with a Zynq chip, which includes a multicore ARM CPU and an FPGA fabric. The former provides the DAQ and slow control interfaces via the software ethernet stack. The latter serves as an interface with the timing system and the ASICs, as well as with any environmental sensors for monitoring pressure and temperatures inside the cryostat.

The expected DAQ data rate, given the negligible noise of SiPMs in cryogenic conditions and the low spill rate, is extremely low. No form of online triggering is foreseen for physics data. A spill trigger in advance with respect to the spill start is, however, required to enable the ASIC power lines. It will be produced by the DAQ via the Timing System whenever a spill is expected. Additional triggers will be issued in the inter-spill period for any calibration needs.

5.7 GRAIN Assembly and Comissioning

Before the final installation at Fermilab, a preliminary assembly of GRAIN at Laboratori Nazionali di Legnaro LNL is foreseen. In this phase, the majority of the components of the cryogenic system will be mounted together with the Inner Vessel and a complete set of optical detectors. In this phase, the GRAIN Inner Vessel will be mounted inside a Vacuum Tank specifically built to perform tests before the delivery of the GRAIN Vacuum Vessel. This phase will be fundamental for the commissioning of the cryogenic system, for the validation and commissioning of the detector layout and the readout system.

Once the Inner Vessel and the Vacuum Tank are ready, the first step to validate all the technical details of the cryogenic infrastructure and imaging readout system will consist of equipping the Inner Vessel with a mechanical and thermal mock-up of the cameras, along with a prototype of the power and signal cabling that will be required in the final detector layout. The mock-up cameras will feature resistive loads equivalent to the ASIC under development and will allow us to study thermal fluxes and techniques to mitigate the formation of GAr bubbles in the LAr volume.

Since the development of the readout ASIC (Section 5.5.2) is a critical aspect, it is particularly relevant to validate in advance all the remaining open design choices on the readout system. These include, in particular, the choice of connectivity and cabling arrangements inside the cryostat, as well as the solutions to mitigate the thermal load and the bubble formation caused by the electronics and the cables. The circuit boards for the GCB and GCIB, as well as all their components, will be validated in a dedicated integration test. The boards used for this test, which are currently under development, will be mechanically identical to the final design ones and will host all the required components and connectors, except for the ASIC, for which a proxy is represented by resistors dissipating equivalent power over a similar surface area.

DRAFT

5.8 Detector Performance

5.8.1 Reconstruction performance with lens-based detector

The performance of the lens-based detector for neutrino-argon interactions was evaluated by simulating large samples of neutrino events within the GRAIN LAr volume. These simulations followed the official workflow described in [43], using the DUNE flux and the SAND detector geometry, with a particular focus on muon neutrino charged current (CC) interactions. The study considered only single neutrino events rather than full beam spills, as the primary goal was to assess the effectiveness of spatial reconstruction algorithms based on the optical readout. Furthermore, in addition to the absence of background tracks, these single-event simulations assumed a simplified electronics readout model that collects all photons detected by the SiPMs within 500 ns from the interaction time.

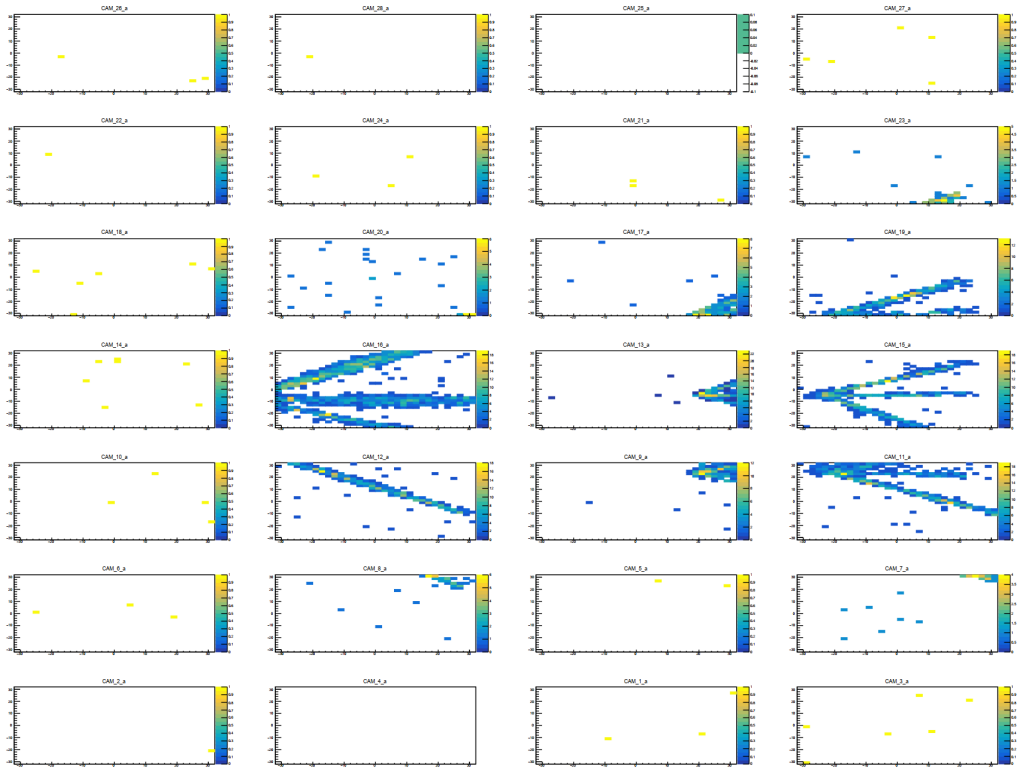
An example of muon neutrino interaction inside GRAIN, as acquired by the layout with 38 lens-based detectors, is shown in Figure 5.27. Three primary particles (a muon, a proton, and a charged pion) are produced in the interaction, all exiting the cryostat and crossing into the tracker volume. The complete set of images recorded by the optical system is shown grouped according to the physical walls on which the cameras are mounted.

For the study of GRAIN's reconstruction performance, a fiducial cut was applied to exclude the layers occupied by cameras on all walls, leaving a 5 cm dead zone around the lenses, as well as the most downstream region of GRAIN. The resulting fiducial volume is defined by $|x| < 350$ mm, $|y| < 550$ mm, and $|z| < 150$ mm when considering only the GRAIN detector for event reconstruction. Within this volume, up to 10 cameras can image the same interaction; however, on average, only about 3 to 4 cameras provide images useful for reconstruction.

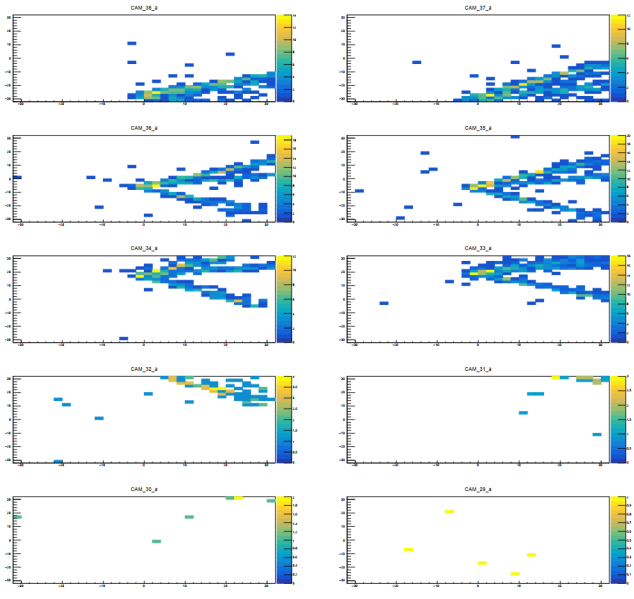
Number of visible tracks Figure 5.28 shows a 2D histogram depicting the number of charged primary tracks per event versus the number of tracks identified as visible by the cameras. This data corresponds to a sample of 15,000 ν_μ CC interactions generated within the GRAIN fiducial volume. A track is considered visible if its projection onto the sensor exceeds 10 pixels in length. As the plot illustrates, most CC interactions produce between 2 and 3 charged particles at the vertex, although events with up to 10 particles can occur at DUNE energies. Many of these particles have short track lengths and low energy, so they are usually not visible in the images. In fact, fewer than 10% of events with 5 or more primary particles are classified by the cameras as having 5 or more visible tracks. For events with 3 primary particles, the cameras detect all three tracks in 32% of cases and only two tracks in 42% of cases. Furthermore, regardless of the true number of primaries, fewer than 8% of events show no visible tracks detected by the cameras.

Vertex reconstruction To reconstruct a vertex for interactions in GRAIN, at least two images must contain the vertex. This, in turn, requires that at least two tracks be reconstructed in each of those cameras, enabling the calculation of their intersection point. These requirements significantly reduce the number of events for which the vertex can be successfully reconstructed. These derived requirements strongly reduce the statistics of events for which the vertex can be found. Out of approximately 7,000 events simulated within the fiducial volume, vertex reconstruction is successful in about 4,000 cases. The results, shown in Figure 5.29, present the differences between the

DRAFT



(a) Left cameras (b) Right cameras



(c) Top cameras (d) Bottom cameras

Figure 5.27: Complete set of 2D images recorded by the optical system for a neutrino interaction in GRAIN. Three tracks are clearly visible, as well as the interaction vertex. In this case, the layout with 38 cameras was considered.

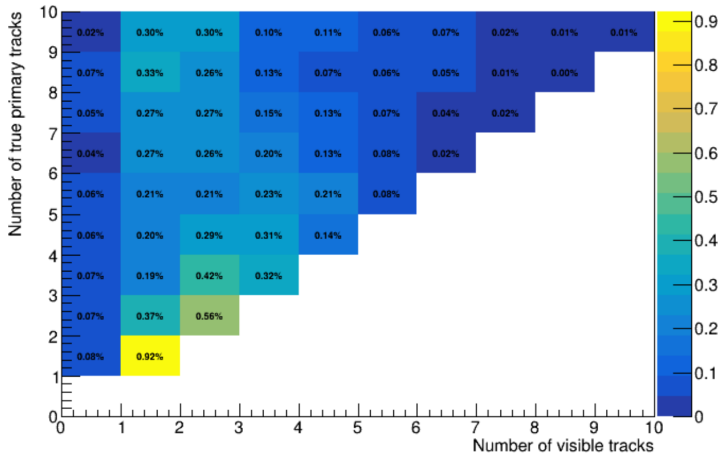
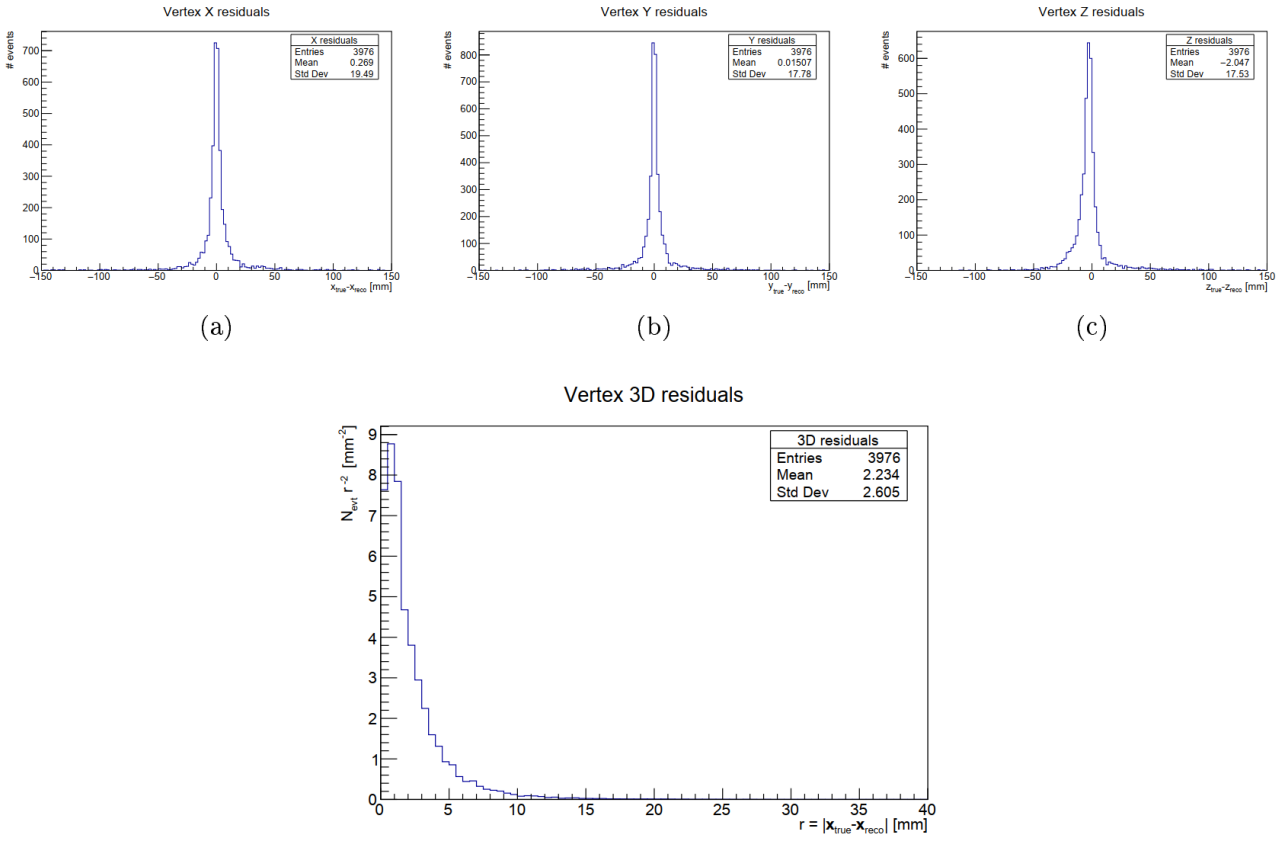


Figure 5.28: Comparison between the number of charged primary tracks in an event and the number of tracks visible to the cameras. The matrix is row-normalized. The data are from 15,000 ν_μ CC interactions with vertices located within GRAIN's fiducial volume.



(a) (b) (c)

Figure 5.29: Top: Residual distributions for the reconstructed vertex coordinates x, y, and z. Bottom: Distribution of the 3D distance (in mm) between the true and reconstructed vertex positions within the GRAIN volume. This plot is normalized so that each bin corresponds to an equal volume in space. Data are from 15,000 ν_μ CC interactions with vertices inside the GRAIN fiducial volume.

reconstructed 3D vertex position and the true Monte Carlo (MC) vertex position. Residuals are displayed for each coordinate individually, as well as for the overall 3D distance between the two points. The 3D histogram was normalized by dividing by r^2, so that each bin corresponds to the same spatial volume. All distributions are centered around zero and symmetric, although a slight negative bias appears in the Z residuals, indicating a tendency for $z_{reco} > z_{true}$. Since the Z-axis aligns with the neutrino beam direction and tracks are generally boosted forward, this biases the Z-coordinate reconstruction. The mean 3D residual is 2.2 mm, primarily influenced by the uncertainty in Z, while the median residual is 1.4 mm. A further improvement in the performance of the interaction vertex position reconstruction in GRAIN is expected when the downward tracker information is also exploited. A preliminary study on a sample of $\nu_\mu CC$ interactions inside GRAIN, Once one or more tracks are recognized and fitted in the STT tracker, an improved reconstruction 25 of the interaction vertex position inside GRAIN can be inferred. This is more effective when at least a couple of tracks are reconstructed: in this case, the simple interception of the two most rigid tracks generally identifies a more precise position of the vertex. The improvement thus obtained can be appreciated in Figure 5.30, for the sample of events with a reconstructed track multiplicity between two and three. In the figure plots, the errors on vertex coordinates from the track crossing are compared with those affecting the preliminary reconstruction based on the MC hit spread and energy deposit in the LAr volume.

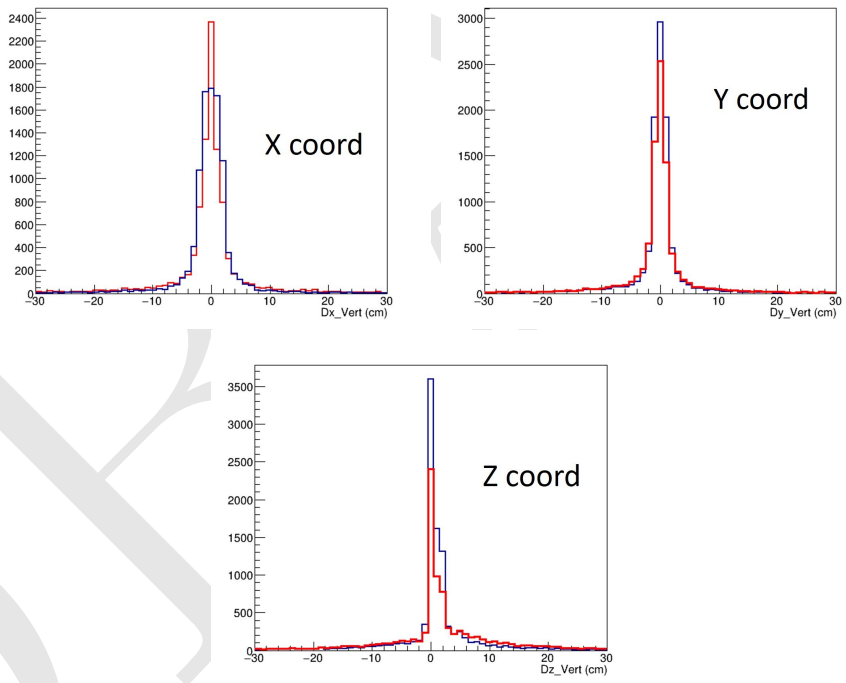


Figure 5.30: Error distributions for the reconstruction of interaction vertex coordinates in GRAIN, using MC information about energy deposit by charged particles in liquid argon (black histogram) and from the intersection of the two most rigid reconstructed tracks (red histogram). The plots refer to the event sample with one, two, or three reconstructed tracks.

End-point track reconstruction The position of each track's end-point within the GRAIN volume is crucial, as it helps determine whether the track is fully contained in LAr or if a corresponding match with the downstream tracker should be expected. The end-point reconstruction achieves results comparable to vertex reconstruction, with a mean distance of about 7 mm between the true

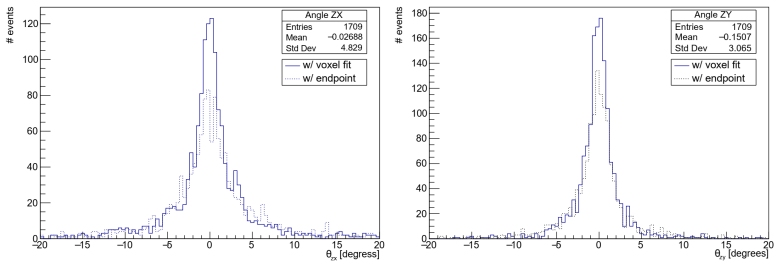
and reconstructed end-point positions. This information is used to classify tracks as either fully contained within GRAIN or not. To define containment, a 5 cm buffer layer near the vessel's inner walls was applied: any track whose end-point lies within this buffer is labeled as not contained. This classification can be compared against truth-level information from the tracker, where tracks are marked as not contained if they have associated hits in the tracker. In the sample of 15,000 ν_μ CC events, approximately 97% of exiting tracks are correctly identified as not contained. However, only around 74% of tracks without associated tracker hits are labeled as contained. This discrepancy arises from the large buffer layer, tracks stopping inside the cryostat, and tracks at large angles that only reach the electromagnetic calorimeter (ECAL). Despite these challenges, the purity of the reconstructed categories remains close to 90%. These results are summarized in Table 5.3.

Table 5.3: Percentages of tracks classified as contained or not, based on both true (simulation) and reconstructed information.

Reco vs. True	Contained	Not contained
Contained	247 ($\sim$ 3%)	8269 ($\sim$ 97%)
Not contained	3301 ($\sim$ 74%)	1186 ($\sim$ 26%)

Track direction reconstruction To extract the 3D direction of tracks, two independently methods were applied, in the first one the direction is directly extracted by the knowledge of vertex and end-point, while for the second one the output of the voxel-based stereo reconstruction (see Section XX) was used. In the latter approach, tracks are represented as clusters of voxels in space. A 3D fit is performed over these voxel clouds to determine the actual shape and direction of the track, which may not be a straight line due to the influence of the magnetic field. Figure 5.31 shows the angular differences, θ_{zx} and θ_{zy}, between the true and reconstructed track directions in GRAIN for both methods. The results are based on a sample of 1,000 neutrino interactions, each producing one muon, one pion, and one proton in the final state.

ref al primo capitolo



(a) Angle ZX (b) Angle ZY

Figure 5.31: Angles between the true and reconstructed track directions for the xz and yz projections respectively.

The means of the distributions are centered at zero, with standard deviations of 5° for θ_{zx} and 3° for θ_{zy}. The larger spread in the xz projection arises from the poorer precision in estimating the x coordinate, as previously noted in the context of track endpoint reconstruction. Overall, GRAIN's ability to accurately determine track directions in LAr is crucial. Within the SAND global event reconstruction framework, GRAIN uniquely provides this directional information for tracks stopping in LAr, and it also aids in refining the back-propagation of particle trajectories

from the downstream tracker. The mean of the distributions is centered at zero, and the standard deviation is 5° for θ_{zx} and 3° for θ_{zy}. The larger spread in the xz projection is due to the poorer ability to estimate X coordinates, as already discussed when considering track endpoints. Overall, the capability of GRAIN to determine the correct direction of the track in LAr is important since, within SAND global event reconstruction, GRAIN is unique in being able to provide this information for tracks that stop in LAr. However, it will also contribute to correcting and adjusting the back-propagation of the particle trajectories from the tracker.

5.8.2 Reconstruction performance with Coded Mask detector

GRAIN reconstruction technique with the Coded Aperture camera design is based on an iterative Maximum Likelihood Expectation-Maximization (MLEM) algorithm. The algorithm computes the probability that a given initial distribution of the photon source within the detector could have produced the observed images, according to a mathematical model of the detection process. Among all possible source distributions, the one with the highest probability is identified as the *Maximum Likelihood Estimate* of the original photon source distribution. In practice, starting from an initial three-dimensional, non-negative distribution—assumed uniform in the absence of other information—the algorithm iteratively updates the estimate of the photon source distribution until the required accuracy for numerical convergence is achieved.

To evaluate the reconstruction performance of GRAIN's coded-mask-based system, a MC simulation was performed, generating a sample of muons and ν_μ charged current quasielastic (CCQE) interactions. The MLEM algorithm is applied to all camera images, with the reconstruction fiducial volume divided into voxels measuring $18 \times 18 \times 18\,\mathrm{mm}^3$. The fiducial volume boundaries are defined by the curved walls of the inner vessel and planes parallel to the cameras, located approximately 1 cm from the mask surface. The number of iterations for the algorithm is fixed at 200 per event, balancing computational runtime with the convergence of the maximum likelihood estimation.

Following reconstruction, the output undergoes an initial post-processing step where voxels with scores exceeding 5% of the maximum value are selected. The reconstructed data is then analyzed in two stages: track finding and track fitting. During track finding, voxels are clustered and associated with potential particle tracks. Due to the specific characteristics of the reconstruction output, a specialized algorithm was necessary. A method based on an extended 3D Hough transform was developed, incorporating voxel scores as weights. Although a preliminary version of this algorithm is available, ongoing studies are focused on improving its efficiency.

For the studies detailed in this section, a "fast" clustering method is used, associating selected voxels with MC truth energy deposits based on spatial proximity. An example of event reconstruction and voxel clustering is shown in Figure 5.32. Once voxels are clustered, tracks are fitted under the assumption that particle trajectories within GRAIN are approximately straight. The fitting minimizes the weighted sum of squared distances between the track and the voxels, where the weights correspond to voxel scores. However, this straight-line approximation is insufficient for low-momentum particles. For these cases, the development of more advanced fitting techniques or integration with the tracker's Kalman Filter (KF) is planned for future improvements.

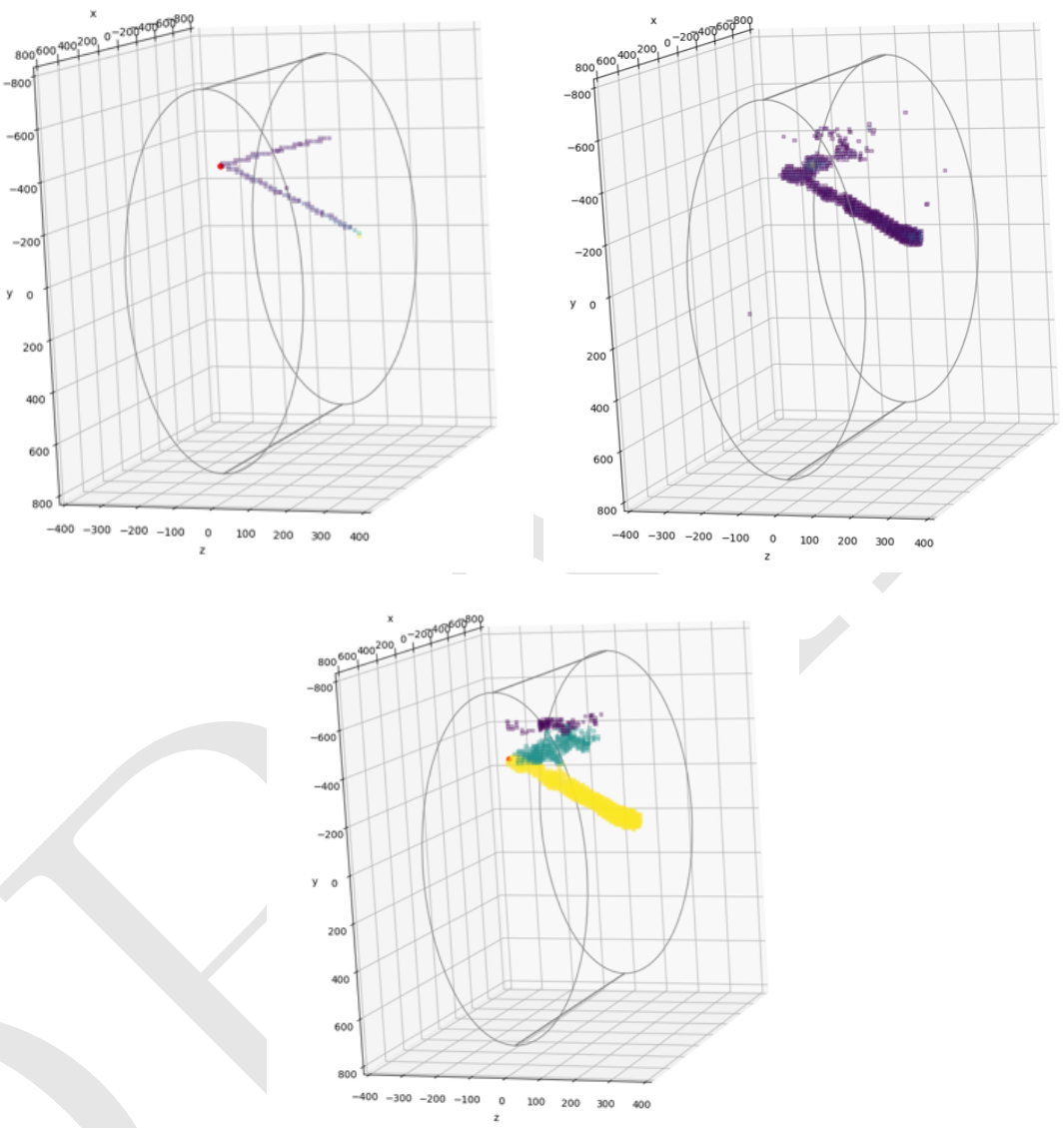


Figure 5.32: Top left: Energy deposits from MC tracks. Top right: The same event reconstructed using the coded aperture mask algorithm. Bottom: Voxel clustering based on distance to MC tracks. The red dot indicates the MC vertex, while voxels are colored by cluster (violet voxels are unassociated with any track).

Single track reconstruction performance A MC sample of 1,000 muons with energy 1 ± 0.3 GeV crossing the GRAIN volume was simulated using Geant4. The muons originate within the region $|X, Y| < 30$ cm at $Z = -50$ cm, with angles ranging from 0° to 20° relative to the z axis. Figure 5.33 shows the residual distribution of the track position at $Z = 0$, as well as the angular difference between the reconstructed and true tracks.

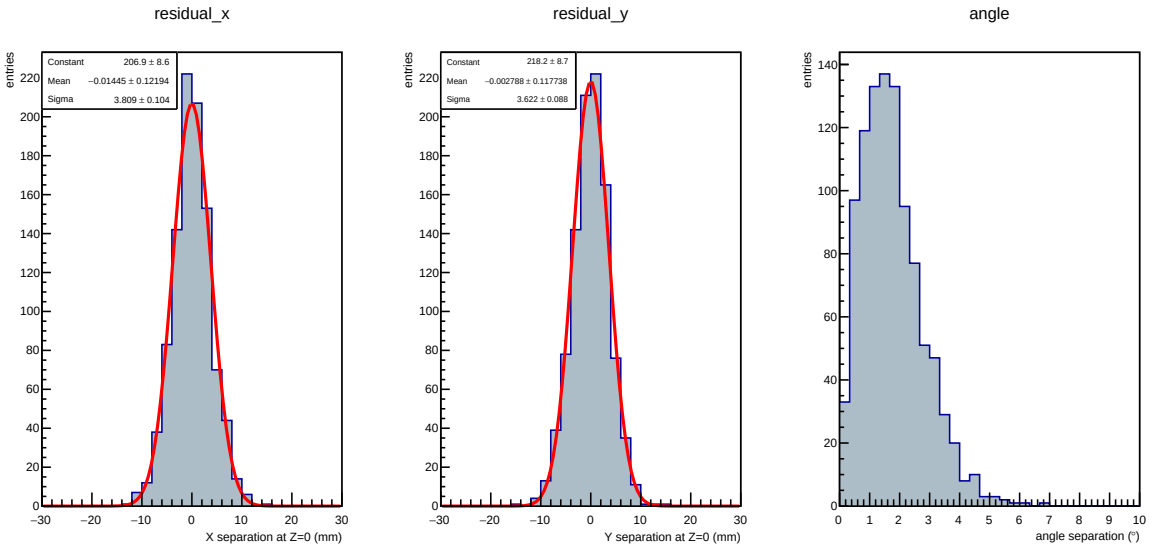


Figure 5.33: Left and Center: Residual distributions of muon track positions at $Z = 0$, with Gaussian fits overlaid. Right: Angular difference between reconstructed tracks and MC truth data.

Vertex reconstruction performance A MC sample of 4,350 ν_μ CCQE interactions was generated using the Energy Deposition Simulation (EDEP-SIM) software. The interactions are constrained to a region of the inner vessel at least 10 cm away from the camera planes. For vertex position evaluation, events were selected if they contained at least two tracks with reconstructed lengths greater than 50 mm and minimum deposited energies above 20 MeV. This selection yielded an efficiency of 46%, resulting in a total of 2,000 selected events. For each event, the two best reconstructed tracks, based on fit quality, were chosen. The reconstructed vertex position is determined as the median point of the segment connecting these two tracks. The reconstructed vertex positions were then compared to the MC truth, with the results shown in Figure 5.34. The vertex resolution is approximately 10 mm along each axis, consistent with the voxel size of $18 \times 18 \times 18\,\text{mm}^3$. A notable bias of about 10 mm along the beam axis is observed and needs to be take into account accordingly.

5.8.3 Acceptance enhancement with GRAIN

In a dedicated study, the acceptance was studied for different particle species by simulating a sample of 100×10^3 events of neutrino interactions in GRAIN, both CC and NC. In the simulations GRAIN was instrumented with a set of 53 cameras as described in section 5.4.3 and a fiducial volume was set on x and y coordinates ($|x| < 350$ mm and $|y| < 550$ mm). Finally the thresholds chosen for particles to be detectable in each subsystem are:

- STT: at least 6 digits in the yz plane, in which curvature occurs. This condition guaranties

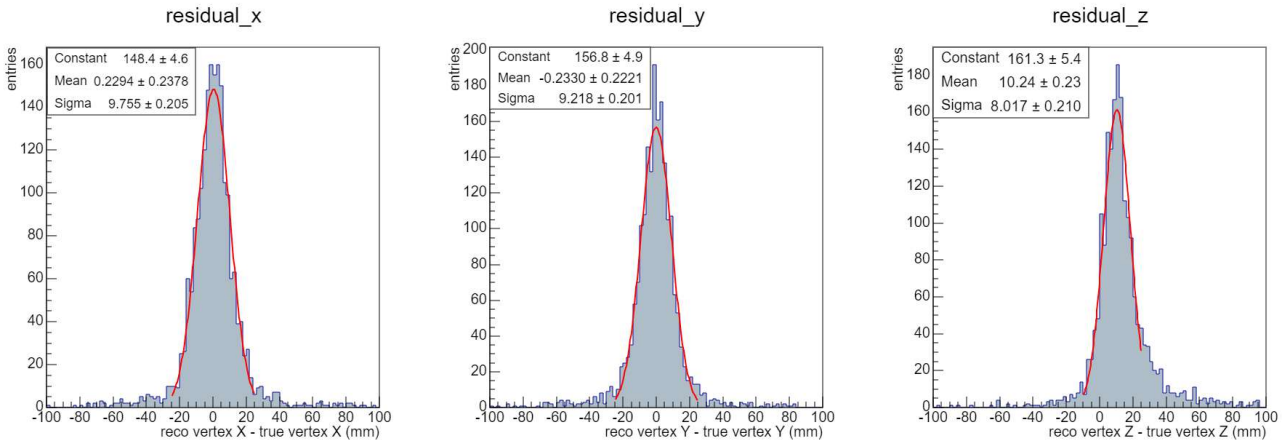


Figure 5.34: Residual distributions of the vertex position along each axis; the z axis (beam direction) exhibits a significant bias. Gaussian fits are overlaid on the distributions.

that the track could, in principle, be fitted to determine its momentum.

- ECAL: at least 100 keV of deposited energy in the scintillating fibers, taking into account light attenuation. This corresponds roughly to a threshold of 1.1 PEs.
- GRAIN: at least 2 cameras must image the track for the particle to be deemed visible, and a successful 3D endpoint reconstruction is required for it to be considered detected. The first condition represents the best possible result achievable in GRAIN with the current geometry and assuming a perfect reconstruction, while the second condition measures what is achieved by the current algorithm.

The average acceptance per particle species is summarized in Table 5.4, showing the fraction of detectable muons, protons, pions, and neutrons in each subdetector of SAND.

Table 5.4: Fraction of primary particles (muons, protons, charged pions and neutrons) reconstructed in STT, GRAIN and ECAL from a 100×10^3 ν_μ FHC sample. For GRAIN, the fraction of visible particles, i.e. particles that are imaged by at least two cameras, is also reported. For neutrons, the STT threshold is ≥ 1 digit, with a deposited energy > 250 eV.

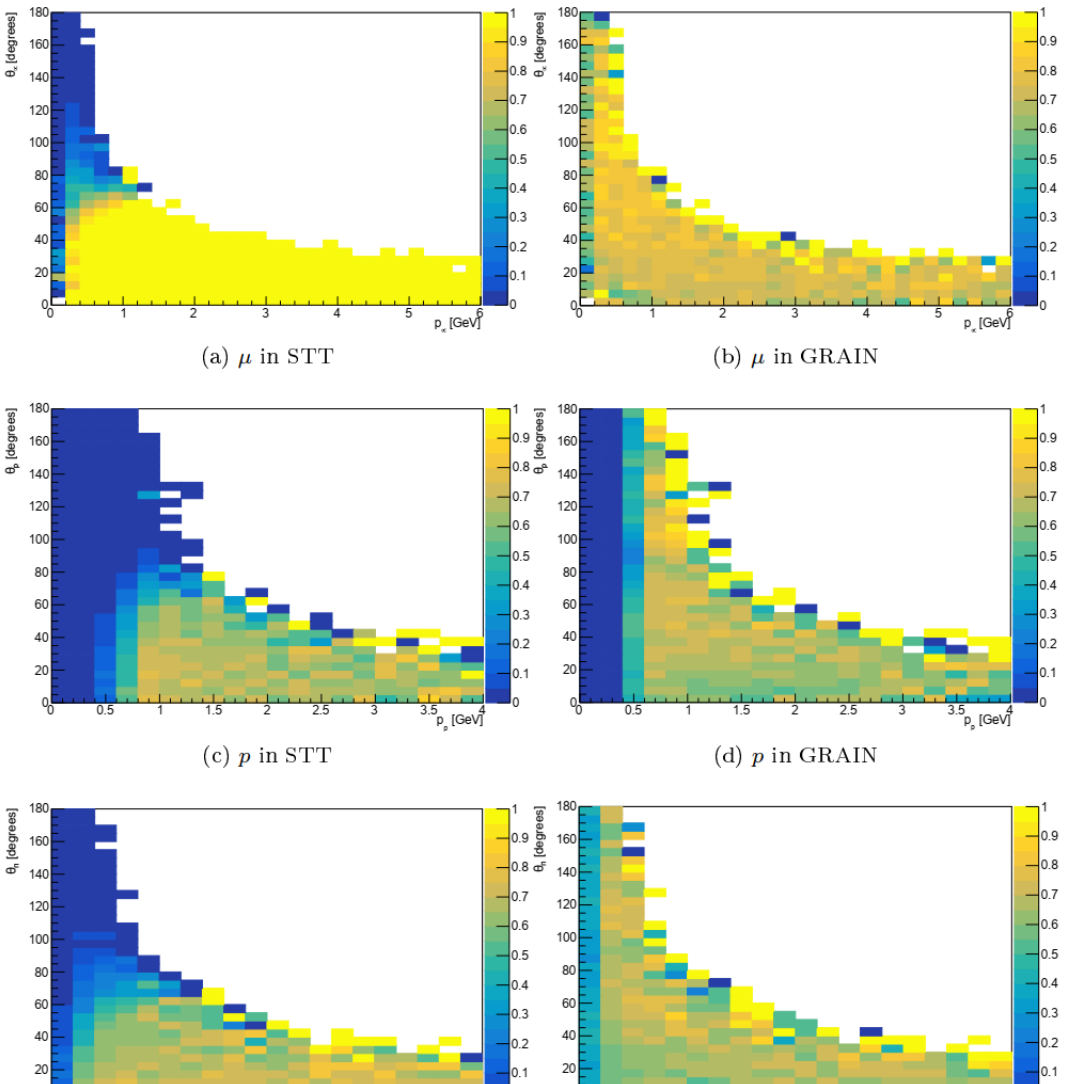
Particle	STT	GRAIN rec	GRAIN vis	ECAL
Muons (μ)	91.6%	76.3%	79.9%	97.7%
Protons (p)	13.3%	23.3%	24.7%	16.6%
Pions ($\pi^\pm$)	42.0%	58.8%	61.9%	72.2%
Neutrons (n)	24.7%			75%

These detection efficiencies are also shown as a function of the particle momentum and angle with respect to the beam in Figure5.35, visualizing the accessible phase space. Since FHC means mostly ν_μ events, a muon is always present. They are generally boosted in the direction of the neutrino beam, so $\theta < 60°$. Because of this, most muons are able to exit GRAIN and cross into the STT, producing long tracks that also reach the ECAL. The average STT acceptance is, in fact, $\sim 92\%$, roughly uniform from low to high momentum (see Figure 5.35a). Moreover, given

the 4π hermiticity, every muon is generally detected by the ECAL as it leaves SAND, bringing its acceptance close to 98%. The acceptance for GRAIN is around 76%, but visible muons are close to 80%. This means that there is still a small margin for GRAIN reconstruction to be improved in the future without changing the geometrical configuration. Figure 5.35(b) shows the phase space acceptable for GRAIN. Despite the average acceptance being smaller than for STT, which is expected to improve, the available phase space is larger, and GRAIN can also access large angles. Concerning protons, the STT average acceptance is instead very low (close to 13%). Proton multiplicity can be high (up to about 10), but most of them are, in fact, very short tracks, close to the vertex and stopping in liquid argon. Since they travel only a few centimeters, their tracks are often less than 10 pixels long, and only 25% are visible in the images. GRAIN is able to recover most of those, achieving an average of 23% detection efficiency. As shown in Figure 5.35d, the momentum threshold for detection in this scenario is 0.4 GeV. This limit could be improved only by pushing GRAIN optical readout into imaging smaller tracks. Recognizing tracks below 10 pixels in length is possible for good quality images, but the activity in the vertex region may cause overlaps, making shorter tracks indistinguishable. However, selecting more exclusive event topologies allows for an increase in acceptance. For example, considering ν_μ CCQE-like events in which a muon is produced alongside any number of protons while vetoing the presence of pions or neutrons (0πNp0n), protons carry a larger fraction of the original neutrino energy, and up to $\sim 50\%$ are visible in GRAIN (with $\sim 46\%$ being reconstructed). Charged pions $pi\pm$ have lower multiplicity than protons, and they are generally more energetic, so a larger fraction is detectable in the STT ($\sim 42\%$). The fraction reconstructed in GRAIN is around 59%, with a visible fraction of 62%. Similarly to muons, despite their currently lower efficiency, GRAIN covers a wider phase space, including large θ and back-going pions, which would otherwise only be detected by the ECAL. Neutrons are detected only through the signal induced by interactions in the calorimeter or, with a lower probability, in the STT. Neutrons do not leave tracks in GRAIN, so no attempt was made at reconstruction inside LAr. However, about 11% of neutrons stop in the LAr volume, so it could, in principle, be possible to look for isolated blips inside GRAIN. The detection efficiency in the ECAL is enhanced due to the large percentage of lead, which leads to an abundant production of secondary particles in inelastic interactions. Considering the 1.1 photoelectron threshold, about 75% of neutrons are detected in the ECAL. Given the lower density, the STT detection efficiency is $\sim 25\%$. In this case, at least one or more digits are required, with a total energy deposition > 250 eV. Overall, the combined detection efficiency for ECAL/STT is $\sim 80\%$. The neutron energy deposits are not proportional to their kinetic energy, which is then reconstructed using the time-of-flight technique by utilizing the time and position of the neutron clusters and the vertex information. This is particularly important in anti-neutrino events, where neutrons would otherwise be responsible for a large fraction of missing energy.

5.8.4 Neutrino energy reconstruction

The neutrino energy is reconstructed using the total momentum method. Assuming the target nucleon to be at rest (no Fermi motion), the 4-momentum is conserved in the interaction. The incoming neutrino 4-momentum is therefore equal to the sum of the 4-momenta of the outgoing interaction products, which can, in principle, be reconstructed in the detector. The effectiveness of this method relies on the ability of the detector to measure all outgoing particles. This is affected by experimental challenges, such as accurately measuring the momenta of neutral species, as well as final state interactions that produce a bias between the true energy and the visible energy by smearing the outgoing topology or momenta. In the combined analysis, the best mo-



(a) μ in STT (b) μ in GRAIN

(c) p in STT (d) p in GRAIN

(e) $\pi^{\pm}$ in STT (f) $\pi^{\pm}$ in GRAIN

Figure 5.35: Detection efficiency in STT and GRAIN for muons, protons, and pions, as a function of the particle momentum p and angle θ with respect to the neutrino beam, visualizing the accessible phase space.

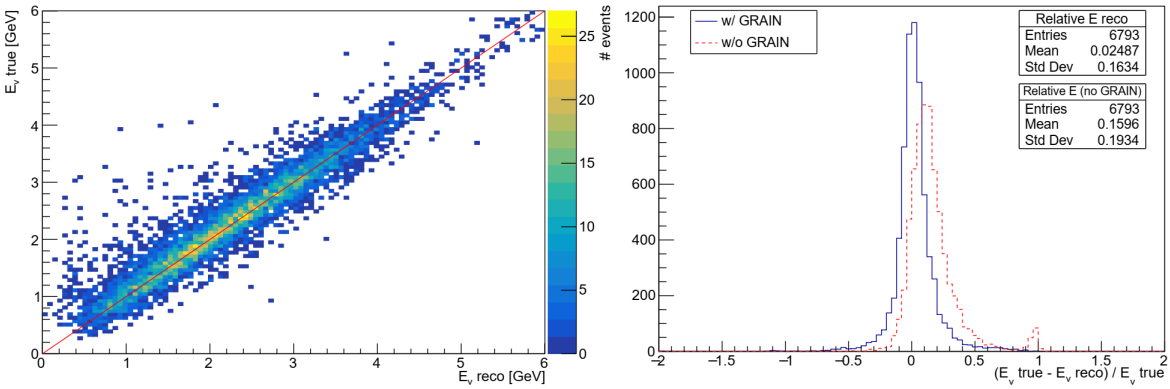
mentum estimate is found by looking at the information available from GRAIN, ECAL and STT for each primary particle. Considering charged particles, several possibilities exist depending on the detector elements with which they are reconstructed. These can be divided into four groups:

- STT (+ECAL): if the particle is reconstructed by the STT, and optionally also by the ECAL, the best estimate of its momentum is taken from the track curvature at its entrance point in the tracker. In the fast reconstruction, this is computed using the Gluckstern parameterization [47] and a multiple-scattering correction to smear the true momentum. The direction is taken from the vertex to the STT entrance point. The ECAL information is not used.
- STT + GRAIN (+ECAL): if the particle is reconstructed by the STT and GRAIN, and optionally also by the ECAL, the momentum is computed starting from the STT estimate and adding the energy deposited in GRAIN to correct for the energy loss between the vertex and the entrance in the STT. The deposited energy in GRAIN is computed as a 20% smear on the true value, given the preliminary performance on single tracks. The direction at the vertex is taken as the GRAIN reconstructed 3D direction. The ECAL information is not used.
- GRAIN (+ECAL): if the particle is reconstructed by GRAIN, its momentum is computed by using the 3D reconstructed direction and considering the energy deposited as the best estimate for its kinetic energy. The underlying assumption is that the particle is stopping in LAr. This is not always true, leading inevitably to a bias, since for non-stopping particles, the deposited energy is, in fact, not proportional to the kinetic energy. If the particle is also reconstructed by the ECAL, the cluster energy in the ECAL is added to the kinetic energy estimate, again assuming a stopping particle. However, particles that are also exiting the ECAL are poorly reconstructed. In the future, a curvature fit should be attempted using the GRAIN reconstructed tracks and ECAL clusters for those cases.
- ECAL only: if the charged particle is reconstructed solely by the ECAL, it is either a back-going particle or a particle at a large angle that is missed by GRAIN. Assuming it is stopping, the total cluster energy is used as an estimate for the kinetic energy, and the direction is taken from the vertex to the start of the ECAL cluster. For these cases, similarly to GRAIN, the estimate can generally be poor since the ECAL alone is not meant for reconstructing the momentum of particles that are passing through. Because of this, the reconstruction quality of particles that do not shower inside is low, and most of their energy is missed. A future improvement would be to use the ToF technique for these cases.

In this fast reconstruction, the flow for neutral particles is different. For detectable neutrons, the kinetic energy is reconstructed using the distribution obtained from a previous performance study employing the time-of-flight technique. From that study, $\Delta E/E_{true} < 0.2$ for about 40% of neutrons, and the neutron direction is determined from the position of the STT or ECAL cluster. For other neutral species, such as pions and photons, their momentum is reconstructed from that of their charged daughters, looking for associated showers in the GRAIN or electron pairs in the STT. Given the complexity of neutrino interactions, the reconstruction performance of the neutrino energy was studied, considering exclusive channels based on the selection of specific final topologies. Selections based on the final topologies are common practice since the underlying interaction mechanisms are not accessible experimentally. For this particular study, muon neutrino interactions are divided as a function of pion ($\pi\pm$) multiplicity in the final state. Since there is no

DRAFT

particle identification, the selection is performed on the true Monte Carlo final state. Samples are built with a defined number of pions (0π, 1π, 2π, or $> 2\pi$), any number of protons (Np), and either zero or any number of neutrons (0n or Nn). It is common to set no conditions on the number of protons, as many of them can go undetected experimentally, so no meaningful selections are possible with the data. Similarly, samples in which neutrons are completely excluded are not realistic, as they would be hard to achieve experimentally and have been included only for comparison. The simplest sample is 0πNp0n, also known as ν_μ CCQE-like, in which the final state particles are a muon and one or more protons. In addition to this topological selection, only events in which the vertex was successfully reconstructed in the fiducial volume are considered for the computation of the neutrino energy.

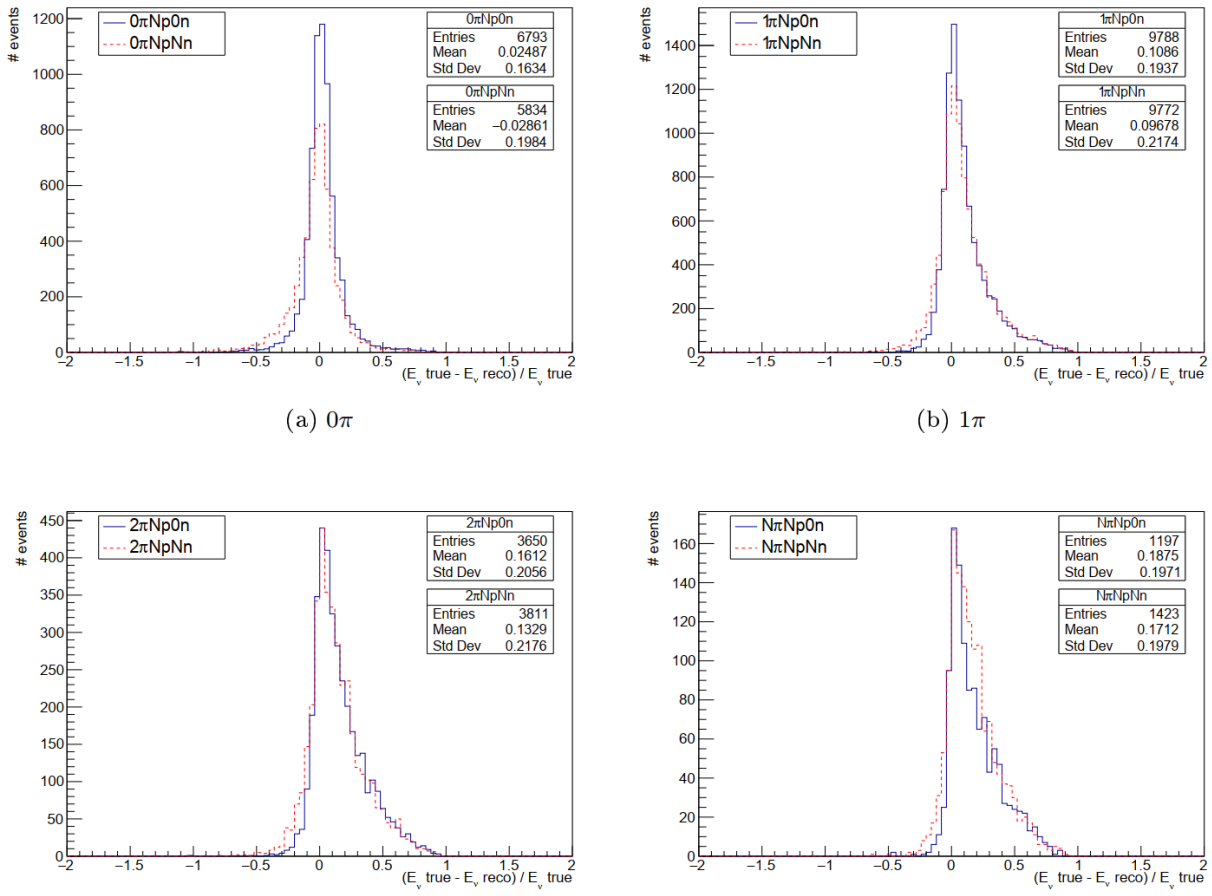


(a) E_ν^{reco} vs E_ν^{true} (b) $(E_\nu^{\text{reco}} - E_\nu^{\text{true}})/E_\nu^{\text{true}}$

Figure 5.36: Neutrino energy reconstruction for a sample of ν_μ 0πNp0n events in the fiducial volume of GRAIN for which the vertex reconstruction was successful. Comparison between true and reconstructed E_ν (a) and relative energy residual (b) for each event. The red dotted histogram in (b) shows the same quantity without GRAIN energy contribution.

The performance about the reconstructed neutrino energy for these events is reported in Figure 5.36, showing the comparison between true and reconstructed neutrino energy (on the left) and the relative energy residual distribution (on the right). It is worth noting that in this sample, most muons are forward-going, and their momentum is estimated via their curvature in the tracker. The other available species in this selection are protons, which are less likely to be reconstructed; however, the requirement of a reconstructed vertex further selects events in which at least one proton is detected either in GRAIN or STT. This reduces the statistics from the original sample but increases the quality of the energy reconstruction. In particular, it cuts out events in which energetic protons are detected only by the ECAL, which would bias the reconstruction. In the end, the overall energy residual achieved with the currently limited reconstruction is $\frac{\Delta E_\nu}{E_\nu} \simeq 2.5\%$. Figure 5.36 (b) also shows the effect of the energy contribution from GRAIN to the computation of the neutrino energy. For the same events, the red dotted histogram shows the relative energy residual when ignoring the correction given by the energy deposited in GRAIN. In that case, the bias increases, and an accumulation of events is also seen for $\frac{\Delta E_\nu}{E_\nu} \simeq 1$, which corresponds to events for which $Ereco_\nu \to 0$ since the energy of key particles that would have been reconstructed by GRAIN is missing.

The same plots with the neutrino energy relative residuals for samples with an increasing number



(a) 0π (b) 1π

(c) 2π (d) $> 2\pi$

Figure 5.37: Relative neutrino energy residuals for samples of muon neutrino interactions with 0π, 1π, 2π and $> 2\pi$ events (with or without neutrons) in the fiducial volume of GRAIN for which the vertex reconstruction is successful. For visually comparing topologies with and without neutrons, roughly the same event statistics are considered, despite topologies with neutrons being more common in a typical FHC sample.

of pions (0π, 1π, 2π, and $> 2\pi$) are shown in Figure 5.37. The solid blue line represents samples without neutrons in the final state (Np0n), while the red dotted line is used for samples that allow neutrons (NpNn). For better comparison of the two distributions in each plot, similar event statistics was selected despite events with neutrons being more common in a typical FHC sample (especially with increasing pion multiplicity). No increase in the bias is observed when comparing Np0n and NpNn samples in all cases, and the spreads of the distributions are similar.
This is a very important result, as it shows that SAND is able to constrain neutrons emerging from ν-Ar interactions well. This capability is mostly derived from having the LAr target enclosed inside a 4π ECAL and will be unique to SAND in the Near Detector. It is therefore a key contribution from GRAIN to ND physics, as ND-LAr will not be able to reconstruct or contain outgoing neutrons.

A complementary study was performed on events whose charged particles enter the downstream tracker and can be fully reconstructed, including their charge and momentum, thanks to the magnetic field. A sample of ν_μ CC interactions occurring inside the GRAIN volume was simulated with FLUKA and was used for such a study. Figure 5.38 shows the multiplicity distribution of charged tracks leaving LAr volume and crossing at least three STT layers in the case of ν_μ CC inside GRAIN. It is worth noting that, for the ν_μ flux foreseen by DUNE, in more than 80% of events, at most three charged primary particles generated in GRAIN are able to enter the tracker. Tracks in STT were reconstructed by the usage of the global transform method described in Section **??** , which works particularly well in the case of clean events with few tracks.

ref al primo capitolo

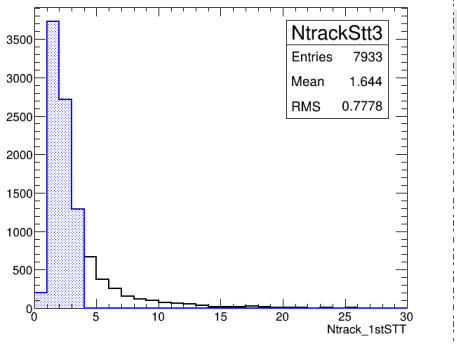


Figure 5.38: Multiplicity distribution of charged tracks entering STT from ν_μ CC interactions in GRAIN. For more than 80% of events, the track multiplicity is at most three (shaded area).

For the event sample of ν_μ CC interactions in GRAIN with at most three tracks reconstructed in the tracker, the corresponding particles can be identified with high efficiency from the curvature sign of the track fitting curves (muon: $\sim$ 100%, proton: $\sim$ 99%, pions: $\sim$ 98%). The value of the curvature in the bending plane, when coupled with the evaluation of the dip angle in the orthogonal view, allows for the estimation of particle momentum. Thus, the total energy of each particle when entering the tracker can finally be measured for such an event sample.

In order to obtain the total interacting neutrino energy, the contribution given by the energy deposited by all primary particles in the liquid argon in GRAIN must be taken into account. This contribution can be partially estimated from the path-length of each charged particle escaping GRAIN and originating a reconstructed track, from the vertex up to the tracker entry point. To this aim, the relation between path-length and energy loss in liquid argon by a minimum ionizing

particle (i.e., a muon or charged pion), as well as by a proton of energy in a proper range, can be used. A sample of simulated ν_μ CC interactions in GRAIN has been used for this purpose. Figure 5.39 (left plot) shows the distribution of the specific energy loss of the muons generated in such interactions, from the interaction vertices up to the entry points in the tracker (in this case, the MC information on the vertex and muon track is used). The right plot of the same figure also shows the specific energy loss for any charged particles produced in the ν_μ CC interactions and reaching the tracker for the event sample with a maximum of three reconstructed tracks.

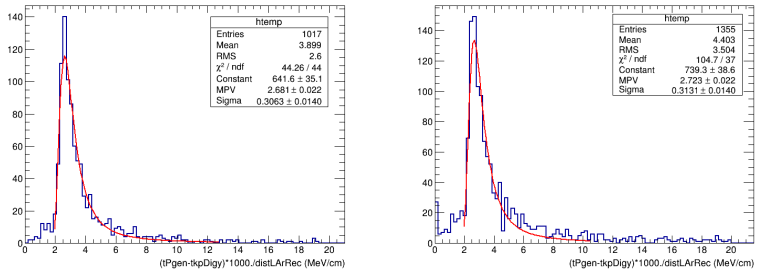


Figure 5.39: Left plot: specific energy loss of muons generated in ν_μ CC interactions in GRAIN, evaluated from the path-lengths between the interaction vertices up to the entering points in the tracker. Right plot: the analogous specific energy loss for any charged particles produced in the interactions and reaching the tracker, limited to the event sample with three reconstructed tracks at maximum. To be noted that the mechanical structure of GRAIN crossed by the particles before reaching the tracker also contributes to their energy losses.

In Figure 5.40 the event by event relation between path-length and energy loss is reported both for the muon (left plot) and any charged particle (right plot) originating a track, in the sample of ν_μ CC interaction events with at most three reconstructed tracks in the tracker. The scatter plots can be quite well fitted by a polynomial function, whose parameters are then used to infer the energy loss from the measured path-length based on the reconstructed track. In Figure 5.40, the parabolic fit for both scatter plots is included.

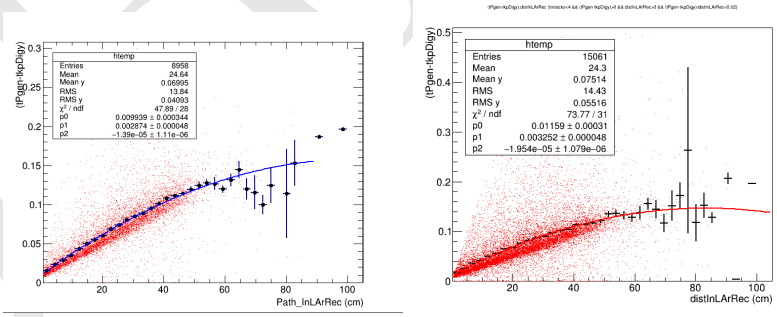


Figure 5.40: Event by event relation between path-length and energy loss in GRAIN for the muon (left plot) and any charged particle (right plot) produced in ν_μ CC interaction and originating a track, for the sample of events with at most three reconstructed tracks. The scatter plots are both fitted by a straight line.

The momentum of each charged particle entering the tracker is first reconstructed from the curvature radius of the fitted track. Then, by adding the track energy loss before entering the tracker, evaluated from the reconstructed path-length inside GRAIN, based on the Monte Carlo

parametrization described above, the initial particle momentum can be estimated. The results are reported in Figure 5.41 for both muon (left plot) and any charged particle (right plot) in the events of ν_μ CC interaction with at most three reconstructed tracks. Each plot shows the reconstructed momentum relative error distribution before (dashed histograms) and after the addition of the contribution (ΔE) of energy loss in GRAIN (solid histograms with the superimposed Gaussian function fit). The width, and in particular the peak offset of each distribution from zero, clearly decrease as a result of the ΔE addition.

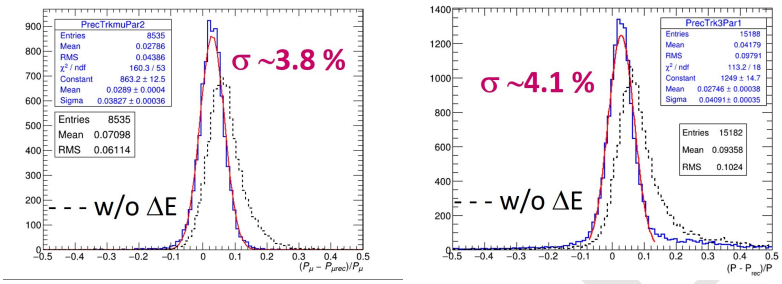


Figure 5.41: Relative error on the momentum reconstruction of the charged particles generated in GRAIN and entering the tracker. The error distribution based only on the reconstructed track in the tracker (dashed histograms) is compared with that corrected for the energy loss in GRAIN estimated from the path length on the basis of the Monte Carlo parametrization (solid histograms). In the latter case, the fit with a Gaussian function is also superimposed, which allows to estimate the resolution and the offset from zero.

For the considered sample of events from ν_μ CC interactions in GRAIN, producing at most three reconstructed tracks, the overall neutrino energy can be estimated. For this aim, two further contributions must be taken into account. The first one includes the possible clusters in the electromagnetic calorimeter ECAL not related to the reconstructed tracks (*off-track clusters*): these are usually due to primary neutrons that interact in ECAL. The other one refers to the energy deposited in the liquid argon by the interaction products, mainly near the ν_μ vertex, and not appearing outside as tracks detectable in the tracker or in ECAL. The latter contribution, which amounts to about 13% from MC simulation, can, in principle, be measured by the photo-detection system foreseen for GRAIN. Figure 5.42 shows the resolution on the estimate of the overall interaction neutrino energy from the reconstructed tracks, with the addition of the energy loss in GRAIN and the energy deposited in potential off-track clusters in ECAL (dashed histogram). It is evident that a large amount of energy is missing. The offset from zero strongly reduces, and the width of the error distribution significantly decreases when the fraction of energy released in GRAIN that does not escape has been added (solid histogram with the superimposed Gaussian fit).

5.9 Calibration System

A calibration system is generally required to convert detector device signals into physical quantities or properties related to the physical processes under study. For a neutrino interaction detector, this involves correlating the signals with the properties of particles produced in the interaction: track, charge, momentum, energy, time of flight (ToF), particle ID, and so on. A measurement of

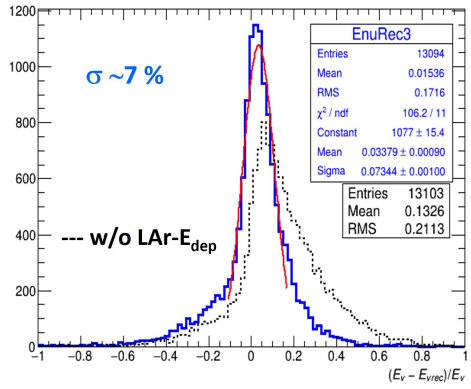


Figure 5.42: Relative error on the overall energy of a ν_μ interacting in GRAIN by CC and producing at most three charged particles detected in the tracker. From the reconstructed tracks with the addition of the energy loss in GRAIN and the energy deposited in possible off-track clusters in ECAL the dashed histogram is obtained. The width of the distribution and the peak offset from zero are strongly reduced when the fraction of energy deposited in GRAIN and not escaping it ($\sim 13\%$) is added (solid histogram with the superimposed Gaussian fit).

these properties is fundamental to reach the main target of GRAIN, which is to gather a complete description of the interacting neutrino features: energy, flavor, and interaction channel.

In the specific case of GRAIN, the detector devices are the SiPM matrices collecting the scintillation light photons in the entire sensitive LAr volume through lenses and/or coded masks. Thus, an effective calibration system for GRAIN must be able to:

- calibrate the position reconstruction algorithms for interaction vertices and particle tracks;
- synchronize the timing between the different cameras and between GRAIN and the other SAND subdetectors;
- perform energy calibration as a function of the tracks and vertex position in the volume.

Regarding the calibration of the position reconstruction, a set of artificial light sources will be placed inside the inner volume to facilitate the reconstruction of point-like sources at well known distances. Regarding the time synchronization between the cameras, this will be performed first by means of test signals sent by the DUNE Timing System and received by the different cameras and the various SAND subdetectors. Finally, an effective synchronization between GRAIN and the calorimeter will be performed by crossing muons.
Finally, for the energy calibration, precise requirements must be set for the equalization of all the SiPM inside GRAIN and for the dynamic range, which is the maximum number detectable by the electronics before saturation. In particular, all SiPMs will be selected with a very similar breakdown voltage in order to achieve global gain equalization, even if all channels are expected to operate at the same voltage. In addition, the calorimetric reconstruction of the deposited energy will be possible only if the dynamic range of the electronics readout does not affect the reconstructed number of photons. As shown in the inset of Figure 5.43, for neutrino interactions inside the GRAIN volume, a deposited energy of up to about 1 GeV is expected.

DRAFT

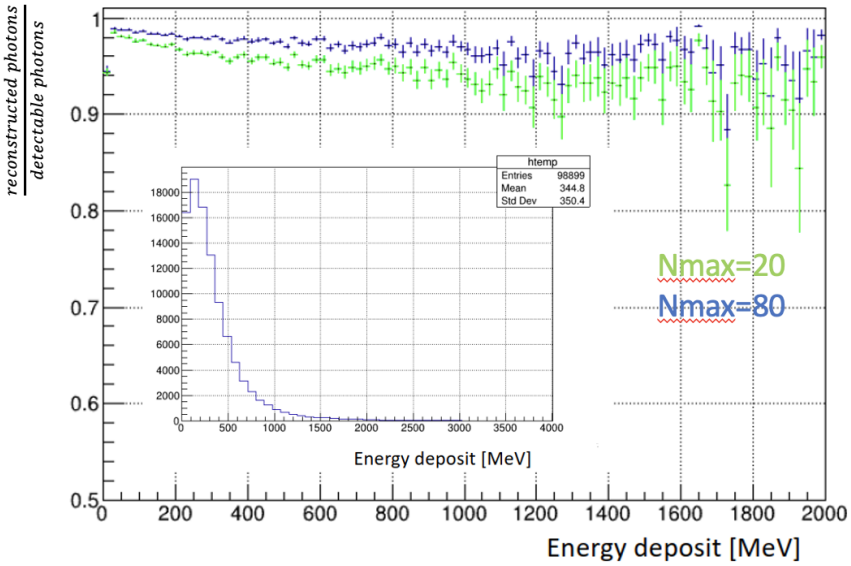


Figure 5.43: Ratio of the reconstructed number of photons over the detectable one as a function of the energy deposited in the LAr volume as resulted from simulating a dynamic range for electronics readout of 20 (in green) or 80 (in blue) for neutrino interactions with vertex in GRAIN.

In this range of values and with the lens-based optical readout, more than 96% of the photons can be counted if the dynamic range is higher than 80; for this reason, a value of 100 was requested for the ASIC design.

Thus, for the energy calibration of tracks in GRAIN, two possible approaches could be adopted:

- calorimetric measurement of the total released energy (which means extracting the whole energy released in GRAIN from the total number of collected photons by all SiPM matrices),
- track-by-track energy loss evaluation, which involves evaluating the associated amount of collected photons for each reconstructed track.

The two approaches are complementary; however, in either case, several factors must be taken into account, such as the relation between energy deposit and scintillation light emission, the photon absorption length, the geometrical acceptance of the photo-detection system, which depends on the vertex and track position inside the cryostat, and the SiPM photon detection efficiency.

Regarding photon detection efficiency, a proper calibration method will be developed to standardize the gain and the baseline of each SiPM among the different matrices, in such a way as to achieve a common $ADC - N_{PE}$ calibration curve.

Thus, several physics processes can be envisaged as useful "standard candle" processes to calibrate the energy deposit measurement in GRAIN, using experimentally collected events (both on prototypes and on the ν beam). Among them, there are:

- minimum ionizing particles (muons),

- natural or artificial radioactive sources,
- charged pions also detected in the tracker;
- other, less abundant sources (stopping muons, muon decay electrons, neutral pions, ...);

On the other hand, some ad-hoc light source devices, such as LEDs, could also be anticipated for calibration purposes.

Energy deposit evaluation with muons The easiest solution for GRAIN energy calibration is based on the energy deposit in LAr by a minimum ionizing particle (MIP), such as muons coming from beam interactions outside GRAIN (~ 1 per spill) and from cosmic rays ($\mathcal{O}(10)$ muons crossing GRAIN during a $\mathcal{O}(20)$ μs gate window).

Fix missing section references based on new organization.

As known, the specific energy loss of a MIP traveling through a generic material is roughly $\langle dE/dx \rangle \sim 2\,\mathrm{MeV}/(\mathrm{g\ cm^{-2}})$. For LAr, the expected value would be $\langle dE/dL \rangle \sim 2.5\,\mathrm{MeV/cm}$, which implies $\langle N_0 \rangle \sim 10^5$ photons/cm as the average number of scintillation photons per unit path-length (assuming a photon emission of $\sim 4 \times 10^4$ photons/MeV). This value was confirmed by MC simulations, where a sample of ν_μ CC interactions, both in ECAL and in the magnet yoke of SAND, was generated using GENIE, [43] and the events with a muon crossing GRAIN were selected. Figure 5.44 reports the specific energy loss dE/dL distribution (left) and the correlation between ΔL and ΔE_{loss} thus obtained (right).

Nevertheless, the specific energy loss can be precisely estimated for a particular material through MC simulations or experimental data. Thus, the relation between muon path-length and energy loss can be exploited to gain knowledge of the energy deposited in LAr, which in turn can be related to the amount of detected photons.

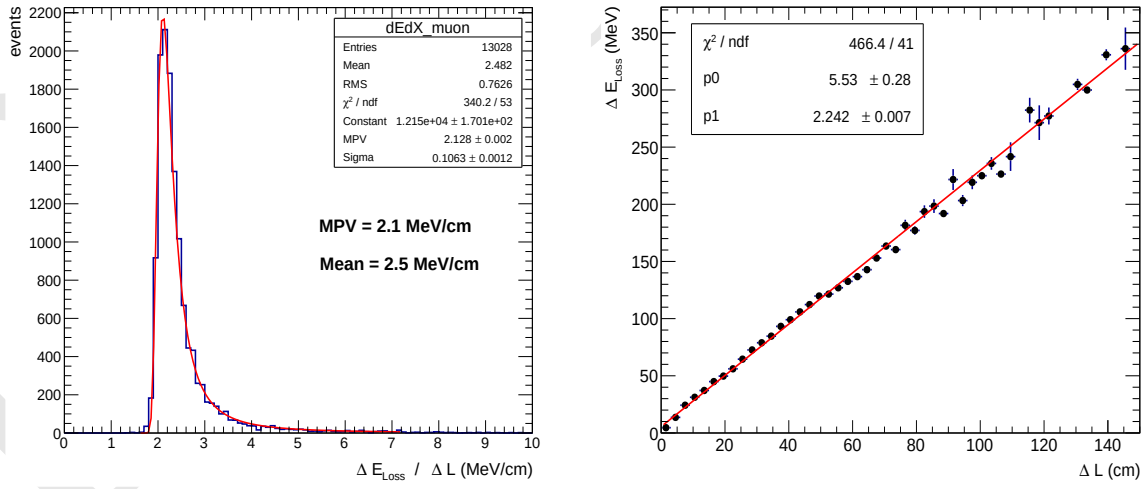


Figure 5.44: Specific energy loss with the superimposed fit by a Landau function (left plot) and correlation between ΔE_{loss} and ΔL (right plot) for the sample of muons generated in ν_μ CC interactions of the beam originating outside of and crossing GRAIN.

In order to test the entire calibration procedure and obtain a realistic calibration curve, the full geometry of the photo-detection system, the SiPM efficiency, and the readout electronics must be included in the simulation. A first test of this method was performed by considering the setup based on 53 lens-cameras, according to the configuration shown in Figure 5.14.

To obtain a first calibration curve relating the number of collected photons (N_{phot}) to the energy deposit (ΔE_{loss}) in LAr, it is convenient to start with well-known muons crossing a limited region of GRAIN. For this purpose, well-collimated 1 GeV muons were generated, impinging on different regions of the GRAIN volume at various angles. A focused muon beam was generated along the Z-axis, with the impact point $(X, Y, Z) = (0, 0, -250\,\text{mm})$ in the reference frame, whose origin is in the center of GRAIN, and the Z-axis is parallel to the minor axis of each elliptical surface (Figure 5.14). This MC muon beam is shown in the left plot of Figure 5.45: the aperture of muon tracks with respect to the Z-axis is due to the multiple scattering experienced by muons along the path length in LAr. The right plot in the same figure reports the distribution of the total energy deposit by beam muons at the end of the path length. Peak and average values are in line with expectations according to the specific energy loss in LAr (Figure 5.44).

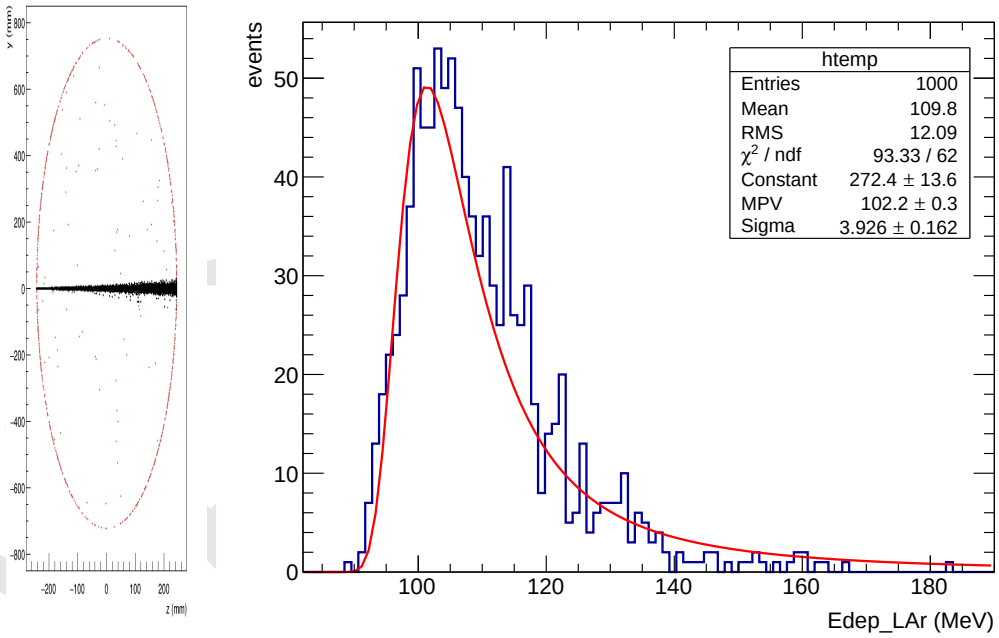


Figure 5.45: Left. MC simulated muon beam (B1) crossing GRAIN through the center along the Z-axis used for testing the calibration procedure. The aperture of muon tracks around the Z-axis is due to the multiple scattering suffered by muons along the path-length in LAr. Right. Distribution of total energy deposit by the beam muons along their path-length in LAr. The fit by a Landau function is superimposed.

Figure 5.46 reports the relation between the energy deposited by the beam muons and the number of photons collected by the entire photo-sensor system (left plot). It can thus be considered the calibration curve for the response of the photo-sensor system to an energy deposit in the central region of GRAIN. The distribution of the number of collected photons per MeV, which accounts for the spread of that correlation ($\sim 3\%$), is shown in the right plot of the same figure.

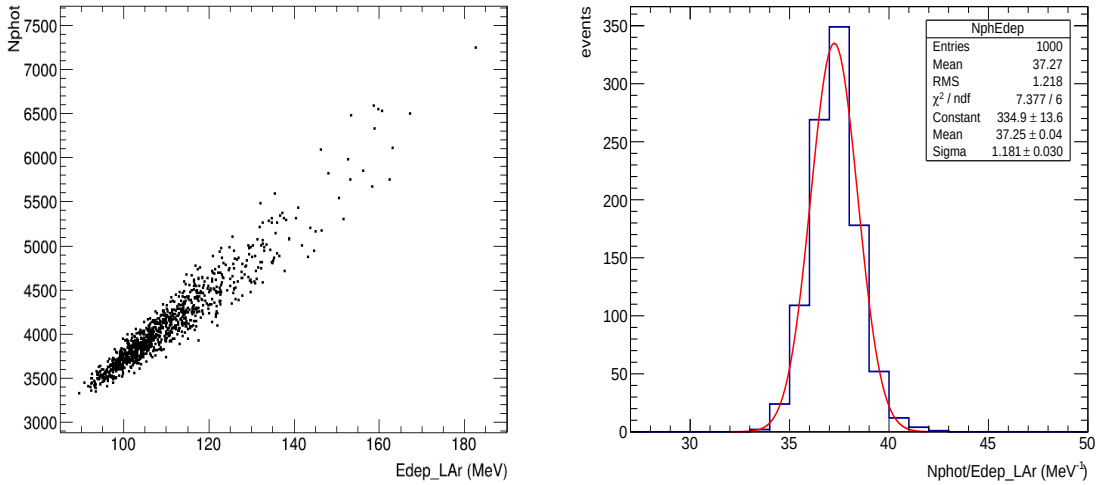


Figure 5.46: Left. Correlation between the muon energy deposit and the amount of photons collected by the lens-based setup of 53 cameras. Right. Ratio between the number of photons and the energy deposit. The parameters from the Gaussian fit provide the mean value and standard deviation of the distribution.

From the right plot in Figure 5.46, it is evident that the mean number of collected photons resulting from an energy deposit of approximately 100 MeV is very low ($\sim 1/10^3$ of the total emitted photons). Consequently, a large variability in the calibration curves can be expected, depending on the geometrical acceptance of the photo-sensor setup. This is particularly true in the case of the lens-based system, where the camera arrangement exhibits a top/bottom asymmetry. This is, in fact, the possible cause of what is observed as a result of a muon beam that crosses the GRAIN volume, always parallel to the Z-axis but at a distance of 300 mm from the center on the Y-axis, towards the top side. This outcome is illustrated in Figure 5.47 and 5.48. It can be observed that, in this case, despite the lower total energy deposit in liquid argon, the mean number of collected photons is higher than in the case of a beam passing through the center of GRAIN, as a consequence of a larger acceptance by the nearer and more numerous top cameras.

As a conclusion from these preliminary outcomes, it is clear that if a clean sample of well-aligned muons crossing GRAIN is selected from the data, a muon based calibration procedure is, in principle, possible. In addition, a detailed calibration procedure tuned with MC simulations can be useful in obtaining a proper calibration function for a set of volumes inside GRAIN and for various topologies. On the other hand, for reliable energy calibration, the vertex position and the event topology (number of tracks and their positions and directions inside the detector) are fundamental for correctly estimating the deposited energy from the total number of collected photons by all cameras.

For the above reasons, a variety of additional mono-energetic muon beams crossing the liquid argon volume were simulated, with several orientations and different impact points on the upstream X-Y surface of GRAIN. Figure 5.49 and Figure 5.50 show two other examples of such simulated 1 GeV energy muon beams. In the first instance, the muon beam, lying in the Y-Z plane, impacts at $Y = -250$ mm on the GRAIN front surface with an inclination such that the center of the LAr volume is crossed (red beam). In the figure, it is shown superimposed on the black muon beam

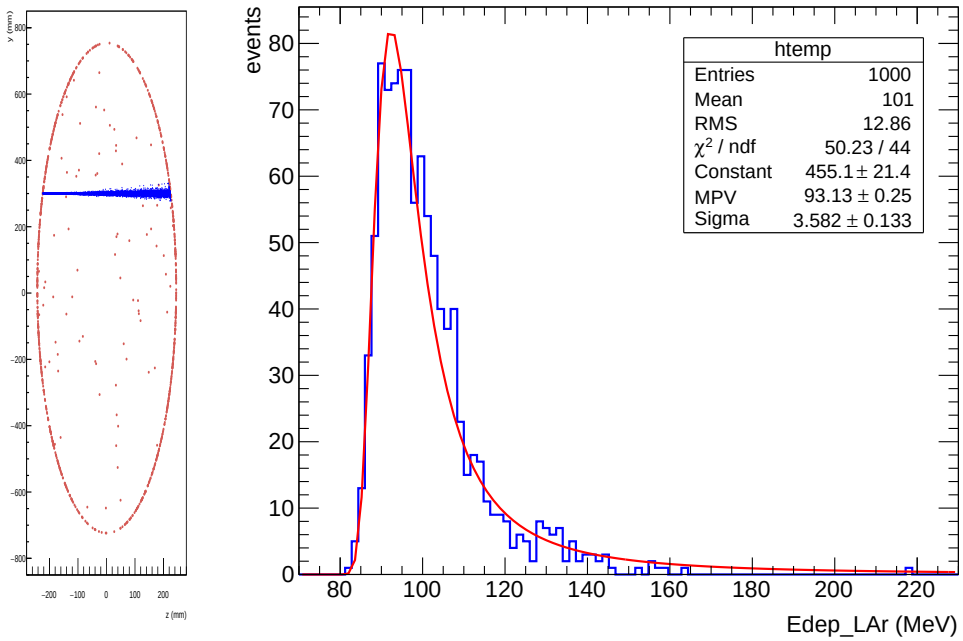


Figure 5.47: Left: MC simulated muon beam crossing GRAIN along a direction parallel to the Z-axis at a distance of 300 mm from the center on the Y-axis. Right: Total energy deposit by the muons shown in the left plot, along their path in LAr. The fit by a Landau function is superimposed.

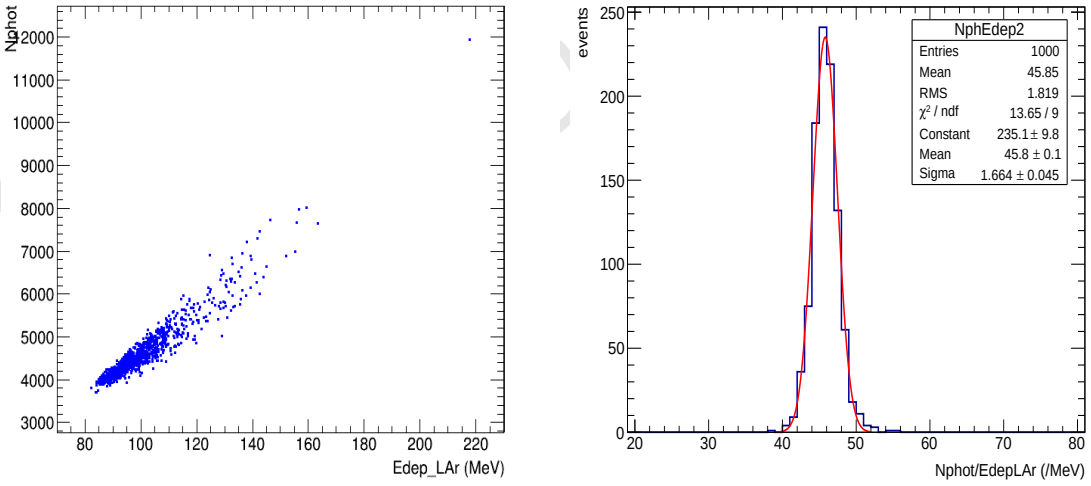


Figure 5.48: Left: Correlation between the energy deposit of the muons in the beam and the amount of photons collected by the lens-based setup of 53 cameras. Right: Ratio between the number of photons and the energy deposit. The Gaussian fit provides the mean value and standard deviation of the distribution.

that was sketched in Figure 5.45.

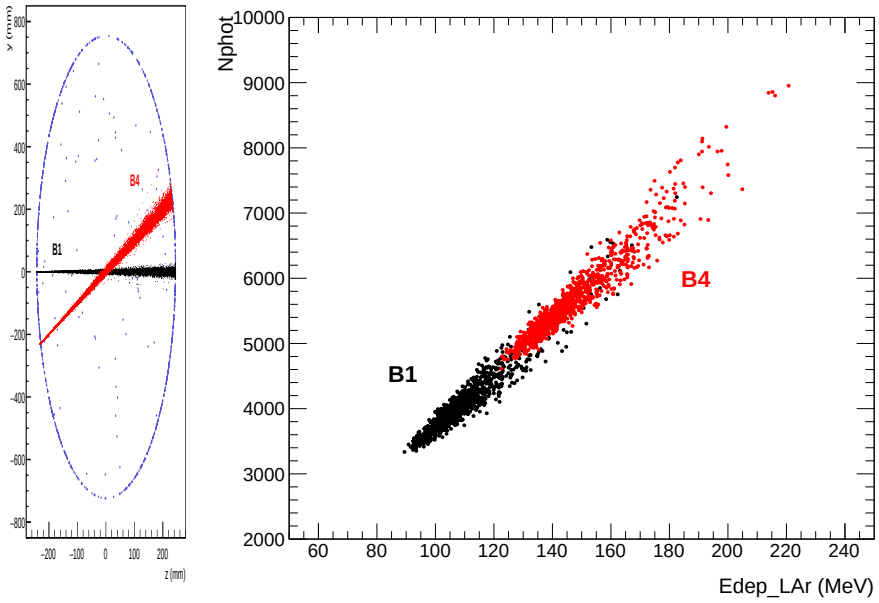


Figure 5.49: Left. MC simulated muon beam (B4, red beam) lying on the Y-Z plane and impacting at $Y = -250$ mm on the GRAIN front surface, with an inclination in such a way to cross GRAIN through the volume center. The superimposed horizontal muon beam (B1, black beam) previously illustrated in Figure 5.45 is also shown. Right. Scatter plot describing the correlation between the muon energy deposit and the amount of photons collected by the lens-based setup of 53 cameras for the two beams shown in the left panel.

The second example includes two other muon beams crossing GRAIN. The first one is parallel to the Z axis, while the second one is inclined in such a way as to intersect the other beam at $X = 0$, $Y = -250$ mm, and $Z = 0$. In the right panels of the same figures, the scatter plots report the amount of photons collected by the 53 cameras of the considered optical setup versus the energy deposited in LAr for the muon beams just described (sketched in the respective left panels). The correlations arising from those scatter plots clearly indicate that the ratio between the collected scintillation photons and the deposited energy, as a first approximation, only depends on the average position of the tracks with respect to the center of GRAIN and not on their directions. As a consequence, this result suggests that, once the ratio $Edep/Nphot$ is taken as a calibration constant, the knowledge of that ratio as a function of the location where the energy deposit occurred in LAr should allow obtaining a complete detector calibration.

With this purpose, two samples of simulated events of neutrino interactions occurring in the SAND magnet yoke or in the calorimeter ECAL, thus externally to GRAIN, were generated using the designed DUNE ν_μ beam and the GENIE code. Out of such samples, the events with an isolated muon going through the GRAIN volume were selected. The MC simulations indicate that, on average, one isolated muon every two beam spills (which means a rate of ~ 0.5 Hz) is expected to cross GRAIN coming from this kind of events. Such a rate could be enough to ensure sufficient muon statistics for the calibration procedure. The left panel of Figure 5.51 shows the Y-Z distribution of ν_μ interaction vertex positions for those events inside the magnet yoke, together

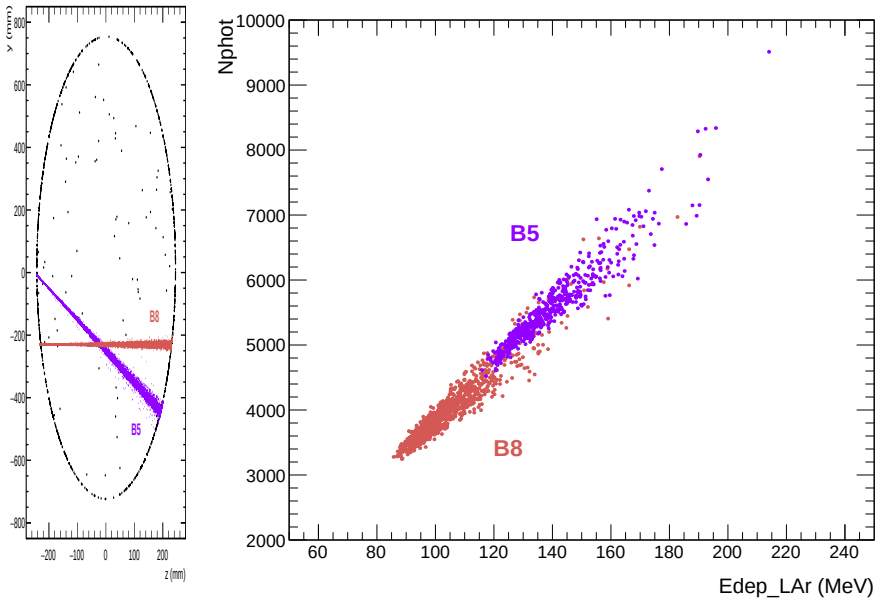


Figure 5.50: Left. MC simulated muon beams both lying on the Y-Z plane. The first one (B8, brown beam) is parallel to the Z axis, the second one (B5, violet beam) is inclined in such a way to intersect the other beam at $X = 0$, $Y = -250$ mm, and $Z = 0$. Right. Scatter plot describing the correlation between the muon energy deposit and the amount of photons collected by the lens-based setup of 53 cameras for the two beams shown in the left panel.

with the entering points of the corresponding muons in GRAIN.

The analogous points in the Y-Z view are shown in the right panel of Figure 5.51 for the case of neutrino interactions in the entire ECAL volume, including the two end-caps.

The muons of the first sample ("yoke muons") were then used to determine the calibration function. To this end, the X-Y surface of GRAIN from -50 cm to 50 cm for both coordinates has been subdivided into a grid of 100 cells, each with dimensions 10 cm $\times$ 10 cm. Thereafter, the distribution of the ratio, $Edep/Nphot$, between the deposited energy in GRAIN and the number of collected photons for the muons crossing each cell, based on the path-length average position, has been considered and fitted with a Gaussian function. The mean value from the Gaussian fit was finally taken as the calibration function value at the central position of the respective cell. The grid of mean values thus obtained could be fitted by a quadratic function of the X and Y coordinates like the following: $F_{cal} = a\ x^2 + b\ y^2 + c\ x\ y + d\ x + e\ y + f$. Despite the limited statistics available here (about 13×10^3 surviving events in total), the fit converged to the function represented in Figure 5.52, where the fit coefficients are also reported.

In order to complete the calibration procedure test, the calibration function $F_{cal}(x, y)$ has also been applied to an independent sample of events, namely the "ECAL muons" (i.e., the isolated muons coming from the beam neutrino interactions in ECAL and going through GRAIN). The left plot of Figure 5.53 shows the distribution of energy loss of such muons in the LAr volume. After evaluating the average (x,y) position of each muon track in the GRAIN volume, the muon energy

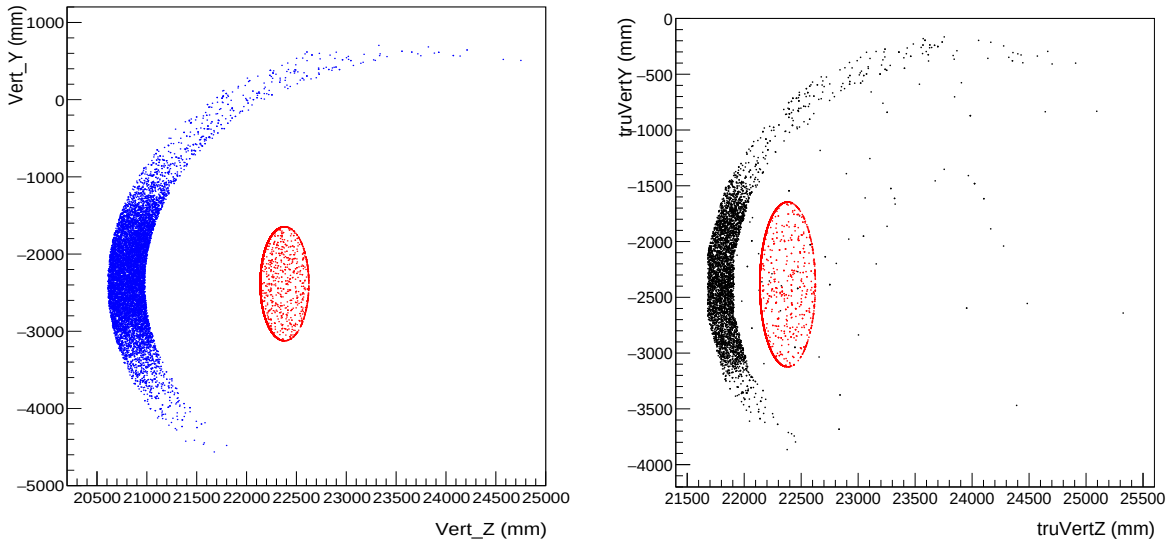


Figure 5.51: Left. Y-Z view scatter plot of the ν_μ-CC interaction vertex positions (blue dots) in the magnet yoke for the events with the muon crossing GRAIN. The entering points of the muons in the GRAIN volume can also be seen (red dots). Right. The analogous points of interaction vertices (black dots) and muons (red dots) entering GRAIN volume in the Y-Z view for the case of neutrino interactions in the whole ECAL volume, including the two end-caps.

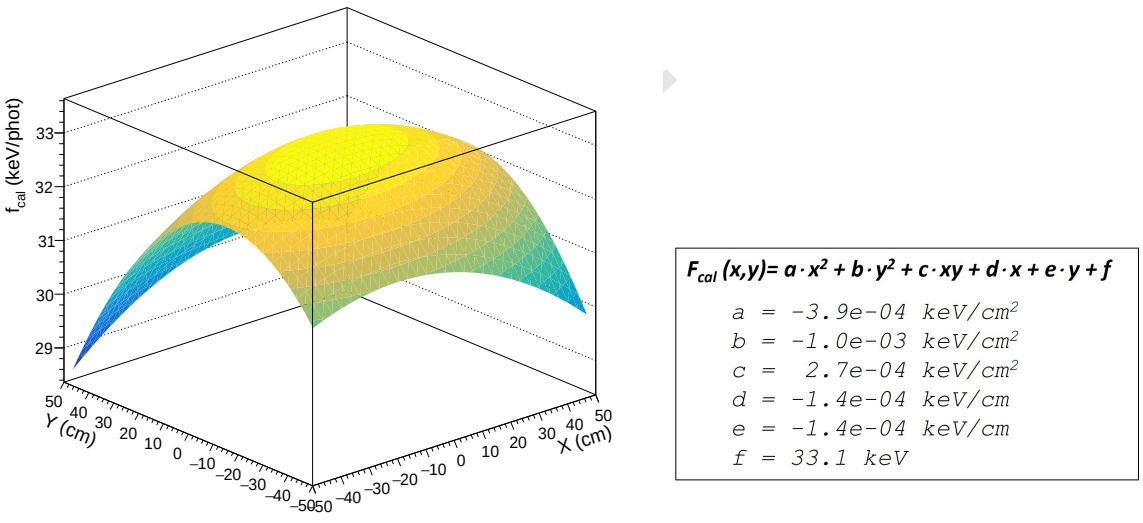


Figure 5.52: Calibration function obtained by fitting the mean values of the $Edep/Nphot$ ratios in the GRAIN volume with the most general quadratic function of X and Y coordinates. Each mean value is the result of the Gaussian fit of the $Edep/Nphot$ ratio distribution in each of the 100 cells of a grid on the whole X-Y GRAIN surface. On the right, the values of the function coefficients, as they result from the fit, are reported.

deposit is estimated from the amount of collected photons by applying the calibration function $F_{cal}(x, y)$. In the right plot of Figure 5.53, the relative difference between the reconstructed and true energy deposits is reported for such a muon sample. It can be seen that the relative difference distribution is peaked at ~ 0, while its standard deviation is $\sigma = 4.5\%$.

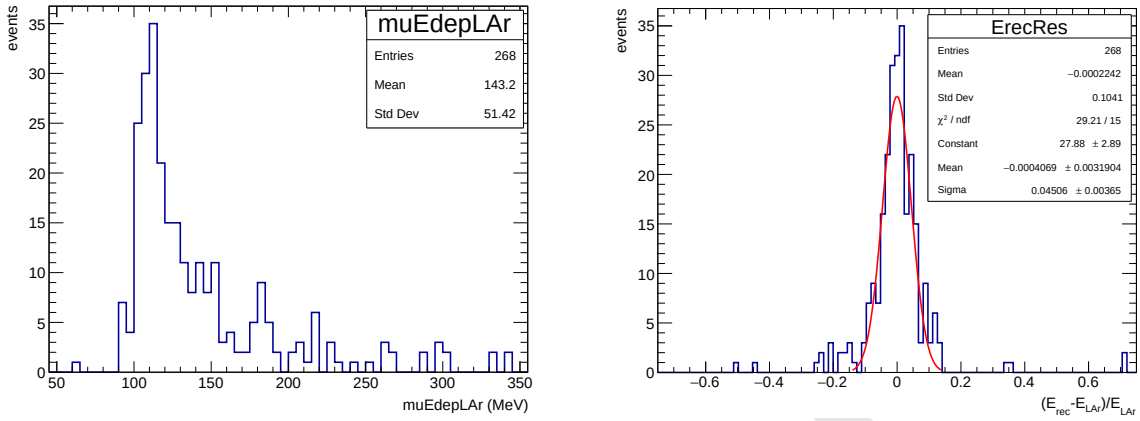


Figure 5.53: Left panel. Distribution of energy deposited in liquid argon by "ECAL muons" (i.e. muons produced in beam neutrino interactions in ECAL) crossing GRAIN volume. Right panel. Plot of relative difference between the muon energy deposit reconstructed through the calibration procedure described in the text and the true one.

Mandatory steps of the described calibration procedure are, of course, the selection of the isolated muons crossing GRAIN, produced by external neutrino interactions, and the precise evaluation of their path-length and average position inside the liquid argon volume. Both of those requirements can be achieved by exploiting the information provided also by ECAL and the tracker.

probabilm manca una parte conclu- siva..ma verrà scritta dopo la revisione se richiesta LDN

DRAFT

Chapter 6

Straw Tube Tracker

6.1 A Compact Modular Design

The Straw Tube Tracker (STT) is designed to offer control over the configuration, chemical composition, and mass of the neutrino targets, similar to electron scattering experiments [48], by physically separating the neutrino targets from the actual tracking system of negligible mass. A large number (70-100) of thin planes – each typically 1-2% of radiation length X_0 – of various passive materials with high chemical purity and comparable thickness are alternated and dispersed throughout active layers – made of four straw planes – of negligible mass in order to guarantee the same acceptance for final-state particles produced in (anti)neutrino interactions (Section 6.18.1). The STT allows minimizing the thickness of individual active layers and approximating the ideal case of a pure target detector – the targets constitute about 97% of the mass – while keeping the total thickness of the stack comparable to one radiation length. Each target plane can be removed or replaced with different materials during data taking, providing a flexible target configuration.

The average density (and sensitive mass) of the STT can be fine-tuned from $0.005\,\mathrm{g/cm^3}$ when no targets are present, up to a maximal value of about $0.17\,\mathrm{g/cm^3}$ with targets. A broad range of target materials can be installed, provided they can be manufactured in the form of thin planes. Physics measurements are obtained effectively by averaging over the many alternating targets, each of which is individually transparent to final state particles (1-2% X_0), making them relatively insensitive to construction tolerances. Every target element must be weighed before installation in order to control the total target mass with high accuracy. The single hit space resolution for the straws is required to be $< 200\,\mu\mathrm{m}$. Particle identification is available throughout the STT volume by exploiting the ionization signals dE/dx from charged particles, the transition radiation from high energy electrons, momentum-range relations, and time of flight. The momentum scale of charged tracks can be calibrated to better than 0.2% in STT using a constraint from the invariant mass of the reconstructed $K^0 \to \pi^+\pi^-$ decays (Section 6.17.2).

The low average density $\rho \leq 0.17\,\mathrm{g/cm^3}$ and the overall dimensions, which are comparable to one radiation length, allow for an accurate reconstruction of the four-momenta of the visible final state particles, as well as the event kinematics in a plane transverse to the beam direction. The

DRAFT

lightness of the tracking straws and the chemical purity of the targets, together with the physical spacing among the individual target planes, make vertex resolution less critical in associating the interactions with the correct target material. For events with a single reconstructed charged track, the corresponding uncertainty is given by the ratio between the thickness of the straw walls ($< 20\,\mu$m) and that of a single target layer, which is typically below 0.5%. For events with at least two reconstructed charged tracks, this uncertainty is reduced to less than 0.1%, thanks to a vertex resolution ($\ll 1$ mm [49]) that is much smaller than the target thickness.

6.2 Nuclear and "Solid" Hydrogen Targets

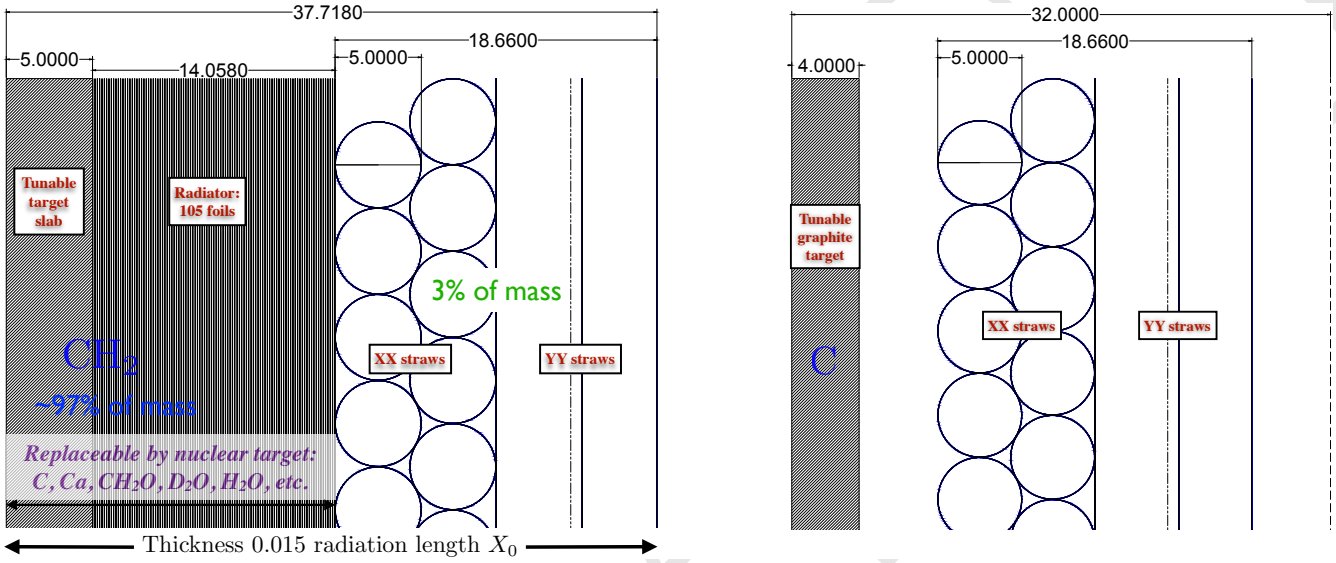


Figure 6.1: Left: Drawing of a STT module including three main elements (left to right): (a) a tunable plastic CH_2 target; (b) a radiator with 105 polypropylene foils for $e^{\pm}$ particle ID (PID); (c) four straw layers XXYY. Right: Drawing of a STT module equipped with a graphite (pure C) target. The thickness of the graphite plate is tuned to provide the same fraction of X_0 as the CH_2 modules. The space introduced by the C-composite frame is also shown. The pure tracking modules are identical but with the C target removed, for a total thickness of 28 mm.

The control of the neutrino targets provided by STT allows the implementation of a "solid" hydrogen (H) target by subtracting measurements on dedicated graphite (pure C) targets from those on polyethylene/polypropylene (hereafter labeled by their common brute formula CH_2) targets [48,50]. The high resolution of STT allows for the selection of the charged current (CC) interactions on hydrogen within the CH_2 targets before subtraction, using a kinematic analysis based on energy-momentum conservation. This approach achieves purities of the selected H samples in the range of 80-95%, depending on the specific process considered [17,18]. This technique can be applied to all available exclusive and inclusive topologies in both neutrino and antineutrino CC interactions on H. Modules equipped with graphite plates are interleaved with CH_2 modules throughout the STT volume in order to guarantee the same detector acceptance for CH_2 and C targets (Section 6.18.1). The graphite targets are an essential element of the "solid" hydrogen concept: they automatically provide all types of interactions, as well as reconstruction effects relevant to achieving a model-independent subtraction of the small residual C background in selecting the $\nu(\bar{\nu})$-H interactions.

The most basic element of STT is a planar tracking module consisting of two straw double layers along orthogonal directions (XXYY). As shown in Figure 6.1, all STT modules share a common tracking module, which has a total thickness of 28 mm, including the support frame (Section 6.5.1). Most of the modules are equipped with a combination of CH_2 targets and a radiator mounted in front of a XXYY tracking section. The design of one default STT module consists of three main elements:

- Four layers of low-mass straws arranged in XXYY orthogonal planes, with 5 mm diameter, 19 μm walls, 20 μm gold-plated tungsten-rhenium (3%) wire, operated with a Xe/CO_2 70/30 gas mixture at 2 bar absolute pressure.
- The straws are preceded by a radiator composed of 105 polypropylene CH_2 foils 18 μm thick, inter-spaced by 117 μm air gaps. The configuration of the radiator is optimized for the e/π separation (Section 6.18.4) using Transition Radiation (TR). The total thickness of CH_2 in a single radiator is 1.89 mm.
- A high-density polyethylene CH_2 target (HDPE) slab is placed in front of the radiator. The thickness of this slab, 5 mm, can be tuned in order to achieve the desired target mass and detector density.

In some modules, the CH_2 target and radiator are replaced by a 4 mm graphite target (Figure 6.1). The thickness of the graphite plates is tuned to match the same fraction of radiation length as the combined CH_2 material (6.89 mm) of the target and radiator present in the other STT modules, as discussed in Section 6.18.1. Both the modules equipped with a graphite target and the ones without a target (tracking modules) are operated with an Ar/CO_2 70/30 gas mixture at 2 bar absolute pressure.

6.3 Detector Requirements

The main design parameters of the detector can be directly derived from two key requirements for the integrated target/tracker system (Section 6.1):

- Distributed target mass concept with overall dimensions comparable to one radiation length;
- Multiple passive target layers individually removable and transparent to final state particles.

The STT design is heavily constrained (Table 6.1) by the need to be inserted into the limited space of the existing KLOE magnet. The total magnetized volume available is only 35.7 m^3, with a maximum detector thickness of about 3 m, excluding the upstream space to be equipped with the active liquid Ar target, GRanular Argon for Interactions of Neutrinos (GRAIN). Taking into account the need to install the passive targets within a restricted fiducial volume for physics studies – defined by a typical distance of 20 cm from the surface of the surrounding 4π calorimeter – the average radiation length X_0 must then be $\geq$ 2.8 m. The main target materials required for the "solid" hydrogen technique are CH_2 plastic and graphite, with the latter in a relative proportion of 0.12–0.25 with respect to the former [17]. The corresponding requirement on the radiation length then translates into a maximal average density of $\leq 0.17\,g/cm^3$ within a fiducial volume of about 26.7 m^3, for a maximal fiducial mass of about 4.5 t (Table 6.1). The possibility of running with a reduced density (i.e., number of targets) must also be taken into account by the detector design.

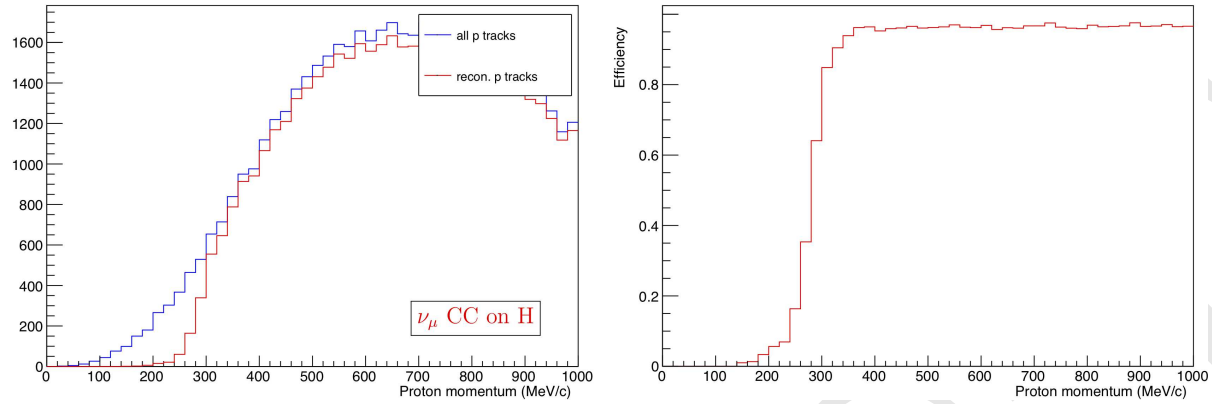


Figure 6.2: Acceptance for protons from ν_μ CC interactions on H obtained with a thickness of the individual passive targets around 0.015 X_0.

Target and module thickness The passive targets must have comparable thicknesses in terms of radiation length, regardless of their material composition. The thickness of individual targets is constrained by the need to guaranty a large acceptance for final state particles produced in (anti)neutrino interactions, most notably for those on the H target. To this end, protons are the most critical particles due to their large energy loss combined with relatively small momentum. In order to obtain the minimal number of hits (≥ 4) required for track reconstruction (Section 6.18.1), a particle typically has to cross at least two consecutive detector modules with the corresponding passive targets. This requirement effectively determines a threshold for proton reconstruction, depending on the thickness of the individual targets. Full detector simulations with the GEometry ANd Tracking (Geant4) package indicate that a target thickness of about 0.015 X_0 allows for maintaining an average acceptance $> 95\%$ for protons produced in interactions on H (Figure 6.2). From the total length of the fiducial volume and the thickness of the individual targets, the maximum thickness allowed for each STT module can be directly derived, which must be less than 4 cm, including any dead space (Table 6.1).

Momentum resolution and scale uncertainty The active tracking modules must be based on thin gaseous detectors to minimize their mass compared to the passive targets with which they are interleaved. The nominal magnetic field value $B = 0.6\,\mathrm{T}$ for the KLOE magnet defines an upper limit on the required momentum resolution $< 5\%$ (Table 6.1) for a track length $L = 1\,\mathrm{m}$ from multiple scattering (MS), given the maximum average density. The track sampling is determined by the maximal thickness of the STT modules, with at least two points per module required in the YZ bending plane perpendicular to the magnetic field direction. A conservative single hit resolution $< 200\,\mu\mathrm{m}$ at atmospheric pressure (Table 6.1) is required for the tracking modules. This value guaranties that the measurement contribution to the momentum resolution is comfortably below the MS one over the entire range of available momenta exceeding $10\,\mathrm{GeV/c}$ for $L \sim 1\,\mathrm{m}$ at the maximal density of $0.17\,\mathrm{g/cm^3}$. The corresponding contribution to the momentum resolution, with all targets removed, is only 0.4% (0.3%) for $p = 1\,\mathrm{GeV}/c$ and $L = 1\,\mathrm{m}$ at 1(2) bar absolute pressure, providing enough flexibility for the target configuration. The single hit resolution also affects the reconstruction of the primary vertex, which must be located with an accuracy much better than the target thickness, $\ll 1\,\mathrm{mm}$, in all coordinates. The uncertainty in the determination of the overall momentum scale is expected to be one of the leading uncertainties in the determination of the (anti)neutrino fluxes using exclusive processes on H [18], which requires an accuracy better

Table 6.1: Summary of the main requirements for the design of the STT.

Item description	Requirement	Comment
Average radiation length X_0	≥ 2.8 m	Comparable to total thickness of FV
Average density ρ	$\leq 0.17\,\mathrm{g/cm^3}$	From minimal radiation length
Maximal fiducial mass m_{FV}	$\lesssim 4.5$ t	From FV of 26.7 $\mathrm{m^3}$ and average density
Thickness of individual targets	$\sim 0.015 X_0$	For $> 95\%$ acceptance of p from H
Thickness of individual modules	< 4 cm	From FV length and target thickness
Momentum resolution	$< 5\%$	From MS with $B = 0.6$ T & $L = 1$ m
Single hit resolution	$< 200\,\mu$m at 1 bar	Value at 2 bar scaled by $1/\sqrt{2}$
Momentum scale uncertainty	$\Delta p/p < 0.2\%$	Relative flux and E_ν scale
Particle identification (PID)	TR, dE/dx charge	ν_e, $\bar{\nu}_e$ CC (TR) and p/π/K (dE/dx)
Readout dynamic range	$\sim 10^3$	Charge measurement for PID (p,$e^{\pm}$)
Straw geometry	XXYY	L-R ambiguities, X-Y symmetry
Straw diameter	5 mm	Module thickness & large angle tracks
Straw wall thickness	$< 20\,\mu$m	Vertex location for single tracks $< 0.5\%$
Tracking fiducial mass	$< 5\%$ of $\mathrm{m_{FV}}$	Small compared with target mass
Operating gas pressure	2 bar absolute	Mechanical design & performance
Wire centering	$< 100\,\mu$m	Guaranteed by self-centering design
Assembly tolerances	$\sim 100\,\mu$m	Not critical with wire self-centering
Ar leak rate per module	$< 4 \times 10^{-4}$ liter/min	Operation with Xe/$\mathrm{CO_2}$ at 2 bar
Maximal power dissipation	< 15 mW/channel	Total dissipation of integrated readout
Nominal gas flow rate	5 nliter/min/module	Self-cooling design

DRAFT

than 0.2%. The same quantity is also relevant for the calibration of the absolute (anti)neutrino energy scale E_ν from the measured interactions.

Particle identification One of the main physics goals for SAND is to measure the ν_μ, $\bar{\nu}_\mu$, ν_e, and $\bar{\nu}_e$ fluxes as a function of energy. It must also measure various exclusive channels in both CC and NC interactions on different nuclear targets. Both goals require excellent capabilities for particle identification integrated throughout the entire volume of the tracking detector (Section 6.18.4). The selection of ν_e and $\bar{\nu}_e$ CC interactions is particularly challenging, as they represent only tiny fractions of the beam composition, with the latter corresponding to about 0.2% of the leading ν_μ CC component in the forward horn current (ν_μ mode) (FHC) beam. The presence of multiple pions in both CC and NC interactions demands electron identification, providing an overall e/π rejection in excess of 10^3. The 4π ECAL surrounding the tracker cannot deliver such separation alone. Detailed detector simulations with the Geant4 package have shown that the ECAL can, at most, provide a residual pion contamination of 5-8% for an electron efficiency of around 90%, due to a combination of various effects, such as relatively low energies, Bremsstrahlung emissions, overlapping clusters, and pile-up effects. Considering that most of the primary $e^\pm$ produced in ν_e and $\bar{\nu}_e$ CC (about 93-98%) are characterized by energies above 0.5 GeV ($\gamma \geq 1000$), the possibility of exploiting the Transition Radiation (TR) would be necessary (Table 6.1) to deliver the required additional rejection factor in the range $100 \div 1,000$ (Figure 6.3). The TR capability proved to be essential in the analysis of NOMAD data [51, 52], in spite of the much less demanding statistics. It is worth noting that some of the most critical measurements expected from SAND are characterized by the presence of $e^\pm$, such as ν_e, $\bar{\nu}_e$ CC, ν-e elastic scattering, NC π^0, etc. In addition to the electrons, the tracker must also be capable of identifying $p/\pi/K$ hadrons for the measurement of exclusive channels required for both the flux measurements and the study of (anti)neutrino interactions on nuclear and hydrogen targets. This task can be achieved by exploiting the energy deposited within the gas by the ionization (dE/dx) of charged particles (Table 6.1). Both the TR and dE/dx measurements share the need to measure the total charge deposited, in addition to the drift time. To this end, a dynamic range of about 10^3 is needed from the electronic readout to cover energy depositions from minimum-ionizing particles to protons and $e^\pm$, taking into account the broad energy and angular spectra expected.

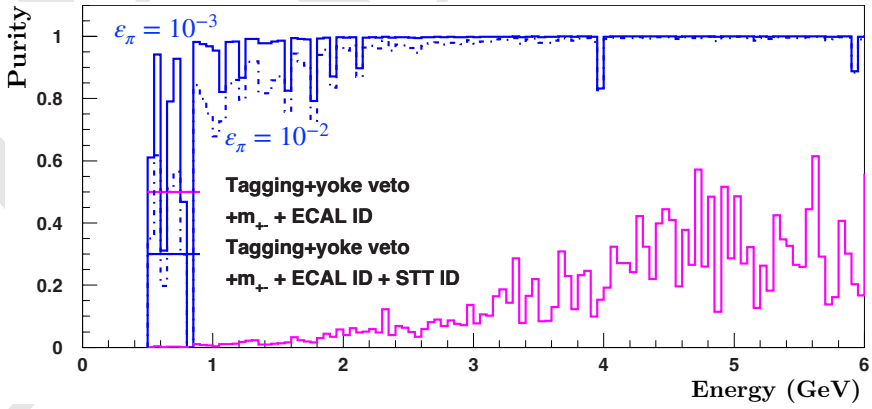


Figure 6.3: Effect of the electron identification in STT on the selection of $\bar{\nu}_e$ CC interactions in the FHC beam. Additional background rejection from the muon tagging and veto, and from the electron identification in ECAL are included for comparison.

Self-supporting tracking modules with ultra-thin straws The possibility of replacing individual targets during data taking is essential for fulfilling the broad physics program of precision measurements and searches for new physics. Furthermore, the passive target layers must be characterized by high chemical purity and well-controlled mass. These requirements demand that the individual tracking modules be self-supporting and decoupled from the target planes, which therefore cannot play any significant role in the mechanical construction. Given the limited total thickness allowed for the STT modules, the construction of planar tracking modules that satisfy such criteria and have transverse dimensions of up to about 4 m is challenging. Ultra-thin straw tubes provide an excellent solution to this problem, minimizing the mass of the active layers and allowing the construction of self-supporting modules with a relatively simple mechanical structure by exploiting operation with internal overpressure. Straw tubes are also widely used for TR detection, which is necessary to achieve the required electron identification capability, as discussed above.

Straw geometry and configuration The straws are arranged in double layers, with the centers staggered by half of the diameter. This geometry allows for the resolution of left-right ambiguities around the wires within each double layer. The staggered layers also provide an effective averaging of the resolution and efficiency as a function of the radius within the straws, since for tracks perpendicular to the straws, the sum of the drift times in both layers is approximately constant. Taking into account that the entire tracker is designed to have dimensions comparable to the radiation length, and the large number of tracking modules, further averaging is obtained by considering the many straws $\mathcal{O}(100)$ crossed by tracks. Each tracking module includes two double straw layers, XXYY, oriented along orthogonal directions (Table 6.1) transverse to the beam. This choice provides symmetry along both the X and Y coordinates, motivated by the need to achieve maximal resolution in the reconstruction of transverse plane kinematics and in the vertex location. Extensive simulations were performed to evaluate the impact of such a geometry on track reconstruction, as discussed in Section 6.7.1. Results indicated that a third stereo orientation is not required, since potential ghost tracks can be resolved using the surrounding 4π ECAL and by alternating the location of the electronic readout in even and odd modules. The use of a XXYY geometry for the straws also considerably simplifies the design of the tracking modules. The diameter of the straws is directly constrained by the total thickness allowed for the modules. Taking into account the space required for the passive targets, the tracking modules must have an overall thickness of around 3 cm, including any supporting mechanical frame. In general, larger straw diameters quickly reduce the maximum number of modules/targets that can be fitted within the limited magnetic volume available. A smaller straw diameter also increases the track sampling in the plane transverse to the beam, thus improving the reconstruction of large angle tracks. It is worth noting that particles produced in (anti)neutrino interactions have broad angular distributions (e.g., protons and pions). The choice of straws with 5 mm diameter was found to provide a good compromise between compactness, transverse sampling, and practical manufacturing considerations. Since only interactions within the passive target layers are used for physics measurements, the total mass of the straws must be minimized. This latter is dominated by the thickness of the straw walls, which can be constrained by the need to associate interactions with the correct target material with an accuracy $\mathcal{O}(10^{-3})$. In particular, for single-track events like $\bar{\nu}_\mu \mathrm{H} \to \mu^+ n$, the target plane where the interaction occurred can be determined by noting the absence of straw tube hits preceding the presumed target, combined with the presence of hits in the tubes following the target. The corresponding uncertainty is given by the ratio of the thickness of the straw walls to that of a single target layer. An upper limit on the thickness of the straw walls $< 20\,\mu$m (Table 6.1) corresponds to an uncertainty of about 0.5%. The total fiducial mass

of the tracking modules must not exceed approximately 5% of the mass of the passive targets.

Engineering and operational constraints The use of ultra-thin straw tubes requires the application of constant tension on their walls in order to keep them straight. To this end, an internal overpressure is used to pre-load the sealed straws rather than applying external tension. The advantages include simplified assembly and a guarantee of straw circularity. The tracking modules are operated with an internal pressure of 2 bar absolute (Table 6.1), which provides automatic cancelation of the forces applied by the straw walls and by the straw wires on the mechanical structure of individual modules for a self-supporting design (Section 6.5.4). The wires must be kept at the center of the straws with an accuracy better than 100 μm to provide a symmetric field distribution. A self-centering design was developed with the addition of precision spacers (Section 6.5.1), making the tolerances in the assembly of the modules non-critical for detector functionality. The detection of TR requires the use of a Xe/CO_2 gas mixture, making the gas tightness of the modules more critical. A gas leak rate per module $< 4 \times 10^{-4}$ liter/min with Ar is required (Section 6.12.1), corresponding to a Xe leak rate that is approximately 0.11 times smaller. The electronic readout is directly integrated into the mechanical frames to achieve self-contained tracking modules that can be easily extracted, inserted, and manipulated. The total power dissipation has to be < 15 mW per channel (Section 6.7.1). A self-cooling design using the internal ionization gas was found to be adequate to remove such modest power (Section 6.8). The corresponding nominal gas flow rate is 5 nliter/min/module.

6.4 Initial STT Configuration and Upgrades

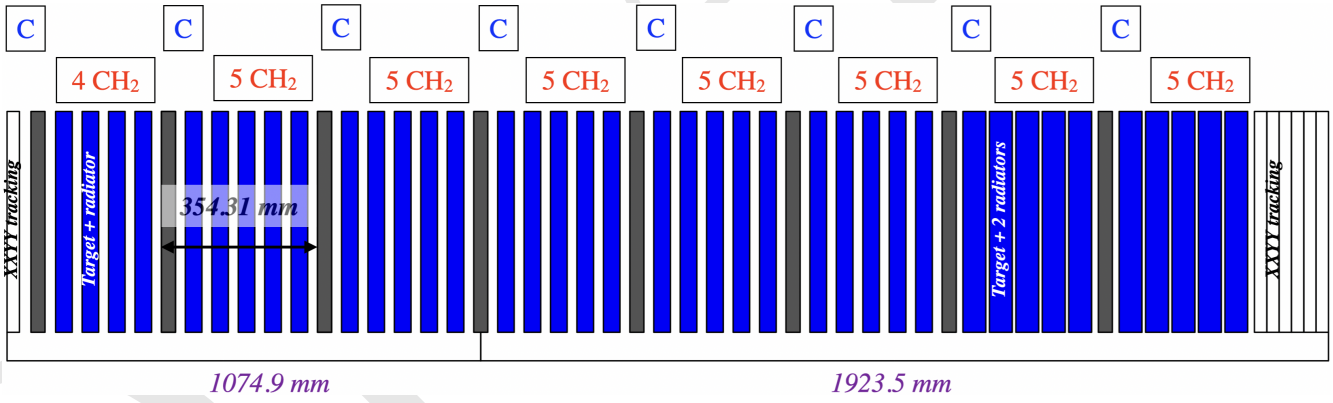


Figure 6.4: Sketch of the module arrangement in the initial STT configuration. Each module has a common tracking part with XXYY straw layers. The C modules (black) are equipped with a graphite target, while the CH_2 modules (blue) have both a HDPE target and one or two polypropylene radiators.

Initial STT configuration The STT and related nuclear targets partially fill a magnetic volume corresponding roughly to a cylinder of 4 m diameter, with the 3.38 m axis perpendicular to the beam direction and along the magnetic field ($B = 0.6$ T) direction. The detector has a total length of 2998 mm and is located downstream of a 925 mm region along the central diameter of the cylinder, where the GRAIN active liquid argon (LAr) target is located. The default STT configuration to be installed in SAND for the initial data collection is shown in Figure 6.4 and is composed of a total of 54 modules (Section 6.5.1):

- 29 modules equipped with a CH_2 target and one radiator, about 37.7 mm thick;
- 10 modules equipped with a CH_2 target and two radiators, about 51.8 mm thick;
- 8 modules equipped with a graphite target and 32 mm thick;
- 7 tracking modules without targets and only the four XXYY straw layers, 28 mm thick.

The thickness of the individual CH_2 targets varies depending on the number of radiators present in order to guarantee the same total CH_2 thickness of 6.89 mm across all 39 CH_2 modules. The location of the radiators across the CH_2 modules was optimized for the $e^{\pm}$ identification with transition radiation (Section 6.18.4). One module with a graphite target is located exactly in the center to allow a symmetric configuration of the remaining modules, with two modules sharing an identical height. The total number of straws in the entire STT is 136,192. The reference fiducial volume is defined by a cut of 20 cm from the edges and corresponds to a total fiducial mass of 2.334 t of CH_2 and 544 kg of graphite. The average STT density within the fiducial volume is about 0.11 g/cm^3, including all nuclear targets, the radiators, the straws, and the related materials (Figure 6.5). All modules are equipped with integrated readout boards using the default VMM3a ASIC chip (Section 6.7.2). The gas mixture used initially will be Ar/CO_2 70/30 for all modules. Table 6.2 summarizes the corresponding key numbers.

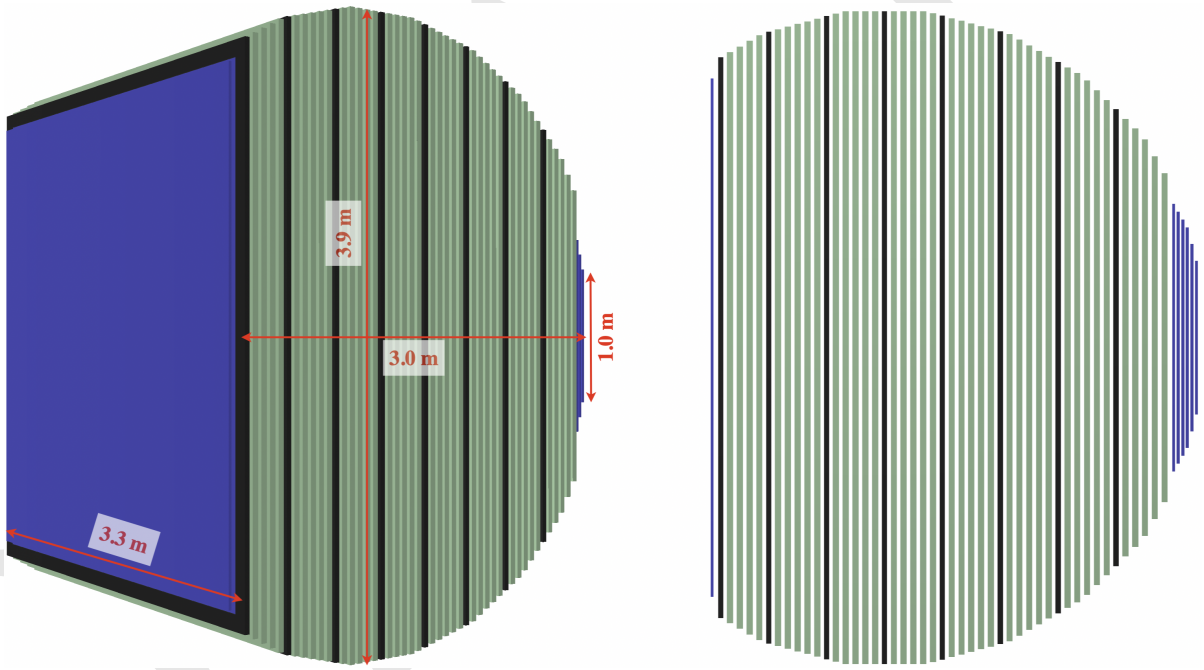


Figure 6.5: Views of the detailed geometry of the initial STT configuration implemented in the Geant4 simulations, showing the modules equipped with graphite (black) and CH_2 (green) targets, and the tracking modules (blue). The magnetic field $B = 0.6$ T is along the X axis of the cylindrical volume, while the neutrino beam is coming from the left side along the Z axis.

Super-module units The individual STT modules are assembled into super-modules, which are the basic detector units conceived for transportation and insertion/extraction into/from the magnet (Section 6.5.3). A total of 8 super-modules integrate both tracking and target components and are supplemented by one additional super-module located downstream of the detector stack, which includes 6 purely tracking modules. The configuration of the main super-modules includes the

Table 6.2: Summary of key numbers for the initial and maximal upgrade configuration of STT.

Item description	Initial STT	Maximal STT
Total number of straws/wires	136,192	215,746
Total straw length (km)	430	700
Straw outer diameter (mm)	5	5
Average straw length (m)	3.16	3.19
Maximal straw length (m)	3.75	3.75
Total straw film area (m^2)	6,751	10,990
Total straw internal volume (m^3)	8	14
Total detector length (mm)	2,998	2,998
Average density (g/cm^3)	0.11	0.17
Average radiation length X_0 (m)	4.3	2.8
Fiducial (20 cm) C mass (t)	0.544	0.544
Fiducial (20 cm) CH_2 mass (t)	2.334	3.863
Total number of modules	54	84
Number of modules with CH_2 target & radiator	29	45
Number of modules with CH_2 target & 2 radiators	10	0
Number of modules with CH_2 target only	0	24
Number of modules with graphite target	8	8
Number of tracking modules (no target)	7	7
Number of straw planes	216	336
Number of modules per super-module	6	10
Number of super-modules	8+1	8+1
Number of FE boards	2,128	3,371
Modularity of FE boards (channels)	64	64
ASIC in FE boards	VMM3a	Custom
Number of HV channels	108	168
Number of LV channels	126	186
Number of data acquisition (DAQ)/DTS interface boards	18	18
Number of LV distribution boards	18	18

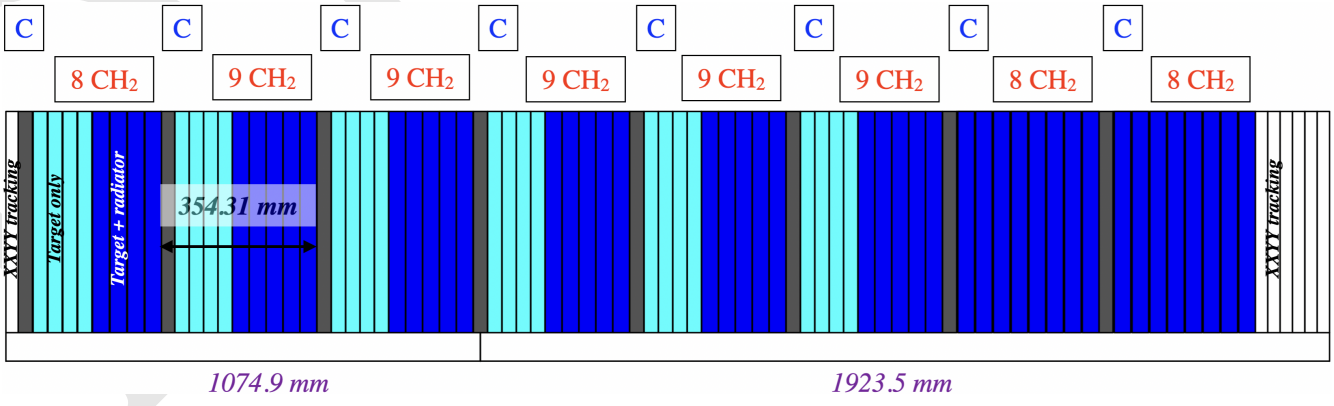


Figure 6.6: Sketch of the module arrangement in the maximal upgrade configuration for STT.

following elements:

- An upstream module equipped with a graphite target.
- 5 modules equipped with both a CH_2 target and a radiator.
- The individual modules are separated by equal air gaps in order to obtain a total super-module thickness of 354.31 mm. Such gaps are placeholders for future potential upgrades with the possible addition of up to 4 extra modules.
- In the most upstream super-module, one CH_2 module is replaced by an upstream tracking module without a target to identify tracks originating outside of the STT volume.
- In the two most downstream super-modules, all 5 CH_2 modules are equipped with targets and 2 radiators to maximize TR detection with a reduced number of modules (Section 6.18.4).

Planned upgrades The initial STT configuration is conceived to provide enough flexibility for future detector upgrades and already includes all service connections and infrastructure to support the insertion of additional modules. The following main upgrades are planned:

- Addition of up to 30 extra STT modules, based on the common tracking modules and equipped with a variety of targets and/or radiators.
- Replacement of the integrated VMM3a readout boards with ones using a custom ASIC developed for STT (Section 6.7.3).
- Filling the STT modules equipped with radiators with the Xe/CO_2 70/30 gas mixture, replacing the initial Ar/CO_2 mixture (Section 6.11). The Xe filling can be completed together with the upgrade of the readout in order to minimize the potential losses associated with the Xe recuperation before opening the frames of the modules.

Figure 6.6 shows the maximal upgrade configuration for STT obtainable by adding a total of 30 CH_2 modules, of which 24 do not have a radiator. The corresponding key numbers are given in Table 6.2. It is noted that some of the additional modules can be equipped with target materials different from CH_2 [50, 53], depending on the physics program of the upgraded STT.

6.5 Engineering Model

6.5.1 Design of STT Modules

The design of the STT is driven by the need for a compact tracking module that is individually replaceable and of relatively simple construction. These considerations translate into the following general design requirements:

- Self-supporting tracking modules minimizing the total thickness and mass;
- High level of detector integration for a self-contained design minimizing operational risks and allowing for a module reconfiguration;
- Optimization for mass production with reduced costs and a simplified assembly procedure, without compromising performance.

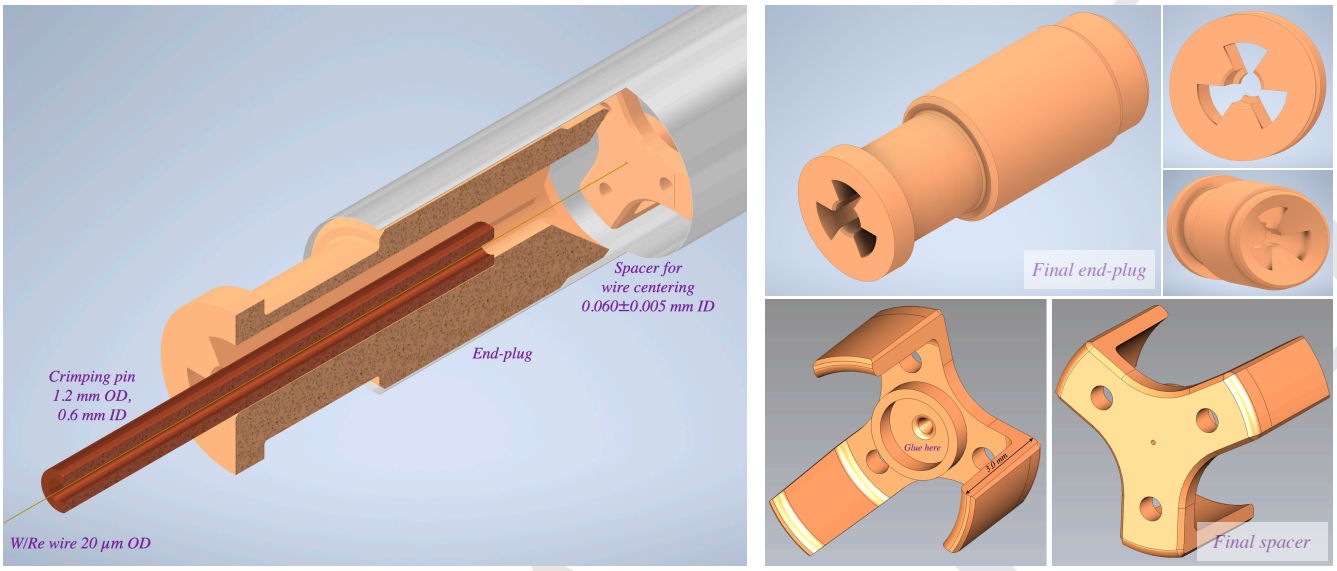


Figure 6.7: Drawing of the various straw components with end-plug, spacer, and pin for the STT. The details of the final end-plug and spacer are shown on the right panels.

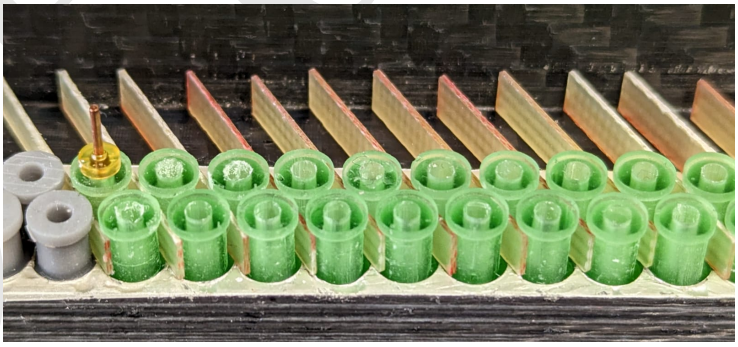


Figure 6.8: Small temporary FR4 bars are inserted to mechanically block the end-plugs during the wiring procedure of the straws in the 1.2 m STT CERN prototype (Section 6.12.4).

DRAFT

End-plugs, wire spacers, and crimping pins An important element in the design of the STT modules is represented by the straw components, including the end-plug, the wire spacer, and the crimping pin. These three parts are closely related to each other but are optimized for separate functions, as illustrated in Figure 6.7. A crimping pin of relatively large inner diameter (0.6 mm) is used exclusively to hold the wire under tension without slippage, while an extra spacer is located close to each end-plug for precise centering of the wire within the straw walls themselves. The use of an internal overpressure of 1 bar relative guarantees the required circularity of the straws. Such an approach effectively decouples the straws from the support frame and results in a number of advantages:

- Better control of wire centering accuracy. The spacer is a single component that can be produced industrially by injection molding with tight tolerances. The conventional approach using a precision pin relies instead on two components (pin and end-plug), each of which is affected by its own fabrication tolerances.
- Simplified assembly procedure. The self-centering of the wires with glued spacers is insensitive to the misalignment of the end-plugs and pins.
- Reduced costs and easier supply of the parts. Both the pins and the end-plugs can be produced industrially with relaxed tolerances, as they are not critical.

The pins are made of oxygen-free copper (Cu-DHP 99.90) and are gold plated for reliable electrical contacts (Section 6.13.5). They are 15 mm long and have an external diameter of 1.2 mm. The crimping of the pins is performed with the same pneumatic tool developed for the mass production of the ATLAS Transition Radiation Tracker (TRT) (Section 6.12.1). The wire spacer has an external diameter of 4.88 mm to fit an inner diameter of the straws of 4.91 mm at atmospheric pressure. The total height of the spacer is 3 mm, which is larger than the straw radius to prevent flipping during insertion into the straw. The central hole has a diameter of only 60 μm, with a conical shape that allows for straightforward insertion of the wire (Figure 6.7). Taking into account the tolerances achieved in industrial production (Section 6.13.4), the spacer guarantees self-centering of the wire with an accuracy of better than 65 μm. The end-plug is produced industrially by injection molding in transparent polycarbonate and fulfills the two functions of holding the pin and optimizing the impedance for the gas flow through the straws (Figure 6.7). It has a total height of 13 mm, with the bottom 8 mm to be inserted into the straws. Its complex external shape is determined by the wiring and assembly procedures (Section 6.5.2). The reduced external diameter in the top section allows for the sealing of an entire double straw layer by pouring Stycast 1266 glue around all end-plugs. During the wiring process, temporary FR4 bars are inserted to mechanically block the end-plugs, as shown in Figure 6.8. This technique allows for the replacement of the few wires failing the tension measurement and/or the HV tests before the final sealing (Section 6.13.10).

Anode wires The wires are made of a tungsten alloy with 3% rhenium content for increased tensile strength, vibration strength, and breaking point. The wire diameter is 20 μm and the surface is electrolytically etched, polished, and covered with a 0.3 μm gold coating (Section 6.13.6). The choice of the wire diameter is motivated by two main considerations:

- Minimize the required wire tension that is transferred to the C-fiber frame during the wiring procedure (Section 6.5.4);

DRAFT

- Guarantee an appropriate gas gain for the operation of the detector with internal overpressure by keeping the applied voltage below 2.0 kV.

The nominal wire tension applied is 50 gf (gram-force), which is safely below the limit of elastic deformation of 75 gf, as measured using calibrated weights. Strict quality controls are performed during the module assembly to guarantee that all wires are within the maximum acceptance range 50 ± 5 gf (Section 6.13.10). Extensive wiring tests were performed (Section 6.12.1) before the final validation with the construction of the 1.2 m (Section 6.12.4) and full-scale (Section 6.12.9) STT prototypes. The number of internal wire spacers per straw varies depending on the actual straw length and its orientation (horizontal or vertical). A minimum number of two spacers located close to the end-plugs is required for short vertical straws, while a maximum number of 4 spacers with two intermediate ones is needed for the longest 3.75 m straws. The free span of the wire between supports is expected to be, on average, about 1.25 m. Note that the PANDA straw tracker also uses 20 μm W/Re wires stretched with a tension of 50 gf over a total span of around 1.5 m without internal supports [54]. The maximal gravitational wire sag is estimated to be about 22 μm for horizontal straws with a free span of 1.25 m. The corresponding combined wire-centering accuracy is better than 87 μm, including both the effects of the wire spacers and the gravitational sag. The gravitational wire sag is expected to have a negligible effect on the vertical straws, for which the wire-centering accuracy is essentially determined by the wire spacers. The use of internal wire supports adds local inefficiencies along the wire. Assuming a total loss of efficiency over the entire 3 mm height of the spacers, the resulting average reduction of the efficiency for a single straw is less than 0.3%. Considering that, on average, a track crosses a large number of straws $\mathcal{O}(100)$, the effect on the track reconstruction efficiency was found to be negligible (Section 6.18.1). The location of the spacers is not required to be very precise and will be slightly staggered in different layers.

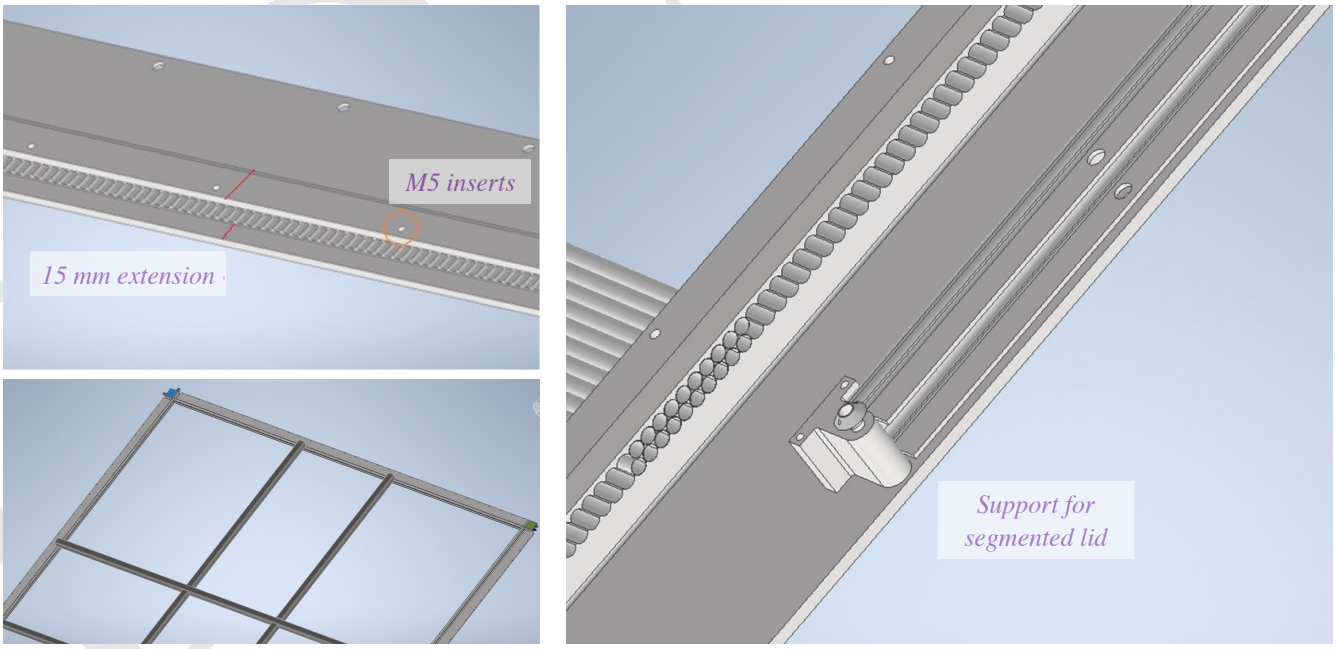


Figure 6.9: Details of the C-fiber frame for the STT tracking modules.

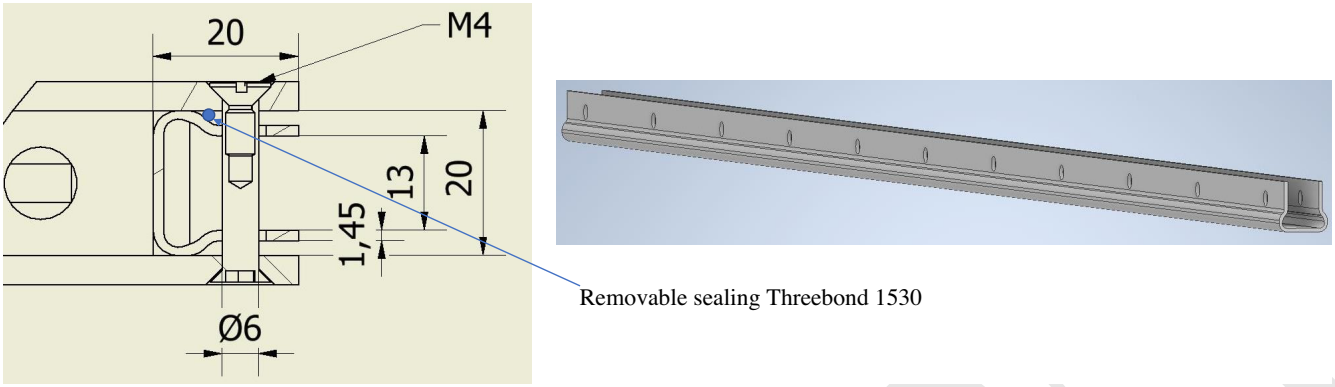


Figure 6.10: Details of the removable lid and sealing of the STT frame.

Carbon-composite support frames The support frames of the STT modules must satisfy opposite constraints. They must provide primarily mechanical support for the straws and the anode wires, with adequate stiffness against deformations during assembly and manipulation. They must also concurrently add minimal mass to the overall material budget of the STT and minimize the thickness of the tracking modules. Additional technical requirements include:

- The frame structure must align the straws with an accuracy of 0.1 mm.
- The frame structure must facilitate the assembly procedure, including the gluing of the straws, wiring, sealing, etc.
- The frame must hold the maximum pressure of 2 bar with an appropriate safety factor.
- The frame must guarantee the gas tightness with a leak rate comparable to or smaller than the diffusion rate through the straw walls.
- The frame structure must avoid excessive straw compressions in the absence of internal overpressure during construction, handling, and transportation.
- The frame must guarantee that in operating conditions the minimum required tension is maintained on the wires and straws.
- The frame structure must integrate the readout electronics and the gas distribution.
- The frame structure must have features allowing the insertion of the modules into the supporting external structure inside SAND.
- The frame must allow easy access to the straws and readout electronics for maintenance and repair.

The frames of the STT tracking modules are fully made of C-composite material, with the exception of the 4 aluminum corner blocks with the gas and electrical connections. The main structural elements are composed of 18 plies of C-fiber twill fabric PrePreg M46J with 60% fiber content and 220 g/m^2. The layers are alternated along two orthogonal directions at 0° and 90°. The resulting module of elasticity along those two directions is required to be no less than 100 GPa (Section 6.13.7). The bottom half of the frame to be screwed to the assembly table is made of 4 elements, each integrating one side panel and a straw holder profile. The top half of the frame is split into 8 parts, including 4 covers for the top straw layer with an integrated straw holder profile and 4 side panels to complete the assembly. This design feature provides open access to the

straw ends for wiring, tests, and sealing purposes before the completion of the module assembly (Figure 6.11). The side panels extend by 15 mm over the area with the straws and have threaded M5 inserts on the inner sides (Figure 6.9) to allow the insertion of a temporary C-fiber cross-bracing (Section 6.5.2). The frame has a maximum width of 105 mm and an overall thickness of only 28 mm, including the four XXYY straw layers. Connection holes are spaced 100 mm apart along the external perimeter of the side panels to secure the removable lids and accommodate the fixtures for the external support of the modules. Figure 6.10 shows the details of the removable lids closing each side of the frame. The lids are made of 7 plies of the same PrePreg M46J used for the other frame elements, alternated at 0° and 90°. The sealing of the lids is achieved with removable Threebond 1530 glue added all along their profiles. Figure 6.11 shows the complete assembly of a STT tracking module with the complete C-fiber frame. The maximal weight of the largest tracking modules 3.9 m × 3.3 m is about 33 kg each, including the frame, straws, Al corner blocks, connectors, readout, etc.

Removable target planes The STT tracking components with XXYY straw layers are common to all 54 modules. The removable targets and radiators are mounted in front of the corresponding tracking modules during the super-module assembly (Section 6.5.3). The graphite target is composed of individual graphite tiles of dimensions 595 mm × 595 mm × 4 mm (Section 6.12.7), which are stacked to form a vertical wall and held together by thin C-fiber woven tape – 50 mm wide – running along both sides of the tile edges (Figure 6.13). The two tapes are stitched together in the middle, creating a "pocket" holding individual tiles. The complete graphite target extends only within the nominal STT fiducial volume, starting 20 cm from each surface of the surrounding ECAL. Overall, the C-fiber tape contributes to less than 0.2% of the fiducial mass of the graphite target, so the chemical purity of the tape itself is not critical. Figure 6.12 shows a complete assembly of the largest STT module equipped with a total of 30 graphite tiles. A similar design is used for the CH_2 target, which is made of high-density polyethylene (HDPE) tiles 595 mm × 595 mm × 5 mm, produced by injection molding and held together by polypropylene tapes of identical CH_2 chemical composition (Figure 6.12). Thin frames made of T700 C-composite material, 90 mm wide and with the same connection holes along the external edges as the frame of the tracking modules, are used to support the tile assembly for both targets.

Removable radiator assembly A radiator made of 105 polypropylene foils 18 μm thick is interleaved between each CH_2 target and the corresponding tracking module. The radiator foils are clamped together between 8 thin frame panels made of T700 C-composite material with the same connection holes along the external edges. In the central area within the STT fiducial volume, the foils are kept apart with a constant spacing of about 117 μm by small pads made of adhesive polypropylene film (Section 6.12.7). Details of the radiator assembly are shown in Figure 6.13. The use of an embossing pattern on one side of each foil will also be investigated for the mass production of the radiators. Alternatively, the possibility of using radiators made of polypropylene-polyethylene fiber mats [55] is also considered instead of film radiators [56, 57].

6.5.2 Assembly Procedure

The self-centering of the wires within the straws themselves (Section 6.5.1) makes the assembly tolerances non-critical, resulting in relaxed requirements for the tooling and module assembly. The assembly procedure was further optimized to minimize the corresponding operations (Section 6.14.2). In order to facilitate the assembly process, the C-fiber frame supporting the straws is supplied

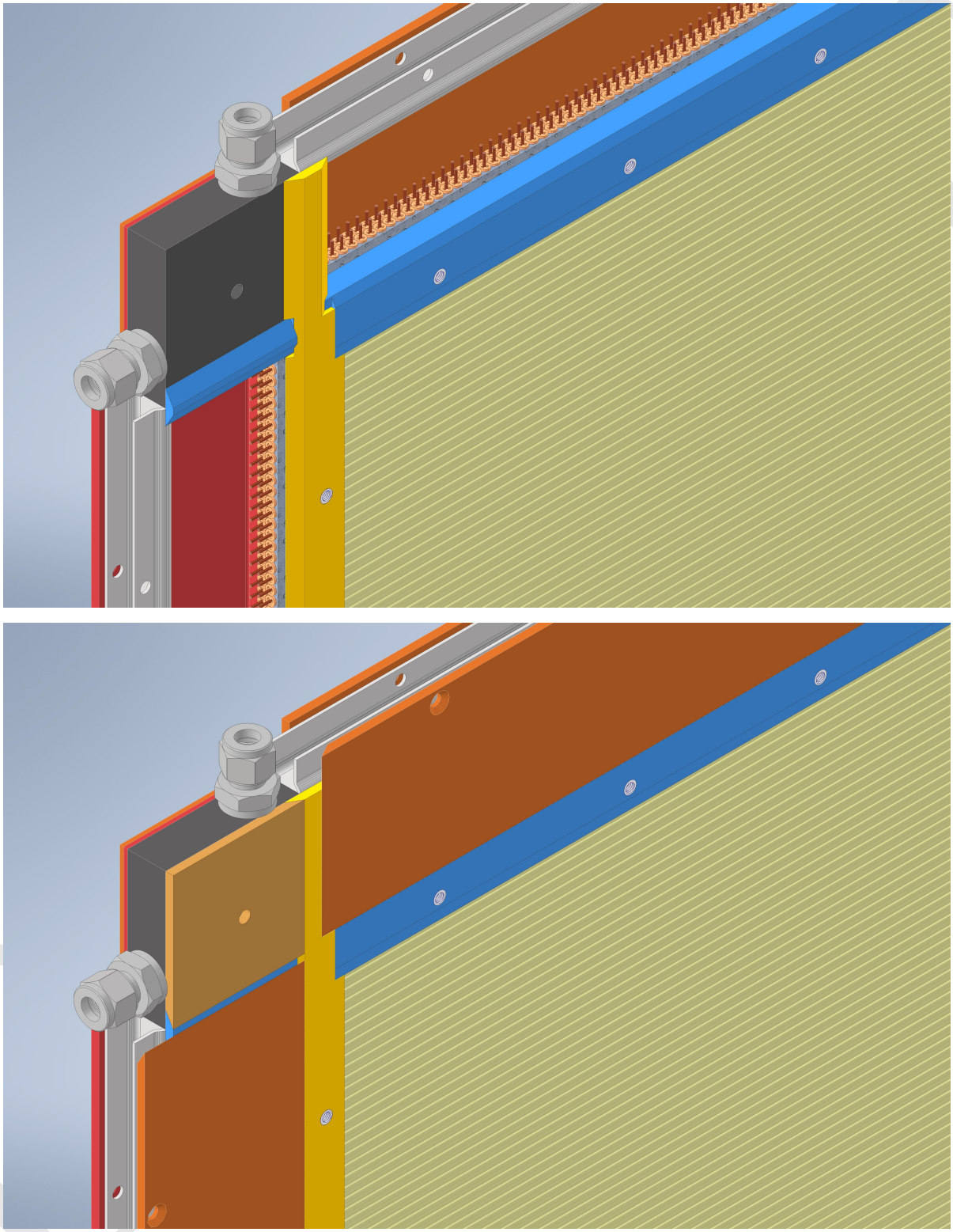


Figure 6.11: Details of a STT tracking module with C-fiber frame and four XXYY straw layers without (top picture) and with (bottom picture) the top C-fiber covers completing the assembly.

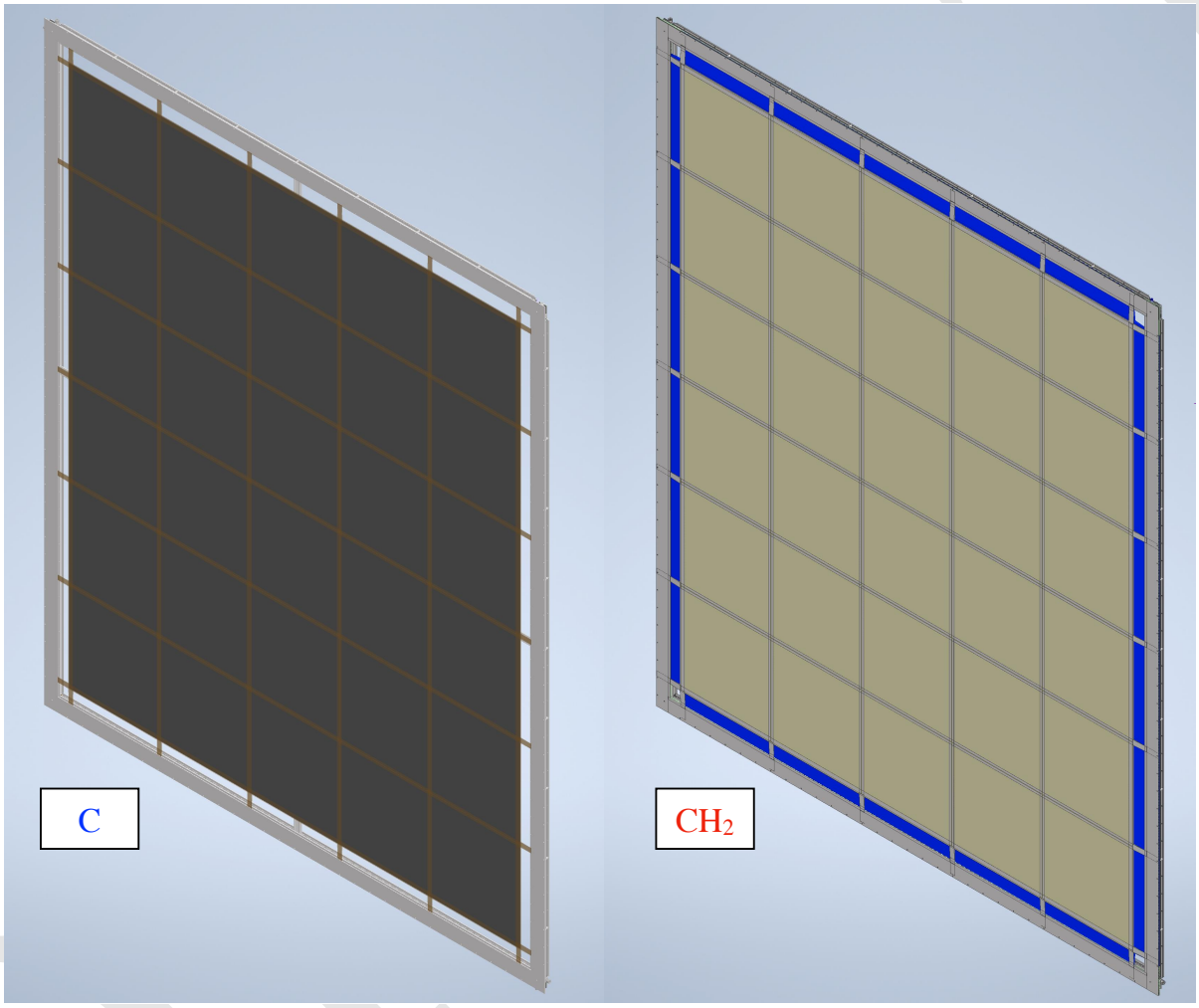


Figure 6.12: Drawing of the complete assembly for the largest STT modules (3.9 m × 3.3 m) equipped with graphite target (left) and polyethylene/polypropylene target and radiator (right). Both target materials are obtained from 595 mm × 595 mm tiles held together by C-fiber/polypropylene tapes.

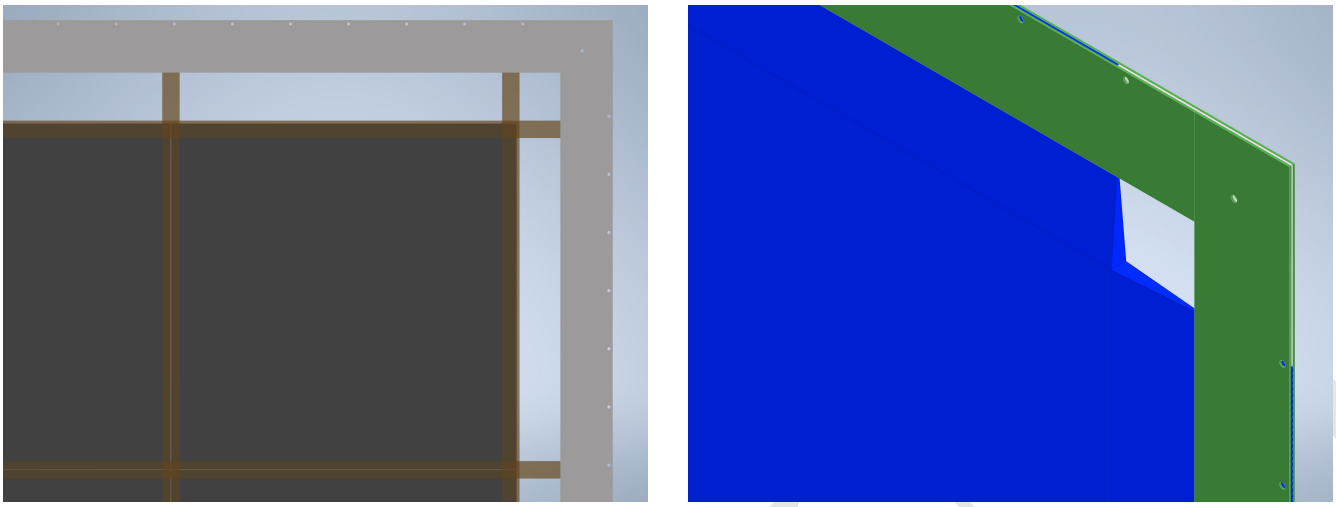


Figure 6.13: Left picture: Details of the tile assembly in the STT graphite target. Right picture: Details of the radiator assembly for the STT modules equipped with CH_2 targets.

by the industrial vendor (Section 6.13.1) in the form of 12 separate parts, supplemented by the 4 aluminum corner blocks (Section 6.9.2) with related C-fiber covers, and the 4 removable lids sealing the gas manifolds, which are split into a total of 10 segments (Figure 6.10). The straw holder profiles are split into two parts, with each half directly integrated into the corresponding side part of the frame during the manufacturing process. After quality checks, the straws produced with the ultrasonic welding technology are prepared for assembly by gluing temporary 3D-printed plugs at both ends and inflating them with an internal pressure of about 2.5 bar relative. This assembly overpressure is required to provide enough mechanical rigidity to the straws, as well as to pre-load them with an initial tension T_0 (Section 6.5.4). To this end, a total of 32 straws are connected to a common 3D-printed collector using flexible plastic tubes (Figure 6.14) to guarantee accurate regulation of the assembly pressure and the related tension T_0. The use of internal overpressure has two main advantages over the application of external tension: (a) simplified straw handling and assembly procedure; (b) guaranteed circularity of the straws, allowing for a more accurate gluing process. The initial length of the straws exceeds the required length so that they can extend on both sides beyond the straw holders onto the corresponding alignment profiles mounted on the assembly table. The assembly procedure of the STT modules includes then proceeds through the following steps:

- The bottom half of the C-fiber frame, including 4 side panels with the corresponding straw holders, is glued together with Araldite 2011 and screwed to the assembly table using the holes on the external edges of the frame. During this step the four aluminum corner blocks are secured with precision pins inserted into their central holes and glued to the bottom frame with 3M 2216 B/A glue. The heights of the 4 straw holder profiles with respect to the table are measured and, if needed, adjusted with the insertion of thin calibrated tapes to achieve a flatness within about 100 μm.
- Thin 3D-printed plastic spacers are glued to the table at regular intervals to prevent a sagging of the bottom straw layer. Small blocks 3D-printed are added on the two sides of the first straw layer to avoid lateral movements of the straws.

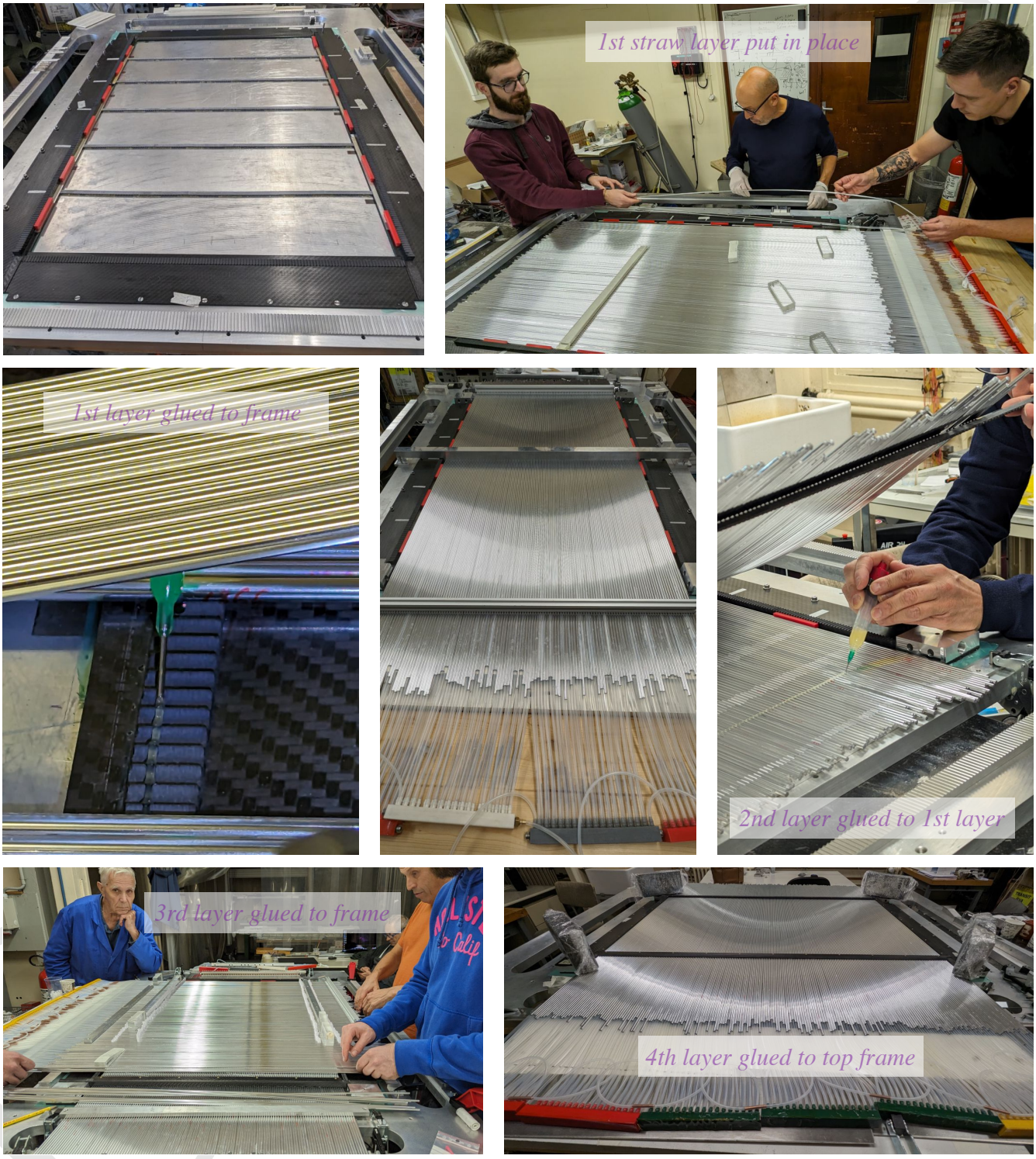


Figure 6.14: Assembly procedure for the 1.2 m STT CERN prototype (Section 6.12.4): gluing of the four XXYY layers of straws inflated at the assembly pressure to the C-fiber frame.



Figure 6.15: Assembly procedure for the 1.2 m STT CERN prototype (Section 6.12.4): cutting of straws, end-plug termination, wiring, sealing, and completion after quality tests.

- The first straw layer is put in place on the bottom straw holders and on the external alignment profiles. The straws are closely packed into each layer resulting in a self-alignment to the straw holders during the assembly procedure.
- The first straw layer is glued to the bottom straw holders with Araldite 2011. Simple flat profiles are used to push down all straws keeping them into the same plane defined by the straw holders. A period of 24 hours is required for complete glue polymerization before gluing the next layer.
- During the gluing of the first layer small drops of Araldite 2011 are dispersed between straws in a few points sperated by approximately by 50 cm along the straw length.
- The second straw layer is put in place and glued to the first layer. During this step the small triangular gaps within the double layer are filled with glue within the region of the straw holders (12 mm thick).
- During the gluing of the second layer small drops of Araldite 2011 are dispersed between straws in a few points sperated by approximately by 50 cm along the straw length.
- Two top profiles of the frame are added and glued with both Araldite 2011 to the second straw layers to complete the assembly of the corresponding double layer and with 3M 2216 B/A to the aluminum corner blocks. A period of 24 hours is required for complete glue polymerization.
- Thin 3D-printed plastic spacers are added on the two sides of the third straw layer to avoid lateral movements of the straws.
- The third straw layer, orthogonal to the first two, is put in place and glued with Araldite 2011 to the corresponding straw holders. A period of 24 hours is required for complete glue polymerization.
- During the gluing of the third layer small drops of Araldite 2011 are dispersed between straws in a few points sperated by approximately by 50 cm along the straw length.
- The fourth straw layer is put in place and glued to the third layer with Araldite 2011. At this stage the remaining two top profiles of the frame are added and glued to the fourth layer to complete the XXYY assembly. A period of 24 hours is required for complete glue polymerization.
- During the gluing of the fourth layer small drops of Araldite 2011 are dispersed between straws in a few points sperated by approximately by 50 cm along the straw length.
- The straws are cut flush with the top frame profiles on all 4 sides to remove the excess length. Until this stage no forces are applied to the frame since the straws are self-supported by the internal overpressure of 2.5 bar relative. The cutting of the straws results in a loss of the internal pressure and in the transfer of their initial tension T_0 onto the frame elements. Although the frame is designed to withstand such a tension with minimal deformations, no deflection is introduced until the frame is fixed to the assembly table.
- The cut straw edges are cleaned from any residual debris.
- The silver conductive paint SCP26G is applied at both ends of the straws and to the straw holder inner surface to create a ground plane creating an electrical contact between the inner and outer metallization of the straw walls.
- Check of the electrical contact between the inner Al metallization of the first straw layer and the outer Al metallization of the fourth straw layer, as well as between the ground planes on the 4 sides of the assembly.

DRAFT

- One side of the straws is terminated with the end-plugs produced by injection molding, which are directly glued to the straw walls.
- A temporary cross-bracing made of squared C-fiber tubes is screwed to the 4 top frame profiles in order to provide additional external support before the frame assembly is completed. The main goal of this cross-bracing is to prevent a bending of the frame elements under the tension of the anode wires.
- The partial XXYY frame assembly together with the external C-fiber cross-bracing is released from the table and put in a vertical position against a wall ready for the wiring process. The assembly is fixed to appropriate wall profiles via precision pins inserted into the central holes of the 4 corner blocks.
- The anode wires are cut to an approximate length and prepared by gluing the required number of spacers onto them with Henkel Loctite 406.
- The wires with the spacers are inserted into the straws along one direction (within a double layer) and stretched at the nominal tension of 50 gf.
- The top side of the straws is terminated with the end-plugs, which are mechanically blocked with the insertion of temporary FR4 bars.
- The wires are fixed by crimping the pins at both ends with the pneumatic crimping tool. This process proceeds from the center of each frame side towards the corners.
- The following quality tests are performed on all wires: (i) measurement of the electrical resistance of the wires to be consistent with 300 Ω/m; (ii) high voltage test at 1.2 kV in air and measurement of the leak current to be within a few nA for a group of 64 channels; (iii) measurement of the wire tension to be within 50 ± 5 gf. Wires failing any of the tests are replaced (Section 6.13.10).
- Sealing with Stycast 1266 glue poured around the neck of the end-plugs to create a monolithic assembly at the top of the entire double layer. The ground plane is embedded into the glue during such a process, which is also protecting it from oxidation.
- Rotation of the module by 90° and repetition of the wiring and sealing procedure with Stycast 1266 at the top of the second double straw layer.
- Rotations of the module to complete the sealing with Stycast 1266 at the opposite sides for both double straw layers.
- Temporary sealing of the frame with dedicated Plexiglass covers and check for the gas tightness. Any detected leak is fixed with the application of appropriate glue.
- Final gluing of the four top sections of the C-fiber frame to complete the permanent assembly. Calibrated aluminum cylinders are used to hold the top section in the correct position.
- Mounting of the C-fiber lids closing the four sides of the frame. The two sides equipped with the integrated readout boards (Section 6.7.1) are sealed with removable Threebond 1530 glue, while the two opposite sides are sealed with permanent Araldite 2011 glue.
- Final quality tests of the completed module: long-term high voltage test, functional test and gain measurement of the straws with a ^{55}Fe source.

Table 6.3 lists the various types of glue and contact paint used in the assembly of the STT modules. The viscosity of the glue used between straws is optimized to avoid excessive spreading over the straws. All glues and materials used are compatible with gaseous detectors and were tested in previous experiments. Given the negligible radiation environment with the LBNF (anti)neutrino

DRAFT

beams and the operation at room temperature around 20°C, no significant aging of the various materials is expected. The STT assembly procedure was validated with the construction of the 1.2 m (Section 6.12.4) and full-scale (Section 6.12.9) STT prototypes. Figures 6.14 and 6.15 illustrate the various steps followed during the assembly of the 1.2 m prototype. In Section 6.14.2 the tooling and requirements for the module assembly units are summarized, while Section 6.13.10 describes the corresponding quality controls and acceptance criteria.

Table 6.3: List of the various types of glue and contact paint used in the assembly of the STT modules.

Item	Type	Use
Araldite 2011	Glue	Between C-fiber frame elements and between straws and frame
3M 2216 B/A	Glue	Between Al corner blocks and C-fiber frame
Stycast 1266	Glue	Final sealing around the end-plugs and straw holders
Threebond 1530	Glue	Removable sealing of the lids of the frame
SCP26G	Silver paint	Conductive paint between ground planes and straw metallization
Henkel Loctite 406	Glue	Block spacers onto anode wire

6.5.3 Super-module Assembly

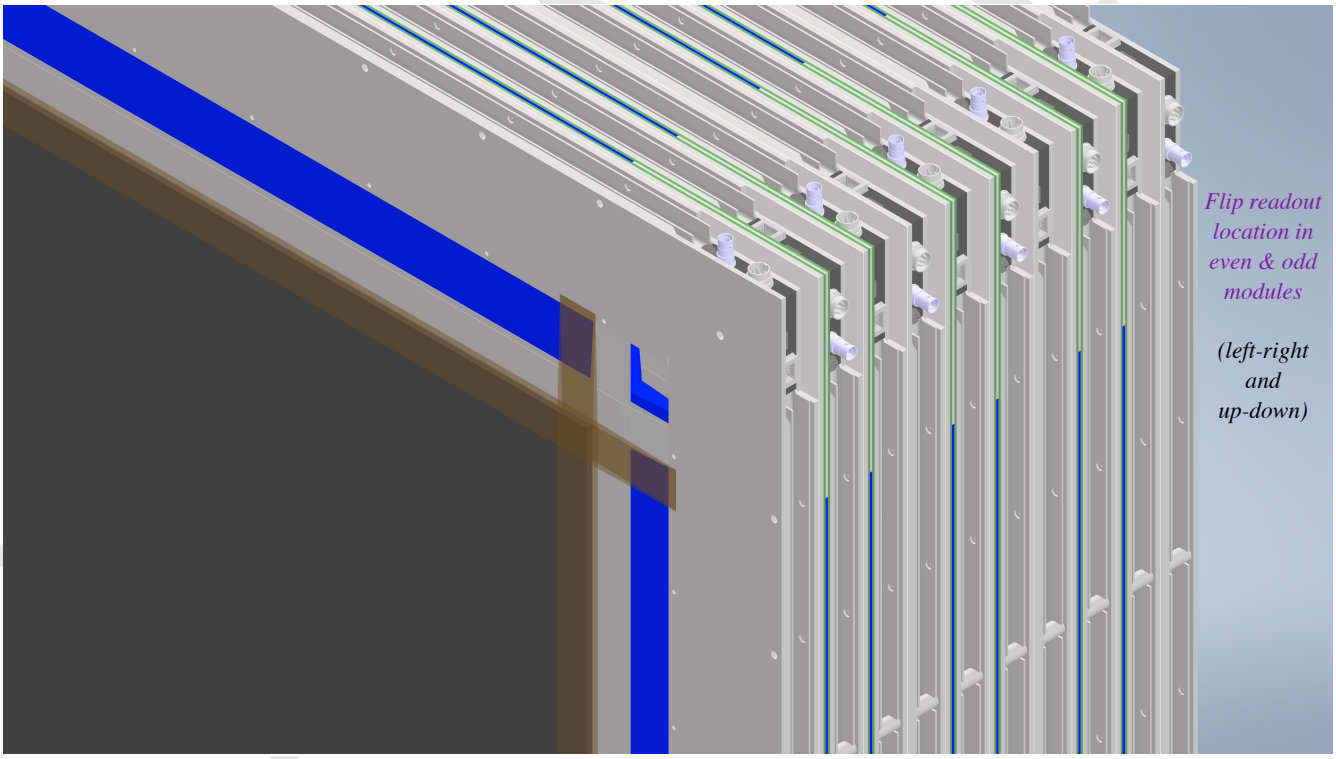


Figure 6.16: Details of a super-module assembly for the maximal STT including one module with C target, 3 modules with CH_2 target without radiator, and 6 modules with both CH_2 target and radiator.

As described in Section 6.4, the basic units for insertion/extraction into/from the magnet are the super-modules, composed of 6 (10) STT modules each in the initial (maximal) STT configuration. Figure 6.16 shows a super-module assembly for the maximal STT. The super-module assembly is about 354 mmwide and provides high mechanical rigidity against out-of-plane movements, as well

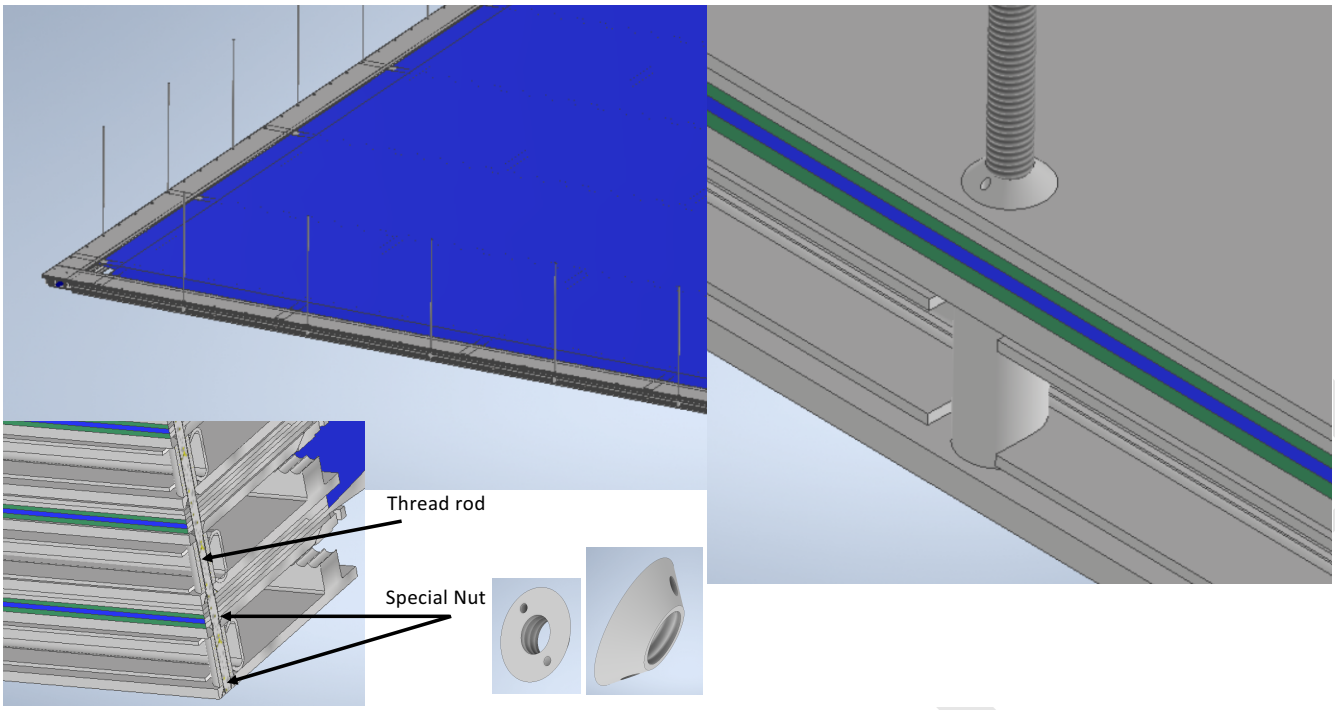


Figure 6.17: Details of the assembly of a STT super-module showing the connecting rods and nuts.

as protection for the straws within the tracking modules. A locking mechanism based on threaded rods and special blocking nuts (Figure 6.17) is used to clamp together the STT modules within the super-module. These rods are separated by 400 mm and are inserted on the right and left sides of the modules, leaving the top and bottom edges free. The super-modules are assembled in the vertical position, as shown in Figure 6.18. A temporary external frame is used to support the tracking modules and targets during the assembly (Figure 6.19). The various panels are held in the vertical position by strips connected to threaded inserts and are then moved into their final position by sliding on linear guides.

The STT modules are self-contained, with the four sides sealed by removable lids. All input and output connections are made through the four corner elements, which are located along the edges of each super-module. This configuration minimizes the length of the electrical cables and the gas pipes and allows easy access to the connections after opening the end caps of the magnet. The maximal weight of the largest super-modules, including 10 modules – one with a graphite target and 9 with plastic targets, of which 6 with radiators (Figure 6.16) – is about 1.1 t.

6.5.4 Mechanical Analysis

Mechanical analysis of straw assembly The mechanical properties of the straw materials were fed into both analytical and finite element analysis (FEA) to determine the straw deformations under the action of the internal overpressure. The geometry of the straw included an asymmetric seam similar to the one obtained from ultrasonic welding (Section 6.13.2). The results were in agreement with the measured values of elongation, tension, and radial deformation described in Section 6.12.1. A radial deformation of 11 (10.5) μm per bar was obtained from the FEA (analytical) calculation, to be compared with the measured value of 10 μm. The calculated longitudinal

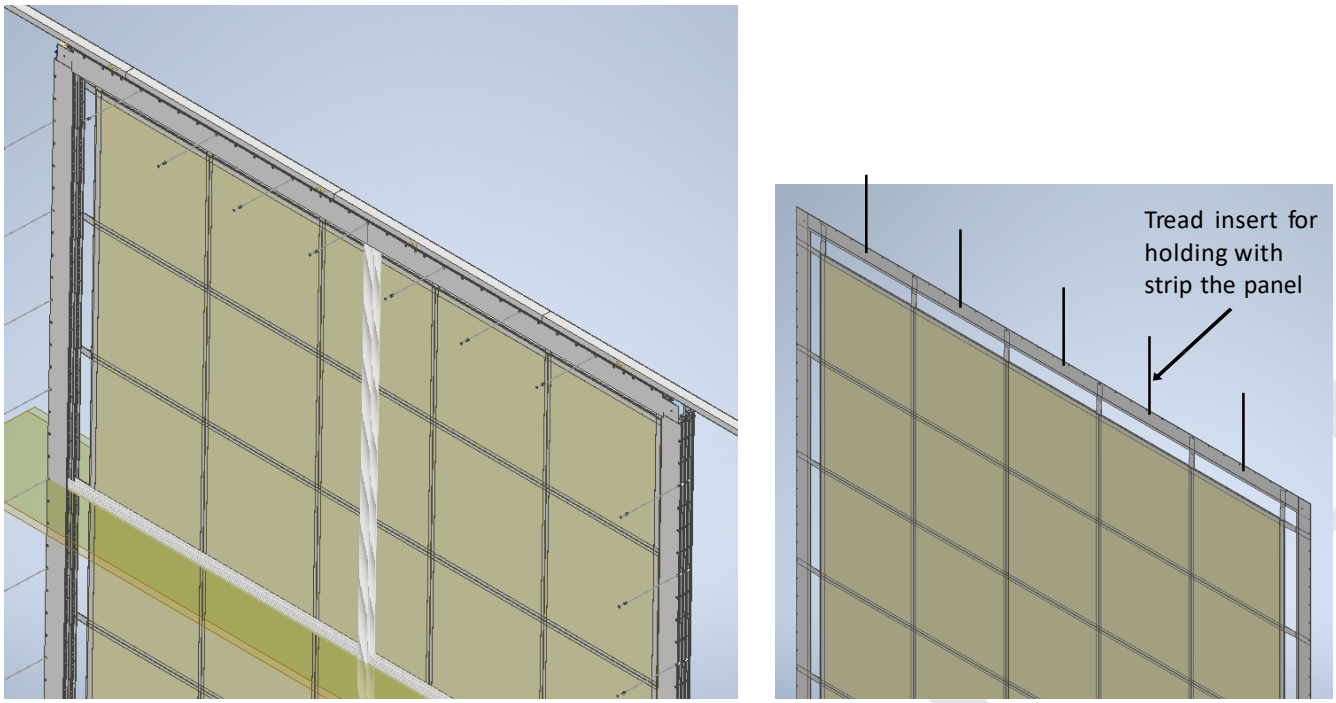


Figure 6.18: Assembly of the various elements of a STT super-module in the vertical position.

elongation for a 4 m straw at 2 bar relative was 2.5 mm, consistent with the measurement of about 2.8 mm. The lateral deformations (bending) of the straws were then simulated with a maximal length of 4 m due to the internal pressure in two different cases: (i) only one end of the straw is restrained by the straw holder; (ii) both ends of the straw are constrained by the straw holders. Figure 6.21 illustrates the results. When one end of the straw was left free, a relatively large deflection of about 70 mm at 2 bar relative was observed. However, once both ends are fixed in place by the straw holders, the maximal deflection at the midpoint is reduced to only 16 μm. This observation validates the use of the straw holder profiles themselves, together with similar external profiles mounted on the assembly table, for self-alignment of the straws during the assembly procedure of the STT modules (Section 6.5.2).

Role of overpressure for assembly and operation The STT takes advantage of the operation with internal overpressure, as demonstrated by PANDA [54] and COSY-TOF [58]. In particular, the design of the STT modules is based on the interplay of two different pressure values:

- An assembly pressure of ~ 2.5 bar relative to pre-loading the straws with an initial tension T_0;
- A lower operating pressure of 1 bar results in a corresponding tension T_{op} applied on the walls of the straws.

The assembly pressure is directly determined from the operating pressure, as it is chosen so that during the STT operation, the outward force applied by the pressure on the frame elements balances the sum of T_{op} plus the inward tension applied by the wires. The outward force is proportional to the total opening area of the straws. Under such conditions, the total net force acting on the

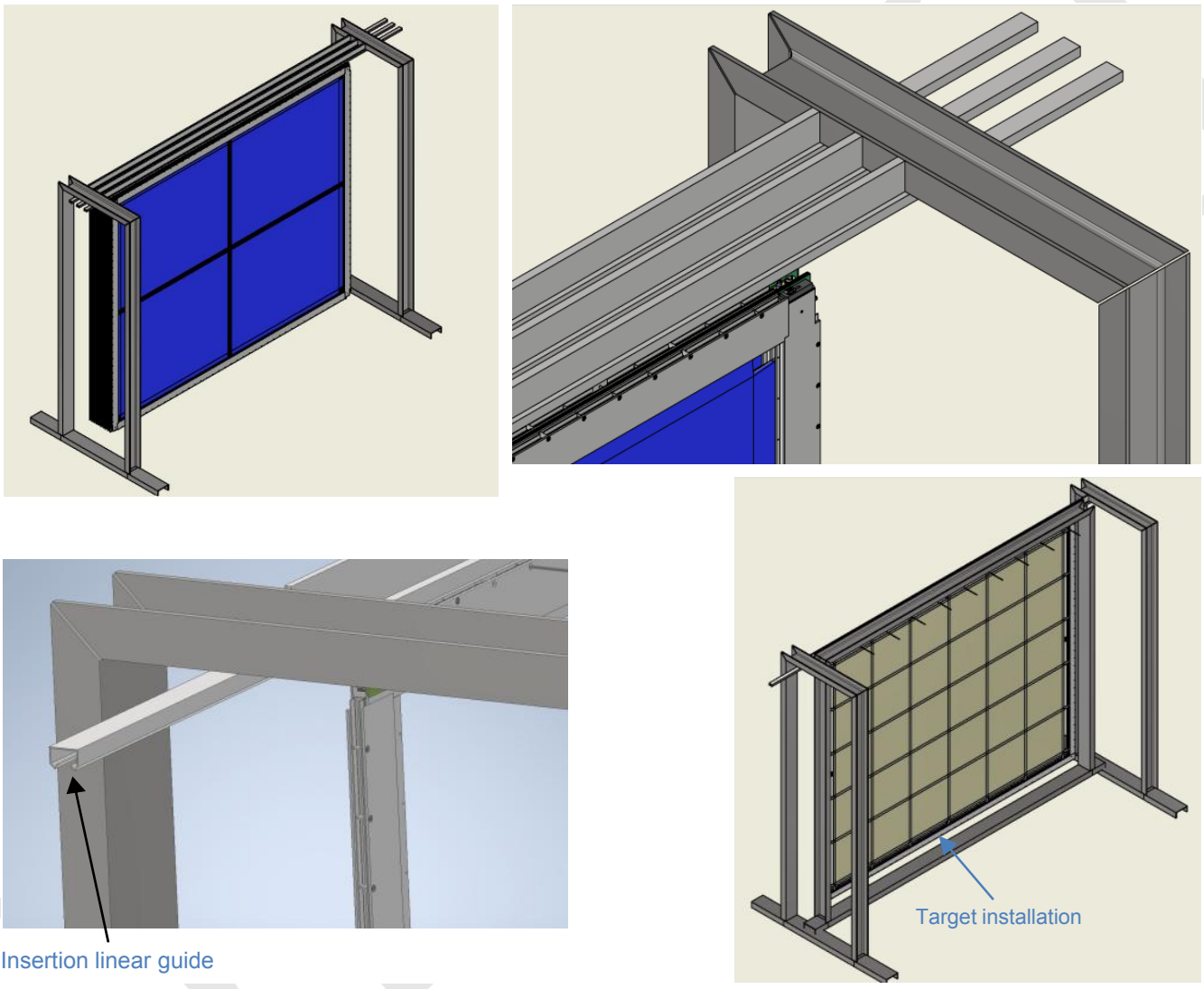


Figure 6.19: Details of the assembly procedure of a STT super-module with the dedicated external support structure.

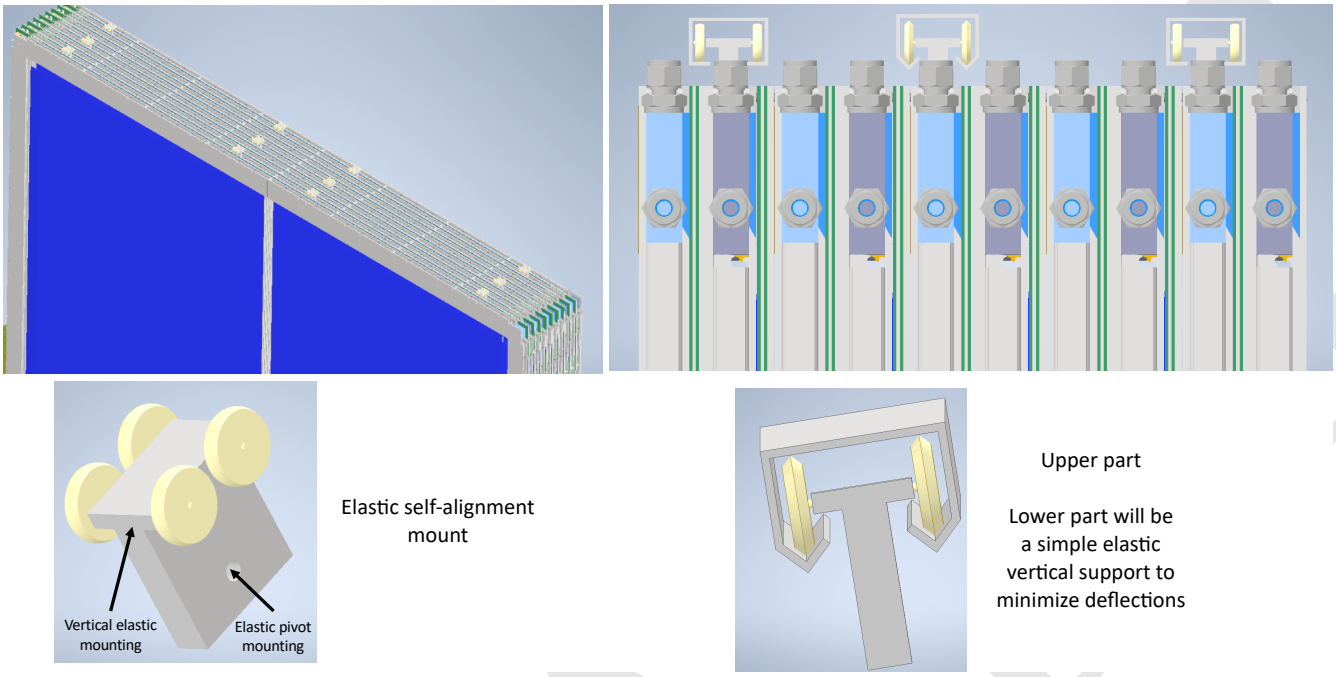


Figure 6.20: Drawing of the fixtures to hang the STT super-modules from the external support structure.

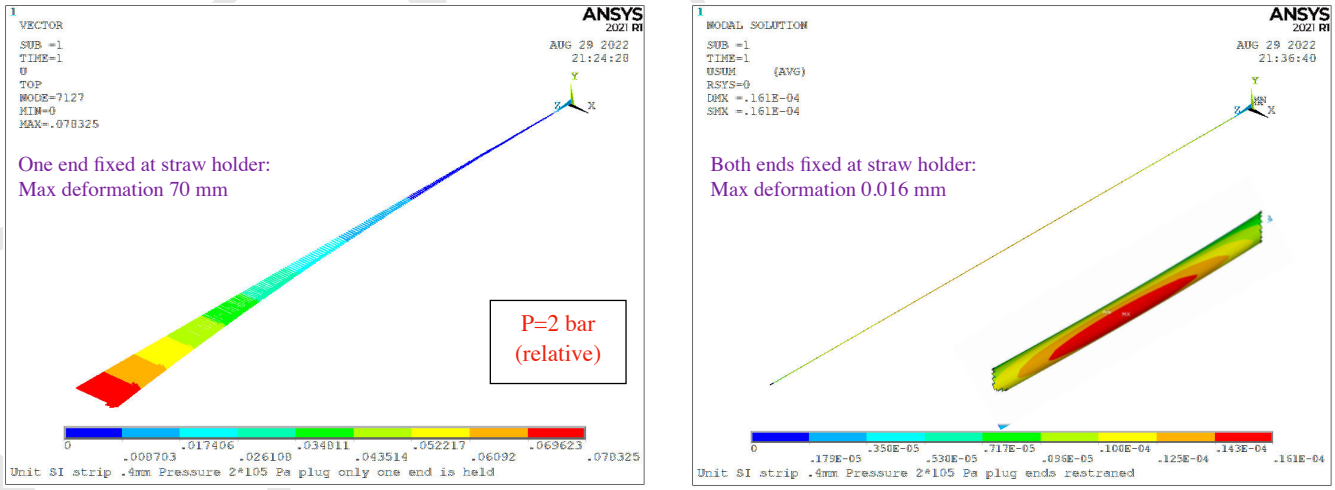
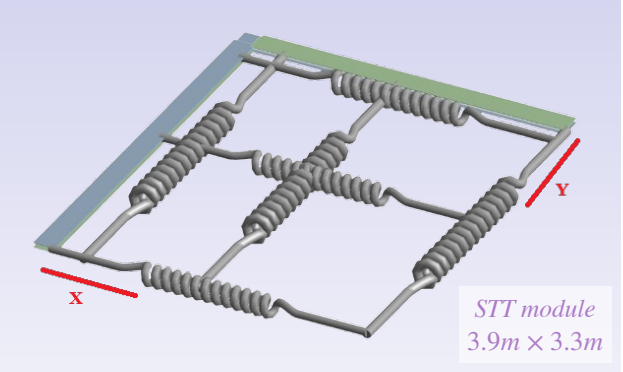
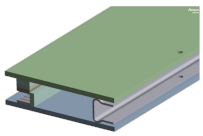


Figure 6.21: Analysis of deformations for a 4 m straw with a welded seam at 2 bar relative internal pressure under two different boundary conditions: (a) only one end is fixed at the straw holder (left plot); (b) both ends are fixed at the straw holders (right plot).

frame vanishes. Note that the same result is valid in the direction perpendicular to the plane of the modules, since the opposite forces applied by the internal pressure on the side panels cancel each other within the super-module assembly (Section 6.5.3). Extensive simulations based on FEA were conducted to validate and optimize the concept under varying conditions.





Layer	Deformation (mm)	Limit (mm)
1°	2.75	3.69
2°	2.75	3.69
3°	3.25	3.09
4°	3.25	3.09

Total deformations are the sum at both straw ends.
Long straws are 1° and 2° layer. Short straws are 3° and 4° layer

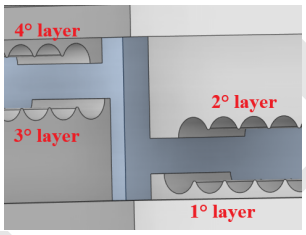


Figure 6.22: Maximal deformations of the full-scale STT module during assembly (1 bar absolute pressure) compared with the initial straw elongation from the pre-load at the assembly pressure of 2.5 bar relative. The values refer to the sum at both sides of the straws for an unconstrained frame.

Mechanical analysis of full-scale modules Both the straws and the wires effectively behave like springs (ropes) and apply tension on the frame proportional to their respective longitudinal elongations. The load is defined by the initial conditions, which are a 50 gf tension for the wires and the tension T_0 from the assembly pressure for the straws. Considering the largest STT module 3.9 m × 3.3 m, the corresponding initial elongations are 13.7 (11.5) mm for the long (short) wires, and 3.69 (3.09) mm for the long (short) straws. In operating conditions, the frame deformations vanish by design, as the 1 bar relative pressure guarantees that the straws and the wires are stretched under tension at the nominal length of the frame. However, during the module assembly or manipulation, the straws are expected to occasionally be at atmospheric pressure. In order to study the frame behavior under such temporary conditions, the detailed spring (rope) behavior of the W/Re wires and of the straws was implemented in the FEA simulations. Results are summarized in Figure 6.22. In the absence of the wires, the compression of the straws is self-limited by the fact that the force vanishes exactly once they return to their un-stretched length. The maximal frame deformations in the middle of each side therefore cannot exceed the initial straw elongation, regardless of the properties of the frame material. This picture changes once the wires are included. Since their initial elongation is much larger compared to that of the straws, the tension that they apply to the frame practically never vanishes and can potentially drive the frame deformations past the initial elongation of the straws. Increasing the assembly pressure helps to compensate for such an effect by extending the initial elongation of the straws and the corresponding load T_0. The complete system is non-linear, due to the interplay of the different elastic deformations. In the worst case, the maximal compression of the straws was less than 80 μm per side (Figure 6.22) with the assembly pressure of 2.5 bar relative. Furthermore, the relative displacement between nearby straws within a given plane is below 7 μm, as shown in Figure 6.23. Such deformations are relatively safe as they are well within the expected construction tolerances.

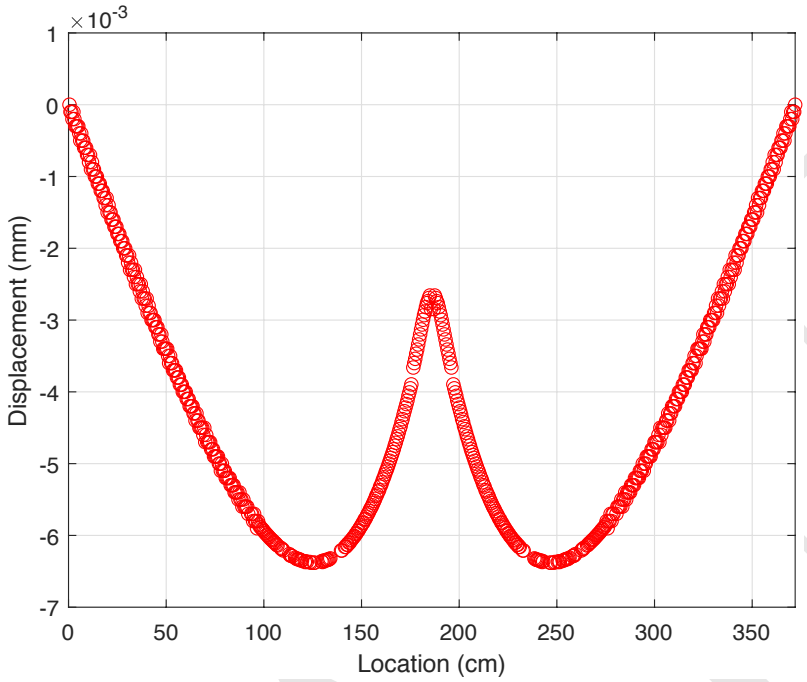


Figure 6.23: Relative displacement between nearby straws (n and $n+1$) in the full-scale STT module, due to frame deformation during assembly (1 bar absolute pressure). The values are obtained for an unconstrained frame.

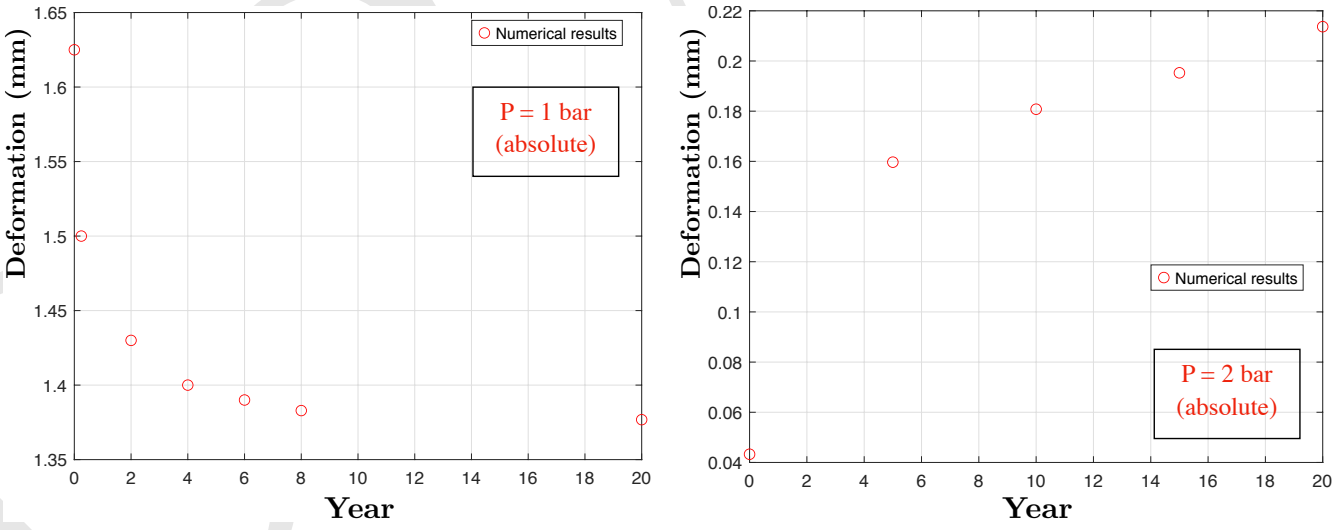


Figure 6.24: Variations in the maximal straw elongation and related frame deformations due to the creep rate expected over a period of 20 years for the full-scale STT module. Left plot: Maximal deformation per side of an unconstrained STT module at 1 bar absolute pressure (Figure 6.22). Right plot: Maximal deformation per side of an unconstrained STT module at the operating pressure of 2 bar absolute.

Long-term effects of straw relaxation A progressive relaxation of the straw material is expected over time, resulting in a reduction of its tension. The corresponding creep (relaxation) rate was measured for the STT straws, showing a characteristic logarithmic dependence as a function of time (Section 6.15.2). In order to evaluate the impact of such an effect on the operation of the STT modules, the measured creep rate was implemented in the FEA and a data-taking period of 20 years was simulated. As described in Section 6.13.9, the straws are stored for 100 days with an internal pressure of 3 bar relative to stabilize their plastic film before the module assembly. The residual creep rate expected during operation is therefore substantially reduced by the logarithmic behavior. Figure 6.24 summarizes the results of the mechanical analysis of the largest STT module 3.9 m×3.3 m. The maximal variation in the frame deformations from the relaxation with the straws temporarily kept at atmospheric pressure (e.g. during module manipulation) is less than 250 μm after 20 years. The corresponding reduction in the tension is automatically compensated by the operation with an internal overpressure of 1 bar relative, which is acting as a natural spring. The overall net effect on the frame deformations is therefore a minimal outward deflection of about 200 μm per side after 20 years.

6.6 Detector Technology

The core technology required to build STT is well established [59] as various straw trackers have been successfully built and operated in the past decades [60–62]. The STT detector concept is similar to the ATLAS TRT [55, 56, 63] and COMPASS [64, 65] straw tracker, which have been smoothly operated for close to 20 years. In particular, the ATLAS TRT is a large straw detector with about 300×10^3 straws, while the COMPASS straw tracker is based on planar modules about 4.5 m × 3.2 m and 40 mm thick with a geometry very similar to the STT modules. Low mass straws have been successfully developed for various modern experiments for precision physics or the search for rare processes including NA62 [66], COMET [67], Mu2e [68], PANDA [54], and SHiP [69]. All the components required to build the STT can be manufactured industrially by vendors to be assembled into the final STT modules at the project production centers.

The use of the straw tube technology offers a number of advantages:

- Each straw is a self-contained detector unit. If a sense wire is broken the corresponding channel can be electrically isolated without impact on the overall performance.
- The electric field is radially symmetric and the hit resolution is independent from the incident angle of the particles.
- Safe operation with a large internal overpressure, resulting in a simplified mechanical structure of the tracker and an improved resolution.
- Common grounding of all straws with only anode wires and no field wires, allowing a lighter support structure.
- Flexible straw layout allows thin self-supporting modules, which are functionally and mechanically independent.
- Transition Radiation (TR) capability for the $e^{\pm}$ identification (π rejection $\sim 10^{-3}$) using a Xe gas mixture.

DRAFT

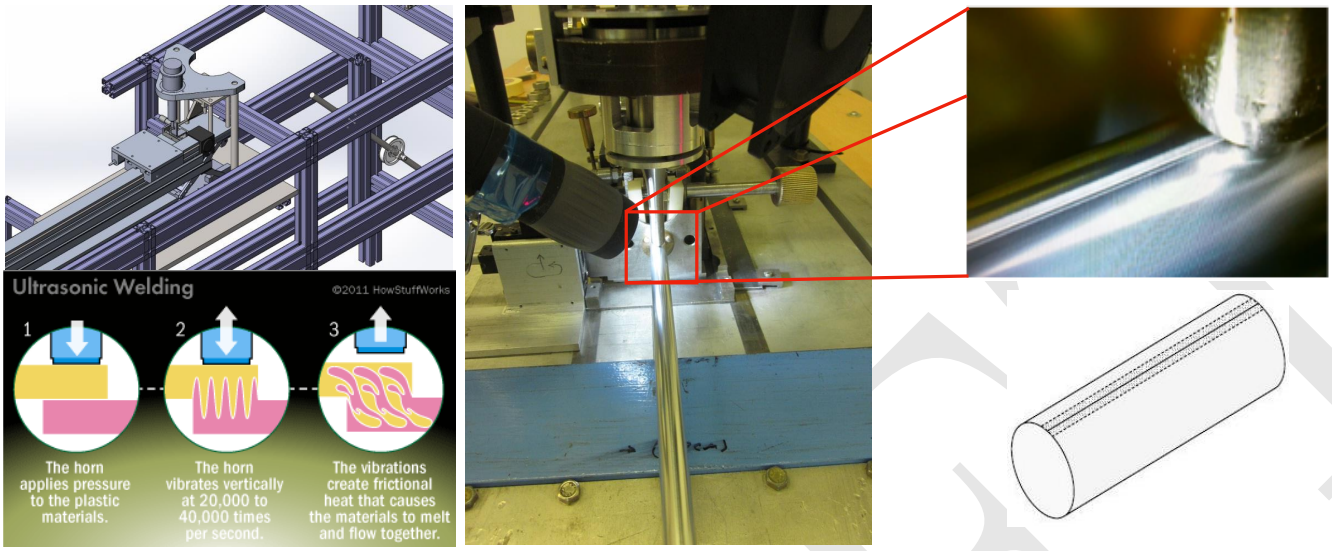


Figure 6.25: Illustration of the ultrasonic welding technology for the production of cylindrical straws from a single strip of aluminized Mylar film. The welding head is connected to a 27 kHz Ultrasonic generator Giminey AUS-0,1/27-OMA.

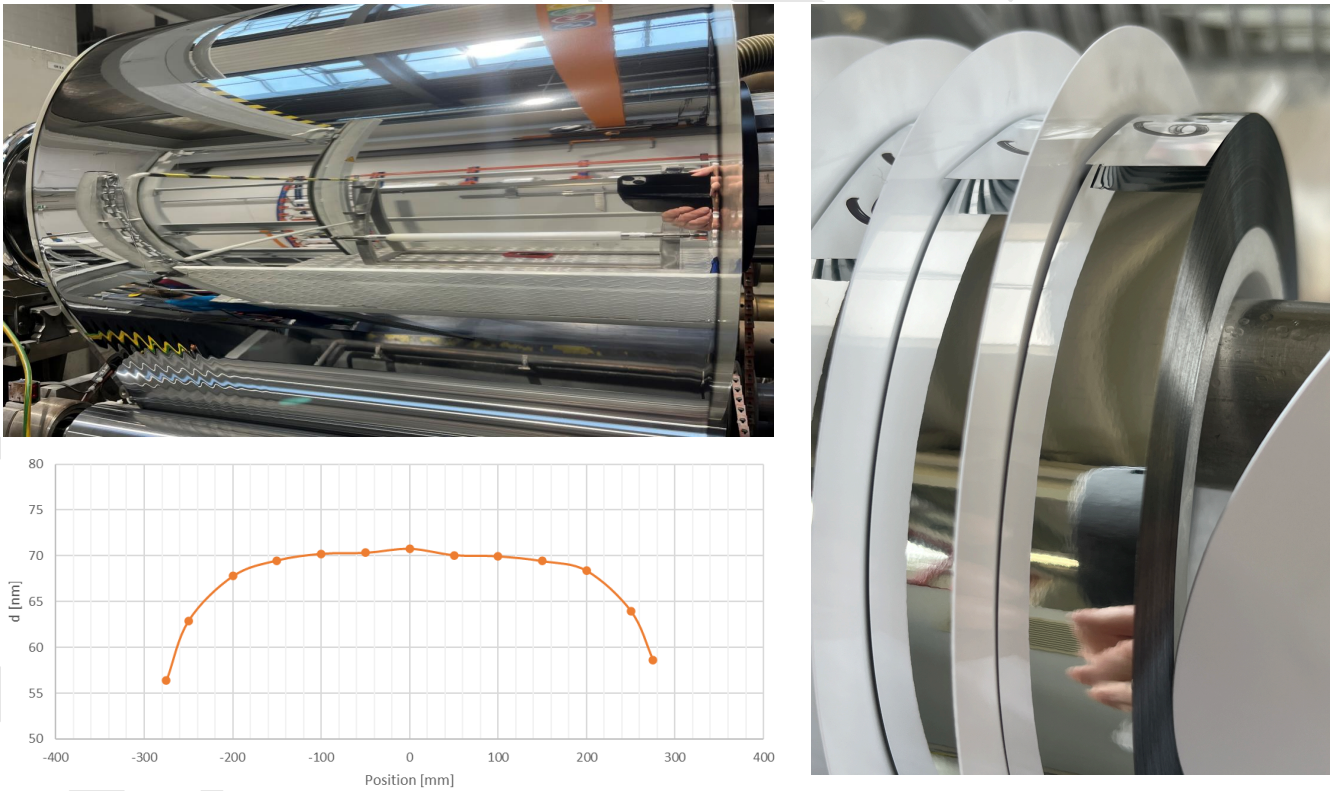


Figure 6.26: Production of film for the STT straws at Fraunhofer FEP: 19 μm Hostaphan RNK19 with double side Al metallization 70 nm thick. The film is cut into strips with width $16.20 \pm 0.03\,\mu$m.

Ultrasonic welding The mass of the straws for the STT was minimized using single-wall straws fabricated with the ultrasonic welding technology, which was developed by JINR and CERN for the NA62 experiment [66]. This technique does not require multiple over-woven layers nor gluing of the plastic films, reducing the total mass and simplifying the straw production. A single Mylar film is rolled and attached to itself in a straight line using ultrasonic welding as schematically shown in Figure 6.25. This method allows the straws to be pre-tensioned using an initial over-pressure of 2.5 bar relative during the assembly of the STT tracking modules. The corresponding seam width is about 600 μm, which is small enough to maintain the circular shape of the cross-section with an internal operating pressure exceeding about 0.2 bar relative. The straws produced with ultrasonic welding technology are characterized by improved mechanical properties and gas tightness compared with the ones produced with the older winding technology, as discussed in Section 6.12.1.

The material selected for the straw production is the base film Hostaphan RNK19 19 μm thick, with a double aluminum metallization 70 nm thick on both film sides. The industrial production of the film was developed together with Fraunhofer FEP and is illustrated in Figure 6.26. Two different coating procedures were tested. The first one uses a special cooling drum, which delivers an improved heat transfer (GKW). This GKW in combination with an electron beam gun evaporation is part of a special machine setup at FEP to the roll coating machine novoFlex. A second procedure uses a boat evaporator and a standard cooling drum for the metallization, resulting in a reduced production time and cost. Both procedures were found to give consistent results with a rather uniform thickness of the Al metallization and no major wrinkles observed across the film roll. After completing the metallization the film is cut into strips 16.20 ± 0.03 μm wide and rolled onto coils with 76 mm inner diameter containing about 300 m of total film each (Figure 6.26).

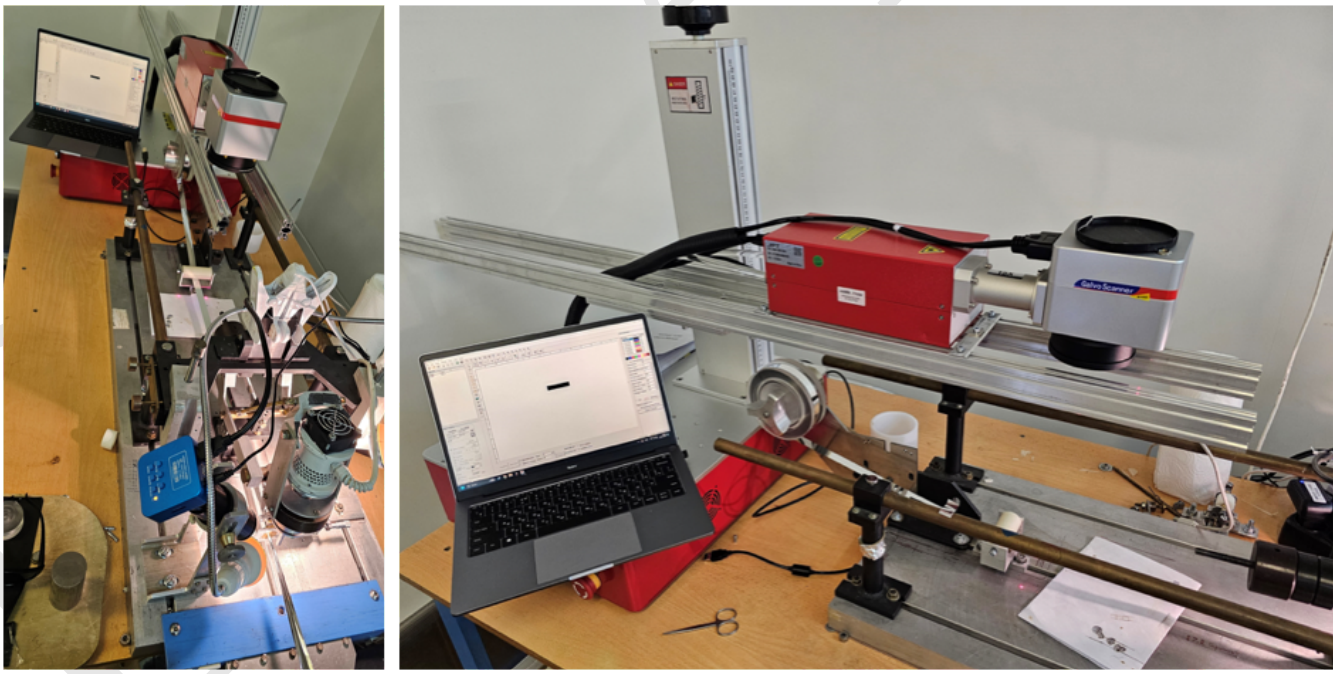


Figure 6.27: Integration of a UV laser with 355 nm wavelength into the straw production line. After passing through the laser, the tape is directed to the ultrasonic welding head.

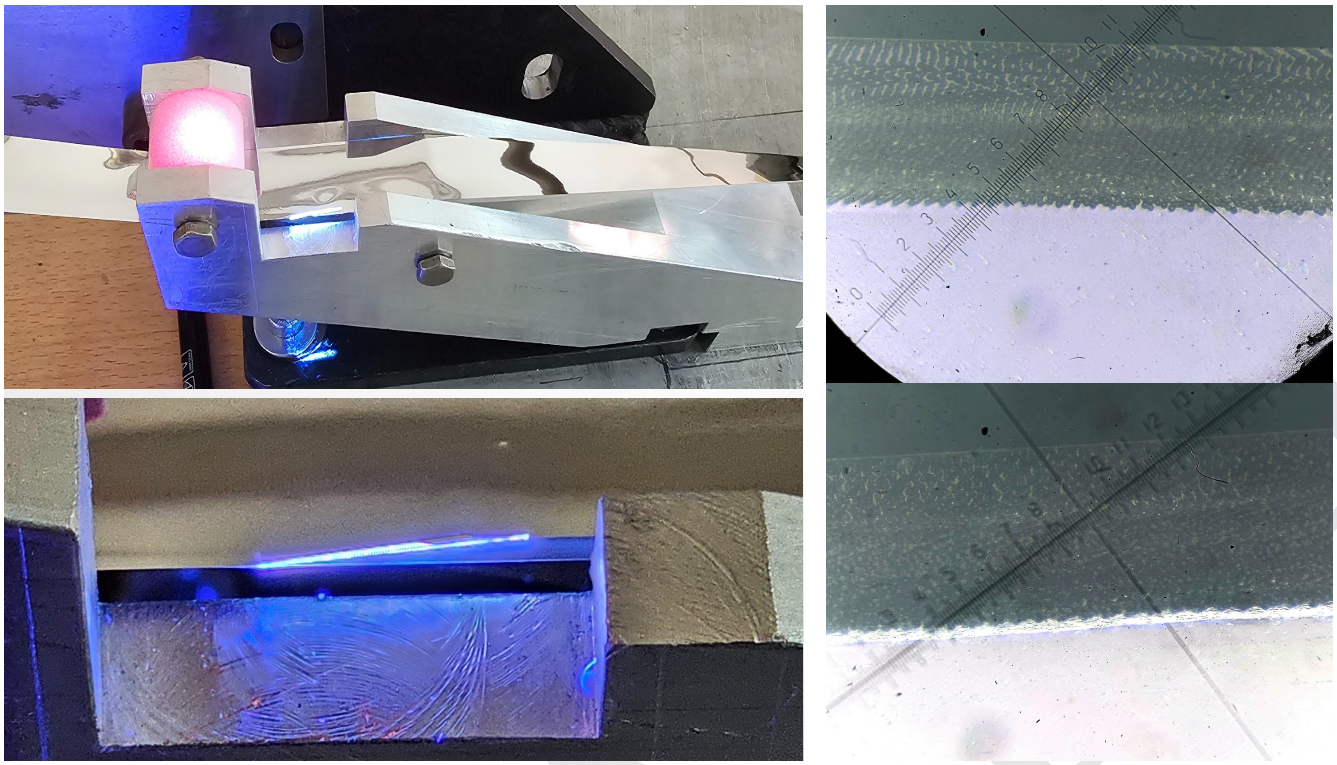


Figure 6.28: Details of the removal of the aluminum metallization in the welding area on one side of the Fraunhofer film with the 355 nm laser.

For the first time, a film with double aluminum metallization on both film sides has been used for the production of straws using the ultrasonic welding technology. The advantages are a better protection of the base film with reduced gas permeability, reduced impedance with both aluminum layers connected to the common ground, and a reduced sensitivity to ambient parameters and straw aging. Dedicated tooling was developed in order to achieve a stable and efficient welding process ready for the mass production of the straws. In particular, a UV laser with 355 nm wavelength was directly integrated into the straw production lines equipped with the ultrasonic welding technology (Figure 6.27). The laser is used for the removal of the aluminum metallization in a welding area of about 500 μm on one side of the Fraunhofer film, as illustrated in Figure 6.28. The tape unwound from the coil and moving with constant speed first passes below the UV laser to be then directed under the ultrasonic head for the welding of the complete straw. The procedure was validated during the production of the straws for the 1.2 m (Section 6.12.4) and full-scale (Section 6.12.9) STT prototypes.

Straw production line The main functional blocks of a straw production line equipped with the ultrasonic welding technology are shown in Figure 6.29. The corresponding hardware components are listed in Figure 6.30. The production settings, geometry, and materials for the STT were optimized during the fabrication of the large number of straws required for the various STT prototypes (Section 6.12). The following facilities are currently operational and available for mass production: (i) a 5 m long straw production line at JINR originally developed for NA62; (ii) a double 5 m long straw production line installed in 2024 at GTU, Georgia; (iii) a 2 m long straw production line operated by GTU at JINR originally developed for COMET. The straw production

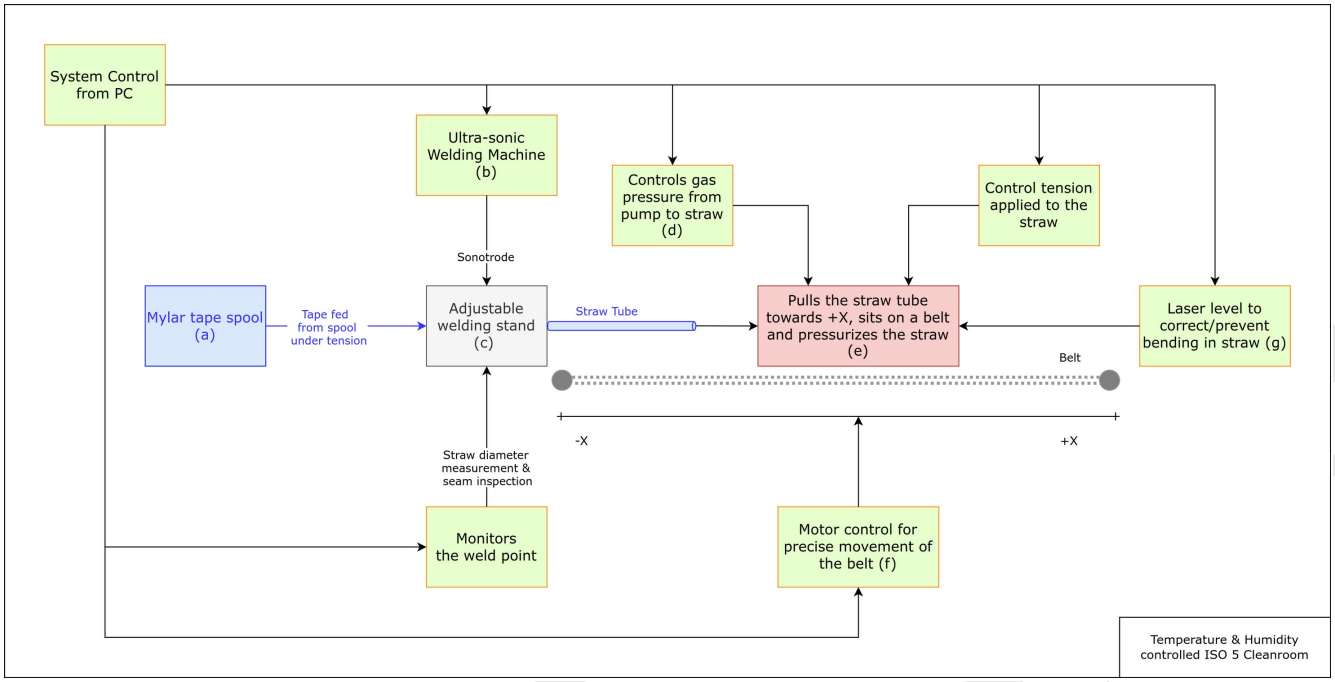


Figure 6.29: Main functional blocks for a straw production line with ultrasonic welding technology.

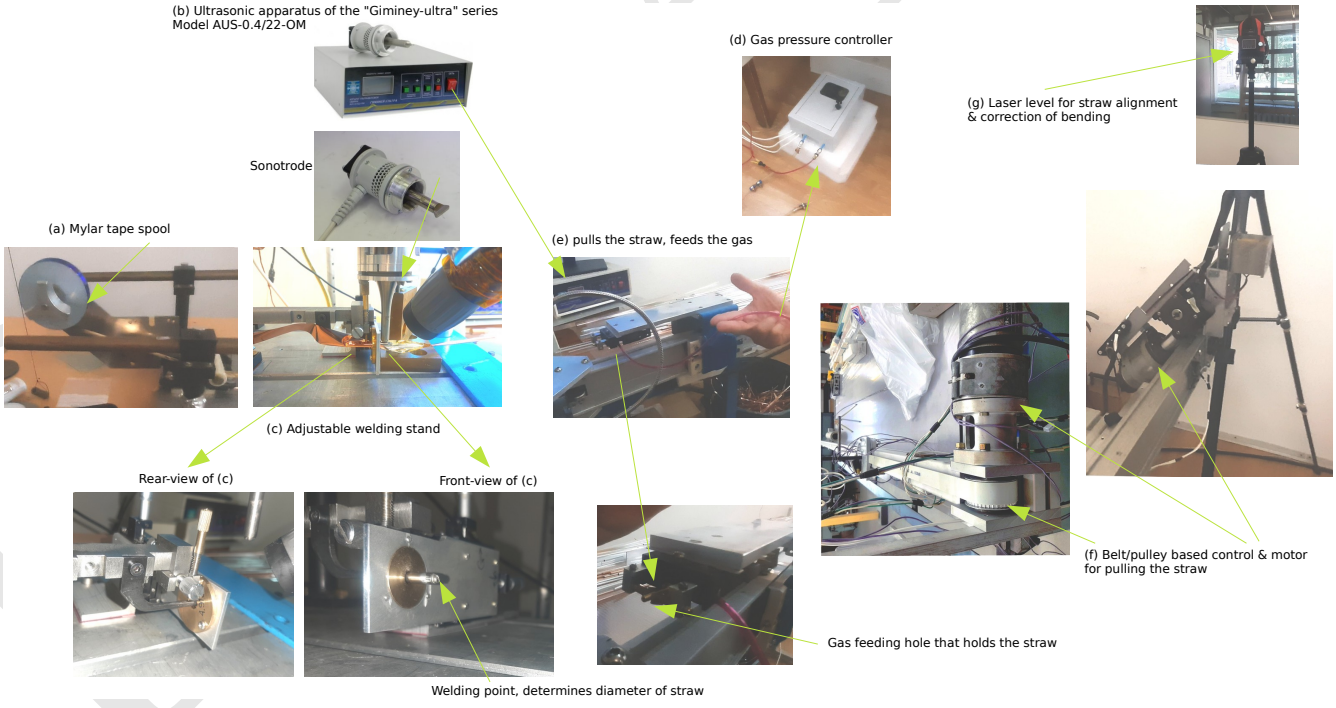


Figure 6.30: Main components in a straw production line with ultrasonic welding technology.

facilities include an ISO class 5 cleanroom with regulated temperature and humidity, as well as multiple quality control stands for various tests. Quality controls performed in parallel with the straw production include optical dimensional tests, inner and outer seam inspection with optical microscope, over-pressure test, leak tests, tension and aging tests (Section 6.13.9). The tested production capability of such lines is about 50 straws/day for 5 m straws, including all quality controls.

6.7 Electronic Readout

6.7.1 Integrated Readout Boards

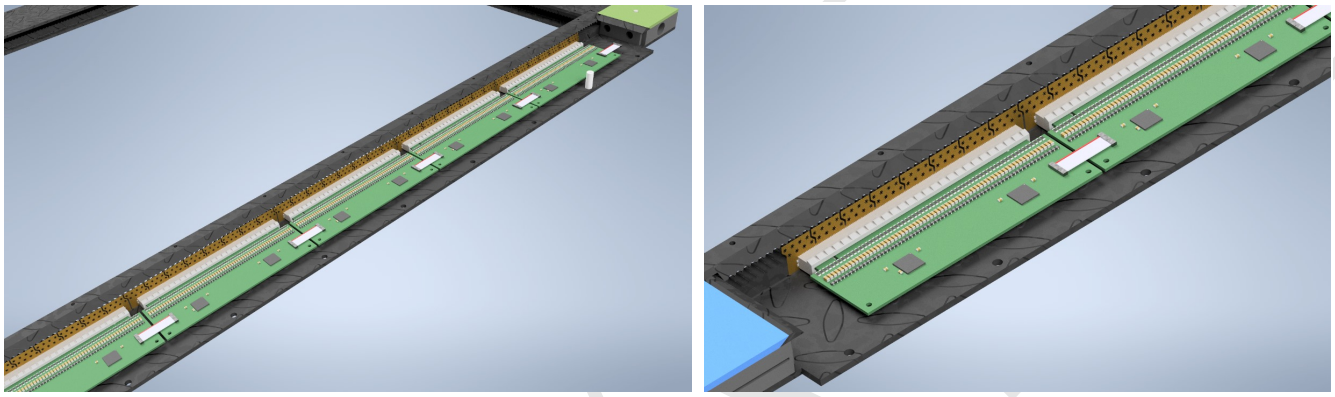


Figure 6.31: Readout boards integrated into the C-fiber frame of one STT module.

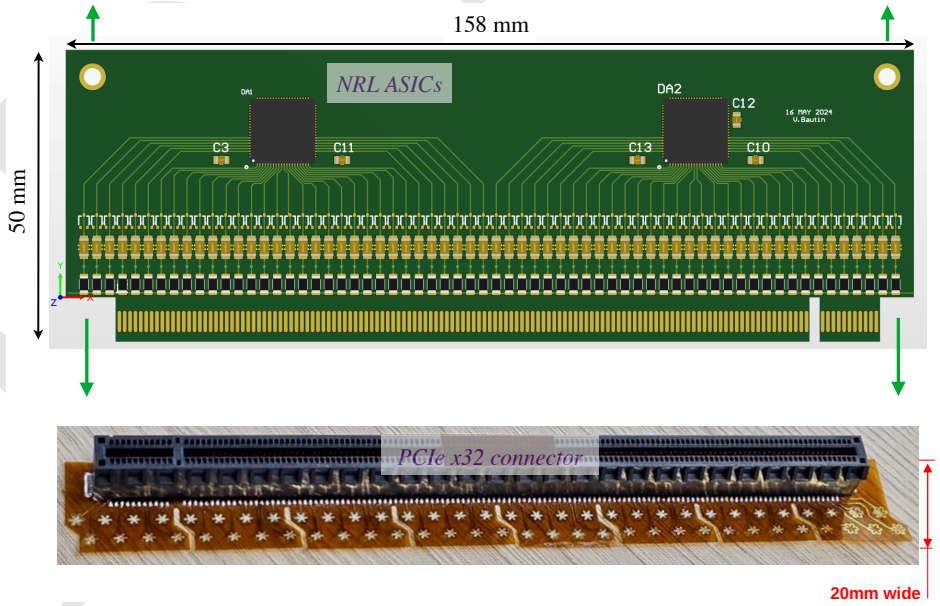


Figure 6.32: Top picture: Integrated board reading 64 straws with ASIC and micro-controller (MCU). Bottom picture: Flexible kapton PCB with PCIe connector.

The design of the electronic readout for the STT follows two main principles:

- Self-contained straw tracking modules which can withstand multiple extractions, insertions and manipulation without damages;
- Early digitization of the signals close to the straw pins, avoiding the extraction of analog signals from the modules.

The implemented solution is based on small low-power readout boards directly integrated within the C-fiber frame of the STT modules. A potential drawback of this choice is represented by the need to access the electronics for detector maintenance. As a mitigation, a highly modular design was developed, in which the readout boards can be replaced through the removable side lids in the C-fiber frames (Section 6.5.1). All electronics and capacitors will be also extensively tested before installation. The single hit space resolution for the straws is required to be $< 200\,\mu$m at 1 bar absolute pressure and the time resolution to be better than 1 ns. A simultaneous measurement of the signal charge is required for particle identification via dE/dx and transition radiation, as well as for noise suppression.

Modular MCU-controlled boards Strict low-power consumption requirements combined with the relatively modest rates led to the development of a micro-controller-based (MCU) readout electronics concept for STT. The design is based on compact modular boards reading 64 channels minimizing the signal path from the straws. Figure 6.31 illustrates how the boards are installed within the C-fiber frame of a STT module. Each readout board includes an analogue front-end with 64-channel ASICs, as well as a digital back-end data processing using STM32G4 Series of mixed-signal MCUs (Figure 6.32). The resulting digital output signal is directly fed to the DAQ system of the experiment via bi-directional connections also providing the input clock and trigger signals. The total power consumption of the readout board is dominated by the ASIC chip and is ≤ 0.8 W including the ASIC, MCU, linear regulators (LDO), and all other components.

Flexible kapton PCBs with PCIe connector The connection of the straws with the readout boards is achieved with a flexible kapton printed circuit board (Figure 6.32), which is directly glued at the bottom of the C-fiber frame on the side of each straw double layer. The base kapton film is $50\,\mu$m thick and is covered by coverlay protection $50\,\mu$m thick on the trace side. Each kapton PCB connects 64 straws to one readout board via a PCIe x32 connector. This configuration results in a typical length of the traces between the straw pins and the connector of only about 10 mm. The electrical contact with the crimped pins of the straws is provided by holes characterized by 6 inward-pointing "petals" with double side Ni/Au coating ($1\,\mu$m Ni, $0.05\,\mu$m Au). The thickness of the kapton PCB is chosen to optimize its rigidity for good and stable contacts. It was verified that the crimping pin external diameter of 1.2 mm provides good electrical contact.

The possibility to add small plastic caps on top of the pins is also considered to secure the contacts. The PCIe connector allows a straightforward replacement or upgrade of the readout boards by extracting them after opening the corresponding lid of the C-fiber frame, similarly to the replacement of a memory card in a PC.

HV and low voltage (LV) protections The traces on the kapton PCB provide a combined HV and signal connection to the straw wires. The integrated readout boards include an appropriate HV decoupling capacitor (1206 package, maximal voltage available from 2.0 kV up to 3.0 kV) and a resistor for each channel. All HV capacitors will go through a long-term test at a higher voltage

DRAFT

before being used. Each board also includes a solid state relay (SSR) with a SiC MOSFET rated up to a maximal voltage of 3.3 kV and maximal current of 30 nA to allow a remote switching of the HV, as well as low voltage surge protections.

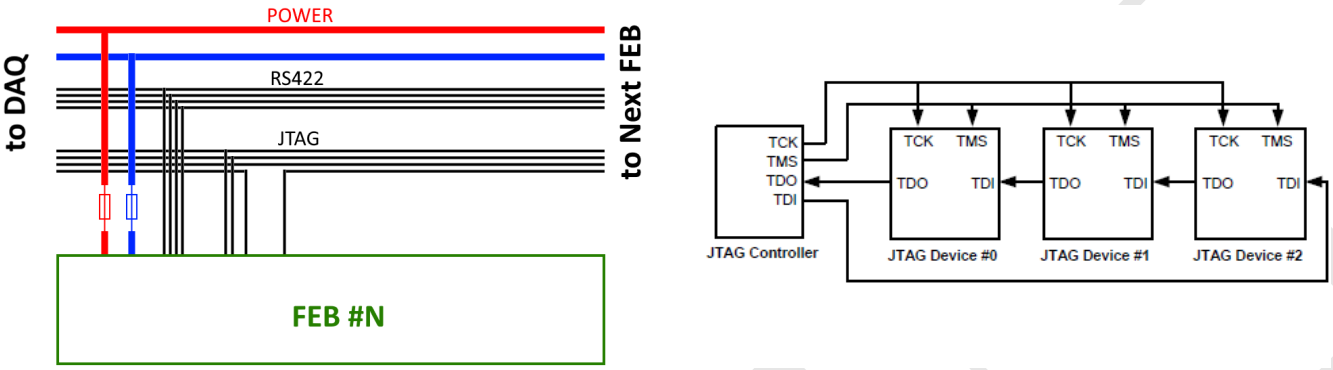


Figure 6.33: Left picture: Schematic diagram of the BUS interface connecting in parallel the STT integrated readout boards. Right Picture: Schematic diagram of the JTAG connections to update the firmware across all readout boards.

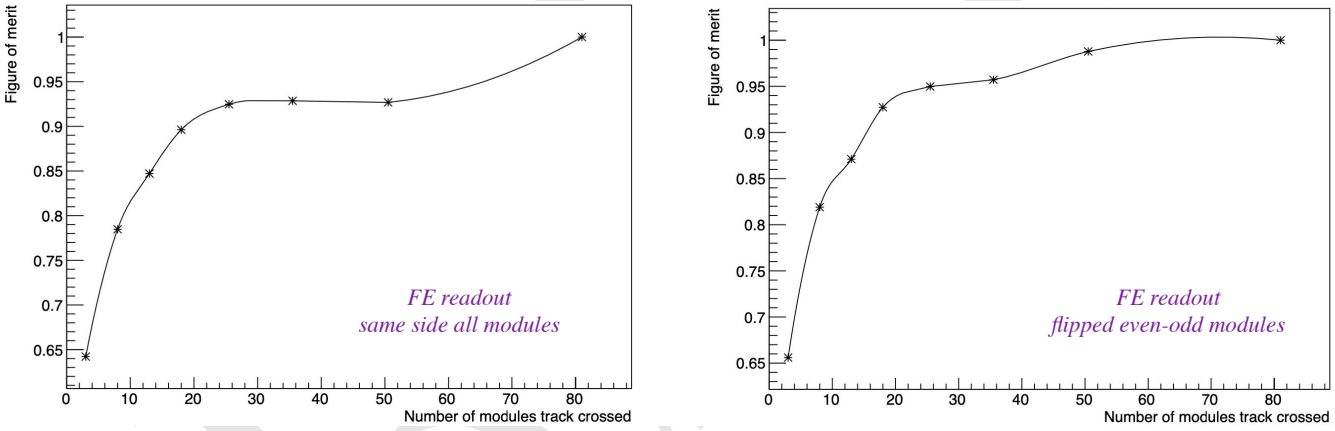


Figure 6.34: Rejection power against the ghost tracks reconstructed in STT obtained by alternating the location of the readout boards in even and odd STT modules.

Parallel BUS interface The straws are readout from a single side and all the readout boards connecting a double straw layers are integrated into one side of the C-fiber frame, which can then include up to a maximum of 24 boards. The boards are connected in parallel via a BUS interface (Figure 6.33) so that the failure of a single board does not affect the data taking of the remaining ones. A transceiver LTC2855 provides a reliable RS422 driver supporting up to 256 nodes per BUS and maintaining a high output impedance over the entire common mode range when disabled or when the supply is removed. A JTAG chain connection (Figure 6.33) is used to flash all boards when a firmware update is required.

Rejection of ghost tracks The use of a projective XXYY straw geometry with a single side readout in STT could potentially result in the reconstruction of ghost tracks when hits from multiple tracks are present. The rejection of ghost tracks was studied using ν_μ CC interactions

randomly simulated with GENIE+Geant4 within the STT fiducial volume. It was found that about 84% of the tracks can be matched to an energy deposition in the 4π surrounding ECAL, which can resolve the ambiguity generating the ghost tracks. Furthermore, only about 7.5% of the track pairs cross the same STT modules across their entire length. It was, therefore, concluded that ghost tracks are generated only for 1.5% of the track pairs that are crossing the same modules in STT but are not matched to an ECAL cell. Tracks were reconstructed from a 3D matching after separate 2D circular fitting of tracks in the YZ bending plane and linear fitting in the XZ plane. The straw hits are obtained as drift circles from the measured time $\Delta t = t_{\text{drift}} + t_{\text{wire}}$ after subtracting the propagation time along the wire, t_{wire}, from the actual drift time, t_{drift}. For ghost hit combinations, the reconstruction involves subtracting an incorrect propagation time, resulting in a larger χ^2 from the track fit. A combination of χ^2 from the separate YZ and XY fits was used to reject ghost tracks. Figure 6.34 shows the resulting rejection power against the ghost tracks. It was found that by alternating the location of the single readout in even and odd STT modules (left-right and up-down), it is possible to significantly enhance the rejection of ghost tracks, depending on the STT timing resolution assumed. Results are summarized in Table 6.4. The residual fraction of ghost tracks is reduced to 0.1-0.3% of the total. The detector geometry with XX and YY staggered double layers appears, therefore, adequate, and a third orientation of the straws is not needed.

Table 6.4: Average rejection power against the ghost tracks reconstructed in STT with different readout configurations and timing resolutions.

Configuration	Resolution 1 ns	Resolution 2 ns	Resolution 5 ns
FE same side (1-10 modules)	0.763	0.724	0.702
FE same side (>10 modules)	0.889	0.855	0.824
FE alternated (1-10 modules)	0.787	0.754	0.729
FE alternated (>10 modules)	0.917	0.889	0.849

Design variants with different ASICs Design variants of the STT readout board with a similar layout and components, but different ASIC chips are available. The modularity of the boards and the use of the PCIe connectors provide a flexible design, allowing for easy exchange of individual STT readout boards. In particular, the performance of two readily available ASIC chips, characterized by different architectures, was tested (Figure 6.35): (i) the VMM3a chip reading 64 channels; (ii) the NRL chip reading 32 channels. Readout boards equipped with VMM3a are planned for the initial STT data taking to minimize project risks (Section 6.7.2). The NRL analog chip was developed for space applications and is interesting due to a dual sub-channel architecture, including a fast shaper with a threshold discriminator for time measurement and a separate slow shaper with peak detection for energy measurement. Although the nominal settings available in the NRL chip are not optimal (minimum gain 9.2 mV/fC) for the STT readout, a similar architecture is planned for the custom ASIC being developed for the STT upgrades (Section 6.7.3), considering the need for simultaneous time and charge measurements in STT. The NRL chip has a lower power consumption with respect to the VMM3a as it does not include the complex digital functionality of the latter.

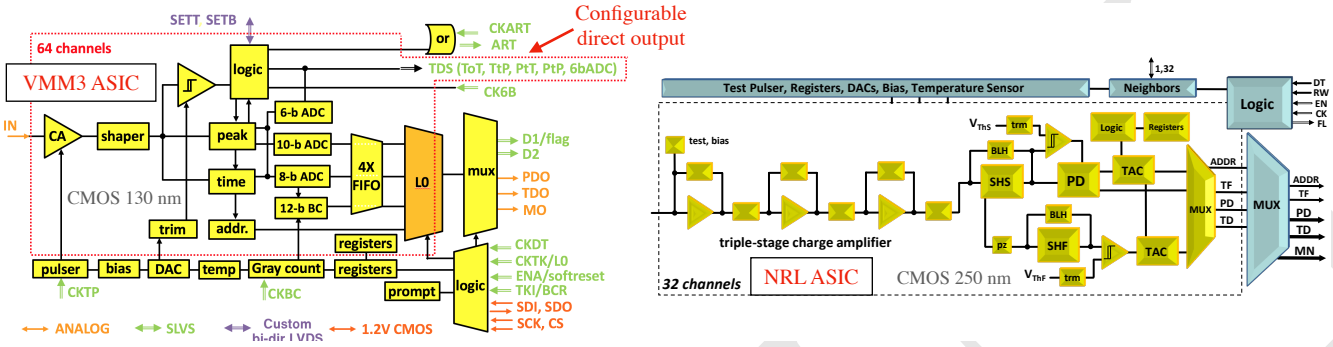


Figure 6.35: Left picture: Architecture of the existing VMM3 chip reading 64 channels. Right picture: Architecture of the existing NRL chip reading 32 channels.

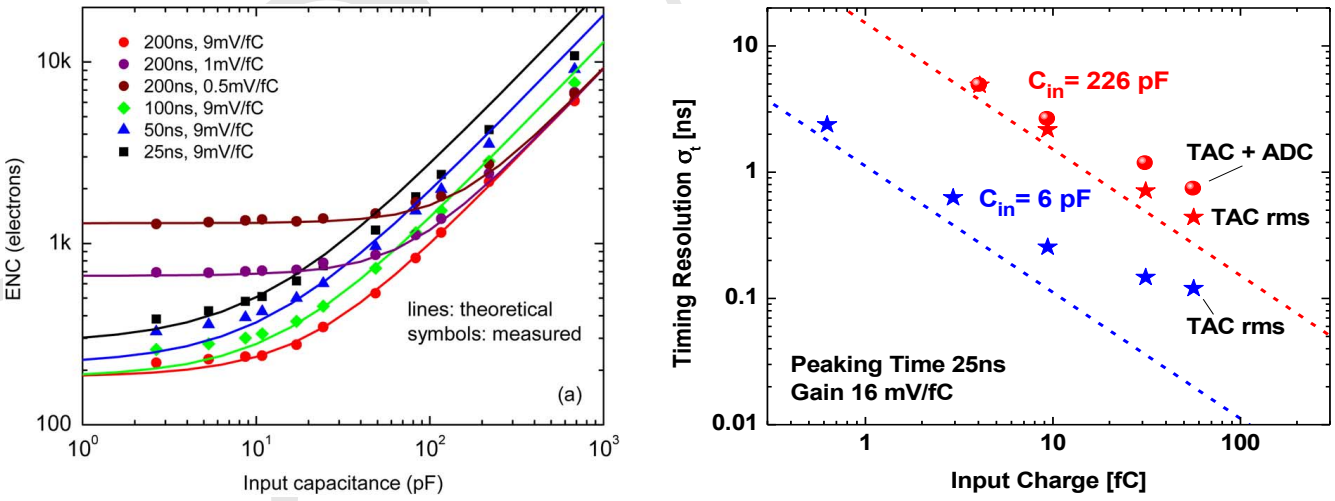


Figure 6.36: Left plot: VMM3a equivalent noise charge for a variety of ASIC gain and shaping time settings [70]. Right plot: VMM3a time resolution as a function of input charge [71].

6.7.2 VMM3a Readout

VMM3a design The VMM3a is a low-power, high-performance, 64 channel ASIC well suited for compact detector readout electronics [70–72] using the GF 130 nm CMOS process (formerly IBM). It was originally developed in the context of the ATLAS New Small Wheel Upgrade to handle the pile-up rate expected at high luminosity. This instrument is the largest MicroPattern Gaseous Detector (MPGD) developed to date with 2.4×10^6 channels, which required industrial production of the VMM3a with related quality and reliability tests. The analog front-end specification of the ASIC allows dual-polarity operation, matches the input capacitance from sub-pF to several hundred pF, measures the maximum input charge amounting to up to 2 pC, and possesses a shaping filter peaking time that allows sub-nanosecond timing resolution. A schematic overview of each VMM3a ASIC channel is shown in Figure 6.35. The preamplifier shaping circuit can be configured to use one of four different peaking times (25, 50, 100, and 200 ns) and eight gain settings (0.5, 1, 3, 4.5, 6, 9, 12, 16 mV/fC). The VMM3a ASIC also has several tail-cancellation options which can be selected by configuration. A channel-specific discriminator triggers on input signals above a configurable threshold to initiate digitization of the amplified pulse with a 10-bit analog-to-digital converter (ADC). Discriminator thresholds are adjusted by a global 10-bit Digital to Analog Converter (DAC) with additional channel-specific 5-bit trimming DACs. A configurable direct output mode allows for the extraction of the analog signals from the chip to be interfaced with an external ADC. In particular, it is planned to take advantage of this feature for the STT readout boards, effectively using only the analog front-end of the chip. Each VMM3 chip can provide detector hit charge and time measurements for 64 individual straws, allowing the use of compact readout electronic boards fully integrated within the frames of the STT modules [73].

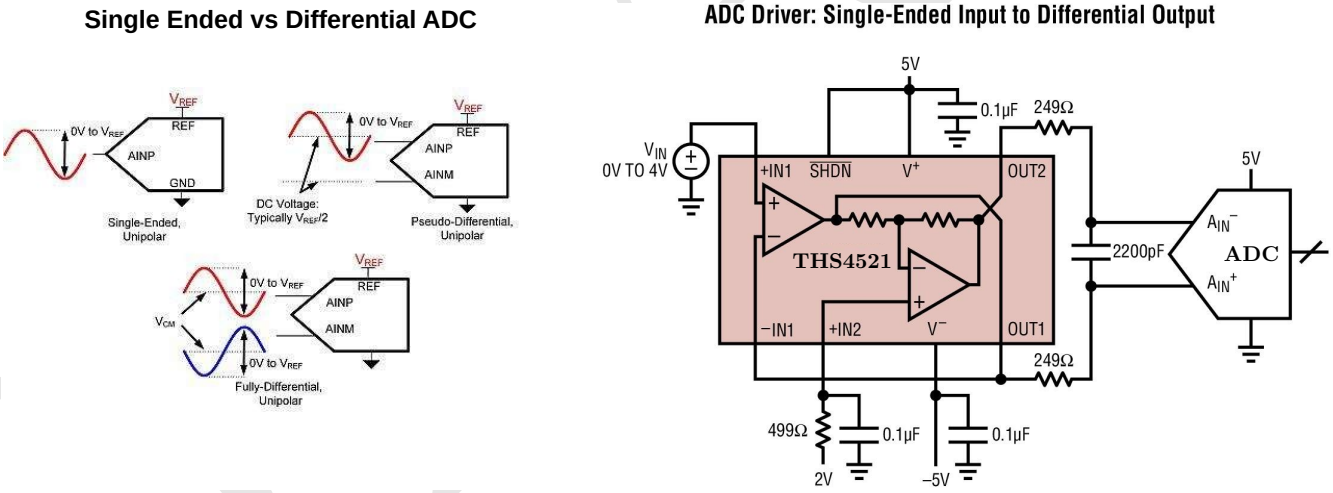


Figure 6.37: Schematics of the differential driver implemented for the VMM3a direct output to a dual ADC on the STT readout boards.

VMM3a performance The electronic noise performance of the VMM ASIC chips has been measured in lab measurements for a range of preamplifier gain and shaping time settings, as shown in Figure 6.36 [70–72]. An equivalent noise charge (ENC) of better than 1000 e^- can generally be achieved with input capacitance less than 100 pF for a variety of shaping time settings. The VMM3a can therefore match the STT low charge threshold requirements, given that the straw tubes in STT have a capacitance of about 10 pF/m (less than 40 pF for the longest straws) and

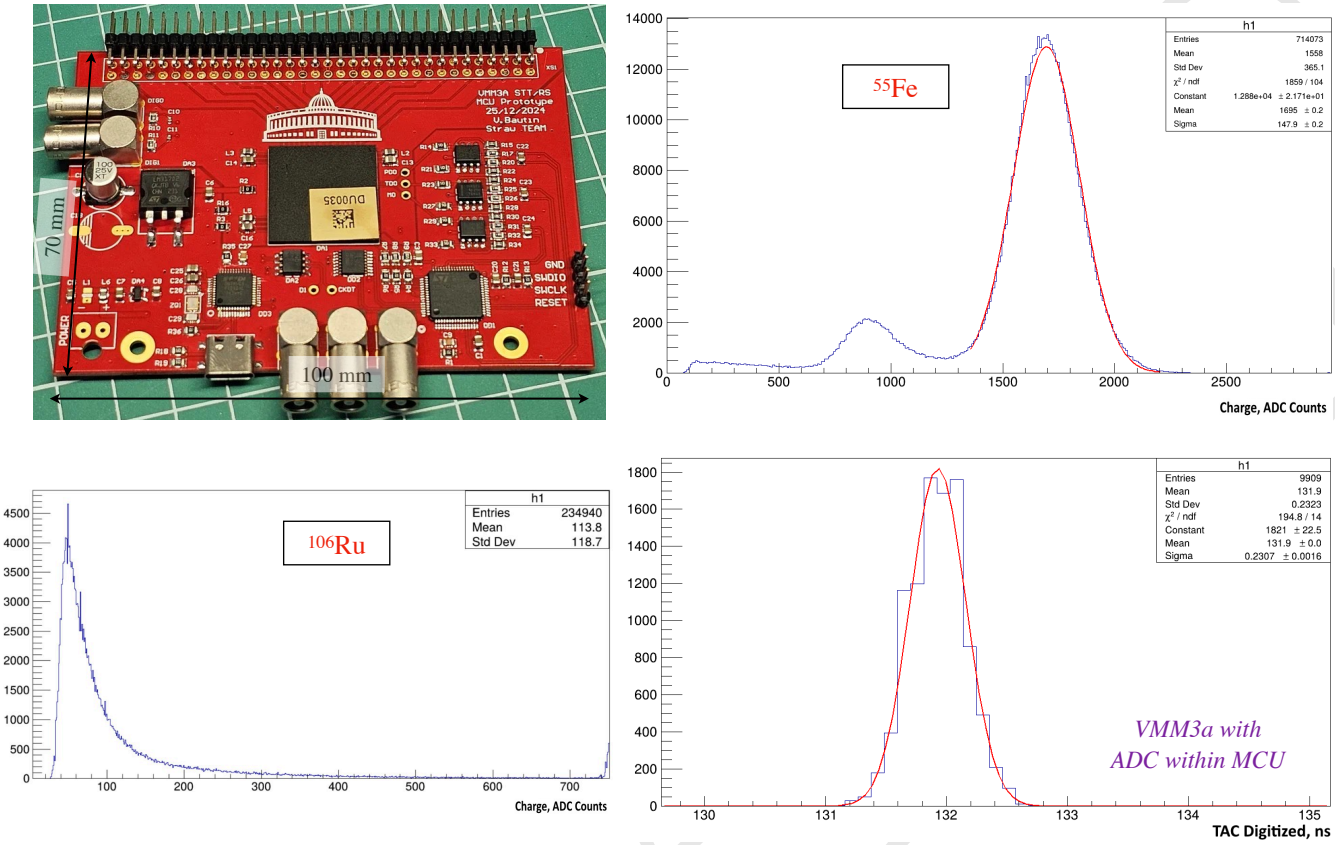


Figure 6.38: Test of a readout board equipped with VMM3a, MCU, and differential drivers for the internal 12-bit 4MSPS ADC of the MCU. The charge measured from the straws in a STT prototype is shown for ^{55}Fe (top right) and ^{106}Ru (bottom left) sources. The timing resolution obtained with test pulses (300 fC) and a 350 ns TAC slope is given in the bottom right plot.

Table 6.5: Timing resolutions obtained from a readout board equipped with VMM3a, MCU, and differential drivers for the internal ADC of the MCU with test pulses (300 fC) and different TAC slopes.

	TAC slope 100 ns	**TAC slope 350 ns**	**TAC slope 650 ns**
Slew rate	10 V/μs	2.8 V/μs	1.5 V/μs
Bin size	30 ps	110 ps	200 ps
Timing resolution	70 ps	230 ps	440 ps

will be operated with a typical gas gain of 2.5×10^4 or above. The time resolution of the VMM3a was also measured in the lab, and the results are summarized as a function of input charge in Figure 6.36. Time resolutions better than 1 ns are obtained for 10-40 pF input capacitance and input charges greater than a few fC, with much better time resolution achievable with higher input signal amplitude. The VMM3a can therefore satisfy the STT time resolution requirements given the expected gain and input capacitance.

The signal/noise (S/N) ratio for minimum ionizing particle (MIP) can be estimated with the VMM3a readout. Given the straw capacitance < 40 pF, the equivalent noise charge (ENC) from the VMM3a front-end is approximately 1000 e^-. With the Xe/CO_2 (Ar/CO_2) 70/30 gas mixture operated at an absolute pressure of 2 bar, the total number of electron–ion pairs produced by a MIP is expected to be 497(208) per centimeter, with 78(56) primary pairs per centimeter. Assuming an average track path of 0.39 cm within the straws, about 194 (81) total electron–ion pairs are produced per MIP, corresponding to a S/N ratio of 4,850 (2,025) for a nominal gas gain of approximately 2.5×10^4. Most of this charge is expected to be collected with a 50 ns shaping time.

Analog front-end with external ADC The VMM3 chip is operated in an external ADC mode to bypass the integrated digital back-end, which proved to be a limiting factor in the test beam exposures (Section 6.12.8). Given the modest straw occupancy of about 3% expected in STT (Figure 6.39), the digital processing is expected to require relatively low power, motivating the the development of a MCU-based implementation with separate analog FE ASIC and digital back-end processing. As discussed in Section 6.7.1, both the analog ASIC and the MCU for the digital back-end are located on the same readout board, minimizing the signal path. A maximal drift distance of 2.5 mm in the STT straws implies that the charge is expected to be collected within a time window of about 50 ns (Figure 6.40). Therefore, a common peaking time of 50 ns can be used to perform both charge and time measurements in STT with appropriate time-walk corrections. The performance of the VMM3a was tested in direct analog output mode using prototype boards in which the internal 12-bit, 4 MSPS ADC integrated within the MCU was used for signal digitization. To this end, fully-differential dedicated drivers were implemented separately for the peak detection output (PDO), the time detection output (TDO), and the monitoring output of VMM3a, as illustrated in Figure 6.37. The benefits include improved ADC resolution, as well as an increased common mode rejection in noisy environments. Figure 6.38 shows the results obtained from charge measurements with a small STT prototype operated with Ar/CO_2 70/30 and ^{55}Fe and ^{106}Ru sources. The timing resolution achievable was tested by injecting test pulses with an equivalent charge of 300 fC and by varying the programmable slope of the Time to Amplitude Converter (TAC) in the VMM3a from 100 ns to 650 ns. Results are summarized in Table 6.5. With a TAC slope of 350 ns a timing resolution of 0.23 ns was obtained (Figure 6.38). The corresponding timing resolution for straw signals was found to be consistent with the STT requirements.

Optimization of the TAC slope and readout timing The choice of the TAC slope for the STT readout was optimized by simulating inclusive CC and NC interactions in the entire SAND detector including the magnet, ECAL, GRAIN, and the STT, as well as in the surrounding rocks of the ND hall. A complete GENIE+Geant4 detector simulation was used, and a full 9.6 μs beam spill simulation was obtained by randomly overlapping the STT and ECAL hits from all the events generated within the spill with their own timing information. The STT straws were split into groups of 64 channels, each assigned to an individual VMM3a readout board. For each value of

the TAC slope Δt_{TAC} a clock frequency $f_{clock} = 2/\Delta t_{\mathrm{TAC}}$ was used. All hits occurring in the 64 channels within a time window $\Delta t = t_{\mathrm{stop}} - t_{\mathrm{start}}$ were accepted, where t_{start} is the time of the arrival of the first signal on one of the 64 wires, and the common t_{stop} is given by the end of the clock interval following the one during which the start signal occurred. After the common stop a dead-time to process the received hits was introduced for each readout board. Different conservative options were considered for the dead-time, including both fixed values ranging from 500 ns to 1.500 ns and a variable value equal to 500 ns times the number of hits recorded within the 64 straws connected to the VMM3a readout board. After the dead-time the readout board becomes active again. Results for the fraction of STT hits within the 9.6 μs neutrino spill accepted by the VMM3a readout are summarized in Table 6.6. The impact of the few lost hits on the acceptance and reconstruction of particle tracks was found to be negligible, as discussed in Section 6.18.1.

Table 6.6: Fraction of all STT hits within the 9.6 μs neutrino spill recorded by the VMM3a readout for different values of the acquisition time. The last row corresponds to a variable time equal to 500 ns times the number of hits within the 64 straws connected to the VMM3a readout board.

Acquisition time	TAC 60 ns	TAC 100 ns	TAC 350 ns	TAC 650 ns
500 ns	96.3%	93.1%	90.2%	96.5%
1.000 ns	96.4%	93.2%	90.2%	96.5%
1.500 ns	96.4%	93.3%	90.4%	96.5%
Variable	96.6%	93.5%	90.8%	96.7%

6.7.3 Custom ASIC Upgrade

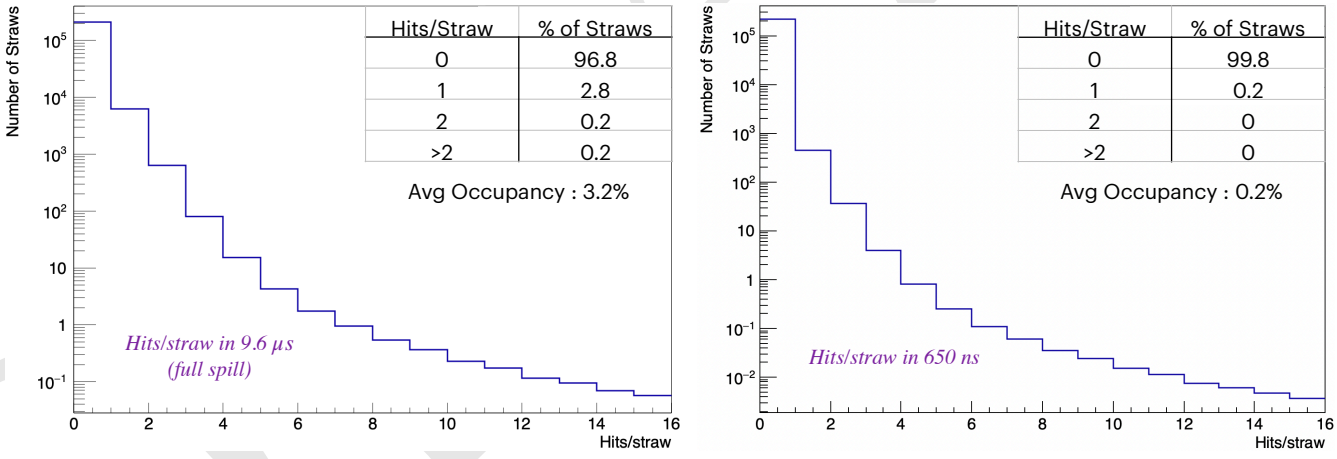


Figure 6.39: Expected straw occupancy in STT within a full 9.6 μs neutrino spill (left plot) and a time window of 650 ns (right plot).

As discussed in Section 6.7.2, readout boards equipped with the existing VMM3a chip are planned for the initial STT data taking to minimize project risks. In parallel, a custom ASIC is being developed to provide simultaneous high-precision measurements of both the amplitude and time of arrival, specifically optimized for the STT and intended for future detector upgrades.

Garfield++ and LTspice simulations In order to define the requirements for the custom ASIC the combined detector and readout response have been studied with simulations including two main

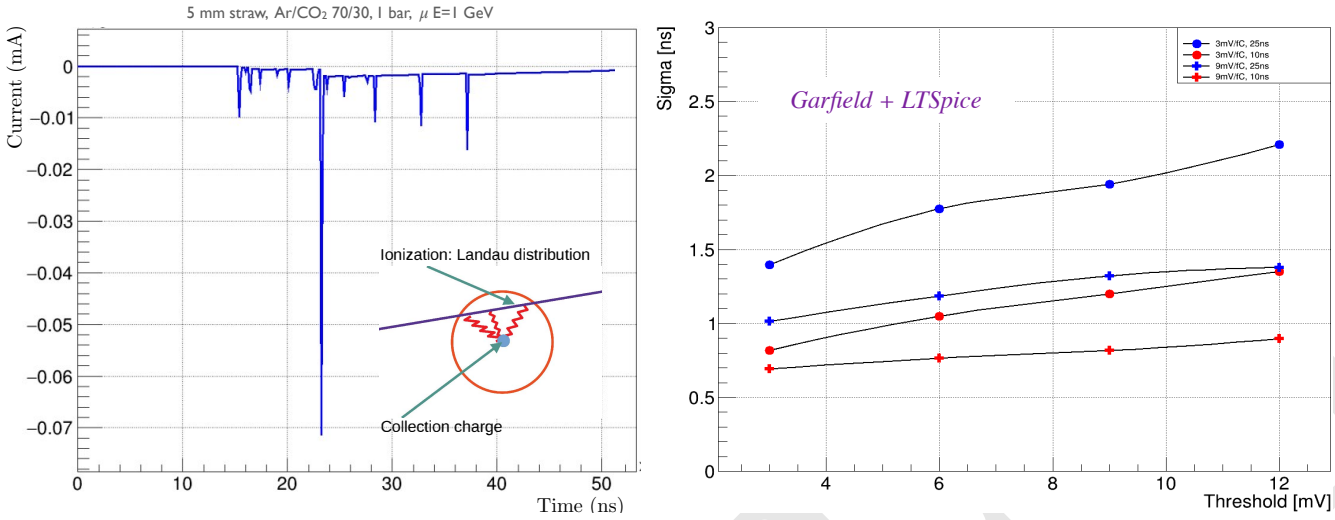


Figure 6.40: Left plot: Typical signal from a muon crossing the STT straws. Right plot: Expected straw timing resolution as a function of the threshold for different values of the peaking time and electronic gain. The curves are not corrected for time walk.

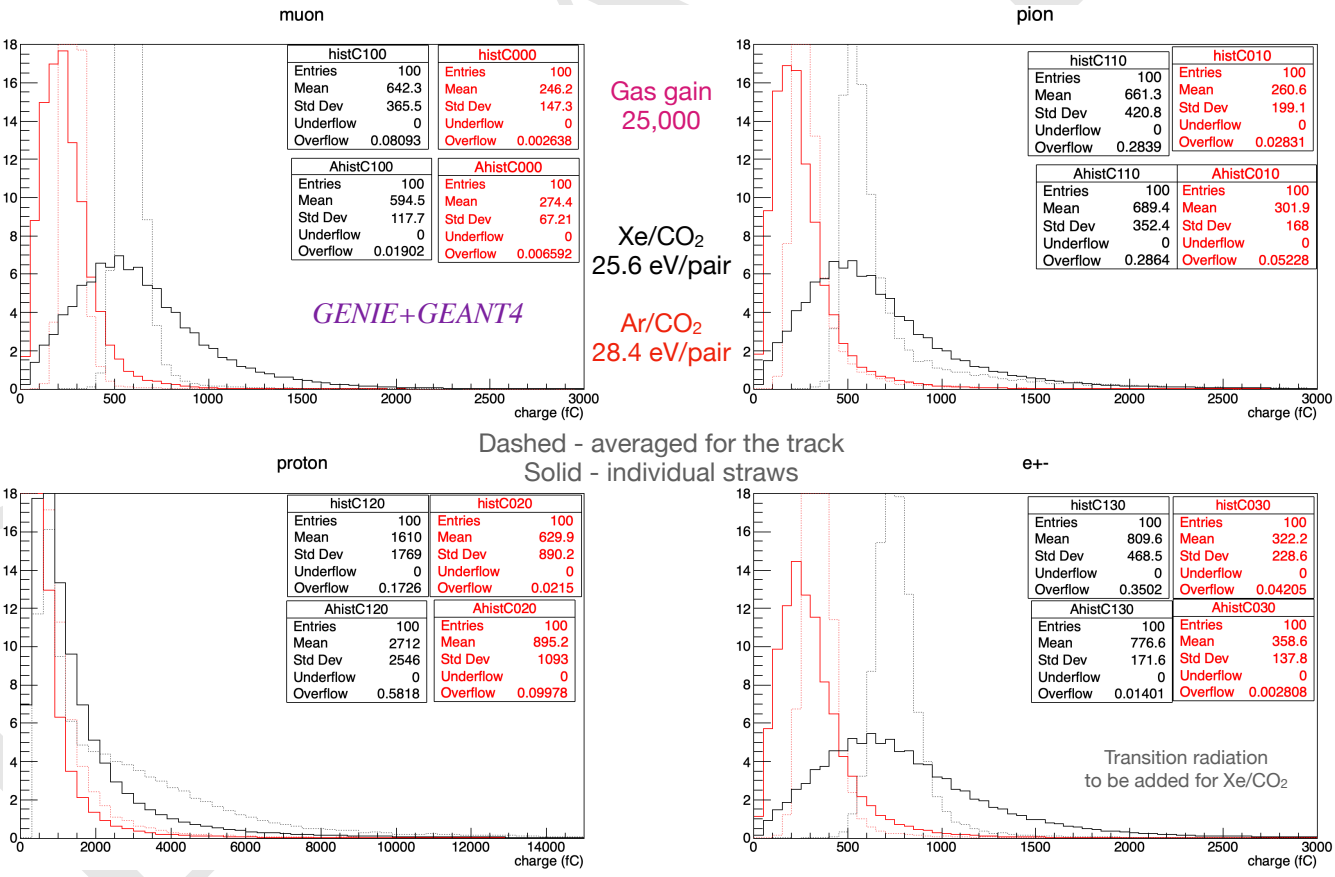


Figure 6.41: Expected charge deposition in the STT straws for different particles with both the Xe/CO_2 and Ar/CO_2 gas mixtures.

aspects: (a) understand and model the basic physical processes taking place in the gas inside the straws, and develop suitable simulation and software tools able to reproduce the physical processes and predict the detector performance; (b) model the response, signal shaping and processing of the STT readout electronics including both the analog front-end and the digital back-end. The first step was based on the Garfield++ package, which is the modern evolution of the well-established simulation code widely employed to evaluate the performance of wire-based gaseous detectors. This package can read 3D field maps computed by Finite Element Method (FEM) or Boundary Element Method (BEM) programs, and can provide a full microscopic simulation of the electron transport processes (scattering, diffusion, amplification), using the electron-atom scattering cross-sections from Magboltz. Figure 6.40 shows the simulation of a typical signal collected at the central wire in a straws crossed by a 1 GeV muon. Fluctuations from both the primary electron-ion pairs produced and the following gas amplification are visible. An optimization of the timing resolution should be based on the early charge signal within about 10-25 ns, while for the energy deposition it is required to maximize the total collected charge in the straw over a longer time period of about 50 ns. The simulated Garfield++ signal from the straws was then used as input for the LTspice package which models the details of the FE electronics readout including the amplification and shaping stages. The LTspice package (Analog Devices) provides a commonly used SPICE simulator software, schematic capture, and waveform viewer with enhancements and models for improving the simulation of analog circuits. The straw tube was essentially considered as a current source with signals similar to the one shown in Figure 6.40. Timing resolutions below 1 ns can be achieved with a peaking time around 10 ns combined with gains of 9 mV/fC or higher even without time-walk corrections.

Table 6.7: Requirements for the custom ASIC planned for the upgrade of the initial STT.

Feature	Requirement
Modularity	64 channels
Input capacitance	10-40 pF (optimize for 40 pF)
Input kapton cable	$\sim$ 1 cm traces + PCIe connector (capacitance $<$ 1 pF)
Architecture	Dual sub-channel with independent gain and shaper: i. Fast shaper & high gain for time measurement ii. Slow shaper & low gain for energy measurement
Technology	180 nm, 1.8 V ($\sim$ 1.5 V linear swing)
Packaging	QFN100 $12 \times 12\,\mathrm{mm}^2$
Minimum charge	4 fC (time measurement), 20 fC (energy measurement)
Maximal charge	10 pC (energy measurement)
Dynamic range	1,000 (energy measurement)
Timing resolution	$<$ 1 ns
Gain settings	i. 6, 9 mV/fC for time measurement ii. $\leq$ 0.5 mV/fC for energy measurement
Peaking times.	i. 10, 25 ns fast shaper ii. 50, 100 ns slow shaper
Power consumption	$<$ 10 mW/channel
Expected rates	$\ll$ 1 kHz

GENIE and Geant4 simulations The detector response obtained with Garfield++ and LTspice was implemented within Geant4 simulations of the complete STT detector. To this end, the

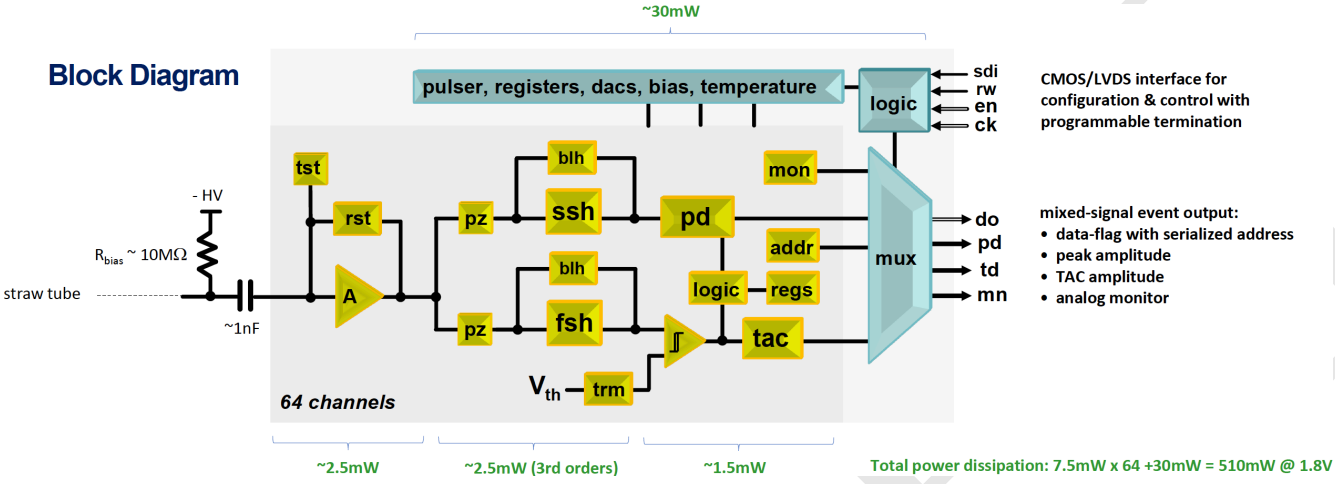


Figure 6.42: Architecture of the custom ASIC for the STT readout.

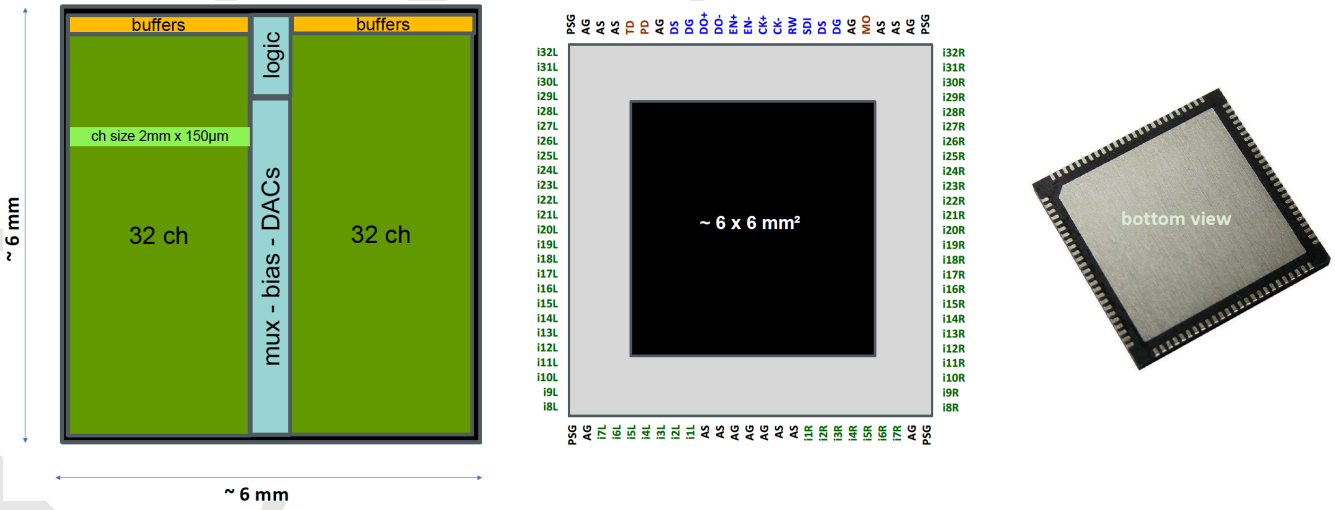


Figure 6.43: Floor-plan and packaging of the custom ASIC for the STT readout.

(anti)neutrino interactions expected in SAND were simulated using the default FHC (neutrino mode) and RHC (antineutrino mode) beams with the GENIE event generator. The main goals were twofold: (i) to evaluate the straw occupancy, hit multiplicity, charge deposition, timing and trigger logic expected in a realistic data taking; (ii) to study the impact of the straw and readout performance on the track reconstruction and particle identification in the STT. Results provided critical feedback for the optimization of the STT readout system and related requirements. The expected average straw occupancy over an entire 9.6 μs neutrino spill is only 3.2%, with only 0.4% of the straws having more than one hit (Figure 6.39). Most of the straws with multiple hits are actually crossed by e^+e^- conversions, with two tracks having the same timing. Particles produced in (anti)neutrino interactions include μ, π, p , $e^{\pm}$, etc. with a broad range of energies and angles, requiring a dynamic range of the analog FE of about 1,000 with maximal expected charges up to a few pC (Figure 6.41).

ASIC requirements and architecture The requirements for the custom ASIC obtained from simulation studies are listed in Table 6.7. A collaboration with the designer of both the VMM and NRL chips (G. De Geronimo) for the implementation of such requirements resulted in the definition of a preliminary architecture of the custom ASIC shown in Figure 6.42. The sub-circuits and functional blocks present are largely inherited from the well-established VMM and NRL chips. Some of the salient features include a charge amplifier linear up to 10 pC, a fast shaper with programmable gain followed by a high-speed low-hysteresis discriminator for time measurement, a slow shaper with independently programmable gain followed by peak detection for charge measurement, and a programmable low-noise time-to-amplitude converter. No radiation hardness is required, given the modest rates expected in STT. The planned chip layout is shown in Figure 6.43. The selected technology is 180 nm operating at 1.8 V with at least 1.5 V of linear swing. This choice is motivated by the easier industrial production with the possibility of using multi-project wafers (MPW) for the prototyping stage, as well as by the reduced costs for both the production masks and the chips. The packaging foreseen is the QFN100 12 mm × 12 mm (Figure 6.43).

6.8 Cooling System

6.8.1 Self-Cooling Design

The integration of the FE boards within the frames of the STT modules, which also serve as gas manifolds, imposes some constraints. In order to guarantee the gas tightness required to operate with internal overpressure, the FE boards are installed directly inside the gas manifolds, avoiding a large number of electrical contacts passing through the manifold walls, which could increase the risk of gas leaks. While this design choice allows for good sealing of the gas circulating within the modules, it makes the cooling of the FE readout electronics more challenging. Considering the relatively low power density present in the STT modules, a self-cooling design was developed for the STT using the ionization gas flowing inside the straws to cool the integrated readout boards within the gas output manifold of the sealed C-fiber frame. The basic idea is to take advantage of the large volume ($\sim 8\,\mathrm{m}^3$) of pressurized gas (2 bar) inside STT by exploiting fluid dynamics to optimize the heat removal by the gas exiting from the straws. The advantages are reduced detector costs and an overall material budget. However, the use of gas cooling imposes limitations on the maximum power dissipation of the integrated readout boards < 15 mW/channel. In order

to increase the lifetime and reliability of the readout boards, it was required that the maximal temperatures on the boards are below 40° C under all reasonable variations of the parameters studied. This value is much lower than the recommended maximum case temperature of 50° C for the VMM3a.

Detector layout and total power dissipation The STT readout boards are installed only on the two sides (separately for vertical and horizontal straws) of the C-fiber frame used as an output gas manifold to prevent the heated gas from entering the straws. The corresponding layout is shown in Figure 6.31. The location of the readout boards is flipped (Section 6.7.1) in even and odd STT modules (left-right and up-down), resulting in a uniform distribution of the power dissipation over the four sides of the detector. Each board has two separate copper ground planes for the analog and digital circuitry (Section 6.9.3), which help to spread out the heat generated by the various chips over the board area. It is also noted that the C-fiber frame is partially conductive along the two main directions of the fibers, further improving heat distribution. The maximal power dissipation is about 0.8 W per board with the VMM3a chip (which dissipates 0.6 W alone) and is expected to be reduced to 0.65 W per board with the custom ASIC. Since at most 24 boards are installed on a single side of the frames, the maximal power to be removed from each manifold is about 19 W linearly distributed over a length of about 4 m. The total power dissipation for the initial STT equipped with VMM3a readout boards is less than 1.7 kW, uniformly distributed on an external detector surface of about 55 m^2, resulting in less than 31 W/m^2. Given the negligible radiation environment associated with the (anti)neutrino beams, the interactions are not expected to release any significant power within the straws.

Pulsed readout operation The integrated readout of the STT modules is designed for continuous operation, and all the thermal analyses performed (Section 6.8.2) are based on the corresponding power dissipation. However, during data taking, only a single beam spill of 9.6 μs is available within each 0.7 s accelerator cycle. A warning signal alerts of the arrival of the neutrino spill about 4 ms in advance. A pulsed operation of the readout boards is therefore foreseen, in which only the MCU unit is continuously active, while the ASIC power is turned on by the MCU about 0.1 s before the start of the 9.6 μs spill and switched off after the spill. The timing of the ASIC active window can be synchronized with the early warning signal. Since the ASIC accounts for most of the readout power, such a pulsed operation would result in a reduction of the total power dissipation by about 80%, with 0.18 W per readout board and about 380 W total for the initial STT, corresponding to 6.9 W/m^2 uniformly distributed on the external detector surface.

6.8.2 Thermal Analysis

Analysis of full-scale modules Detailed thermal simulations were performed to validate the self-cooling design and to optimize the layout and the location of the readout boards. The internal gas flow, the ambient temperature, and the expected boundary conditions were varied with the final 3D engineering model of the full-scale STT modules and 24 initial VMM3a boards per side. To this end, a Xe/CO_2 70/30 gas mixture is used, while the Ar/CO_2 mixture provides a slightly more efficient cooling performance. Actually, most of the gas cooling power is due to the excellent cooling properties of the large CO_2 fraction. The resulting thermal maps are shown in Figure 6.44 for the vertical straws and a nominal gas flow of 5 normal liters per minute (NLPM) in the entire STT module. The heat is contained within the section of the output gas manifold and the input gas quickly thermalizes at the ambient temperature within the straws. The maximal

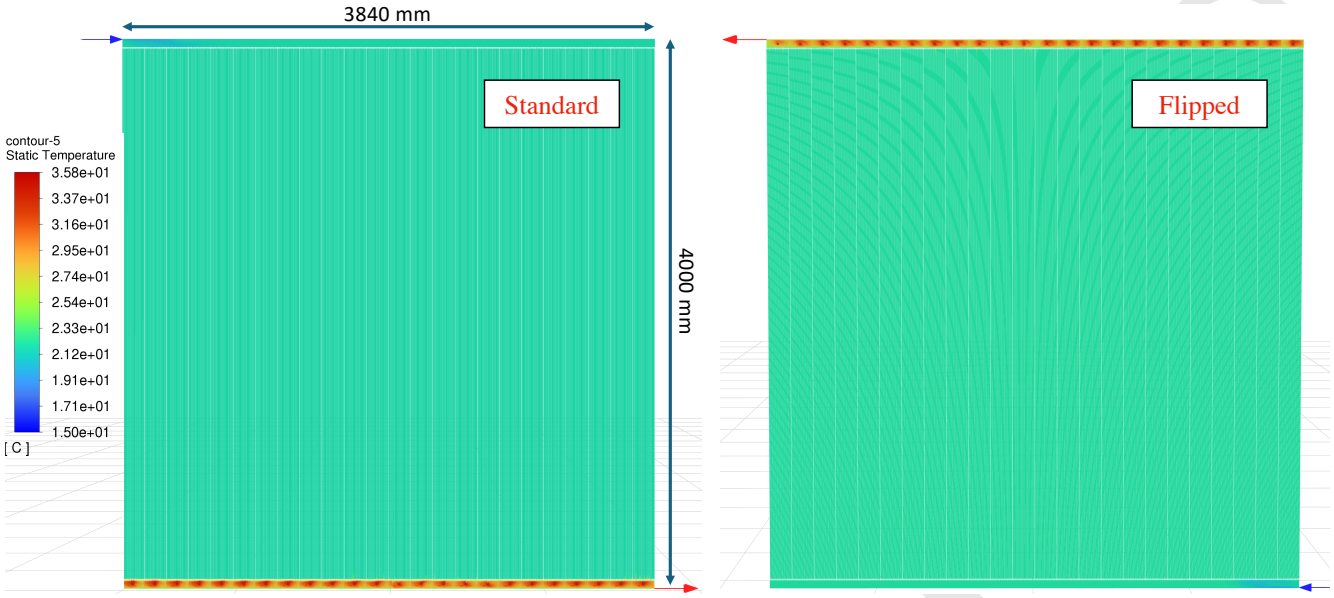


Figure 6.44: Thermal map of a full-scale STT module from FE analysis with a nominal gas flow of 5 NLPM and Xe/CO_2 70/30 gas mixture.

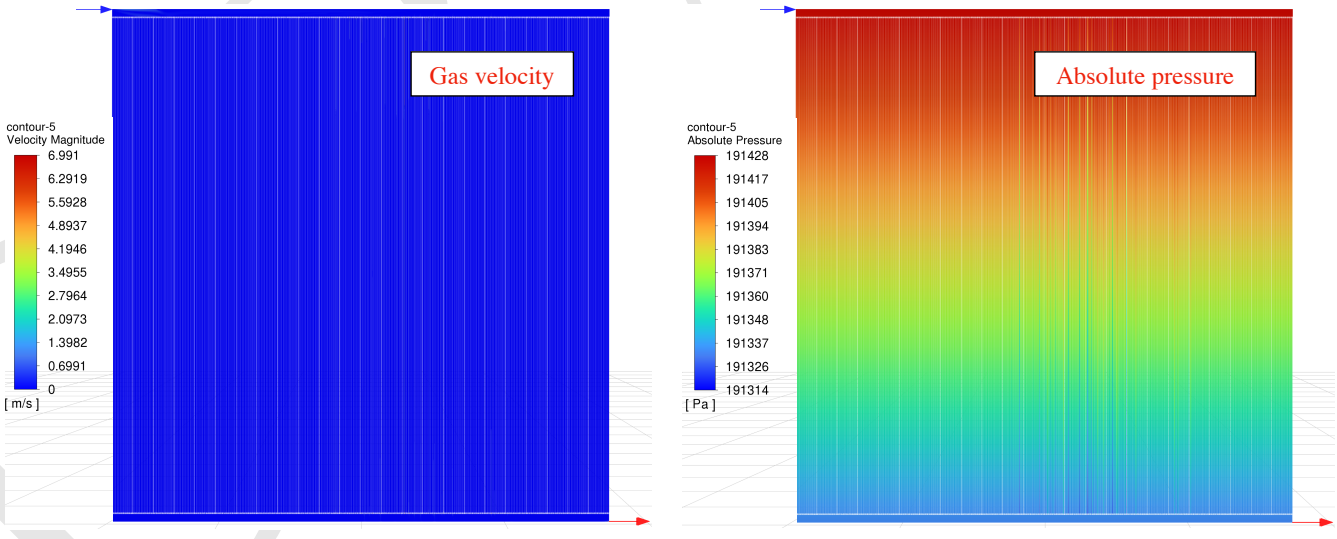


Figure 6.45: Map of gas flow in a full-scale STT module from FE analysis with a nominal value of 5 NLPM and Xe/CO_2 70/30 gas mixture.

temperature reached during steady operation is below 36°C on the surface of the VMM3a chips. No significant variations are observed in the thermal maps nor in the maximal temperature when the readout boards are moved from the bottom to the top sections of the C-fiber frame, in both configurations serving as output gas manifolds. This result justifies the choice to alternate the location of the readout boards in even and odd STT modules (left-right and up-down), as discussed in Section 6.7.1. The gas is moving relatively slowly within the straws, resulting in a negligible variation of the internal pressure along the straws (Figure 6.45).

Analysis of a super-module In order to evaluate the cooling performance under realistic operating conditions representative of the final detector installed within the magnet, a comprehensive thermal analysis was conducted on a super-module assembly comprising a maximum stack of ten STT modules with their corresponding targets and radiators (Figure 6.46).

A detailed simulation of the internal structure of all C-composite panels was performed, including the various C-fiber layers and the epoxy matrix, with their individual thermal properties (Section 6.5.1). The location of the readout boards is flipped in even and odd modules, giving a total of 5 manifolds with readout boards per super-module side. The resulting temperature maps are shown in Figure 6.47 for a nominal gas flow of 5 normal liters per minute (NLPM) in each module and an ambient temperature of 20°C. The maximal temperature on the VMM3a chips was found to be below 35°C. Figure 6.48 shows the dependence of the maximal VMM3a temperature from the ambient temperature and the gas flow. Variations are found to be relatively smooth, allowing for the definition of a broad range of parameters for safe operation. In particular, variations of the ambient temperature of ±5°C are consistent with the requirement of maximal chip temperatures below 40°C (Section 6.15.4). In the calculations a natural convection was assumed for the external air surrounding the super-module assembly. The corresponding heat transfer coefficient was varied between 1 and 25 W/m^2K, as shown in Figure 6.49. In all conditions studied the natural convection was found to be adequate, with a relatively small impact on the maximal chip temperatures.

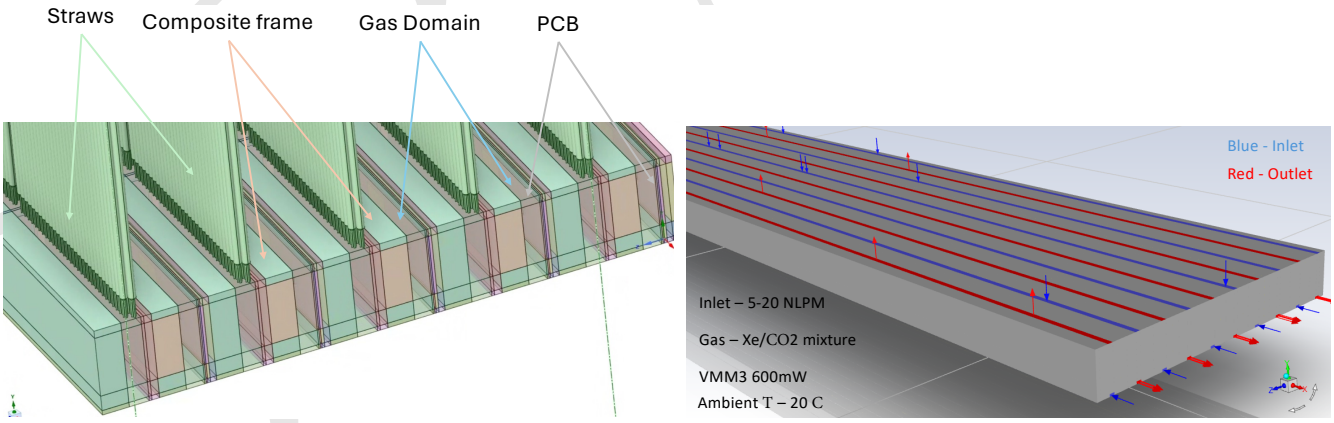


Figure 6.46: Setup implemented for the thermal analysis of a full-scale STT super-module.

The nominal volume gas flow rate required for the self-cooling of the STT modules (5 NLPM) corresponds to a complete exchange of the internal gas volume in the straws in about one hour. This value is not critical for the gas system and is much larger than the maximum drift time of about 60 ns. The STT modules are split into two separate distribution circuits: one distribution feeds the STT modules with Xe/CO_2, and a second distributes the Ar/CO_2 gas mixture to the

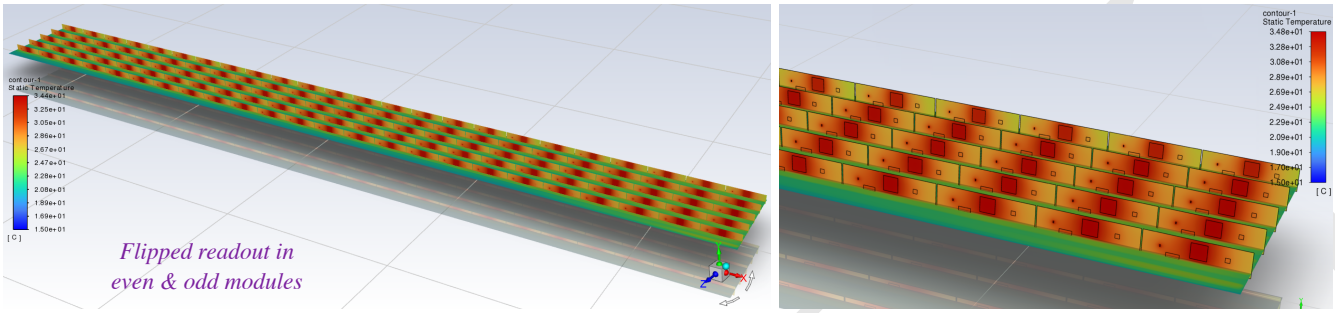


Figure 6.47: Temperature map from the thermal analysis of a full-scale STT super-module.

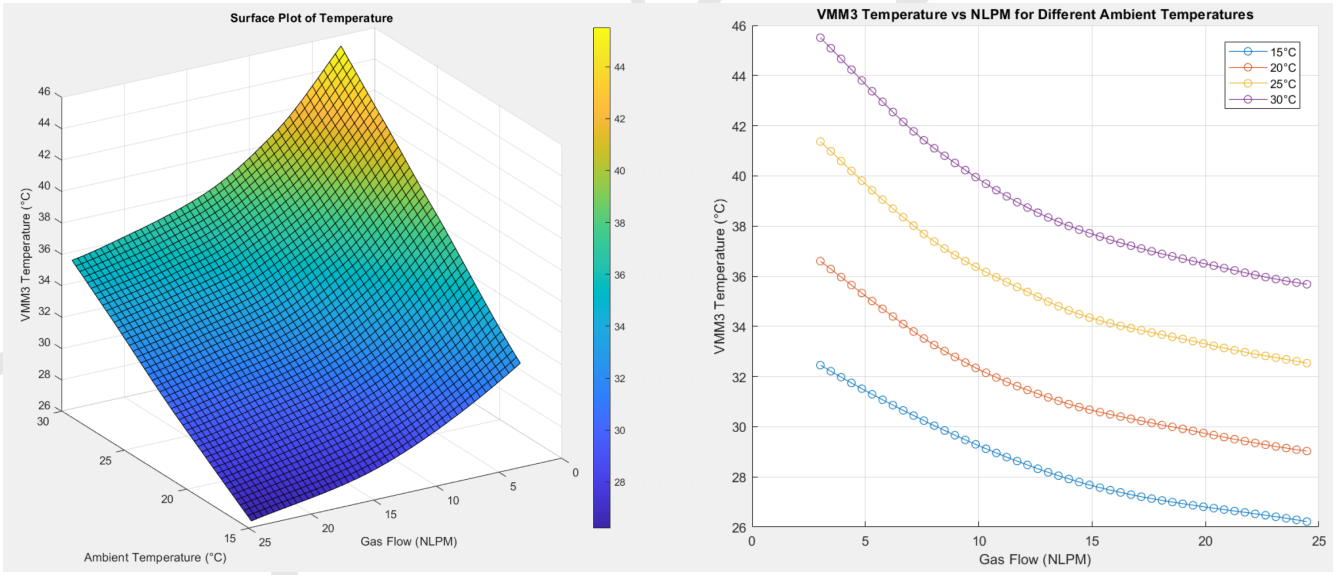


Figure 6.48: Results from the thermal analysis of a full-scale STT super-module: dependence of the maximal VMM3a temperature on the internal gas flow and the external ambient temperature.

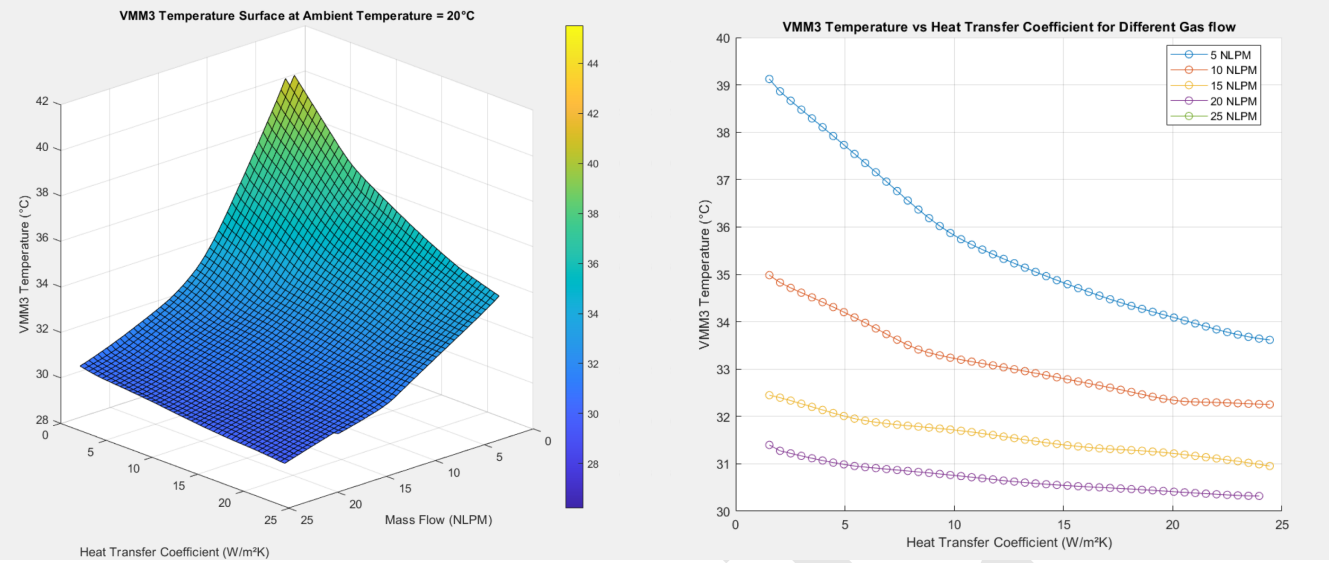


Figure 6.49: Results from the thermal analysis of a full-scale STT super-module: dependence of the maximal VMM3a temperature on the internal gas flow and the heat transfer coefficients of the external air assuming natural convection.

modules. The maximal volume gas flow expected for each distribution circuit is below 15 nm^3/h (Section 6.11).

The thermal simulations of a super-module with a realistic description of the internal structure of the C-composite frames indicate that the anisotropic properties of the latter help to largely confine the heat within individual modules (Figure 6.50). The thermal conductivity along the direction perpendicular to the plane of the module is indeed much smaller than that in-plane along the two directions of the C-fibers (oriented at 0° and 90°). As a result, the temperature in the input gas manifolds of the nearby modules without readout boards does not show major variations. In order to verify the gas temperature within the straw layers fed by such input manifolds, the simulation included full length straws (about 4 m) and end-plugs. Figure 6.50 shows that the gas inside the straws quickly becomes thermalized to the ambient temperature (20° C) and that excellent temperature uniformity is achieved along the entire 4 m length of the straws. This latter point is critical for stable gas gain along the straws, which is relevant for the charge measurement required for particle identification (Section 6.18.4).

Table 6.8: Maximal temperatures on the VMM3a chips for the continuous and pulsed operation modes. An active window of about 4 ms is assumed for the VMM3a chip in the latter case.

	Continuous	**Pulsed**
Maximal temperature	37.4° C	23.3° C

Pulsed operation The results discussed above indicate that the VMM3a readout boards can be safely operated in continuous mode within the C-fiber frames of the STT modules. However, the possibility of switching off the VMM3a chips – dissipating most of the total power – outside of the neutrino spill appears desirable. Such a pulsed operation can be controlled by the MCU, which

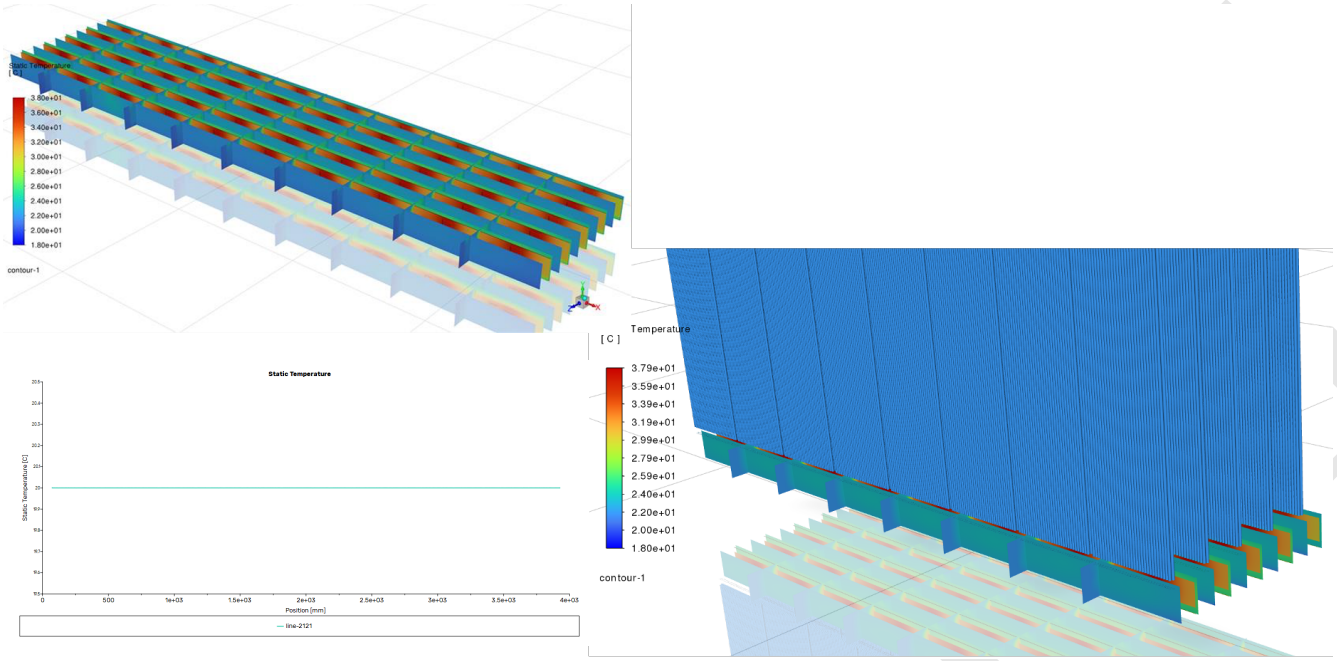


Figure 6.50: Results from the thermal analysis of a full-scale STT super-module: temperature uniformity of the gas along the straws.

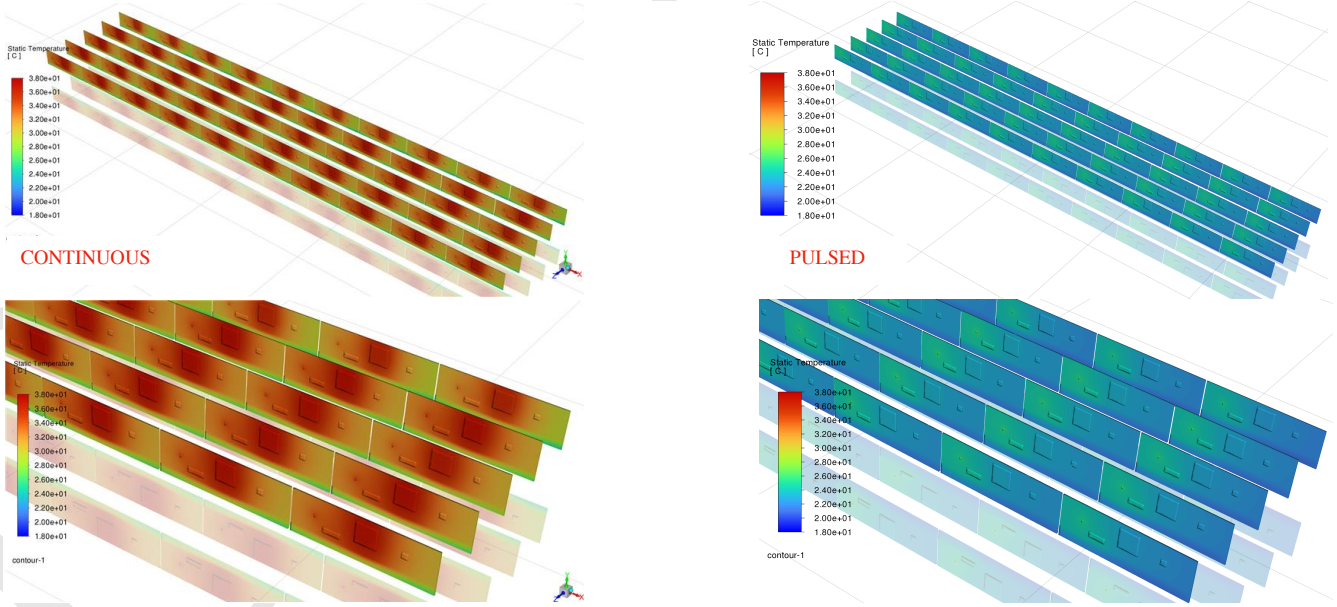


Figure 6.51: Results from the thermal analysis of a full-scale STT super-module: comparison of the temperature maps for the continuous operation (left) and pulsed operation (right) modes for the VMM3a chips. An active window of about 4 ms is assumed for the VMM3a chip in the latter case.

is kept permanently operational (Section 6.8.1). In order to evaluate the impact of the pulsed operation, the thermal analysis of the STT super-module was repeated, assuming the expected active window of 4 ms for the VMM3a chips during the overall accelerator cycle of 0.7 s. Figure 6.51 shows a comparison between the thermal maps obtained with the continuous and pulsed operations. The maximal temperature is reduced from 37.4° C to 23.3° C with the pulsed operation (Table 6.8). The corresponding power dissipation is reduced by almost 80%. A duration of the active VMM3a window of a few ms does not appear to be critical for the VMM3a chip. Figure 6.52 shows the maximal temperature reached as a function of the duration of the active time window for the VMM3a. Limited temperature variations are found below 10 ms. The lowest temperature obtained when the VMM3s is permanently switched off is higher than the ambient temperature of 20° C, due to the power dissipation by the MCU, LDOs and the other components of the readout boards.

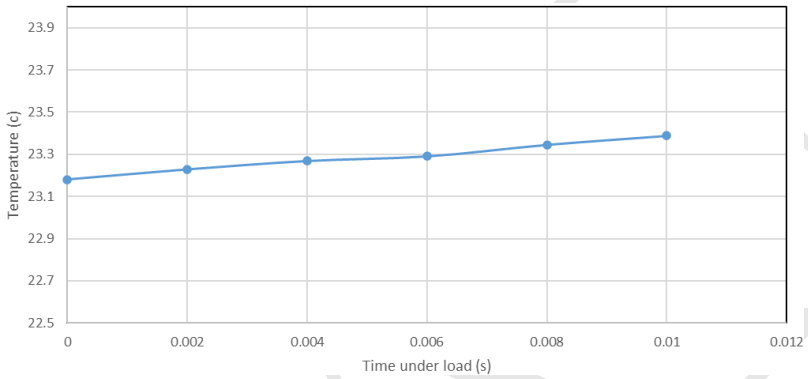


Figure 6.52: Results from the thermal analysis of a full-scale STT super-module: maximal temperature reached as a function of the duration of the active time window for the VMM3a for a pulsed operation.

6.9 System Integration

A high level of detector integration is required to minimize the mass and thickness of the STT modules (Section 6.5), as well as to simplify the detector installation and reduce the external components (and mass) required. Some of the technical solutions implemented in the STT design include the installation of the readout boards integrating the analog front-end, the digital back-end processing, as well as the HV distribution to the straws within the sealed C-fiber frames of the modules, and a combined HV + signal connection of the straws. Aspects such as the cooling of the integrated boards (Section 6.8), the grounding scheme, and the external input/output connections thus become essential elements of the design of the STT modules.

All service connections are integrated within the frame of the modules, while all gas and electrical connections are routed through the four aluminum corner blocks (Figure 6.53). The connectors will be permanently glued to the Al corner blocks and the internal holes filled with resin once the complete wiring is in place to guarantee the required gas tightness. Each STT half-module is designed operate independently from the remaining ones, providing a standalone solution only requiring input/output electrical cables and gas pipes. Besides space and cost savings, this design offers the advantage of a fully modular detector (Section 6.15.1).

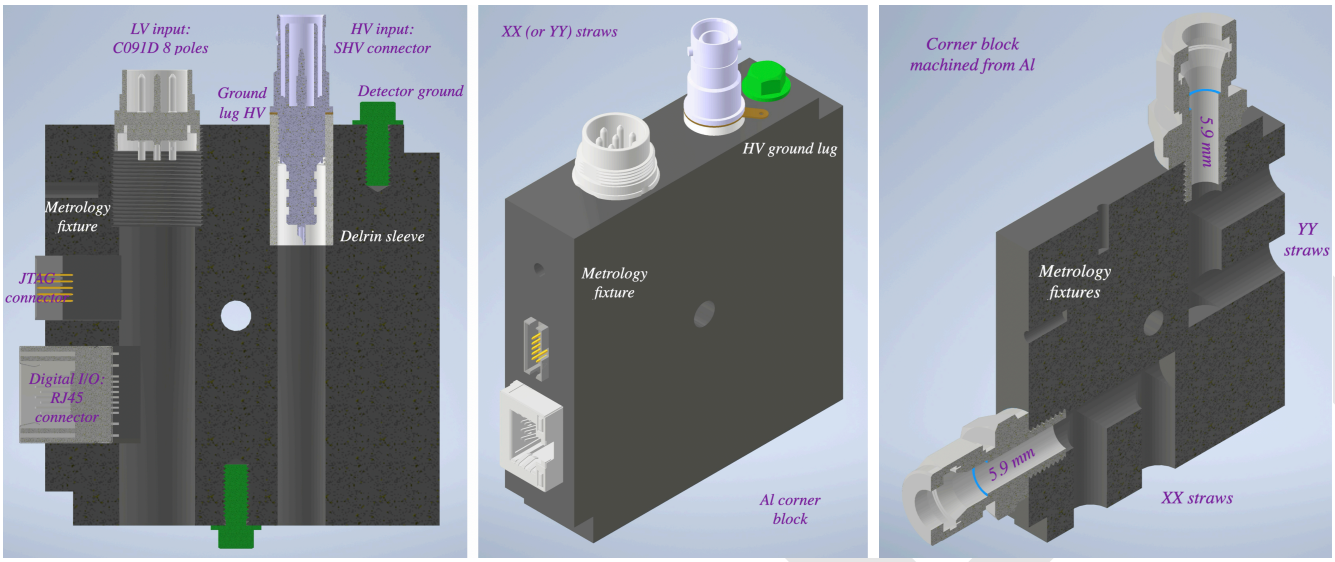


Figure 6.53: Details of the electrical input/output connections (left and middle pictures) and of the gas inlet/outlet connections (right picture) for the STT modules (independent for XX and YY layers).

6.9.1 Gas Connections

Each STT module is directly connected to the corresponding circuit within the gas distribution rack (Section 6.11) via one input tube and one output tube. Both such tubes are made of PVDF plastics, providing a high electrochemical stability and gas tightness, and are terminated by brass ferrules (Figure 6.54). The inner diameter of these input/output PVDF tubes was chosen to be 8 mm (Table 6.9) to guarantees an overall pressure drop $\lesssim$ 1 mbar for both the Ar/CO_2 and Xe/CO_2 gas mixtures over lengths of 10-15 m with the nominal gas flow of 5 NLPM (Section 6.8.2). The 8 mm PVDF tubes have a minimal bending radius of 65 mm.

In order to simplify the gas connections and maximize the gas tightness of the modules, the hollow cavities of the mechanical frames are used as gas manifolds. Two sides of the module constitute the separate gas input manifolds for the vertical and horizontal straws. Similarly, the remaining two sides are the gas output manifolds. The end-plugs (Figure 6.7) are designed to offer an optimal impedance to the gas flow from/to the common manifolds. Each gas manifold serves a double layer of straws. Figure 6.53 shows an engineering drawing of the gas connections. Two gas inlets/outlets with an internal diameter of 5.9 mm are directly connected to an aluminum corner block. This latter has an internal structure with two independent cavities servicing the vertical and horizontal straws and directing the pressurized gas to the input/output manifolds via two separate holes per side. The role of this internal distribution is to guarantee a more uniform gas flow reducing the turbulence. The two inlets/outlets for the vertical and horizontal straws in each corner block are connected through a T-shaped metal joint to the single input/output PVDF tube per STT module via two short PVDF tubes with an internal diameter of 6 mm (Table 6.9). The minimal bending radius of the latter is 18 mm, making them ideal for the gas connectors located on the top and bottom sides of the detector. Figure 6.54 shows a T-joint, as well as a stainless steel caps which can be used to close the gas circulation in a STT half-module (XX or YY layers).

Table 6.9: List of input/output gas tubing for the initial (maximal) STT with approximate lengths.

Link	Tube type	Terminations	Quantity	Length
Distribution rack to STT modules	PVDF 8 mm ID	Brass ferrules	54 (84)	15 m
STT modules to distribution rack	PVDF 8 mm ID	Brass ferrules	54 (84)	15 m
T-joints to inlets	PVDF 6 mm ID	Brass ferrules	108 (168)	0.3 m
Outlets to T-joints	PVDF 6 mm ID	Brass ferrules	108 (168)	0.3 m

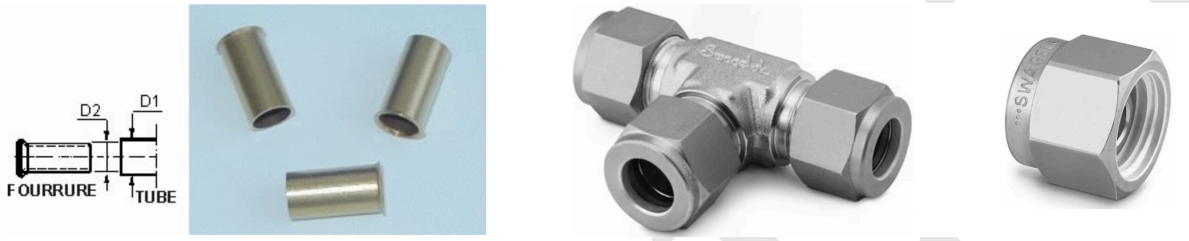


Figure 6.54: Terminations for the gas connections: brass ferrules to be inserted into the PVDF tubing (left), T-joint between one 8 mm tube and two 6 mm tubes (middle), and stainless steel tube cap to close a straw double layer (right).

6.9.2 Electrical Connections

A compact modular readout board was developed to be directly integrated within the output gas manifolds as shown in Figure 6.31. The readout of the vertical straws is based on a total of 20 boards reading a total of 1,247 straws. This board configuration is common to all STT modules – which share the same number of vertical straws – and are installed at the top and bottom sides of the frames in even and odd modules. The readout of the horizontal straws requires a variable number of boards, depending on the height of the module considered. The largest modules located in the central part of the magnetic volume have 24 readout boards, installed within the left (or right) side output manifold. Conversely, the smallest modules at the edge of the magnetic volume have only 7 boards.

All input/output electrical connections are split between the two corner blocks, which are not used by the gas inlets and outlets. A single HV channel is used per double layer of straws, corresponding to two HV channels per STT module and a total of 108 (168) channels for the initial (maximal) STT configuration. A maximal voltage of 2.0 kV per channel is required, given the operating voltage of about 1.6 kV at 2 bar absolute pressure for a gas gain of about 2.5×10^4. Each corner dedicated to the electrical connections integrates a teflon SHV 5 kV input connector servicing one half-module, as shown in Figure 6.53. A single DIN connector Amphenol C091D with 8-pin male contacts is used to feed 4 LV lines into each straw double layer (STT half-module) via the corresponding electrical corner block:

- 3.5 V line feeding all MCUs in each STT half-module, for a total maximal current < 0.9 A;
- 3×1.5 V lines feeding ≤ 8 VMM3a each, for a total maximal current < 3.5 A per line. With the custom ASIC upgrade the supplied LV lines will be increased to 2.5 V using dedicated adjustable trimpots located on the corresponding LV distribution boards.

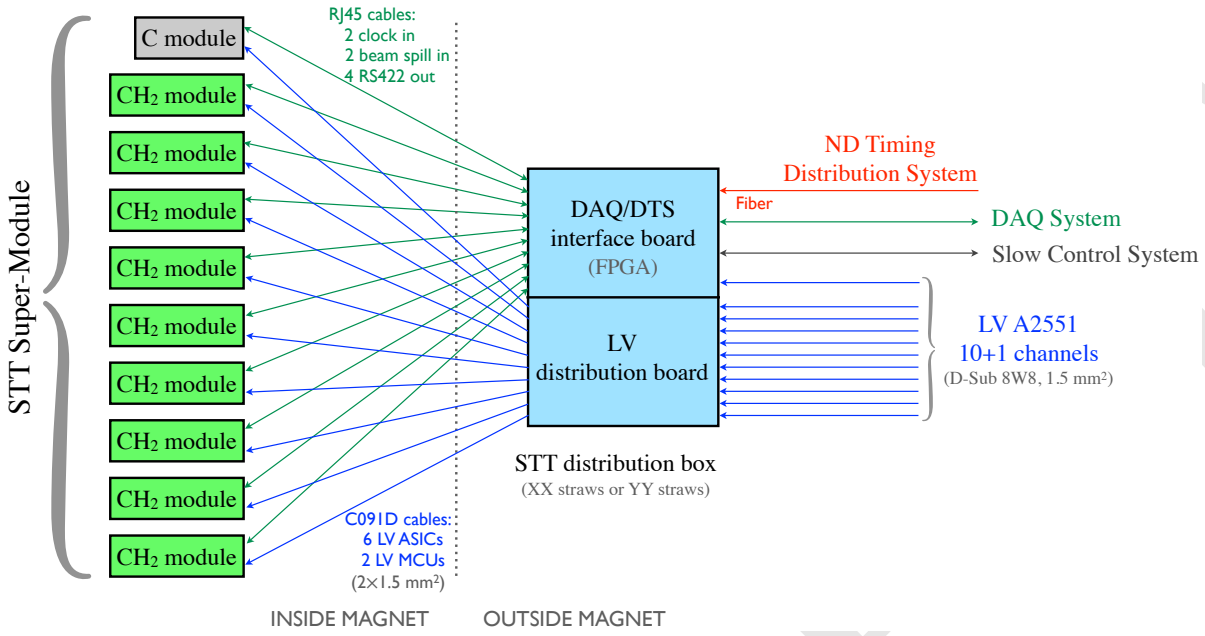


Figure 6.55: Schematic diagram of the DAQ/DTS and LV connections for one Super-Module of the maximal STT. For the LV and digital I/O cables, the number of wires associated with each function (two wires per line) is shown.

The presence of LDO regulators for each input voltage on the STT readout boards does not require dedicated LV sense lines. Remote (dis)connection for the LV lines is available on each readout board. The LDO powering the ASIC will have a "Power Off" option controlled by the MCU. The MCU itself can be power cycled through the JTAG chain, if needed.

A single LV channel per double layer of straws (half-module) is used. Each LV channel is split into the 4 separate lines of the C091D 8-pin connector on the electrical corner block by an LV distribution board. Two LV distribution boards are required to feed a complete STT super-module, including 6(10) modules for the initial (maximal) STT configuration, corresponding to a total of 18 LV distribution boards. Figure 6.55 illustrates the LV connections of the distribution boards. One additional LV channel is required to power each LV distribution board. The total number of LV channels is therefore 126 (186) for the initial (maximal) STT configuration. Each LV channel provides a 5 V input to the distribution boards, with maximal power < 20 W. The distribution boards includes a LDO regulator and an adjustable voltage (trimpot) on each LV output line, for a total of 40 lines per distribution board. The possibility to vary the output voltage of each LV line adds flexibility allowing a straightforward installation of readout boards with different ASICs.

As discussed in Section 6.7.1, all the electronic boards reading a double straw layer are connected in parallel via a BUS interface (Figure 6.33). A single combined RJ45 connector is used in the electrical corner blocks (Figure 6.53) for the digital input/output lines of each STT half-module. The interconnections between boards can use either ribbon cables or flexible printed cables (FPC), as illustrated in Figure 6.56. The 8 wires connected to the RJ45 connector are used for the following digital input/output signals:

- 2 input wires for the machine clock;

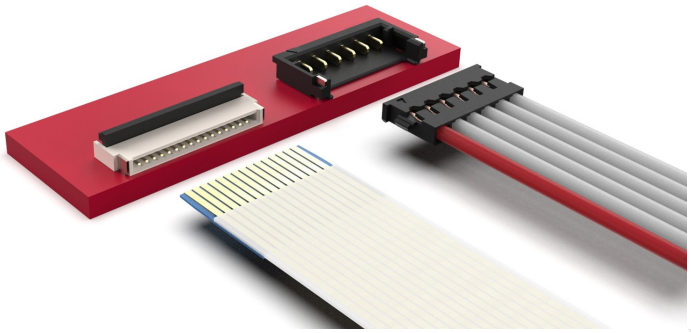


Figure 6.56: Flexible printed cable (left) and ribbon cable (right) for the interconnection of the STT readout boards within the C-fiber frame.

- 2 input wires for the beginning of beam spill;
- 4 output wires with the RS422 digital signals.

An RS422 receiver converting the output signals to LVDS is mounted on the DAQ/DTS interface boards equipped with FPGA (Section 6.10). A clock frequency of 62.5 MHz is distributed by fiber to all DAQ/DTS interface boards and from those to the STT modules via the RJ45 connection. A single JTAG connector is completing the digital connections available through the electrical corner blocks (Figure 6.53) for the firmware update of all the electronic boards reading each STT half-module. A permanent cable connection of the JTAG lines to the DAQ is not required, since frequent firmware updates are not expected after detector commissioning and initial operation.



Figure 6.57: Common ground plane obtained during the assembly of the 1.2 m STT prototype (Section 6.12.4) with the application of the silver conductive paint SCP26G at both ends of the straws.

6.9.3 Grounding

All straws within a module share a common grounding, which is connected to the walls of the straws (cathodes) via a ground plane on the inner surface of the straw holders in the C-fiber frame. The ground plane is obtained during the module assembly with the application of the silver conductive paint SCP26G (Section 6.5.2) at both ends of the straws (Figure 6.57). The ground plane is then embedded into the Stycast 1266 used for the final sealing of the modules. A single ground contact close to the electrical corner blocks connects all the straws. Each electrical corner block also includes a connection to the detector ground via a corresponding ground screw (Figure 6.53).

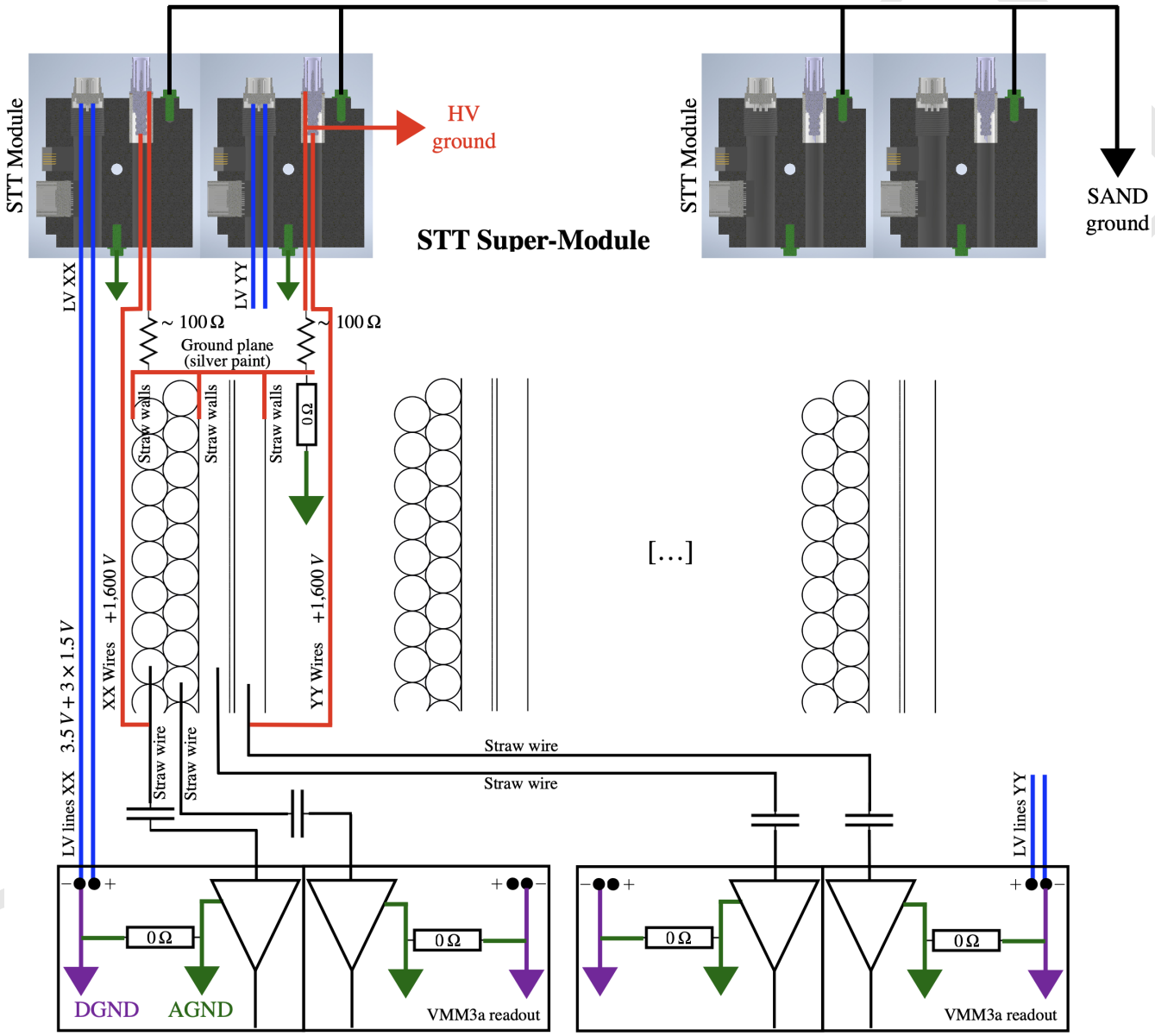


Figure 6.58: Diagram of the grounding scheme for a STT Super-Module.

Figure 6.58 illustrates the grounding scheme for for a STT super-module (Section 6.5.3). The C-composite material used for the frame of the modules has directional properties as it is characterized by excellent electrical (and thermal) conductivity along the orientation of the fibers, while the epoxy matrix (40% by volume) is mostly insulating. As a result, a significant electrical resistance is present between the STT modules facing each other within the super-module assembly. This condition allows a simple implementation of a star connection of the detector ground with the general SAND reference ground via the ground contact integrated into the electrical corner block (for either XX of YY straws) of a single STT module. All other corner blocks within the given super-module are in turn connected in parallel to that one (Figure 6.58). Additional connections to the external SAND ground can be easily implemented in case the noise conditions of the final installation require them.

The HV channels feeding a double straw layer each have a common floating ground (Section 6.9.4). The HV return on each SHV connector is electrically insulated from the corresponding Al block with the insertion of a Delrin sleeve (Figure 6.53) and is connected to the common ground plane via a "ground breaking" resistor of the order of 100 Ω. This resistor typically drops only a few mV since the HV currents are very small and it prevents the return current from the LV lines and the analog ground (AGND) to flow through the HV lines. The SHV connector has an additional ground lug made of brass, to which a ground wire can be soldered in case the noise conditions require the HV ground to be connected back to the detector ground. The common ground plane of the straws is connected to the detector ground (corner blocks) and the AGND defining the polarization of the detector via a minimal ($\sim 0\,\Omega$) resistance. A dedicated RC filter is present on the HV line.

The LV power is distributed from the remote DC supplies to the integrated readout boards via the corresponding LV distribution board (Section 6.9.2). Each LV channel has individually floating (return) ground (Section 6.9.4) connected to the 4 LV return lines feeding a double straw layer (XX or YY). The negative LV returns are connected to the readout ground via a minimal ($\sim 0\,\Omega$) resistance. Each readout board has two separate ground planes for the analog (AGND) and digital (DGND) circuitry, which can be decoupled by connecting a dedicated RC filter. The VMM3a itself has different grounds for the input circuitry, for the amplification/shaping, and for the digital outputs. The readout AGND is in turn connected to the detector ground via a minimal ($\sim 0\,\Omega$) resistance.

6.9.4 HV and LV Components

A maximum of 108 (168) channels supplying < 2.0 kV is required for the initial (maximum) STT (Table 6.2). A total of 9 (14) CAEN 7030DP modules are sufficient, each with 12 channels rated at 3 kV/1 mA (1.5 W) output range and with SHV common floating connectors. The output voltage can be set with a resolution of 50 mV.

A maximum of 126 (186) channels supplying 5 V to the LV distribution boards with a current < 4 A each is required for the initial (maximum) STT (Table 6.2). To this end, a total of 16 (24) CAEN A2551 modules are employed, each providing eight individual floating channels of 8 V/12 A (60 W) with dual D-Sub 8W8 output connectors. The output voltage can be set with a 0.2 mV resolution.

Table 6.10: Configuration of the HV and LV modules for the initial (maximal) STT.

Mainframe	Modules	Quantity
CAEN SY4527 1	HV 7030DP	3 (4)
	LV A2551	4 (6)
	PS A4533	1
CAEN SY4527 2	HV 7030DP	2 (4)
	LV A2551	4 (6)
	PS A4533	1
CAEN SY4527 3	HV 7030DP	2 (3)
	LV A2551	4 (6)
	PS A4533	1
CAEN SY4527 4	HV 7030DP	2 (3)
	LV A2551	4 (6)
	PS A4533	1

Both the HV and the LV modules can be combined into the universal multichannel power supply system CAEN SY4527 in order to optimize the total power consumption. Table 6.10 shows the corresponding configuration for the maximal STT. A total of 4 mainframes SY4527 are required, each equipped with an additional double power supply unit A4533, increasing the maximal rated power to 1.2 kW.

6.9.5 Cabling

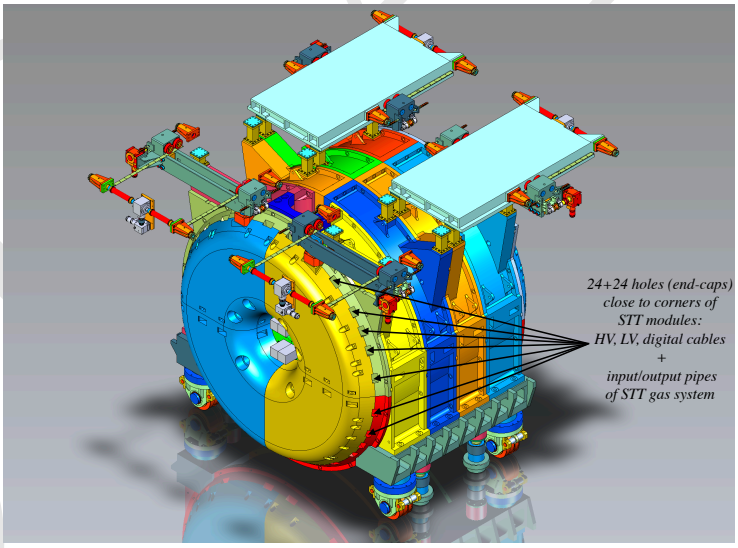


Figure 6.59: Drawing of the closed magnet showing the access for the STT services including the HV, LV, and digital cabling, as well as the gas pipes.

All electrical connections with the STT modules are routed through the 24 holes present between each end-cap and the barrel yoke of the magnet (Figure 6.59). Such gaps directly face the corners of the STT modules with the relevant electrical connectors, as described in Section 6.9.2. The gas pipes are also routed through the corresponding holes which are not used for the electrical connection on each side of the magnet, since the gas inlets/outlets are located at opposite corners

Table 6.11: List of cables for the initial (maximal) STT with approximate lengths.

Link	Cable type	Connectors	Quantity	Length
LV A2551 to LV distribution	$4 \times 1.5\,\text{mm}^2$ 0.6/1 kV	D-Sub 8W8	63 (93)	1 m
LV distribution to STT modules	$4 \times 1.5\,\text{mm}^2$ 0.6/1 kV	C091D 8-pin	432 (672)	8 m
HV 7030DP to STT modules	Coaxial 5 kV DC	SHV	108 (168)	8 m
STT modules to DAQ/DTS interface	GigE Cat 6	RJ45	108 (168)	8 m

of the STT modules. All input and output connections to the STT modules can be directly accessed by opening the end-caps, without extracting the modules from the magnet. Table 6.11 summarizes the cables required for the electrical connection of the initial (maximal) STT.

The four CAEN SY4527 mainframes hosting all the HV and LV modules (Section 6.9.4) are mounted into 4 separate racks to be installed at the four ends of the two mezzanines on the magnet in order to distribute the cabling load. The distance between such racks and the corner blocks of the various STT modules is less than 8 m. The expected total power consumption for the maximal STT is < 5 kW. Each LV distribution board is housed together with the corresponding DAQ/DTS interface board in a common shielded case (distribution box), as shown in Figure 6.55. The 18 distribution boxes are located within the same 4 racks with the four CAEN SY4527 mainframes. The distance between such distribution boxes and the corner blocks of the STT modules is less than 8 m. The LV cabling is based on shielded cable $4 \times 1.5\,\text{mm}^2$ 0.6/1 kV throughout. The connection between the CAEN A2551 modules and the LV distribution board uses a single run $1.5\,\text{mm}^2$ per channel ($\Delta V < 0.1$ V) terminated with D-Sub 8W8 connectors at both ends. The connection between the LV distribution and each STT half-module (XX or YY straws) utilizes a double run $2 \times 1.5\,\text{mm}^2$ per channel ($\Delta V < 0.3$ V) terminated with C091D 8-pin female connectors at both ends. A right-angle C091D female connector is used for the LV cables feeding the top and bottom sides of the STT modules in order to reduce the corresponding bending radius of the cables. The CAEN 7030DP modules are directly connected to the STT half-modules via a coaxial 5 kV DC cable with SHV connectors at both ends. The digital input/output of each STT half-module is connected to the corresponding DAQ/DTS interface board with a twisted, shielded GigE Cat 6 cable featuring an RJ-45 click-lock plug on both ends. The DAQ/DTS interface board is in turn connected to the central DAQ system with a single digital cable and to the DUNE timing system with an optical fiber cable.

6.9.6 Metrology Fixtures

Each aluminum corner block includes dedicated metrology fixtures for the laser survey of the location of the STT modules (Figure 6.53). Precision holes with a diameter of $3.175^{+0.010}_{-0.000}$ mm and 11.5 mm deep allow the temporary insertion of magnetic holders for 0.5 in steel reflective spheres acting as targets for imaging (camera) metrology. The reflective ball rests in the conical section of the holder, which has a magnet built into the nest to hold it (Figure 6.60). A similar system was adopted for the straw tracker of the Mu2e experiment at Fermilab. A total of 6 precision holes are available for each STT module: two in each of the corners with the gas connections and one in each of the corners with the electrical connections (Figure 6.53). Three points are required to fully determine the orientation of each STT module. Typically, two targets are inserted into the opposite corners with gas connections, and a third one is connected to one of the remaining

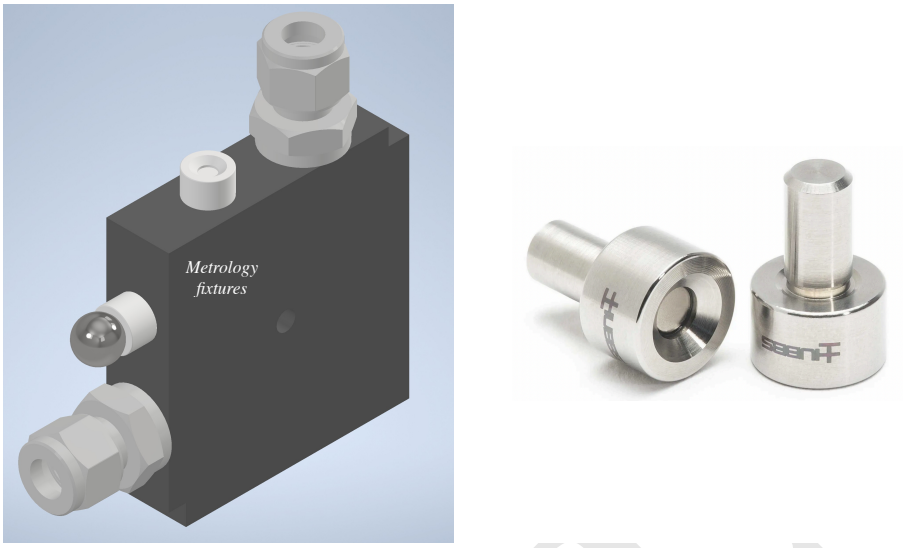


Figure 6.60: Details of the metrology fixtures used for the laser survey of the location of the STT modules. Spherical 0.5 in laser targets can be mounted magnetically onto removable precision holders.

corners. The extra holes are provided for convenience to facilitate the metrology survey under different installation configurations.

6.10 Data Acquisition and Slow Control System

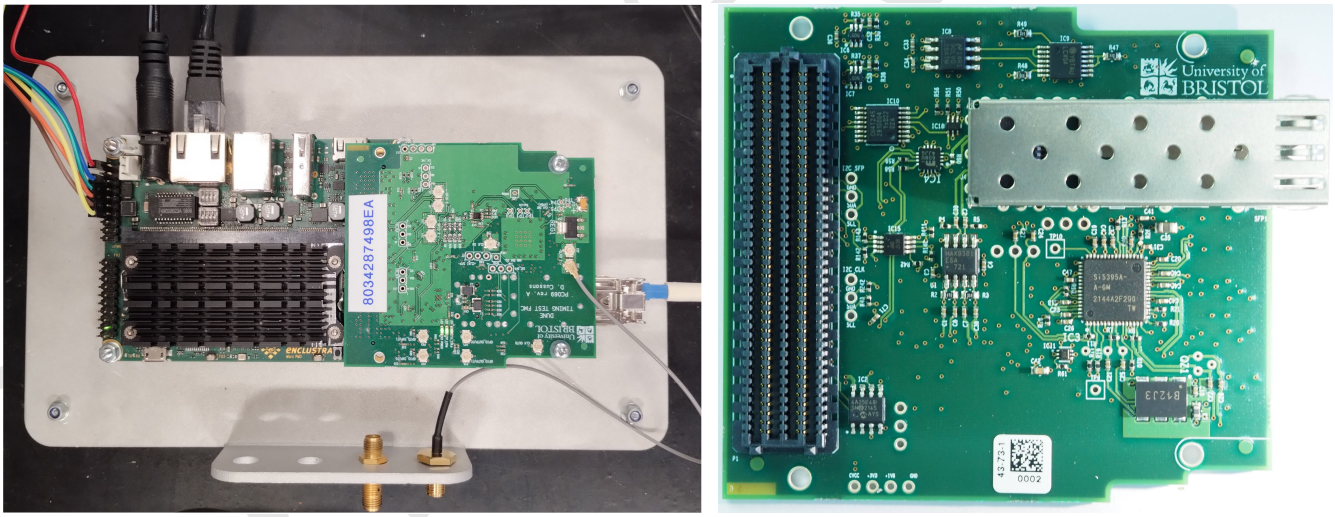


Figure 6.61: Reference prototype hardware for the FPGA Mezzanine Cards (FMC) developed by the DUNE DAQ group as timing endpoint and DAQ interface.

The STT modules are connected to the central DAQ and timing system via 2 DAQ/DTS interface boards (Section 6.9.5) per super-module, as shown in Figure 6.55. The DAQ/DTS interface boards are equipped with an FPGA and have the following functions:

- Act as STT end-points for the DUNE Timing System (DTS);

- Distribute the input signals from the machine clock and the beginning of the neutrino spill to the STT modules;
- Collect the digital RS422 output signals from the STT modules and route them to the central DAQ system;
- Interface the central Slow Control system with the STT modules.

Each interface board has 10 digital input/output lines with RJ45 connectors, directly linked to the corresponding STT half-modules part of a single super-module assembly. The DUNE DAQ group developed a reference prototype hardware of FPGA Mezzanine Cards (FMC) that mounts onto an FPGA board (Enclustra, Nexys Video), as shown in Figure 6.61. Such a prototype board has the main functionality and I/O interfaces required for STT and can be used as a basis for the design of the DAQ/DTS interface boards. It has a single mode fiber carrying clock and synchronization messages with a 62.5 MHz clock, a 64-bit timestamp, and a clock recovery with a Si5395 PLL-based clock generator.

The straws are operated in a common-stop mode, each of them measuring a time difference $\Delta t = t_{\text{stop}} - t_{\text{start}}$. The start signal, t_{start}, is given by the arrival of the drift electrons from a particle crossing the straw at the anode wire, in coincidence with the neutrino spill. The stop signal, t_{stop}, is given by a common delayed signal from the beginning of the spill within the 9.6 μs spill. The measured time difference Δt corresponds to the common delay time, Δt_{delay}, minus the sum of the interaction time from the beginning of the spill, Δt_{int}, the time of flight (ToF) of the particle from the interaction point, Δt_{tof}, the drift time of the electrons within the straw, Δt_{drift}, the signal propagation time along the sense wire, Δt_{wire}, and the signal propagation time in the electronic circuits, Δt_{elect}:

$$\Delta t = \Delta t_{\text{delay}} - (\Delta t_{\text{int}} + \Delta t_{\text{tof}} + \Delta t_{\text{drift}} + \Delta t_{\text{wire}} + \Delta t_{\text{elect}})$$

This time can be corrected for Δt_{delay}, Δt_{wire}, and Δt_{elect} as soon as the coordinate of the hit along the wire is known, e.g., from the hits in the perpendicular straws of the preceding or following layers within the same tracking module. The track reconstruction can then correct for Δt_{tof} and Δt_{int} (common to all hits from the same event) using an iterative fitting procedure. In addition to the time measurement, the total charge deposited in each straw by the crossing particle is also recorded for particle identification (Section 6.7).

6.11 Gas System

The initial (maximal) STT is composed by 54 (84) modules. A maximal number of 45 STT modules (39 for the initial STT) will be operated with a Xe/CO_2 (70%/30%) gas mixture, while a maximal number of 39 STT modules (15 for the initial STT) will be operated with an Ar/CO_2 (70%/30%) gas mixture. The total inner volume of the straws is about 8 (14) m^3 for the initial (maximal) STT (Table 6.2), out of which about 5.8 (7.5) m^3 with Xe/CO_2 and 2.2 (6.5) m^3 with Ar/CO_2. The STT modules will be operated at an internal absolute pressure of 2 bar. Since the gas mixture flow is also used to cool the integrated readout electronics, to ensure a good cooling capacity a nominal average gas flow ≤ 5 normal liters per minute per module is considered for the design of the gas system. The corresponding total mixture flow for the initial (maximal) STT should be $\lesssim 12(14)$ nm^3/h for the Xe/CO_2 and $\lesssim 5(12)$ nm^3/h for the Ar/CO_2, respectively. Given the relatively large detector volumes and the gas flow rates expected, re-circulation systems will be used for the STT

modules working with both Ar/CO_2 and Xe/CO_2 mixtures. The basic function of the gas system is to prepare the two mixtures and to distribute them to the STT modules. The injection of fresh Ar/CO_2 and Xe/CO_2 mixtures will be used only to compensate for small leaks over long periods. The envisaged gas system consists of several modules which profit of the design experience and standards adopted for the gas systems of the LHC experiments at CERN. The gas system will be running on PLC [1] and it will be controlled/monitored using the standard WinCC-OA SCADA [2] interface. For all values (pressures, flows, mixing ratios, etc.) warnings, alarms and interlocks can be configured according to the specific detector needs.

Two stages are foreseen for the STT gas system:

- An initial gas system used at the beginning of the data taking with the initial STT and based on Ar/CO_2 for all 54 modules. Figure 6.62 shows an overview of the initial gas system with the main functional modules.
- A maximal gas system, which includes separate Ar/CO_2 and Xe/CO_2 systems, able to support the maximal STT configuration. Figure 6.63 shows an overview of the maximal gas system with the main functional modules. The upgrade from the initial to the maximal gas systems can be completed together with the upgrade of the readout (Section 6.4) in order to minimize the potential losses associated with the Xe recuperation before opening the frames of the modules. Part of the additional modules required for the Xe/CO_2 system will be refurbished from the gas system of the ATLAS TRT after decommissioning.

All components of the STT gas system will be installed in the ND hall, separated from the detector, with the exception of the distribution modules, which will be located directly on the mezzanines of the SAND magnet. In the following sections, some of the relevant modules will be briefly described for both the initial and maximal STT gas systems.

Primary supply The gas system will be connected to a primary supply network for Ar, Xe, CO_2, and N_2 (the latter is mainly used to control pneumatic valves). Given the use of closed circulation systems, a limited injection of fresh gases is expected over time. Therefore, the use of separate bottles of Ar, Xe, CO_2 and N_2 is foreseen for the primary gas supply. These bottles will be located in the ND hall at some distance from the detector.

Mixer modules The working principle of the two mixer modules, Ar/CO_2 and Xe/CO_2, is the same. The flows of each gas component will be controlled by Mass Flow Controllers (MFCs). The mixing ratio will be adjusted and monitored by the software controls. Each mixer unit will contain two sets of MFCs: the first called *run* is used for normal operation, while a second set with higher flow capacity will be employed for a fast filling of the detector with the run mixture (*fill*). In order to operate within the optimal range for stability and consistency, the MFCs will normally be operated at about 60-70% of their maximum capacity. Since, during normal runs, both mixers will inject new gas only occasionally, the injection flow will be on the order of 10 nl/h for both, while the *fill* set will have a maximum capacity of about $2\,nm^3/h$. The possibility of a detector

[1] Programmable Logic Controller

[2] WinCC-OA is a supervisory control and data acquisition (SCADA) and human-machine interface (HMI) system from Siemens.

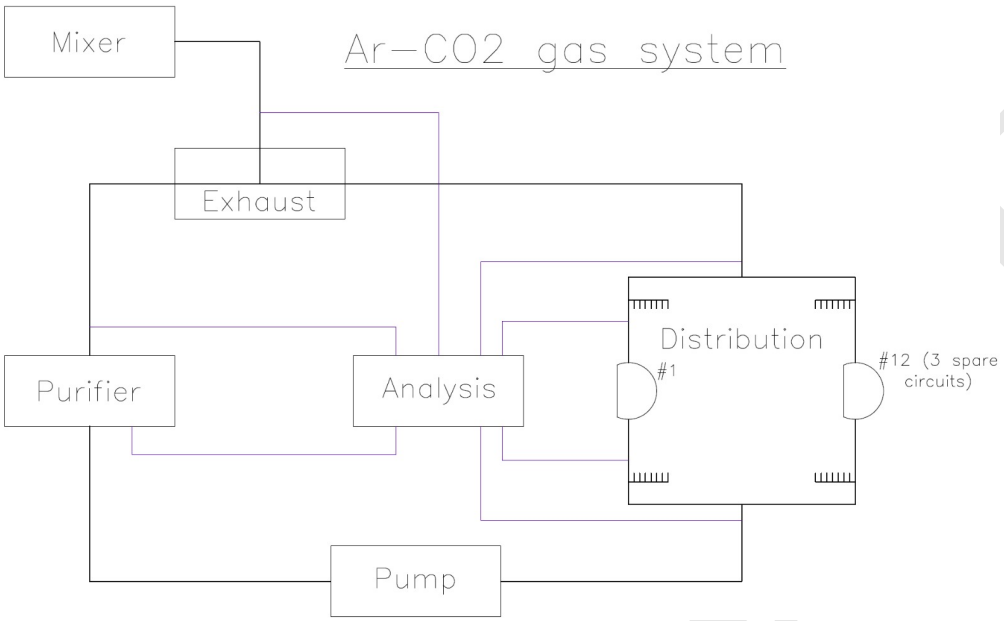


Figure 6.62: Overview of the main functional modules in the initial gas system for the STT. The 54 modules of the initial STT are split into 9 distribution circuits all using a Ar/CO_2 gas mixture.

purge with a neutral gas (i.e. N_2) is foreseen in the design of the mixer module. Figure 6.64 shows the drawing of a typical mixer module.

Closed-loop circulation modules To reduce operational costs, both the Ar/CO_2 and the Xe/CO_2 mixtures are circulated in closed loop circuits. The circulation loop is distributed over three different areas:

- Fresh mixture supply, purifier and exhausted modules can be located in service area also far from the detector;
- Circulation pump module should be located close to the experimental hall;
- Pressure controllers and final distribution modules should be located very close to the detector to minimize the pipe work.

The mixture circulation in the main loop is ensured by the pump module. Figure 6.65 shows a typical design of a pump module. Flow capacity and pump input pressure are tuned by means of an automated regulation valve in a by-pass loop around the pump [3]. A manual by-pass loop is also present. The pump input pressure is normally used as a set-point for the operation of the modules.

Initial distribution module All STT distribution modules are designed to include up to 12 separate circuits each, including some spare ones. The initial distribution module will contain 9 individual supply and return circuits (plus 3 spares) with Ar/CO_2 only (Figure 6.62). Each circuit will be connected to 6 STT modules in parallel using a distribution manifold (Figure 6.66). Supply and return flows will be read by means of flow measurement cells developed at CERN for the gas

[3] Frequency controlled pump can also be used

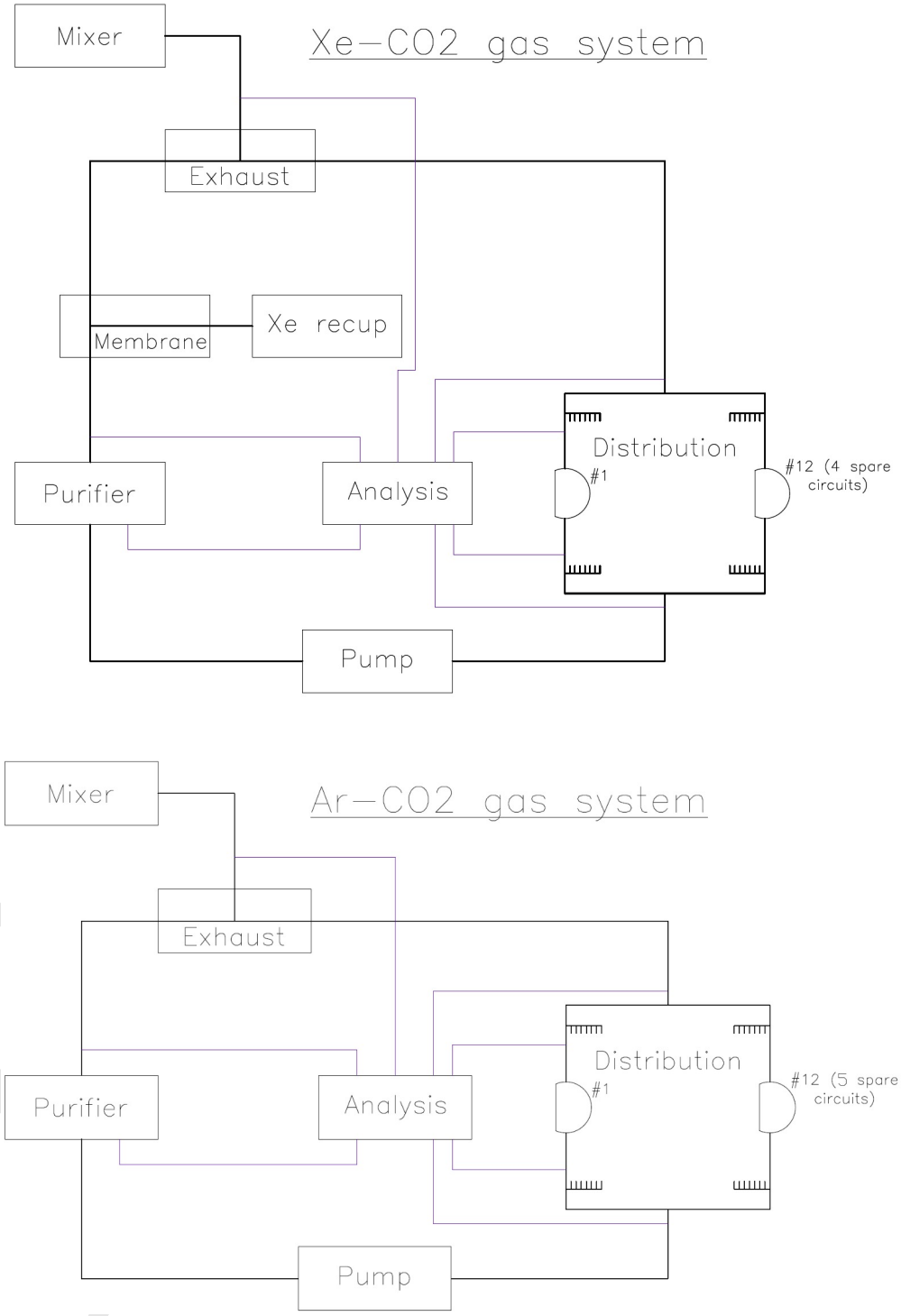


Figure 6.63: Overview of the main functional modules in the maximal gas system for the STT including separate Ar/CO_2 and Xe/CO_2 systems and able to support the maximal STT configuration. The distribution modules include 8 circuits for Xe/CO_2 and 7 circuits for Ar/CO_2.

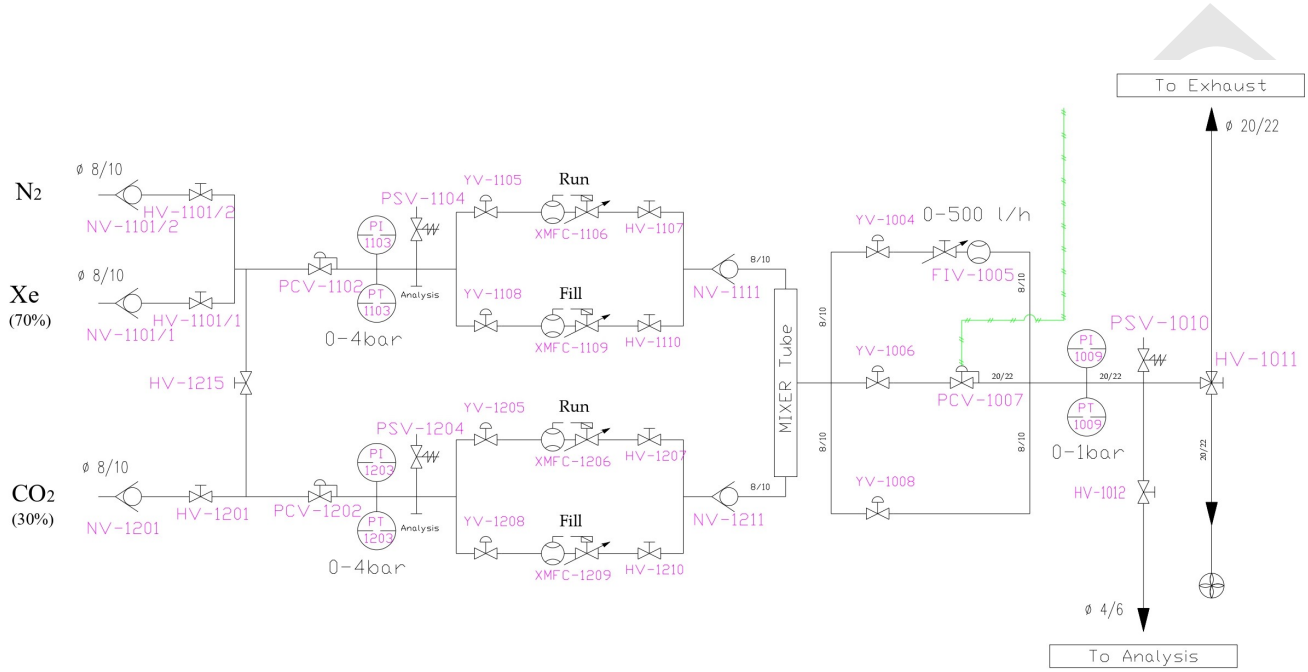


Figure 6.64: Layout of the Xe/CO_2 gas mixer module for STT.

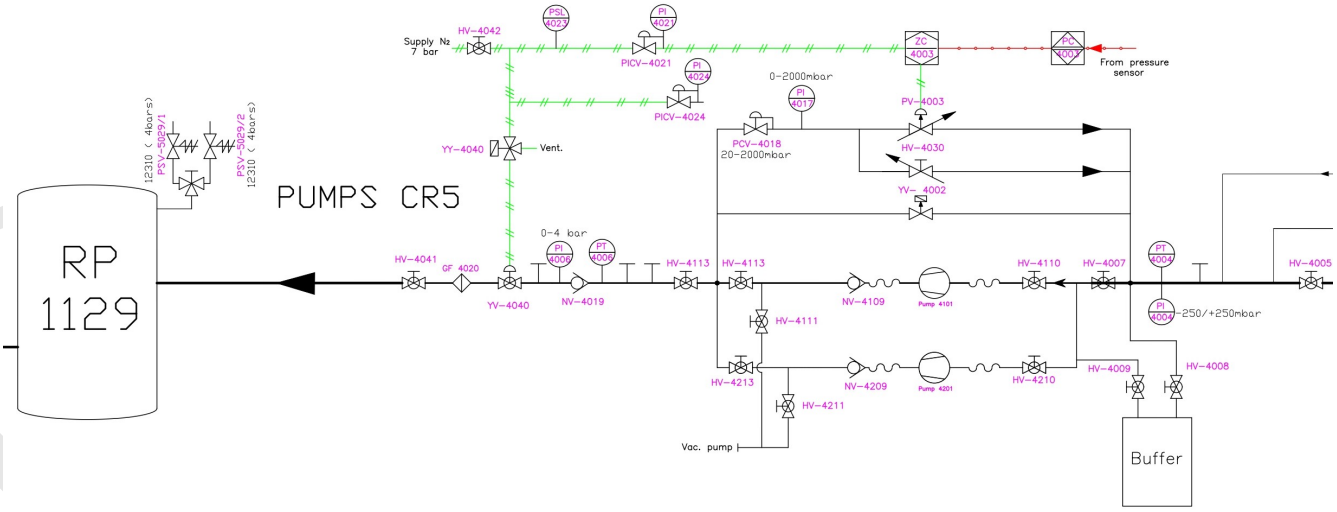


Figure 6.65: Layout of a typical gas compressor module for STT.

systems of the LHC experiments. Manual needle valves will allow for the adjustment of the flow in the individual channels. On the return lines, automated regulation valves will control the pressure in the STT detector. Insulation valves and an absolute pressure sensor will be installed on each channel before and after each STT module. This implementation allows for the insulation of each module and the performance of leak tests. Figure 6.67 shows a preliminary layout of the distribution module. A maximum of three supply and return circuits can be mounted in a standard rack with dimensions 60 cm (W) × 90 cm (D) × 200 cm (H). A total of 3 racks are required for the initial STT gas distribution system, to be installed on a mezzanine on the magnet.

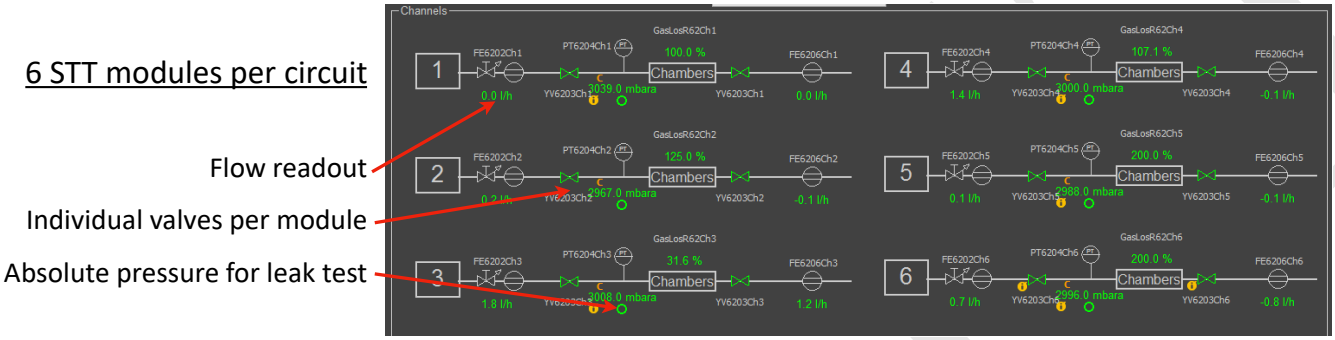


Figure 6.66: Schematic diagram of one of the gas distribution circuits feeding 6 STT modules.

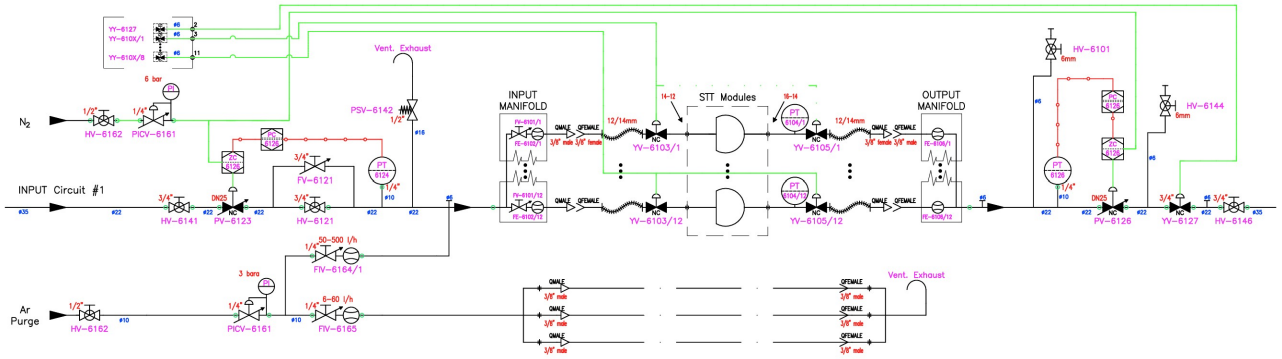


Figure 6.67: Preliminary layout of the gas distribution module for STT.

Maximal distribution module Two separate distribution modules are foreseen for the maximal STT: one with 8 circuits (plus 4 spares) for Xe/CO_2 and a second one with 7 circuits (plus 5 spares) Ar/CO_2 (Figure 6.63). Each circuit will be connected to 6 STT modules in parallel using a distribution manifold (Figure 6.66), similarly to the initial distribution module described above. A total of 5 racks – only 2 in addition to the ones present in the initial distribution module – are required for the maximal STT gas distribution system, to be installed on a mezzanine on the magnet.

Purifier modules Since impurities can accumulate during operation in the gas re-circulation, a purifier module is included in the design for both the Ar/CO_2 and Xe/CO_2 systems. It can be equipped with material able to remove O_2 and H_2O from the gas mixture. The removal capacity of other specific impurities (if any) will have to be tested and measured. The module contains two

24 liters cartridges filled with the suitable cleaning agent (normally molecular sieves and metallic catalysts are used for water and oxygen removal respectively). The purifier cycle is completely automated. During standard operation one cartridge is used for mixture cleaning, while the other is regenerated or ready and waiting for operation. Regeneration of metallic catalysts require the use of H_2. To this end, a bottle of non-flammable Ar/H_2 mixture 97.5%/2.5% is used since the purifier modules will be installed in the ND hall. Given the requirements on the maximal O_2 contamination and the gas flow rates in operating conditions, the use of about 1-2 bottles per months is expected.

Xe recuperation A Xe recuperation module will be added to the Xe/CO_2 gas system to minimize operational costs particularly during emptying of the detector. The recuperation system will use cryogenic separation (by means of liquid N_2) to isolate Xe mainly from N_2 and CO_2 and will be installed in the ND hall. Figure 6.68 shows the example of the Xe recuperation system developed for the ATLAS-TRT detector at the CERN LHC. This module can be refurbished after decommissioning to be reused for the STT.

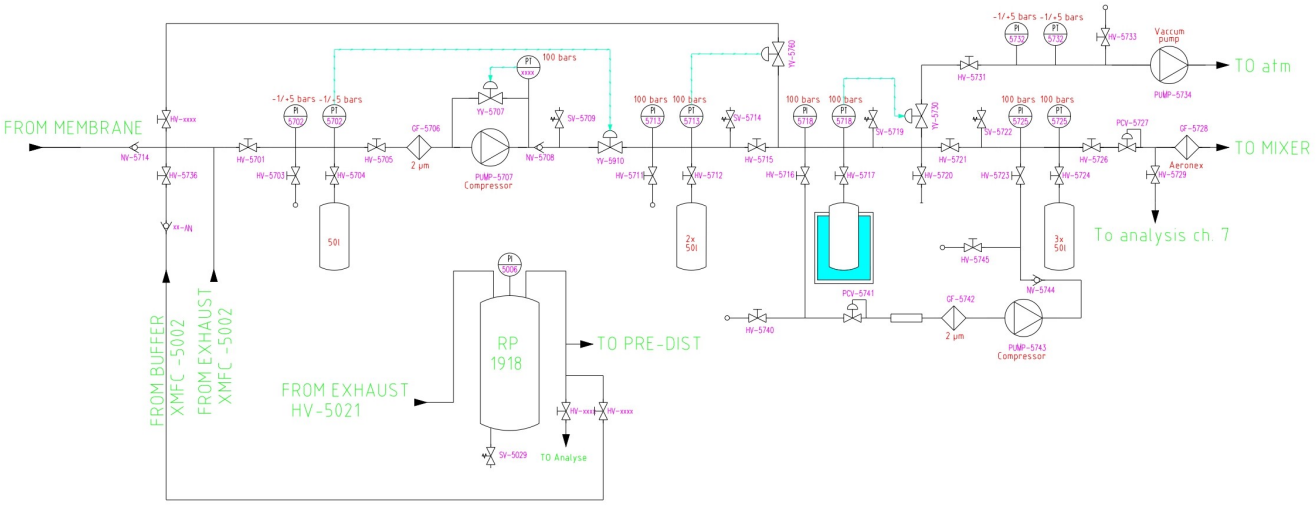


Figure 6.68: Example of the Xe recuperation system developed for the ATLAS TRT at the CERN LHC.

Gas analysis A gas analysis module is used to continuously monitor with an automated cycles O_2, CO_2, and H_2O concentrations in both the Ar/CO_2 and Xe/CO_2 gas mixtures. A gas chromatograph is also added to the analysis module used in the Xe/CO_2 gas system to monitor the N_2 concentration. The chromatograph can be refurbished from the ATLAS-TRT gas system after decommissioning. The analysis modules are completely automated: they can be programmed to sample all gas streams (for example supply and returns of distribution circuits) including references or calibration gases. Expert operators can trigger remotely the analysis of specific lines at any moment. The analysis time of each stream can be tuned to compensate for the different pipe length between the analysis rack and the sampling point. The gas, after being analyzed is re-injected into the circulation loop.

Construction, operation and resource estimate The STT detector will be equipped with separate gas re-circulation systems for the STT modules operated with the Ar/CO_2 and Xe/CO_2

mixtures. The new system is designed based on well-established functional modules developed for the LHC experiments. The PLC and WinCC-OA SCADA interface are used internally to control and monitor all relevant parameters and for the regulation loops. An external interface to the Ignition framework used at Fermilab can be used. The following components of the initial Ar/CO_2 gas system have to be installed in the ND hall:

- 2 compressors (1 spare): each approximately 110 cm (W) × 90 cm (D) × 120 cm (H), 450 kg;
- 1 control rack for the compressors: 60 cm (W) × 90 cm (D) × 200 cm (H);
- 2 racks for gas buffers (at 2 bar): 80 cm (W) × 80 cm (D) × 200 cm (H);
- 1 rack for the gas mixer: 60 cm (W) × 90 cm (D) × 200 cm (H);
- 1 rack for the gas analysis: 60 cm (W) × 90 cm (D) × 200 cm (H);
- 1 rack for the gas purification: 60 cm (W) × 90 cm (D) × 200 cm (H);
- 1 rack for the gas exhaust: 60 cm (W) × 90 cm (D) × 200 cm (H);
- 1 control rack for the gas distribution: 60 cm (W) × 90 cm (D) × 200 cm (H).

The total power requirement for the two pumps is 11 kW 3 phase (4 poles) at 480 V and 60 Hz. A water supply line at about 15° C is needed for cooling the compressors. The additional components required for the later Xe/CO_2 partial filling and the maximal STT upgrade to be considered for the ND hall space include:

- 1 compressor: approximately 110 cm (W) × 90 cm (D) × 120 cm (H), 450 kg;
- 1 control rack for the compressors: 60 cm (W) × 90 cm (D) × 200 cm (H);
- 2 racks for gas buffers (at 2 bar): 80 cm (W) × 80 cm (D) × 200 cm (H);
- 1 rack for the gas mixer: 60 cm (W) × 90 cm (D) × 200 cm (H);
- 3 racks for the gas analysis: 60 cm (W) × 90 cm (D) × 200 cm (H);
- 1 rack for the gas purification: 60 cm (W) × 90 cm (D) × 200 cm (H);
- 2 racks for Xe recuperation: 60 cm (W) × 90 cm (D) × 200 cm (H);
- 1 rack for the gas exhaust: 60 cm (W) × 90 cm (D) × 200 cm (H);
- 1 rack for the membrane module: 60 cm (W) × 90 cm (D) × 200 cm (H);
- 1 control rack for the gas distribution: 60 cm (W) × 90 cm (D) × 200 cm (H).

The power and cooling requirements are similar to the ones for the Ar/CO_2 system.

Some of the components of the STT gas system will be refurbished from the gas system of the ATLAS TRT, expected to be decommissioned in 2026, resulting in an overall cost reduction. Table 6.12 lists such components. The construction schedule for the STT gas system will take about 50 weeks considering a fully available and expert team at CERN. A supervision team will also be needed. It is composed by 1 physicist and 2 technical engineers (or PhD students). The latter will be trained at CERN for the future operation and maintenance of the gas system.

DRAFT

Table 6.12: List of the components to be refurbished from the gas system of the ATLAS TRT.

Item	Quantity	Comment
Gas analysis system	3	CO_2 and O_2 concentration above 0.1%
Chromatograph	2	For the analysis module
Xe recuperation system	1	50 liter tank + components and compressors
Operational membrane rack	1	For Xe/CO_2 system
Spare pumps for membrane rack	2	
Spare membranes	2	
Xe mixer and buffer	1	For Xe/CO_2 system
Ar mixing rack	1	For Ar/CO_2 system

6.12 Prototyping and Tests

6.12.1 Measurements of Straw Properties

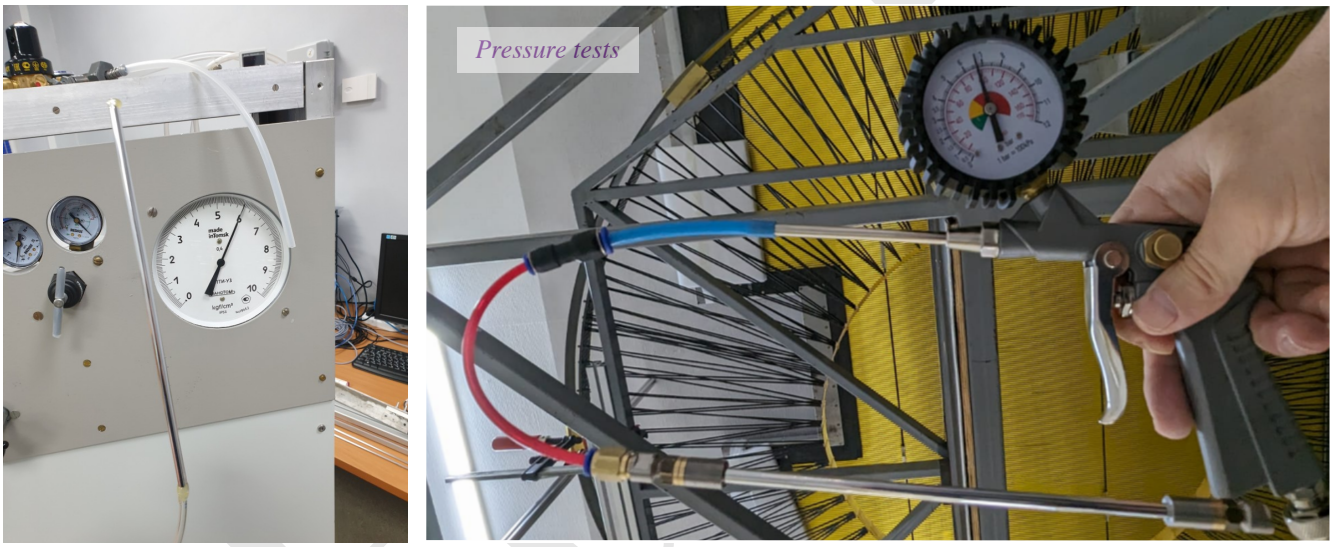


Figure 6.69: Pressure tests of straws with 20 μm walls for STT. A maximal pressure of 7 bar relative was achieved without permanent deformations.

Mechanical Tests Extensive tests of the straws under varying internal pressure have been performed in order to evaluate their mechanical properties. The straws produced with ultrasonic welding and the Fraunhofer film 19 μm thick with double Al metallization were successfully tested up to 7 bar relative (Figure 6.69), which is still within the elastic regime of the material. The pressure resulting in a straw breakage was found to be about 9 bar relative, mostly due to instabilities at the seam-material boundary.

The straw deformations caused by the internal pressure and the resulting tension on the straw walls were studied for two different wall thicknesses, 12 μm and 20 μm. Such deformations proved important to tune the parameters of the assembly procedure of the STT modules (Section 6.5.2), as well as the STT operating conditions. Results are summarized in Figure 6.70. A minimal overpressure of about 0.25 bar is required to guarantee the circularity of the straws, given the

thinness of the walls. Above this value, the straw diameter increases by approximately 10 μm per bar of additional pressure, exhibiting a linear behavior. The internal overpressure also results in an elongation stretching the straws and putting their walls under tension. Straws behave like natural springs (ropes) within the elastic limit of their material, as shown by the linear deformations in Figure 6.70. The measured elongations and tensions are listed in Table 6.13 for both the nominal STT operating pressure (1 bar relative) and the assembly pressure. The use of 12 μm walls results in substantially larger elongations and higher tensions. For this reason, 19 μm walls were selected, as they are mechanically less critical and allow a more efficient mass production. The measured deformations are in good agreement with the finite element calculations (Section 6.5.4), validating the STT engineering model and the related mechanical analysis.

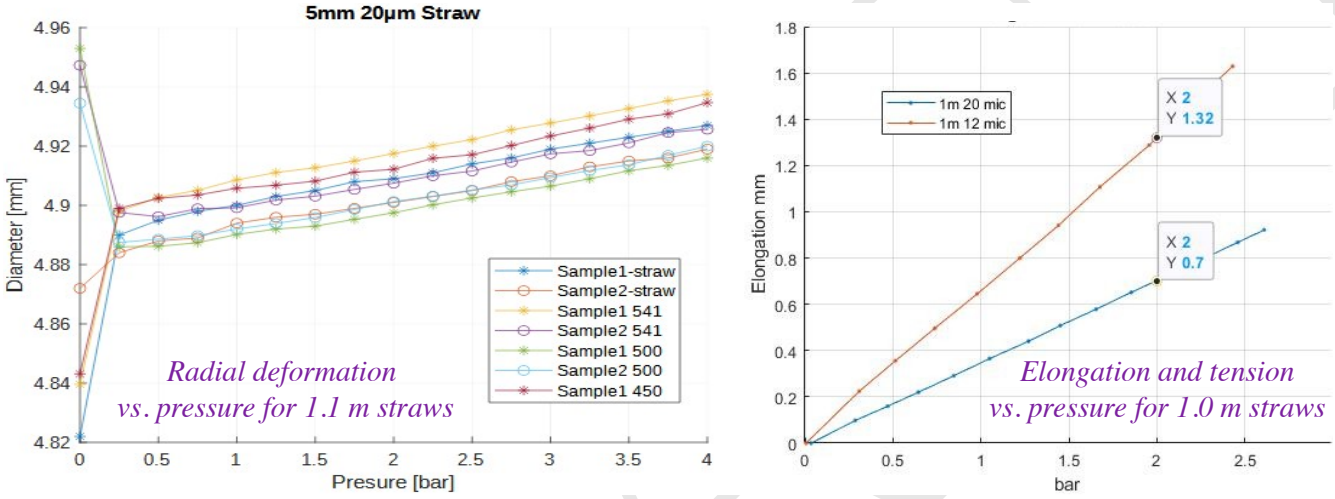


Figure 6.70: Measurement of the increase in the outer diameter (left plot) and of the straw elongation (right plot) as a function of the internal relative pressure for different values of the wall thickness.

Table 6.13: Measurement of the straw elongation and tension with an internal pressure of 1 bar and 2.5 bar relative for different values of the wall thickness.

Diameter	Length	Wall thickness	Elongation		Tension	
			1 bar	2.5 bar	1 bar	2.5 bar
5 mm	1 m	12 μm	0.66 mm	1.65 mm	78.5 gf	196 gf
5 mm	1 m	20 μm	0.35 mm	0.88 mm	56.0 gf	140 gf

Gas Leak Measurements The gas leak rate of the straws produced with ultrasonic welding using the final Fraunhofer film 19 μm thick with double Al coating 70 nm+70 nm (Section 6.6) was measured. The same straws are used for the assembly of the second 1.2 m C-fiber prototype (Section 6.12.4) and of the full-scale prototype (Section 6.12.9). The test rig (Figure 6.71) consisted of a digital pressure gauge connected to a straw end and a valve to shut down the gas flow. The straws were inserted into a sealed glass tube flushed with dry air to reduce the H_2O contamination and initially pressurized to 2.5 bar absolute. The relative pressure drop within the straw and the mole number leaked out are determined from the equation of state:

$$n = \frac{pV}{RT} \qquad \frac{\delta n}{n} = \frac{\delta p}{p}$$

from the measured internal pressure p_{straw}, external pressure p_{lab}, temperature T, relative humidity, and volume of the straw V_{straw}. The variations are obtained at constant temperature and volume. The internal pressure was continuously monitored for a few days after the straw was filled with different gases, including CO_2, Ar, Xe, and air. A simultaneous measurement with a straw from the Mu2e experiment, produced with conventional winding technology and 14 μm film with a coating of 80 nm Al + 20 nm Au, was performed to obtain a reference calibration. Results are summarized in Table 6.14. The measured leak rates of the STT straws are significantly lower than those of the Mu2e straws, due to the ultrasonic welding technology and the double metallization on both sides of the film. The result can be used to estimate the diffusion rate expected for the entire initial STT with both the Ar and Xe gases. An exponential dependence of the diffusion rate upon the square of the atomic radius of gas is expected [74] giving a scale factor Xe/Ar around 0.11. The initial STT has a total gas volume of about 5.8 m^3 filled at 70% with Xe and about 2.2 m^3 filled at 70% with Ar (Section 6.11). The expected total gas leakage from the diffusion through the straws at the nominal operating pressure of 1 bar relative is therefore about 1.079 liters/year for Ar and 314 liters/year for Xe.

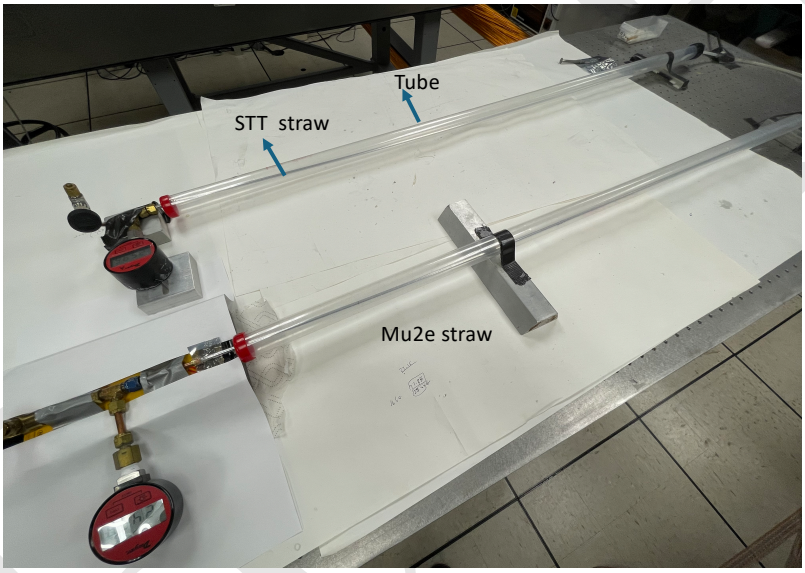


Figure 6.71: Measurement of the gas leak rate for the STT straws produced with ultrasonic welding using the Fraunhofer film 19 μm thick with double Al coating 70 nm+70 nm, and an initial pressure of 2.5 bar absolute. A straw from the Mu2e experiment is used as reference.

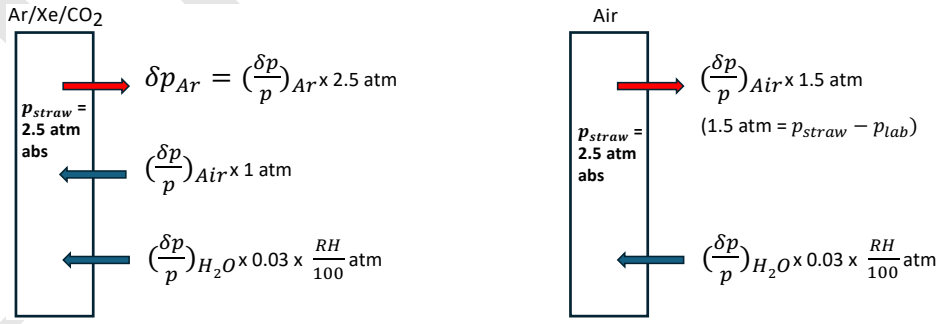


Figure 6.72: Determination of the leak rate for CO_2, Ar, Xe, and air from the measurements.

Gas Gain vs. High Voltage The gas gain as a function of the high voltage applied was measured using irradiation with ^{55}Fe sources and a gas mixture of Ar/CO_2 70/30 at 1 bar absolute pressure.

Table 6.14: Measurement of the gas leak rate for the STT straws compared with a reference Mu2e straw.

Gas type	$\delta p/p$ per hour		
	Mu2e straw	STT straw	Ratio
CO_2	18.0×10^{-4}	8.0×10^{-4}	2.3
Air	3.0×10^{-4}	0.8×10^{-4}	3.7
Ar	1.7×10^{-4}	0.4×10^{-4}	4.2

Since the constant current (I_0) observed at lower voltages corresponds to the nominal ionization current, a direct evaluation of the gas gain at higher voltages can be obtained by normalizing the measured current curve to the initial value $G = I/I_0$ [75]. The setup of the measurement is shown in Figure 6.73. A negative high voltage was applied to the walls of a single STT straw, while the 20 μm W/Re wire was connected to the ground potential. Two ^{55}Fe sources were used to increase the irradiation rate. Count rates were measured, and the signal was digitized using a TQDC readout. The ionization current I_0 is calculated from a fit to the rate of the digitized spectrum. Results for the gas gain as a function of the HV applied are shown in Figure 6.73. The default gas gain of 2.5×10^4 is achieved with a voltage of about 1.4 kV at 1 bar absolute pressure. The corresponding operating point at 2 bar absolute pressure is reached around 1.6 kV.

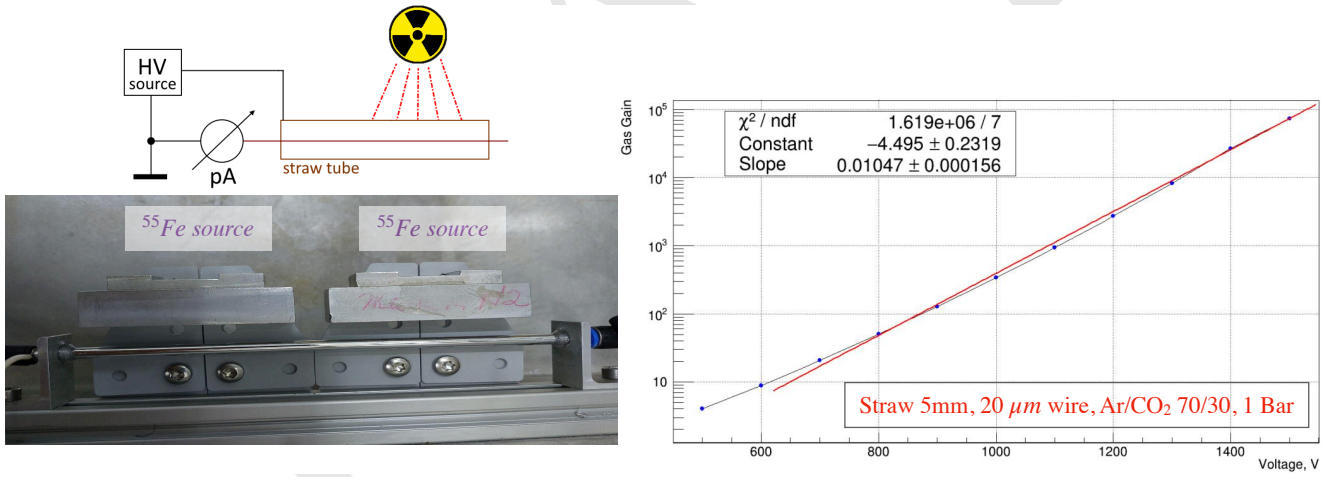


Figure 6.73: Measurement of the gas gain as a function of the applied HV for STT straws at 1 bar absolute pressure. A gain of 2.5×10^4 is reached at HV around 1.4 kV.

6.12.2 Mockup Prototypes

In order to validate the basic STT concept, a small mockup prototype of approximately 0.4 m × 0.4 m was constructed using the same frame design planned for the STT modules (Section 6.5.1). The mockup with four XXYY straw layers was successfully assembled using a frame machined from transparent plexiglass (Figure 6.74). The mockup was pressurized at the nominal 2 bar absolute pressure and functionally tested with a ^{55}Fe source at a voltage of 1.550 V, corresponding to an approximate gas gain of 2×10^4, as shown in Figure 6.74. The completion of the mockup prototype was an important milestone for STT as it allowed a better understanding of the assembly procedure and of the corresponding tooling required. To this end, the mockup was used as a standard test

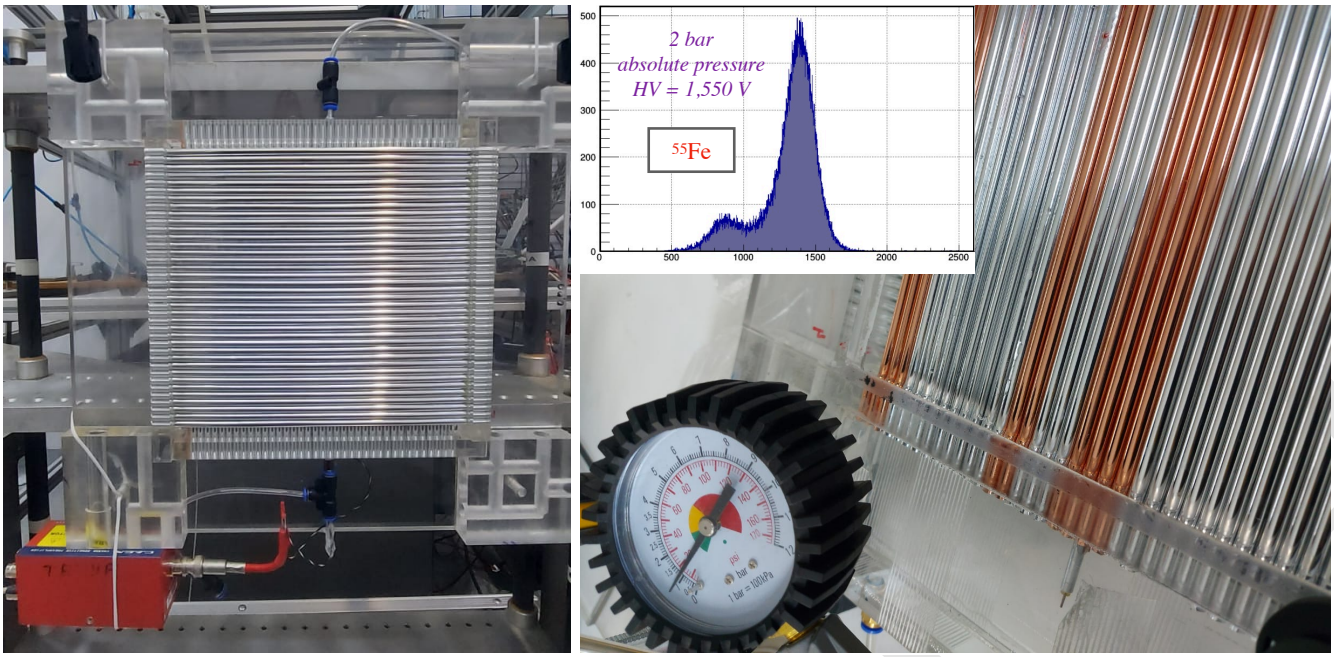


Figure 6.74: Completion and test of a mockup prototype with plexiglass frame and four XXYY straw layers with the same geometry as the STT modules.

bench to validate various elements like the end-plugs, the crimping pins, the readout boards, etc. throughout the design and prototyping stage of the STT modules.

6.12.3 Wiring Tests

The wiring with the newly designed crimping pins was extensively tested. For this purpose, a dedicated setup was constructed using a machined plexiglass frame with multiple holes capable of holding up to 30 wires via the corresponding pins (Figure 6.75). Wires made of W/Re with a 20 μm diameter and produced by LUMA were used, along with the same pneumatic crimping tool developed for the mass production of the ATLAS TRT. The effect of varying the crimping point along the pins, as well as the long-term stability of wire tension after crimping were evaluated. Some of the results are shown in Figure 6.75. An improved reproducibility and long term stability were obtained with the pneumatic crimping tool compared with the manual tool used during the assembly of the 1.2 m STT prototype (Section 6.12.4). The tests were repeated with different pin versions, characterized by varying diameters of the central hole and a different hardness of the copper material. The main parameter for an optimal crimping with the pneumatic tool was found to be the material softness, which was achieved by a thermal annealing at 600°C, followed by a rapid immersion in cold water prior to the gold coating via electrical deposition. Once the pins are soft enough the crimping process with the ATLAS pneumatic tool proved to be successful. No wire slippage was observed in a few weeks after the actual crimping Figure 6.75). A nominal wire tension of 50 gf was used in all tests, which is safely below the expected limit of elastic deformation of 75 gf. The latter value was measured using calibrated weights. Given the relatively short wire length of about 20 cm in the test setup, a systematic uncertainty around 5 gf was estimated on the absolute values of the tension measured, due to the uncertainty in calculating the effective wire length.

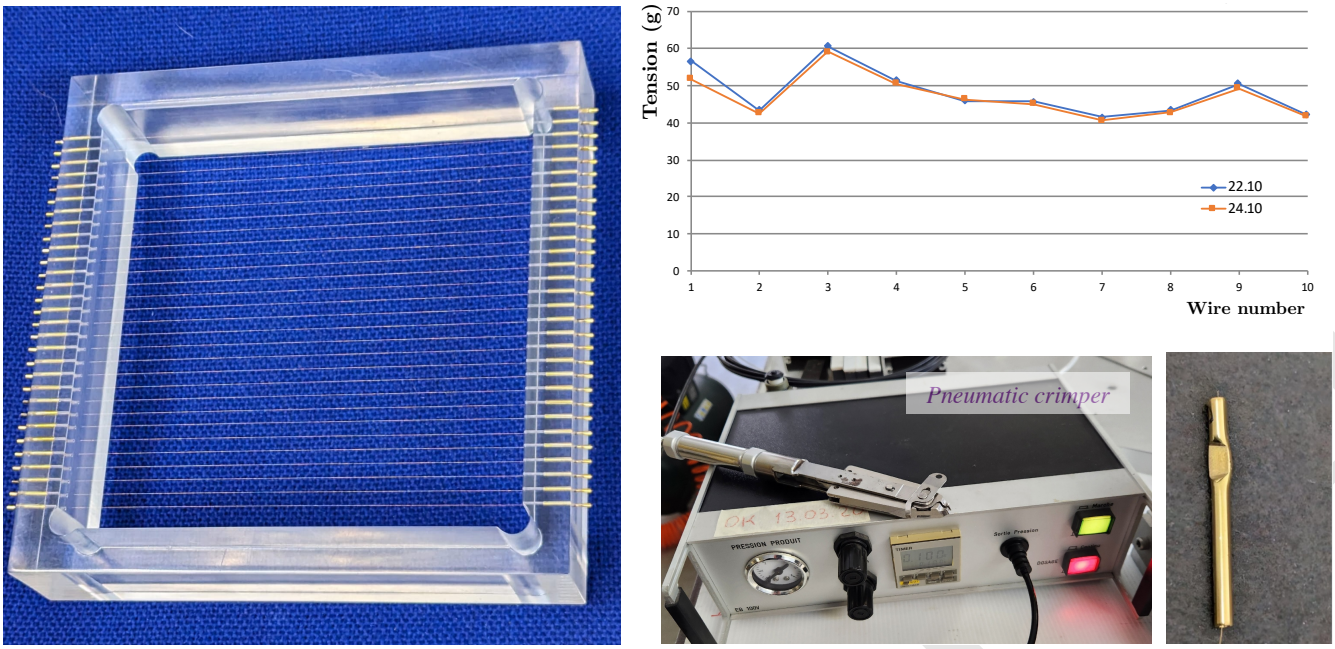


Figure 6.75: Crimping tests with the final pins and the pneumatic tool for mass production developed by ATLAS TRT. The wire tension is measured at different time intervals after the crimping.



Figure 6.76: Wiring tests with a 4 m STT straw in vertical position and four spacers glued to the 20 μm wire.

The complete STT wiring procedure including the spacers was tested with full-size 4 m long straws. The test included the following steps:

- A tooling developed for the COMPASS straw tracker (Section 6.14.2) is used to support the 20 μm W/Re wire under a tension of 50 gf while 4 spacers are glued onto it: two spacers at the wire ends and two spacers equally spaced in between with $\sim$ 1.3 m span;
- A 4 m straw is held under tension in the vertical position by a supporting frame;
- The wire with glued spacers is attached to an ordinary plastic thread;
- The wire with glued spacers is inserted at the top of the vertical straw and the thread pulled down until the wire comes out at the opposite end;
- The straw is terminated with the end-plugs and the wire is fixed by the crimped pins.

Figure 6.76 illustrates the final wiring steps. Both the spacers and the end-plugs used were produced by 3D printing in order to validate their design before the fabrication of the final tooling for the mass production by injection molding (Section 6.13.1). The central hole of the spacers was manually drilled after the 3D printing. Various tests were performed to optimize the viscosity and curing time for the glue. The final solution selected provided a good accuracy in positioning the spacers onto the wire without any significant spread of the glue along the wire nor any hot spot created. The wiring tests successfully demonstrated the wiring procedure to be used during the assembly of the STT modules in realistic conditions. The precision of the 3D printed spacers could not match the one obtained from the injection molding, but was nevertheless adequate.

The wiring procedure with the final production pins, end-plugs, and spacers was optimized and validated during the assembly of the second 1.2 m STT prototype in Pisa (Section 6.12.4). The spacers were not directly glued to the wire, but instead they were constrained by two small drops of Henkel Loctite 406 glue, as shown in Figure 6.77. Three spacers per wire were used. A pressure of about 5 bar was found to provide an optimal crimping with the ATLAS pneumatic tool and a nominal wire tension of 50 gf. The crimping success rate was similar to the one obtained with the old ATLAS pins used for the 1.2 m CERN prototype (Section 6.12.4), with no significant wire slippage observed over a few weeks. Figure 6.77 shows the testing of multiple wires and the measurement of the wire tension from the vibration resonance.

6.12.4 Prototypes of a 1.2 m STT Module

In November 2023 a 1.2 m $\times$ 0.8 m prototype with about 700 straws in four XXYY layers and based on a complete C-fiber frame identical to the one of the STT modules (except size) was successfully completed and tested at CERN (Figure 6.78). The end-plugs for the straw termination were produced by 3D printing to test them before the mass production by injection molding (Section 6.13.3). The aluminum assembly table used had alignment profiles similar to the straw holders at the four sides, as well as the possibility to rotate around two orthogonal axes. The wiring with 20 μm W/Re LUMA wires was performed in the vertical position with a nominal tension of 50 gf applied (Section 6.13.10). The number of instrumented straws was 64 in the XX double layer and 64 in the YY double layer. Figure 6.79 shows some results from the functional test of the prototype with a gas mixture of Ar/CO_2 70/30 and a voltage of 1.45 kV. The total time required for the assembly and test was about 1.5 months by 5 people, including the trial of alternative options for some of the assembly steps. No major issues were found during the assembly and small

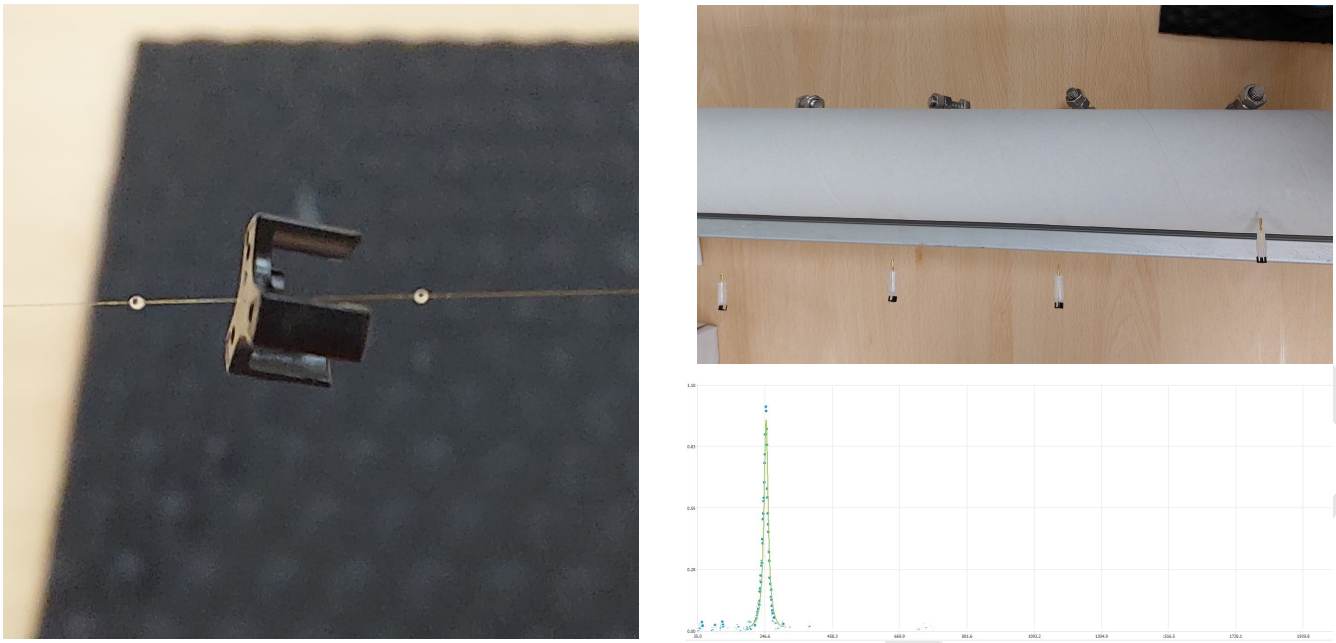


Figure 6.77: Validation of the wiring procedure with the final production pins, end-plugs, and spacers during the assembly of the second 1.2 m STT prototype in Pisa.



Figure 6.78: Construction and test of the first 1.2 m prototype of a STT tracking module at CERN with 4 XXYY straw layers and C-fiber frame.

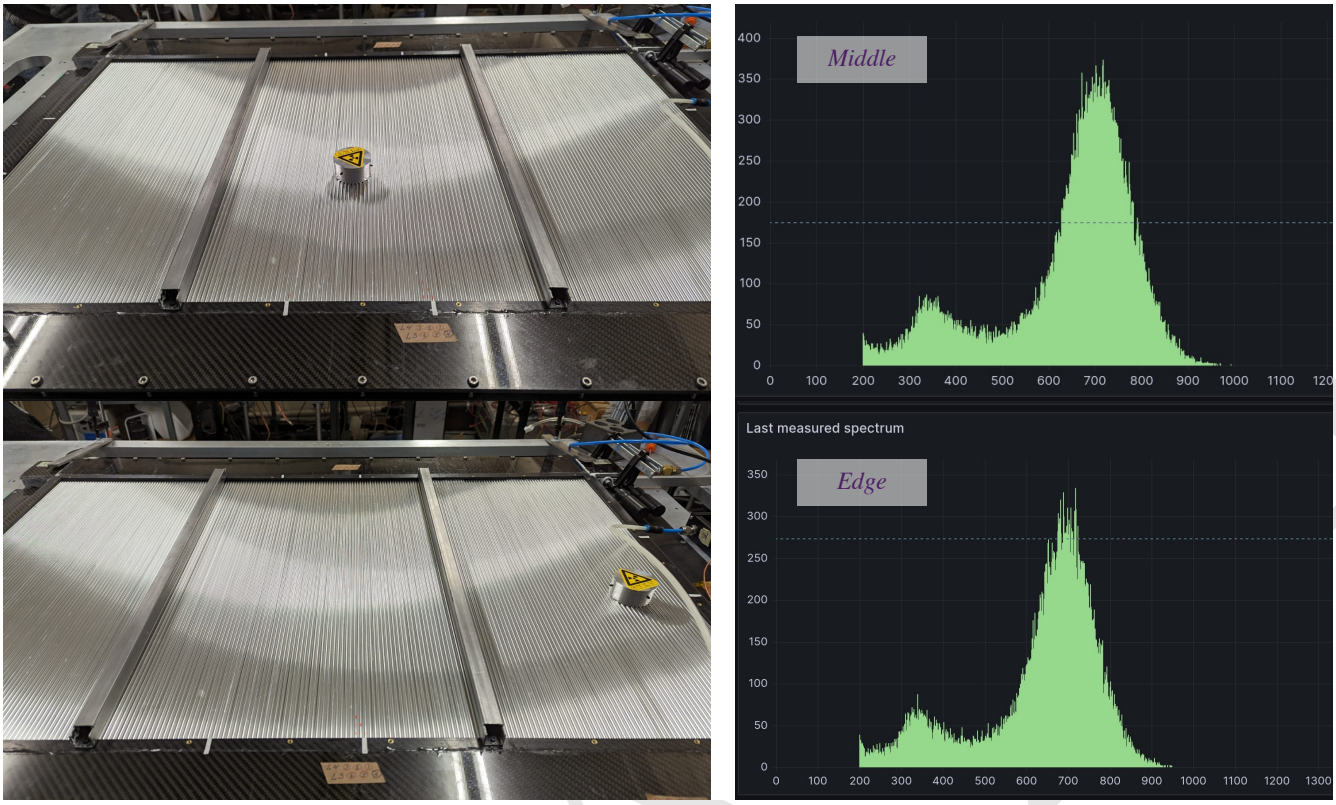


Figure 6.79: Test of the first 1.2 m STT prototype with a ^{55}Fe source at CERN.

improvements were identified to be implemented in the next iterations. The demonstration of this realistic STT prototype was a major milestone for the STT technology, allowing to establish an end-to-end assembly procedure (Section 6.5.2) and to validate the design of the tracking modules and related components. The CERN prototype also provided an important test bench for the optimization of the detector integration (Section 6.9) and of the STT integrated readout boards (Section 6.7.1).

A second 1.2 m STT prototype similar to the CERN one and incorporating the small improvements identified has been assembled at Pisa Istituto Nazionale di Fisica Nucleare (INFN). No major change in the design was required with respect to the first prototype. This second prototype is based on the final components validated for mass production and used for the full-scale prototype as well (Section 6.12.9). The main change is the use of the spacers produced by injection molding (Section 6.13.4) for the wire self-centering. All the straw used (about 700) were produced with the final Fraunhofer film (Section 6.13.2). Figures 6.80 and 6.81 show various steps of the assembly procedure for the second 1.2 m prototype in Pisa. The wiring procedure with the final pins, end-plugs, and spacers was successfully validated (Section 6.12.3).

6.12.5 Prototypes of Readout Boards

Complete prototypes of the integrated STT readout boards and the related flexible kapton PCBs (Section 6.7.1) were tested with the 1.2 m C-fiber prototype at CERN, as shown in Figure 6.82. The prototype boards had the correct form factor to be mounted within the C-fiber frame (158 mm ×

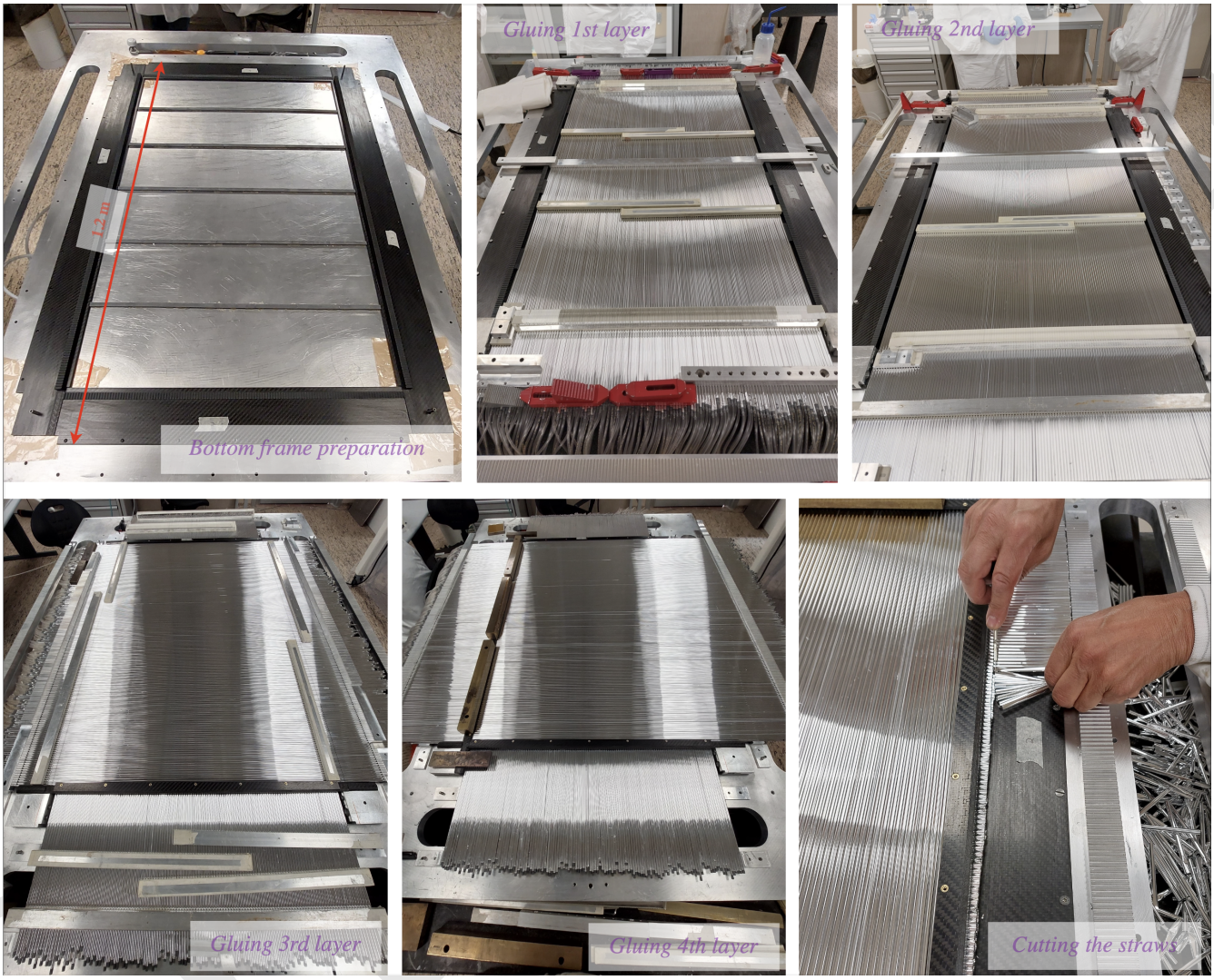


Figure 6.80: Assembly of the second 1.2 m STT prototype in Pisa: gluing of the four XXYY layers of straws inflated at the assembly pressure to the C-fiber frame and cutting of the straws.



Figure 6.81: Assembly of the the second 1.2 m STT prototype in Pisa: application of the silver paint to the ground plane, wiring of the straws with the final pins, end-plugs, and spacers, measurement of the wire tension, measurement of the wire resistance, sealing with stycast glue and teflon molds, pressure test with temporary plexiglass covers, completed prototype at testbeam.

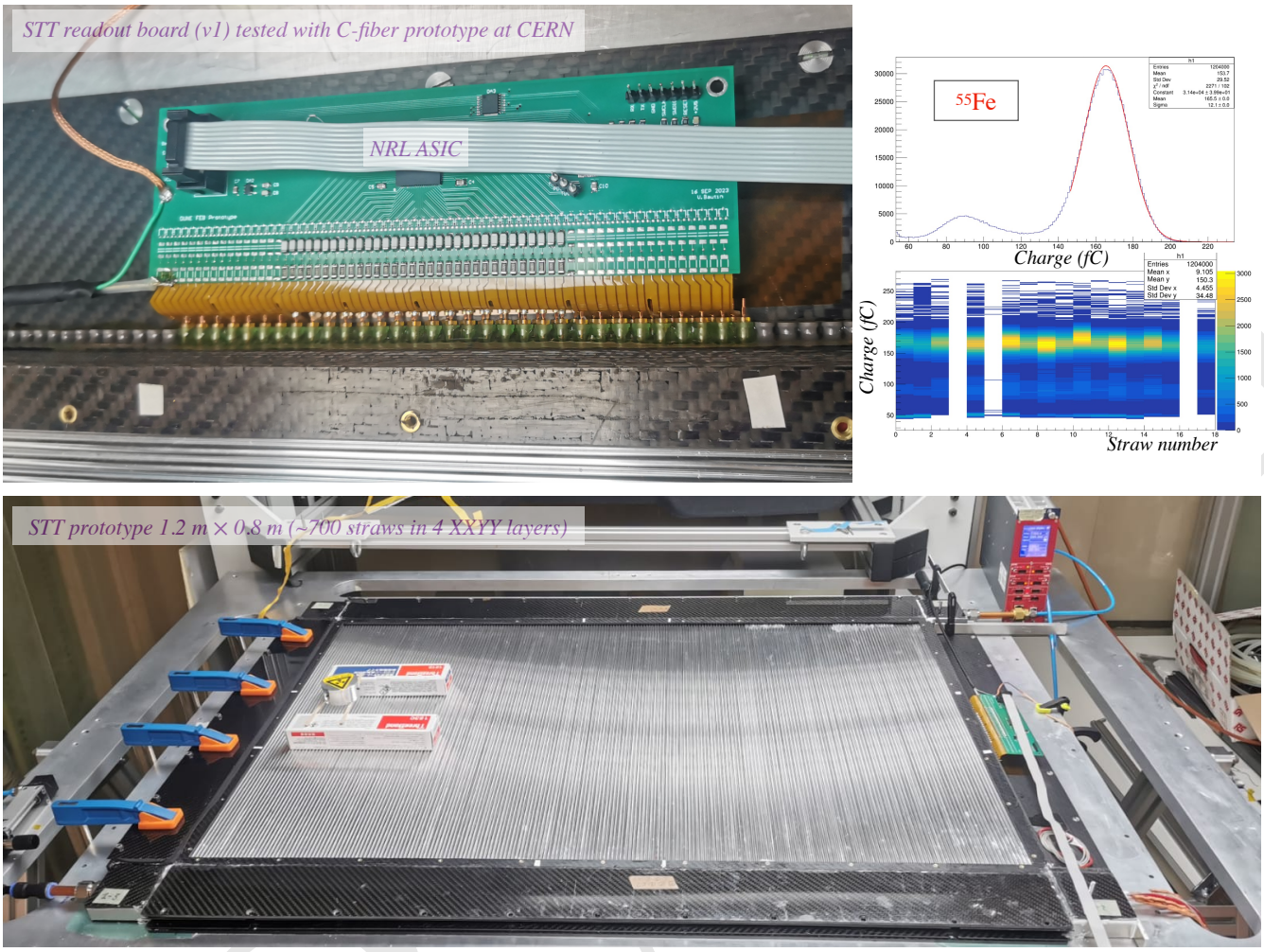


Figure 6.82: Tests of a prototype of the integrated readout boards with the 1.2 m C-fiber STT prototype at CERN. The gaps appearing in the response correspond to three dead channels in the NRL chip used.

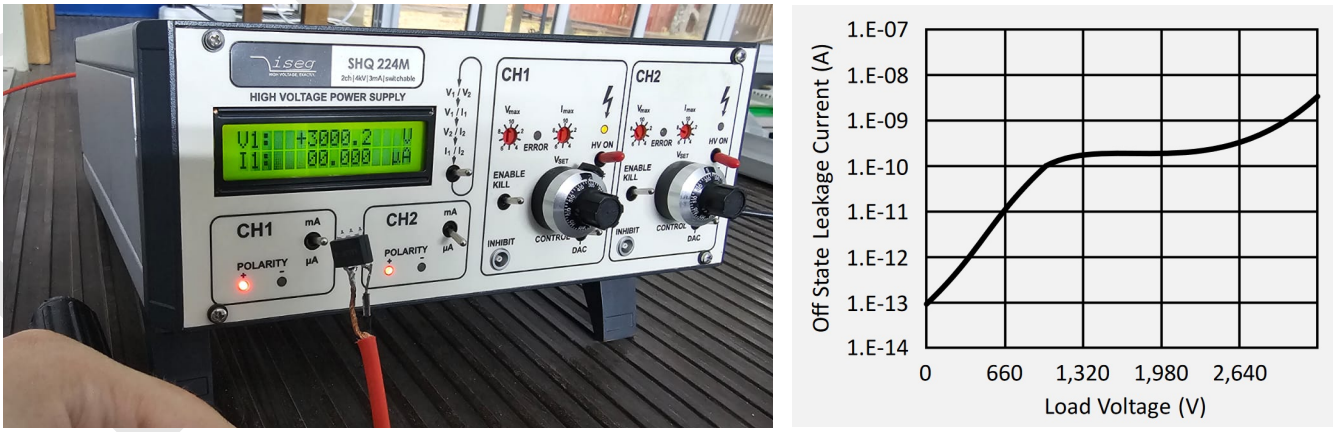


Figure 6.83: Tests of the solid state relay for the STT readout boards at 3.0 kV.

50 mm) and complete functionality, including HV and LV supplies, ASIC, MCU, LDO regulators, etc. The first version tested was based on a single NRL analog chip reading 32 straws and had the kapton PCB directly soldered to the readout board. Results obtained with a ^{55}Fe source are shown in Figure 6.82. An excellent charge resolution with low noise levels was observed across all instrumented straws. The tests demonstrated the concept of integrated readout for STT and provided useful insights for further design improvements. They also allowed a debugging and optimization of the related firmware controlling the MCU and the interface with the DAQ. The final revised board includes a modular PCIe x32 connector for easier installation/replacement, combined with a fixed kapton PCB directly glued to the straw holder on the side of each double straw layer (Section 6.7.1).

Figure 6.83 shows quality tests of the leakage current performed on some samples of the solid state relay used to remotely connect/disconnect the HV on the integrated STT readout boards (Section 6.7.1). No measurable current was detected up to applied voltages of 3.0 kV.

6.12.6 Mockup Cooling Prototype

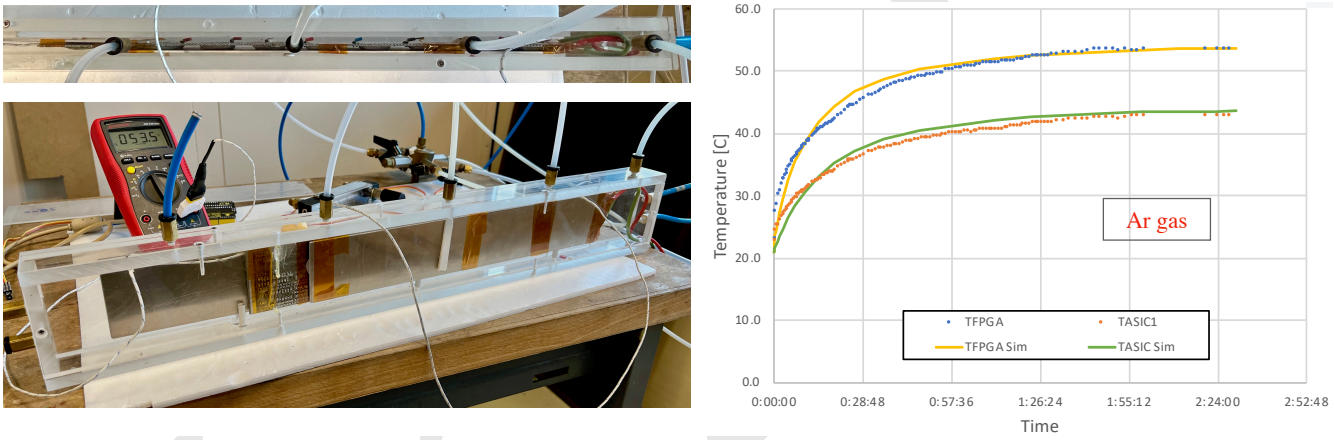


Figure 6.84: Construction and test of a mockup cooling prototype (left picture) at CERN. The measured temperatures as a function of time are compared with FE simulations (right picture) to validate the cooling model.

In order to validate the results of the thermal analyses a mockup prototype was built using a plexiglass frame with the same geometry as a section of the STT modules and dummy readout boards with simple resistors dissipating the power expected from the various chips. The mockup prototype was flushed with pure Ar gas at 1 bar absolute pressure. The temperatures on the mockup chips were measured with sensors as a function of time for different values of the gas flow. Complete temperature maps of the setup were also created using an infrared camera. Figure 6.84 shows the test setup and the results obtained. The test conditions were simulated with the same software implementation used for the thermal analysis of the STT modules (Section 6.8.2) and the results were compared with measurements. Overall, the measured temperature profiles as a function of time showed an excellent agreement with the corresponding simulations, as illustrated in Figure 6.84. The absolute values of the temperatures in the test setup were higher than those expected in the actual STT modules due to differences in the operating conditions. However, simulations were found to correctly trace the dependence on the boundary conditions and operating

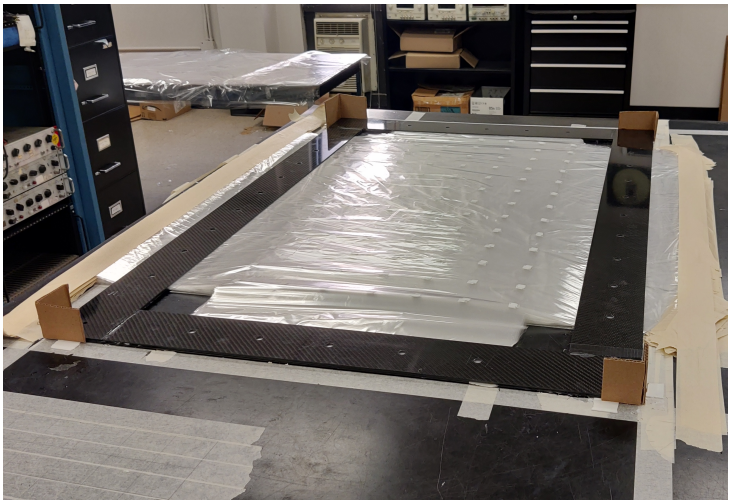
conditions.

6.12.7 Target and Radiator Prototypes



Figure 6.85: Prototype of the STT graphite target 1.5 m × 1.0 m including two machined tiles 595 mm × 595 mm × 4 mm and a T700 C-composite frame 3.6 mm thick. The material used is isostatic graphite with a purity of 100 ppm. The cross-bracing is made with carbon-fiber tape 50 mm wide.

Prototypes of the graphite target from different industrial suppliers were tested to validate their mechanical and chemical properties, as well as the target assembly foreseen for the STT (Section 6.5.1). The dimensions of the graphite tiles tested were 595 mm × 595 mm × 4 mm, as the ones in the actual STT targets. The material chosen is isostatic graphite, a material characterized by micro particles and an isotropic structure and properties, created through the isostatic pressing (CIP) of micro particles. Isostatic graphite is much stronger than conventional graphite due to its micro particle structure, offering a highly reliable material with a small characteristic variation. The grain size for the samples from the selected vendor was 8-10 μm, the density 1.82 g/cm^3, the elastic modulus 12 GPa, and the hardness (shore) 65. The graphite tiles for the STT targets were machined to guarantee tight tolerances on the thickness (4 mm) and dimensions (Figure 6.85).



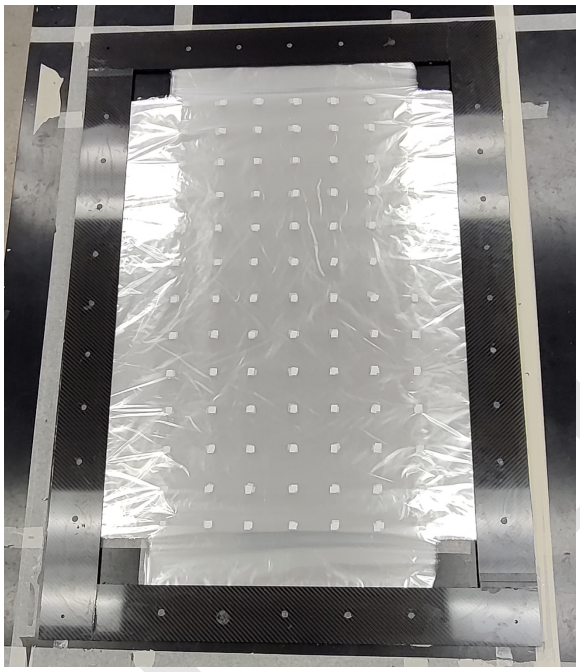


Figure 6.86: Construction of a 1.2 m × 0.8 m prototype of the STT radiator with T700 C-composite frame and 105 polypropylene foils.

The tests performed indicated that the selected material and design is consistent with the STT requirements.

A complete 1.5 m × 1.0 m prototype of the graphite target based on the same design as in the actual STT targets was constructed to validate the mechanical design. The prototype includes two tiles of isostatic graphite with the standard dimensions, a frame composed of 8 staggered plates made of T700 C-composite material, and a cross-bracing supporting the tiles made of C-fiber woven tape 50 mm thick and with a weight of less than 200 g/m^2. The total thickness of the C-composite frame was 3.6 mm. The 8 individual plates are glued together and to the the C-fiber cross-bracing using Araldite 2011 glue. The cross-bracing tapes on both sides of the tiles are connected together in the middle points by a few mm of double adhesive tape, supplemented by stitches at the crossing points. The surface of the graphite tiles was protected with the application of a permanent, matte spray designed for pencil drawings. Figure 6.85 shows the completed prototype. Extensive tests indicated that such a mechanical assembly is self-supporting and can withstand all the manipulations expected to mount/unmount the graphite targets from the STT tracking modules.

A 1.2 m × 0.8 m prototype of the radiators was constructed, following the same design as the STT modules (Section 6.5.1), except for the size. The radiator prototype has a frame that includes 8 staggered plates made of T700 C-composite material, which hold a stack of 105 polypropylene foils 18 μm thick and separated by 120 μm air gaps in the central region. The total thickness of the frame assembly is 5.49 mm, including the foil stack clamped between the C-fiber plates. The spacing between the foils is maintained through the addition of a grid of small squared pads made of 120 μm adhesive polypropylene film on one side of each foil. The pads are aligned throughout

the 105 foils. The foils are stretched and fixed to the frame with 3D printed circular inserts with 10 mm diameter. The total radiator thickness in the central region is 14.37 mm. Figure 6.86 shows the radiator prototype, which was designed to be mounted onto the corresponding 1.2 m × 0.8 m prototypes of the STT tracking modules (Section 6.12.4).

6.12.8 Test Beam Measurements

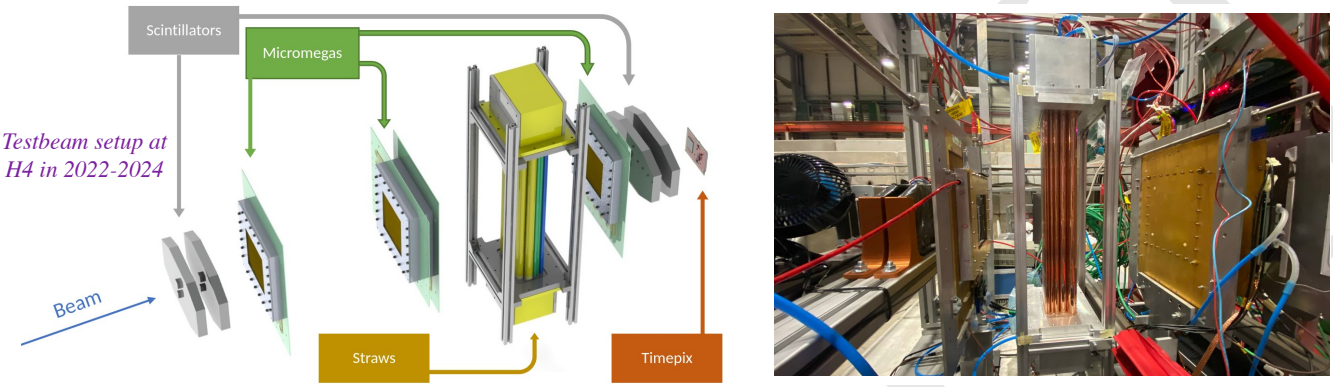


Figure 6.87: Test beam setup with a small STT prototype to test different readout systems in the SPS H4 and H8 beamlines at CERN used in 2022-2024.

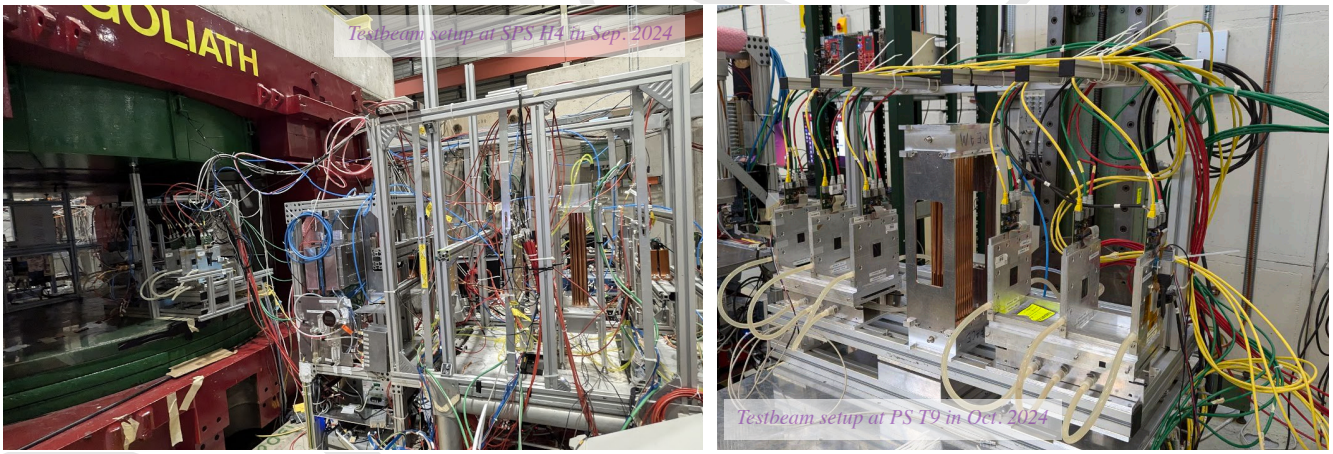


Figure 6.88: Test beam setups with small STT prototypes to test different readout systems in the SPS H4 and PS T9 beamlines at CERN installed in 2024.

A permanent test beam setup was prepared and repeatedly exposed to μ, π, and e at the H4 and H8 beamlines at CERN from 2022 to 2024. This setup includes a small straw tracker prototype with the same geometry and straws as STT (5 mm diameter, 20 μm wire), a MicroMEGAS external trackers (3X + 1Y) with a pitch of 250 μm, scintillators for time reference, and an external Si tracker with 50 μm × 50 μm pixels (Figure 6.87). The primary goal was to evaluate the STT performance for tracking and particle identification with different options for the readout system. A second improved setup was installed in 2024 for test beam exposures at both the SPS H4 and the PS T9 beamlines at CERN (Figure 6.88). This upgraded setup used a new high precision ($\sim$ 6 μm) AZALEA silicon tracker with 6 planes, each having a 18.4 μm pitch. Runs with and

without B field, as well as both time and charge measurements as a function of the internal gas pressure, thresholds, and magnetic field, were taken. Data collected at H4 included high energy μ and π, while the T9 program focused on e, π, μ, and p of low energies ($\leq 2\,\text{GeV}$), together with some cross-calibration runs at 15 GeV.

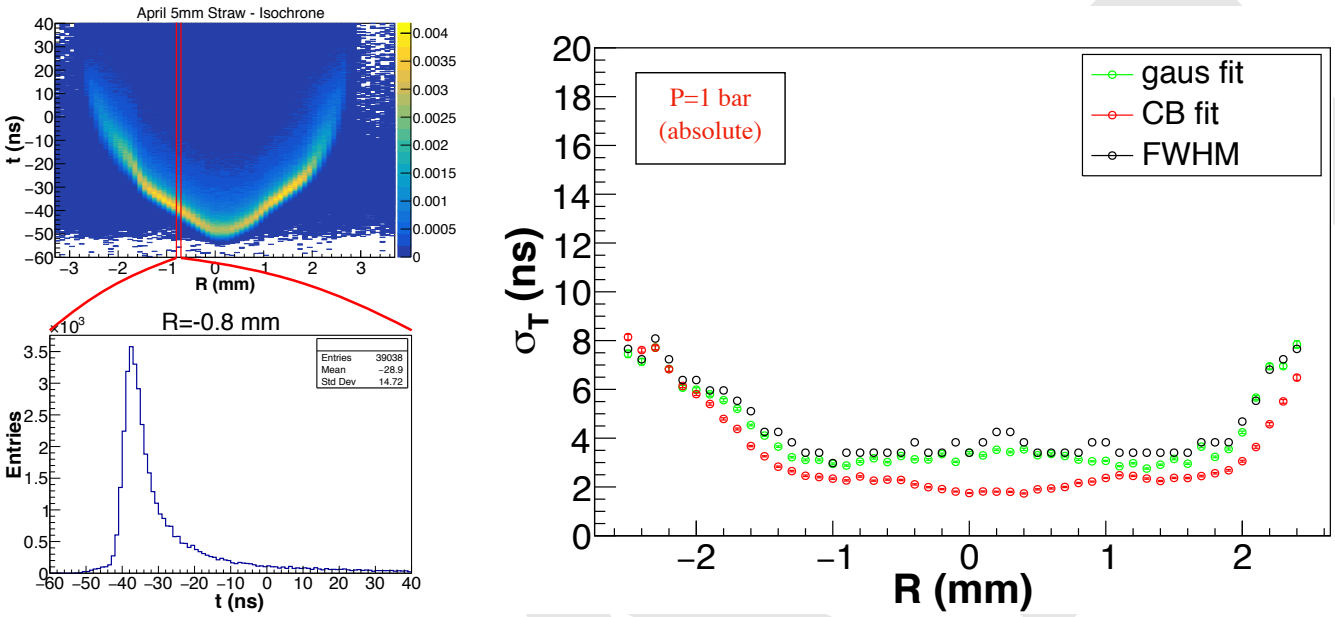
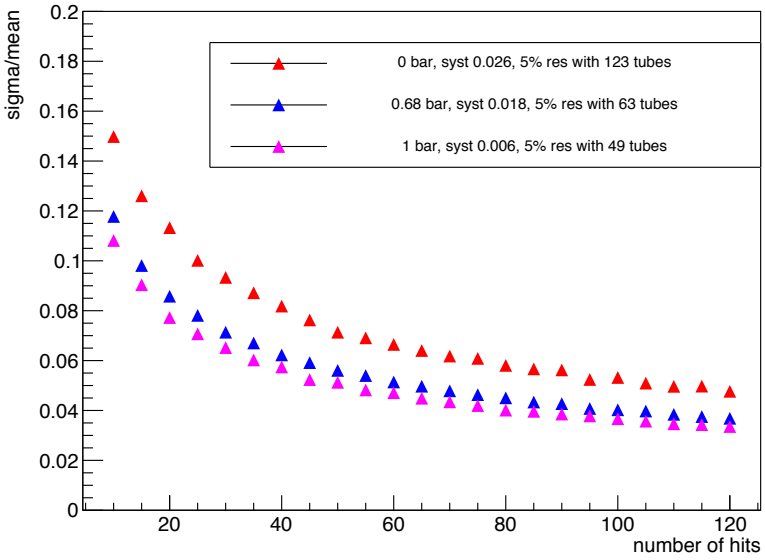


Figure 6.89: Preliminary timing resolution of straws measured at the SPS H4 test beam in 2023.

The various exposures allowed the test of two spare front-end boards from the Mu2e experiment equipped with the VMM3 chip, as well as an alternative readout based on the TIGER ASIC [76]. In particular, two main settings were tested for the VMM3 readout: (i) a peaking time of 25 ns with a gain of 3 mV/fC for the time measurements; (ii) a peaking time of 200 ns with a gain of 0.5 mV/fC for the charge measurements. The TIGER chips instead have a fixed peaking time of 60 ns with a gain of 12 mV/fC. The time-to-distance relationship (r-t) for the straws was calibrated after a recursive alignment with the external trackers, as shown in Figure 6.89. Preliminary results showed low levels of electronic noise and indicated a timing resolution of a few ns with both chips, in spite of the use of non-optimal electronic gains and peaking times (Figure 6.89). The measured timing resolutions were found to be roughly consistent with the expected single hit spatial resolution of $\leq 200\,\mu\text{m}$ in STT. However, we found that the performance was limited by the integrated ADCs and the digital path within the VMM3. To simultaneously fulfill the requirements for the drift time and the charge measurements, a readout based on the direct analog output of the VMM3 combined with an external ADC (Section 6.7.2) was developed. The dE/dx deposited by particles in the straws was also measured. To this end, the recorded energy deposition was divided by the corresponding track length within each straw, as determined through the interpolation from the precision external tracker. A truncated mean, discarding 30% of the highest values, was used to suppress the tail in the corresponding Landau distribution. The test beam results obtained with the VMM3 readout are summarized in Figure 6.90 as a function of the number of hits (straws crossed) for different values of the internal pressure. Improvements in dE/dx resolution were observed by increasing the gas overpressure p, consistently with the expected $1/\sqrt{p}$ behavior. The measured dE/dx resolution was implemented into the detector simulations to evaluate the corresponding particle identification capabilities (Section 6.18.4).



$$\sigma^2_{dE/dx}(N) = \sigma^2_{\text{syst}} + \frac{\sigma^2_{\text{stat}}}{N}$$

Relative pressure	σ_{syst}	σ_{stat}
0.00 Bar	0.026	0.450
0.68 Bar	0.018	0.369
1.00 Bar	0.006	0.352

Figure 6.90: Preliminary dE/dx for muons from the charge measured in straws at the SPS H4 test beam in 2023.

6.12.9 Full-Scale 3.9 m Prototype of a STT Module

Preparations for the construction of a full-scale 3.9 m × 3.3 m prototype of the largest STT modules ("Module 0") are in progress. This prototype is based on the final design of the C-fiber frames (Section 6.5.1) validated with the 1.2 m prototypes (Section 6.12.4) and with detailed mechanical analyses (Section 6.5.4). It includes a total of 2,742 straws arranged into four XXYY layers, with 1,495 XX horizontal straws 3.15 m long, and 1,247 YY vertical straws 3.75 m long. The 26 parts composing the C-fiber frame have been produced industrially with the same tooling foreseen for the series production of the STT modules (Section 6.13.1). Figure 6.91 shows a dry assembly test of the completed frame together with the cross-bracing tool to be used during the wiring process and made of C-fiber (T700) square tubes. The procurement of all required components including end-plugs, spacers, crimping pins, and W/Re wire has been completed. The tooling for the assembly of the full-scale STT prototype will be partially based upon the tooling developed for the construction of the COMPASS straw tracker (Section 6.14.2). The preparation of all the required tooling has been completed. The large assembly table 5.04 m × 3.5 m × 0.9 m is shown in Fig. 6.92 and is composed of two main parts: (i) a newly designed support structure constructed from light aluminum beams; (ii) a refurbished top plane made of multiple steel plates. After being mounted, the various elements of the table were aligned to achieve an accuracy of about 100 μm on the flatness of the top plane. The assembly table will be replicated at the various STT production sites equipped with module assembly units (Sec 6.14.2), once validated by the construction of the STT pre-production "Module 0". The construction of the full-scale STT prototype will concurrently offer an excellent training opportunity in view of the mass production of the detector. To this end, at least one person from each of the main STT production sites 6.14.3 will participate to the construction activities.

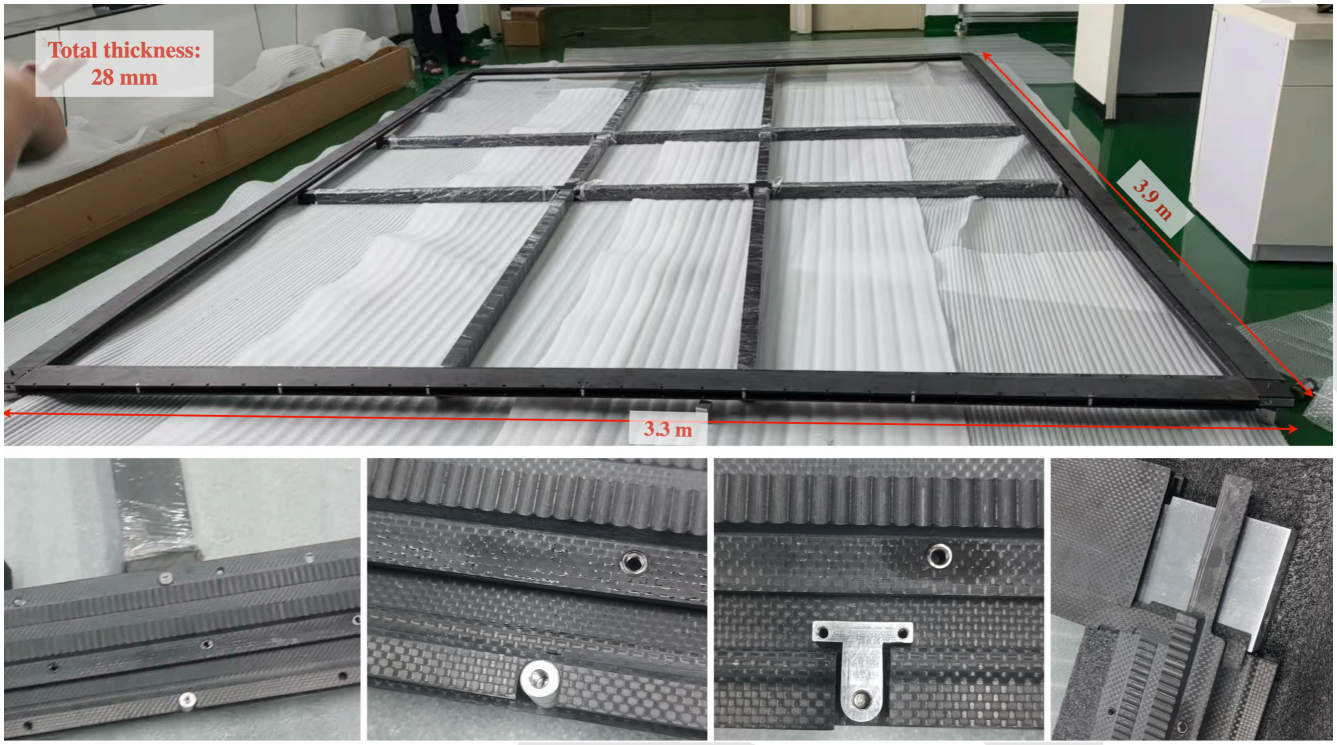


Figure 6.91: Preparation for the assembly of a full-scale 3.9 m × 3.3 m prototype ("Module 0") of a STT tracking module with 4 XXYY straw layers: dry assembly test of the C-fiber frame with the temporary cross-bracing with C-fiber square tubes. The latter is part of the tooling required for the Module Assembly (MA) units.



Figure 6.92: Assembly table used for the construction of the full-scale 3.9 m × 3.3 m STT prototype with C-fiber frame ("Module 0"), including a newly designed support structure (left picture) and a refurbished top steel plate (right picture).

6.13 Quality Controls for Mass Production

6.13.1 Industrial Supply Chain

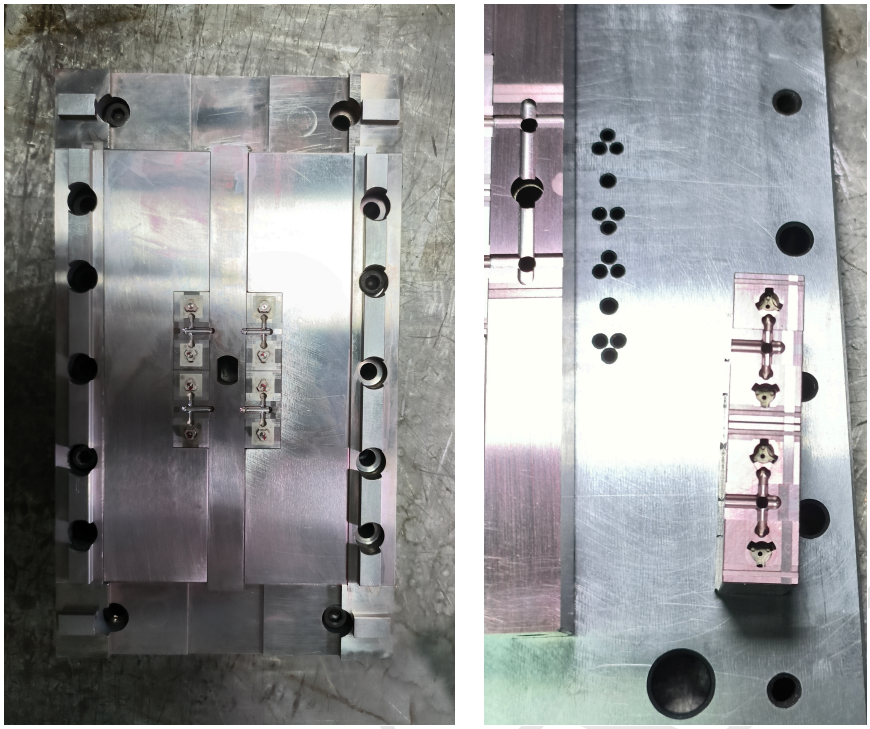


Figure 6.93: Mold for the industrial production of the STT spacers: 8 cavities with a lifetime of 4 million spacers.

Table 6.15: Tooling completed for the industrial production of the STT parts. For all parts, the tooling lifetime largely exceeds the total number of pieces required for the maximal STT configuration.

STT part	Material	Mould cavities	Lifetime	Maximal required
Wire spacer	Polycarbonate	8	4,000,000 pieces	800,000 pieces
End-plug	Polycarbonate	8	4,000,000 pieces	450,000 pieces
Module frame	Carbon composite	1	5,000 pieces	84 pieces

The STT is specifically optimized for the mass production of a detector with $\mathcal{O}(10^5)$ channels. Two specific areas were targeted for this purpose:

- Industrial production of all components required for the assembly of the STT modules;
- Simplified assembly procedures minimize both assembly time and tolerance requirements.

As an essential element of the design process (Section 6.5), for each STT component a primary vendor has been selected together with one or more backup vendors. The main criteria used were the technical capabilities, the quality of the samples received, the lead times, and the quoted costs for the parts. The technical requirements, as well as the quality controls and acceptance criteria to be implemented in the production of each component, were agreed upon with the suppliers. Having an efficient industrial supply chain in place creates a solid foundation for the mass production of



Figure 6.94: Molds for the industrial production of the C-fiber frames of the STT modules.

the STT modules. Collaborations with industrial suppliers were undertaken for the development of many individual components. The process included both feedback from the vendors and evaluation of samples from various revisions of the parts. Custom tooling was developed for the industrial production of some STT parts, as summarized in Table 6.15. For all parts the tooling lifetime largely exceeds the total number of pieces required for the maximal STT configuration. Before fabricating the final production tooling, the design of the end-plugs and the spacers was validated with 3D-printed parts used in the assembly of various STT prototypes. Similarly, the design of the C-fiber frame was tested and finalized with the 1.2 m prototypes (Section 6.12.4) before the fabrication of the final full-scale tooling. Figure 6.93 shows the precision mold for the polycarbonate spacers. Figure 6.94 shows the molds for the various elements of the C-fiber frames, which can be used to produce STT modules of any size ranging from 1 m up to 4 m.

6.13.2 Tests of Straw Welding

Extensive quality controls were conducted on the seam region resulting from the ultrasonic welding of the cylindrical straws. Multiple samples of the STT straws produced with the Fraunhofer film (Section 6.6) were examined by scanning electron microscopy (SEM) and energy dispersive X-ray spectroscopy (EDS) at CERN in order to obtain a targeted analysis of both the external surface and the cross-section of the samples. Figure 6.95 shows an illustration of the results obtained. The welding process used provides a strong consistent weld with homogeneous and straight weld boundaries. No major deviations were observed among the different samples analyzed. The average weld width was measured to be 568.8 μm. The analysis of the weld cross-section did not reveal indented marks representing critical points or damage to the substrate material. The fraction of the completed weld interface with the films fused together was found to be in the range of 75-80% in all samples, corresponding to widths of 426-454 μm. The average weld thickness ranged from

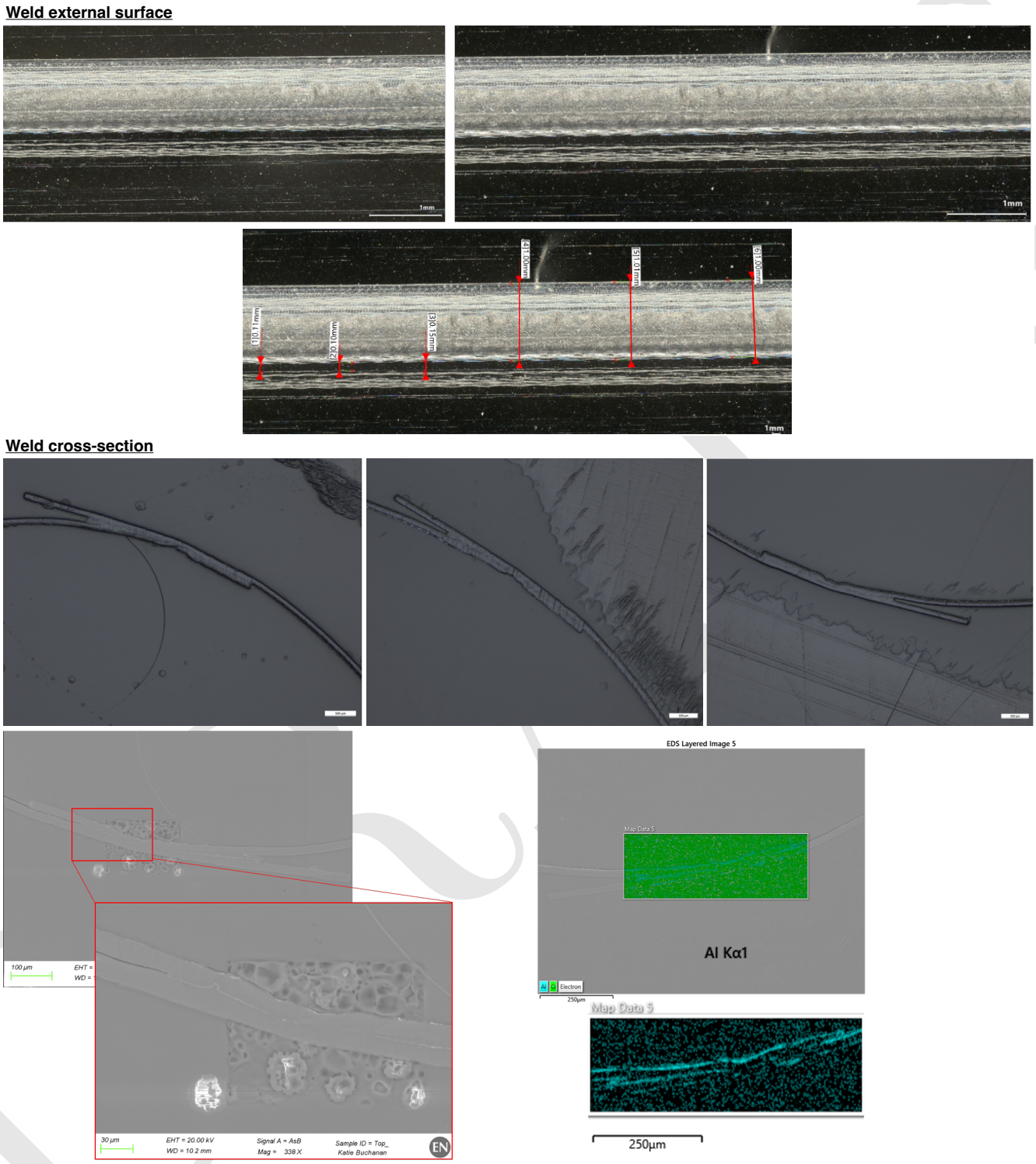
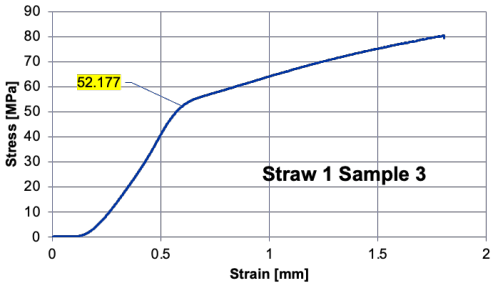
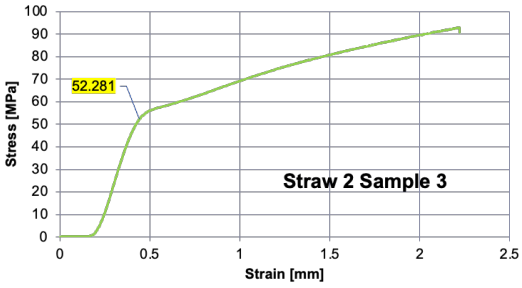
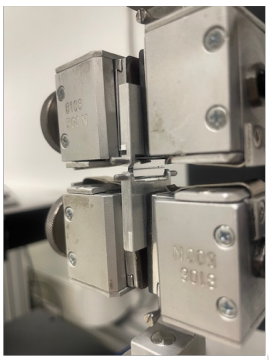


Figure 6.95: Microscopic inspection of the weld external surface (top pictures) and of the weld cross-section (bottom pictures) for the STT straws with SEM-EDS techniques.

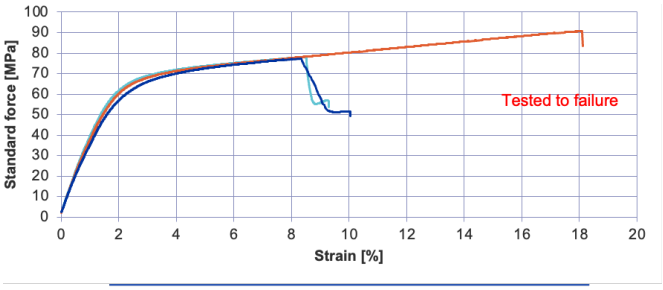






	Straw 1	Straw 2
Yield point (MPa)	52.35 ± 2.86	51.79 ± 4.87

Figure 6.96: Transverse tests of the mechanical strength of the welding for the STT straws produced with the final Fraunhofer film and with the removal of the Al coating by UV laser (Section 6.6).



	Longitudinal	Transverse
Yield point (MPa)	58.02 ± 5.00	52.21 ± 2.47

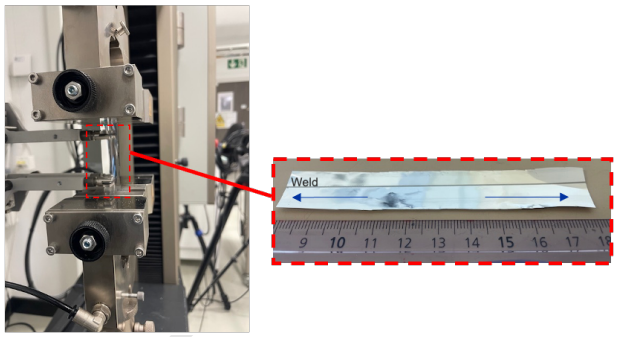


Figure 6.97: Longitudinal tests of the mechanical strength of the welding for the STT straws produced with the final Fraunhofer film and with the removal of the Al coating by UV laser (Section 6.6).

	JINR 2010 (36µm)	JINR 2022 (19µm)	DUNE 2024 (19µm)	DUNE 2025 (19µm)	Longitudinal	Raw material (Red)	Raw material (Green)
Stress at break σ_t (MPa)	103.5 ± 0.9	102.2 ± 20.8	95.99 ± 19.64	72.09 ± 12.89	-	-	-
Force at break (N)	36.0 ± 1.4	31.0 ± 16.7	27.62 ± 5.14	38.21 ± 7.08	-	-	-
Force at break per unit length (N/mm)	2.40	2.06	1.82 ± 0.37	2.75 ± 0.49	-	-	-
Number of samples			5	10	3	6	6
Yield (MPa)			37.93 ± 4.66	52.21 ± 2.47	58.02 ± 5.00	89.18 ± 0.86	91.18 ± 1.08

Figure 6.98: Results of the transverse and longitudinal tests on the straw welding for the STT straws produced with the final Fraunhofer film and with the removal of the Al coating by UV laser (DUNE 2025). A comparison is shown with straws produced with the same film without the removal of the Al coating (DUNE 2024), as well as with a different film used for the first prototype STT at CERN (JINR 2022), and with NA62 [66] straws (JINR 2010). The results for the raw material refer to the final Fraunhofer film with good (green) and bad (red) quality Al coating, respectively.

35.5 μm to 39.0 μm depending on the sample.

Mechanical tests of the weld strength were performed on different cut sections of the straw walls using a video-extensometer with stickers on the aluminum grip. All measurements were performed on a Zwick/roell Z010 mechanical testing machine. Results are summarized in Figure 6.96. For the final STT straws made from 19 μm Hostaphan RNK19 base film with the Al coating removed by UV laser (Section 6.6), an average yield point of 52.21 ± 2.47 MPa was measured. The average force at break was 38.21 ± 7.08 N, corresponding to a force per unit length of 2.75 ± 0.49 N/mm. These values are significantly higher than the previous straws produced with the same film but without the removal of the Al coating by UV laser, as shown in Figure 6.98. The welding is also stronger than the one in the straws produced with a different film used for the first STT prototype at CERN, as well as in the NA62 straws using the same RNK19 base film and a different metallization. The mechanical properties of the welding along the longitudinal direction were also tested with the final straws produced after the removal of the Al coating by UV laser (Figure 6.97). The corresponding longitudinal yield was found to be close to that along the transverse direction. In both cases, the measured values for the welding are lower than the raw material, as summarized in Figure 6.98.

6.13.3 Tests of End-plugs

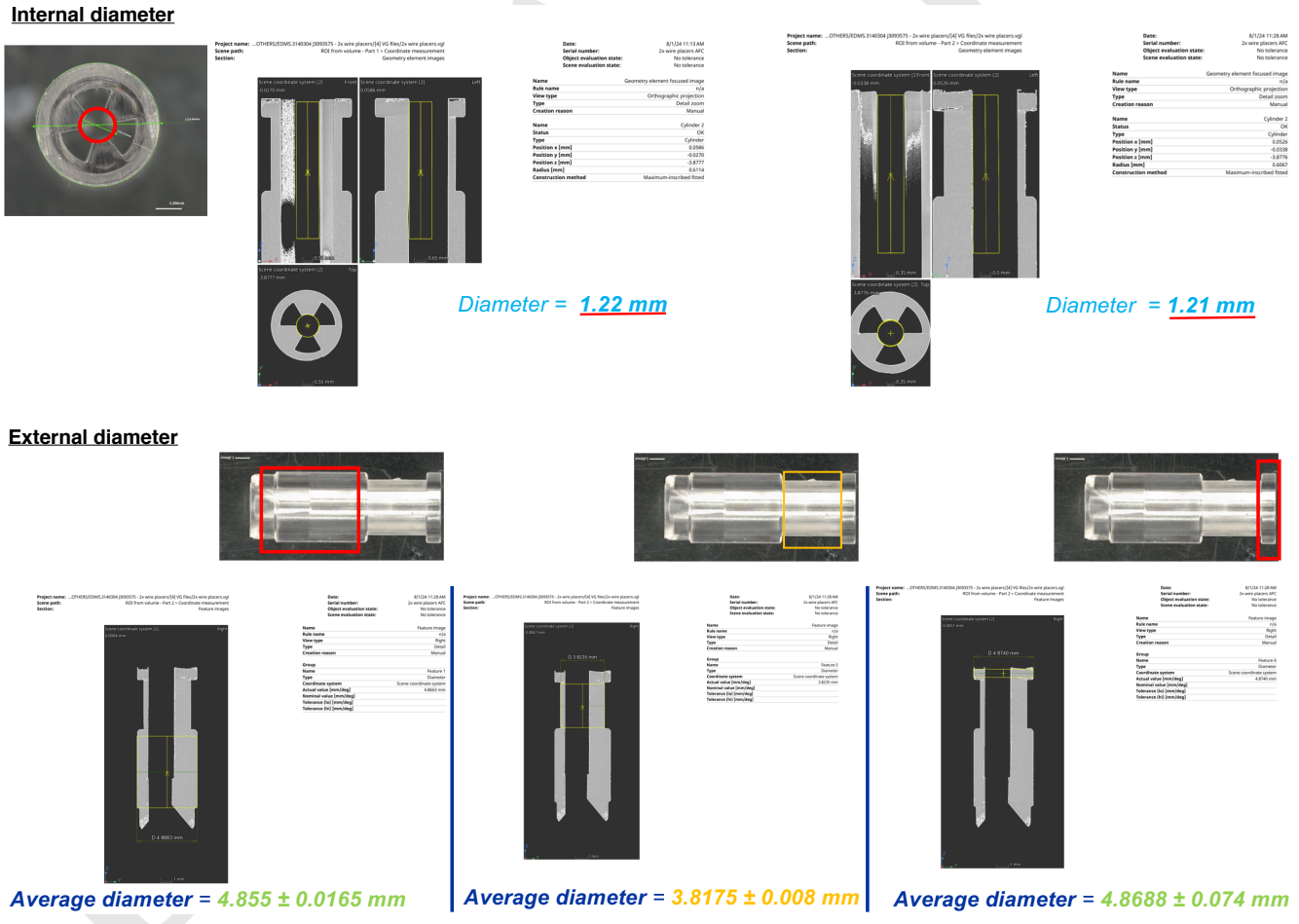


Figure 6.99: Inspection of final end-plugs for STT by CT scan.

Microscopic inspections were performed on the final samples of the end-plugs industrially produced

by injection molding (Section 6.13.1) with transparent polycarbonate. Figure 6.99 illustrates the main measurements performed. The external surface which will be in contact with the straw walls was found smooth and free from imperfections. A small nodule residual of the plastic injection point, not exceeding 250 μm as, is visible on the neck of all samples produced. However, this feature is not critical since the region will not be in contact with the straw and will be encapsulated within the stycast glue used for the final sealing. A good consistency was found across samples with the quality of all measured parameters exceeding the specifications. The diameter of the inner hole for the insertion of the crimping pin was found 1.21 ± 0.01 mm. The average external diameter was measured to be 4.855 ± 0.0165 mm. An excellent consistency in dimensions and finish was found within a production run of 10,000 pieces. During mass production both the external diameter and the diameter of the inner hole are checked on each piece using calibrated holes and pins, in addition to visual inspection.

6.13.4 Tests of Wire Spacers

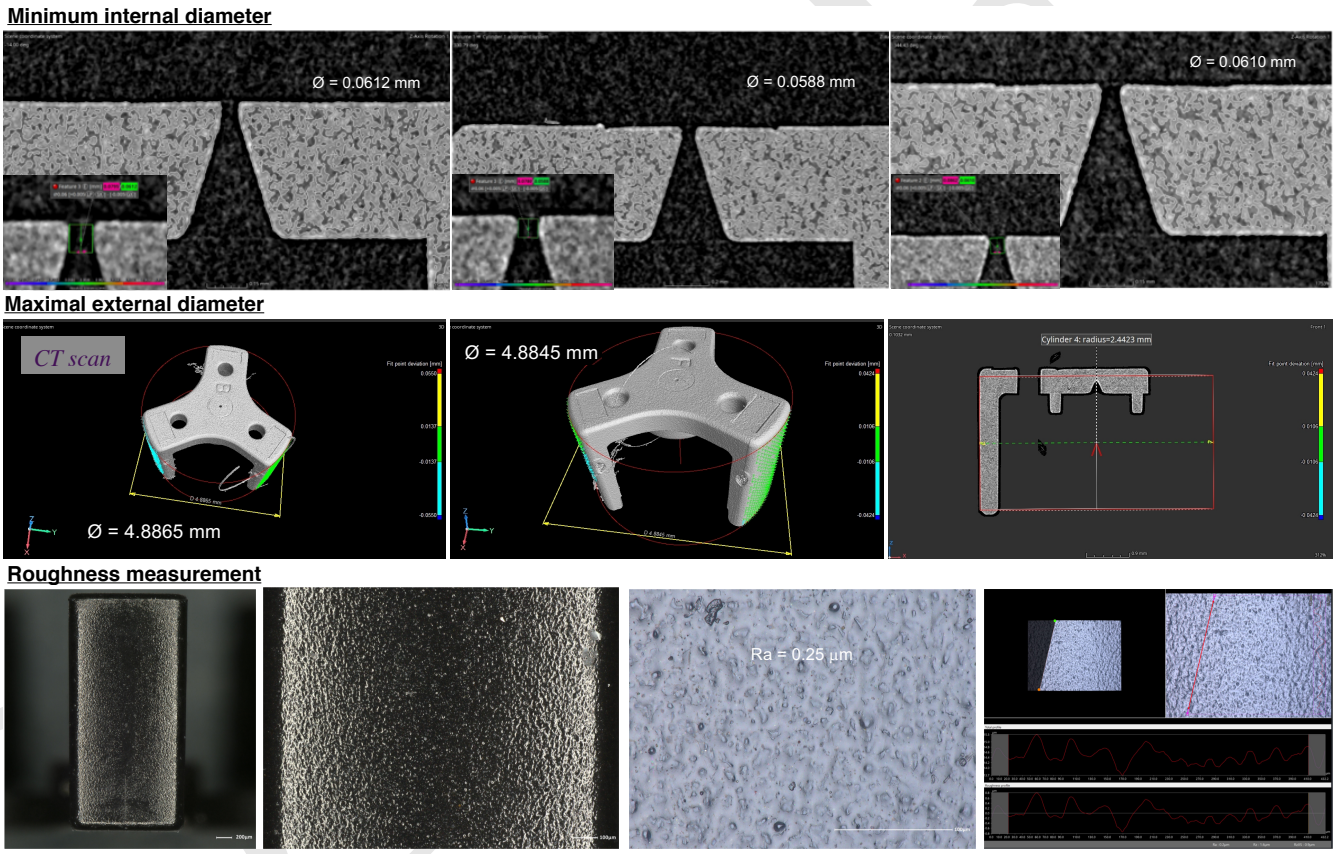


Figure 6.100: Quality inspections of the STT wire spacers by microscopy and CT scan: (a) minimum diameter of the inner hole holding the wire (top); (b) maximum external diameter (middle); (c) roughness of the external surfaces (bottom).

The wire spacer is a critical element for the STT design as it determines the accuracy to which the wires are self-centered within the straws. Stringent quality tests were performed on the spacers industrially produced by injection molding (Section 6.13.1) with black polycarbonate. In particular, the following critical quantities were measured on multiple samples:

- Minimum diameter of the inner hole holding the wire. The inner hole must have negligible eccentricity and a diameter $< 80\,\mu$m.
- Internal radius of the edges of the inner hole. The minimum radius of curvature must not be larger than the wire diameter as sharper edges can potentially damage the wire.
- Maximum external diameter of the surfaces in contact with the straw walls. The difference between the external diameter and the inner diameter of the straws at 1 bar absolute pressure (4.91 mm) must be smaller than the radius of the central hole to minimize the wire offset.
- Roughness of the external surfaces in contact with the straw walls. A smooth external surface is required to facilitate the insertion of the spacers into the straws without scratching the inner metallization.

The parts received were subjected to microscopic inspections and complete 3D internal mapping by computed tomography (CT) scans. Roughness values were measured using a Keyence VHX 7000, with a resolution of $0.1\,\mu$m. Figure 6.100 summarizes the results. The minimum diameter of the inner hole was found to be $61 \pm 2\,\mu$m when averaged over all samples. The average internal radius of curvature of its edges was $21 \pm 3\,\mu$m. The average maximum external diameter was measured as 4.873 ± 0.012 mm. The roughness of the external surfaces measured across the samples was averaged at $R_a = 0.25\,\mu$m. All tests indicated a quality of the production parts exceeding the specifications. Considering the tolerances on the inner diameter of the straws produced for the STT (Section 6.13.9) and the metrology results obtained for the production spacers, an average accuracy in the self-centering of the wires of $65\,\mu$m or better was estimated. An excellent consistency in dimensions and finish was found within a production run of 15,000 pieces. During mass production, both the diameter of the inner hole and the external diameter are checked on each piece using 2.5-dimensional optical inspection equipment. The absence of residual burrs along the edge of the inner hole and on the external surface is also checked on all pieces.

6.13.5 Tests of Crimping Pins

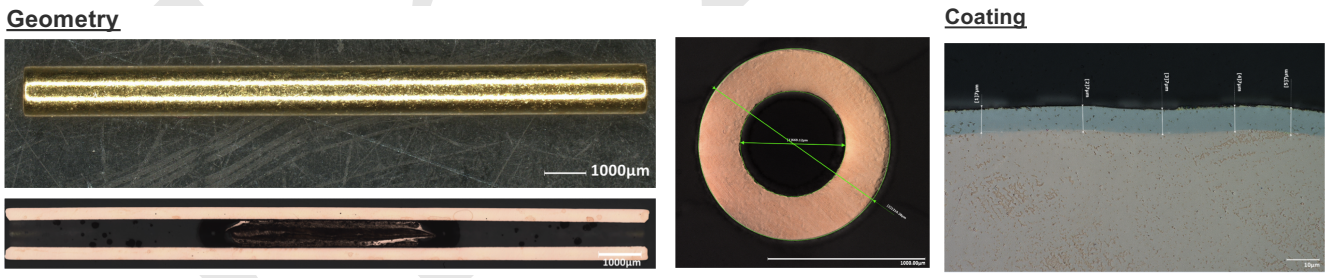


Figure 6.101: Microscopic inspection of gold-plated Cu-DHP crimping pins.

Microscopic and mechanical tests were conducted on various samples of crimping pins produced by the selected industrial supplier. The pins are machined from oxygen-free 99.90% Cu-DHP copper, as in the pins used for the ATLAS TRT. A thermal annealing at 600°C followed by immersion in cold water is used to soften the base material for a more reliable crimping (Section 6.12.1). A gold coating $0.05\,\mu$m thick is applied by electrical deposition on a Ni substrate over the surfaces. Figure 6.101 summarizes some of the results obtained from the tests. The external diameter was measured as 1.21 ± 0.01 mm averaged over all samples. The gold coating on the surface had a very smooth and homogeneous finish, with good scratch resistance and excellent electrical conductivity.

A remarkable consistency in dimensions and finish was found across the 20,000 pieces received. During mass production the external diameter is checked on all pieces with a direct insertion into samples of the STT end-plug (Section 6.13.3).

6.13.6 Tests of Anode Wires

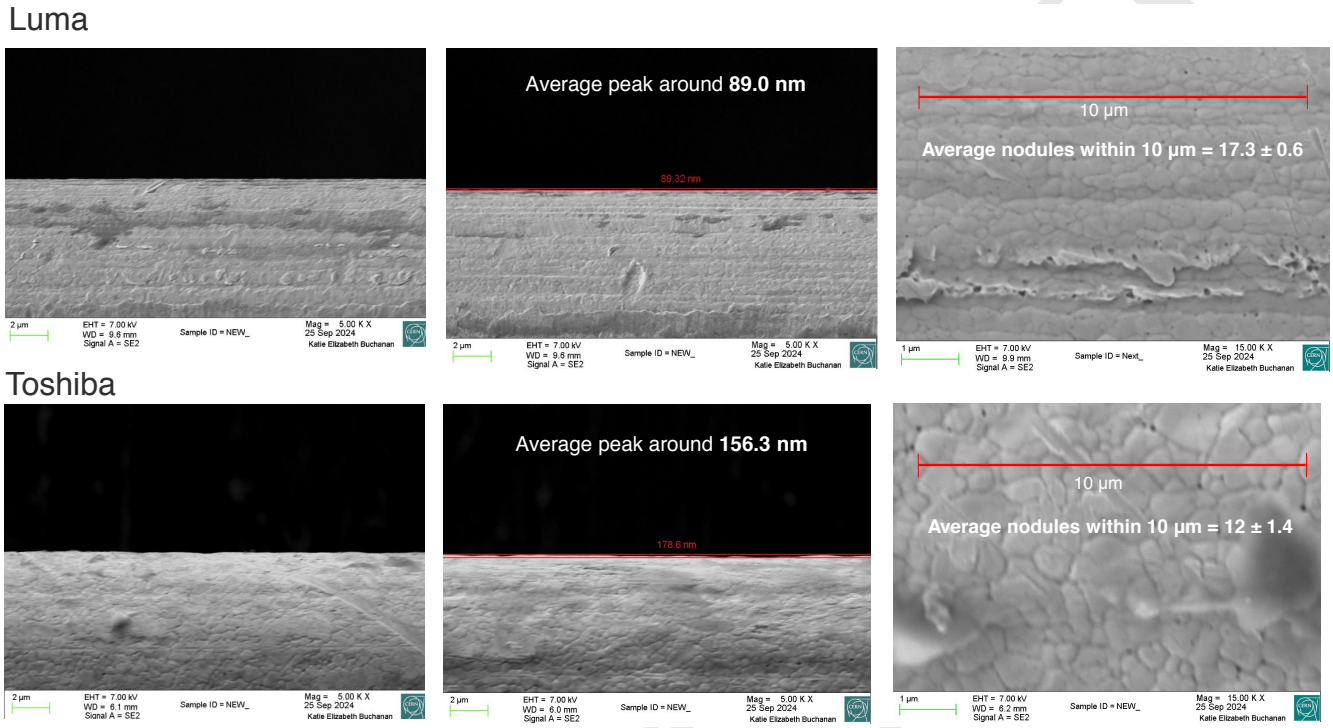
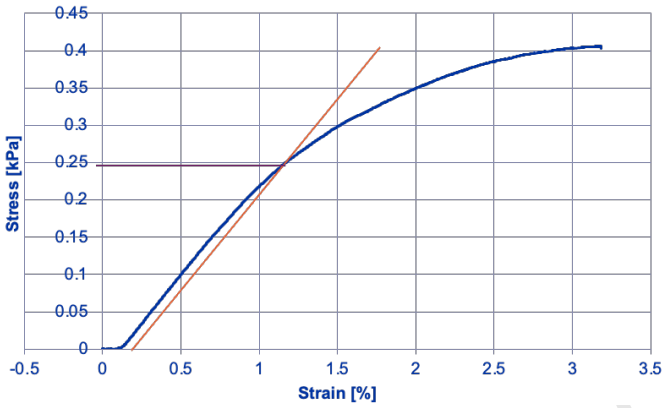


Figure 6.102: Inspection of gold-plated W/Re wires (20 μm diameter) from Luma and Toshiba by SEM.

Two different samples of the anode wire, produced by LUMA in Sweden and Toshiba in Japan, were analyzed. In both cases, the wire was made of a tungsten/rhenium (97/3) alloy with a nominal diameter of 20 μm and a gold surface coating. The thickness of the gold coating differed in the two samples: about 0.20 μm for LUMA and about 0.85 μm for Toshiba. The wire samples were examined by scanning electron microscopy (SEM) to determine the surface properties. Results are summarized in Figure 6.102. The measured diameter is close to the nominal value in both samples: 20.25 μm for LUMA and 20.19 μm for Toshiba, to be compared with an expected tolerance of 0.8 μm. The surface coating was found to be homogeneous in both cases. The LUMA wire had finer nodules in the coating, having an average number of 17.3 per 10 μm compared to an average number of 12 per 10 μm for Toshiba. An analysis of the surface roughness showed that the Toshiba wire had larger peaks in the coating, with an average of around 150 nm, compared to an average of around 90 nm for the LUMA wire. The difference in the surface roughness found could be related to the rather different thicknesses of the corresponding gold coatings. After consultation with Toshiba, a nominal gold coating thickness of 0.3 μm was finalized for the STT anode wires. All quality tests will be repeated with new wire samples featuring such a coating. The possibility of an additional drawing step after the Au-coating is also evaluated to further increase surface smoothness. Consistent quality was found for both LUMA and Toshiba wires within the initial procurements of about 20 km of wire.

A mechanical assessment was performed on the Toshiba W/Re wire with 0.3 μm gold coating to understand the elastic limit and breaking point. All measurements were performed on the same Zwick/roell Z010 mechanical testing machine used to evaluate the strength of the straw welding (Section 6.13.2). The 20 μm wire was wrapped around a pin and tested at a speed of 0.1 mm/min. A total of 9 different wire samples obtained from the same spool were measured. The results summarized in Figure 6.103 indicate a yield stress of 0.26 ± 0.04 kPa and a force at break of 1.28 ± 0.04 N on average.

During mass production, the breaking strength of the wire is checked using a few wire segments for each wire spool received, by using calibrated weights of 65 g. The entire spool is rejected in case of wire breakage. For each production batch the wire diameter is also measured with microscopic inspection and the wire is rejected in case the diameter is out of tolerance.



	Yield Stress (kPa)	Force at break (N)
Samples 1-9	0.26 ± 0.04	1.28 ± 0.04

Figure 6.103: Mechanical tests of the the gold-plated W/Re wires (20 μm diameter) from Toshiba.

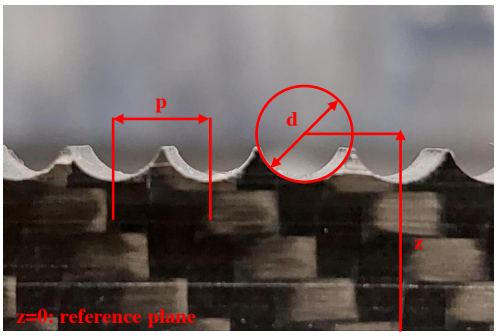
6.13.7 Tests of C-fiber Frames

Table 6.16: Tolerances and acceptance ranges for the industrial production of the C-fiber frames of the STT modules. The measured parameters are defined in Figure 6.104.

Parameter	Nominal	Tolerance	Acceptance range
Pitch p	5 mm	$\pm$0.01 mm	4.99 – 5.01 mm
Diameter d	5 mm	$0.00 + 0.05$ mm	5.00 – 5.05 mm
Height z_1	7.17 mm	$-0.05 + 0.00$ mm	7.12 – 7.17 mm
Height z_2	16.5 mm	$-0.05 + 0.00$ mm	16.45 – 16.50 mm

The quality control procedures for the C-fiber frames were defined with both the 1.2 m (Section 6.12.4) and full-scale (Section 6.12.9) STT prototypes. The most critical elements for the assembly of the STT modules are the 8 profiles forming the four straw holders, which are subject to dedicated measurements (Figure 6.104). The following acceptance tests are performed on each C-fiber frame:

- Flatness within 300 μm over the entire length of the frame elements;
- Modulus of elasticity for the fabricated parts not smaller than 100 GPa along the two main directions of the fibers. The modulus of elasticity is measured by performing four point



1. Place the component under a CMM
2. Measure pitch (p), diameter (d) and center height from reference plane (z) as function of the coordinate (y)
3. Each measurement is repeated at three different x-coordinates: -5 mm, 0, 5 mm

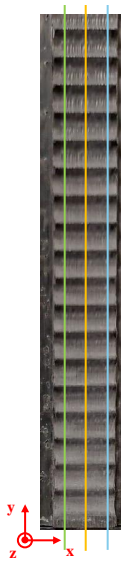




Figure 6.104: Measurement of the pitch, diameter, and height of the holes in all the straw holders of the CF frame.

flexural tests along the main frame elements according to the ASTM D7264 and ISO 14125 specifications.

- For all straw holder profiles, the following quantities are measured with a coordinate-measuring machine (CMM) as a function of the position along the profile: (i) pitch (p) of the holes; (ii) diameter (d) of the holes; (iii) height (z) of the hole centers from a reference plane. Discrete points on the surface of the frame elements are sensed with a laser probe.
- All measured values of the pitch, diameter, and height must be within the tolerances listed in Table 6.16 over the entire length of the longitudinal coordinate.

In case of non-conformity with the required specifications, the parts are rejected. A total of 54 C-fiber frames of varying heights are required for the initial STT, all of which can be fabricated using the existing tooling described in Section 6.13.1. The implementation and results of the acceptance tests described above were confirmed during the procurement of the C-fiber frame for the full-scale (Section 6.12.9) STT prototype. The average modulus of elasticity for the C-fiber frame of the full-scale STT prototype was measured to be 122.6 GPa.

6.13.8 Tests of VMM3a Chips

The VMM3a ASIC has a well-established supply chain including supported production masks and packaging. Around 45,000 VMM3a chips were successfully produced and tested for the electronic readout of the resistive Micromegas and sTGC detectors in the NSW upgrade of the ATLAS experiment. To this end, an automatized system of quality controls was developed, including a custom test board (VMMT) with removable sockets for the VMM3a chips, an optical code reader, and dedicated software with a number of pre-defined settings and a database. The testing is based on the noise, alive channels, and functionality for both the peak detection output (PDO) and the time detection output (TDO) of the chips in positive and negative polarity. An automated test

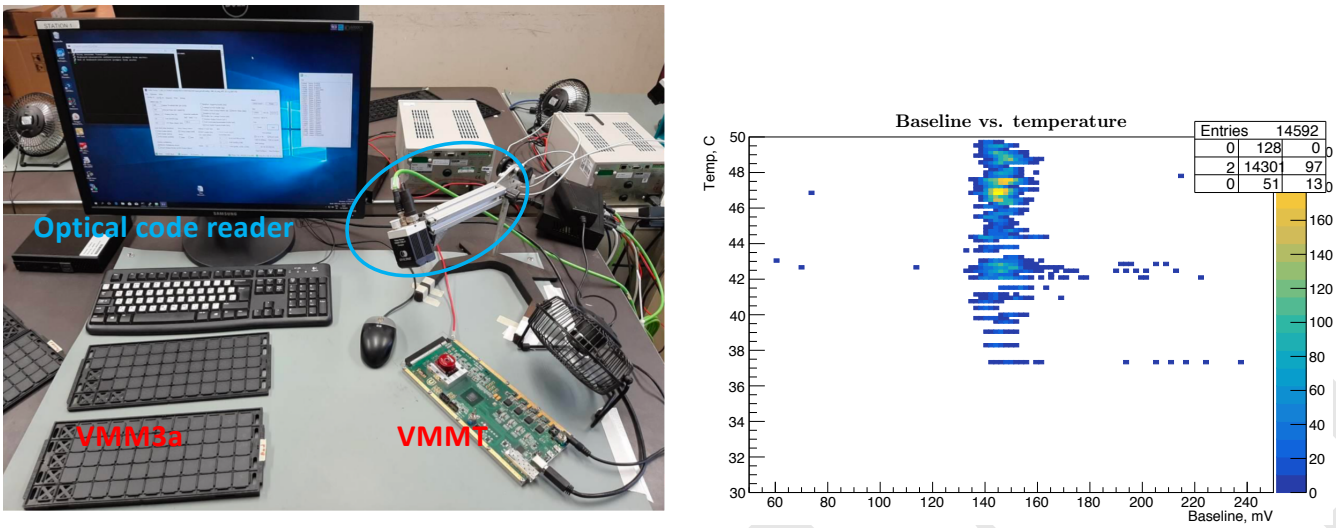


Figure 6.105: Acceptance tests of VMM3a chips for STT with automatized VMMT setup developed for ATLAS NSW at CERN. The number of channels in the plot corresponds to 228 tested chips from two complete wafers.

pattern generator is used to test the packaged chips on the bench-top with the VMMT board. The chips are categorized in three bins based on the acceptance criteria:

- "Good" with all 64 channels fully functional.
- "Passed" with only 1 or 2 channels failing at least one of the acceptance criteria. It is still possible to use the chips for prototyping and test activities or when less than 64 readout channels are needed.
- "Failed" with more than 2 channels failing at least one of the acceptance criteria. The chips are rejected.

To meet the readout requirements of the STT prototyping and initial module production, 454 VMM3a chips were procured, corresponding to four complete wafers from two separate production runs. The packaged chips were tested at CERN using the automated VMMT procedure developed for the NSW (Figure 6.105). The average yield was found to be about 70% for the "Good" fully functional chips. Figure 6.105 shows an example of the distribution of the baseline as a function of the chip temperature as obtained from the computerized tests. A total of 2,128 VMM3a chips is needed for the readout of the initial STT (Table 6.2). Taking into account the measured yield, the number translates into the production of 27 wafers with about 3,051 untested chips. During mass production, each VMM3a packaged chip will undergo the same acceptance tests described above, and only the ones in the "Good" bin will be mounted onto the STT readout boards (Section 6.7.2).

6.13.9 Quality Controls for Straw Production

The straws undergo stringent acceptance tests at the Straw Production (SP) units (Section 6.14.1) in order to ensure a more reliable assembly of the STT modules later. The first step is a visual and dimensional inspection of the tape rolls, followed by a measure of the surface conductivity on

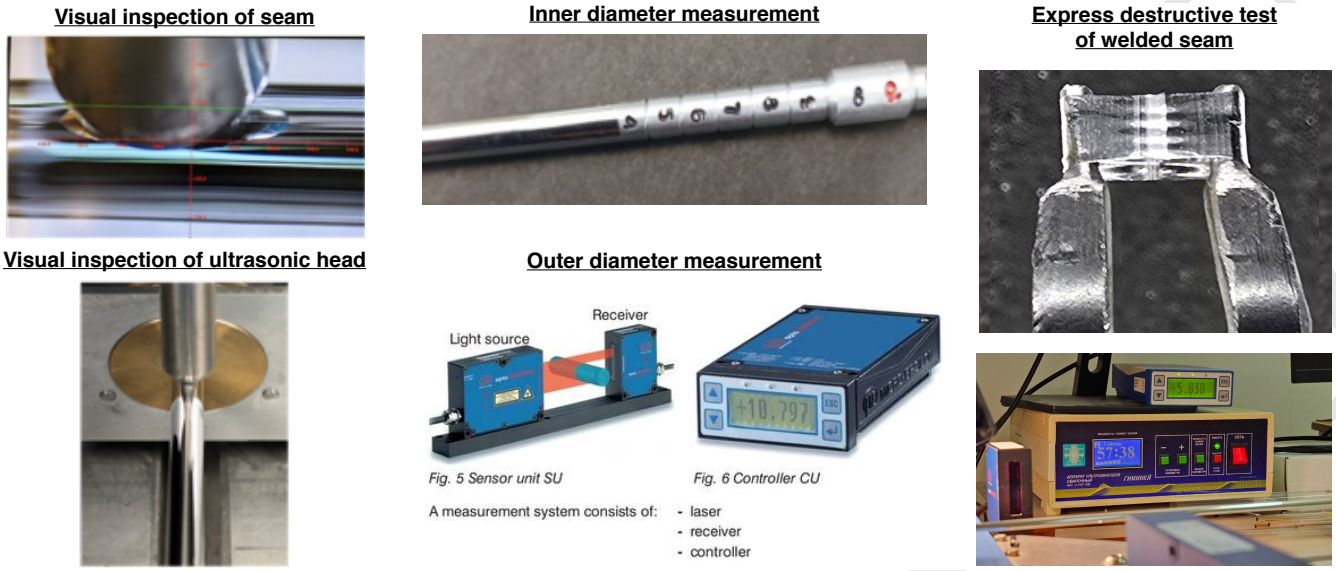


Figure 6.106: Quality controls for the straw production in STT: visual inspection, inner and outer diameter measurements, and express destructive test of the welded seam.

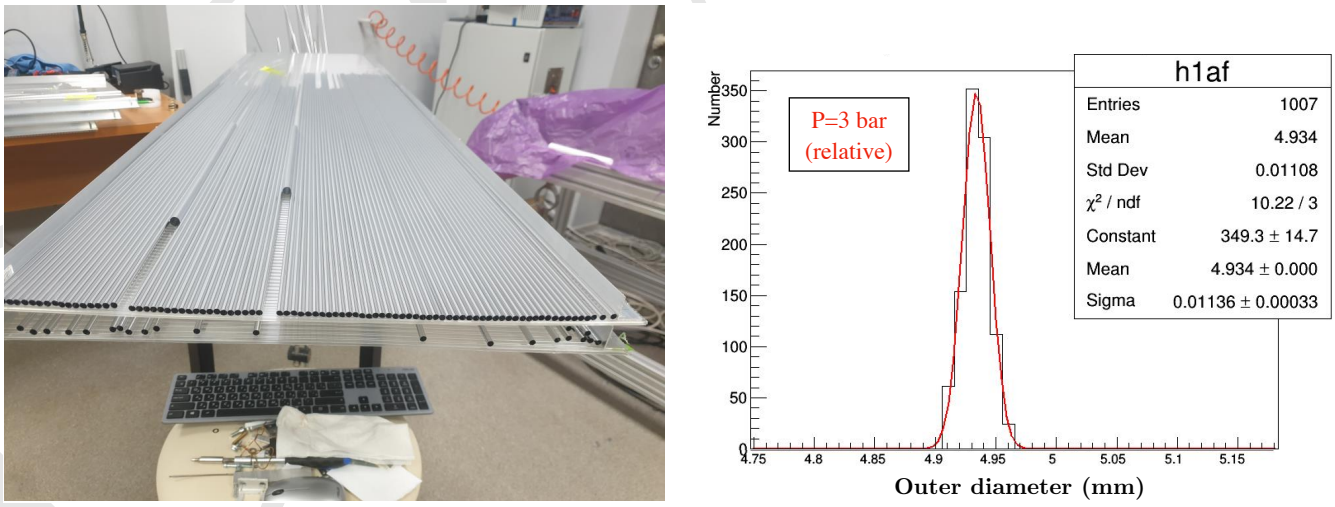


Figure 6.107: Distribution of the straw outer diameter measured during the production for the STT prototypes.



Figure 6.108: Quality controls for the straw production in STT: short-term pressure test at 5 bar relative and long-term storage at 3 bar relative.

both sides of the tape. The straws produced with the ultrasonic welding are longer than the final length required. After production they are cut to the approximate length needed by the MA units. Each straw is then subject to the following quality controls and tests:

- Continuous microscopic inspection of the welded seam. During the straw production the ultrasonic welding process is continuously monitored with a magnifying camera and visible defects appearing at any point along the straw seam result in an immediate rejection of the straw. This quality control is currently performed by an operator, but an AI-based automated procedure is planned to further increase the speed during mass production.
- Continuous measurement of the outer straw diameter. During straw production, the outer diameter of the straw is continuously monitored using a precision optical system (laser) with an internal pressurization of 1.3 bar absolute. Consistency with the nominal value of 4.95 ± 0.01 mm (corresponding to 4.98 mm at 3 bar relative) is required. Any measured value outside of the acceptance range results in an immediate rejection of the straw.
- Measurement of the straw inner diameter. The inner diameter of each straw is measured at both ends after production using a precision caliper. The inner diameter must be consistent with the nominal value of 4.91 ± 0.01 mm at atmospheric pressure. Straws falling outside of this acceptance range are rejected.
- Express destructive test of the welded seam. Two small segments of about 5-10 mm are cut from both ends of each straw and radially stretched until breakage. Early failures before reaching the elastic limit of the material due to incomplete welding result in the rejection of the entire straw.
- Short-term high pressure test. Straws within the acceptance range of the inner diameter are inflated at a relative pressure of 5 bar for a period of less than one minute in order to quickly detect potential weak spots in the welded seam by accelerating their mechanical failure.

DRAFT

- Long-term high pressure storage. All straws produced are inflated with Ar gas at a relative pressure of 3 bar and stored in a horizontal position for a period of 100 days. During this period, the straws are regularly checked. Any straw developing gas leaks or an abnormal pressure loss is rejected. The primary goal for the long-term storage is to stabilize the mylar film reducing the creep rate expected during the operation of the assembled STT modules. Our measurements (Section 6.15.2) indicate that the creep rate has a logarithmic dependence over time, with most of the material relaxation occurring in the initial 100 days. Straws will be used for module assembly continuously as they are produced, eliminating the need for simultaneous storage of all straws.

The quality controls described above were tested during the production of the straws for the 1.2 m (Section 6.12.4) and full-scale (Section 6.12.9) STT prototypes (Figure 6.106), with the exception of the long-term storage. Figure 6.107 shows the distribution of the outer diameter measured during the straw production, with a standard deviation of 10 μm achieved. Figure 6.108 gives some examples of the short-term and long-term pressure tests.

6.13.10 Quality Controls for Module Assembly



Figure 6.109: Checking the ground connections of the straws during the assembly of the 1.2 m STT prototype at CERN.

The STT modules are subject to a number of quality controls and strict acceptance tests at the Module Assembly (MA) units (Section 6.14.2) both during and after the completion of their assembly. Visual and dimensional inspections of the various components received from the industrial suppliers are performed first, to ensure compliance with the required specifications. The bottom half of the C-fiber frame is mounted on the assembly table and its flatness is measured along all 4 sides. The following quality controls and tests are then performed on each STT module at various stages of the assembly procedure:

- Check of the ground connection for all straws. The electrical contacts between the inner Al metallization of the first straw layer and the outer Al metallization of the fourth straw layer, as well as between the ground planes on the 4 sides of the assembly are checked. An additional application of the silver conductive paint SCP26G is used in case missing ground contacts are found.
- Measurement of the electrical resistance for all wires after the crimping of the pins. The measured values must be consistent with an expected value of about 300 Ω/m. Wires with



Figure 6.110: Measurement of the wire resistance (left picture) and HV test (right picture) during the assembly of the 1.2 m STT prototype at CERN.

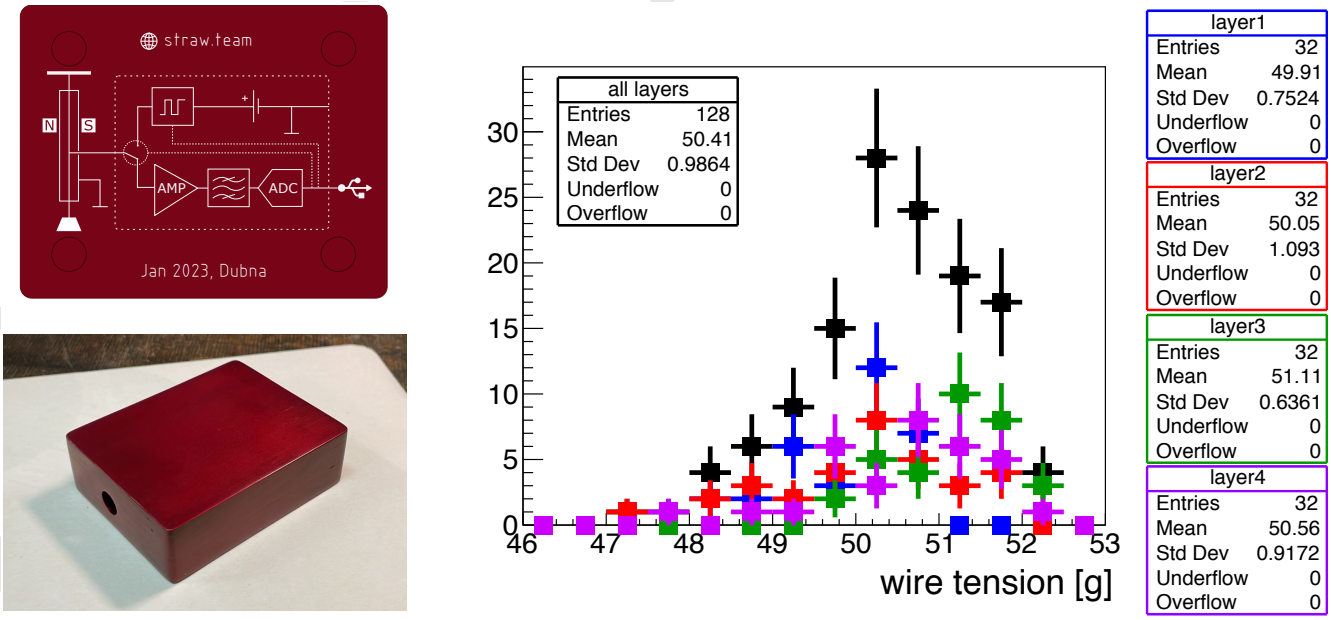


Figure 6.111: Measurement of the wire tension during the assembly of the 1.2 m STT prototype at CERN. The nominal tension is 50 gf. The total fraction of wires replaced after QC was $2/128 = 1.6\%$ (1 HV leak current, 1 crimped w/o weight).

abnormal values of the resistance are immediately replaced.

- Short-term high voltage test for all wires passing the electrical resistance test. The test is performed in air with a nominal HV value of about 1.2 kV. The maximal leak current is required to be within a few nA for a group of 64 channels. Wires which cannot hold the nominal voltage or with abnormal values of leak current observed are immediately replaced.
- Measurement of the tension for all wires passing the short term HV test. The wire tension is measured using a standard technique based on sending a pulse within an external magnetic field and measuring the straw oscillation. The measured tension must be within 50 ± 5 gf. Wires falling outside of this range are immediately replaced. Because the wire tension is critical for the stability of the straw operation, the wire tension has to be measured at each step to ensure there is no major tension loss due to slippage of the wire inside the crimping pin, partially inserted HV plugs, transportation, measuring errors during the STT assembly etc.
- Pressure and gas tightness test after the sealing of the completed module. The gas tightness test of the assembled STT module is carried out by measuring the pressure drop in the closed detector gas volume filled with Ar at the STT operating condition of 2 bar absolute pressure for a few hours. Internal pressure, atmospheric pressure, and temperature are recorded during the gas tightness test. The leak rate can be evaluated by fitting the pressure drop trend measured. In order to avoid substantial losses of the Xe gas, it is required that the total leak rate of the module does not exceed twice the average diffusion rate expected from the straw walls alone based on the measurements (Section 6.12.1). This requirement corresponds to an average leak rate for the STT modules of less than 4×10^{-4} liter/min with Ar gas at 2 bar absolute pressure. In case an excessive leak rate is detected, its origin within the module is identified, the sealing procedure is updated, and the gas tightness measurement is repeated until the module satisfies the acceptance criteria.
- Long-term high voltage test after passing the gas tightness test to identify faulty channels (discharge or large leakage current). This test is performed over a period of 4 days with an active gas mixture of Ar/CO_2 70/30 at 2 bar absolute pressure and a voltage of 1.5 kV. During the long term high voltage test the current and the number of trips are monitored. In case of large currents or repeated trips, that particular high voltage channel is investigated to identify the faulty straw.
- Functional test and gain measurement of the straws. During the long-term HV test with Ar/CO_2 70/30 at 2 bar absolute pressure and 1.5 kV, the straws are scanned using a ^{55}Fe source. Uniform gas gain along the straw tube is important for the safety of the detector and for optimal performance. The STT design guarantees minimal deformations in the straws: the operating overpressure results in a circular shape of the straws, while the spacers allow a self-centering of the wires within the straw, regardless of the assembly tolerances. The gas gain will be checked in 3 points along the straws to verify that no abnormal conditions are present.

Most of the quality controls described above were tested during the construction of the 1.2 m (Section 6.12.4) and full-scale (Section 6.12.9) STT prototypes. Figure 6.109 illustrates the checks of ground connections, Figure 6.110 shows an example of the corresponding electrical resistance and HV tests, while Figure 6.111 summarizes the results of the wire tension measurements. The fraction of wires that had to be replaced during the assembly was found to be only about 1.6%, mostly due

to abnormal HV leakage current and human errors during the manual crimping procedure.

6.14 Detector Construction

The construction of the STT includes two main functional blocks:

- Production and testing of straws using ultrasonic welding technology;
- Assembly and testing of the complete STT modules from the supplied components (straws, frame, wires, end-plugs, spacers, pins, etc.).

The two steps are functionally independent and can operate either from the same site or from different sites. In the latter case, the straws are shipped to the assembly sites after passing all quality controls and acceptance criteria (Section 6.13.9). This scheme provides flexibility in the organization of the STT construction. The required resources and infrastructure are quantified in terms of straw production units and module assembly units, respectively.

6.14.1 Straw Production unit

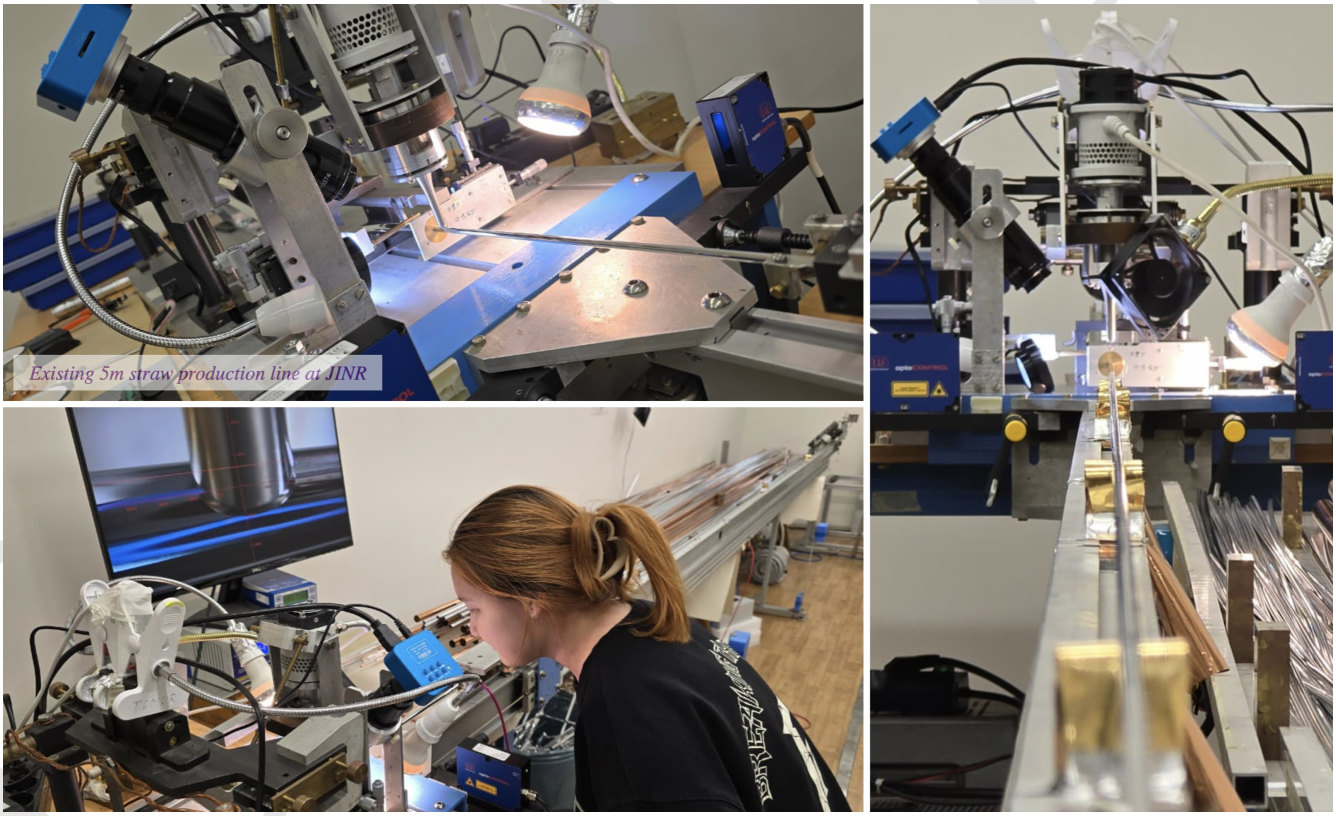


Figure 6.112: Existing straw production unit capable of producing 5 m long straws at JINR.

A basic Straw Production (SP) unit includes the following:

- A straw production line capable of fabricating the longest STT straws (4 m) equipped with

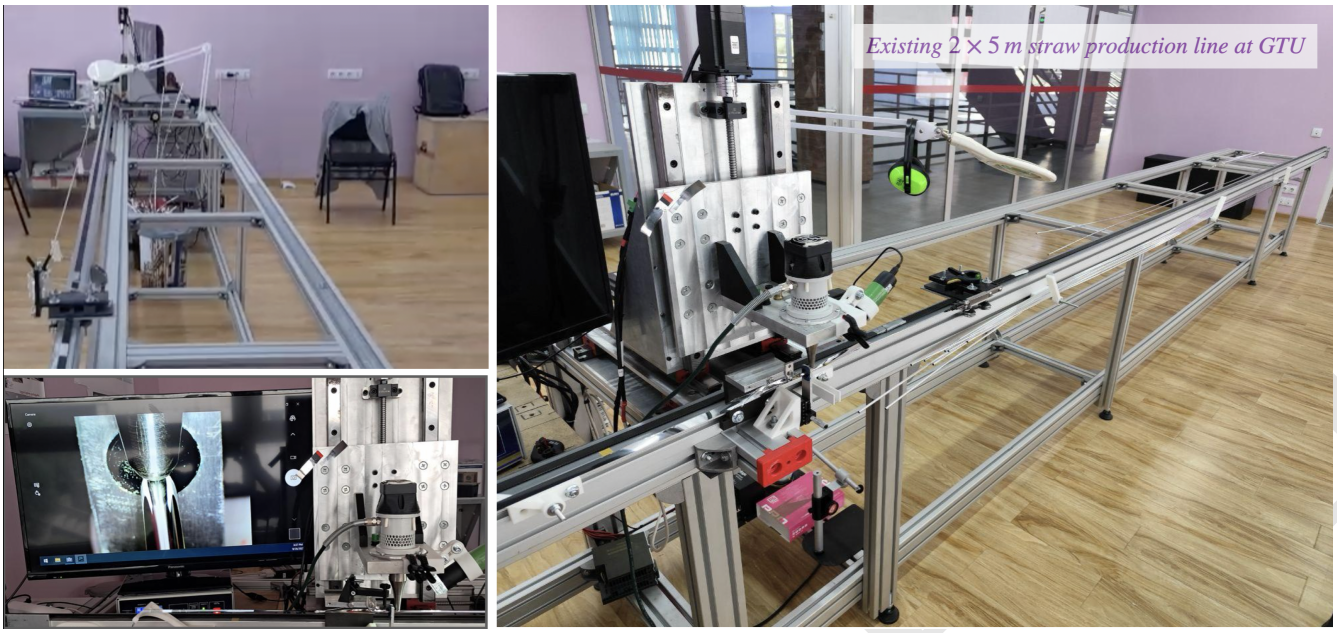


Figure 6.113: Existing $2\times$ 5 m straw production line (equivalent to 2 SP units) at GTU in Tbilisi.



Figure 6.114: New straw production unit capable of producing 5 m long straws at INP, Kazakhstan.

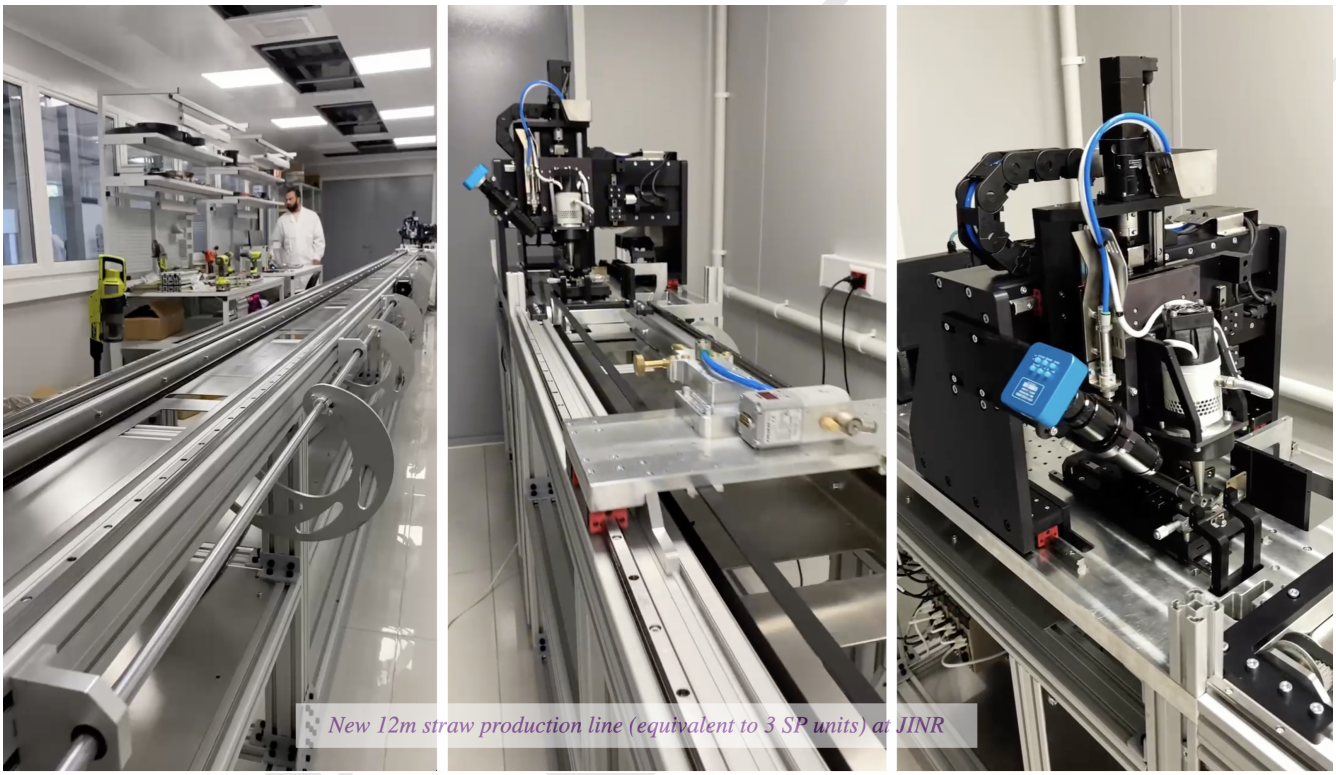


Figure 6.115: New automatized line capable of producing 12 m long straws (equivalent to 3 SP units) completed at JINR in 2025.

DRAFT

ultrasonic welding technology (Section 6.6). The welding process is automatized and the SP line is based on the existing facilities operational at JINR and GTU.

- A test station for the required quality controls (Section 6.13.9) to be performed in parallel with the actual straw production.
- No strict clean-room certification is required for the production of the STT straws.
- A total person-power of 4 people is required to operate a single SP unit, regardless of the length of the SP line: two people for the straw production and two people for the quality tests. A double SP unit like the one available at GTU requires a total of 6 people.
- An average straw production rate of 50 straws/day with 8 working hours per day including QC was verified for 5 m straws at the existing JINR facility.
- An appropriate shelf space is required to store the straws at a relative pressure of 3 bar in a horizontal position for a period of 100 days (Section 6.13.9). Since the assembly of the STT modules proceeds partly in parallel with the straw production, the maximal number of straws stored at any given time corresponds to the production expected during the 100 day period, i.e. about 5,000 full-length straws per SP unit.

A minimal number of 3 SP units is required for the construction of the initial STT. Assuming an average number of 230 working days per year with 8 working hours per day, the total straw length of 430 km needed (Section 6.2) can be produced in about 2.5 years by such units:

$$430.000\,\mathrm{m}/(50\,straws/day \times 5\,\mathrm{m} \times 3\,SP\,units \times 230\,day) = 2.49\ years$$

which is safely below the total scheduled construction time of over 4 years for the initial STT (Section 6.14.6). It must be noted that the existing facilities at INP, GTU, and JINR, listed in Table 6.17, already provide 7 ST units corresponding to more than twice the requirements. Figure 6.112, Figure 6.113, and Figure 6.114 show the existing 5 m long lines at JINR, GTU, and INP, respectively. In addition, a new automatized line capable of producing 12 m long straws, equivalent to 3 SP units alone, was completed at JINR in 2025 (Figure 6.115) and will be duplicated at INP. The advantages of such a longer line are an increase production speed and a reduction of the person-power requirements compared with the equivalent number of separate SP units. The total personpower required for their operation is estimated to be 6 people at the GTU facility, 4 people at the INP/JINR facilities, and only 3 people at the new 12 m long facility at JINR.

Table 6.17: List of existing SP units available for the STT straw production in 2025.

Production line	Length	SP units	FTE	Comment
INP/JINR	5 m	1	4	Used for "Module 0"
GTU	2×5 m	2	6	Used for "Module 0"
INP	5 m	1	4	Completed
INP/JINR	12 m	3	3	Completed
Total		7	17	Minimal SP units 3

6.14.2 Module Assembly Unit

A basic Module Assembly (MA) unit includes the following:

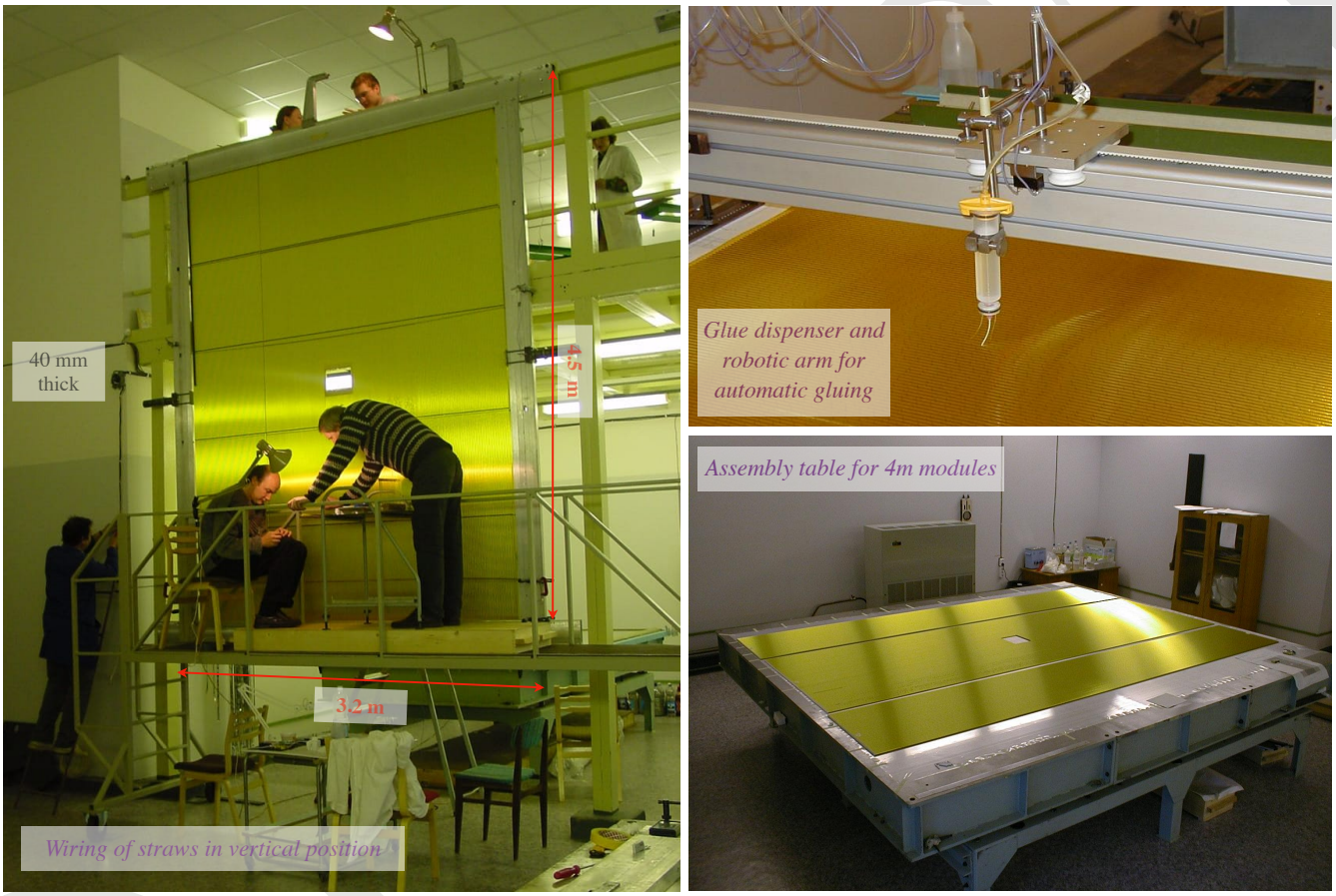


Figure 6.116: Module assembly tooling for the assembly of 4 m modules developed for the COMPASS straw tracker.

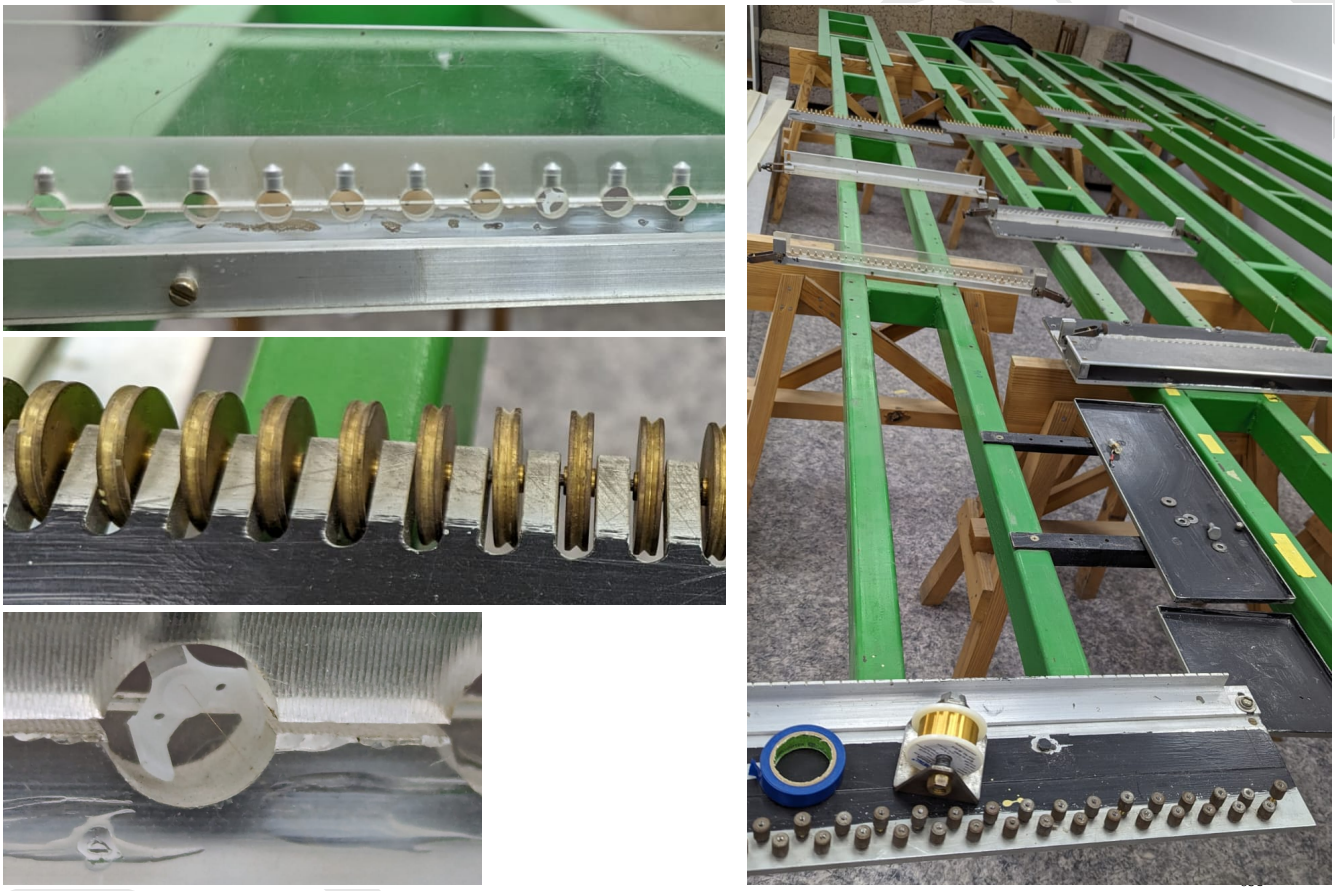


Figure 6.117: Module assembly tooling developed for COMPASS to glue spacers on 4 m long wires before insertion into the straws.



Figure 6.118: Module assembly tooling for external support of full-scale STT frames during the wiring and assembly process based on cross-bracing with C-fiber square tubes.

- An assembly table $5.04\,\mathrm{m} \times 3.5\,\mathrm{m} \times 0.9\,\mathrm{m}$ capable to fit the largest STT modules $3.9\,\mathrm{m} \times 3.3\,\mathrm{m}$ with a flatness requirement of $100\,\mu\mathrm{m}$. The table is composed of two main parts: (i) a support structure constructed from light aluminum beams; (ii) a top plane made of multiple steel plates (Fig. 6.92). The design of the assembly table will be validated with the construction of the full-scale STT prototype (Section 6.12.9). A second table per assembly site is required to allow a parallel workflow for the module tests and part of the initial assembly steps.
- A robotic arm equipped with an automatic glue dispenser similar to the one developed for the assembly of the modules of the COMPASS straw tracker (Figure 6.116).
- Frames and holders for gluing the spacers to the wires before insertion into the straws. This tooling was developed for the assembly of the modules of the COMPASS straw tracker (Figure 6.117).
- External cross-bracing made of C-fiber squared tubes for the temporary support of the frames of the STT modules during the wiring and assembly process, as shown in Fig. 6.118 and Fig. 6.91.
- Pneumatic crimping tools for the wire pins developed for the mass production of the ATLAS TRT (Figure 6.75). A total of 5-10 crimping tools per MA unit is required to have enough spare tools in case of breakage during mass production.
- A test station for the required quality controls (Section 6.13.10) to be performed in parallel with the actual module assembly.
- A total space of about $150\,\mathrm{m}^2$ is required including test and storage space.
- A ceiling height $\geq 5\,\mathrm{m}$ is required to allow the largest modules to be held in a vertical position for the wiring and the final sealing.
- No strict clean-room certification is required for the assembly of the STT modules.
- A total person-power of 7 people is required to operate a single MA unit, including both the assembly and the quality controls, based on the experience with the construction of the 1.2 m (Section 6.12.4) and full-scale (Section 6.12.9) STT prototypes.
- An average production time of about 2 months/module is expected once a steady operation of the MA unit is reached after a training during the first three years of operation.

A minimal number of 3 MA units is required for the construction of the initial STT over a period of about 4 years. Such MA units could be operational either from different sites or from a single site equipped with the corresponding assembly tables and related tooling. It is conservatively assumed that each MA unit will assemble 1 module in the first year of operation, 2 modules in the second year, 4 modules in the third year, and 6 modules/year afterwards. The total personpower required to operate 3 MA units is estimated to be 21 people. A single MA unit is currently available at JINR based on the existing COMPASS and ATLAS tooling and will be replicated after the completion of the construction of a full-scale STT prototype (Section 6.12.9). Up to six MA units are planned at various production sites, significantly exceeding the minimum required number.

As discussed in Section 6.5, the STT design was optimized to simplify the operations at the MA units. In particular, two main features are relevant:

- Self-alignment of the straws during assembly. The straws in each layer are pressurized at 2.5 bar relative, closely packed and aligned to the corresponding straw holder profiles in the

C-fiber frame, supplemented by similar alignment profiles installed on the assembly table.

- Self-centering of wires within the straws themselves. Extra spacers close to the straw ends provide accurate wire centering ($< 65\,\mu$m), effectively decoupling the straws from the mechanical frame.

The first feature avoids complex alignments, while the second one makes the assembly tolerances non-critical, resulting in relaxed requirements for the tooling and assembly procedure. Once the wires are self-centered with high accuracy by design, the unknown absolute wire position within a STT module can be obtained by in-situ alignment, without the need for dedicated X-ray scans. To this end, the large number of muons passing through, originated by (anti)neutrino interactions in the rocks surrounding the detector, can be used (Section 6.17.1).

6.14.3 Production Sites

Country	STT Institutions	Contributions	Planned Contributions
Italy	INFN Pisa, Bologna	Management Design and engineering Procurement of film, prototype frames, assembly tooling Testbeam exposures Construction of prototypes Simulations and reconstruction Analysis and physics studies	Assembly of STT modules (at FNAL) ASIC and readout
Georgia	GTU	Design and engineering Tests of straw properties Construction of 2.5 SP units Product of straws for prototypes Construction of prototypes Simulations and analysis	Setup 1 MA unit Production of straws Assembly of STT modules
India	Delhi IIT Guwahati IIT Kanpur NISER Panjab	Procurement of components Tests of straw properties Readout and testbeam exposures Simulation and reconstruction Analysis and physics studies	Construction of 1 SP unit Setup 3 MA units Production of straws Assembly of STT modules Readout electronics
Kazakhstan	INP, Almaty (+ JINR)	Design and engineering Readout and testbeam exposures Tests of straw properties Construction of 4 (+1) SP units Construction of prototypes Simulations and analysis	Construction of 3 SP units Setup 1 MA unit Production of straws Assembly of STT modules Readout electronics
USA	Duke University USC (FNAL)	Management Design and engineering Procurement of straw components, targets/radiator, VMM3a, readout, full-scale frame prototype and tooling Readout and testbeam exposures Tests of straw properties Simulations and reconstruction Analysis and physics studies	Construction of 1 SP unit Setup 1 MA unit (FNAL) Readout electronics

Figure 6.119: Summary of contributions to the STT from the participating institutions.

A STT production site is a laboratory located at one of the collaborating institutions or at Fermilab and is equipped with one or more SP units (Section 6.14.1) and/or one or more MA units (Section 6.14.2). In principle, the initial STT can be constructed using a single production site equipped with the required SP and/or MA units. However, multiple sites in different countries are being prepared to provide additional flexibility and improve the project sharing among collaborating institutions. As outlined in Figure 6.119 up to 7 STT production sites are planned, located at INP in Kazakhstan, at GTU in Georgia, at Delhi University, IIT Guwahati, and Panjab University in India, at Fermilab, and at Duke/USC in the US. Each production site will be equipped with a variable number of SP units and/or MA units, depending on the local infrastructure available.

The STT production site in the US will be divided among the participating institutions in Figure 6.119 and Fermilab. A single SP unit will be installed and operated at Duke/USC, while a MA unit is planned to be set up at Fermilab. The straws produced by the various SP units will be shipped at Fermilab, where the MA unit will be operated primarily by personnel sent by the collaborating institutions, under the coordination of Fermilab personnel. The space requirements at Fermilab are about 150 m^2 with two tables, one for assembly and one spare for tests. The tooling and person-power requirements are the same as listed in Section 6.14.2.

Table 6.18: Requirements of FTE for the construction of the initial STT. Each FTE assumes a working time of 8 hours per day for a total of 230 working days per year.

Task	Units	FTE		Comment
		Nominal	Minimun	
Straw production	3	INP/JINR 5m: 4		Existing facility
		GTU 2×5m: 6		Existing facility
			INP/JINR 12m: 3	Existing facility
Module assembly	3	21	21	Single or multiple sites
Fermilab integration	1	7	7	Targets & readout

The estimate of the total FTE requirements for the construction of the initial STT is based on the following assumptions for the production times:

- Production of all straws in a conservative period of 2.5 years (Section 6.14.1);
- Assembly of all 54 STT modules in a period of about 4 years (Section 6.14.2);
- Integration and installation at Fermilab over a period of about 2.5 years (Section 6.14.5).

Table 6.18 summarizes the various SP and MA units and the corresponding requirements in terms of FTE. Overall, a total of 4 SP sites and 6 MA sites will be operated by the collaborating institutions. The production of the straws requires 10 FTE using 3 SP units 5 m long and only 3 FTE with the new 12 m SP line (Section 6.14.1). The assembly of the 54 STT modules requires 21 FTE, assuming a minimum of 3 MA units available. The installation and integration at Fermilab requires a total of 7 FTE, as discussed in Section 6.14.5. All the required personnel will be provided by the collaborating institutions and include technicians, students, scientists, and engineers. The corresponding labor costs vary depending on the location of the production sites and on the qualification of the personnel ("uncosted labor").

6.14.4 Transportation to Fermilab



Figure 6.120: Transportation of the COMPASS straw tracker (4.5 m × 3.2 m modules) from JINR to CERN. No damage was found on the modules at CERN.

The transportation of the STT modules from the various production sites (Section 6.14.3) to Fermilab will be performed via water and/or ground. The modules will be shipped without targets nor radiators in order to reduce the corresponding weight, as well as potential damages to the tracking modules. Targets and radiators will be added to the various super-module assemblies on the Fermilab site before installation (Section 6.14.5). The basic shipping unit is a stack of 5 STT tracking modules, which will be prepared for transportation as a super-module assembly (Section 6.5.3) using appropriate threaded rods and nuts. The total thickness of such stacks is about 140 mm, while the maximal weight is about 165 kg for the largest modules 3.9 m tall and 3.3 m wide.

The COMPASS experiment successfully delivered similar straw tracker modules about 4.5 m × 3.2 m and only 40 mm thick over a distance of about 3000 km from JINR to CERN by ground transportation (Figure 6.120). Although the COMPASS modules were shipped individually within custom crates, no damage was found on the modules at the arrival at CERN. The COMPASS experience provides a valuable input for the transportation of the STT modules.

The dimensions of a super-module assembly with 5 of the largest STT tracking modules, including adequate protection packaging, is consistent with the use of standard 20 ft High Cube (HC) containers for transportation. Figure 6.121 shows a sketch of the corresponding arrangement inside the container. A basic shipping unit is fitted diagonally at an angle of about 49° into the inner space of the container 2.7 m × 2.35 m. The super-module assembly has to be first secured onto a supporting triangular space-frame structure before the insertion into the container. The close

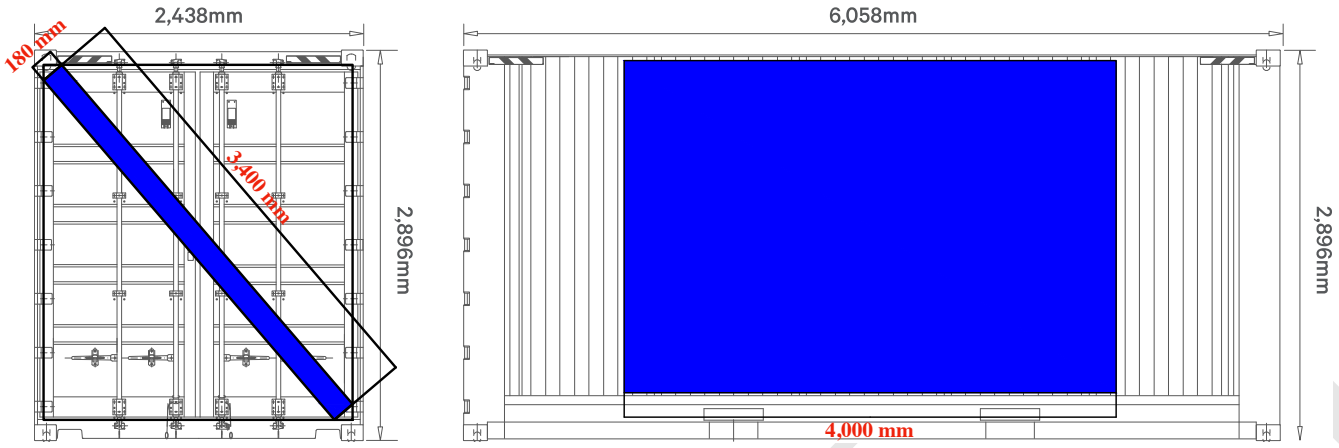


Figure 6.121: Five of the largest STT tracking modules (without targets) clamped together in a super-module assembly can be shipped to Fermilab via water/ground using a standard 20ft HC container.

container also provides extra protection for the STT modules against accidental damages. The use of a commercially available standard container can reduce shipping costs and simplify the various operations required for both water and ground transportation. Considering that all the STT modules share a common width of about 3.3 m and have variable heights ranging from about 3.9 m down to about 1 m, a maximum of 8 containers 20 ft HC will be required for the transportation of the 54 modules of the initial STT from the production sites to Fermilab. Alternatively, a total of 4 standard 40 ft HC containers for the entire initial STT can also be used. Each 40 ft HC container can transport 3 super-module assemblies of 5 modules each, given the average height of 3.27 m for the STT modules.

6.14.5 Installation and Integration at Fermilab

The 54 modules of the initial STT will arrive at Fermilab assembled into 11 basic shipping units, each composed of 5 tracking modules without targets. Those shipping units will be delivered within standard 20 ft HC or 40 ft HC containers (Section 6.14.4). After unloading the containers the shipping units will be moved to an on-site storage and test facility, where they will be inspected and disassembled into individual modules. Each STT tracking module will undergo various tests to verify that no significant damage occurred during the transportation from the production sites to Fermilab:

- Measurement of the tension for all wires. The same procedure followed during the module assembly will be used (Section 6.13.10). The measured tension must be within 50 ± 5 gf. Wires falling outside of this range are disconnected by removing the corresponding crimped pins and appropriately marked in the detector database.
- Instrumentation with the final integrated readout boards. The required readout boards are inserted into the corresponding PCIe connectors (Section 6.7.1) located at the bottom of two sides of the frame and connected to the LV, HV, and digital input/output wires (Section 6.9.2).
- Gas tightness test after the sealing of the removable lids. The gas tightness of the STT module equipped with the final readout boards is tested by measuring the pressure drop

in the closed detector gas volume filled with Ar at the STT operating condition of 2 bar absolute pressure for a few hours. It is required that the total leak rate of the module does not exceed twice the average diffusion rate expected from the straw walls alone based on the measurements (Section 6.12.1). In case an excessive leak rate is observed, its origin is identified, the removable lids are resealed, and the gas tightness measurement is repeated until the module satisfies the acceptance criteria.

- Functional test and gain measurement of the straws. This test is performed over a period of 4 days with an active gas mixture of Ar/CO_2 70/30 at 2 bar absolute pressure and a voltage of 1.5 kV (Section 6.13.10). During this period the current and the number of trips are monitored, and the straws are scanned with a ^{55}Fe source. In case of large currents, repeated trips, or abnormal operating conditions the corresponding channels are disconnected from the readout boards by removing the corresponding HV resistor and appropriately marked in the detector database.

Once the functional tests are completed, the STT tracking modules are assembled into the final 8+1 super-modules (Section 6.5.3) in the vertical position as shown in Figure 6.18. At this stage the various graphite and plastic targets and radiators are added in the super-module assembly. The fixtures to hang the super-modules to the external mechanical structure (basket) supporting both GRAIN and the STT are added and secured to the top sections of the relevant modules (Figure 6.20). The maximal weight of the largest super-modules including 10 modules – one with graphite target and 9 with plastic targets, out of which 6 with radiators (Figure 6.16) – is about 1.1 t. Individual super-modules are finally inserted into the basket within the SAND magnet using dedicated mechanical rails. Service connections including the various gas pipes, LV, HV, and digital cabling (Section 6.9.5) are then completed. The total person-power required at Fermilab is estimated to be 7 people, the same as for a single MA unit (Section 6.14.2).

6.14.6 Organization and Schedule

The STT project includes 11 academic institutions from 5 countries: INFN and the University of Pisa, Italy; INFN and the University of Bologna, Italy; Georgian Technical University (GTU) in Tbilisi, Georgia; IIT Guwahati, India; IIT Kanpur, India; National Institute of Science Education and Research (NISER) Bhubaneswar, India; Panjab University, India; Delhi University, India; Institute for Nuclear Physics (INP) in Almaty, Kazakhstan; Duke University, USA; University of South Carolina (USC), USA. These groups have been efficiently working together since 2021, making significant contributions (Figure 6.119) to the design and prototyping of the STT. They have good working relationships and shared knowledge. Many of the collaborators from the participating institutions have extensive and long-standing experience (over a few decades) with straw tube detectors, including ATLAS TRT, COMPASS, NA62, NA64, Mu2e, COMET, SHiP, etc. Most institutions have contributed to the construction, commissioning, and operation of large detectors for HEP experiments, like ATLAS, CMS, OPERA, K-LOng Experiment (KLOE), etc. There is also a wealth of experience with neutrino detectors and experiments, including NOMAD, OPERA, MINOS, NOvA, LBNE, DUNE, etc. In particular, some institutions have been instrumental in the SAND proposal [32] and have also been deeply involved in DUNE since its inception, as well as in its previous incarnation, LBNE, since 2009.

Figure 6.122 shows the preliminary organizational chart for the construction of the STT. A steering

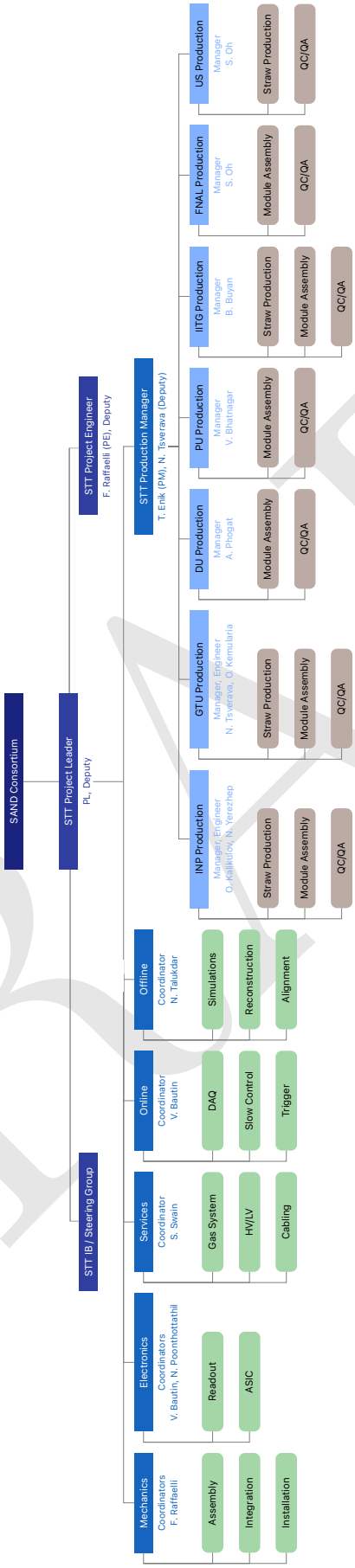


Figure 6.122: Preliminary organizational chart for the construction of STT.

DRAFT

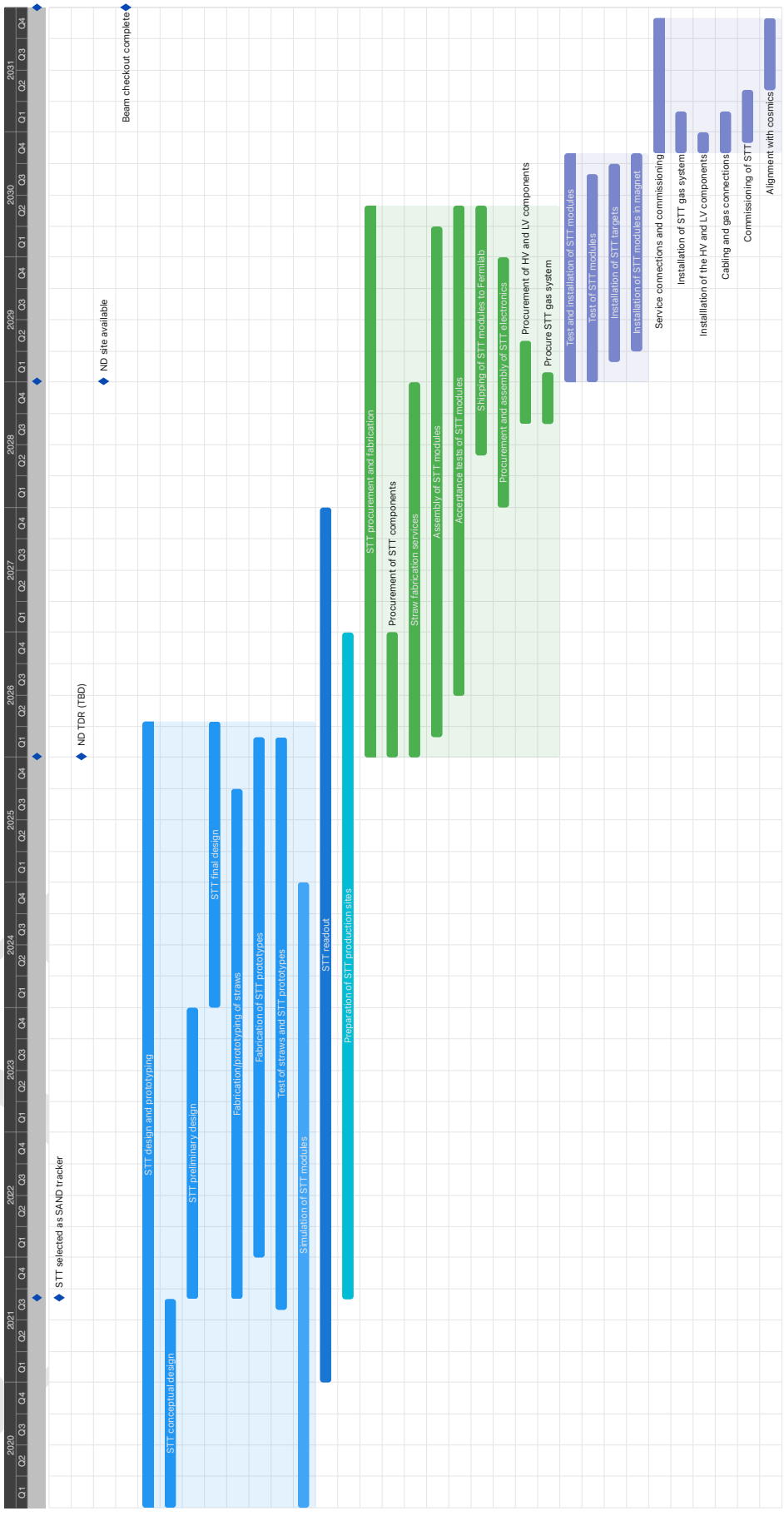


Figure 6.123: Preliminary schedule for the construction of the initial STT including contingency.

group, comprising one representative from each collaborating institution, is acting in consultation with the project leader and deputy to guarantee the sharing of critical decisions among all international parties. A project engineer (and deputy) provides managerial support on technical aspects. Based on the contributions in Figure 6.119, up to seven STT production sites are planned: INP (Kazakhstan), GTU (Georgia), Delhi University, IIT Guwahati, and Panjab University (India), Fermilab, and Duke/USC (US). Each production site will be equipped with a variable number of SP units and/or MA units, depending on the available local infrastructure. Strict quality control procedures and acceptance criteria will be required across all production sites, as described in Section 6.13.9 and Section 6.13.10. In order to guarantee a consistent quality of the STT modules assembled at different production sites, a production manager (and deputy) will coordinate the production and QC at sites, including verifications by inspections. A joint training of the production and assembly personnel is being conducted at the existing facilities during the prototyping activities. Common purchases of the detector components, subject to stringent quality controls, are foreseen through the validated industrial supply chain (Section 6.13.1).

The preliminary schedule for the construction, installation, and commissioning of the initial STT is shown in Figure 6.123. The planning is based on recent progress and developments, as well as ongoing prototyping activities. The initial STT must be fully operational and ready to take data in SAND with the first neutrino beam, which is expected to be delivered in the last quarter of 2031. A softer milestone is represented by the availability of the beneficial occupancy of the ND hall at the end of 2028. The installation of the first STT modules in the magnet is planned to start shortly after that date, partially overlapping with the fabrication. A total period of slightly over four years is allocated for constructing the 54 STT modules required for the initial STT, including schedule contingency. After the arrival at Fermilab, the STT modules will be tested and equipped with various targets and radiators before the installation of the final assembled super-modules in SAND. After the completion of the installation and the corresponding service connections, the detector commissioning will be completed with a cosmics run, followed by an initial alignment with the beam, without the magnetic field. The final detector design is expected to be completed in the first half of 2026, including the test of the full-scale "Module 0" prototype. The preparation of the STT production sites proceeds in parallel with the completion of the design and prototyping. The procurement of the industrial components required for the construction of the STT modules is expected to start in 2026 and be completed by the end of the year. A complete readout based on the VMM3a chip is already available ahead of schedule.

6.15 Operating Conditions

6.15.1 Operational Modularity

Table 6.19: Modularity for the operation of the main elements of STT.

Item	Straws/channel	Modularity	Comment
Gas distribution	395-1,495	395-1,495	Each half-module (XX or YY) independent
Readout I/O	64	64	Readout board & ASIC modularity
High Voltage	395-1,495	64	SSR on individual readout boards
Low Voltage	395-1,495	64	LV protection on individual readout boards

As described above, the STT is characterized by a highly modular design, both mechanically and functionally. The main advantages are twofold:

- Robustness against manipulation allows for easy modification of the detector configuration, including targets, number of modules, etc.;
- Robust operation minimizing operational risks associated with the failure of components.

From the mechanical standpoint each STT tracking module integrates two half-modules composed of straw double layers, which are functionally independent. The basic operational modularity is therefore given by the (variable) number of straws in each half-module, ranging from a minimum of 396 up to a maximum of 1,495 for the largest modules. These numbers correspond to only 0.3-1.1% of the initial STT configuration (Table 6.2). The STT gas distribution has such modularity with separate inlet/outlet tubes (Section 6.9.2). The operational modularity of all the electrical components including HV, LV, and readout is defined by the 64-channel integrated readout boards, as described in Section 6.9. Remote (dis)connection for the LV lines is available on each readout board. The LDO powering the ASIC will have a "Power Off" option controlled by the MCU. The MCU itself can be power cycled through the JTAG chain, if needed. Each board also includes a solid state relay with a SiC MOSFET to allow a remote switching of the HV, as well as low voltage surge protections. In case of related malfunctioning due to HV trip, LV over-current, ASIC or MCU failure, wire breakage, etc. only less than 0.05% of the initial STT is affected. Table 6.19 summarizes the operational modularity for the various components. In all cases the operational modularity is enough to guarantee no disruption on the data taking in case of failures. The affected detector elements can be easily disconnected and safely replaced or repaired during one of the beam-off periods.

6.15.2 Straw Creep Rate

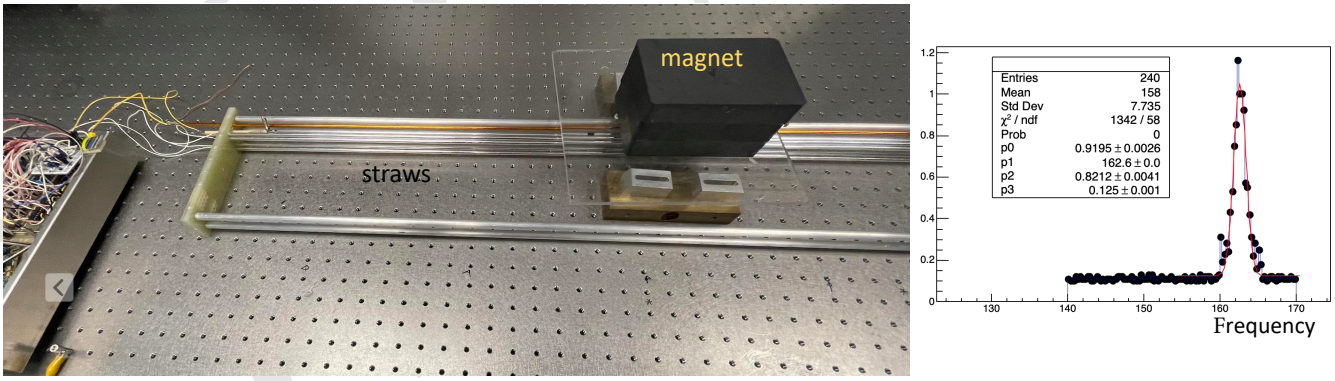


Figure 6.124: Measurement of the creep rate for the straws used in STT. The tension of the straw is determined from a resonant excitation (third harmonics) using an external magnet.

Thin plastic films under tension undergo a permanent modification of the material over time, known as relaxation. This effect has been verified in various straw trackers [77] and must be taken into account in the design and operation of the detector. To this end, the creep (relaxation) rate was measured for straws produced with two different film types: the one used for the first 1.2 m STT prototype (v0) built at CERN and the one used for the second 1.2 m and full-scale prototypes

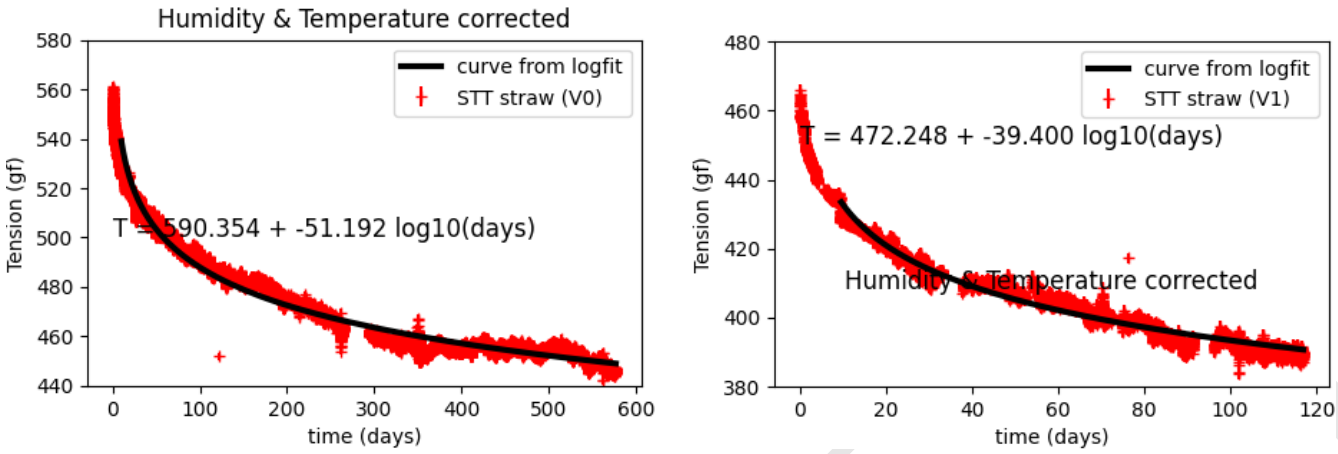


Figure 6.125: Measurement of the creep rate for two different straw types used for the first 1.2 m STT prototype (v0) and for the second 1.2 m and full-scale prototypes (v1). The measured tension is fitted with a logarithmic function $p_0 + p_1 \log_{10}(t)$ with t in days.

(v1). Both films had a nominal thickness of 19 μm walls and featured double Al metallization. Straw tubes were pre-tensioned (T_0) and glued to a fixed frame, as shown in Figure 6.124. The tension of the straw was continuously measured every 15 minutes from a resonant excitation (third harmonics) using an external magnet, along with the ambient pressure, temperature, and humidity. After correcting the data for the temperature and humidity variations detected, the dependence of the straw tension on time shown in Figure 6.125 was obtained. A logarithmic behavior is observed, with most of the relaxation occurring in the initial 50 days. A fit to the normalized tension T/T_0 with the function $p_0 + p_1 \log_{10}(t)$ results in a slope $p_1 = -0.084$ for the straw produced with the final Fraunhofer film (Table 6.20). This measurement indicates an expected tension reduction of about 17% after the initial 100 days, followed by an additional 18% reduction over the next 20 years. Similar results were obtained from both film types in spite of the differences in the base material. As discussed in Section 6.13.9, all straws produced for the STT will be subject to a long-term storage at 3 bar relative pressure for 100 days, in order to allow the material to stabilize before the assembly of the STT modules. Therefore, only the residual 18% creep rate is expected over 20 years of STT operation.

Table 6.20: Straw creep rate obtained from a fit to the normalized tension T/T_0 with the logarithmic function $p_0 + p_1 \log_{10}(t)$. Results for two different straw types used in the first 1.2 m STT prototype (v0) and in the second 1.2 m and full-scale prototypes (v1) are reported.

Film type	p_0	p_1	Comment
v0	1.045	-0.091	First 1.2 m STT prototype
v1	1.007	-0.084	Final Fraunhofer film

The measured creep rate can be used to evaluate an upper limit on the variation in the straw length expected from the relaxation over a period of 20 years:

$$\left[1 - \frac{p_0 + p_1 \log_{10}(7300)}{p_0 + p_1 \log_{10}(100)}\right] 3.5\,\text{mm} = 0.65\,\text{mm}$$

where the longest 3.75 m straws, an operational pressure of 1 bar relative, and an assembly pressure of 2.5 bar relative, corresponding to an initial straw elongation of about 3.5 mm (Section 6.12.1) are assumed. The actual variation in the straw length will be smaller than the upper limit above since the straws are glued to the C-fiber frame and are subjected to the additional forces applied by both the frame and the wires, as obtained from the complete mechanical analysis of Section 6.5.4. The internal overpressure provides a natural spring mechanism that automatically compensates for variations in straw elongation within the elastic limit during the STT operation (Section 6.5.4). A conservative requirement is that any variation in the straw elongation due to humidity, temperature, etc., must be kept < 0.65 mm over a data-taking period of 20 years.

6.15.3 Relative humidity

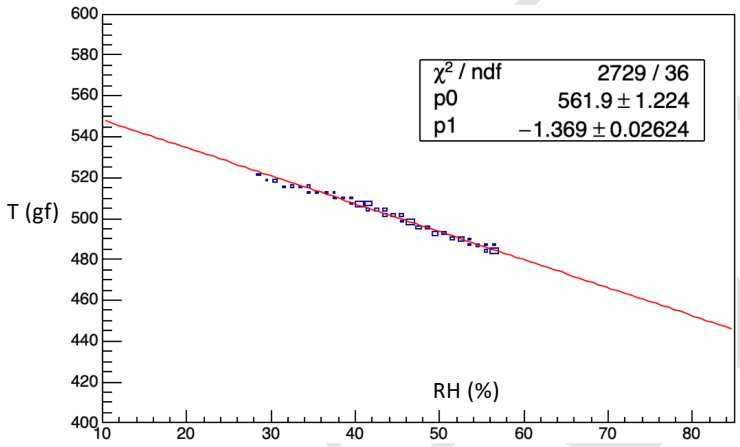


Figure 6.126: Measurement of the variation in the straw tension as a function of the relative humidity (%) for the straws used in STT.

The dependence of straw tension on the ambient relative humidity (RH) was measured with the straws produced for the STT prototypes with 20 μm walls and double Al metallization. Results are shown in Figure 6.126. A linear fit with respect to the relative humidity gives a humidity coefficient of 0.8×10^{-6} cm/cm/%RH. The maximal variation in the straw length expected due to humidity can then be estimated as:

$$0.8 \times 10^{-5}\,\text{mm/cm/\%RH} \times 375\,\text{cm} \times 50\%\ \text{RH} = 0.15\,\text{mm}$$

where the longest 3.75 m straws and an extreme variation of 50% RH are assumed. The resulting variations in the straw length due to the relative humidity are well below the expected creep rate (Section 6.15.2). The ambient humidity, therefore, will not be critical for the STT operation. The internal overpressure will automatically compensate for the corresponding variations in straw elongation. Both the humidity and temperature will be monitored during data taking. Straw elongations due to humidity are reversible once the humidity is brought back to nominal values, contrary to the permanent effect of the creep rate.

6.15.4 Ambient temperature

The maximal variation in the straw length expected from ambient temperature can be estimated using the coefficient of linear expansion of the base Mylar film quoted by the vendor of 17×10^{-3}

mm/m/°C. For the longest 3.75 m straws, this yields:

$$17 \times 10^{-3}\,\mathrm{mm/m/}^{\circ}C \times 3.75\,\mathrm{m} = 0.064\,\mathrm{mm/}^{\circ}C.$$

In order to keep the maximal variations well below those expected from the 20-year creep rate (Section 6.15.2), the ambient temperature must be controlled within ±5°C. This requirement is relatively modest, as typical commercial air conditioning achieves an accuracy of about 1°C. The temperature will be continuously monitored during data taking. Straw elongations due to humidity are reversible, similar to the case of temperature. As in the latter case, the internal overpressure will automatically compensate for the corresponding variations in straw elongation.

A second aspect to consider in defining a safe temperature range for the STT operation is the cooling of the readout boards integrated into the C-fiber frames of the STT modules. A detailed thermal analysis of the complete super-module assembly indicates that a variation of the ambient temperature within 20 ± 5°C is compatible with a maximal temperature on the VMM3a chips well below 40°C (Section 6.8.2).

6.15.5 Detector aging

The primary aging effect is expected to be related to the progressive relaxation of the straw material over time. The corresponding creep rate was measured for the STT straws (Section 6.15.2) and found to follow a logarithmic behavior as a function of time. In order to reduce its impact on the STT operation, all the straws undergo a long-term storage for 100 days at 3 bar relative pressure (Section 6.13.9) before their use in the module assembly. The residual effect is expected to be limited to a reduction in the straw tension of about 18% over a period of 20 years. Such an aging effect was implemented in detailed FE analyses of the STT operating conditions, resulting in maximal frame deformations in the outward deflection of about 200 μm per side after 20 years over a length of 3.9 m (Section 6.5.4).

The design of the STT modules is based on the use of an internal overpressure of 1 bar relative to balance the sum of the opposite tensions applied by the walls of the straws and by the wires. Similarly, the forces induced by the pressure on the side panels of nearby modules cancel each other within the super-module assembly. Under such conditions, the total net force acting on the frame is vanishing in operating conditions. The C-fiber frames are therefore subject to a negligible stress during their lifetime, reducing the probability of developing the microscopic defects typically associated with the aging of the corresponding materials.

All glues and materials used in the construction of the STT modules are compatible with gaseous detectors and were tested in previous experiments. The gas mixtures Xe/CO_2 and Ar/CO_2 70/30 used in STT are safe and non-flammable. Given the negligible radiation environment with the LBNF (anti)neutrino beams and the operation at room temperature around 20°C, no significant aging of the various materials is expected. It is also worth mentioning that straw trackers like the ATLAS TRT [55, 56] and the COMPASS [64, 65] one have been successfully operated for close to 20 years in environments with much higher radiation.

DRAFT

Risk ID (placeholder)	Risk title	Risk area (RBS)	Prob.	Impact	Rank	Mitigations and Responses
RT-131-ND.05-501	Delay in custom ASIC development for STT	Management Risk / Planning	10%	Low	Low	Complete readout based on existing VMM3a available, which satisfies the main STT requirements and will be used for STT construction/testing and for initial data taking. The custom ASIC upgrade is not on critical path and can proceed in parallel. The modular design of the readout boards with PCIe connector allows easy replacements/upgrades.
RT-131-ND.05-502	Delay of the full-scale STT prototype	Management Risk / Planning	35%	Moderate	Medium	Schedule contingency allowed up to mid 2026, with final engineering proceeding partially in parallel with the preparation of the production sites. Procurement and test of the main components required for full-scale prototypes already completed.
RT-131-ND.05-503	Delay in module assembly during the STT construction	Management Risk / Planning	20%	Moderate	Medium	The STT design makes each individual module functionally independent, allowing the operation of the detector with less modules. We plan an initial STT configuration with 54 modules, which fulfills the main physics scopes and allows a substantial schedule contingency. Additional 30 modules are foreseen for a later STT upgrade.
RT-131-ND.05-504	Inconsistent quality across the STT production sites	Technical Risk / Quality	20%	Low	Low	Strict QA/QC procedures and acceptance criteria will be required across all production sites. A production manager will coordinate the production and QA/QC at sites, including verifications by inspections. Common purchases of the detector components required for assembly and a joint training of the assembly personnel are foreseen. In addition, the initial STT configuration could be produced at a single assembly site equipped with 3 assembly tables.
RT-131-ND.05-505	Difficulties in procurement of C-fiber frames for STT	External Risk / Vendors	35%	Low	Low	Verification of quality of prototype C-fiber frames. Qualification of different vendors during prototyping activities and selection of backup vendors.
RT-131-ND.05-506	Difficulties in the procurement of W/Re wire for STT	External Risk / Vendors	20%	Low	Low	Qualification of different vendors during prototyping activities and selection of backup vendors. Quality tests of wire samples from all selected vendors at CERN.
RT-131-ND.05-507	Problems encountered during tests of custom ASIC prototypes	External Risk / Industry	20%	Low	Low	Development of custom ASIC for STT based upon sub-circuits and functions largely inherited from the well-established NRL and VMM3a chips, which have been tested with STT prototypes. Direct involvement of the designer of NRL and VMM3a chips in the development of the custom ASIC for STT.
RT-131-ND.05-508	Problems with the tooling for the assembly of STT modules	External Risk / Facilities	20%	Moderate	Medium	Construction and test of STT full-scale prototype ("module 0") will be used to validate the tooling and identify potential issues. Initial tooling based on the ones developed for the COMPASS straw tracker with modules of similar size and geometry as in STT.
RU-131-ND.05-511	Price variations from market changes	External Risk / Market	20%	Low	Low	For most items obtained quotes from multiple vendors and monitor costs over time. The contracts for the purchase of the main components are expected to be signed by 2026.
RU-131-ND.05-512	Foreign exchange rate fluctuations	External Risk / Market	20%	Low	Low	STT core costs based on quotes from a mixture of currencies from selected vendors in different countries. The procurement of most components should occur by 2026, thus reducing long-term uncertainty in exchange rate fluctuations.
RT-131-ND.05-513	Delay in the availability/ approval of funding / resources	Management Risk / Funding and Resources	35%	Moderate	Medium	Value engineering resulted in a reduction of core costs for the initial STT configuration. Funding proposals for STT have been submitted to funding agencies by participating institutions, exceeding the estimated core costs. A firm support by the DUNE management is required.
RT-131-ND.05-514	Damage of STT modules during shipping to Fermilab	Management Risk / Logistics	5%	Low	Low	Five STT modules will be connected together as a shipping unit in a super-module assembly. The shipping will be done via water/ground transportation using standard 20ft or 40ft HC containers. We will take advantage of the shipping experience of similar COMPASS modules from JINR to CERN. We will engage an engineering/shipping firm from an early stage of the production process.
RT-40ND-ND.05-515	Gas leakage in a STT module	Technical Risk / Reliability and Performance	1%	Low	Low	Each STT half-module (XX or YY straw double layer) is fed by independent parallel gas input/output lines, with an individual valve and pressure sensor for each module. Depending on the type of leak detected the affected half-module can be either moved from the Xe/CO_2 to the Ar/CO_2 distribution, or disconnected altogether from the gas distribution, without stopping the STT data taking. The STT design allows to fix leakages during one of the beam-off periods.
RT-40ND-ND.05-516	Failure of STT gas system including pump	Technical Risk / Reliability and Performance	1%	Low	Low	A second backup pump is included into the STT gas system allowing a quick switch without major losses of data taking while the faulty pump is being repaired.
RT-40ND-ND.05-517	Leakage/breakage of STT straws	Technical Risk / Reliability and Performance	<0.01%	Low	Low	Strict QA/QC protocols and acceptance criteria will be used during the straw production, similar to the ones implemented for the NA62 straw tracker, in which no straw breakage was observed over many years of operation. The quality of the straw welding has been validated with dedicated tests at CERN and found to exceed the one of the NA62 straws.
RT-40ND-ND.05-518	Failure of a STT integrated readout board	Technical Risk / Reliability and Performance	1%	Low	Low	The STT readout boards are connected in parallel with a robust BUS interface so that the failure of a readout board does not affect the remaining ones. The failure of a readout board implies the temporary loss of 64 straws, corresponding to 0.05% of the initial detector, and does not require to stop the data taking. The affected board can be replaced during one of the beam-off periods.
RT-40ND-ND.05-519	High voltage short circuit/failure	Technical Risk / Reliability and Performance	1%	Low	Low	Each STT readout board is equipped with a Solid-State Relay (SSR) allowing to remotely disconnect HV in case an over-current is detected. The effect of a HV short circuit/failure is a temporary loss of 64 straws, corresponding to 0.05% of the initial detector, and does not require to stop the data taking.
RT-40ND-ND.05-520	Low voltage short circuit/failure	Technical Risk / Reliability and Performance	1%	Low	Low	Each STT readout board is equipped with surge protections and LV fuses confining the effect of a LV short circuit within the individual board. The effect of a LV short circuit/failure is a temporary loss of 64 straws, corresponding to 0.05% of the initial detector, and does not require to stop the data taking.
RT-40ND-ND.05-521	Broken wire in a STT straw	Technical Risk / Reliability and Performance	<0.1%	Low	Low	The breakage of a wire in a STT straw requires to temporarily disconnect the corresponding readout board via the SSR, taking offline 64 straws. The broken wire is self-contained within the straw and will not be removed, the affected channel will be permanently disconnected by removing the HV resistor on the board during one of the beam-off periods.
RT-40ND-ND.05-522	Aging of STT straws	Technical Risk / Reliability and Performance	<0.5%/ year	Moderate	Low	The use of ultrasonic welding with double Al metallization protects the straws. The main aging effect expected is a relaxation of the tension on the straw walls over time, given that STT operates at room temperature with negligible irradiation. We will store all straws for 100 days at a pressure of 3 bar to allow a stabilization of the film before module assembly. The residual relaxation expected is 18% during 20 years, which does not have significant effects on the detector performance. Impact of humidity on the straws is reversible and can be corrected by monitoring temp. and humidity.

Figure 6.127: Risk register for the STT project.

6.16 Risk Register and Contingencies

Potential risks during both the STT construction and operation were evaluated, identifying 20 risks encompassing threats and uncertainties. All risks were classified as technical, management, or external, following the Fermilab Risk Breakdown Structure (RBS) for project management. For each risk, a preliminary assessment of the probability of occurrence and of the impact on the STT costs and schedule was performed. Adequate mitigation and responses were defined and taken into account in the planning, as well as in finalizing the STT design. All 20 STT risks were implemented into the standard format of the Fermilab risk register with corresponding metadata, tentatively labeled LBNF/DUNE and LBNF/DUNE Operations. The risks are ranked according to the Lab-standard Risk Rank matrix. Figure 6.127 summarizes the resulting risk register for the STT. This risk register is continuously updated to reflect the progress on the various STT activities.

A qualitative risk analysis was performed to determine the impact of all risks on the STT core costs and schedule using a MC simulation. The modeling of the cost estimate uncertainties (EU) includes the following:

- For each item entering the STT core cost estimate, a -5%+25% uncertainty with 100% probability is assumed;
- For each item quoted in currencies different from USD ($) a ±25% exchange rate uncertainty with 100% probability has been assumed;
- The cost impact of each risk from the STT register (Figure 6.127) was added separately, using the corresponding probability distribution.

A total of 10,000 STT projects were simulated, and the contingency on the STT core costs was defined at the 95% confidence level. All input costs are based on direct vendor quotes and on the purchases of the components for the various STT prototypes (Section 6.12). The nominal core cost (without labor) is 2,757 k$, corresponding to an average cost per module of 51,057 $ and about 20 $/channel, including the complete STT with modules, readout, targets, gas system, services, cabling, tooling, etc. Results of simulations provide a total cost for the initial STT of 3,352 k$ (without labor) including contingency (Figure 6.128).

6.17 Alignment, Monitoring, and Calibration

6.17.1 Alignment and Monitoring with Rock Muons

Table 6.21: Number of passing through muons originated from interactions in the rocks expected on average per straw in STT with the FHC beam.

Time period	Muons/straw
One day	1,366
One week	9,561

The large number of single, passing muons that originated from CC interactions in the rocks of the ND hall surrounding SAND can be used for the in-situ alignment and monitoring of the

DRAFT

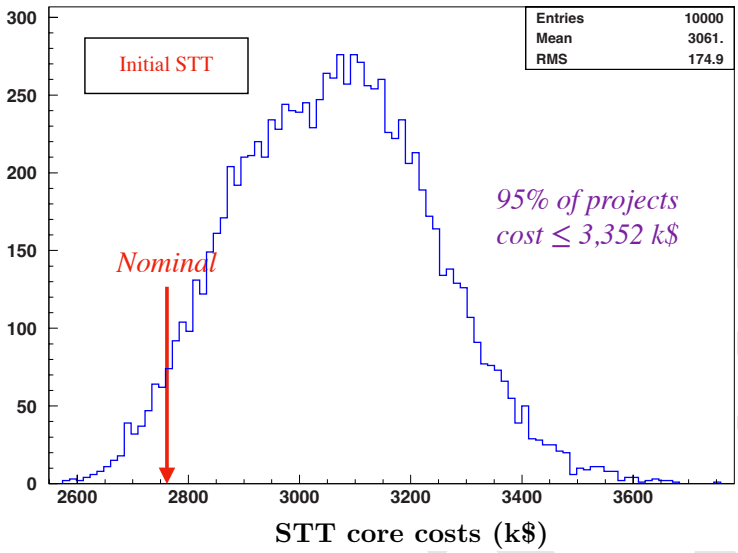


Figure 6.128: Monte Carlo (MC) simulation of 10,000 projects with variations of the core costs based on the STT risk register. The cost contingency is defined to cover 95% of simulated project.

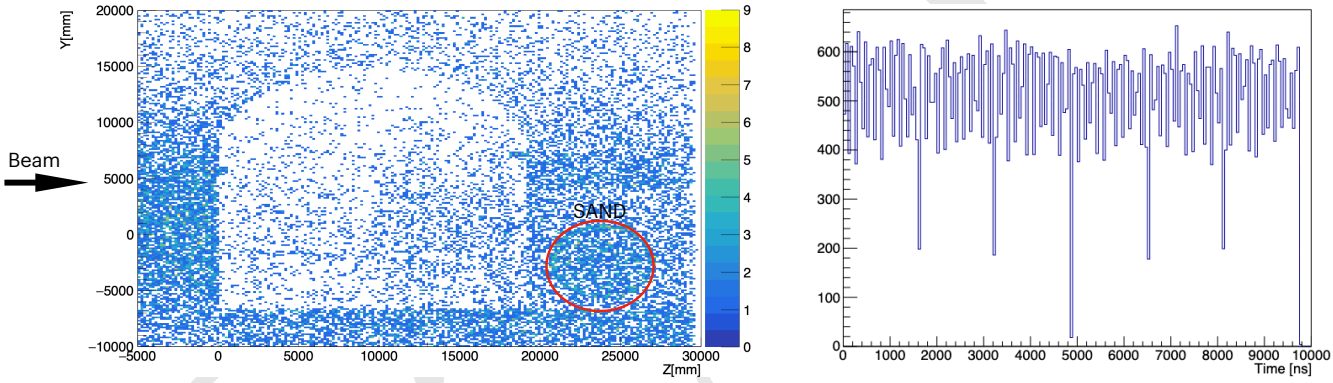


Figure 6.129: Left figure: Vertex distribution of simulated ν_μ CC interactions randomly generated in SAND and in the surrounding ND hall. Right figure: Event timing distribution of the events generated within a 9.6 μs neutrino spill showing the beam structure.

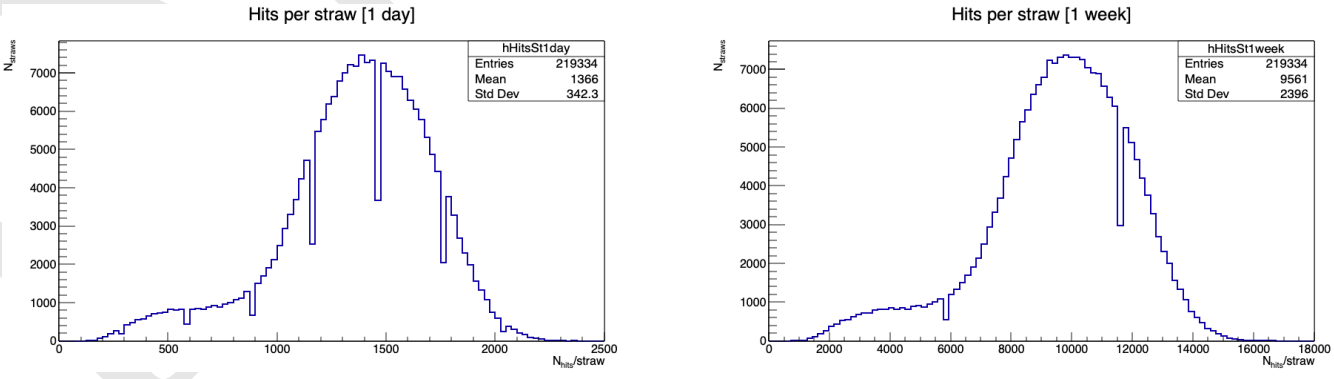


Figure 6.130: Number of passing muons originated from interactions in the rocks crossing each straw of the maximal STT in one day (left plot) and one week (right plot) with the FHC beam.

STT. Detailed GENIE+Geant4 simulations were performed for a full (anti)neutrino spill (9.6 μs, 7.5×10^{13} protons on target (POT)), including the entire SAND detector and the geometry of the surrounding ND hall (Figure 6.129). Events were randomly generated within the spill according to the mass distributions and the corresponding hits in STT combined. An average number of 2,454 hits from rock muons is found within the tracking volume of the maximal STT in a single spill, with an average occupancy of about 0.01 hits/straw. Figure 6.130 shows the corresponding distributions of the number of hits per straw from rock muons expected in one day and one week of data taking. The average numbers are 1,366 muons/straw and 9,561 muons/straw, respectively (Table 6.21). It is remarkable that even with the maximal STT configuration, each of the 219,334 straws (Table 6.2) is crossed by $\gtrsim$ 2,000 muons per week of data taking.

The expected number of rock muons crossing the straws obtained from the simulations (Table 6.2) allow for an in-situ alignment of the entire STT on a weekly basis. Although major detector changes are not expected on such a short timescale, the muon signals will be used to continuously monitor the response of each straw over time. In case some variations are detected, a dedicated alignment and calibration of the detector using MIP muons will be performed. As discussed in Section 6.14.2, the possibility of performing frequent in-situ alignments results in relaxed requirements on the tolerances of the tooling and the assembly procedure for the STT modules. Furthermore, dedicated X-ray scans of the modules are not required before their installation in SAND.

The VMM3a chip (Section 6.7.2) also has a built-in calibration pulser circuit that can be used to calibrate and monitor the gain of the electronics chain. This pulser circuit will be used to obtain a gain mapping of each straw to be uploaded into the STT database.

After the installation of the STT into the magnet, a laser survey of the location of each module can be performed using the metrology fixtures integrated into the aluminum corner blocks (Section 6.9.6). This survey will provide the initial position of the STT modules along the magnet axis, as well as their orientation. During the commissioning following the completion of the STT installation (Section 6.14.5) a first rough alignment of the wires can be performed with cosmics before the beam is delivered to the detector.

Once the beam is available, an initial data taking session without a magnetic field (magnet off) is foreseen to determine the initial alignment parameters. The exact duration of such an alignment run will depend on the initial intensity of the beam, which is expected to be somewhat lower than the nominal intensity. Based on the rates expected for the nominal beam in Table 6.21, a few days of initial data taking with the magnet off should be sufficient to determine the initial STT alignment for all straws. The subsequent alignments can then be performed during regular data taking with the nominal magnetic field.

6.17.2 Calibration with V^0 Decays

The determination of the energy for charged tracks in the STT is based on the momentum measurement in the magnetic field (spectrometer). The uniformity of the magnetic field in the KLOE solenoid implies less stringent requirements on the accuracy of the corresponding B field mapping. The absolute calibration of the track momenta can follow the procedure used by the NOMAD experiment, using the mass peak of the $K^0_s \to \pi^+\pi^-$ decays reconstructed within the tracking volume (V_0 vertices). An overall momentum scale uncertainty of 0.2% [78] was achieved by NOMAD

Table 6.22: Number of $K^0_s \to \pi^+\pi^-$, $\Lambda^0 \to p\pi^-$, and $\gamma \to e^+e^-$ decays (≥ 6 YZ hits) which can be reconstructed within the STT volume for both the initial and maximal STT configurations.

Interactions	**Initial STT**			**Maximal STT**		
	FHC 1 year					
	$K^0_s \to \pi^+\pi^-$	$\Lambda^0 \to p\pi^-$	$\gamma \to e^+e^-$	$K^0_s \to \pi^+\pi^-$	$\Lambda^0 \to p\pi^-$	$\gamma \to e^+e^-$
CC in STT FV	39,277	58,691	1,360,262	58,843	89,804	3,312,578
NC in STT FV	15,261	21,467	366,710	21,474	32,169	901,682
CC in SAND	15,452	44,953	1,221,248	15,452	44,953	1,221,248
NC in SAND	8,897	15,921	419,101	8,897	15,921	419,101
Total	78,887	141,032	3,367,320	104,666	182,847	5,854,610
	RHC 1 year					
	$K^0_s \to \pi^+\pi^-$	$\Lambda^0 \to p\pi^-$	$\gamma \to e^+e^-$	$K^0_s \to \pi^+\pi^-$	$\Lambda^0 \to p\pi^-$	$\gamma \to e^+e^-$
CC in STT FV	27,195	44,941	752,242	38,267	67,347	1,849,644
NC in STT FV	10,562	13,656	298,670	14,862	20,464	734,382
CC in SAND	10,474	33,170	638,463	10,474	33,170	638,463
NC in SAND	4,489	8,728	246,157	4,489	8,728	246,157
Total	52,720	100,495	1,935,530	68,092	129,709	3,468,650

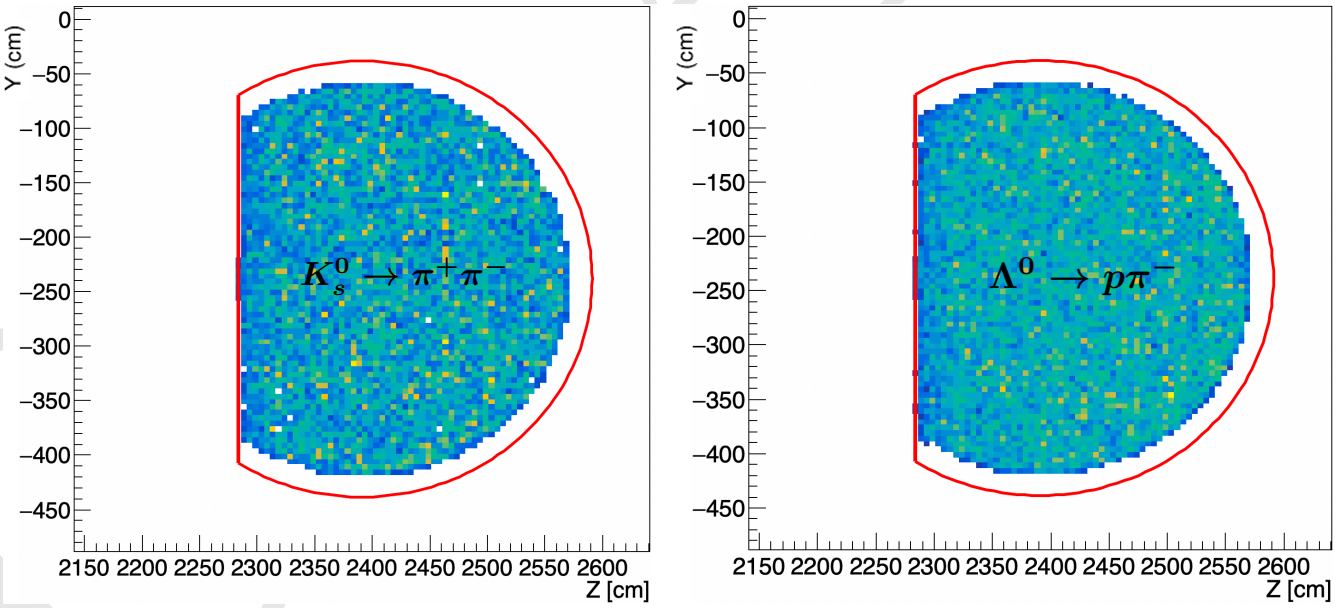


Figure 6.131: Distribution of $K^0_s \to \pi^+\pi^-$ (left plot) and $\Lambda^0 \to p\pi^-$ (right plot) decays within the initial STT fiducial volume. The particles are originated from inclusive ν_μ CC interactions with the default FHC beam. The red line represents the outer surface of the STT volume.

with this method. It must be emphasized that this uncertainty is a key parameter in determining the sensitivity of the various measurements used to constrain the systematic uncertainties affecting the long-baseline analyses in DUNE, as well as the precision measurements and searches for new physics included in the SAND physics program. The unique combination of low density and relatively large fiducial mass offered by STT allows for the collection of a large statistics of V^0 decays, uniformly distributed throughout the STT fiducial volume (Figure 6.131). The K_s^0 decays within the STT fiducial volume are reconstructed at an average distance of about 8 cm from the primary vertex, which is much larger than the expected vertex resolution. Table 6.22 summarizes the total V^0 statistics expected in one year of data taking with both the initial and maximal STT configurations, with a requirement of ≥ 6 YZ hits on both tracks. The corresponding acceptance for $K_s^0 \to \pi^+\pi^-$ is found to be 89.0% in the initial STT. In addition to the inclusive CC and NC events originating in the STT fiducial volume, the V^0s produced in CC and NC interactions within the magnet and ECAL surrounding the STT, as well as in GRAIN, are also considered. Although only a small fraction of those particles has a decay vertex reconstructed in STT, the large mass of the magnet and ECAL still results in sizable overall numbers. A total of about 78,887 K_s^0 decays are expected to be reconstructed within the tracking volume of the initial STT configuration in one year of data taking with the FHC beam (Table 6.22). The corresponding K_s^0 statistics reconstructed in a four year run with the initial STT is over 10 times larger than the sample available in NOMAD, in addition to the improved resolution and detector segmentation. This allows the momentum scale to be calibrated using $K_s^0 \to \pi^+\pi^-$ decays with an accuracy better than 0.2%.

The tracking and identification of protons can be calibrated using identified V_0 vertices from the $\Lambda^0 \to p\pi^-$ decays, as in NOMAD. Similar considerations as for the K_s^0 can be made. A total of approximately 141,032 Λ^0 decays are expected to be reconstructed within the tracking volume of the initial STT configuration in one year of data taking with the FHC beam (Table 6.22), requiring ≥ 6 YZ hits on both tracks. The corresponding acceptance is found to be 86.8% in the initial STT. Identified Λ^0 decays also provide a good constraint on systematic uncertainties related to hadronic energy and vertex reconstruction, since the hadron final state particles are the same as in the $\nu_\mu H \to \mu^- p \pi^+$ process on hydrogen used for flux determination. Furthermore, both Λ^0 and K_s^0 decays can be used to constrain the systematic uncertainty on the muon angle reconstruction, which is relevant for the analysis of the Q^2 distribution and other kinematic variables.

The electron (positron) reconstruction and identification efficiency in STT can be calibrated in-situ with the large sample of photon conversions into e^+e^- pairs. The average conversion rate of single γ in the initial (maximal) STT is about 19 (28)% and in about 32 (46)% of the π^0 produced in ν_μ CC interactions, at least one photon from the π^0 decay converts into a e^+e^- pair within the STT volume. Table 6.22 summarizes the total number of photon conversions expected in the initial and maximal STT with a requirement of ≥ 6 YZ hits on both tracks.

6.18 Detector Performance

Extensive studies of the detector performance and physics sensitivity were conducted to optimize all aspects of the STT design. The consistency of the initial STT configuration with the SAND physics goals was evaluated, and extensive comparisons with the maximal STT configuration were made. In order to obtain a realistic assessment of the STT performance, the studies are based on full-spill simulations, including all types of interactions within SAND and the surrounding ND

hall, as well as full track reconstruction based on a Kalman Filter (KF). The time and charge measurements obtained from test beam exposures of various STT prototypes were implemented into the simulation and reconstruction programs. In the following sections, some of the main results are summarized.

6.18.1 Particle acceptance

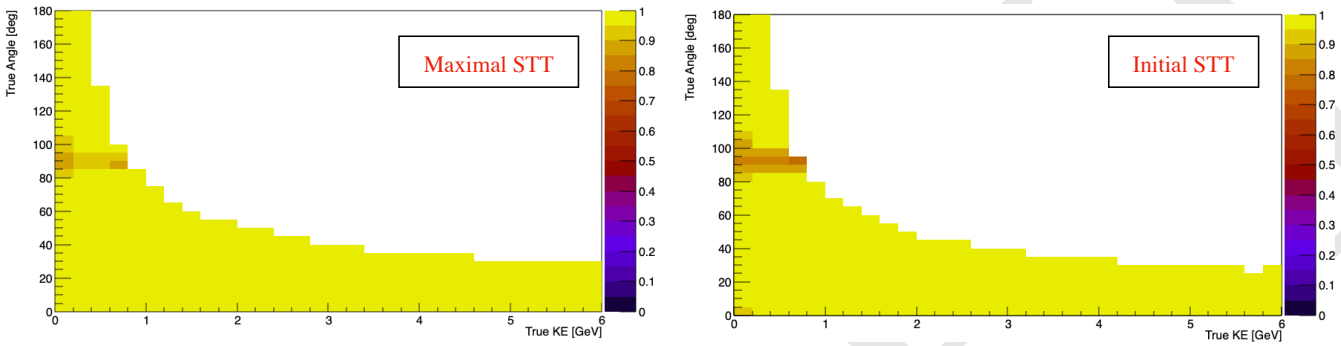


Figure 6.132: Muon acceptance for inclusive ν_μ CC interactions with the FHC beam in the maximal (left plot) and initial (right plot) STT.

Table 6.23: Fraction of tracks originated from different charged particles produced in inclusive ν_μ CC (FHC) and $\bar{\nu}_\mu$ CC (RHC) interactions, which have ≥ 4 YZ hits within the STT volume for both the initial and maximal STT configurations.

Particle	Origin	Initial STT		Maximal STT	
		FHC	RHC	FHC	RHC
μ^-	Primary	99.5%	–	98.8%	–
μ^+	Primary	–	99.9%	–	98.9%
π^-	Primary	94.0%	93.0%	92.8%	92.0%
π^+	Primary	94.5%	93.4%	93.3%	92.6%
p (from H)	Primary	96.8%	94.4%	95.0%	92.7%
p (from C)	Primary	76.6%	66.7%	76.3%	67.0%
$K^\pm$	Primary	96.6%	95.6%	95.1%	95.3%
$e^\pm$	From π^0	96.4%	95.6%	95.7%	95.0%

Initial and maximal STT configurations Detailed comparisons of the particle acceptance in the initial and maximal STT configurations were performed with complete GENIE+Geant4 detector simulations. A requirement of at least four YZ hits in the STT tracking volume was applied, with an energy deposition in each straw above 250 eV, corresponding to approximately ten ion pairs. This condition allows for the reconstruction of the momentum of the track in the presence of a vertex constraint. For single track events without a reconstructed vertex, ≥ 6 YZ hits are required. Figure 6.132 shows the muon acceptance as a function of the muon kinetic energy and angle with the beam direction for inclusive ν_μ CC interactions with the FHC beam. The high track sampling, due to the compactness of the STT tracking modules (only 28 mm thick), and the low average density, results in an approximately uniform acceptance over the full 4π angle. The acceptance is consistently above 99% for angles $\theta < 80°$ and $\theta > 100°$. This result can be explained

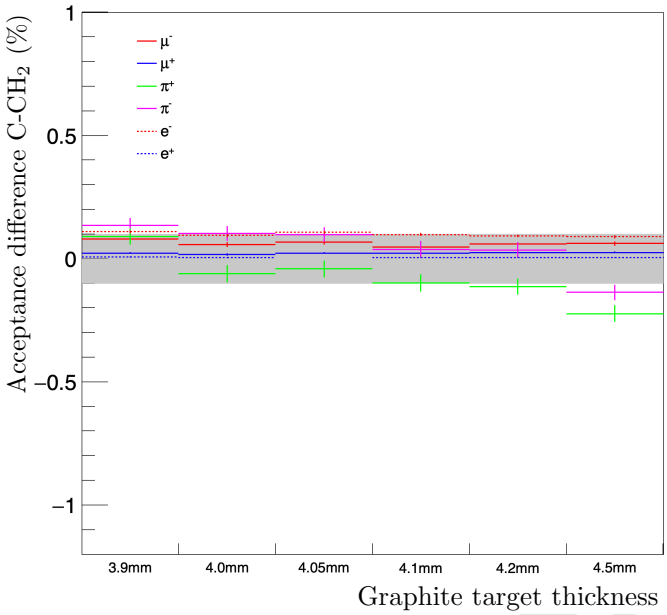


Figure 6.133: Difference in acceptance between the CH_2 and C targets in STT.

by the fact that the higher track sampling in the transverse direction (0.12% X_0) compared to the longitudinal direction (0.32% X_0) partially compensates for the smaller number of straw planes crossed at larger angles. A small acceptance dip is observed for tracks emitted at angles close to 90° with respect to the beam, as they can travel largely within one of the passive targets. However, Such tracks are kinematically suppressed, and the STT acceptance is still around 85-90% even for tracks emitted perpendicularly to the beam direction. No major difference is observed between the initial and maximal STT configurations. In the former case, the increased spacing between nearby STT modules (Figure 6.4) results in a slight broadening of the acceptance dip around $\theta = 90°$. Table 6.23 summarizes the average acceptance values for different particles produced in inclusive CC interactions with both the FHC and RHC beams. The lower density of the initial STT is responsible for the somewhat improved values of the average acceptance of all particles.

Optimization of the target thickness For a fixed combined thickness of the CH_2 targets and radiators, the thickness of the graphite targets was optimized to minimize the corresponding difference in the acceptance. As shown in Figure 6.133, the acceptance difference between different targets can be kept within 10^{-3} for all particles. This result is essential for the "solid" hydrogen technique, as it implies that the subtraction procedure between different materials can be considered model-independent within this level of uncertainty. Furthermore, the detector acceptance effectively cancels in comparisons between the selected interactions on different target nuclei. Similar results are obtained for both the initial and maximal STT configurations, as they use identical targets.

Optimization of the energy threshold A nominal energy threshold $E_{\text{Hit}} = 250\,\text{eV}$ is applied to hits from individual straws, corresponding to approximately 10 ion pairs. The dependence of the particle acceptance on the specific threshold used was studied with inclusive ν_μ CC FHC interactions. Table 6.24 summarizes the results for a minimum number of hits ≥ 4 in the YZ bending plane. A variation of the energy threshold between 200 eV and 300 eV was found to have a negligible impact on the acceptance of all charged particles detected in the initial STT volume.

Table 6.24: Effect of the energy threshold on the acceptance of different charged particles produced in inclusive ν_μ CC FHC interactions, which have ≥ 4 YZ hits within the initial STT volume.

Particle	Origin	E_{Hit}>200 eV	E_{Hit}>250 eV	E_{Hit}>300 eV
μ^-	Primary	99.5%	99.5%	99.5%
π^-	Primary	94.0%	94.0%	94.0%
π^+	Primary	94.5%	94.5%	94.4%
p (from H)	Primary	96.8%	96.8%	96.8%
p (from C)	Primary	76.6%	76.6%	76.6%
$K^\pm$	Primary	96.6%	96.6%	96.6%
$e^\pm$	From π^0	96.4%	96.4%	96.4%

Table 6.25: Effect of the wire spacers on the acceptance of different charged particles produced in inclusive ν_μ CC (FHC) interactions, which have ≥ 4 YZ hits within the initial STT volume.

Particle	Origin	No spacers	With spacers
μ^-	Primary	99.5%	99.5%
π^-	Primary	94.0%	94.0%
π^+	Primary	94.5%	94.4%
p (from H)	Primary	96.8%	96.8%
p (from C)	Primary	76.6%	76.6%
$K^\pm$	Primary	96.6%	96.6%
$e^\pm$	From π^0	96.4%	96.3%

Effect of the wire spacers The use of internal wire supports adds local inefficiencies along the wire. Assuming a total loss of efficiency over the entire 3 mm height of the spacers, the resulting average reduction of the efficiency for a single straw is less than 0.3% (Section 6.5.1). The impact of the wire spacers on particle acceptance (≥ 4 YZ hits) was studied with inclusive ν_μ CC FHC interactions. The results shown in Table 6.25 indicate that the selected spacers have a negligible impact on the acceptance of all charged particles detected in the initial STT volume.

6.18.2 Track Reconstruction

Table 6.26: Reconstruction efficiency for muons in inclusive ν_μ CC interactions with the FHC beam. The acceptance values correspond to the requirement of ≥ 4 YZ hits in STT. Full track reconstruction based on KF is used.

Configuration	Acceptance	Reconstructed	Rec. efficiency
Initial STT	99.4%	99.1%	99.7%
Maximal STT	98.8%	98.2%	99.1%

A full track reconstruction was implemented using a KF [79], which allows for the calculation of the trajectory of a charged particle from its properties at a specific point. This process of propagation or extrapolation is used to predict the properties of the particle after it has traveled a certain distance within the STT, taking into account a detailed mapping of the geometry and materials for both the initial and maximal STT configurations. Numerical integrations are performed using

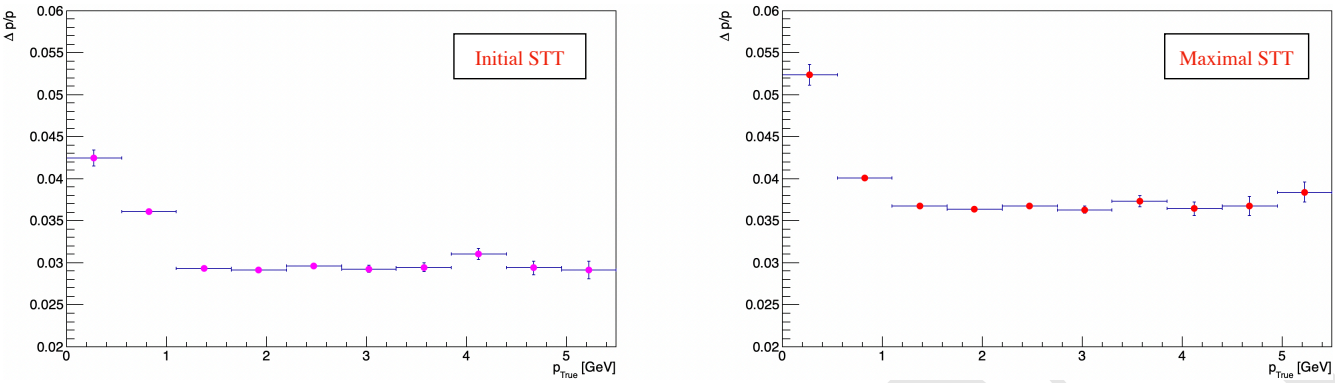


Figure 6.134: Momentum resolution as a function of the momentum for muons in inclusive ν_μ CC within the FV of the initial (left plot) and maximal (right plot) STT. Full track reconstruction based on KF is used with minimal cuts ≥ 4 YZ hits.

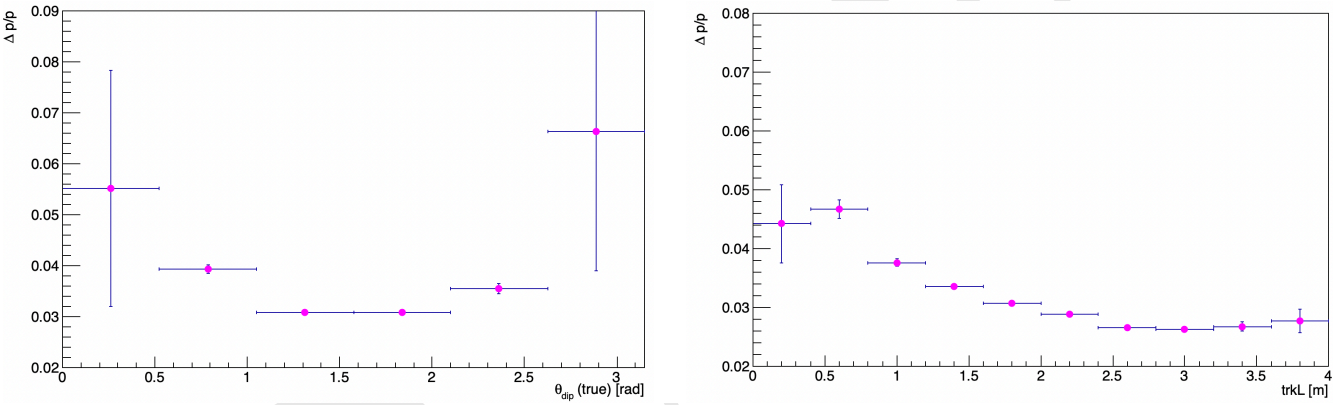


Figure 6.135: Momentum resolution as a function of the dip angle (left plot) and track length (right plot) for muons in inclusive ν_μ CC within the fiducial volume (FV) of the initial STT. Full track reconstruction based on KF is used with minimal cuts ≥ 4 YZ hits.

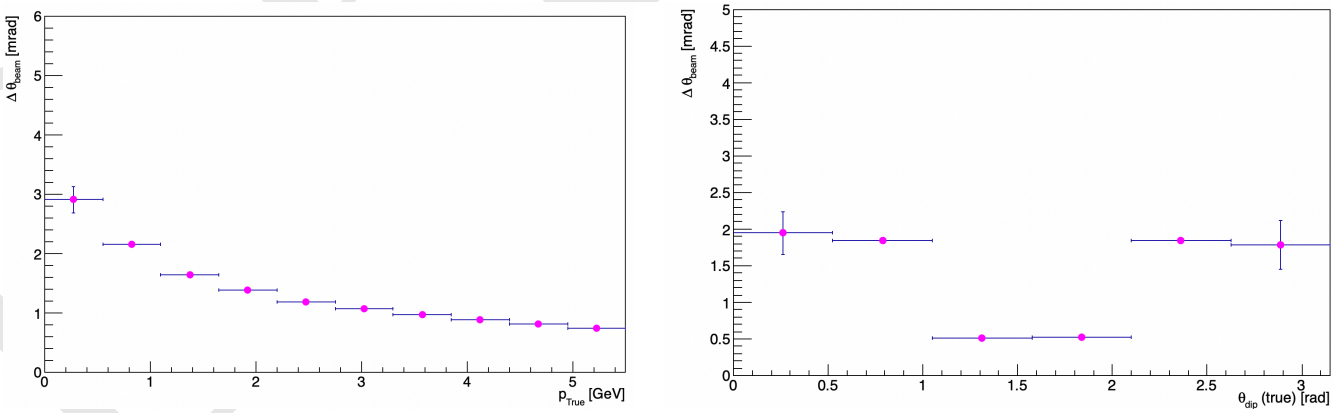


Figure 6.136: Angular resolution as a function of the momentum (left plot) and dip angle (right plot) for muons in inclusive ν_μ CC within the FV of the initial STT. Full track reconstruction based on KF is used with minimal cuts ≥ 4 YZ hits.

the Runge-Kutta-Nystrom method. Drift circles obtained from the timing of the measured hits in the straws provide the input for the reconstruction. Topological and timing information from the detected hits are used to cluster the hits associated with a given particle as a placeholder for dedicated pattern recognition. During the digitization, the drift circle radii are smeared with an expected resolution of $200\,\mu\text{m}/\sqrt{2}$ at 2 bar absolute pressure, while the position along the wires is smeared with a resolution of 10 mm. This latter assumption is conservative since the coordinate along the wire can be simply obtained from the closest orthogonal layer with a resolution of $5\,\text{mm}/\sqrt{12} = 1.44\,\text{mm}$. An average single hit resolution of better than $200\,\mu$m at 1 bar absolute pressure was demonstrated with test beam exposures of STT prototypes with VMM3 readout (Section 6.12.8). The track seeding is performed without MC truth by fitting a helix to the hits (drift circles) in order to obtain the initial parameters for the Kalman fit.

Initial and maximal STT configurations The performance of the track reconstruction was studied with minimal selection cuts in both the initial and maximal STT configurations. For events within the default STT fiducial volume (20 cm from the edges), all tracks with at least four YZ hits in the STT tracking volume and an energy deposition above 250 eV, corresponding to approximately ten ion pairs, were considered. The average reconstruction efficiency of muons from inclusive ν_μ CC events in the FHC beam is 99.7% for the initial STT and 99.1% for the maximal STT (Table 6.26). The corresponding average momentum resolution is 3.0% for the initial STT and 3.6% for the maximal STT. Figure 6.134 shows the dependence of the momentum resolution on the muon momentum for both configurations. The lower density of the initial STT results in improved momentum resolution. The dependence on the dip angle of the track is rather smooth (Figure 6.135) thanks to the high track sampling with small cylindrical straws. Figure 6.136 shows the angular resolution as a function of track momentum and dip angle for the initial STT. For momenta $\gtrsim 2$ GeV, an angular resolution below 1 mrad is obtained. A fit with a double Gaussian function to the residual distribution gives an average angular resolution of $\sigma_{\text{core}} = 0.5$ mrad and $\sigma_{\text{tail}} = 1.6$ mrad for the initial STT. Similarly to the momentum reconstruction, the angular resolution of the initial STT is improved by about 20% with respect to the maximal STT.

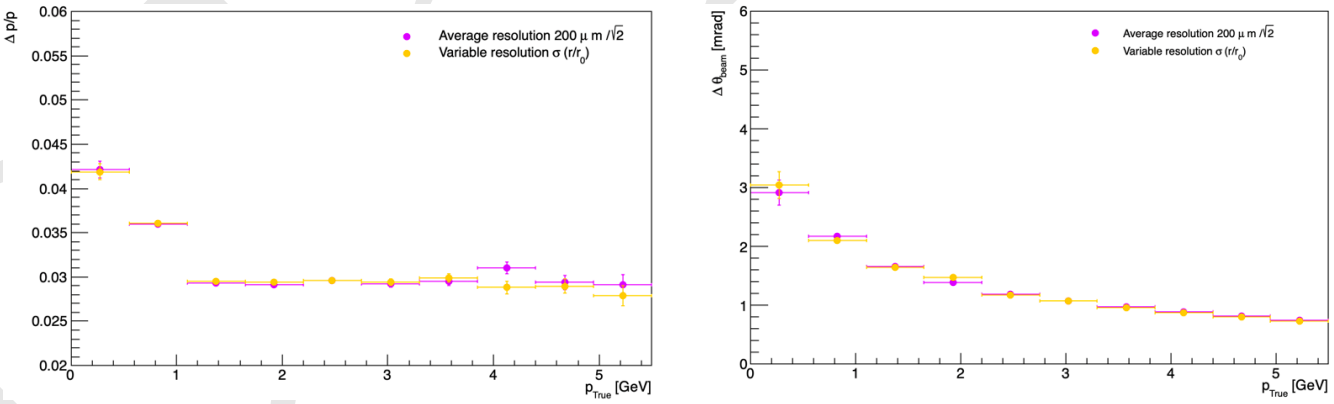


Figure 6.137: Comparison of the momentum (left plot) and angular (right plot) resolutions obtained with the measured radial dependence of the single hit $\sigma(r/r_0)$ and with an average resolution of $200\,\mu\text{m}/\sqrt{2}$.

Radial dependence of single hit resolution For the track reconstruction, a conservative resolution of $200\,\mu$m was assumed at 1 bar absolute pressure, which has already been demonstrated with test beam exposures using VMM3 readout in non-optimal conditions (Section 6.12.8). Although

better resolutions are expected, the chosen average value was mainly intended to define an upper limit on performance. However, the characteristic space-drift time relation $r(t)$ within the straws typically results in a dependence of the single hit resolution on the radial distance from the wire, $\sigma(r)$, with worse values at the anode (wire) and better values at the cathode (straw walls). The resulting functional shape is defined by the distribution of the electric field intensity along the straw radius, which is in turn sensitive to the operating gas gain (around 2.5×10^4 for STT). For a fixed gas gain, the dependence on the relative distance from the wire r/r_0 with respect to the straw radius r_0 was found to be roughly independent of the straw diameter. In order to study the impact on the track reconstruction in the initial STT, the measured $\sigma(r/r_0)$ was implemented in the digitization. Figure 6.137 shows the corresponding momentum and angular resolutions obtained from a complete Kalman filter reconstruction for muons in inclusive ν_μ CC interactions with the FHC beam. The values obtained with the measured $\sigma(r/r_0)$ are consistent with those using the average resolution of 200 μm at 1 bar absolute pressure. The result can be understood by considering that if a track crosses a straw close to the wire in one layer, it typically will cross the straws in the following layer (less than 5 mm apart) close to the wall, thus effectively averaging the resolutions within the double staggered layers (Section 6.3). A further averaging is obtained from the many straws $\mathcal{O}(100)$ crossed by tracks in STT. In principle, the use of $\sigma(r/r_0)$ in the process of converting the measured time intervals into radial coordinates may allow one to reconstruct the track parameters more accurately.

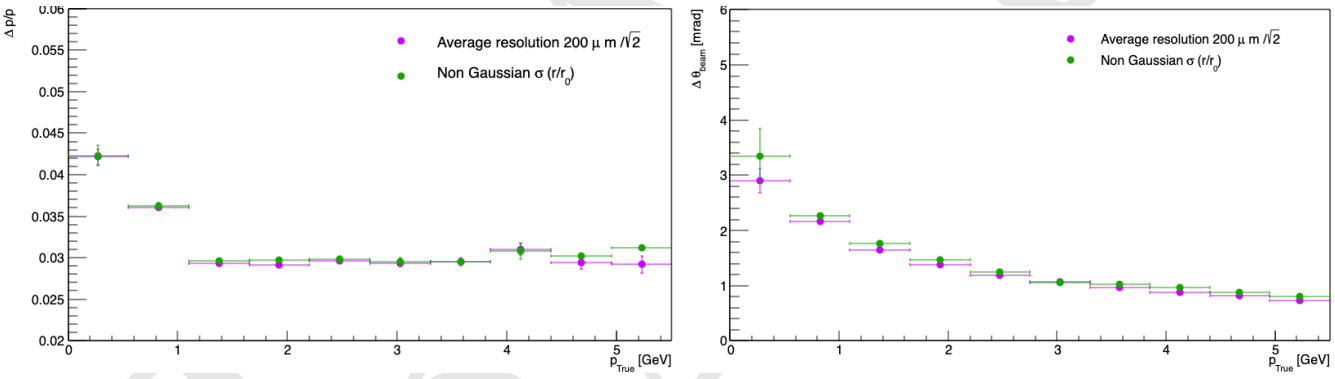


Figure 6.138: Effect of non-Gaussian tails in the single hit resolution from test beam measurements on the momentum (left plot) and angular (right plot) resolutions of muon tracks reconstructed with the Kalman filter in the initial STT.

Effect of non-Gaussian tails in the single hit resolution In order to study the impact of non-Gaussian tails on the single hit resolution in track reconstruction, the complete timing resolution from the r-t relationship measured during the test beam exposures of the STT prototypes (Figure 6.89) was implemented into the digitization. Figure 6.138 shows the corresponding momentum and angular resolutions obtained from a complete Kalman filter reconstruction for muons in inclusive ν_μ CC interactions within the fiducial volume of the initial STT. The effect observed is marginal, with the values obtained from the measured non-Gaussian tails being consistent with a simulation based on a Gaussian resolution.

Resolutions for pion and proton tracks The reconstruction of pion and proton tracks follows the same workflow used for the muons. The digitization of the hits in the straws is independent of the type of particle originating them. Every track with ≥ 4 YZ hits with energy deposition exceeding

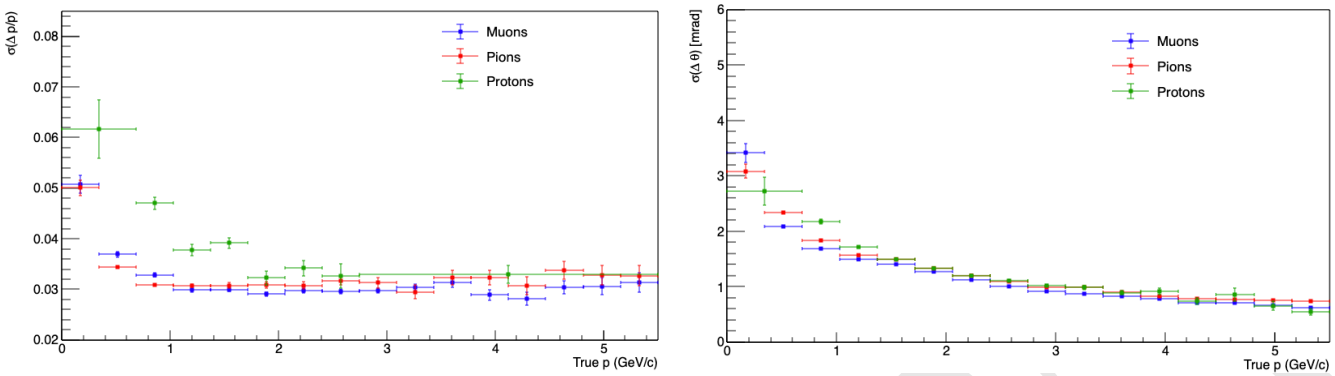


Figure 6.139: Momentum (left plot) and angular (right plot) resolutions as a function of the momentum for muon, pion, and proton tracks from inclusive ν_μ CC interactions reconstructed with the Kalman filter in the initial STT.

250 eV is reconstructed with KF assuming the energy loss corresponding to the pion or proton mass, respectively. The performance of the reconstruction is evaluated with tracks from inclusive ν_μ CC interactions generated in the fiducial volume of the initial STT with the FHC beam. Pions and protons have, on average, significantly lower momenta compared to the current muon, as they are part of the hadronic system. The corresponding momentum and angular resolutions are therefore compared for fixed momentum bins in Figure 6.139. A similar tracking performance is obtained for muons and pions with the initial STT, with a momentum resolution around 3% above 1 GeV and an angular resolution below 1 mrad above 2 GeV. High energy protons have comparable resolutions as well, while for momenta below 0.5 GeV a degradation is observed mainly due to the shorter track length of protons compared to muons and pions with the same momentum. This effect is demonstrated by the fact that the resolutions for fixed bins of track length are similar (Figure 6.140). Overall, the proton momentum resolution is below 5% in most of the available phase space. It must be noted that protons originated from CC interactions on hydrogen are characterized by significantly harder momenta compared to interactions on nuclei. In the former case about 95.8% of protons have a momentum above 300 MeV .

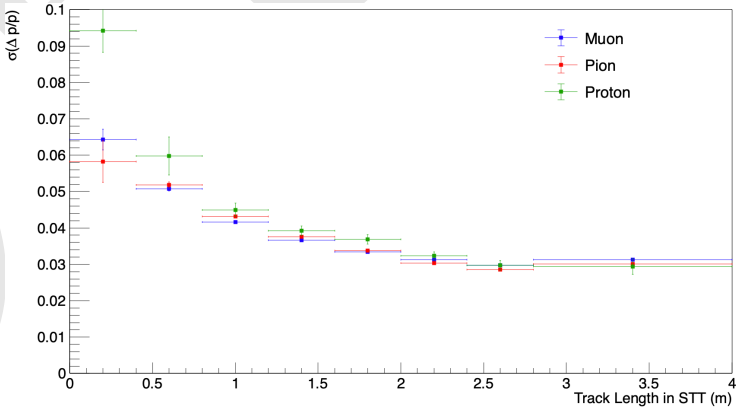


Figure 6.140: Momentum resolutions as a function of the track length for muon, pion, and proton tracks from inclusive ν_μ CC interactions reconstructed with the Kalman filter in the initial STT.

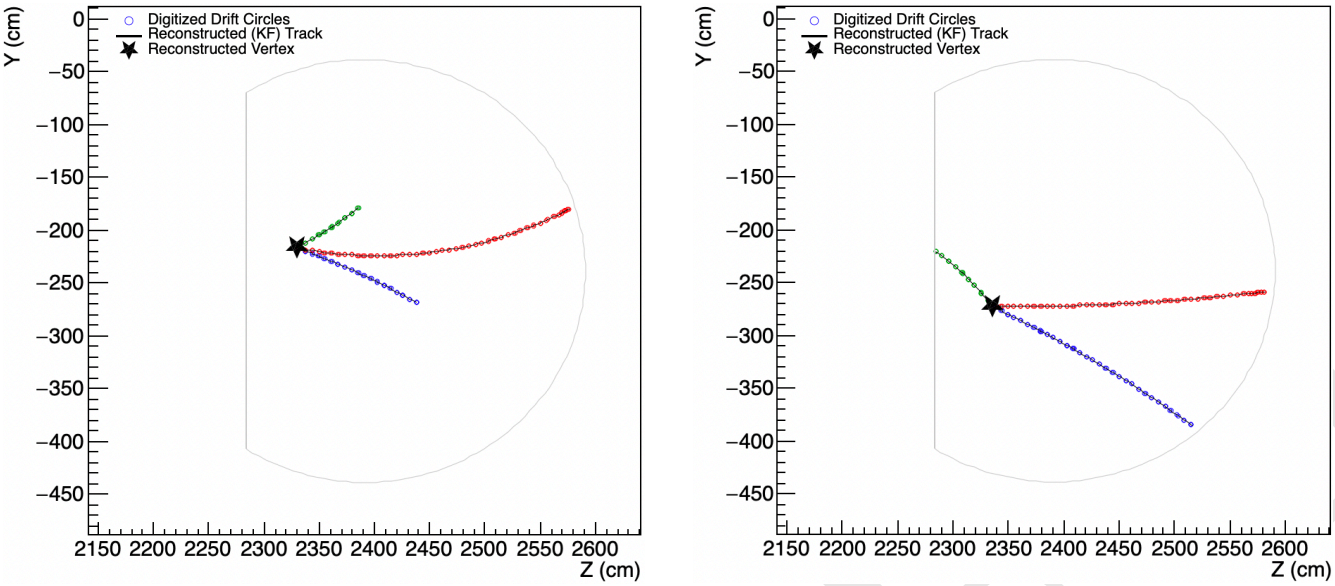


Figure 6.141: Reconstruction of the primary vertex for inclusive ν_μ CC interactions in the initial STT: the YZ views (bending plane) for two events with $N_{\text{trk}}^{\text{rec}} = 3$ are shown for illustration. Full track reconstruction based on KF is used for all tracks with ≥ 4 YZ hits and the resulting vertex location is obtained as the point of minimal distance in 3D space.

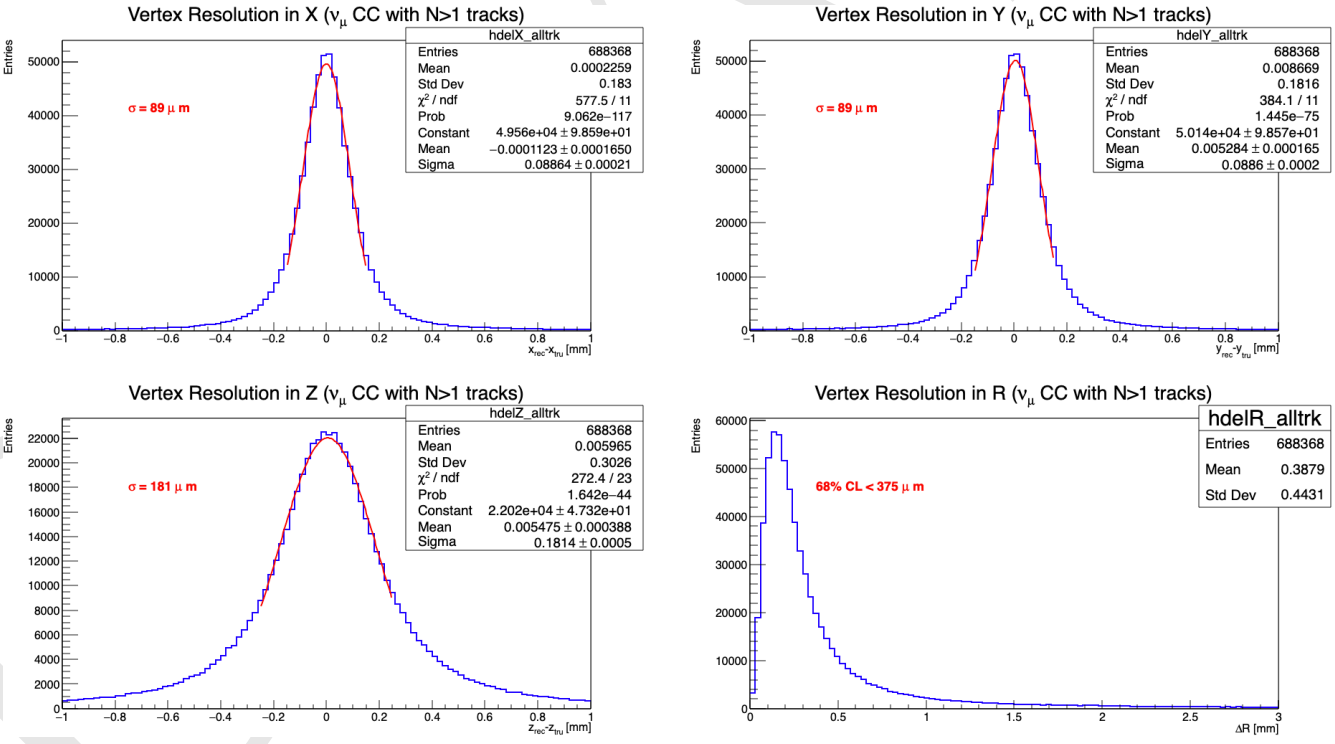


Figure 6.142: Resolution on the reconstructed position of the primary vertex for inclusive ν_μ CC interactions with $N_{\text{trk}}^{\text{rec}} > 1$ charged tracks in the initial STT. Full track reconstruction based on KF is used for all tracks with ≥ 4 YZ hits and the resulting vertex location is obtained as the point of minimal distance in 3D space.

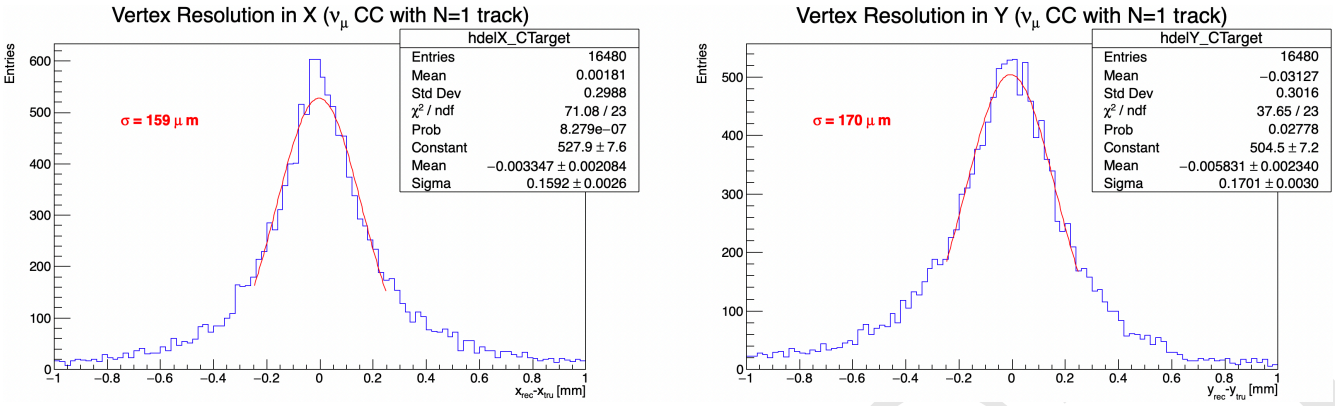


Figure 6.143: Resolution on the reconstructed position of the primary vertex for single track ($N^{\text{rec}}_{\text{trk}} = 1$) QE $\bar{\nu}_\mu p \to \mu^+ n$ interactions in the initial STT. Full track reconstruction based on KF is used for the single muon with ≥ 4 YZ hits, which is extrapolated backward from the first detected hit to the average z position within the identified target plane, weighted by the corresponding mass distribution.

6.18.3 Vertex Reconstruction

A location of the primary interaction vertex within the targets with an accuracy $\ll 1$ mm is necessary for a good control of the chemical composition and mass of the (anti)neutrino target materials. The reconstruction of the primary vertex requires the presence of at least two reconstructed tracks and it directly depends on the detector granularity and track sampling. To this end, the performance of the initial STT was tested with inclusive ν_μ CC interactions generated with the default FHC beam and GENIE+Geant4 in the STT fiducial volume (20 cm from the ECAL surface). All primary tracks with ≥ 4 YZ hits in the event were reconstructed with the KF described in Section 6.18.2. For events with a number of reconstructed tracks $N^{\text{rec}}_{\text{trk}} > 1$ the primary vertex was then defined as the point of minimal distance $\Delta R = \sqrt{(\Delta x)^2 + (\Delta y)^2 + (\Delta z)^2}$ among such tracks in the 3D space (Figure 6.141). The algorithm could find a proper vertex point in all such events. Figure 6.142 shows the corresponding results on the reconstructed position of the primary vertex. On average, vertex resolutions of $\sigma(x) = 89$ μm, $\sigma(y) = 89$ μm, and $\sigma(z) = 181$ μm were achieved for all events with $N^{\text{rec}}_{\text{trk}} > 1$ reconstructed tracks in the initial STT. No significant systematic offset was observed on each of the reconstructed vertex coordinates. A mild dependence of the vertex resolution on the number of reconstructed primary tracks was found, with both $\sigma(y)$ and $\sigma(y)$ varying from about 108 μm for $N = 2$ to about 73 μm for $N > 3$ (Table 6.27). It is important to note that the same resolutions are achieved on $\sigma(x)$ and $\sigma(y)$ in the transverse plane with respect to the beam direction. This result is a direct consequence of the symmetric X-Y geometry of the four straw layers in each STT module, as well as of their orientation along two orthogonal directions (Section 6.3).

For events with a single reconstructed track ($N^{\text{rec}}_{\text{trk}} = 1$) a full 3D reconstruction of the primary vertex is not possible. However, the target plane where the interaction occurred can be determined by noting the absence of straw tube hits preceding the presumed target combined with the presence of hits in the tubes following the target. The only reconstructed track available is then extrapolated backward from the first detected hit to the average z position within the identified target plane, weighted by the corresponding mass distribution. Figure 6.143 shows the results on

the reconstructed position of the primary vertex in the (x, y) transverse plane for QE $\bar{\nu}_\mu p \to \mu^+ n$ interactions, either on H or on nuclei. Average vertex resolutions of $\sigma(x) = 159\ \mu m$ and $\sigma(y) = 170\ \mu m$ are achieved by the algorithm. It is worth noting that the uncertainty in associating single track interactions to the correct target material is given by the the ratio between the thickness of the straw walls and the one of a target plane, as the walls of the straw layers adjacent to the passive target cannot be resolved from the latter. The choice of 19 μm straw walls for the STT corresponds to an uncertainty of about 0.5% (Section 6.3).

Table 6.27: Resolution on the reconstructed position of the primary vertex as a function of the number of reconstructed tracks $N_{\rm trk}^{\rm rec}$ for inclusive ν_μ CC interactions in the initial STT. Full track reconstruction based on KF is used for all tracks with ≥ 4 YZ hits and the resulting vertex location is obtained as the point of minimal distance R in 3D space. The range $R < \Delta R$ corresponds to 68% C.L.

Tracks	$\boldsymbol{\sigma(x)}$ [μm]	$\boldsymbol{\sigma(y)}$ [μm]	$\boldsymbol{\sigma(z)}$ [μm]	$\boldsymbol{\Delta R}$ [μm]
$N_{\rm trk}^{\rm rec} = 2$	108	107	200	495
$N_{\rm trk}^{\rm rec} = 3$	93	92	180	375
$N_{\rm trk}^{\rm rec} > 3$	73	75	163	285
All $N_{\rm trk}^{\rm rec} > 1$	89	89	181	375

6.18.4 Particle Identification

Transition Radiation Some of the most critical measurements expected from SAND are characterized by the presence of $e^\pm$, such as ν_e, $\bar{\nu}_e$ CC, ν-e elastic scattering, NC π^0, etc. The selection of ν_e and $\bar{\nu}_e$ CC is particularly challenging, as they represent only tiny fractions of the beam composition, with the latter corresponding to about 0.2% of the leading ν_μ CC component in the FHC beam. Considering that most of the primary $e^\pm$ produced in ν_e and $\bar{\nu}_e$ CC (about 93-98%) are characterized by energies above 0.5 GeV ($\gamma \geq 1000$), a Transition Radiation (TR) identification providing a rejection factor against pions in the range 100÷1,000 is required (Section 6.3).

The TR capability for $e^\pm$ identification is obtained in STT by adding a thin radiator to most of the modules equipped with plastic CH_2 targets (Figure 6.1). Each individual radiator is about 14 mm thick and, in the default design, is composed of 105 polypropylene CH_2 foils 18 μm thick, inter-spaced by 117 μm air gaps (Section 6.2). The detection of the TR photons emitted in the radiator is performed by filling the following XXYY straw layers with a Xe/CO_2 70/30 gas mixture at 2 bar absolute pressure. The use of Xe gas is motivated by the absorption length around 10 mm for the typical TR photon energies in the range of 3-15 keV.

The design of the radiators and the detection of the resulting TR photons in STT was optimized to match the average performance of the NOMAD TRD [52], which proved to be critical in the analysis of (anti)neutrino interactions. Figure 6.144 shows a comparison between the TR detection planes in STT and in NOMAD, which are both based on cylindrical straws. An equivalent Xe thickness at 1 bar absolute pressure was calculated, taking into account the straw diameter, the gas mixture, and the operating pressure. The value for individual STT modules is about 22 mm, to be compared with an effective Xe thickness of around 10 mm for NOMAD TRD modules (Figure 6.144). It is worth noting that in STT the total Xe volume is split into 4 independent layers – each about half of the one in NOMAD TRD – resulting in a smaller ionization loss by pions, and thus in a better e/π separation in spite of the higher operating pressure.

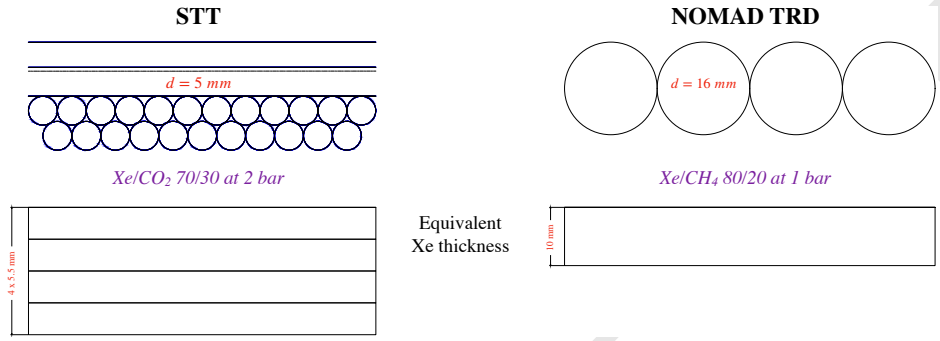


Figure 6.144: Comparison between TR detection planes in STT and NOMAD TRD [52]. The equivalent Xe thickness at 1 bar is calculated taking into account the operating pressure and the Xe fraction within the gas mixtures, in addition to the geometrical dimensions.

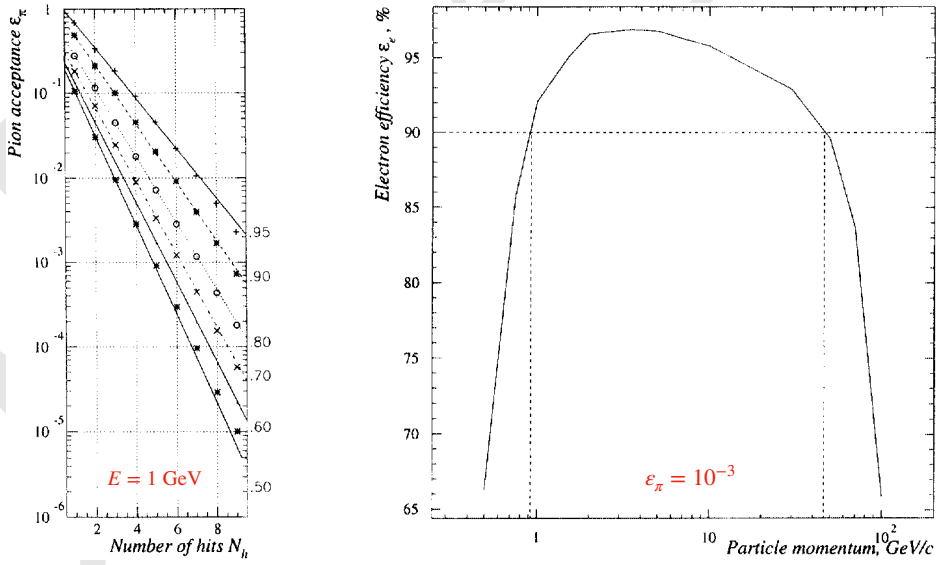


Figure 6.145: Performance of the TR electron identification in NOMAD TRD [52]. Left plot: pion acceptance for fixed electron efficiencies as a function of the number of modules crossed (9 in total). Right plot: electron efficiency for a fixed 10^{-3} pion acceptance as a function of the electron momentum.

The measured TR performance for electron identification in the NOMAD TRD is summarized in Figure 6.145, as a function of the number of modules crossed by the particle. A typical pion rejection factor of 10^{-3} for an electron efficiency exceeding 90% was achieved with the maximal number of 9 modules, down to energies well below 1 GeV. A significant $e^{\pm}$ identification capability was still provided close to the lower limit for TR emission of 0.5 GeV.

Detailed simulations of the TR production and detection were performed for both the STT and the NOMAD TRD modules (with 105 polypropylene foils each) using the code developed for the ATLAS TRT [80] and validated with test beam measurements [81]. These simulations take into account the radiator and module geometry, the materials used (self-absorption), as well as the gas composition and operating conditions. The number of detected TR photons was studied as a function of the electron energy, the energy threshold in the detection planes, and the modules crossed by the particle. While a build-up effect across consecutive detection planes is present for the NOMAD TRD, the larger equivalent Xe thickness and the presence of the 5 mm CH_2 target slab (Section 6.2) practically decouple individual STT modules. In order to compare the performance of the two detectors, the average number of TR photons detected per module was calculated across 9 consecutive modules. Results are shown in Figure 6.146 as a function of the electron energy for different thresholds. Overall, two STT modules are roughly equivalent to a single NOMAD TRD module for $E \gtrsim 1$ GeV. At lower energies, the STT performance is substantially better than that of NOMAD, with an increase in the number of TR photons detected by about 60% at 0.5 GeV.

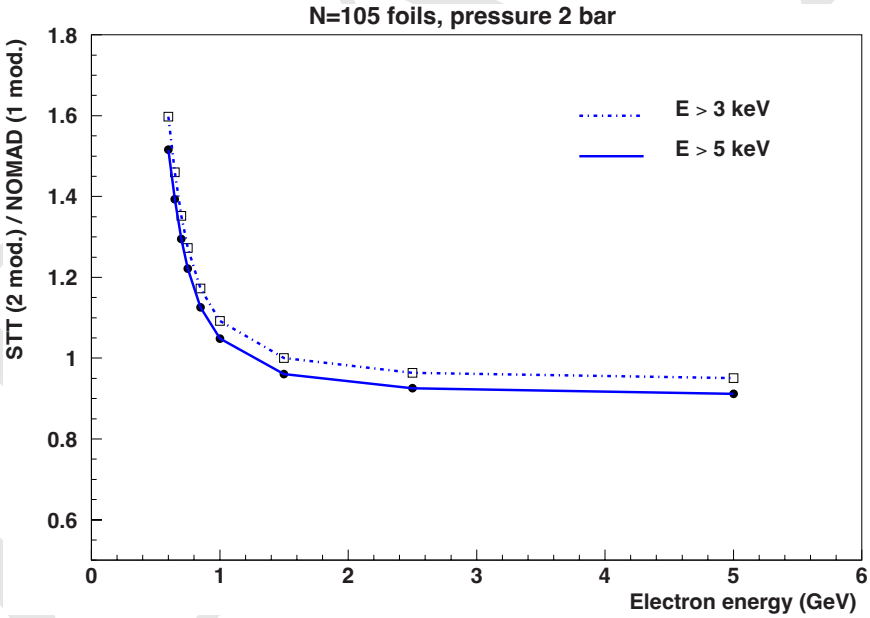


Figure 6.146: Ratio between the numbers of detected TR photons for electrons crossing two STT modules (with 105 foils each) and a single NOMAD TRD module (with 315 foils).

The equivalence between two STT modules and a NOMAD TRD module (Figure 6.146) can be used to obtain realistic estimates of the $e^{\pm}$ identification capability of STT using the TR. To this end, the pion rejection measured by the NOMAD TRD [52] was parametrized as a function of the number of modules crossed, the particle energy, and the electron efficiency. The parametrization was then implemented into complete GENIE+Geant4 detector simulations of ν_e and $\bar{\nu}_e$ CC interactions with both FHC and RHC beams. The total number of radiator modules in the initial STT is 39 (Table 6.2), which is much larger than the 9 in the NOMAD TRD. Results for the pion rejection

in the initial STT are shown in Figure 6.147. Overall, the STT has improved $e^{\pm}$ identification compared with NOMAD. The fraction of tracks with pion rejection > 100 was found to be in the range of 80–85% for all beam components (Table 6.28), which is consistent with the detector requirements outlined in Section 6.3. Most of the tracks with pion acceptance $> 10^{-2}$ originate from events located in the last downstream super-module or close to the edge of the detector, limiting the total number of STT modules crossed by the particle (Figure 6.148). In order to improve the $e^{\pm}$ identification achievable for such events, the 10 CH_2 modules within the last two super-modules in the initial STT have been instrumented with 2 radiators each (Figure 6.4). Simulations performed with the ATLAS TRT code [80] show that such a configuration increases the average number of TR photons detected by a factor of 1.54 compared to the standard modules with a single radiator. In the maximal STT configuration, the increased number of modules naturally enhances the TR performance, and all 16 CH_2 modules within the last two super-modules are equipped with a single radiator (Figure 6.6).

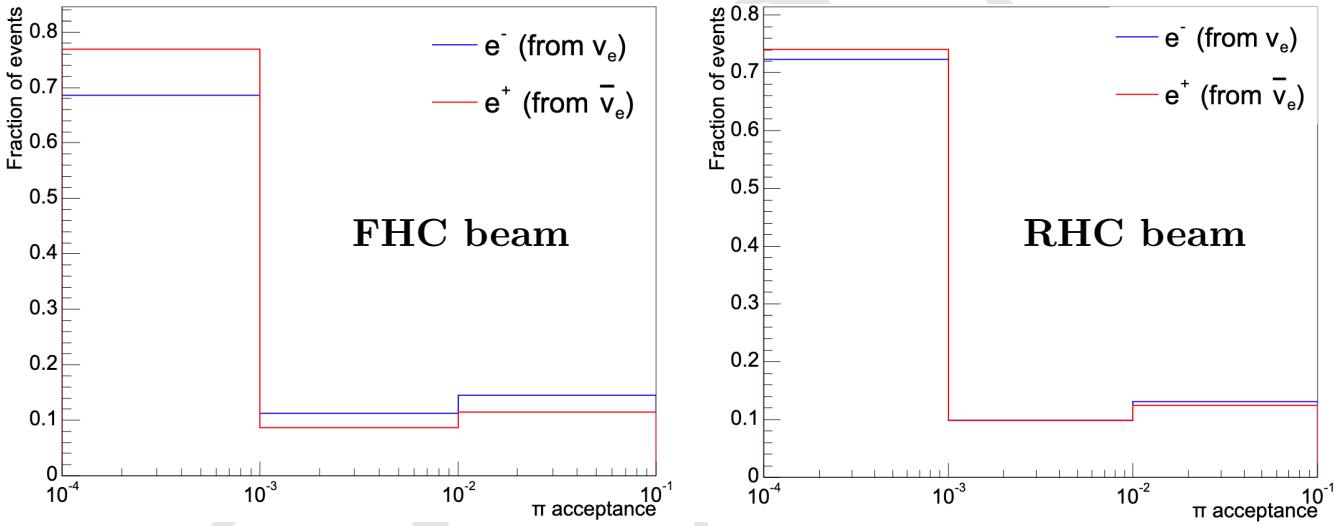


Figure 6.147: Pion acceptance for 90% $e^{\pm}$ efficiency in ν_e CC and $\bar{\nu}_e$ CC within the FV of the initial STT. Both the FHC (left plot) and RHC (right plot) beam modes are shown for completeness.

Table 6.28: Fraction of $e^{\pm}$ from ν_e CC and $\bar{\nu}_e$ CC events with a pion rejection > 100 in the initial STT.

Pion rejection	ν_e CC FHC	$\bar{\nu}_e$ CC FHC	$\bar{\nu}_e$ CC RHC	ν_e CC RHC
> 100	80%	84%	83%	85%

Energy loss dE/dx The identification of $p/\pi/K$ hadrons is required for the measurement of exclusive channels relevant to both flux measurements and the study of (anti)neutrino interactions on nuclear and hydrogen targets (Section 6.3). This task can be achieved by exploiting the ionization energy loss dE/dx by charged particles within the active straws. The dE/dx resolution obtainable from the charge measurement with the VMM3 readout of the STT was studied with dedicated test beam measurements performed at CERN with muon and pion beams (Section 6.12.8). The measured dE/dx resolution was used as input for complete GENIE+Geant4 simulations of inclusive ν_μ CC interactions in the initial STT to understand the performance that can be realistically achieved in the experiment. Figure 6.149 shows that a clear advantage is obtained at 2 bar abso-

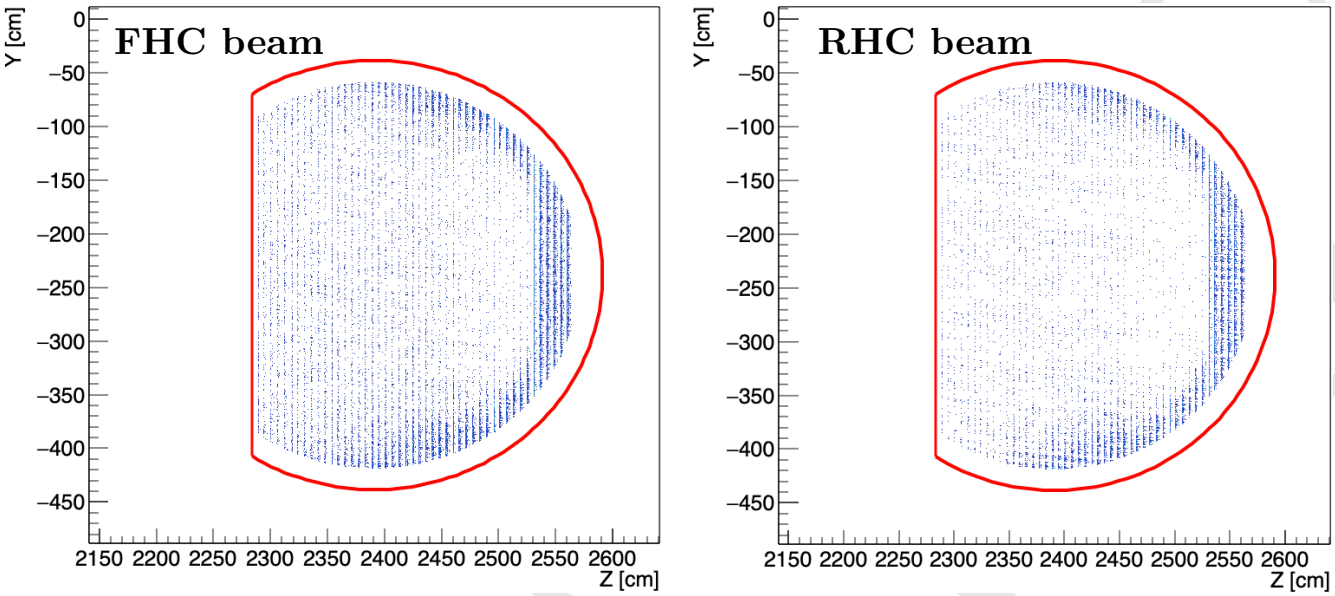


Figure 6.148: Vertex distribution of $e^{\pm}$ tracks from ν_e CC FHC (left plot) and $\bar{\nu}_e$ CC RHC (right plot) characterized by a pion rejection from TR < 100 in the initial STT.

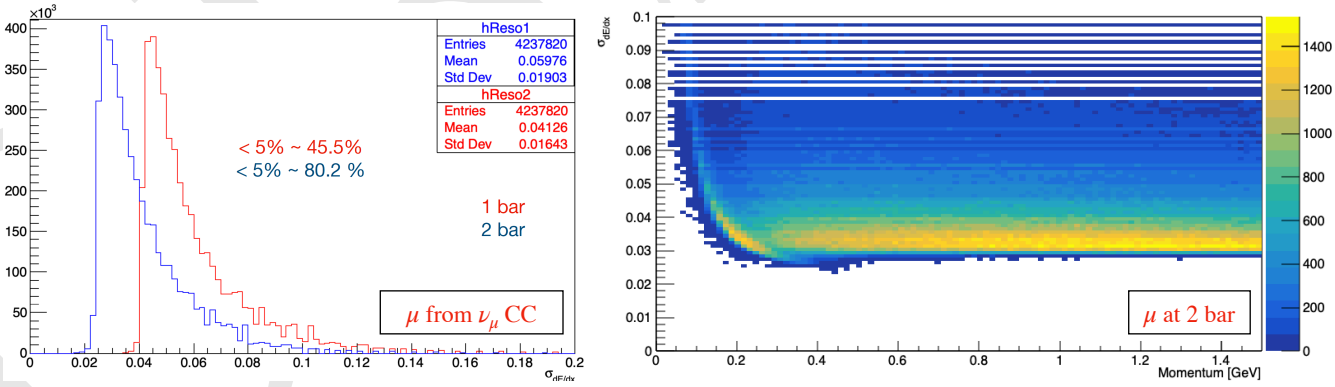


Figure 6.149: Expected dE/dx resolution for muons in ν_μ CC interactions with the FHC beam within the STT fiducial volume based on the test beam measurements.

lute pressure. In such operating conditions, more than 80% of the muons have a dE/dx resolution better than 5%, with typical values around 3% for momenta $\gtrsim 0.2\,\mathrm{GeV}$.

6.18.5 Application to $\bar{\nu}_\mu \mathrm{H} \to \mu^+ n$ with Initial STT

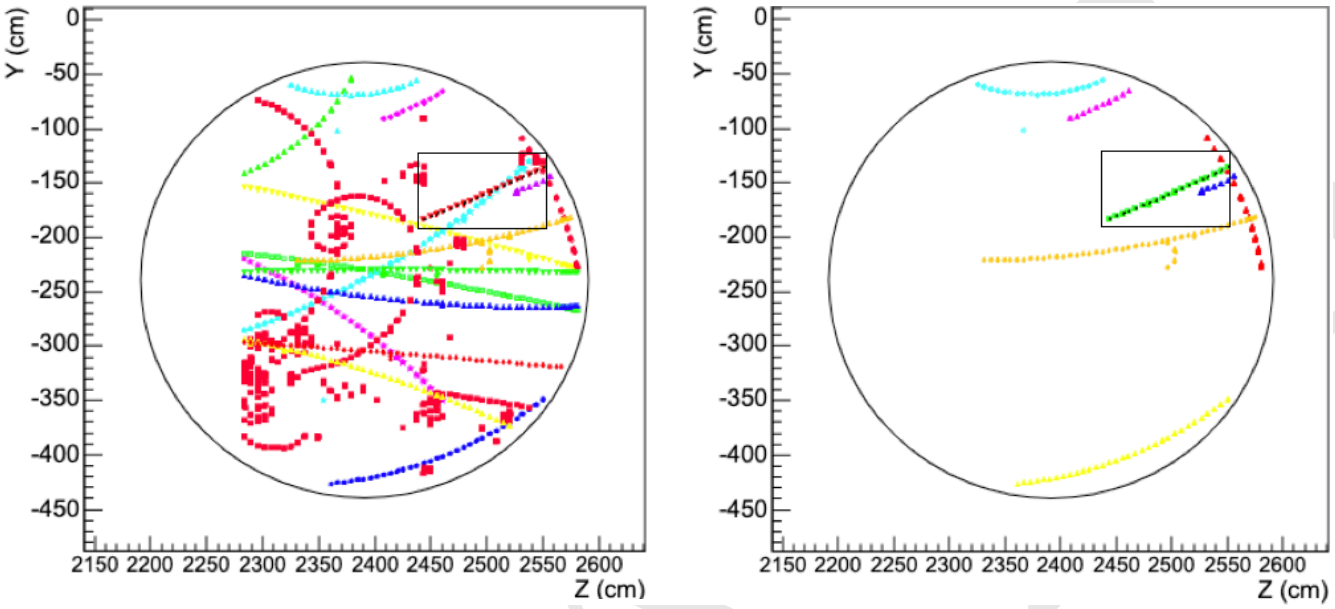


Figure 6.150: Example of hit distribution in the initial STT within a 9.6 μs spill before (left picture) and after (right picture) clustering.

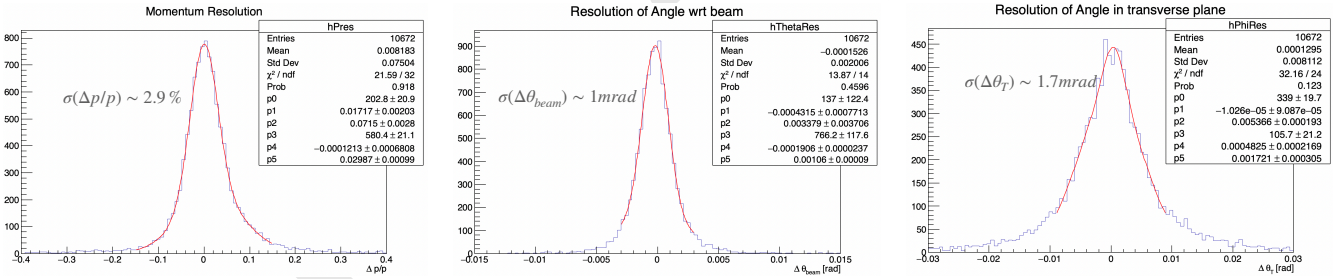


Figure 6.151: Resolutions on the reconstructed momentum (left plot), angle with respect to the beam direction (middle plot), and angle in a plane transverse to the beam direction (right plot) for muons produced in $\bar{\nu}_\mu \mathrm{H} \to \mu^+ n$ interactions with the initial STT. Full track reconstruction based on KF is used with minimal cuts ≥ 4 YZ hits.

The physics sensitivity achievable with the initial STT configuration was evaluated with a few representative analyses. The example from the selection of $\bar{\nu}_\mu \mathrm{H} \to \mu^+ n$ interactions is illustrative, as this channel is relevant for the determination of the $\bar{\nu}_\mu$ relative and absolute flux, as well as for the determination of the axial form factor and radius of the nucleon [82].

Inclusive CC and NC interactions were simulated using the default RHC beam across the entire SAND detector—including the magnet, ECAL, GRAIN, and STT — as well as in the surrounding rocks of the ND hall. Complete GENIE+Geant4 simulations were used, with each event assigned

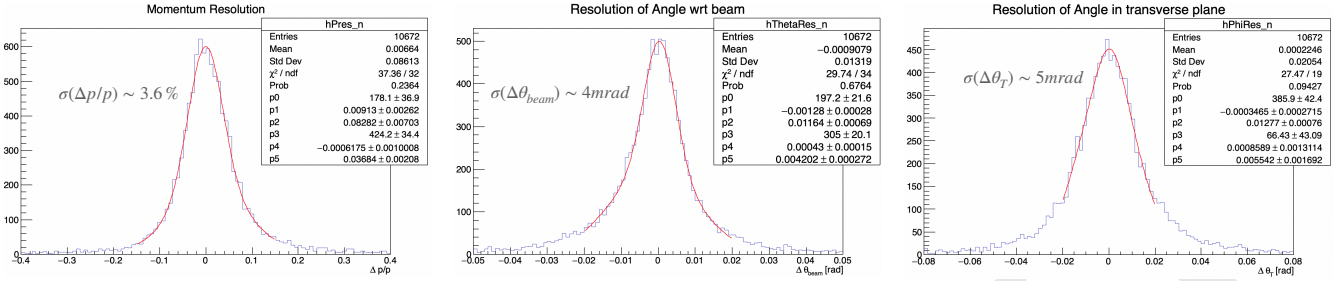


Figure 6.152: Resolutions on the reconstructed momentum (left plot), angle with respect to the beam direction (middle plot), and angle in a plane transverse to the beam direction (right plot) for neutrons produced in $\bar{\nu}_\mu \mathrm{H} \to \mu^+ n$ interactions with the initial STT. The neutron kinematics is calculated using energy-momentum conservation from the muon reconstructed with a KF and minimal cuts ≥ 4 YZ hits.

a timestamp randomly generated according to the detailed timing structure of a 9.6 μs beam spill. The number of interactions that occurred in each simulated spill is generated from a Poisson distribution with the mean equal to the average number of expected events based on 7.5×10^{13} POT/spill and the target mass of the various SAND components and the ND hall. The full spill simulation is then obtained by overlapping the STT and ECAL hits from all the events generated within the spill with their respective timing information. Figure 6.150 illustrates the resulting typical hit distribution in STT within a spill.

The first step in the event reconstruction is the clustering of the hits detected within a spill based on their topological contiguity and timing consistency. The presence of hits in the most upstream tracking STT module or in the active STT region outside of the FV is used to reject clusters associated with external interactions. Clusters consistent with single isolated tracks originating within the STT fiducial volume were selected (Figure 6.150). A circular fit is used to select positively charged muon tracks, which are then reconstructed based on a KF (Section 6.18.2). Figure 6.151 shows the resolution obtained on the momentum, on the angle with respect to the beam direction, and on the angle in a plane transverse to the beam direction for muons in $\bar{\nu}_\mu \mathrm{H} \to \mu^+ n$ interactions with the initial STT and minimal cuts ≥ 4 YZ hits. A good reconstruction of the transverse plane kinematics is particularly relevant for the separation of the interactions on H from the corresponding backgrounds arising from interactions within the C nucleus. For signal events, the momentum vector of the primary neutron can be directly calculated from energy-momentum conservation using the measured energy and angle of the μ^+ [17]. Results are shown in Figure 6.152.

The line-of-flight (LoF) of the neutron is defined as the straight line connecting the first hit on the muon track to the earliest interaction point of the neutron (Figure 6.153). This latter can be either within the STT or in the surrounding ECAL. In both cases, the hits are digitized taking into account the detector readout and the position of the interaction point is inferred from the corresponding detected cluster. The momentum vector of the neutron is obtained from the measured neutron direction and the energy E_n calculated from energy-momentum conservation. Figure 6.153 shows the corresponding angular resolution on the measured neutron direction.

The selection of $\bar{\nu}_\mu H \to \mu^+ n$ closely follows the analysis of Ref. [17]. After reconstructing an isolated positive track consistent with a muon, the correct neutron must be attached to it. To this

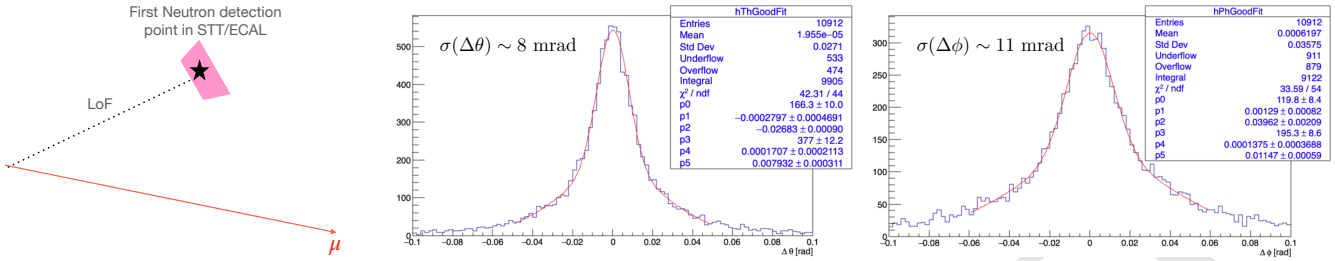


Figure 6.153: Reconstruction of the neutron line-of-flight from the first hit on the muon track to the earliest interaction point of the neutron in either STT or ECAL for $\bar{\nu}_\mu \mathrm{H} \to \mu^+ n$. The resolutions obtained on both the angle with respect to the beam direction ($\Delta\theta$) and the angle in a plane transverse to the beam direction ($\Delta\phi$) are shown.

end, an algorithm based on reconstructed topological information was developed without using any MC truth. The average detection efficiency for the primary neutron in signal events is about 75%, including those detected in both STT and ECAL (Figure 6.154). The corresponding energy thresholds applied were 2.5 photoelectrons for ECAL cells and 250 eV for STT straws. However, the ambiguity arising from the large number of random neutrons detected within the neutrino spill must be taken into account. The first step is to create a list of potential neutron candidates within the given spill, defined as any disconnected neutral cluster or energy deposition in either STT or ECAL. These neutral clusters can be produced by any primary or secondary neutron from either the H signal or the background events, but also from other neutral particles, including hadrons and photons. The initial number of neutron candidates found for each genuine $\bar{\nu}_\mu H \to \mu^+ n$ event is, on average, 136 neutral clusters per spill. In addition to the list of neutron candidates, a second list of all the detected activities from any (anti)neutrino interactions that overlapped with the signal event within the same spill is created. The rejection of the random clusters is performed by combining reconstructed timing and topological information of both the neutron candidates and the detected activities into a Multilayer Perceptron (MLP) discriminant. Figure 6.154 shows that such a discriminant provides a good separation between the primary neutron from signal events and random clusters. Overall, the correct neutron candidate is selected in about 92.5% of the cases (Table 6.29).

Table 6.29: Results from the selection of the neutron candidates in $\bar{\nu}_\mu H \to \mu^+ n$ events based on the MLP discriminant shown in Figure 6.154.

	Correct primary n	**Self-secondary n**	**Random background**
Fraction	92.5%	0.5%	7.0%

After the selection of the neutron candidate, the complete event kinematics for $\bar{\nu}_\mu H \to \mu^+ n$ interactions on hydrogen is reconstructed. The resolution achievable on many of the kinematic variables is dominated by the reconstruction of the neutron direction rather than that of the μ^+ momentum vector, given the excellent momentum and angular resolutions of the STT. The kinematic selection is based on a multi-dimensional discriminant optimized for the complete set of variables for the separation of H and C interactions in Ref. [17] (Figure 6.155). The dominant background is from charged current quasielastic (CCQE) interactions. Table 6.30 summarizes the number of selected events in one year of data taking with the initial STT. The results obtained with

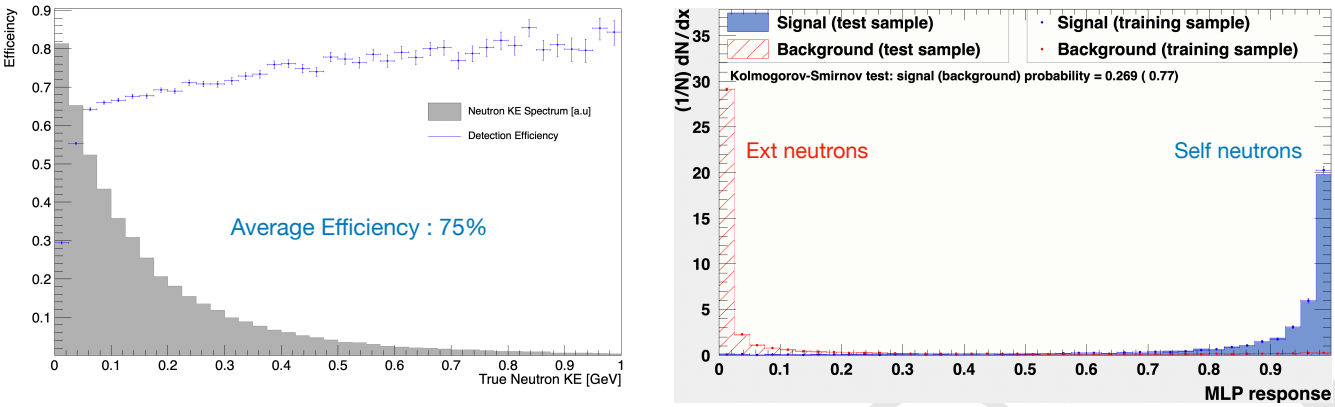


Figure 6.154: Left plot: Detection efficiency for the primary neutron from $\bar{\nu}_\mu H \to \mu^+ n$ events in the initial STT including the ones detected in both STT and ECAL. The energy thresholds applied are 2.5 photoelectrons (PEs) for ECAL cell and 250 eV for STT straw. Right plot: Separation between the correct primary neutron in signal events and random clusters.

full-spill simulations and realistic reconstruction are not far from Ref. [17]. Further improvements are expected with more refined digitization and reconstruction algorithms. The complete selection is applied to events originating in both the plastic CH_2 and the graphite targets. The selected events from the C targets are then scaled by the ratio between the total fiducial masses of C within the graphite and CH_2 targets and are subtracted from those in the latter. Figure 6.156 illustrates the corresponding reconstructed Q^2 distribution after the subtraction for one year of data taking. The uncertainties include the effect of background subtraction. A similar analysis was also validated with the data from the NOvA near detector, which is characterized by a relatively large H content of about 11%. A good agreement was found between NOvA data and predictions, with a total of about 35,000 $\bar{\nu}_\mu H \to \mu^+ n$ selected after the kinematic analysis [83].

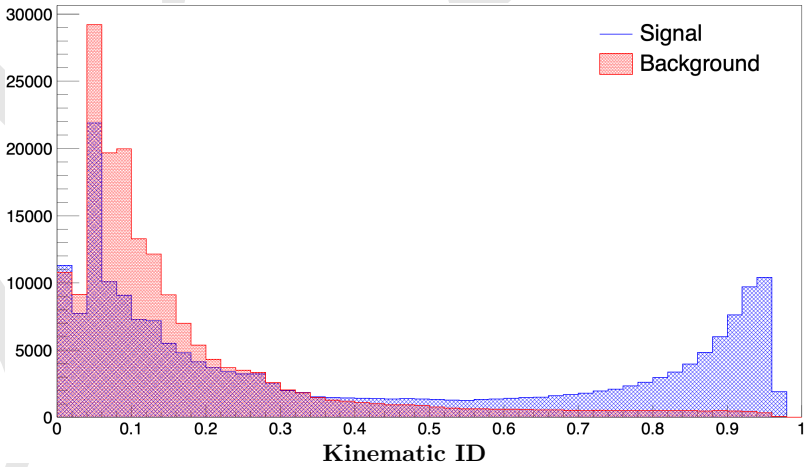


Figure 6.155: Distributions of the discriminant used for the kinematic selection of the $\bar{\nu}_\mu H \to \mu^+ n$ signal from the backgrounds (mostly from interactions on the carbon nucleus) in the initial STT. The input variables are the same as in the corresponding analysis of Ref. [17].

Table 6.30: Expected number of $\bar{\nu}_\mu H \rightarrow \mu^+ n$ events after the complete selection of the neutron candidate and the kinematic analysis in the initial STT for one year of data taking. Backgrounds include contributions from all internal and external CC+NC interactions within a 9.6 μs spill.

Selected signal	CCQE bkgnd	non-CCQE bkgnd	Total bkgnd	Purity
100,166	34,653	5,112	39,756	71.6%

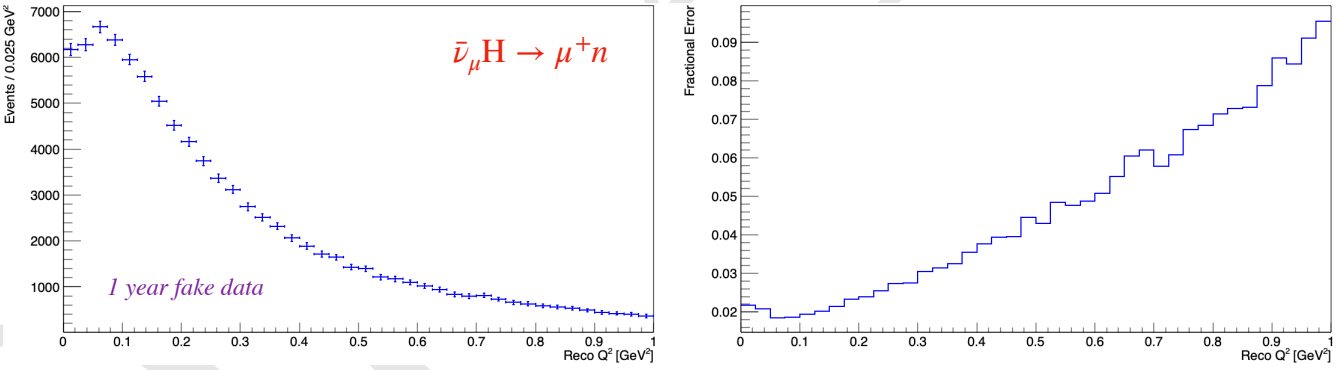


Figure 6.156: Left plot: Reconstructed Q^2 distribution in the final selected $\bar{\nu}_\mu H \rightarrow \mu^+ n$ events after subtraction of the C backgrounds using the corresponding interactions in the graphite targets. The errors include the effect of the background subtraction and the distribution corresponds to one year of data taking with the initial STT. Right plot: Relative errors on the same reconstructed Q^2 distribution shown on the left.

Chapter 7

Drift Chamber

In progress

DRAFT

Chapter 8

DAQ Architecture

This section describes the architecture of the Data acquisition (DAQ) system, as well as the closely related Timing, Trigger, and Calibration interfaces, and the runtime configuration of the Front-end (FE) electronics. Each of the SAND subdetectors implements a different architecture for their FE, but must conform to a common standard for interfacing with the DAQ, as well as with the Detector Control System (DCS) and Detector Safety System (DSS) described in Sections 9 and 9.5. The element of a subdetector readout system that implements one or more of these standard interfaces will be called an *Endpoint* for the respective interface. The implementation of, e.g., the timing distribution, the data processing, or the configuration of the readout boards that takes place inside the Endpoint(s) or between the Endpoint(s) and any separate front-end board (FEB) is the responsibility of the respective subdetector and will not be discussed in this section. In SAND, there will be a 1-to-1 correspondence between the DAQ and the timing Endpoints, with each subdetector comprising more than one endpoint; the exact number depends on the layout, modularity, and expected data throughput of that specific subdetector. The DAQ and the Timing system used in SAND are based on the DUNE-DAQ framework [84,85] and conform to the design implemented by the other near detectors (NDs) and the far detectors (FDs). The design is summarized here in Sections 8.3 and 8.6 respectively, and more in depth information is available in the SAND-DAQ interface control document (in preparation).

8.1 Description of the SAND subsystems and their interfaces

The following sections provide a description of the SAND subsystems and their interfaces with the DUNE DAQ and Timing System.

8.1.1 GRAIN

GRanular Argon for Interactions of Neutrinos (GRAIN) is a 1 t liquid argon detector with optical readout. It is equipped with approximately 60,000 silicon photomultipliers (SiPMs), arranged in 1024-channel matrices, each read out by a single cryogenic application-specific integrated circuit (ASIC), up to eight of which are connected to one GRAIN Warm Interface Board (GWIB). Four GWIBs are installed on each side of the GRAIN cryostat, for a total of eight. A GWIB implements

all required hardware and firmware to interface with the ASICs, the DUNE DAQ, and the Timing System. In the baseline design, the GWIB is based on a Xilinx Ultrascale+ family device. The ASIC is self-triggering and is capable of continuous acquisition. It is designed to operate on a 312.5 MHz clock. Due to the high performance and high channel density, the combined ASIC power consumption is significant and would exceed the capacity of the cryogenic cooling system. A reduction in power consumption can be achieved by turning off parts of the circuit outside the time window of interest for data collection. This window includes the full duration of the spill (10 µs duration over a 1.2 s repetition period [86]). Additional windows may include periods for calibration and alignment data taking, such as for cosmic rays or test pulse acquisition. The GWIB must be aware of the spill arrival time at least 4000 µs (this value is a conservative estimate) in advance of the neutrinos entering the SAND volume, in order for the ASIC power-saving features to settle into the ON state and for the necessary reconfigurations, if any, to take place.

8.1.2 Tracker

The choice of tracker for SAND has not yet been finalized; the two options are STT (Section 6) and drift chamber (Section 7). From a data acquisition perspective, the two solutions are similar: in both cases, the number of readout channels is on the scale of 10^5, and the occupancy and data throughput are relatively low. In the following, the STT option will be taken as a reference, but similar considerations would apply to the drift chamber.

8.1.3 ECAL

The SAND Electromagnetic calorimeter (ECAL) is a fine sampling lead-scintillating calorimeter equipped with photomultiplier tube readout. The barrel section of the endcap consists of 24 modules equipped with 60 PMTs at each end. Endcap modules vary in size from 10 to 60 channels. The total number of readout channels is 4,880. The performances measured in the past in the KLOE experiment include a time resolution of $54\,\mathrm{ps}/\sqrt{E(GeV)} \oplus 140\,\mathrm{ps}$. Reaching this same performance is of great importance in order to achieve the target momentum resolution for neutrons (which is measured via time of flight (ToF)). Therefore, the contribution of the timing distribution system must be significantly smaller. Possible solutions for the Front End electronics are still being investigated within the DUNE SAND Consortia and in collaboration with CAEN S.p.A. The various options for front end are discussed in 4.5.2, but they all share a common backend in the CAEN FERS concentrator. Differences in the front end are not expected to lead to significant differences in data rates or acquisition modes. CAEN engineers have conducted a preliminary study on the integration of the DAQ and DTS endpoint in a modified FERS concentrator. No showstoppers have been identified so far, and the integration effort is presently underway.

8.2 DUNE-DAQ and DTS Systems

The Trigger and DAQ system (TDAQ) is responsible for receiving, processing, and recording data from the various components and subdetectors that are part of the DUNE experiment. This system:

- provides timing and synchronization to the detector electronics and calibration devices;
- receives and buffers data streaming from the detector components;

DRAFT

- extracts information from the data at a local level to subsequently form trigger decisions;
- builds trigger records, defined as a collection from selected detector space-time volumes corresponding to a trigger decision;
- carries out additional data reduction and compression as needed; and
- relays trigger records to permanent storage.

The main challenge for the DUNE TDAQ lies in the development of effective, resilient software and firmware that optimize the performance of the underlying hardware. The design is driven not only by data rate and throughput considerations but also — and predominantly — by the stringent uptime requirements of the experiment. The TDAQ is composed of a set of systems, as represented in Figure 8.1, where their relationship is also described.

All systems rely on the functionality provided by the DAQ control, configuration and monitoring subsystem (CCM) and data quality monitoring (DQM), which are the glue of the overall TDAQ, transforming the set of components into a coherent system. The DAQ trigger subsystem (DAQ TS) and Data filter are responsible for the selection and compression of data. The Dataflow system provides the communication layer to exchange data (i.e., it is used by the other systems intersecting with it in the diagram). In addition, it implements the data collection functionality, i.e., the logic for building trigger records as well as the organization of data into files. The DAQ readout system (DAQ RO) receives the data streams from the FE boards, processes them to extract information for the trigger, and buffers data while the trigger is forming a decision.

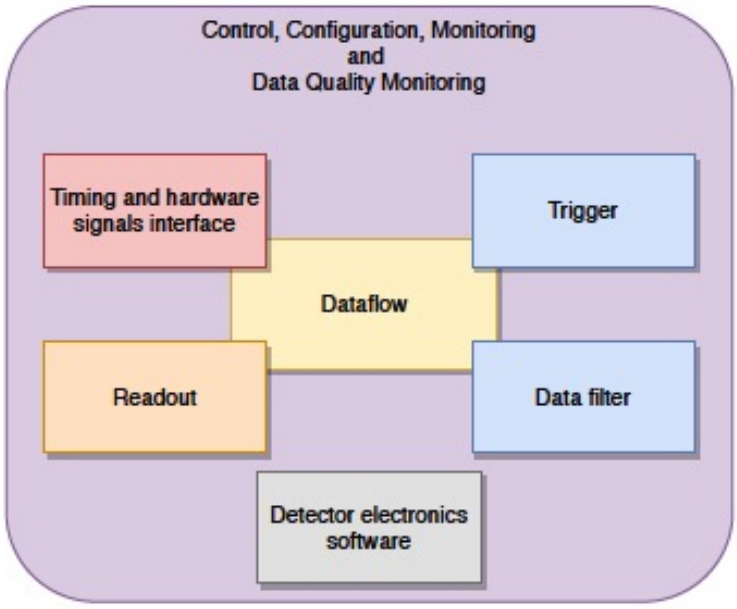


Figure 8.1: Diagram showing the relationships between TDAQ systems. It also shows, in grey, the detector electronics software, which is not part of TDAQ but will be developed fully embedded into the CCM environment.

The Deep Underground Neutrino Experiment (DUNE) Timing and Synchronization Subsystem (DTS) is in charge of distributing the clock, synchronizing the ND sub-module, as well as timestamping hardware signals that may be used for triggering, such as calibration pulses. The Detector

electronics software is not part of the TDAQ responsibility; it is part of the individual SAND subdetectors that will implement a different architecture for their FE boards. A data quality monitoring (DQM) processes data samples in near real-time to provide fast information on the quality of the data; while the CCM monitors the DAQ itself, the DQM monitors the usability of the data flowing through the system. A high performance Ethernet network interconnects all the elements and allows them to operate as a single, distributed system. At the output of the TDAQ the high-bandwidth Wide Area Network (WAN) allows the transfer of data from the subdetectors to the central storage area. The TDAQ for the whole of DUNE ND is designed and developed coherently by a joint team on the basis of the FD design.

The DAQ Endpoints will be connected via an optical Ethernet link to a switch that will aggregate the data streams of the System for on-Axis Neutrino Detection (SAND) detectors and transmit them to the upstream ND-DAQ system. The DAQ Endpoints will also include an interface for the control and configuration of the front-end electronics, encapsulating configuration parameters specific to a subdetector in the common communication framework provided by the DUNE-DAQ system. The requirements of SAND in terms of data volumes are modest, at least when compared with those of FD. The data rate is therefore not a main driver of the DAQ implementation, which is characterized by high bandwidth links. The planned number of endpoints is driven primarily by the desire to respect the modularity of the underlying subdetector, as well as to optimize cabling paths for the endpoints. The limited data throughput of SAND allows sharing of the same physical connection between the control and configuration interface and the data readout interface; however, the two interfaces can be kept separate for the subdetectors that require this. A summary of the output data rate and the number of endpoints for each subdetector is shown in Table 8.1. Note that the higher rate of hits in GRAIN is due to the high number of channels activated by a single particle.

Table 8.1: Expected data rates

Subdetector	ECAL	GRAIN	Tracker
Approximate hit size [bits]	50-100	128	50
Hits per spill [#]	5×10^3	3×10^5	1×10^4
Hits from calibration sources/cosmics [#]	1×10^4	6×10^5	1×10^4
Total data rate [Mbps]	1	11.5	1
Endpoint count	8	8	10-100

8.3 Physical Interfaces

The physical solutions adopted for timing distribution, synchronization, and data transmission are discussed below.

8.3.1 Timing

Timing and synchronization messages are distributed on OS2 single mode fiber. The timing system will use 1000Base-BX-20 SFP modules, which transmit at 1310 nm and receive at 1550 nm. The timing endpoints on the detector will use matching 1000Base-BX-20 SFP modules, which transmit at 1550 nm and receive at 1310 nm.

- Downlink: The timing system will normally transmit continuously. This is to allow the DUNE-SAND endpoints to receive a clock at any time. However, the DUNE-SAND endpoints must have the capability of recovering from an interruption in the timing data stream. The DUNE SAND consortium is responsible for receiving the optical signal at the endpoints listed above and distributing it to the front-end electronics.
- Uplink: Each SAND timing endpoint will implement the DTS protocol.
- Link Speed: This is set to 62.5 MHz.
- Clock Jitter: < 10 ps.
- Clock skew between endpoints: < 30 ps over the timescale of one spill, < 100 ps overall.
- Fiber Connection: The transceivers on the DAQ side have an LC connector. The DAQ is responsible for providing the optical fanouts.
- Firmware: The DAQ consortium is responsible for providing the firmware (compatible with integration in firmware based on AMD/Xilinx US+ FPGAs) that implements the timing endpoints.

8.3.2 Data

Data may be transmitted using OM3/OM4 multimode fiber pairs supporting either the 1 Gigabit or 10 Gigabit Ethernet standard over the required distance.

- Link: Data transmission is bi-directional. Control and configuration commands to the endpoints may be sent via the readout path.
- Fiber Connection: The SAND consortium is responsible for the fiber patch cords that will connect the endpoints to a patch-panel located on the SAND electronics shelves.
- Firmware: The DAQ consortium will provide the firmware (compatible with integration in firmware based on AMD/Xilinx US+ FPGAs) that implements the 10G transmitter endpoint. If a 1G implementation is used instead for some detectors, it may be implemented in software, the implementation of which will have to be agreed upon with the DAQ consortium.

8.4 Data formats and protocols

The following sections are dedicated to the formats and protocols adopted for timing and data transmission.

8.4.1 Timing

Timing and synchronization messages are distributed using the DTS protocol described in [87]. The timing system provides a common firmware block to decode the timing protocol, which will be incorporated into the overall firmware design for the receiving FPGA in each endpoint component. In addition to the clock, the timing system will distribute timestamps and time synchronous commands. At a minimum, the DTS shall forward an accelerator-derived warning signal no less than 4000 µs before the arrival of each spill from the accelerator. It should also allow for synchronization with the beam with an accuracy comparable to that of the timing system itself (100 ps).

8.4.2 Data

Given the relatively low data throughput of the SAND subdetectors (see Table 8.1), the definition of the data format and transmission protocol does not pose significant challenges. The data will be formatted according to the specifications provided by the DUNE-DAQ framework. There will be a common header associated with the subdetector-specific organization of the signal information.

8.5 Data synchronization

The data format of the packets transmitted from SAND includes the DUNE timestamp field as outlined in Section 8.4.1. The timestamp value represents the time at which physics signals are converted into electronic signals by the different DUNE SAND frontend motherboards. The DTS is responsible for aligning the timestamp distributed by the DTS endpoints to the detector electronics across a DUNE detector module. The timestamp is guaranteed to be aligned with the correct clock cycle at the DTS firmware interface. It is the responsibility of SAND subdetectors to correct the timestamp value for the delays due to the transmission, processing, or packaging of the sampled data between the sensors and the UDP transmission block.

8.6 Synchronous Interfaces

The synchronization of the SAND subdetectors will be based on the DUNE DAQ timing and synchronization subsystem (DAQ TSS) [88], a set of hardware, firmware, and software tools initially developed for the FD and subsequently adopted by the ND. The DAQ TSS delivers clock, timestamps, and other synchronous signals to a certain number of end-points. These signals are distributed over optical fibers using a custom protocol based on duty cycle shift keying, on a separate physical interface from that of the DAQ Endpoints, but located on the same circuit board and connected to the same programmable device. The timing system will feature the ability to correct the recovered clock signal phase to achieve synchronization with an error substantially smaller than the clock period.

8.6.1 Performance requirements for synchronization

Given the good timing performance of SAND subdetectors and the desire to perform data analyzes that require accurate ToF measurements, the following minimum performance is required of the timing system:

- a skew less than 30 ps root mean square (RMS), after corrections, between any two different endpoints *when measured over the duration of one spill*;
- a skew less than $\mathcal{O}(100\,\text{ps})$ RMS, after corrections, between any two different endpoints *when measured over a longer duration*;
- a skew less than $\mathcal{O}(100\,\text{ps})$ RMS between any endpoint in SAND and the device(s) measuring the timing of the beam.

The first requirement is motivated by internal ToF measurements between different subdetectors and different modules of the same subdetector. When taking into account the additional inter-

channel skew introduced by the readout system (which is estimated at 10 ps), it results in a timing error introduced by the clock distribution system that is sufficiently low not to degrade the intrinsic timing performance of the subdetectors. The second requirement is motivated by the need to perform accurate calibrations between detectors. As these take place over a longer timescale than a single particle interaction, additional phenomena can influence timing accuracy (e.g., thermal and voltage variations in fibers, converters, etc...). These make it harder to limit the skew, but a larger skew can be accepted as statistical analysis can partially compensate. The third requirement intends to constrain the error in synchronization between SAND and the accelerator in order to be sensitive enough to disentangle the bunch structure in the spill.

A critical requirement is the implementation of a spill warning signal that will reach the SAND endpoints in advance with respect to the first particles from the spill. The minimum amount of time for this warning has not yet been established, but an estimate of 4 ms is assumed.

The timing requirements of SAND are summarized in Table 8.2. Since several specifications of the SAND subdetectors are still under development, the values in the table must be taken as estimates based on the current knowledge of the system.

Table 8.2: SAND Timing requirements. Since several specifications of the SAND subdetectors are still under development, the values in the table must be taken as estimates based on the present knowledge of the system.

Id	Description
1	The DTS shall distribute to all SAND endpoints a clock with a nominal period of 16 ns.
2	The skew between any two SAND endpoints, and between any endpoint and the nominal absolute timescale, after all applicable corrections by the DTS, shall be at most 30 ps.
3	The standard deviation of the distribution of rising edge actual - nominal arrival times shall be 1. less than 20 ps when measured in a window of 100 µs 2. less than 100 ps overall measured at the output of each endpoint PLL
4	The DTS shall forward an accelerator-derived warning signal at least 4000 µs before the arrival of each spill from the accelerator, with a precision of at least 1 ns (ideally 100 ps). Note: the requirement can be satisfied with two separate signals, one early, one accurate

8.6.2 Trigger and Calibration

The readout systems of all the SAND subdetectors have self-triggering capabilities that are more than sufficient to limit data rates to a manageable level when data is acquired only in the vicinity of the spill. A global trigger is therefore unnecessary for SAND when acquiring beam data, and a simple *beam-gate* needs to be provided. A gate should include signals with sufficient advance warning in order to, for example, enable those front end elements that support power gating (such as the GRAIN ASIC).

In addition to beam data, the acquisition of auxiliary data for calibration and alignment purposes will be supported. It is not expected that the amount of data produced during the calibration procedures will significantly affect the overall data throughput of SAND and each DAQ Endpoint; however, a set of commands and synchronous signals will be needed to perform this task, starting and synchronizing the acquisition of calibration data across SAND or a specific subdetector. These commands and signals can be easily accommodated within the standard communication frameworks provided by the DUNE-DAQ and the DUNE Timing Systems.

DRAFT

Chapter 9

Detector Control and Safety systems (DCS-DSS)

The Detector Control System (DCS) has exclusive control of the SAND detector, excluding the control of the cryogenic system related to the magnet. This control is independent of the DCS, as it involves safety aspects critical for the people on site and the operation of the experiment.

The DCS is built on equipment compliant with Fermilab regulations and will require dedicated training for its maintenance. The system will be based on the Ignition system. The monitoring data collected by the DCS will be made available to the DAQ system as Detector status, authorizing the data acquisition sequence to proceed. A brief description of the different subsystems and how the DCS manages them is given below.

9.1 DCS Devices

- **Detector Power Control**: The detector power control (DPC) consists of the power supplies that provide power to the different parts of the detector. The DCS is in charge of processing the requests from the operators and sending the commands to the power supplies. Additionally, the DCS monitors and archives the power supply parameters, such as currents, voltages, and temperatures, allowing for an analysis of the system behavior over time. A Detector Safety System (DSS) system is also implemented and connected to the DCS, displaying an alarm in case any of the configured limits are exceeded. Depending on the severity of the alarms, corrective actions may be taken automatically to protect the detector.
- **DAQ Rack Control**: The DCS system monitors all working parameters of the racks and is able to cut power if the ambient temperature rises beyond a set threshold. It also controls the staged re-powering of racks during a cold start procedure in order to limit the instantaneous load on the electric distribution system.
- **External Systems**: The cryogenics control system does not belong to the Detector DCS but to the Cryo DCS system. However, the DCS and the DCS cryogenics control system continuously exchange information.

9.2 Unifying Standards

The DCS provides a homogeneous environment in which all its parts can be integrated.

The communication protocols used to interact with different hardware components are, in most cases, fixed by the manufacturers. Therefore, the DCS has to be able to support a variety of communication mechanisms and abstract those such that their differences are not visible to the higher levels of the supervisory system, as well as to the operators. The communication layers used within SAND detectors and their main characteristics are listed here:

- open platform communications (OPC) Classic (OLE1 for Process Control Data Access): The OPC Classic specifications are widely used in the Industry as the standard interface for hardware communication. The OPC Classic specifications provide a middle-ware to decouple the hardware specific elements from the software in charge of its control.
- OPC unified architecture (OPC-UA): The OPC-UA was designed to enhance and surpass the capabilities of the OPC Classic specifications. Its functionality remains the same, but with several improvements that ease its operation.

9.3 Detector Operation

The software chosen to operate the DCS is a commercial supervisory control and data acquisition (SCADA) toolkit: Ignition. Ignition is based on a distributed product where quasi-independent processes called managers execute different tasks. Those managers do not need to run on the same machine and may be distributed, along with the Ignition internal database, to several computers running on Linux. A critical component in the SAND DCS is the Access Control component. With the access control enabled, every user logs in with his personal account to perform any DCS action. Three authorization levels are in use: Monitor, Operator, and Expert. Depending on the user's rights, different actions can be blocked or hidden to protect the detector integrity and to better guide the user.

Another critical interface in the SAND DCS system is the integration with the DUNE-DAQ slow control. In case of emergency situations, the DCS will operate and control such interfaces even when the DAQ is running.

9.4 Basic and Advanced Operations

The basic operation of the detector uses a simplified interface that allows the operators to execute their tasks smoothly, minimizing unintended actions and, therefore, increasing the stability of the system. For monitoring purposes, the interface uses simple color coding to be as straightforward as possible. It is based on two main concepts:

- Dynamic objects, where all the graphical items are dynamic and thus can be used to navigate through the different parts of the detector to see its dedicated panels.
- Data widget, where the datum displayed on the DCS interface is more than a pure value,

DRAFT

and the operators may perform some extra actions, such as plotting its historical values or checking its status.

For advanced detector operations, specific and more detailed panels can be designed. Rather than using an FSM to move the detector — or its sub-components — to a preset state, the advanced panels allow the experts, accredited by access control, full control of the different parts of the detector. The advanced panels connect with the lowest level architecture of the detector, allowing the experts to modify operational parameters, set limits for alerts, or directly control critical devices.

9.5 Detector Safety Systems (DSS)

The DSS is an independent safety system that interacts directly with the Cryogenics and the other SAND detector sub-components to assure the safety of the equipment, people, and various power supplies.

The function of the DSS is to detect abnormal and potentially harmful situations, minimizing the resulting damage to the experimental equipment by taking protective actions in order to bring the detectors to a "safe state". DSS serves as an equipment protection layer between the Live Protection System (Level 3 alarms at Fermilab), which provides the highest level of safety, and the Slow Controls or Detector Control System (DCS), which perform normal operations. DCS may handle a lower level of safety.

DSS complements existing systems such as DCS or the Live Protection System, and the subdetector safety systems that provide an internal subdetector safety level are also complementary to DSS.

Based on the requirements mentioned above, the following specifications have been defined for the DSS.

- Be highly reliable and available, as well as simple and robust.
- Provide a cost-effective solution for experimental safety.
- Operate permanently and independently of the state of DCS and the Live Protections System, being able to take immediate actions to protect the equipment.
- Be scalable so that it may evolve with the experiments during their assembly, commissioning, operation, and dismantling (a time-span of approximately 20 years).
- Be maintainable throughout the lifetime of the experiment.
- Be configurable so that changes in the setup can be accounted for.
- Be able to connect to all sub-systems, services, and subdetector safety systems.
- Exchange information or signals with DCS and the Live Protection System.

9.5.1 DSS Devices

The detector safety system will be based on SIEMENS PLC architecture that will be connected directly to the DUNE-SAND power supplies as interlocks, and it will be integrated into the Ignition

DRAFT

SCADA system as well.

9.5.2 DSS Control Hardware

DSS can adopt the standard industrial solution for critical systems by using a Programmable Logic Controller (PLC) with a redundant CPU to avoid detector downtime. The choice of the SIEMENS S7-1500H, in particular the CPU 1517H, provides an optimal solution for redundancy and high availability systems.

A backup PLC CPU synchronized with the primary PLC CPU ensures that no data is lost in the switchover in case of failure. The switchover time between the failing primary CPU and the backup is less than 100 ms. The synchronization of the CPU's is achieved via a module/optical fiber capable of up to 3 km.

The PLC network uses the industrial Ethernet protocol PROFINET, connecting the CPU's with the remote extension I/O in a ring configuration. The PLC ring configuration ensures the proper functioning of redundancy, taking into account all possible failure cases of the CPU and/or remote I/O.

The CPUs are installed in a rack called DSS CPU racks, and the remote extension I/O is also installed in the DSS Extension rack. The primary CPU is installed either on the surface or in the service cavern, while the backup CPUs are installed in the experimental cavern. Both CPUs are synchronized by means of optical fibers.

The DSS remote expansion racks are the end-points of the DSS signals. DSS signals are only connected by hardware through cables. The CPU's racks contain I/O modules for connecting DSS signals. External software protocols or field buses cannot connect to DSS.

- DSS can receive digital input in PLC logic levels: Low = 0 V, High = 24 V;
- DSS can send digital output signals in dry relay contact format;
- DSS can receive analog signals: 0-10 V, 4-20 mA, 0-20 mA, PT100, and PT1000 types.

The design of DSS signals in electrical circuits is referred to as fail-safe due to its intended design to default to the safest mode in the event of a common failure, such as a broken connection in the wiring.

The size of the DSS, in other words, the number of DSS Remote Expansion racks, depends on the number of signals to be processed.

DSS racks can be strategically placed in the experimental cavern in order to minimize the routing of the DSS cables.

The back-planes allocate the different DSS I/O modules; 4 types of I/O modules are used in the default configuration.

- 32 Digital Input Module

- 32 Digital Output Module
- 8 Analog Input Module
- 8 RTD Input Module

The I/O modules are plugged into the back-plane, as shown in Figure 9.1, according to the configuration required by the application. They communicate through the back-plane with the first module, which is the Profinet communication module linked to the communication ring.

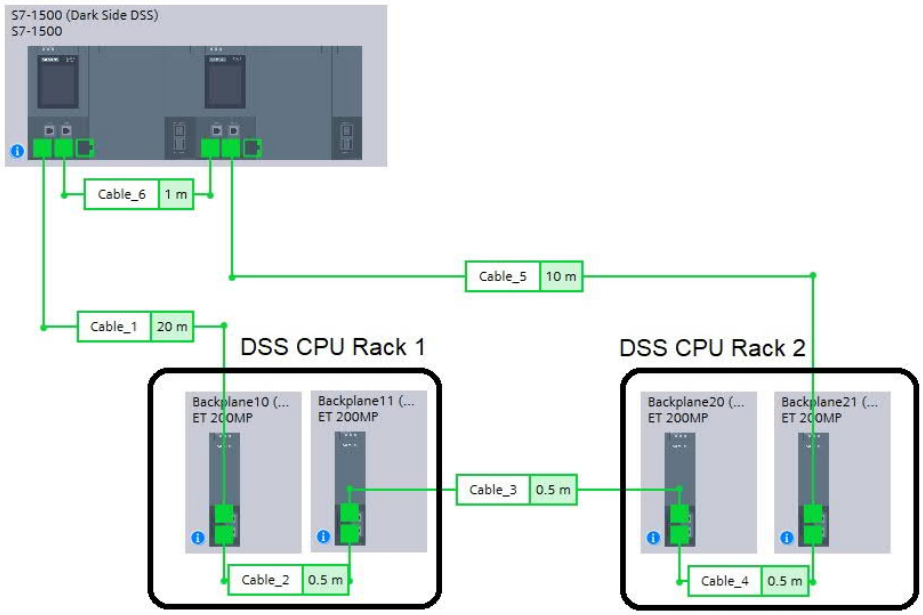


Figure 9.1: Basic layout of a DSS system with only two CPU racks: one in the service cavern and the second one in the experimental cavern. They are connected in a ring topology with the I/O back-planes to ensure redundancy. Each rack contains 2 I/O back-planes.

The design of the racks is uniform for all DSS racks, maintaining the same layout and components to minimize assembly time and costs, as well as to simplify operation and maintenance. The typical initial hardware format of the DSS is a 19' rack with a height of 56U, but it can also be produced in other formats, such as expansion mini-crates or industrial cubicles. One of the key aspects of the DSS is the power supply circuit, which needs to be highly reliable and readily available, as well as simple and robust. The DSS PLC and all associated instrumentation are powered by 24 VDC (Volts Direct Current).

The 24 VDC is generated from a reliable 220 VAC power supply.

The cables driving the signals to and from DSS PLC are physically connected to specific modules, depending on the signal type.

- The digital input signals are optocoupled and over-voltage protected for all incoming signals to DSS.
- The digital outputs are interfaced using electromechanical relays to transmit the signals with dry relay contacts.

- The analog signals and PT100/P1000 sensors are also interfaced with the PLC module in order to simplify cable routing.

DRAFT

Chapter 10

Installation & Integration

Installation and Integration includes the activities taking place at Fermilab upon the delivery of equipment from SAND's collaborating institutions. This section describes:

- How the activities are organized, the decision-making processes, the related responsibility chain, and the way SAND Consortium interacts with the ND I&I team (DUNE-ND Project) and Fermilab's infrastructure;
- The applicable codes and the process of approval for using equipment at Fermilab;
- Organization of the transport of equipment from the SAND consortium's collaborating institutions to Fermilab, storage, and local transport inside Fermilab, and the related sharing of responsibility;
- The experimental hall and the related facilities for assembly, installation, testing, and operation; a description of the test areas required at Fermilab for testing, pre-assembly, and QA/QC processes following transport;
- The helium cryogenic system to be installed in the underground hall to supply the superconducting magnet;
- SAND's installation sequence in the ND hall;
- Critical lifts and the standard way they will be handled;
- Risk categories associated with Installation and Integration and a short description of management and mitigation strategies;
- The gas protocols applied for activities at Fermilab.

10.1 Work Organization and Sharing of Responsibilities

The definition of the action plan, sequence of operations, high-level schedule, and the definition and oversight of QA/QC processes are the responsibility of the SAND Technical Leader through interaction with SAND's working groups (WGs). Major technical matters are discussed at the Consortium Technical Board, as is the general progress of the WG activities. High-level technical decisions, particularly those impacting multiple sub-systems, are discussed and made by the Tech-

DRAFT

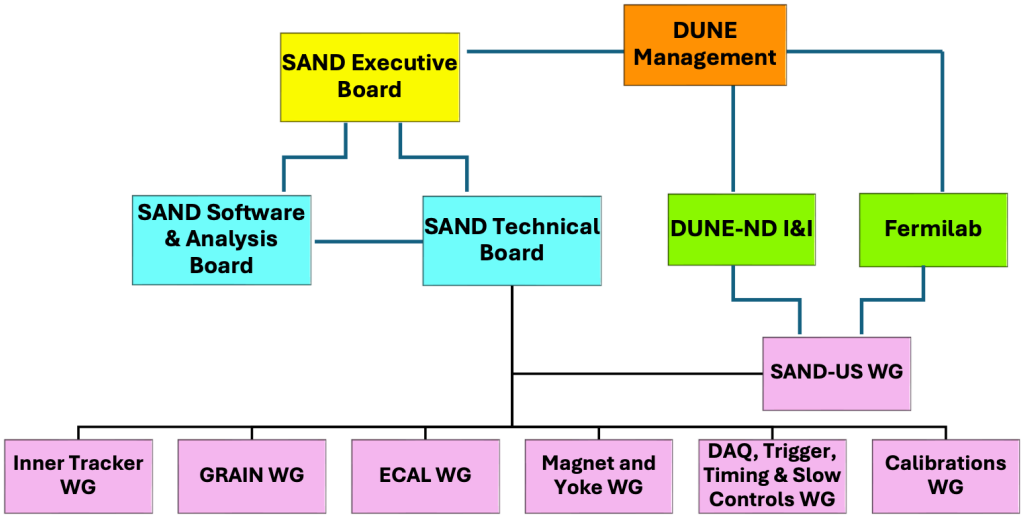


Figure 10.1: Organizational chart for SAND I&I.

nical Board or, if needed, moved to the Consortium Executive Board, and from there to higher-level bodies as deemed appropriate. If a technical decision has potential impacts on data analysis, the matter will be discussed jointly with the Software/Analysis board and then, if needed, moved to higher level bodies following the above process.

During installation, the SAND Technical Board will meet at least monthly, while weekly meetings of the SAND Consortium (SAND General meeting) are used to oversee the progress of the ongoing activities.

The interface between the SAND Consortium and the ND I&I team, as well as Fermilab ES&H and technical services, is provided by the SAND-US group, based at Fermilab. It is the responsibility of the SAND-US group to organize SAND's activities at Fermilab in terms of required local personnel support, logistics, and safety, and to provide the infrastructure in the experimental cavern and elsewhere on the Fermilab site needed for the safe and successful installation and operation of the SAND detector. It is also the responsibility of the SAND-US group to assist the other WGs in preparing documents, tests, and other actions necessary to achieve acceptance for the operation of their sub-systems at Fermilab. The SAND-US group will organize the reviews to obtain Partial Operational Readiness Clearance (pORC) or the final operational readiness clearance (ORC) of the various sub-systems in accordance with the Fermilab Environment, Safety and Health Manual (FESHM) chapter 2005 [89].

SAND installation, integration, and commissioning activities will be organized following the same procedures developed for the installation and commissioning of the ICARUS and SBND detectors, in light of the many similarities with those activities, particularly with ICARUS. Primary in-kind

contributions will come from non-US institutions, and installation, integration, and commissioning will primarily be carried out by their personnel and subcontractors. Experience gained from the SBND installation and commissioning, which proved effective in work safety planning, scheduling optimization, and quality assurance, will be applied.

Detailed written work plans, including hazard analysis and risk mitigation strategies, are developed by the WGs in accordance with FESHM 2060 [89]. Work plans are presented and discussed in weekly meetings organized by the SAND-US group leader sufficiently in advance of the expected work date to implement possible modifications in the workflow and to allow for the necessary preparatory activities. A tentative schedule of the activities related to the work plan is generated after the first discussion and finalized when all required conditions are met. This procedure is implemented as soon as there is work at Fermilab, including work taking place outside the DUNE-ND experimental hall, such as the acceptance tests of the magnet and the ECAL modules.

During installation, toolbox meetings will be held before the start of each work shift. These meetings will be organized by DUNE-ND I&I team to ensure coordination among the installation and commissioning activities for the various ND elements. If needed, additional toolbox meetings will be organized, having at least one interface to transfer information from the previous ones.

Figure 10.1 shows the operational interconnection between the various groups involved in DUNE-SAND installation activities.

10.2 Fermilab Requirements for Equipment Approval

For any system and component received at Fermilab to be qualified for operations, documentation proving compliance with the applicable codes and standards must be provided. To understand the requirements and types of documents necessary for each system or component to prove conformity, various chapters of Fermilab FESHM [89] must be reviewed and adequately followed to the best of one's ability. FESHM 1071 describes all applicable codes and standards for mechanical, cryogenics, electrical, fire protection, and pressure systems required when designing, fabricating, testing, and operating new equipment. The codes also cover the evaluation of features and processes, as well as the assembly of the facility. FESHM 2100 describes the process used to establish equivalent safety performance between U.S. and International engineering design codes and standards for pressure equipment.

10.2.1 Cryogenics and Pressure Engineering Requirements

Most of the sub-systems composing the SAND detector use cryogenic or pressure equipment, or both. These include the following.

- GRAIN has a main cryogenic LAr container, a proximity cryogenic and argon purification plant, and a liquid nitrogen transfer line running from the DUNE-ND hall shaft to the SAND alcove.
- The superconducting magnet has a vacuum vessel, an internal liquid helium / liquid nitrogen distribution circuit for cooling the superconducting coil, proximity valve boxes, and heat exchangers; a helium cryo-cooling plant located on the mezzanine at the north end of the

DUNE-ND hall, helium storage and compressors at ground level, a cryogenic transfer line running from the mezzanine to the alcove, and pressure piping from ground level to the underground mezzanine.

- The inner tracker has a gas distribution system located on the detector platforms and a gas distribution line running from ground level to the alcove.

The relevant FESHM chapters describing the engineering and safety requirements and related procedures for cryogenic vessels, pressure vessels, vacuum vessels, piping, and refrigeration systems are:

- FESHM 5031: Pressure Vessels;
- FESHM 5031.1: Piping Systems;
- FESHM 5031.5: Low Pressure Vessels and Fluid Containment;
- FESHM 5032: Cryogenic System Review;
- FESHM 5032.1: Cryogenic Dewar Installation and Operation Rules;
- FESHM 5033: Vacuum Vessel Safety;
- FESHM 5034: Pressure Testing; and
- FESHM 5035: Mechanical Refrigeration Systems.

In general, for newly built pressure vessels and piping, US regulations require the application of current American Society of Mechanical Engineers (ASME) standards. However, a panel of Fermilab-appointed experts has recognized the substantial equivalence between some international safety codes, including the European Union's Pressure Equipment Directive (PED) compliant codes and the ASME codes related to pressure safety. DOE has approved a variance to the regulation requiring ASME code compliance, allowing the use of non-ASME codes for pressure vessels and piping to be applied to in-kind contributions to the DUNE experiment from international partners, according to evaluation and testing procedures outlined in the relevant FESHM chapters.

The variance applies to some of SAND's components: the GRAIN cryogenic system, the tracker gas system, the external helium system for the magnet, and, in general, to all newly built components involving pressurized gasses. The variance does not apply to KLOE's magnet, as it was built prior to the first European Union Pressure Equipment Directive.

Fermilab has recognized a need to evaluate equipment that does not meet the conditions for approval that would accompany new devices. This may be because the equipment exhibits wear (e.g., corrosion) or because there have been other changes to operating conditions. Alternatively, there may be a need to accept legacy, existing, reused, or relocated pressure equipment, which needs to be transferred to Fermilab from collaborating institutions and operated at the Fermilab site. Such legacy, existing, reused, or relocated equipment could be originally designed and constructed per ASME or the international codes listed in 10 CFR 851 and its recent Variance. On infrequent occasions, it could lack any established code pedigree. In order to address these situations, Fermilab is incorporating into FESHM the ASME/API procedures governing Fitness for Service (FFS) described in API-579, which provides a methodology for the evaluation of pressure safety for existing post-constructed equipment.

DRAFT

The cryogenic pressure components of the KLOE superconducting magnet, which include a small helium vessel located inside the magnet's turret and cryogenic piping, for which no code pedigree could be established, are being evaluated under the FFS framework.

An outside consultant, who is internationally recognized for his expertise in ASME/API FFS methodology, is evaluating the safety of KLOE pressure equipment, including the assessment of risks and consequences of failures; the assessment of inspections and tests; application of FFS methodology for the interpretation of records, inspections, tests, etc.; and the proposal of replacements, repairs, and enhancements needed to mitigate identified risks. This initiative, which is set to conclude in 2025, will provide criteria for the approval of KLOE magnet installation and operation at Fermilab.

10.2.2 Mechanical Engineering Requirements

SAND is composed of a superconducting magnet and an electromagnetic calorimeter (ECAL) reused from the KLOE experiment at the DAΦNE Φ-factory, along with a target/tracking system that is newly designed and developed for the DUNE ND. The components from KLOE will first be decommissioned, refurbished, and tested at Istituto Nazionale di Fisica Nucleare (INFN) before shipping. To facilitate this decommissioning process, many mechanical tooling structures and fixtures are to be refurbished or newly designed and constructed, and then shipped together with the detector components to be used for installation tasks in DUNE-ND hall. Specialized tooling, fixtures, platforms, test apparatus, and materials to perform assembly and installation tasks will also be provided for each of the detector systems. This approach will help ensure that the project's installation schedule is clearly laid out.

All mechanical components, their assembly, and functionality will be evaluated following the guidelines described in FESHM 2100 [89]. Relevant FESHM chapters are:

- FESHM 5100: Structural Safety;
- FESHM 10100: Overhead Cranes and Hoists;
- FESHM 10110: Below-the-Hook Lifting Devices;
- FESHM 10120: Powered Industrial Trucks;
- FESHM 10130: Slings and Rigging Hardware;
- FESHM 10200: Lift Plans; and
- FESHM 10210: Equipment Transport.

Figure 10.2 (a) shows the KLOE ECAL disassembly platform, a special scaffolding necessary for the disassembly and reassembly of the detector with the barrel module extraction/insertion tooling set up on the platform floor. Figure 10.2 (b) shows the frames refurbished for handling ECAL end-cap modules for dismount and transport.

10.2.3 Electrical Engineering Requirements

The KLOE detector operated at the INFN Laboratori Nazionali di Frascati, Italy, and thus all electrical power distribution and equipment adhered to European standards. With the move of the

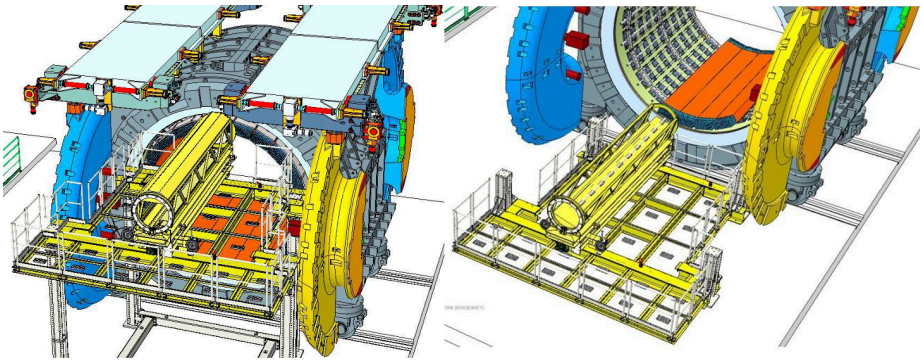


Figure 10.2: (a-left) KLOE ECAL disassembly/assembly platform and barrel module extraction/insertion tooling; (b-right) same as (a-left) with the platform and the extraction/insertion tooling positioned at a lower level.

detector to the Fermilab site, all power distribution must be replaced to adhere to North American standards and comply with the National Electrical Code (NEC). In addition, Fermilab provides several FESHM chapters that are relevant.

All commercially powered equipment should be approved by a US nationally recognized testing laboratory (NRTL) and be installed and used in accordance with the listing. International code equivalencies or codes with reduced inspection requirements are listed in the technical appendix of FESHM 9110: Electrical Utilization Equipment Safety. For all unlisted or non-NRTL electrical equipment, FESHM 9111: Approval of Unlisted Electrical Equipment provides the steps required for evaluation and approval by the Electrical Authority Having Jurisdiction (AHJ).

Custom electronics will be reviewed according to the FESHM 9000 Electrical Safety chapters [89], Fermilab's Electrical Design Standards for Electronics in Experimental Apparatus [**?**], and Fermilab's Electrical Safety ORC Review Guidelines [90]. Custom electronics are defined as any powered equipment that is not commercially available and includes all printed circuit boards, chassis that contain a collection of commercial/custom electronics with internal wiring completed by the user, any commercial equipment with a modification, and any equipment that does not have an NRTL seal. Where an NRTL approved version of an item of equipment does not exist, the procedure set out in FESHM 9111 shall be applied.

For each electrical system (or subsystem), a documentation set should be produced that contains the required list of documents demonstrating that the equipment has been designed and assembled

while respecting safety principles, and that it can be installed, commissioned, operated, and then dismantled safely.

The contents of the documentation shall include:

- Objective of the analysis and scope of the equipment to be analyzed;
- References to design codes or standards that are utilized in the analysis;
- Personnel and qualifications carrying out the analysis;
- A system (or subsystem) level block diagram showing the entire planned installation, including both commercial and custom components. It must include any wire or cable connections with detailed information on wire or cable sizes (AWG or mm^2), lengths, and connectors;
- Analysis showing all system level power paths provides appropriately sized fuses, wires/cables, and connectors;
- Complete schematics of any custom printed circuit boards, along with layout files and a detailed analysis of any power paths or power planes used, must document the use of fuses. If fuses are not used, a note on why they are not required must be provided;
- Identification of any high voltage paths;
- Adherence to electric and mechanical tolerances on all connections; and
- Information on all commercial equipment, including NRTL or equivalent ratings.

These documents shall cover the operational lifetime of the concerned equipment or detector. The versioning of these documents should be maintained and controlled on engineering document management system (EDMS). The documentation provided must contain sufficient detail so that results are reproducible and peer-reviewable.

10.3 Transport and Handling

The delivery of the various SAND detector components to the Fermi National Accelerator Laboratory (Fermilab) site will be the responsibility of the stakeholder or institutional group overseeing their fabrication, testing, and pre-assembly at external locations. Specifically, components of the KLOE detector — including the magnet, yoke, electromagnetic calorimeter (ECAL) modules, mechanical support structures, and assembly tools — will be shipped from the INFN Laboratory in Frascati, Italy, via one or more transport operations organized by INFN. Similarly, GRAIN subcomponents will be delivered from INFN Laboratori Nazionali di Legnaro (LNL) following testing and validation. The inner tracker modules will be transported from their respective integration sites following comparable procedures. Each institutional group is responsible for defining the technical specifications for the transport of their respective subsystems, including environmental constraints, packaging requirements, and handling tolerances. These specifications shall include pre-shipment checks, post-arrival acceptance protocols, and documentation required under the project-wide QA/QC framework.

The SAND-US working group is responsible for:

- Identifying appropriate delivery points and temporary storage areas at Fermilab,

- Coordinating internal transport and staging operations required for testing or partial assembly prior to underground installation,
- Maintaining the inventory of all delivered items, and
- Managing the global delivery schedule in coordination with DUNE planning milestones.

Release of the carrier at the point of delivery (Fermilab) is the responsibility of the contractor, who must confirm successful handoff and initiate the on-site acceptance process. All international shipments must comply with applicable Fermilab and U.S. Government procedures, including customs documentation, import/export control. The contributing institution is responsible for shipping arrangements, cost coverage, and ensuring traceable delivery through approved freight carriers. Coordination with Fermilab's Logistics and Shipping Office is required well in advance of shipping dates.

10.4 Experimental Hall and Facilities

The SAND detector will be installed in the near detector (ND) Cavern at Fermilab, a purpose-built underground facility designed to host the three DUNE near detectors: Near Detector Liquid Argon system (ND-LAr), Temporary Muon Spectrometer (TMS) (the muon spectrometer), and SAND. The hall provides the infrastructure, utilities, and mechanical access required for the transportation, installation, and long-term operation of these systems in proximity to the neutrino beamline. The ND Cavern is an underground structure located downstream of the LBNF beam target. It provides stable environmental conditions, crane coverage, and platforms (mezzanines at the north end of the cavern) to support both the installation and maintenance of detectors. Installation logistics for all major components — including handling constraints and sequencing — are discussed in detail here.

10.4.1 Detector Access and Transport Infrastructure

Delivery of components to the underground hall is carried out via the vertical shaft located at the north end of the facility. Components are transferred from surface-level staging areas into the shaft using the surface building crane (Figure 10.3). For items whose weight exceeds the 15 t capacity of this crane—such as the SAND magnet or parts of the iron yoke—external lifting solutions will be deployed (e.g., mobile or crawler cranes) to lower components directly into the shaft. Once underground, final positioning and assembly operations benefit from the coverage of the 60 t overhead crane installed in the main hall. This crane supports the lifting and rigging of heavy subassemblies within the integration envelope. In addition, a set of floor-mounted rails enables the displacement of partially or fully assembled detectors, allowing flexible reconfiguration during staged installation phases or future maintenance interventions (Figure 10.6).

10.4.2 Space Allocation and Infrastructure Interfaces

The hall layout allocates dedicated volumes to each of the three detectors, with corresponding footprints, access clearances, and service corridors. SAND occupies the downstream-most position in the hall (the alcove) and shares common access paths with the adjacent TMS system. Interface control between detector systems is coordinated through the DUNE ND integration team.

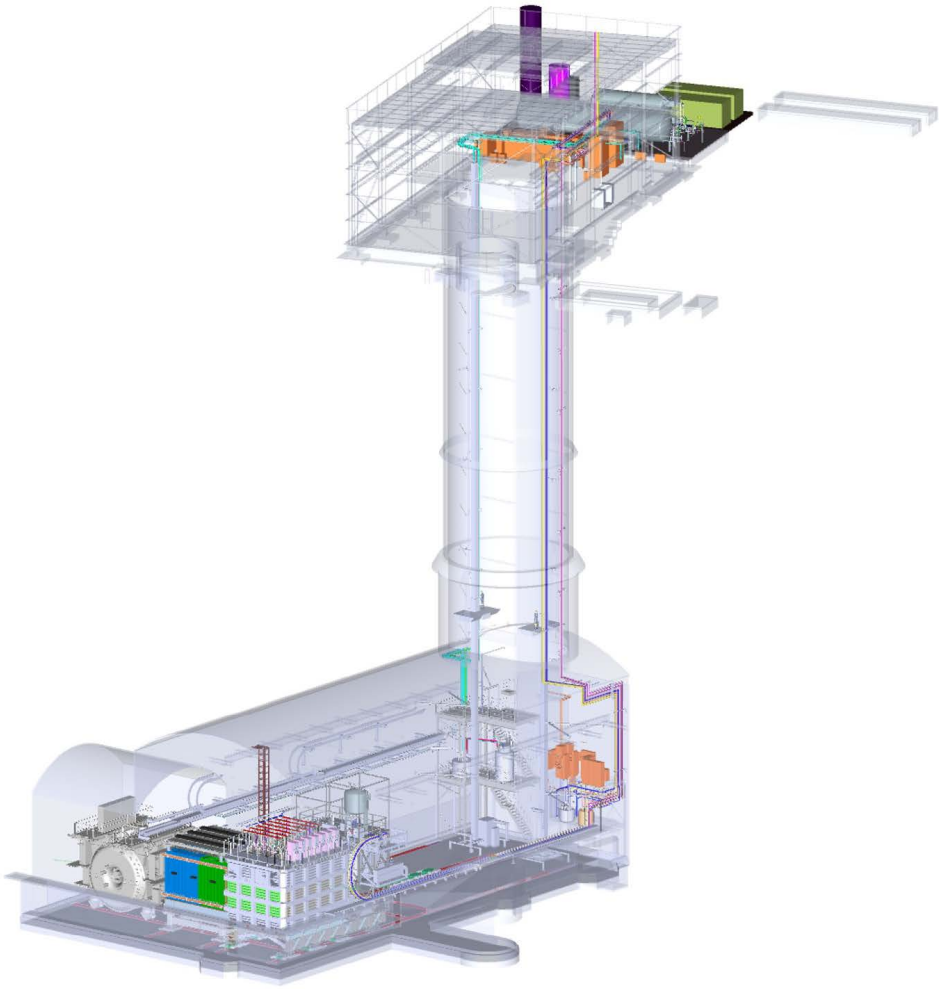


Figure 10.3: 3D Model of the ND experimental facility. The surface building, the shaft, and the underground hall are shown.

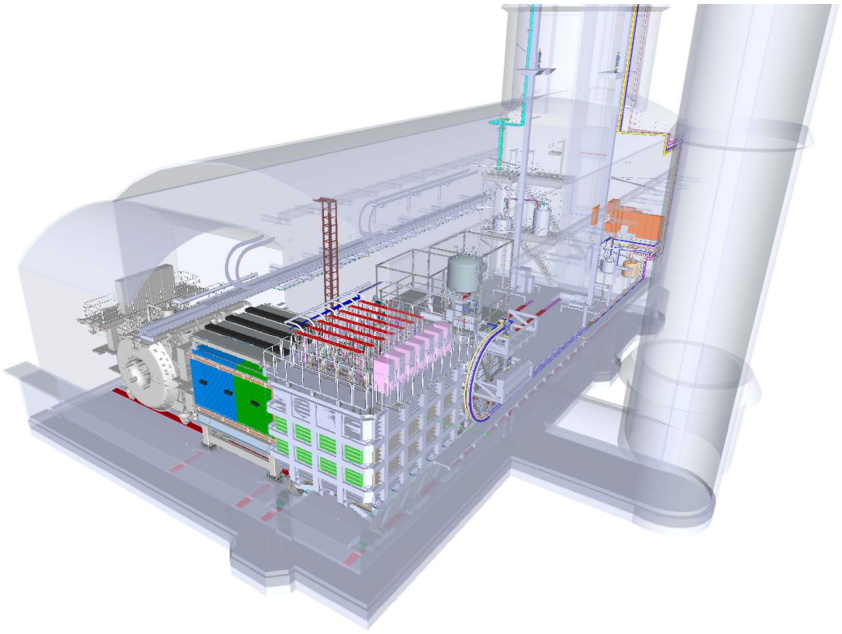


Figure 10.4: 3D Model of the ND experimental facility. The underground hall with the three detectors all positioned on-axis is shown with SAND at the leftmost end; the vertical emergency egress is visible on the right.

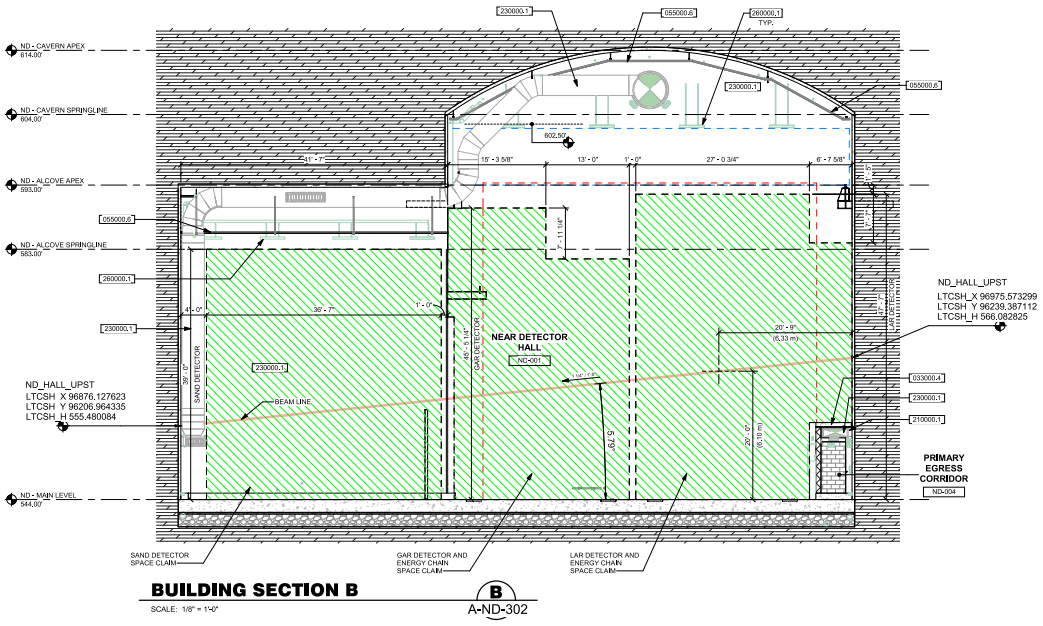


Figure 10.5: Side view of the ND Cavern as seen from the north side. The space assigned to the three detectors (SAND, TMS, and ND-LAr, from left to right) is indicated by the green shaded areas.

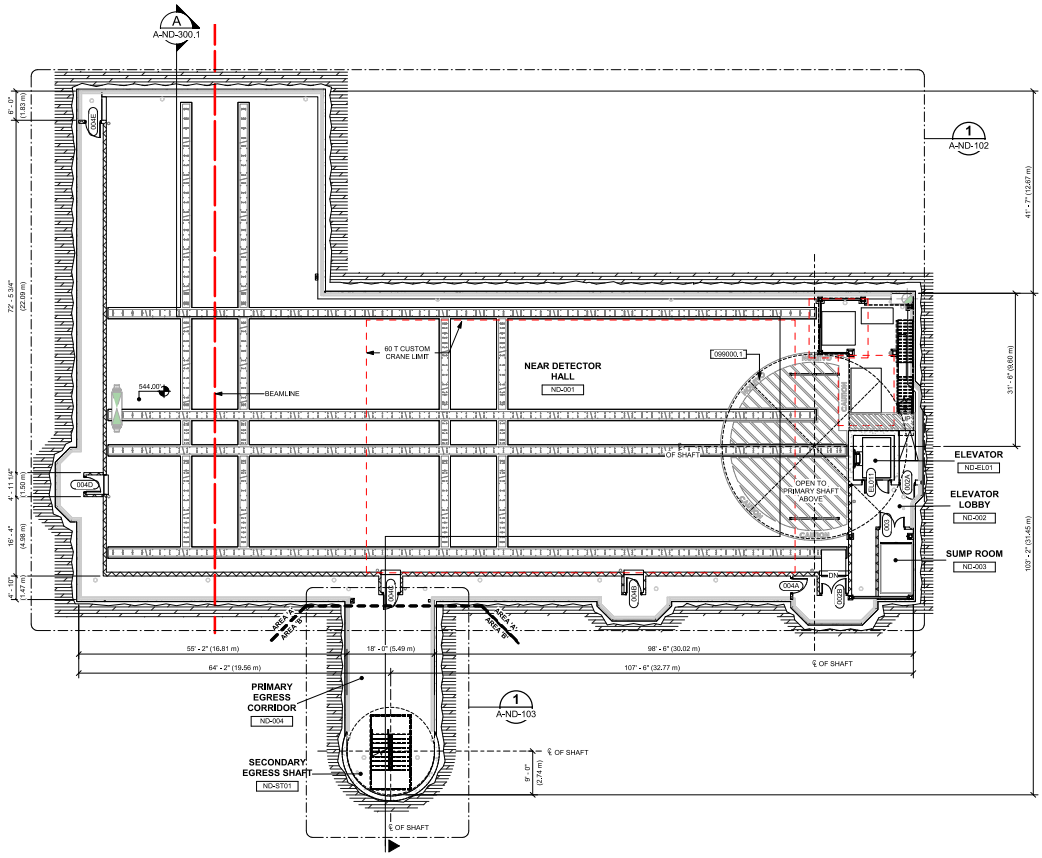


Figure 10.6: Plan view of the ND Cavern. The rail system used for movement of the three detectors is shown. The location of SAND is in the alcove at the top left of the L-shaped floor plan. The beam axis is indicated by the red dashed line.

The ND I&I team provides anchor points, survey monuments, and alignment infrastructure to support detector positioning within the beam coordinate system. Detailed dimensional constraints, access envelopes, and interference mitigation strategies are discussed here.

10.4.3 Facility Services and Utilities

The ND Hall is equipped with the following infrastructure elements relevant to SAND:

- Electrical power: Power panels are available at various locations in the cavern to support the detector installation (welding, power tools, etc.; Figure 10.7). To operate, SAND is provided with dedicated 480 V lines and a separate clean ground (detector ground). Step down transformers, service panels, and power distribution to the experiment are deliverables of the SAND-US group.
- Data and network connectivity: Ethernet and timing links are routed to the hall from the surface-level control rooms and the global DUNE timing system.
- Ambient conditions: The hall is maintained at stable temperature and humidity levels suitable for detector operation and electronics performance.
- Cryogenic and gas systems: These are primarily utilized by other detectors (e.g., ND-LAr); SAND relies on the facility for the supply of liquid nitrogen and compressed air. The helium system required for the operation of the magnet described in Section 10.5 is a deliverable of the SAND Consortium, as well as the gas system required by the inner tracker.
- Lifting systems: The ND Hall includes multiple lifting systems to support installation and maintenance activities.
  - A 60 t overhead bridge crane spans the main hall and serves shared operations across all three detectors. In addition,
  - a dedicated 5 t crane is installed in the alcove area where the SAND detector is located, enabling localized handling of subcomponents during detector integration and future servicing. The dedicated crane is a deliverable of the SAND-US group.
  - Mobile lifting equipment, such as forklifts, scissor lifts, and portable rigging systems, will either be available as part of the facility or rented as needed. These tools facilitate the movement of smaller assemblies, enable vertical access during installation, and support component alignment and fastening procedures in areas beyond crane reach.

10.4.4 Environmental and Safety Considerations

The hall is equipped with safety systems in compliance with Fermilab's ES&H requirements, including:

- Emergency lighting and egress pathways (Figure 10.8)
- Fire detection and suppression
- Oxygen Deficiency Hazard (ODH) monitoring (primarily for cryogenic systems)
- Access control points for personnel and equipment
- Alignment with the operational readiness clearance (ORC) protocols

DRAFT

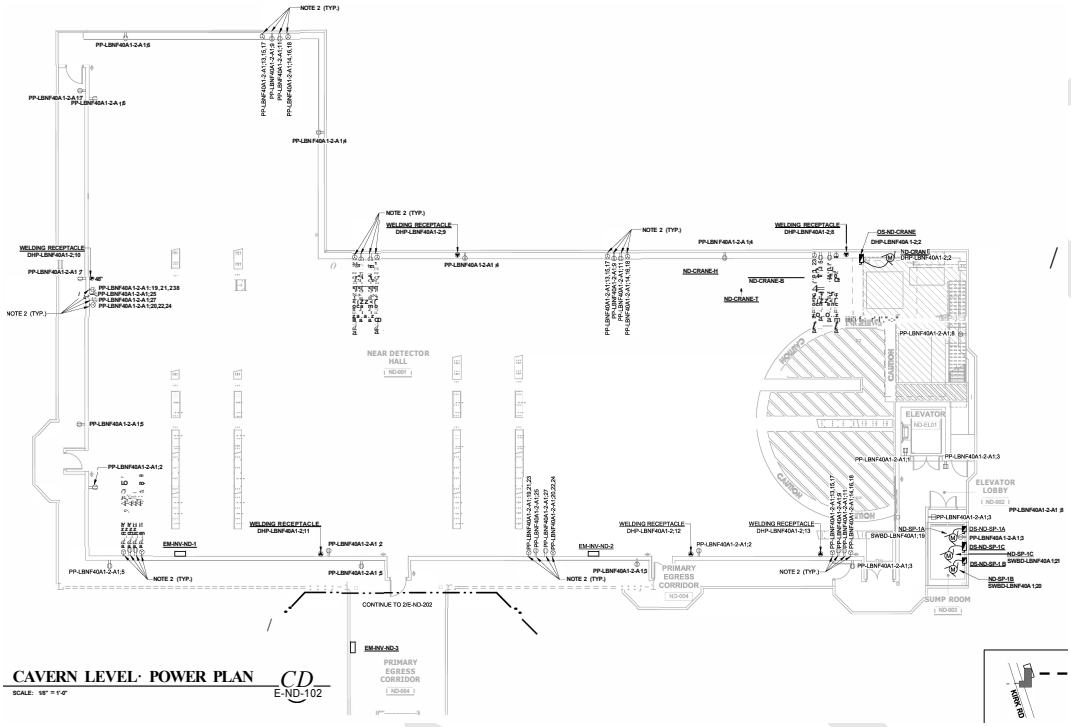


Figure 10.7: Plan of the ND underground hall showing the position and type of electrical outlets.

No additional construction or upgrades to the facility infrastructure are required for the installation of SAND beyond what is already planned for the DUNE ND complex.

10.5 Helium Cryogenics and Distribution

The SAND helium cryogenic system is primarily composed of a helium refrigerator system, a SAND distribution valve box (SAND VB) with a built-in helium sub-cooler, vacuum-jacketed cryogen transfer lines (VJTLs), a warm piping and valve system, gaseous helium storage and buffer tanks, instruments, a monitoring and control system, and a cryo-safety system, including a safety relief system and ODH analysis. A liquid nitrogen system supplied by the ND Cryogenics liquid argon system will provide liquid nitrogen for precooling the helium refrigerator cold boxes. The SAND helium system will share an LN2 phase separator with the ND LAr system.

This section presents the preliminary design of the SAND helium cryogenic system, including the design scheme, process flow diagram, heat load estimates, layout plan, and so forth.

10.5.1 Cooling Requirements

The SAND magnet is an iron shielded superconducting solenoid coil indirectly cooled by a liquid helium thermosiphon cycle. The cryostat of SAND solenoid possesses its own local valve box (called the Service Turret) that includes a Joule-Thomson (JT) valve and a liquid helium reservoir of about 150 liter. All the controls associated with magnet functioning, including cooldown and warm up, are an integral part of the magnet system. Table 10.1 summarizes the main parameters of the SAND solenoid and its cryostat [22, 91].

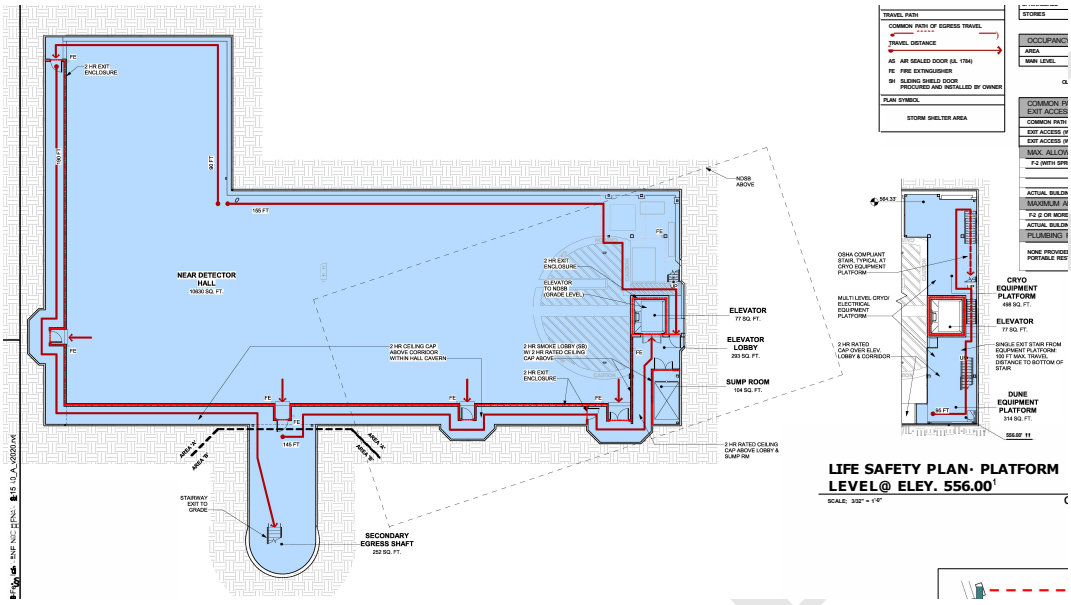


Figure 10.8: Plan of the ND underground hall showing ingress and egress pathways.

Coil assembly	
Central Field (T)	0.6
Layers	2
Turns/layer	368
Ampere-turns	2.14 MA-T
Operating/Design Current (A)	2902/3000
Inductance at full field (H)	3.4
Stored energy (MJ)	14.32
Discharge voltage (V)	250
Peak Quench Temperature (K)	80
Conductor	10 mm × 5 mm Al stabilized NbTi Rutherford cable, wrapped with two half lapped layers of 0.125 mm glass tape
Coil winding method	internally wound coil
Coil support bobbin	5083 Aluminium cylinder
Coil shell inner diameter (m)	5.19
Coil Cold mass (t)	~ 8.5
Radiation shield	two 5 mm thick solid aluminum cylinders with cooling pipes attached to the outside of each
Service Turret	supply and control of LHe including JT valve, supply and control of 70 K helium for radiation shields, gas cooled 3 kA current leads, Instrumentation connections to the coil and radiation screens, LHe reservoir: $\sim$ 150 liter

Table 10.1: Main parameters of SAND magnet and its cryostat with service turret.

Coil cooling scheme	Indirectly cooled through a LHe thermosiphon cycle; gaseous helium at 5.2 K is injected at 3 bara from the helium refrigerator and liquefied through a Joule-Thomson valve into a LHe reservoir
Thermal shield cooling method	cooled by 50-70 K forced gas helium flow from the helium refrigerator system
Current leads	A pair of 3 kA leads, cooled directly by liquid helium from LHe reservoir in the Turret, 300 K GHe returns to the suction side of helium recycle compressor of the refrigerator system
4 K heat radiation and conduction (W)	55
Current leads' GHe cooling flow (g/s)	0.4 (test data)
70 K heat radiation and conduction (W)	530
Operating temperature (K)	4.42-4.5
Operating pressure (bara)	1.2-1.3
300-70 K cool down scheme	300 K and 70 K GHe mixing forced flow, 4-5 bara, $\sim$ 2 weeks
70-4 K cool down scheme	5.2 K 3 bara GHe forced flow, $\sim$ 1 week

Table 10.2: Cooling requirements of SAND magnet.

Table 10.2 presents the cooling requirements of SAND magnet [92].

10.5.2 Design Scheme

Figure 10.10 shows the preliminary design of the process flow diagram (PFD) of the SAND helium cryogenic system. The design allows for the sharing of external helium tanks and truck supply with a second magnet in the system as part of a future upgrade; otherwise, the helium circuit would be completely dedicated to SAND.

The SAND magnet and the local KLOE valve box, connected with a multiple-channel vacuum jacketed helium transfer line (5-in-1 multi-channel transfer line (MCTL)), will be supplied by INFN, Italy. The 5-in-1 MCTL is used for the connection between the KLOE valve box and the SAND magnet service turret. The KLOE valve box connects the 5-in-1 MCTL to a 4-in-1 MCTL from the refrigeration system located near the access shaft. The 5-in-1 MCTL is composed of a 70 K GHe supply line, a 80 K GHe return, a 3 bara/5 K supercritical helium (SHe) supply line, a 4.4-4.5 K return line, a 300-10 K cooldown GHe return line, and vacuum piping to enclose all five lines in it [92]. The helium cryo system will provide the SAND magnet with the following streams of helium gas:

- Supercritical Helium (SHe) at 5.2 K and pressure 3 bara. Inside the service turret on top

of the magnet cryostat, after the final expansion from 3 bara to 1.3 bara, the liquid helium necessary for the operation of the superconducting magnet is collected in the liquid helium reservoir and then delivered to the magnet by a thermosiphon circuit. LHe is used to cool the magnet down from 70-100 K to around 5 K and then maintain that temperature.

- Helium gas at intermediate temperatures (50-70 K, 4-5 bara) is necessary for cooling the magnet from room temperature to 70-100 K and for operating the 70 K thermal radiation shields of the magnets.
- Helium gas at room temperature ($\sim$ 300 K, 13-15 bara, and 4-5 bara): necessary for purging and pumping the entire cryogenic system and cooling down the magnets from room temperature to 70-100 K through mixing with 70 K GHe.

The multi-channel vacuum jacketed helium transfer line (4-in-1 MCTL), connecting the refrigerator system with the magnet, is about 55 m long. The heat load generated by the MCTL is estimated to be about 27.5 W. The heat load from the MCTL will cause an increase in the temperature of the supercritical helium before the JT valve in the magnet service turret, which will result in insufficient liquid helium production through the JT valve to cool the magnet. One liquid helium vessel with a built-in heat exchanger is used to cool the supercritical helium delivered from the cold box to the magnet at a temperature lower than 5 K. The built-in heat exchanger is made of a coiled copper tube and is called the LHe subcooler.

10.5.3 Operation Modes

The SAND helium cryo system is designed to implement the following operational modes and protect the SAND magnet from damage in various failure situations:

- Cool down:
  1. to cool down the magnet and thermal shields from room temperature to 70-100 K (300-77 K mode) by mixed 300 K and 70 K forced GHe flow;
  2. to cool down the magnet and current leads from 70-100 K to 4.4 K (77-4 K mode) by supercritical helium flow, and the thermal shields will be kept cooled at 70 K by 70 K GHe flow.
- Steady state operation: to continuously provide the necessary cooling capacity and support the SAND magnet during stable operation.
- Quench process: The quench phenomenon is the sudden return to a condition of normal conductivity in a superconducting conductor. During the quench process, the joule heating of the conductor, caused by its electrical resistance and the discharge into the magnet of the energy stored in the magnetic field generated by it, leads to very rapid and significant overheating of the superconducting coil, which likely results in permanent damage to the magnet. All the liquid helium contained in the magnet undergoes dramatic and sudden evaporation (e.g., within a few seconds) to absorb the heat generated by the magnet and keep it from burning out. Once a quench occurs, the magnet stops operating and must be placed in a safe situation. As shown in Table 10.1, the stored energy of the SAND magnet is 14.32 MJ and its peak quench temperature is 80 K.
- Re-cool down after quench: After the quench, the magnet can be re-cooled to a superconducting condition and then fully re-energized.

DRAFT

- Warm up: Bring the magnet from 4 K to 300 K, respecting the thermal constraints of the magnet.
- Failure modes include the following possible scenarios: power outage, loss of insulating vacuum, refrigerator malfunction, and so forth; the cryo system and SAND magnet will be placed in a safe situation during various failure modes.

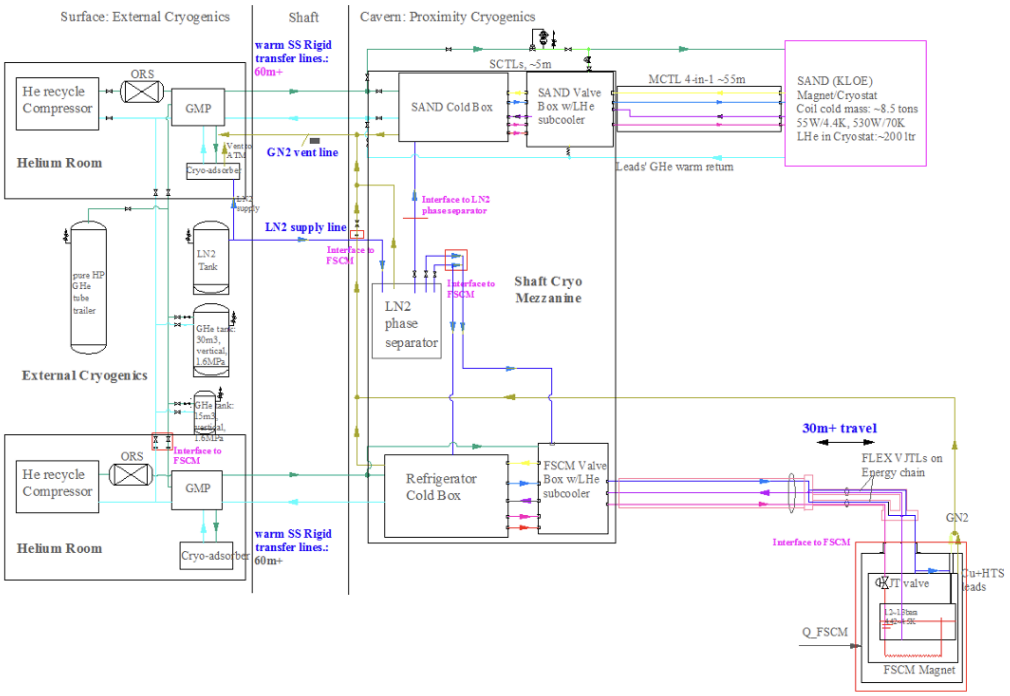


Figure 10.9: Design scheme of DUNE NS helium cryo system

10.5.4 Cryogenic Facilities

As shown in Figure 10.10, the SAND helium cryo system is primarily composed of:

- A customized helium refrigerator system with a cold box that incorporates liquid nitrogen pre-cooling and advanced turbine expanders. The cold box is customized with controls and ports of 70 K GHe supply, 80 K GHe return, 3 bara supercritical helium supply, 4.4 K LHe supply, and 4.4 K GHe return. The refrigerator scope of supply also includes a single water-cooled, oil-flooded screw compressor, an oil removal skid, a gaseous helium management panel, and a cryo-adsorber.
- A SAND distribution valve box with a built-in LHe subcooler (100-150 liter): its functions could be integrated into the refrigerator cold box.
- Single-channel vacuum-jacketed helium cryo-transfer lines (SCTLs, $\sim$ 5 m long) between the cold box and SAND VB include: one 5 K 3 bara supercritical helium supply, one 4.4 K liquid helium supply to the LHe subcooled vessel, one 4.4-4.5 K 1.2-1.3 bara gas helium return from the coil, one 50-70 K gas helium supply for cooldown & thermal shields, and one 60-80 K gas helium return from the thermal shields.
- The refrigerator cold box (CB) precooling liquid nitrogen supply SCTL ($\sim$ 20 m long) and cold gas nitrogen return SCTL ($\sim$ 20 m long) are situated between the LN2 phase separator

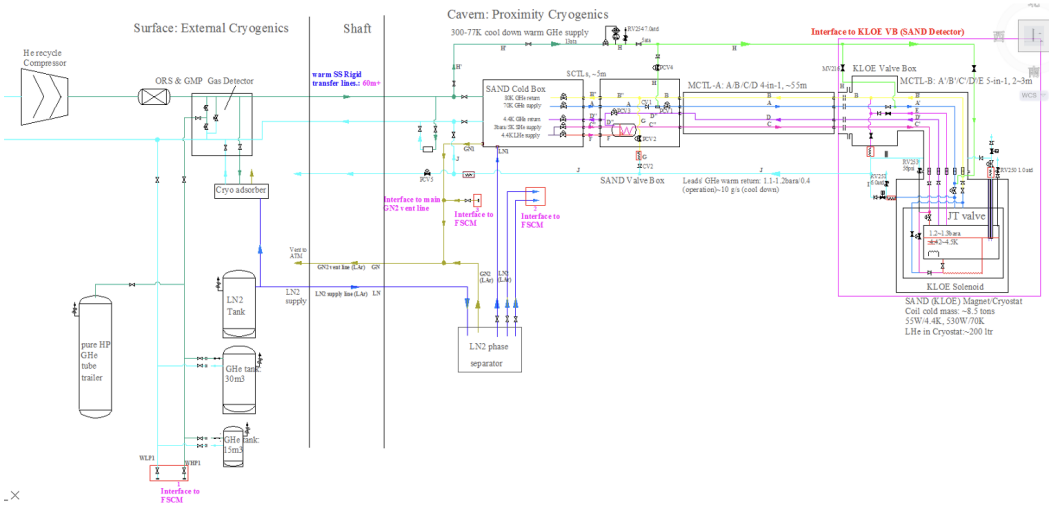


Figure 10.10: Preliminary PFD of DUNE NS SAND helium cryo system

and the CB.

- A 4-in-1 MCTL between SAND VB and local KLOE VB (∼ 55 m long) includes: one 5 K/3 bara supercritical helium supply, one 4.4-4.5 K/1.2-1.3 bara gas helium return from the coil, one 50-70 K gas helium supply for cooldown & thermal shields, one 60-80 K gas helium return from thermal shields, and the above four cryo-lines are enclosed in a warm vacuum jacket. The 60-80 K gas helium return will also be used for cooling the intermediate temperature thermal shield in the MCTL to reduce the heat load to 4 K lines.
- Warm GHe piping and valve system runs 60 m deep from the Surface building through the Shaft into the Cavern. It includes 300 K/13 bara compressor discharge, 5 bara gas helium used for cooldown, pumping, and backfill, and 300 K 1.05-1.3 bara gas helium low pressure return from leads, quench, cooldown, any failure, etc.
- Gas helium storage/buffer tanks: vertical, one 15 m^3 and one 30 m^3, 1.6 MPa design pressure.
- Instrumentation, gas analysis, controls, and human-machine interfaces.
- Cryo-safety features, including an overpressure relief system and Oxygen Deficiency Hazard (ODH) mitigation.

10.5.5 Layout Plan

Figure 10.11 shows the overall layout plan of the NS LHe cryo system. Two GHe storage/buffer tanks and a helium compressor system will be located outside, near the surface building. The warm helium recycle compressor (WCS), oil removal system, gas management panel (ORS & GMP), control cabinet of the WCS & ORS, and external LN2-cooled cryo-adsorber will be accommodated in the surface Helium Room. The cryogenic facilities, including the cold box (CB), SAND VB, and LN2 phase separator, will be located on the Cryo-Mezzanine in the underground Cavern. The shaft connecting the ground and underground is more than 60 m deep. Underground, the horizontal distance between the refrigerator and the SAND magnet is at least 30 m.

DRAFT

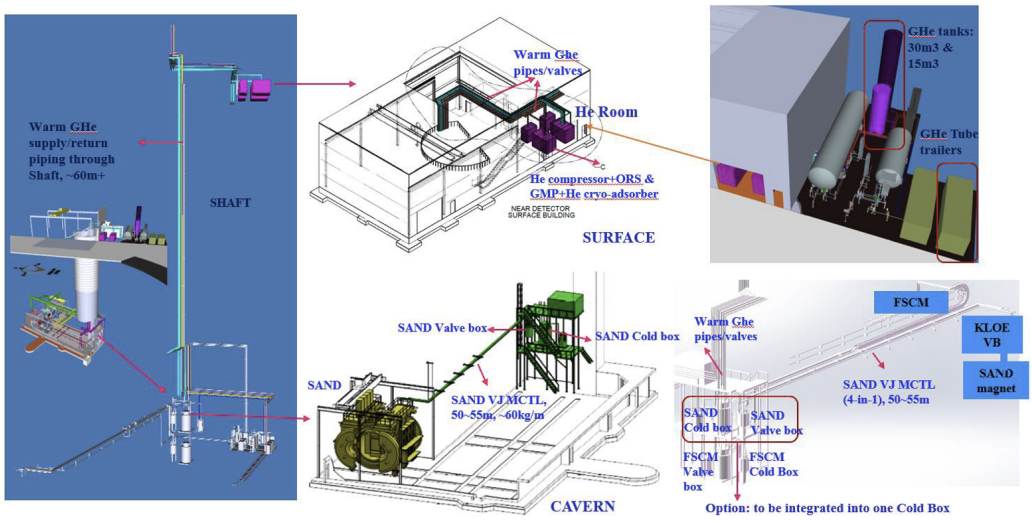


Figure 10.11: Overall layout plan of the NS Cryo LHe cryo system.

10.5.6 Estimated Heat Loads

Tables 10.3 and 10.4 present the estimated heat loads based on the current preliminary design of the SAND helium cryogenic system. Based on tables 10.3 and 10.4, the required cooling capacity is summarized as follows:

- $\geq 120\,\mathrm{W}$ at $4.4\,\mathrm{K}$
- $0.4\,\mathrm{g/s}$ GHe flow for cooling current leads
- $\geq 811\,\mathrm{W}$ at $70\,\mathrm{K}$

Table 10.3: Estimates of heat loads at 4 K

	q_{4K} (W/m)	L (m)	Q_{4K} (W)
Single rigid cryo-transfer lines between CB & SAND VB	0.50	5.0	2.5
	0.50	5.0	2.5
	0.50	5.0	2.5
4-in-1 Multi-channel Rigid cryo-transfer lines	0.50	55	27.5
dshortsand VB			7.7
Sub-total			42.7
Sub-total Heat load from transfer system w/50% contingency			64.0
SAND (KLOE) cryostat & turret			55.0
Sub-total 4 K load			119.0
3 KA Current leads' cooling flow		one pair	0.4 g/s
4 K total heat load w/contingency			153.0

10.5.7 Final Remarks about Cryogenic Helium System

The preliminary design of the Long-Baseline Neutrino Facility (LBNF)/DUNE-US Near Site helium cryogenic system to support the SAND magnet has been carried out since December 2019.

Table 10.4: Estimates of heat loads at 70 K

	q_{70K} (W/m)	L (m)	Q_{70K} (W)
Single rigid cryo-transfer lines between CB & SAND VB	0.50	5.0	2.5
	0.66	5.0	3.3
4-in-1 Multi-channel Rigid cryo-transfer lines	3.0	55	165.0
SAND VB			16.5
Sub-total			187.3
Sub-total Heat load from transfer system w/50% contingency			281.0
SAND (KLOE) cryostat & turret			530.0
70 K total heat load w/contingency			811.0

The design scheme for the NS cryo helium system was proposed, discussed, and studied. The preliminary P&IDs were designed, the preliminary layout plans were developed, and the preliminary calculations and analyzes were performed. A preliminary study of the interfaces, not presented in this document, has been carried out and is reported in [93]. At present, the final design is being carried out. Some modifications to the layout presented in the previous pages are being discussed.

10.6 Installation Sequence

While the design of SAND allows it to be assembled in any order with respect to the the other near detectors, construction will be easiest if it is built first. The first step will be preparation of the hall which includes construction of a crane in the SAND alcove and installation of the cryogenic transfer lines (see Section 10.5.4), electric power feed, and other services below the corbels that support the TMS energy chain. After that, the detector can be assembled in the main cavern. Electric distribution equipment can be installed in the alcove in parallel with the detector assembly in the main cavern, as will the installation of the liquid helium compressor, tanks, purifier, and associated piping and instrumentation.

Figure 10.12 shows a pictorial representation of the assembly activities in the main cavern up to the detector move in the alcove. The first step is to assemble the main portion of the yoke. At that point, the solenoid will be lowered through the shaft. The ND service building is constructed with a removable hatch. The solenoid will be lifted from a truck and lowered through the hatch down the shaft. The 60 t crane in the cavern can be used to position it for insertion. After the solenoid is inserted, the end pieces of the central yoke will be attached. The barrel ECAL modules will be inserted using custom fixtures. The yoke end caps can then be bolted to the yoke and to each other. After they are in position, the upper platforms that contain the cranes to move the endcaps are installed. The endcaps are opened, and the endcap ECAL modules are attached to the yoke pieces. After the tracker support frame is installed (not shown), the detector is ready to move to the alcove. The total duration to this point is estimated to be 9 months.

Local cryogenic elements, instrumentation, and controls; GRAIN; and the tracker modules can be installed either in the main cavern or in the alcove, depending on the space considerations of the other detectors in the cavern. Once the detector is in the cavern, electronics racks and equipment can be installed on the platforms on the upstream and downstream side of the magnet yoke, and

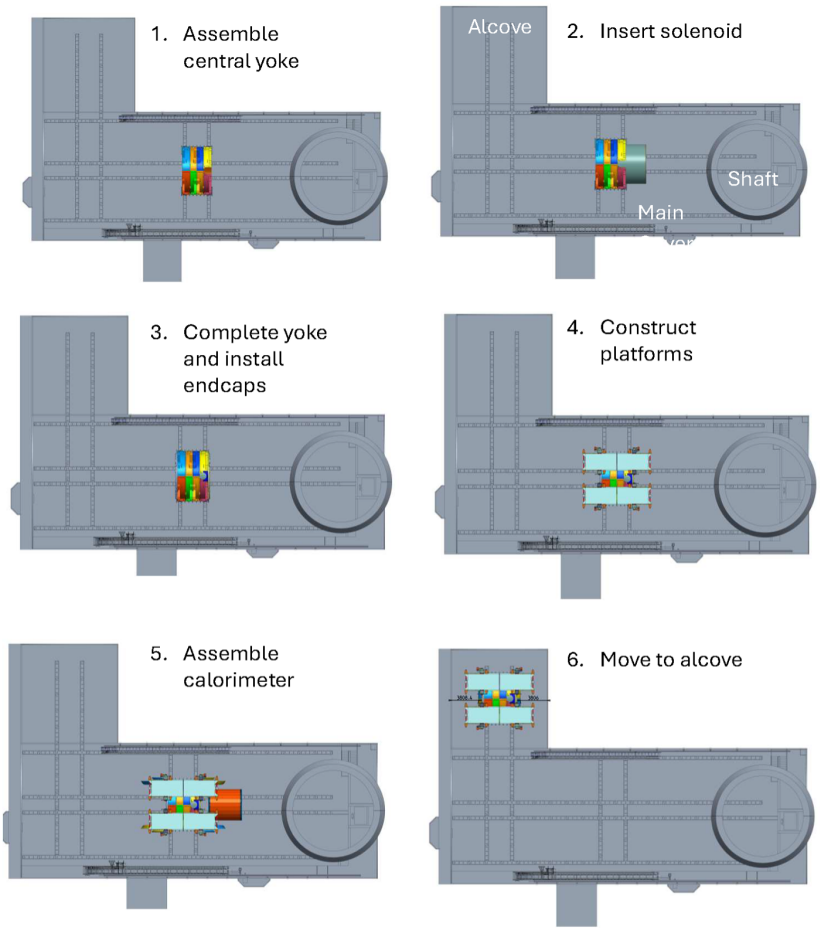


Figure 10.12: Assembly sequence for SAND described in the text.

the detectors can also be cabled up to the readout crates and power supplies. The magnet power supply will be installed on the upstream platform with a low-conductivity water skid nearby. The GRAIN cryogenics will be installed with elements both at the top of the magnet and on the floor. The tracker gas circulation system will be installed on the downstream platform.

In parallel with work in the alcove, the liquid helium coldbox can be installed on the mezzanine and connected to the MCTL. Installation of the piping in the vertical shaft will be coordinated with similar work by ND-LAr as this work will render the shaft inaccessible for deliveries to the cavern.

While electronics can largely be tested as they are installed on a channel-by-channel level, integrated testing of all systems is expected to take sseveral months. A significant commissioning period will also be required for the magnet. All told the commissioning period after installation that is required to be ready for phyics-quality data is expected to be about nine months.

10.7 Critical and Engineered Lifts

According to FESHM 10200 (Lift Plans), a critical lift is defined as a lift that meets any of the following:

- Loss of control of the item being lifted would likely result in the declaration of an emergency.
- The load or item is unique, and if damaged, would be irreplaceable or non-repairable. It is vital to the operation of the system, facility, or project.
- The cost to replace or repair the damaged load item would have a negative impact on the facility, organizational, or DOE budgets to the extent that it would affect program commitments.
- Lifts made with more than one crane or forklift.
  - Exception: a tandem lift with synchronized overhead cranes that utilizes one controller, as long as the item being lifted does not meet any other critical lift criteria.
- Lifts made near electrical, ground, or overhead utilities.
- The lift involves a non-routine or technically difficult rigging arrangement.
- Lifts over items that are considered critical to the lab.
- For steel erection, a lift shall be designated as a critical lift if:
  - The lift exceeds 75% of the rated capacity of the crane, or
  - The lift requires the use of more than one crane.

A Critical Lift designation will require the following:

- Documented step-by-step instructions (according to FESHM 10200, Section 5.4);
- Sign-off approvals from the lift director, technical approver, ESH representative, Division and Section management, Project management, and the qualified operator;
- Independent pre-identification of load weight, load center of gravity, lift attachment points,

and minimum capacities of lifting hardware (slings, below-the-hook lifting devices, shackles, etc.) that will be used for the lift or series of lifts;

- Independent pre-identification of crane(s) or forklift(s) with minimum capacities identified for the configuration to be used;
- Evaluation of hazards associated with the lift may include, but is not limited to, environmental factors, ground support, power lines, and physical obstructions;
- Pre-identified special limiting or stop-work conditions.

Moving components through the shaft from ground level to the underground hall, given the height of the lift, is always considered a critical lift. Procedures for these lifts are developed by the ND I&I team. Installation of most of SAND's components in the underground hall will require a critical lift. Lift plans are developed by the SAND-US WG in cooperation with the relevant SAND WG and any involved companies. Assembly procedures, including lift plans, for the yoke and the magnet will be developed in cooperation with the company in charge of the disassembly in Frascati, which will also be contracted by INFN for the reassembly at Fermilab. Similarly, assembly procedures and lift plans for the ECAL modules, the related platform, and specialized tools will be developed in cooperation with the ECAL WG by retracing and appropriately analyzing the steps of the disassembly activities in Frascati.

The installation of the support structure for the Inner Tracker and GRAIN also requires a lift plan in view of the risk of damage to ECAL modules. The installation in the alcove of the Inner Tracker modules and of the GRAIN main cryostat containing the GRAIN detector will require specialized tools. Appropriate lift plans and procedures will be developed for moving the Inner Tracker modules and GRAIN in proximity to the alcove, securing them in the specialized tools, and moving them inside the support structure to their final position. The installation of the magnet's power supply and the quench protection system will also require a lift plan, given the delicacy, cost, and long lead time required for replacing or repairing the equipment. Lift plans for additional, non-critical equipment (e.g., GRAIN's cryogenic and purification systems or electronic cabinets) will be developed on a case-by-case basis, also considering the status of installation and the risks of damaging already installed critical components.

10.8 Risks

Installation and integration activities are sensitive to risks in the following categories.

Interface compatibility among detector subsystems These risks are largely internal to the other working groups. The most significant interface between detector systems and I&I is space allocation. Given the detailed planning process, this is regarded as a low probability risk. Another risk between systems and I&I is related to power and cooling services provided to the systems. This risk is also a low probability for significant incompatibilities, given the extensive engineering reviews that are planned.

Schedule coordination across international partners There are two classes of risk within this category. The first is delays of the working group activities leading to delayed deliveries at Fermilab. In this case, I&I is impacted by upstream risks. These impacts should be cataloged

as part of those risks. Because the inner detector elements and all electronics and cabling are planned to be installed once SAND is in the alcove, there is considerable flexibility in reordering, and there should be no impact on the construction of the ND-LAr or TMS.

Logistics and transportation constraints The primary limitations on logistics and transportation are access to the shaft from the surface building to the near detector cavern and the minimal staging space available either on the surface near the ND hall or in the cavern. The principal risks are thus conflicts for access to these regions. While every incident is of low impact, the cumulative effect could be large. The mitigations are effective planning and possibly using a second shift for staging material for the next day's work.

Resource availability at Fermilab This category includes many risks, including:

- Availability of Fermilab engineering and technical staff;
- Funding for I&I activities;
- Limitations on partner personnel to work at Fermilab; and
- Availability of lab spaces for prep work on SAND equipment prior to installation.

These risks can be mitigated with effective planning and, in many cases, by reordering work.

Safety and regulatory compliance The work planning process outlined in FESHM chapter 2060 is used to identify hazards associated with all work. As planning for installation progresses, these work plans will be written and fleshed out to account for safety risks.

10.9 Safety

The SAND activity is currently taking place — and will continue to take place — in several laboratories, including Fermilab, LNF, CERN, and others. Each country and each laboratory has its own set of rules aimed at preventing any type of injury. The SAND activity is, and will remain, in full compliance with these rules. The management ensures that all personnel are fully informed about the current safety regulations in each laboratory and that all necessary measures are implemented to guarantee proper adherence to these rules. In addition, all personnel are provided with the appropriate personal protective equipment required to perform their tasks safely.

This section focuses on safety at Fermilab, where SAND will be assembled and will conduct data acquisition for years to come.

The SAND detector will be designed, built, commissioned, and operated following strict adherence to the Fermilab environment, safety, and health (ES&H) policies and the FESHM. Line managers and all affected employees are responsible for environmental stewardship and personal safety at the Batavia work site.

Fermilab and all other affected staff ensure that procedures are established to support the following ES&H policy statements:

DRAFT

- Line managers, supported by the ES&H organizations of Fermilab and other collaborating laboratories, will provide consistent guidance and enforcement of the ES&H program that governs the activities of workers at the SAND site where work is performed.
- Incidents, whether they involve injuries or damage to equipment, facilities, or the environment, can be prevented through the implementation of proper planning and controls. All SAND Project work is planned, and the plans are documented.
- Workers are involved in the work-planning process and continuous improvement, including the identification of hazards and controls.
- Working safely and complying with requirements are vital for a safe working environment. Line managers will enforce disciplinary policies for violations of safety rules.
- Each worker is responsible for their own safety and that of their co-workers. Teams looking out for each other create safe work environments.
- A strong program of independent audits, self-assessments, and surveillance will be employed to periodically evaluate the effectiveness of the ES&H program.
- Any incidents that result in, or could have resulted in, personal injury or illness, significant damage to buildings or equipment, or an impact on the environment will be investigated to determine corrective actions and lessons that can be applied to prevent recurrence. Fermilab encourages open reporting of errors and events.

Safety hazards associated with the SAND Detector are likely related to pressure systems involving both vessels and piping, cryogenic fluids, electrical systems, material movements, and magnetic fields. These hazards are mitigated by adherence to FESHM and to the codes and standards listed in Appendix A.

During the commissioning and operation of the SAND Project. Workers may encounter hazardous conditions and/or emergencies that require resources greater than those available on site. Call ext. 3131 from a lab phone (630-840-3131 from a cell phone) in the event of an emergency situation, such as personnel requiring medical treatment for any reason.

All emergencies must be reported to the Division Safety Officer (DSO) and line management to ensure proper mitigatory efforts are implemented to either eliminate the problem or identify corrective actions that will be tracked to closure. Some emergencies or events may require additional reporting, such as alerting the Event Review Team (ERT). FESHM 3010 outlines additional information on workplace occurrence reporting. As always, questions regarding reporting or actions to take after an incident can be routed directly to the DSO.

DRAFT

Appendix A

Engineering Codes and Standards

DRAFT

Code/Std	Title	Pub. Date	Assoc'd FESHM Chapter (if applicable)
AA ADM-2020	Aluminum Association - Aluminum Design Manual	2020	
ACI-318	Building Code Requirements for Structural Concrete	2019	FESHM 7080 Concrete Anchor Devices
ACI 355.2	Post-Installed Mechanical Anchors in Concrete	2022	FESHM 7080
AIA/NAS - NAS 1514	Radiographic Standard for Classification of Fusion Weld Discontinuities	2015	
AISC 325	Steel Construction Manual	2017	FESHM 5100 Structural Safety
ANSI/AISC 360	Specification for Structural Steel Buildings	2016	FESHM 5100
ANSI B56.1	Safety Standard for Low Lift and High Lift Trucks	2020	FESHM 10120 Powered Industrial Trucks (PITs)
ANSI B56.1	Safety Standard for Low Lift and High Lift Trucks	2020	FESHM 5031.5 Low Pressure Vessels and Fluid Containment
API 520	Sizing, Selection, and Installation of Pressure-relieving Devices	2020	FESHM 5031.5
ASCE-7	Minimum Design Loads and Associated Criteria for Buildings and Other Structures	2017	FESHM 5100, FESHM 7980
ASME A276	Standard Specification for Stainless Steel Bars and Shapes	2013	
ASME B30.20	Below The Hook Lifting Devices	2018	FESHM 10110 Below The Hook Lifting Devices
ASME B31.3	Process Piping	2021	FESHM 5031.1 Piping Systems, FESHM 5034 Pressure Testing
ASME BPVC-V	ASME Boiler and Pressure Vessel Code, Section V: Nondestructive Examination	2021	FESHM 5031.5
ASME BPVC VIII	Boiler Pressure Vessel Code & Boiler Pressure Vessel Code	2021	FESHM 5031, FESHM 5031.5, FESHM 5033 Vacuum Vessel Safety, FESHM 5034 Pressure Testing
ASME BPVC-IX	Welding, Brazing, and Fusing Qualifications	2021	

Table A.1: A.1 - First part - Engineering codes and standards used in the beamline design.

DRAFT

Code/Std	Title	Pub. Date	Assoc'd FESHM Chapter (if applicable)
ASME BTH-1	Design of Below The Hook Lifting Devices	2021	FESHM 10110
ASME PCC-1	Guidelines for Pressure Boundary Bolted Flange Joint Assembly	2019	
ASME Y14.5-2009	Dimensioning and Tolerancing	2009	
ASTM A36	Standard Specification for Carbon Structural Steel	2019	
ASTM A193	Standard Specification for Alloy-Steel and Stainless Steel Bolting for High Temperature or High Pressure Service and Other Special Purpose Applications	2020	
ASTM B209	Standard Specification for Aluminum and Aluminum-Alloy Sheet and Plate	2021	
ASTM B241	Standard Specification for Aluminum and Aluminum-Alloy Seamless Pipe and Seamless Extruded Tube	2016	
ASTM B247	Standard Specification for Aluminum and Aluminum-Alloy Die Forgings, Hand Forgings, and Rolled Ring Forgings	2020	
ASTM B361	Standard Specification for Factory-Made Wrought Aluminum and Aluminum-Alloy Welding Fittings	2016	
ASTM B594	Standard Practice for Ultrasonic Inspection of Aluminum-Alloy Wrought Products	2019	
AWS A5.10 / A5.10M:2017	Welding Consumables - Wire Electrodes, Wires and Rods for Welding of Aluminum and Aluminum Alloys - Classification	2017	
AWS B2.1-8-212	Standard Welding Procedure Specification (SWPS) for Gas Tungsten Arc Welding of Austenitic Stainless Steel (M-8/P-8/S-8, Group 1), 1/16 through 1-1/2 inch Thick, ER3XX, As-Welded Condition, Primarily Pipe Applications	2012	
AWS D1.1/D1.1M	Structural Welding Code – Steel	2020	FESHM 5100

Table A.2: A.1 - Second part - Engineering codes and standards used in the beamline design.

DRAFT

Code/Std	Title	Pub. Date	Assoc'd FESHM Chapter (if applicable)
AWS D1.2/D1.2M	Structural Welding Code – Aluminum	2014	FESHM 5100
AWS D1.6/D1.6M	Structural Welding Code – Stainless Steel	2014	FESHM 5100
IBC	International Building Code	2021	FESHM 5100
NFPA 70	The National Electrical Code (NEC)	$\star$	FESHM 9100 Fermilab Electrical Safety Program
NFPA 70	Standard for Electrical Safety in the Workplace	$\star$	FESHM 9100
SAE AMS 2772G	Heat treatment of Aluminum Alloy Raw Materials	2016	
UL 583	Electrical-Battery-Powered Industrial Trucks	2012	
	Other Fermilab specific codes and pratices		
ACGIH	American Conference of Governmental Industrial Hygienists – Minimal Oxygen Content	2005	FESHM 4240 Oxygen Deficiency Hazards
Fermilab ED0011268	Structural Support Design Guide	2021	
Fermilab ESH-doc-372	Vacuum Window Safety	2022	FESHM 5033.1 Vacuum Window Safety
Fermilab Directorate-doc-34	Fermilab Engineering Manual	2019	
Fermilab ISD	Infrastructure Design Guide		

Table A.3: A.1 - Third part - Engineering codes and standards used in the beamline design. $\star$ = latest addition appproved by Electrical AHJ.

Code/Std	Title	Pub. Date	Assoc'd FESHM Chapter (if applicable)
ACI 355.2	Post-Installed Mechanical Anchors in Concrete	2022	FESHM 7080 Concrete Anchor Devices
ASME B30.9	Slings	2021	FESHM 10200 Lift Plans
ASME B30.26	Rigging Hardware	2020	FESHM 10200
DOE STD-1090	Hoisting and Rigging	2020	FESHM 10200
OSHA 29 CFR 1910	Occupational Safety and Health Standards	Date varies	
	Other Fermilab specific codes and pratices		
Fermilab ESH doc-6970	Equipment Transport		FESHM 10210 Equipment Transport

Table A.4: A.2 - Engineering codes and standards used in the beamline installation and construction.

Glossary

AC Alternating Current; when used in the phrase "AC coupling" refers to a circuit element that filters out low-frequency components, such as constant offsets, leaving higher frequency signal components. The frequency filtering is determined both by a resistor and a capacitor. 22

analog-to-digital converter (ADC) A sampling of a voltage resulting in a discrete integer count corresponding in some way to the input. 55, 105, 205

ArgonCube The name of the core part of the Deep Underground Neutrino Experiment (DUNE) near detector (ND), a liquid argon time-projection chamber (LArTPC). 366

ARgon Test InfrastruCture (ARTIC) Cryogenic facility installed in the DIFILab (Physics Department, University of Genoa, Italy) to test detectors in liquid argon. 126

application-specific integrated circuit (ASIC) ASIC is an integrated circuit designed for a particular use. 77, 114, 117, 126, 318

American Society of Mechanical Engineers (ASME) Professional organization that develops internationally recognized codes and standards in the field of mechanical engineering. 335, 336

Beyond the Standard Model (BSM) Area of physics research with the aim of extending the Standard Model of particle physics to phenomena it presently does not explain. 4, 12

charged current (CC) Refers to an interaction between elementary particles where a charged weak force carrier (W^+ or W^-) is exchanged. 2, 4, 138, 140, 142, 166

DAQ control, configuration and monitoring subsystem (CCM) A system for controlling, configuring and monitoring other systems in particular those that make up the data acquisition (DAQ) where the CCM encompasses RC. 320, 321

charged current quasielastic (CCQE) An interaction where a neutrino scatters from a nucleon, producing a charged lepton and converting a neutron to a proton, or vice versa. 143, 145, 314, 316

European Organization for Nuclear Research (CERN) The leading particle physics laboratory

in Europe and home to the ProtoDUNEs. (In French, the Organisation Européenne pour la Recherche Nucléaire, derived from Conseil Européen pour la Recherche Nucléaire). 77, 363, 364

conventional facilities (CF) Pertaining to construction and operation of buildings and conventional infrastructure, and for LBNF and DUNE project (LBNF/DUNE), CF includes the excavation caverns. 364

charge parity (CP) Product of charge and parity transformations. 5

coefficient of thermal expansion (CTE) It measures the fractional variation of a material's size per unit change in temperature. 132

data acquisition (DAQ) The data acquisition system accepts data from the detector front-end (FE) electronics, buffers the data, performs a trigger decision, builds events from the selected data and delivers the result to the offline secondary DAQ buffer. 89, 137, 174, 201, 318, 319, 361–363, 367, 368

DAQ trigger subsystem (DAQ TS) The subsystem of the DAQ responsible for forming a trigger decision. 320

DAQ timing and synchronization subsystem (DAQ TSS) The portion of the DAQ that provides for timing and synchronization to various components. 323

Detector Control System (DCS) The system is devoted to remotely controlling and monitoring the complex sub-detectors, ensuring safe, reliable operation and high-quality data acquisition. 318, 326–328

Dune Integrated Electronics for NEutrino Beams (DENEB) Name of the dedicated ASIC for GRanular Argon for Interactions of Neutrinos (GRAIN). 129

DOE U.S. Department of Energy. 21

data quality monitoring (DQM) Analysis of the raw data to monitor the integrity of the data and the performance of the detectors and their electronics. This type of monitoring may be performed in real time, within the DAQ system, or in later stages of processing, using disk files as input. 320, 321

dynamic random access memory (DRAM) A computer memory technology. 132

Detector Safety System (DSS) Independent system interacting directly with the Cryogenics and SAND detector sub-components in order to assure the safety of equipment, people, and various power supplies. 318, 326, 328–330

DUNE Timing and Synchronization Subsystem (DTS) Communication system implemented to ensure that all detector components operate on the same clock and share a common time

reference. 320, 322–324

Deep Underground Neutrino Experiment (DUNE) A leading-edge, international experiment for neutrino science and proton decay studies. 2, 320, 361–365, 367, 368

DUNE Precision Reaction-Independent Spectrum Measurement (DUNE-PRISM) a mobile near detector that can perform measurements over a range of angles off-axis from the neutrino beam direction in order to sample many different neutrino energy distributions. 2

electromagnetic calorimeter (ECAL) A detector component that measures energy deposition of traversing particles (in the near detector conceptual design). 5, 20, 24, 27, 51, 92, 142, 336, 338, 365, 366

Energy Deposition Simulation (EDEP-SIM) It is a wrapper around the GEANT4 particle propagation simulation and is intended as a tool to simulate all particle propagation and geometry-related issues. 10, 65, 145

engineering document management system (EDMS) A computerized document management system developed and supported at European Organization for Nuclear Research (CERN) in which some DUNE documents, drawings, and engineering models are managed. 338

equivalent noise charge (ENC) The equivalent noise charge is the input charge that corresponds to a signal-to-noise ratio of 1. 207

far detector module The entire DUNE far detector is segmented into four modules, each with a nominal 10 kt fiducial mass. 369

far detector (FD) The 70 kt total (40 kt fiducial) mass LArTPC DUNE detector, composed of four 17.5 kt total (10 kt fiducial) mass modules, to be installed at the far site at Sanford Underground Research Facility (SURF) in Lead, SD, USA. 110, 318, 321, 323, 365, 368

front-end (FE) The front-end refers a point that is "upstream" of the data flow for a particular subsystem. For example the single-phase (SP) front-end electronics is where the cold electronics meet the sense wires of the TPC and the front-end DAQ is where the DAQ meets the output of the electronics. 114, 117, 318, 320, 321, 362

finite element analysis (FEA) Simulation of a physical phenomenon using the numerical technique called the Finite Element Method (FEM), a numerical method for solving problems in engineering and mathematical physics. 111, 112, 189, 193, 195

front-end board (FEB) Board devoted to managing the detector signal. 318

front-end electronics (FEE) Electronics devoted to acquiring and processing input data. 65, 71, 77, 89, 105

Fermi National Accelerator Laboratory (Fermilab) U.S. national laboratory in Batavia, IL. It

is the laboratory that hosts DUNE and serves as its near site. 25, 27, 92, 338, 364–366, 368

Fermilab Environment, Safety and Health Manual (FESHM) The document that contains Fermilab's policies and procedures designed to manage environment, safety, and health in all its programs. 333–335, 337, 355

forward horn current (ν_μ mode) (FHC) The horn polarity makes it possible to focus positive hadrons, thus producing a ν_μ beam. 65, 170, 307, 309, 310

far site conventional facilities (FSCF) The conventional facilities (CF) at the DUNE far detector site, SURF. 368

fiducial volume (FV) The detector volume within the time projection chamber (TPC) that is selected for physics analysis through cuts on reconstructed event position. 4, 65, 122, 301, 313

gaseous argon (GAr) argon in its gas phase. 113

GRAIN Camera Board (GCB) Printed circuit board (PCB) that hosts the readout and control electronics directly connected to the detector. 128

GRAIN Cold Interface Board (GCIB) Electronic circuit board that connects hardware and software components working at low temperatures. 128, 136

GEometry ANd Tracking (Geant4) A software toolkit developed by CERN for the simulation of the passage of particles through matter using Monte Carlo (MC) methods. 168, 170, 173, 203

GRanular Argon for Interactions of Neutrinos (GRAIN) Subdetector of System for on-Axis Neutrino Detection (SAND). 5, 12, 20, 110, 116, 128, 136, 143, 167, 284, 318, 362, 364

GRAIN Warm Interface Board (GWIB) Electronic circuit board that connects hardware and software components working at ambient temperatures. 128

Heavy Neutral Leptons (HNL) Hypothetical particles that could explain neutrino masses, matter-antimatter asymmetry, and dark matter. 8, 15

high-pressure gaseous argon TPC (HPgTPC) A TPC filled with gaseous argon; a possible component of the DUNE ND. 366

high voltage (HV) Generally describes a voltage applied to drive the motion of free electrons through some media, e.g., LAr. 71, 91

ICARUS A neutrino experiment that was located at the Laboratori Nazionali del Gran Sasso (LNGS) in Italy, then refurbished at CERN for re-use in the same neutrino beam from Fermi

National Accelerator Laboratory (Fermilab) used by the MiniBooNE , MicroBooNE and SBND experiments. The ICARUS detector is being reassembled at Fermilab. 333

Istituto Nazionale di Fisica Nucleare (INFN) Italian institution devoted to nuclear research. 21, 30, 43, 245, 336, 338, 365

Kalman Filter (KF) Algorithm that uses a series of measurements, including statistical noise. 143, 298, 300, 301, 304–307, 312, 313

K-LOng Experiment (KLOE) KLOE is an e^+e^- collider detector spectrometer operated at DAΦNE, the ϕ-meson factory in Frascati, Rome. In DUNE, it will consist of a 26 cm Pb+scintillating fiber electromagnetic calorimeter (ECAL) surrounding a cylindrical open detector region that is 4.00 m in diameter and 4.30 m long. The ECAL and detector regions are embedded in a 0.6 T magnetic field created by a 4.86 m diameter superconducting coil and a 475 t iron yoke. 2, 5, 21, 28, 43, 44, 51, 92, 284, 295

liquid argon (LAr) Argon in its liquid phase; it is a cryogenic liquid with a boiling point of 87 K and density of 1.4 g/ml. 5, 22, 111, 117, 127, 141, 159, 172, 368

liquid argon time-projection chamber (LArTPC) A TPC filled with liquid argon; the basis for the DUNE far detector (FD) modules. 361, 363, 366

Long-Baseline Neutrino Facility (LBNF) The organizational entity responsible for developing the neutrino beam, the cryostats and cryogenics systems, and the conventional facilities for DUNE. 9, 10, 21, 350, 365, 368

LBNF and DUNE project (LBNF/DUNE) The overall global project, including Long-Baseline Neutrino Facility (LBNF) and DUNE. 362

Laboratori Nazionali di Frascati (LNF) Istituto Nazionale di Fisica Nucleare (INFN) laboratory in Italy. 12, 21, 42, 92, 99

Laboratori Nazionali di Legnaro (LNL) INFN laboratory in Italy. 338

low voltage (LV) It refers to electrical systems that typically operate between 50 and 1000 V in alternating current or 75 to 1500 V in direct current. 201

Module Assembly (MA) Integration and mechanical assembly of the detector components. 255, 268, 269, 275, 279, 281, 284, 287

Monte Carlo (MC) Refers to a method of numerical integration that entails the statistical sampling of the integrand function. Forms the basis for some types of detector and physics simulations. 61, 65, 76, 141, 143–145, 158, 294, 364

Multiple Coulomb Scattering (MCS) Scattering of charged particles traversing matter. It is

due to the interaction of the charged particles with the Coulomb potentials of nuclei and electrons. 10

multi-channel transfer line (MCTL) The cryogenic multi-channel transfer line is a "pipe structure" cryostat, which transfers the cryogenic liquid. It makes possible to transfer the cryogenic liquid for a long distance at very low heat loss. 346, 347

MicroBooNE A LArTPC neutrino oscillation experiment at Fermilab. 365

MINERvA Neutrino cross sections experiment at Fermilab. 8

MiniBooNE The Mini Booster Neutrino Experiment, at Fermilab, was designed to fully explore the LSND result. 365

minimum ionizing particle (MIP) Refers to a particle traversing some medium such that the particle's mean energy loss is near the minimum. 55, 157, 207

Multilayer Perceptron (MLP) Neural network having at least one hidden layer and whose neurons use a nonlinear activation function. 314

memorandum of understanding (MoU) A document summarizing an agreement between two or more parties. 21

multi-purpose detector (MPD) A component of the near detector conceptual design; it is a magnetized system consisting of a high-pressure gaseous argon TPC (HPgTPC) and a surrounding ECAL. 368

near detector (ND) Refers to the detector(s) installed close to the neutrino source at Fermilab. 2, 25, 110, 318, 323, 339, 344, 361, 364

Near Detector Liquid Argon system (ND-LAr) LArTPC component of the near detector based on ArgonCube technology. 2, 25, 339, 341, 343

NOvA The NOvA off-axis neutrino oscillation experiment at Fermilab. 284, 315, 366

open platform communications (OPC) Open platform communications is a series of standards and specifications for industrial telecommunication. 327

OPC-UA OPC Unified Architecture is a machine to machine communication protocol for industrial automation developed by the OPC Foundation. OPC stands for Object Linking and Embedding for Process Control. 327

operational readiness clearance (ORC) Final safety approval prior to the start of operation. 333, 337

DRAFT

PCB printed circuit board. 118

photon detection efficiency (PDE) Efficiency in photon collection. 116

photoelectron (PE) An electron ejected from the surface of a material by the photoelectric effect. 66, 133, 315

process flow diagram (PFD) Graphical representation of a process, showing the sequence and relationships between major components. 346, 349

particle ID (PID) Particle identification. 166

photomultiplier tube (PMT) A device that makes use of the photoelectric effect to produce an electrical signal from the arrival of optical photons. 10, 51, 54, 91

protons on target (POT) Typically used as a unit of normalization for the number of protons striking the neutrino production target. 65, 295

Precision Reaction-Independent Spectrum Measurement (PRISM) a mobile near detector that can perform measurements over a range of angles off-axis from the neutrino beam direction in order to sample many different neutrino energy distributions. 25

quality assurance (QA) The process of ensuring that the quality of each element meets requirements during design and development, and to detect and correct poor results prior to production. 24, 27, 106, 107

quality control (QC) The process (e.g., inspection, testing, measurements) of ensuring that each manufactured element meets its quality requirements prior to assembly or installation. 24, 27, 106, 107

RC Depending on context, one of (1) resistive-capacitive (circuit), (2) run control, the system for configuring, starting and terminating the DAQ, or (3) resource coordinator, a member of the DUNE management team responsible for coordinating the financial resources of the project. 361

root mean square (RMS) The square root of the arithmetic mean of the squares of a set of values, used as a measure of the typical magnitude of a set of numbers, regardless of their sign. 130, 132, 323

System for on-Axis Neutrino Detection (SAND) The beam monitor component of the near detector that remains on-axis at all times and serves as a dedicated neutrino spectrum monitor. 2, 20, 65, 321, 323, 324, 364

SAND Detector Simulation and Event Reconstruction Tool (sandreco) This project aims to develop tools to reconstruct neutrino interactions in the SAND detector. 65

DRAFT

SBND The Short-Baseline Near Detector experiment at Fermilab. 333, 365

secondary DAQ buffer A secondary DAQ buffer holds a small subset of the full rate as selected by a trigger command. This buffer also marks the interface with the DUNE Offline. 362

silicon photomultiplier (SiPM) A solid-state avalanche photodiode sensitive to single photoelectron signals. 5, 54, 111, 318

single-phase (SP) Distinguishes one of the DUNE far detector technologies by the fact that it operates using argon in its liquid phase only. 363

Straw Tube Tracker (STT) Tracker in SAND. 5, 9, 165

Sanford Underground Research Facility (SURF) The laboratory in South Dakota where the LBNF far site conventional facilities (FSCF) will be constructed and the DUNE FD will be installed and operated. 363, 364

Time to Analog Converter (TAC) An electronic device that converts the time interval between two input signals into a proportional analog voltage or current. 132

Trigger and DAQ system (TDAQ) System used to manage selection (trigger) and data collection (data acquisition) from detectors. 319, 320

Time-to-Digital Converter (TDC) Device that measures and converts a time interval into a digital code. 55, 105, 132

Transverse Kinematic Imbalance (TKI) The Transverse Kinematic Imbalance is a technique based on the measurement of kinematic imbalances between the outgoing muon and proton in CCQE-like neutrino interactions. It is used to study nuclear effects in neutrino interactions. 6

Temporary Muon Spectrometer (TMS) A muon spectrometer for the Near Detector that will be installed for the initial running period of DUNE, before the multi-purpose detector (MPD) detector component is ready. 2, 25, 339, 341

time of flight (ToF) The time a particle takes to fly between two visible interactions observed in the detector. If combined with the distance traveled by the particle, for example, a neutron, it can be used for energy reconstruction. 56, 61, 154, 229, 319, 323

Time over Threshold (ToT) Time width of a signal pulse over a defined threshold. 77, 133

time projection chamber (TPC) A type of particle detector that uses an E field together with a sensitive volume of gas or liquid, e.g., liquid argon (LAr), to perform a 3D reconstruction of a particle trajectory or interaction. The activity is recorded by digitizing the waveforms of current induced on the anode as the distribution of ionization charge passes by or is collected on the electrode (TPC is also used for "total project cost"). 110, 364, 365

DRAFT

Transition Radiation (TR) Light emission when a charged particle moves across different materials. xiii, xv, 167, 169–172, 175, 195, 307–311

trigger candidate Summary information derived from the full data stream and representing a contribution toward forming a trigger decision. 369

trigger command Information derived from one or more trigger candidates that directs elements of the far detector module to read out a portion of the data stream. 368, 369

trigger decision The process by which trigger candidates are converted into trigger commands. 362, 369

Transition Radiation Tracker (TRT) The TRT is a tracking system based on individual drift tubes (or straws) interleaved with fibers or foils. 177, 195

vacuum ultra-violet (VUV) Ultra-violet light in the range 120-240 nm. 116, 117

working group (WG) A group of persons working together to achieve specified goals. 20, 332, 354

DRAFT

References

[1] DOE Office of High Energy Physics, "Mission Need Statement for a Long-Baseline Neutrino Experiment (LBNE)," tech. rep., DOE, 2009. LBNE-doc-6259.

[2] A. A. Abud *et al.*, "Deep Underground Neutrino Experiment (DUNE) Near Detector Conceptual Design Report," *Instruments* **5** (2021) . https://www.mdpi.com/2410-390X/5/4/31.

[3] M. Adinolfi *et al.*, "The KLOE electromagnetic calorimeter," *Nuclear Instruments and Methods in Physics Research Section A: Accelerators, Spectrometers, Detectors and Associated Equipment* **482** (2002) 364. https://www.sciencedirect.com/science/article/pii/S0168900201015029.

[4] https://docs.dunescience.org/cgi-bin/sso/ShowDocument?docid=36184.

[5] X.-G. Lu, L. Pickering, S. Dolan, G. Barr, D. Coplowe, Y. Uchida, D. Wark, M. Wascko, A. Weber, and T. Yuan, "Measurement of nuclear effects in neutrino interactions with minimal dependence on neutrino energy," *Phys. Rev. C* **94** no. 1, (2016) 015503, arXiv:1512.05748 [nucl-th].

[6] A. P. Furmanski and J. T. Sobczyk, "Neutrino energy reconstruction from one muon and one proton events," *Phys. Rev. C* **95** no. 6, (2017) 065501, arXiv:1609.03530 [hep-ex].

[7] **T2K** Collaboration, K. Abe *et al.*, "Characterization of nuclear effects in muon-neutrino scattering on hydrocarbon with a measurement of final-state kinematics and correlations in charged-current pionless interactions at T2K," *Phys. Rev.* **D98** no. 3, (2018) 032003, arXiv:1802.05078 [hep-ex].

[8] S. Dolan, U. Mosel, K. Gallmeister, L. Pickering, and S. Bolognesi, "Sensitivity of Neutrino-Nucleus Interaction Measurements to 2p2h Excitations," *Phys. Rev. C* **98** no. 4, (2018) 045502, arXiv:1804.09488 [hep-ex].

[9] X.-G. Lu, D. Coplowe, R. Shah, G. Barr, D. Wark, and A. Weber, "Reconstruction of Energy Spectra of Neutrino Beams Independent of Nuclear Effects," *Phys. Rev. D* **92** no. 5, (2015) 051302, arXiv:1507.00967 [hep-ex].

DRAFT

[10] **MINERvA** Collaboration, X. Lu *et al.*, "Measurement of final-state correlations in neutrino muon-proton mesonless production on hydrocarbon at $\langle E_\nu \rangle = 3$ GeV," *Phys. Rev. Lett.* **121** no. 2, (2018) 022504, arXiv:1805.05486 [hep-ex].

[11] S. Dolan, "Exploring Nuclear Effects in Neutrino-Nucleus Interactions Using Measurements of Transverse Kinematic Imbalance from T2K and MINERvA," arXiv:1810.06043 [hep-ex].

[12] X.-G. Lu and J. T. Sobczyk, "Identification of nuclear effects in neutrino and antineutrino interactions on nuclei using generalized final-state correlations," *Phys. Rev. C* **99** no. 5, (2019) 055504, arXiv:1901.06411 [hep-ph].

[13] L. Harewood and R. Gran, "Elastic hadron-nucleus scattering in neutrino-nucleus reactions and transverse kinematics measurements," arXiv:1906.10576 [hep-ex].

[14] T. Cai, X.-G. Lu, and D. Ruterbories, "Pion-proton correlation in neutrino interactions on nuclei," *Phys. Rev. D* **100** (2019) 073010, arXiv:1907.11212 [hep-ex].

[15] **MINERvA** Collaboration, T. Cai *et al.*, "Nucleon binding energy and transverse momentum imbalance in neutrino-nucleus reactions," *Phys. Rev. D* **101** no. 9, (2020) 092001, arXiv:1910.08658 [hep-ex].

[16] **MINERvA** Collaboration, D. Coplowe *et al.*, "Probing Nuclear Effects with Neutrino-induced Charged-Current Neutral Pion Production," arXiv:2002.05812 [hep-ex].

[17] H. Duyang, B. Guo, S. R. Mishra, and R. Petti, "A novel approach to neutrino–hydrogen measurements," *Eur. Phys. J. Plus* **139** no. 11, (2024) 1014, arXiv:1809.08752 [hep-ph].

[18] H. Duyang, B. Guo, S. Mishra, and R. Petti, "A Precise Determination of (Anti)neutrino Fluxes with (Anti)neutrino-Hydrogen Interactions," *Phys. Lett. B* **795** (2019) 424–431, arXiv:1902.09480 [hep-ph].

[19] C. Andreopoulos *et al.*, "The GENIE Neutrino Monte Carlo Generator," *Nucl. Instrum. Methods* **A** no. 614, (2010) 87–104.

[20] **GEANT4** Collaboration, S. Agostinelli *et al.*, "GEANT4 — A Simulation Toolkit," *Nucl. Instrum. Methods* **A** no. 506, (2003) 250–303.

[21] **KLOE** Collaboration, A. Ceccarelli, S. Dell'Agnello, A. Di Virgilio, and S. Moccia, "Survey and alignment of the KLOE experiment at DAPHNE," *eConf* **C971013** (1997) 025.

[22] K. Smith, A. Broadbent, M. Greenslade, S. Harrison, D. Jenkins, J. Ross, A. Street, M. Townsend, J. Wiatrzyk, and J. Franzini, "Progress in the design and manufacture of the KLOE solenoid for the DAPHNE ring at Frascati," *IEEE Trans. Appl. Supercond.* **7** no. 2, (1997) 630–632.

DRAFT

[23] C. Ligi, et al., "DAΦNE CRYOGENIC COOLING SYSTEM: STATUS AND PERSPECTIVES," 2002. https://accelconf.web.cern.ch/e02/PAPERS/MOPLE026.pdf. Proceedings of EPAC, Paris.

[24] M. Modena, "The DAΦNE Cryogenic System," 1997. https://inis.iaea.org/collection/NCLCollectionStore/_Public/29/056/29056136.pdf. LNF-97/046.

[25] W. T. Welford and R. Winston, *The Optics of Nonimaging Concentrators*. Academic Press, New York, first ed., 1978.

[26] https://www.digchip.com/datasheets/parts/datasheet/190/R5946.php.

[27] F. Alemanno, P. Bernardini, A. Corvaglia, G. D. Matteis, L. Martina, A. Miccoli, M. Panareo, M. Panetta, C. Pinto, and A. Surdo, "Study of silicon photomultipliers for the readout of a lead/scintillating-fiber calorimeter," *Journal of Instrumentation* **19** no. 06, (Jun, 2024) T06005. https://dx.doi.org/10.1088/1748-0221/19/06/T06005.

[28] A. Gallo *et al.*, "DAFNE status report," *Conf. Proc. C* **060626** (2006) 604–606. https://inspirehep.net/literature/724788.

[29] R. Wigmans, *Calorimetry: Energy measurement in particle physics*, vol. 107. 2000.

[30] R. Wigmans, "Calorimetry," *AIP Conf. Proc.* **674** no. 1, (2003) 144–168.

[31] M. Anelli *et al.*, "Measurement and simulation of the neutron response and detection efficiency of a Pb-scintillating fiber calorimeter," *Nucl. Instrum. Meth. A* **581** (2007) 368–372.

[32] G. A. et al., "A Proposal to Enhance the DUNE Near Detector Complex," DUNE doc 13262, 2019. https://docs.dunescience.org/cgi-bin/ShowDocument?docid=13262.

[33] C. Bini et al., "Evaluation of the performance of the KLOE calorimeter barrel mo dules at the Cosmic Ray Stand," 1996. http://www.lnf.infn.it/kloe/kdocs/getfile.php?doc_fname=kn154.ps. KLOE Note N.154 February 1996.

[34] M. Adinolfi *et al.*, "The KLOE electromagnetic calorimeter," *Nucl. Instrum. Meth.* **A482** (2002) 364–386.

[35] "S13361-2050 datasheet." https://www.hamamatsu.com/content/dam/hamamatsu-photonics/note=sites/documents/99_SALES_LIBRARY/ssd/s13361-2050_series_kapd1055e.pdf.

[36] "S13615-1050n-16 datasheet." https://www.hamamatsu.com/content/dam/hamamatsu-photonics/sites/documents/99_SALES_LIBRARY/ssd/s13615_series_kapd1062e.pdf.

DRAFT

[37] E. Segreto, "Properties of liquid argon scintillation light emission," *Phys. Rev. D* **103** (Feb, 2021) 043001. https://link.aps.org/doi/10.1103/PhysRevD.103.043001.

[38] D. Akimov, V. Belov, A. Konovalov, A. Kumpan, O. Razuvaeva, D. Rudik, and G. Simakov, "Fast component re-emission in xe-doped liquid argon," *Journal of Instrumentation* **14** no. 09, (Sep, 2019) P09022.

[39] S. Kubota, M. Hishida, S. Himi, J. Suzuki, and J. Ruan, "The suppression of the slow component in xenon-doped liquid argon scintillation," *Nuclear Instruments and Methods in Physics Research Section A: Accelerators, Spectrometers, Detectors and Associated Equipment* **327** no. 1, (1993) 71–74.

[40] E. Grace, A. Butcher, J. Monroe, and J. A. Nikkel, "Index of refraction, rayleigh scattering length, and sellmeier coefficients in solid and liquid argon and xenon," *Nuclear Instruments and Methods in Physics Research Section A: Accelerators, Spectrometers, Detectors and Associated Equipment* **867** (2017) 204–208.

[41] M. Babicz, S. Bordoni, A. Fava, U. Kose, M. Nessi, F. Pietropaolo, G. Raselli, F. Resnati, M. Rossella, P. Sala, F. Stocker, and A. Zani, "A measurement of the group velocity of scintillation light in liquid argon," *Journal of Instrumentation* **15** no. 09, (Sep, 2020) P09009.

[42] M. Andreotti *et al.*, "Coded masks for imaging of neutrino events," *The European Physical Journal C* **81** (2021) 1011. http://dx.doi.org/10.1140/epjc/s10052-021-09798-y.

[43] M. Tenti *et al.*, "Simulation, Reconstruction, and Analysis Framework and Physics Reach of SAND," DUNE doc 36184, 2026. https://docs.dunescience.org/cgi-bin/ShowDocument?docid=36184.

[44] F. Cossio *et al.*, "ALCOR: A mixed-signal ASIC for the dRICH detector of the ePIC experiment at the EIC," *Nucl. Instrum. Meth. A* **1069** (2024) 169817.

[45] M. Aoki, S. Hanamura, T. Masuhara, and K. Yano, "Performance and hot-carrier effects of small cryo-cmos devices," *IEEE Transactions on Electron Devices* **34** no. 1, (1987) 8–18.

[46] G. Wu, G. W. Deptuch, J. R. Hoff, and P. Gui, "Degradations of threshold voltage, mobility, and drain current and the dependence on transistor geometry for stressing at 77 k and 300 k," *IEEE Transactions on Device and Materials Reliability* **14** no. 1, (2014) 477–483.

[47] R. Gluckstern, "Uncertainties in track momentum and direction, due to multiple scattering and measurement errors," *Nucl. Instrum. Meth.* **24** (1963) 381–389.

[48] R. Petti, "Precision Measurements of Fundamental Interactions with (Anti)Neutrinos," in *Proceedings, 27th International Workshop on Deep Inelastic Scattering and Related Subjects (DIS 2019): Torino, Italy, April 8-12, 2019*. 2019. arXiv:1910.05995 [hep-ex].

[49] M. Anfreville, P. Astier, M. Authier, A. Baldisseri, M. Banner, *et al.*, "The Drift chambers of the NOMAD experiment," *Nucl.Instrum.Meth.* **A481** (2002) 339–364,

DRAFT

arXiv:hep-ex/0104012 [hep-ex].

[50] R. Petti, "Probing free nucleons with (anti)neutrinos," *Phys. Lett. B* **834** (2022) 137469, arXiv:2205.10396 [hep-ph].

[51] **NOMAD** Collaboration, J. Altegoer *et al.*, "The NOMAD experiment at the CERN SPS," *Nucl. Instrum. Meth. A* **404** (1998) 96–128.

[52] G. Bassompierre *et al.*, "Performance of the NOMAD transition radiation detector," *Nucl. Instrum. Meth. A* **411** (1998) 63–74.

[53] R. Petti, "An Oxygen Target for (Anti)neutrinos," *Phys. Part. Nucl.* **57** no. 1, (2026) 144–150, arXiv:2301.04744 [hep-ex].

[54] **PANDA** Collaboration, W. Erni *et al.*, "Technical design report for the PANDA (AntiProton Annihilations at Darmstadt) Straw Tube Tracker," *Eur. Phys. J. A* **49** (2013) 25, arXiv:1205.5441 [physics.ins-det].

[55] **ATLAS TRT** Collaboration, E. Abat *et al.*, "The ATLAS TRT barrel detector," *JINST* **3** (2008) P02014.

[56] E. Abat *et al.*, "The ATLAS TRT end-cap detectors," *JINST* **3** (2008) P10003.

[57] G. Bassompierre *et al.*, "A Large area transition radiation detector for the NOMAD experiment," *Nucl. Instrum. Meth. A* **403** (1998) 363–382.

[58] **COSY-TOF** Collaboration, P. Wintz, "A large tracking detector in vacuum consisting of self-supporting straw tubes," *AIP Conf. Proc.* **698** no. 1, (2004) 789–792.

[59] V. D. Peshekhonov, "Coordinate detectors based on thin-wall drift tubes," *Phys. Part. Nucl.* **46** no. 1, (2015) 94–122.

[60] T. Akesson *et al.*, "Study of straw proportional tubes for a transition radiation detector/tracker at LHC," *Nucl. Instrum. Meth. A* **361** (1995) 440–456.

[61] S. Graessle *et al.*, "A straw tracking system to study rare K(L) decays," *Nucl. Instrum. Meth. A* **367** (1995) 138–142.

[62] H. Ogren *et al.*, "The straw tracker for the SDC detector," *Nucl. Instrum. Meth. A* **367** (1995) 133–137.

[63] **ATLAS TRT** Collaboration, E. Abat *et al.*, "The ATLAS Transition Radiation Tracker (TRT) proportional drift tube: Design and performance," *JINST* **3** (2008) P02013.

[64] V. Bychkov *et al.*, "Construction and manufacture of large size straw-chambers of the COMPASS spectrometer tracking system," *Particles and Nuclei, Letters* **2** [**111**] (2002) 64–73.

DRAFT

[65] K. Platzer, W. Dunnweber, N. Dedek, M. Faessler, R. Geyer, C. Ilgner, V. Peshekhonov, and H. Wellenstein, "Mapping the large area straw detectors of the COMPASS experiment with X-rays," *IEEE Trans. Nucl. Sci.* **52** (2005) 793–798.

[66] A. Sergi, "NA62 Spectrometer: A Low Mass Straw Tracker," *Phys. Procedia* **37** (2012) 530–534.

[67] H. Nishiguchi *et al.*, "Development of an extremely thin-wall straw tracker operational in vacuum – The COMET straw tracker system," *Nucl. Instrum. Meth.* **A845** (2017) 269–272.

[68] **Mu2e** Collaboration, M. Lee, "The Straw-tube Tracker for the Mu2e Experiment," *Nucl. Part. Phys. Proc.* **273-275** (2016) 2530–2532.

[69] **SHiP** Collaboration, M. Anelli *et al.*, "A facility to Search for Hidden Particles (SHiP) at the CERN SPS," `arXiv:1504.04956 [physics.ins-det]`.

[70] G. De Geronimo, J. Fried, S. Li, J. Metcalfe, N. Nambiar, E. Vernon, and V. Polychronakos, "VMM1 - An ASIC for Micropattern Detectors," *IEEE Trans. Nucl. Sci.* **60** (2013) 2314–2321.

[71] **ATLAS Muon** Collaboration, G. Iakovidis, "VMM - An ASIC for micropattern detectors," *EPJ Web Conf.* **174** (2018) 07001.

[72] G. Iakovidis, "VMM3a, an ASIC for tracking detectors," *J. Phys. Conf. Ser.* **1498** (2020) 012051.

[73] V. Bautin, M. Demichev, T. Enik, E. Kuznetsova, V. Maleev, R. Petti, S. Nasybulin, K. Salamatin, D. Sosnov, and A. Zelenov, "VMM3 ASIC as a potential front end electronics solution for future Straw Trackers," *Nucl. Instrum. Meth. A* **1047** (2023) 167864.

[74] S. J. Schowalter, C. B. Connolly, and J. M. Doyle, "Permeability of Noble Gases through Kapton, Butyl, Nylon, and 'Silver Shield'," *Nucl. Instrum. Meth. A* **615** (2010) 267–271, `arXiv:0909.2610 [physics.ins-det]`.

[75] T. Ferguson, A. Krivshich, and V. Maleev, "Gas gain and space charge effects in aging tests of gaseous detectors," *Nucl. Instrum. Meth. A* **515** (2003) 283–287.

[76] A. Rivetti *et al.*, "TIGER: A front-end ASIC for timing and energy measurements with radiation detectors," *Nucl. Instrum. Meth. A* **924** (2019) 181–186.

[77] J. S. Bono, J. F. Caron, S. H. Oh, and C. Wang, "The stress relaxation (creep) rate of Mu2e straw tubes," *Nucl. Instrum. Meth. A* **902** (2018) 95–102.

[78] **NOMAD** Collaboration, Q. Wu *et al.*, "A Precise measurement of the muon neutrino-nucleon inclusive charged current cross-section off an isoscalar target in the energy range 2.5 < E(nu) < 40-GeV by NOMAD," *Phys.Lett.* **B660** (2008) 19–25, `arXiv:0711.1183 [hep-ex]`.

DRAFT

[79] R. E. Kalman, "A New Approach to Linear Filtering and Prediction Problems," *J. Basic Eng.* **82** (1960) 35–45.

[80] P. Nevski, "Advances in the simulation of Transition Radiation Detectors," *Nucl. Instrum. Meth. A* **522** (2004) 116–121.

[81] **ATLAS TRT** Collaboration, E. Abat *et al.*, "The ATLAS Transition Radiation Tracker (TRT) proportional drift tube: Design and performance," *JINST* **3** (2008) P02013.

[82] R. Petti, R. J. Hill, and O. Tomalak, "Nucleon axial-vector form factor and radius from future neutrino experiments," *Phys. Rev. D* **109** no. 5, (2024) L051301, arXiv:2309.02509 [hep-ph].

[83] N. Talukdar and R. Petti, "Anti-neutrino elastic scattering on hydrogen in the NOνA ND.," tech. rep., Univ. of South Carolina. NOνA DocDB 63569.

[84] **DUNE** Collaboration, E. L. Flumerfelt, "The DUNE-DAQ Application Framework," arXiv:2405.18583 [physics.ins-det].

[85] A. Abed Abud, C. Batchelor, K. Biery, J. Brooke, G. Crone, D. Cussans, P. Ding, A. Earle, E. Flumerfelt, J. Freeman, A. Habig, R. Halsall, P. Hamilton, N. Ilic, A. Kaboth, W. Ketchum, B. King, J. Klein, P. Lasorak, G. Lehmann Miotto, D. Newbold, D. Oliva, M. Roda, R. Sipos, A. Tapper, A. Thea, and S. Trilov, "Trigger and Data AcQuisition (TDAQ) System Design," CERN EDMS 2812882 v.2, 2023. https://edms.cern.ch/document/2812882/2.

[86] **DUNE** Collaboration, J. Strait *et al.*, "Long-Baseline Neutrino Facility (LBNF) and Deep Underground Neutrino Experiment (DUNE)," arXiv:1601.05823 [physics.ins-det].

[87] "DUNE Timing and Synchronization Interface," CERN EDMS 2209895. https://edms.cern.ch/document/2209895/3.

[88] A. Barcock, D. Cussans, D. Lindebaum, D. Newbold, S. Paramesvaran, and S. Trilov, "Timing and synchronization of the DUNE neutrino detector," *JINST* **18** no. 01, (2023) C01067, arXiv:2210.15517 [hep-ex].

[89] "Fermilab Environment, Safety, and Health Manual." https://eshq.fnal.gov/manuals/feshm/.

[90] "Electrical Design Standards for Experimental Apparatus at Fermilab." https://esh-docdb.fnal.gov/cgi-bin/RetrieveFile?docid=3270.

[91] D. Andrews *et al.*, "Proceedings of the 1997 particle accelerator conference," in *Proceedings of the 1997 Particle Accelerator Conference (Cat. No.97CH36167)*, vol. 3, p. 3413. 1997.

[92] M. Modena, "The DAΦNE Cryogenic System,". https://inis.iaea.org/records/ymw9n-szm49.

DRAFT

[93] "NS LHE Cryogenics: ICD SAND Magnet and LHe Cryogenic [CERN EDMS 2458544]," tech. rep. https://edms.cern.ch/document/2458544/4.

DRAFT